Graeme Hanson

Lawrence Berliner

Editors

Metals in Biology

Applications of High Resolution EPR to Metalloenzymes

Springer

Biological Magnetic Resonance

Volume 29

Graeme Hanson • Lawrence Berliner
Editors

Metals in Biology

Applications of High-Resolution EPR
to Metalloenzymes

Volume 29

x

Springer

Editors
Graeme Hanson
Centre for Magnetic Resonance
The University of Queensland
St. Lucia, QLD 4072
Australia
Graeme.Hanson@cmr.uq.edu.au

Lawrence Berliner
University of Denver
2190 E. Iliff Avenue, Room 202
Denver, CO 80208-0001
USA
berliner@du.edu

Printed on acid-free paper

CONTRIBUTORS

A.V. Astashkin (chap. 6)
Department of Chemistry
1306 E. University Boulevard
University of Arizona
Tucson, Arizona 85721-0041, USA
+1 520-621-9968
+1 520-626-8407 (fax)
andrei@u.arizona.edu

Helmut Beinert (chap. 3) (deceased)
Institute for Enzyme Research
Department of Biochemistry
University of Wisconsin
Madison, WI 53726, USA

Brian Bennett (chap. 10)
Department of Biophysics
Medical College of Wisconsin
8701 Watertown Plank Road
Milwaukee, WI 53226-0509, USA
414 456-4787
414 456-6512 (fax)
bbennett@mcw.edu

David Britt (chap. 8)
Department of Chemistry
University of California Davis
One Shields Avenue
Davis, CA 95695, USA
530 752-6377
530 752-8995 (fax)
rdbritt@ucdavis.edu

Marcin Brynda (chap. 8)
Department of Chemistry
University of California Davis
One Shields Avenue
Davis, CA 95616-8635, USA
530 792-1828
mabrynda@ucdavis.edu

Richard Cammack (chap. 2)
School of Biomedical and Health Sciences
Pharmaceutical Science Research Division
Kings College, London
London SE1 9NH, UK
+44 20-7848-4264
+44 20-7848-4500 (fax)
richard.cammack@kcl.ac.uk

N. Dennis Chasteen (chap. 11)
Department of Chemistry
University of New Hampshire
Parsons Hall, 23 College Road
Durham, NH 03824, USA
603 862-2520
603 862-4278 (fax)
ndc@cisunix.unh.edu

John H. Enemark (chap. 6)
Department of Chemistry
1306 E. University Boulevard
University of Arizona
Tucson, Arizona 85721-0041, USA
520 621-2245
520 626-8065 (fax)
jenemark@u.arizona.edu

Marc Fontecave (chap. 4)
Laboratoire de Chimie et Biologie des Métaux
Institut de Recherches en technologies et
  Sciences pour le Vivant
UMR CEA-CNRS-Université
Joseph Fourier n° 5249
CEA-Grenoble
17 rue des Martyrs
38 054 Grenoble CEDEX 9-France
+33 4-3878-9102
+33 4-3878-9124 (fax)
marc.Fontecave@cea.fr

Serge Gambarelli (chap. 4)
Service de Chimie Inorganique et Biologique
Institut Nanosciences et Cryogénie
UMR-E 3 CEA-UJF et FRE CNRS 3200
CEA-Grenoble, 17 rue des Martyrs
38054 Grenoble CEDEX 9-France
+33 4-3878-3940
+33 4-3878-5090 (fax)
serge.gambarelli@cea.fr

Kieran S. Hadler (chap. 9)
School of Chemistry & Molecular Biosciences
The University of Queensland
St. Lucia, Queensland 4072, Australia
+61 7-3365-4107
+61 7-3365-4299 (fax)
k.hadler@uq.edu.au

Graeme R. Hanson (chaps. 7,9)
Centre for Magnetic Resonance
The University of Queensland
St. Lucia, Queensland 4072,Australia
+61 7-3365-3242
+61 7-3365-3833 (fax)
Graeme.Hanson@cmr.uq.edu.au

Russ Hille (chap. 5)
Dept. of Molecular & Cellular Biochemistry
The Ohio State University
Columbus, OH 43210-1218, USA
Current address:
  Department of Biochemistry
  University of California Riverside
  1463 Boyce Hall
  Riverside CA 92521-0122, USA
  951 827-6354
  951 827-2364 (fax)
  russ.hille@ucr.edu

Ian Lane (chap. 7)
Institute of Molecular Biosciences
The University of Queensland
St. Lucia, Queensland, 4072, Australia
+61 7-3346-2370
+61 7-3346-2090 (fax)
i.lane@imb.uq.edu.au

Sarah C. Larsen (chap. 11)
Department of Chemistry
University of Iowa
Iowa City, Iowa 52242, USA
319 335-1346
319 335-1270 (fax)
Sarah-larsen@uiowa.edu

Fraser MacMillan (chap. 2)
School of Chemical Sciences and Pharmacy
University of East Anglia
Norwich NR4 7TJ, UK
+44 (0) 1603 592766
+44 (0) 1603 592003 (fax)
fraser.macmillan@uea.ac.uk

Nataša Mitić (chap. 9)
School of Chemistry & Molecular Biosciences
The University of Queensland
St. Lucia 4072, Australia
+61 7-3365-4040
+61 7-3365-4273 (fax)
n.mitic@uq.edu.au

Etienne Mulliez (chap. 4)
Laboratoire de Chimie et Biologie des Métaux
Institut de Recherches en technologies
    et Sciences pour le Vivant
UMR CEA-CNRS-Université
Joseph Fourier n° 5249
CEA-Grenoble
17 rue des Martyrs
38 054 Grenoble CEDEX 9-France
+33 4-3878-9107
+33 4-3878-9124 (fax)
emulliez@cea.fr

John R. Pilbrow (chap. 1)
School of Physics
Building 27, Monash University
Victoria 3800, Australia
+61 3-9905-3630
+61 3-9905-3637 (fax)
John.Pilbrow@sci.monash.edu.au

A.M. Raitsimring (chap. 6)
Department of Chemistry
1306 E. University Boulevard
University of Arizona
Tucson, Arizona 85721-0041, USA
+1 520-621-6335
+1 520-626-8407 (fax)
arnold@u.arizona.edu

Gerhard Schenk (chap. 9)
School of Chemistry & Molecular Biosciences
The University of Queensland
St. Lucia 4072, Australia
+61 7-3365-4144
+61 7-3365-4273 (fax)
schenk@uq.edu.au

Sarah J. Smith (chap. 9)
School of Chemistry & Biochemistry
The University of Queensland
St. Lucia 4072, Australia
+61 7-3365-4107
+61 7-3365-4299 (fax)
s.smith3@uq.edu.au

PREFACE

Metalloproteins comprise approximately 30% of all known proteins and are involved in a variety of biologically important processes, including oxygen transport, biosynthesis, electron transfer, biodegradation, drug metabolism, proteolysis and hydrolysis of amides and esters, environmental sulfur and nitrogen cycles, and disease mechanisms. EPR spectroscopy has an important role in not only the geometric structural characterization of the redox cofactors in metalloproteins but also their electronic structure, as this is crucial for their reactivity. The advent of X-ray crystallographic snapshots of the active site redox cofactors in metalloenzymes in conjunction with high-resolution EPR spectroscopy has provided detailed structural insights into their catalytic mechanisms.

This volume forms the second part of a two-volume series on the application of high-resolution EPR to the structural (geometric and electronic) characterization of redox active cofactors in metalloproteins. We have been fortunate to enlist internationally recognized experts in this joint venture to provide the scientific community with an overview of high-resolution EPR and its application to metals in biology. Volume 28, entitled *High-Resolution EPR: Applications to Metalloenzymes and Metals in Medicine*, covered high-resolution EPR methods, iron proteins, nickel and copper enzymes, and metals in medicine. In this volume, *Metals in Biology: Applications of High-Resolution EPR to Metalloenzymes,* we further extend the periodic table into the application of high-resolution EPR to other families of metalloproteins. Specifically, areas covered include: iron–sulfur cluster-containing proteins, molybdenum enzymes, manganese-containing enzymes and photosystem II, cobalt-substituted enzymes, and hyperfine and quadrupole interactions in vanadium proteins and model complexes. John Pilbrow in the Introduction, which follows, provides an eloquent synopsis of each chapter.

Helmut Beinert was a pioneer in the application of EPR spectroscopy to the structural characterization of novel iron–sulfur cluster-containing metalloproteins. Sadly, he passed away during the preparation of this volume, and we are fortunate to have had him contribute a chapter on the involvement of iron–sulfur cluster proteins in catalysis and gene regulation. His expertise and contributions to metal ions in biological systems will be dearly missed.

It is an honor for the editors to facilitate the dissemination of these excellent contributions to the scientific community, and we would like to dedicate this volume to Graeme's wife Lyn and family (Jeffrey, Harry, Johanna, and Adrian),

whose unending support allowed the production of this volume to be completed. Suggestions for future volumes are always appreciated.

Graeme R. Hanson
Brisbane, Australia

Lawrence J. Berliner
Denver, Colorado, USA

CONTENTS

Chapter 1

Introduction

John R. Pilbrow

IRON–SULFUR-CONTAINING PROTEINS

Chapter 2

**Electron Magnetic Resonance of Iron–Sulfur Proteins in
Electron-Transfer Chains: Resolving Complexity**

Richard Cammack and Fraser MacMillan

Chapter 3

Catalysis and Gene Regulation

Chapter 4

**Iron–Sulfur Clusters in "Radical SAM" Enzymes:
Spectroscopy and Coordination**

Serge Gambarelli[1], Etienne Mulliez,[2] and Marc Fontecave

Mononuclear Molybdenum Enzymes

MANGANESE-CONTAINING ENZYMES

Chapter 9

Manganese Metalloproteins

Sarah J. Smith, Kieran S. Hadler, Gerhard Schenk,
Graeme R. Hanson, and Nataša Mitić

NOVEL METALLOENZYMES AND METALLOPROTEINS

LIST OF COLOR FIGURES AND WEBSITE MATERIALS

Please visit http://www.springer.com/978-1-4419-1138-4 to view high-resolution full-color versions of all the color illustrations in this volume.

INTRODUCTION

John R. Pilbrow

School of Physics, Monash University,
Victoria, Australia

I warmly commend this volume, which covers the characterization of iron–sulfur proteins, molybdenum proteins, manganese-containing enzymes, cobalt-substituted enzymes, and vanadyl-substituted proteins using electron paramagnetic resonance techniques. It complements the survey of high-resolution EPR methods, iron proteins, nickel and copper enzymes, and metals in medicine that formed the basis of the previous volume, Volume 28. Readers will find it helpful to have access to both Volumes 28 and 29 in order to obtain a comprehensive overview of the contribution of EPR techniques to metal ions in biology.

While discussion of interpretive difficulties may appear to be incidental in several of the chapters, the importance of recognizing the limitations of particular EPR techniques remains important. These include spectral overlap, particularly for iron–sulfur proteins, and the challenge of the small g-anisotropy for Mo[V] and VO[IV] when seeking to use CW-EPR alone to determine metal ion coordination. Manganese EPR is always challenging, even for isolated Mn[II] ions, but even more so for the coupled systems described in Chapters 8 and 9. High-spin cobalt[II] in distorted "tetrahedral" sites involve spectra from one of the doublets formed from $S = {}^3/_2$. This involves the $S = ½$ spin Hamiltonian, where the resulting "effective" g-factors are field, and thus frequency, dependent. The role and importance of pulsed methods, Davies and Mims ENDOR, ESEEM, and HYSCORE, and the underlying theoretical basis for the interpretation of the resulting data sets are explained as appropriate in context.

An ongoing challenge is to work out key structural units in functioning proteins and enzymes. While information from X-ray crystallography and EXAFS is of immeasurable benefit, it is not often that single crystals of proteins can be obtained. Thus the spectroscopy most often has to be performed in the frozen state.

Address all correspondence to John R. Pilbrow, School of Physics, Building 27, Monash University Victoria 3800, Australia, +61 3-9905-3630, +61 3-9905-3637 (fax) <John.Pilbrow@sci.monash.edu.au>.

This necessitates what is called "orientation selection" spectroscopy, particularly relevant to the many pulsed techniques that are used and discussed in many of the following chapters.

Chapters 2, 3, and 4 relate to iron–sulfur proteins. Chapters 5, 6, and 7 to molybdenum enzymes, while Chapters 8 and 9 concern manganese-containing enzymes. The last two chapters relate specifically to substitution of paramagnetic spins as probes of non-magnetic active sites in proteins. Chapter 10 reports on Co(II)-substituted zinc enzymes, while the final chapter, Chapter 11, introduces the vanadyl oxycation as a probe of metal ion sites in proteins.

1. IRON–SULFUR CLUSTER-CONTAINING PROTEINS

Chapter 2 by Cammack and MacMillan focuses on iron–sulfur clusters, which are among the most abundant electron-transfer groups in biology, first detected and investigated using EPR spectroscopy. [2Fe–2S], [3Fe–4S], and [4Fe–4S] clusters, commonly found in large membrane-bound complexes essential for energy conversion in living cells as essential constituents of the mitochondrial respiratory chain, are readily amenable to EPR investigation via various paramagnetic redox states. They have a wide range of functions, including electron transfer, enzyme catalysis, regulation, and maintenance of protein structure. Examples include photosynthetic plant-type ferredoxins, cytochrome P-450 monooxygenases, the [2Fe–2S] ferredoxins from nitrogen-fixing bacteria, and the Rieske proteins of respiratory and photosynthetic electron-transfer chains. Protein characterization increasingly involves multifrequency EPR with ever higher magnetic fields and microwave frequencies. Multidimensional pulsed correlation EPR spectroscopy, application of a second microwave frequency (PELDOR), or radio frequency (pulsed ENDOR) are described in the context of distance measurements. Samples include macromolecular complexes and membranes, as well as whole cells and tissues. Orientationally disordered spectra observed in the frozen state require orientation-selective ENDOR and ESEEM, high-field spectroscopy, and ^{14}N ESEEM. A newer method, Relaxation Filtered Hyperfine Spectroscopy [REFINE], has been used to select spectra from individual centers having different relaxation rates, such as cluster N2 from NADH:ubiquinone oxidoreductase.

Chapter 3 by the late Helmut Beinert concerns the application of electron paramagnetic resonance (EPR) to analyzing regulatory proteins based on the observation of EPR signals from the various cluster types containing [2Fe–2S], [3Fe–4S], or [4Fe–4S], and eventually superclusters, such as those occurring in nitrogen-fixing systems. The signals are found for the one-electron reduced states with [2Fe–2S] and [4Fe–4S] clusters and for the oxidized form of the [3Fe–4S] cluster and high-potential Fe–S proteins. Beinert's concern was rather to explore the interface between proteins and molecular biology. A particular challenge arises because the active centers of enzymes that normally deal with energy transformation can also be multifunctional, e.g., directing messenger RNA (mRNA) use in the cytoplasm through the cytoplasmic iron-regulatory protein aconitase without the [4Fe–

4S] cluster. The remaining iron regulatory protein [IRP1] converts to c-aconitase in the presence of iron; however, the cluster in c-aconitase disassembles when there is limited iron available and IRP1 then binds to ferritin and transferrin receptor RNA. Beinert also discusses the global microbial control system involving the fumarate nitrate reduction (FNR) protein. In the presence of oxygen, the FNR cluster decays from the [4Fe–4S] to the [2Fe–2S] state. Mössbauer spectroscopy is particularly helpful because the presence of ^{57}Fe permits detection of all Fe species from FNR. Beinert's chapter concludes with this comment: "… in the last two decades EPR has often been called upon as a decisive method for providing critical information on the role of Fe–S clusters in controlling the activity of regulatory proteins both in vitro and in whole cells."

Chapter 4 by Gambarelli, Mulliez, and Fontecave focuses attention on the versatility of the coordination of iron–sulfur clusters in biology. Though cysteine residue is the most favored ligand, providing sulfur coordination, oxygen-based and nitrogen-based residues are also found. The authors point out that low-molecular-weight substrates (citrate for aconitase) and cofactors (S-adenosylmethionine, SAM, for "Radical-SAM" enzymes) are activated through binding to one of the iron sites in [4Fe–4S] clusters. Cluster–SAM complexes are found to be essential intermediates in a number of enzyme reactions for the "Radical-SAM" enzyme superfamily involved in the metabolism of all living organisms. Examples include pyruvate formate lyase and anaerobic ribonucleotide reductase. The background theory regarding hyperfine couplings for ESEEM and ENDOR in metalloproteins is presented. There is also discussion of the strengths and weaknesses of ENDOR and HYSCORE spectroscopy for characterizing metalloprotein coordination. "Blind spots" intrinsic to Mims ENDOR are overcome by obtaining data at a number of τ values.

2. MOLYBDENUM ENZYMES

In Chapter 5, Hille begins by reminding the reader that EPR and related methods have long been used to understand the structure and function of molybdenum-containing enzymes. The author covers the pioneering contributions of R.C. Bray and coworkers, who characterized the different types of EPR signal manifested by the active sites of enzymes such as xanthine oxidoreductase. These are known as "very rapid," "rapid type 1" (or just "type 1"), and "type 2." He then summarizes more recent investigations utilizing a variety of more advanced methods that have contributed significantly to our understanding of the physical and electronic structures of the various EPR-active centers of the enzymes. He discusses comparison with model systems, the significance of EXAFS metal–ligand bond length determinations, and the contribution of EPR spectroscopy, complemented by ^{17}O and Mo isotope enrichment. Hille's final example concerns magnetic interactions in xanthine oxidoreductase, which contains two 2Fe–2S centers that are very similar to those found in spinach ferredoxin, one of which, Fe–S/I, interacts with the Mo center 14.7 Å distant. A good deal is now known about reaction intermediates

formed during hydroxylation by xanthine oxidoreductase, and this has led to improved understanding of the chemical pathways involved.

Enemark, Astashkin and Raitsimring in Chapter 6 provide a comprehensive account of a class of molybdenum enzymes called sulfite oxidases. They review the history of the EPR of molybdenum enzymes as well as the role played by sophisticated pulsed EPR methods. This chapter sits nicely between the previous chapter by Hille and the following chapter by Hanson and Lane. Sulfite oxidases (SOs) are Mo-containing enzymes that catalyze the oxidation of sulfite to sulfate. They occur in humans, avians, plants, and bacteria. The two-electron oxidation of SO_3^{2-} occurs at the Mo center. First, Mo^{IV} is produced, which is then reoxidized to Mo^{VI} by sequential one-electron transfers to the b_5-type heme center. X-ray crystallography reveals that the Mo center is approximately square pyramidal, with an oxo group occupying the apical position. The equatorial positions are occupied by a second oxygen and by three sulfurs, one of which is supplied by a cysteine sidechain. Mo(V) (d^1) and its immediate environment are readily amenable to EPR techniques. With regard to pulsed EPR methods, the authors argue that it is best to begin with 1D techniques such as 2-pulse ESEEM, Mims or Davies ENDOR, and only to use 2D methods (HYSCORE, refocused primary echo, or RP ESEEM, 2D MIMS ENDOR) to resolve ambiguities. The theoretical background essential for understanding and interpreting spectral data from pulsed experiments is fully outlined. The authors draw attention to the difficulty of relating HFI and NQR parameters to structure because of incomplete knowledge regarding the relationship between the g- and molecular coordinate frames.

Hanson and Lane in Chapter 7 describe the application of continuous wave (CW) and pulsed EPR spectroscopy to the geometric and electronic characterization of the Mo(V) active site within dimethylsulfoxide (DMSO) reductase, which belongs to a distinct family of molybdoenzymes. It contains two molydopterin ligands, in contrast to others that have only one. Studies of model molybdenum(V) complexes are also reported. The importance of X-ray structures, where available, elucidation of the low-symmetry Mo sites, the sensitivity of spin Hamiltonian parameters to small changes in the coordination sphere, the role of computer simulations, and the importance of theoretical DFT calculations are all addressed. Molybdenum EPR investigations are assisted by the presence of the normal Mo isotopes, ^{95}Mo and ^{97}Mo, each with nuclear spin $I = 5/2$ and the remaining 74.5% where $I = 0$. Although results are reported for respiratory DMSO reductase, the main emphasis is on periplasmic DMSO reductase, where a rich range of spectra are observed. These are differentiated as low-g and high-g CW-EPR spectra, characterized by average g-factors of 1.96 and 1.98, respectively. Specifically, the electronic and geometric structure of the low-g and high-g EPR signals and their relevance to the catalytic cycle of the enzymes are described. CW- and pulsed EPR studies of a dithionite-reduced sample of DMSO reductase reveal the presence of a sulfur-centered radical localized on the pterin molybdenum cofactor. Through redox potentiometry, the high-g unsplit and split Mo(V) signals are shown to arise from Mo(V) species on the reductive and oxidative sides, respectively, of the catalytic cycle. The retention of a trigonal prismatic geometry around the molybdenum ion

in DMSO reductase upon reduction of the oxidized enzyme (Mo(VI)) through Mo(V) to Mo(IV) indicates that the active site is an example of an entatic state, poised for catalysis.

3. MANGANESE-CONTAINING ENZYMES

In Chapter 8, Brynda and Britt explain that manganese has a variety of roles in enzymes such as arginase that catalyze the hydrolysis of arginine. Since Mn^{II}, Mn^{III}, and Mn^{IV} are all biologically accessible, clearly manganese must play a crucial role in important redox reactions in the Mn_4Ca cluster of Photosystem II (PSII), a large transmembrane protein/cofactor complex that utilizes light energy to oxidize water to molecular oxygen. The authors discuss the requirement for Ca^{2+} and Cl^- cofactors and the role of X-ray crystal structures and X-ray absorption spectroscopy in shedding new light on the structure of the oxygen-evolving complex (OEC). The exact nature of the Mn cluster and its precise role in water oxidation remains unresolved. Synthetic models and quantum mechanical calculations, based on a broken symmetry density functional theory (DFT) approach, are used to evaluate the electronic structure of these Mn complexes so as to illuminate the structural and mechanistic aspects of catalytic water splitting in PSII. The physics of coupled systems is thoroughly outlined. In particular the authors explain how the coupling interaction is simplified by writing the Heisenberg Hamiltonian for polynuclear complexes as a sum of pairwise interaction terms.

In Chapter 9, Smith, Hadler, Schenk, Hanson, and Mitić discuss selective advances in the study of the structure/function relationship of binuclear manganese-dependent enzymes. In the previous volume in this series, Schenk, Mitić, and Hanson reviewed the biochemical, structural, and spectroscopic properties, in particular EPR-related properties, of many binuclear non-heme iron enzymes. Several of these also function in the presence of manganese, for example, ribonucleotide reductase and a purple acid phosphatase from sweet potato. By way of contrast, some enzymes have evolved a specific requirement for manganese, including catalases and arginase. Using the same format as in their previous review on the binuclear non-heme systems, the biochemical and structural properties of the selected enzyme systems are described, followed by a summary of data from several spectroscopic techniques, focusing particularly on the contributions from EPR-related techniques. Where possible, a brief description regarding mechanistic implications is offered. While it is envisioned that this chapter may provide an entry point for the interested researcher, it is also anticipated that specialists may also find the discussion and references helpful for their own research.

4. NOVEL METALLOENZYMES AND METALLOPROTEINS

In Chapter 10, Bennett explains that Co(II) has long been used as a spectroscopically active substitute for Zn(II) in enzymes. The Co(II) ground state is high-

spin $S = {}^3/_2$, what is expected for a near tetrahedral coordination. The analysis of EPR spectra in terms of spin Hamiltonian parameters is described, along with their interpretation in structural terms. There is a fairly full discussion regarding the "effective" g-factors that occur in these systems where the spectra actually arise from isolated doublets of the spin $^3/_2$ system. The applicability of Co(II) as a structural and functional mimic of Zn(II) in enzymes is considered and a brief update of EPR studies in the literature presented. Some 37 cases are tabulated. Obtaining high-quality EPR from high-spin Co(II) that can provide useful information is not trivial, so experimental issues are discussed in some detail. Complementary measurement techniques are very briefly discussed. One case study is provided to show how the EPR of Co(II) can provide mechanistic information on a zinc enzyme, unavailable by other techniques.

Chapter 11 by Larsen and Chasteen concerns investigations using the oxycation VO^{2+} as an EPR spin probe of protein metal binding sites. Its importance has increased significantly because of the availability and now widespread use of high-resolution pulsed EPR methods such as ENDOR, ESEEM, and HYSCORE. Thus isotropic and dipolar components of ligand hyperfine couplings unavailable from CW-EPR can now be measured. Experiments on model complexes supplemented by DFT calculations have led to new insights into how g-factors and ligand and ^{51}V nuclear hyperfine couplings depend on the electronic structure and coordination geometries of VO^{2+} chelates. These results are then used to enhance the understanding of similar data obtained from vanadyl-substituted proteins. A number of examples involving the application of high-resolution EPR of VO^{2+}-containing proteins and tissues samples are reviewed in this chapter.

5. CONCLUSIONS

The chapters in this volume are diverse in subject matter and emphasis, and in the matter of which EPR techniques are most important in each case. They differ in style and yet are unified in that they all relate to the application of EPR spectroscopy to the structural characterization of metal ion active sites in metalloenzymes. The importance of pulsed methods to elucidate metal ligand coordination cannot be overemphasized, though it needs to be pointed out that there are very often difficulties regarding how to relate the g-frame of reference to the molecular frame.

There are many target audiences. Those within the various fields represented here will find much to "get their teeth into." Those considering work on one or more of the systems described will find starting points, valuable information, and useful references. Beginning graduate students will find this volume a useful introduction to EPR applications to metal ions in biology and to the variety of approaches both experimental and theoretical that are the necessary armory for anyone seriously considering entering the field.

This volume complements the previous volume (Vol. 28) and helps to make the point that modern EPR methods are the method of choice when investigating the role of paramagnetic ions and clusters in biology. Of course, EPR data cannot

stand on their own and should be supplemented by information from many other methods such as X-ray crystallography, magnetic circular dichroism, and EXAFS, and electronic absorption, infrared, resonance Raman and Mössbauer spectroscopy.

IRON–SULFUR-CONTAINING

MATERIALS

ELECTRON MAGNETIC RESONANCE OF IRON–SULFUR PROTEINS IN ELECTRON-TRANSFER CHAINS: RESOLVING COMPLEXITY

Richard Cammack[1] and Fraser MacMillan[2]

[1]*Pharmaceutical Science Research Division, Kings College, London*
[2]*School of Chemical Sciences and Pharmacy, University of East Anglia, Norwich, UK*

Iron–sulfur clusters, some of the most abundant electron-transfer groups in biology, were first detected and investigated using EPR spectroscopy. They are commonly found in large, membrane-bound complexes that are essential for energy conversion in living cells. Here we describe the applications of multiple-frequency, pulsed and double-resonance electron magnetic resonance (EMR[†]) methods to investigate the structure and function of these iron–sulfur proteins. Such spectra can be observed from macromolecular complexes and membranes, as well as from whole cells and tissues. A careful choice of sample preparation and measurement parameters is required to partially resolve overlapping spectra from multiple iron–sulfur clusters. Recently the REFINE technique has been presented, which can be used to select the spectra of individual centers having different relaxation rates, such as cluster N2 from NADH: ubiquinone oxidoreductase. Where proteins are difficult to crystallize, EMR methods can provide structural information; ESEEM and ENDOR especially can identify the types of clusters and the nature of their protein ligands. Pulsed EPR and PELDOR are able to provide information about distances between clusters and other paramagnets such as semiquinone radicals or other metals. When crystal structures are known, EMR provides additional information about electronic structures and the disposition of protons. Potentially, EMR techniques can show details of protein movements and the effects of transmembrane potentials. Future directions for research are discussed.

Address all correspondence to Richard Cammack, Pharmaceutical Science Research Division, Kings College, London, 150 Stamford Street, London SE1 9NH, UK, +44 20-7848-4264, +44 20-7848-4500, <richard.cammack@kcl.ac.uk>.
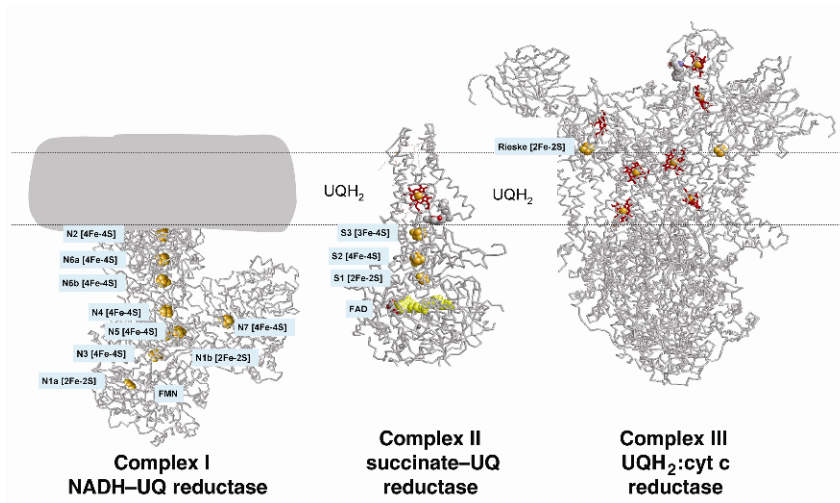
Figure 1. Diagram of the iron–sulfur clusters in complexes of the respiratory chain. Protein Databank structures 1FUG, 1NEK, and 1KYO were drawn with RasMol [132]. Please visit http://www.springer.com/978-1-4419-1138-4 to view a high-resolution full-color version of this illustration.

1. INTRODUCTION

Some of the first biological systems to which EPR spectroscopy was applied were electron-transfer (ET) proteins. A notable success was the establishment of iron–sulfur proteins as essential constituents of the mitochondrial respiratory chain (see Fig. 1), the photosynthetic electron-transfer chain [1,2], and other systems of membrane bioenergetics. Optical absorption spectroscopy had shown that several cytochromes acted as electron carriers in these systems, but when EPR spectroscopy was applied, particularly at temperatures below 77 K, it revealed that iron–sulfur (Fe–S) proteins were even more abundant [3–7]. An important advantage of continuous-wave (cw) EPR spectroscopy is that it can be applied to whole macromolecular protein complexes, organelles such as mitochondria and chloroplasts, and even whole tissues in the frozen state. The individual Fe–S clusters in these systems were identified and named on the basis of their EPR signatures, each cluster giving a spectrum with a characteristic lineshape in either the oxidized or reduced state. As the complexes were isolated, it was found that often several iron–sulfur clusters of different types occur in the same protein. The puzzling abundance of iron–sulfur clusters in the membrane-bound complexes of bioenergetics was later rationalized when it was learned that a sequence of clusters, separated by distances of 1.2–1.4 nm could act as an efficient conductor of electrons, for example, from one side of a membrane to the other [8,9].

An indication of the importance of these proteins is that a number of hereditary neurological diseases have been attributed to deficiencies in iron–sulfur proteins of the mitochondrial respiratory chain [10]. Fe–S clusters have also been implicated in the toxic effects of oxygen radicals and nitric oxide [11,12].

Cw-EPR is able to provide information about the structure and biological function of these Fe–S centers, including:

- The type of Fe–S cluster ([2Fe–2S], [3Fe–4S], [4Fe–4S], etc.). The properties of the different types of cluster were determined by studies on small iron–sulfur ET proteins, the ferredoxins.
- The electronic structures of the clusters, investigated by observation of hyperfine interactions with nuclei of introduced stable isotopes such as ^{57}Fe, ^{33}S, and ^{2}H.
- The redox states of the clusters under different conditions, and the midpoint redox potentials, obtained by preparing samples treated with substrates, or poised at specific potentials using potentiometry.
- The proximity and orientation of the clusters, through the effects of spin–spin interactions on the EPR spectra, which are manifested as increased spin relaxation rates, and/or splitting of EPR signals.
- The location of the clusters in a membrane (inside or outside) from studies of the effects of paramagnetic relaxation agents [13,14].

Recently, advanced electron magnetic resonance (EMR[†]) techniques have been developed (see reviews [15–17]) that extend the scope of paramagnetic resonance in various ways, such as

- refinement of nuclear hyperfine and quadrupolar couplings,
- measurement of spin–lattice and spin–spin relaxation rates,
- resolution of zero-field splittings,
- more precise measurement of electron spin–spin interactions, for determination of longer distances and orientations.

In this review we consider some of the interesting biochemical questions that have been and may be addressed by application of these advanced EMR methods.

1.1. Problems of Complex Electron-Transfer Systems

Membrane-bound ET proteins indeed represent a considerable challenge to many of these new methods, some of which will clearly prove more useful than others. This is primarily due to one or more of the following factors:

- the complexity of the spin systems (high-spin and spin-coupled species);

- spectral overlap of EPR signals leading to difficulties in assignments;
- the low concentration of the paramagnets, which becomes a problem especially for some two dimensional methods where the resolution gained is accompanied by an inherent loss of sensitivity;
- the fact that most transition metal systems can only be studied in the frozen state, leading to disordered spectra;
- distributions of parameters such as g-factors, hyperfine couplings, and electron spin–spin interactions, owing to the random distribution of strain in protein conformation [18].

With the introduction of the first commercial pulsed EPR spectrometers around 1990, it was of great interest to see how these methods could extend the range of applications of EMR in biological systems. The dramatic improvement in sensitivity provided by Fourier-transform techniques in NMR have not yet been replicated in EMR, mainly due to the broad spectral linewidths involved and the very fast electron-spin relaxation rates and short coherence times. Nevertheless the new techniques have provided important information about these complex biochemical systems that could not be obtained in other ways.

The biological application of EMR techniques was developed by using selected model systems that were optimized for signal amplitudes and minimal interferences, and these methods still rely on very careful sample preparation. In addition the interpretation of the results has greatly benefited from a combined approach with other molecular information such as protein sequence and structure, and especially from other spectroscopic techniques such as Mössbauer, magnetic circular dichroism (MCD) and EXAFS, and from DFT calculations.

2. IRON–SULFUR PROTEINS

Fe–S proteins are metalloproteins, widely distributed in almost all organisms, which contain Fe–S clusters [19]. They have a wide range of functions, including enzyme catalysis, regulation, and maintenance of protein structure, but the most frequent activity is in biological ET. These Fe–S proteins of ET chains are large molecules, and often comprise a series of clusters. In view of their importance in systems for the conservation of energy, these proteins have been studied in great detail.

The structures of clusters found in biological electron-transfer chains are illustrated in Figure 2. They comprise iron and sulfide atoms in a number of characteristic structures, coordinated directly to amino-acid residues in the protein, usually cysteine but sometimes also histidine, aspartate, serine, or other residues. The most commonly occurring clusters are the [2Fe–2S], [3Fe–4S], and [4Fe–4S] types whose properties are summarized in Table 1. They were first characterized in
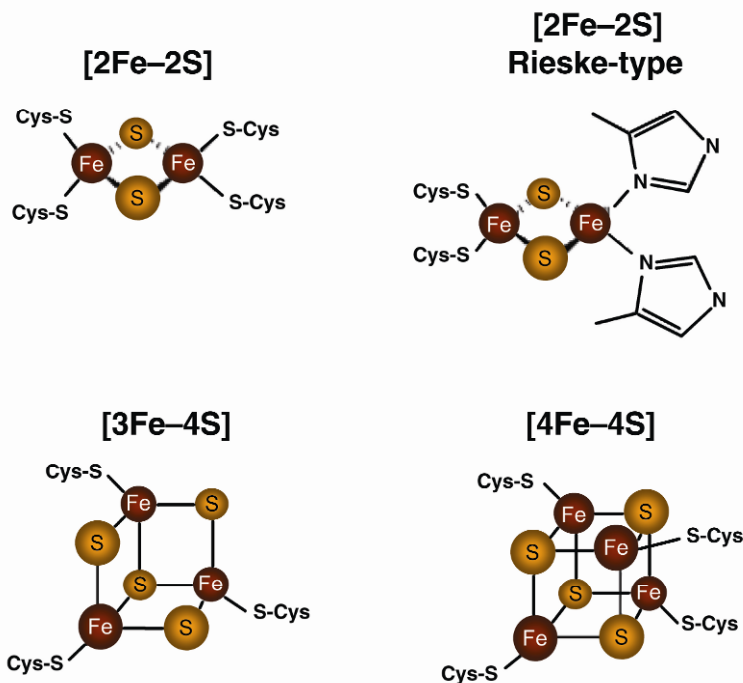
Figure 2. Structures of the most common forms of Fe–S clusters. Please visit http://www.springer.com/978-1-4419-1138-4 to view a high-resolution full-color version of this illustration.

smaller electron-transfer proteins, the ferredoxins [19–21]. In general each cluster is able to transfer one electron, so that it is EPR-detectable in at least one state, either oxidized or reduced.

The majority of Fe–S clusters are paramagnetic ($S = \frac{1}{2}$) in either their oxidized or reduced state. Higher spin states such as $S = 3/2$ or $S = 2$ are also common. Most of them are observable by cw-EPR spectroscopy, and they are potentially good subjects for advanced EMR techniques. Their EPR spectra are usually observed at cryogenic temperatures ($T < 100$ K) and typically have a rhombic or near-axial lineshape.

The structures of the large ET protein complexes reveal that they often have a modular construction in which the cluster-binding domains are homologous to those found in the ferredoxins. The [4Fe–4S] clusters, for example, are often found in pairs, with a polypeptide sequence similar to that of the eight-iron ferredoxins. Therefore studies of the simpler proteins by advanced EMR techniques are very relevant to observations on the complex enzymes.

Table 1. Types of Fe–S Cluster

Designation	Diamagnetic oxidation states*	EPR-detectable oxidation states*	Typical g-factors
[2Fe–2S]	Oxidized (2^+)	Reduced (1^+)	$g = 1.94$
[2Fe–2S]$_{Rieske}$	Oxidized (2^+)	Reduced (1^+)	$g = 1.90$
[3Fe–4S]	Reduced (0)	Oxidized (1^+)	$g = 2.01$
[4Fe–4S]	Oxidized (2^+)	Reduced (1^+)	$g = 1.94$
[4Fe–4S]$_{HiPIP}$	Oxidized (3^+)	Reduced (2^+)	$g = 2.01$

*The charges on the clusters are calculated from the sum of the charges on iron (3^+ or 2^+) and sulfide, ignoring the charges on the ligands.

Notes: N^1, N^2 refer to two nitrogen ligands to the Rieske-type cluster; N1, N2 refer to clusters in Complex I (NADH:ubiquinone reductase).

2.1. Types of Clusters

The [2Fe–2S] proteins are the most intensively studied by advanced spectroscopic techniques. On the basis of amino-acid sequences, several major types of cluster-binding domains can be distinguished:

- the structurally well-characterized proteins typified by ferredoxins from plant-type photosynthesis and cytochrome P-450 monooxygenases;
- a type of cluster found in molybdenum hydroxylases such as xanthine oxidase;
- the [2Fe–2S] ferredoxins from nitrogen-fixing bacteria such as *Clostridium pasteurianum*;
- the Rieske proteins of respiratory and photosynthetic electron-transfer chains, and similar clusters in nonheme iron-containing oxygenases.

The original model for the structure of the [2Fe–2S] clusters [22,23] was confirmed by a combination of Mössbauer, EPR and ENDOR studies (reviewed by [24,25]). Earlier work on ENDOR and ESEEM of [2Fe–2S] clusters has been reviewed [26]. In the oxidized state both atoms are formally Fe(III), $S = 5/2$, antiferromagnetically coupled so that the ground state has $S = 0$. It was first shown using Mössbauer and ^{57}Fe-ENDOR spectroscopy that upon reduction one iron atom becomes reduced to Fe(II), so the resulting net spin is $S = \frac{1}{2}$ and EPR spectra with $g_{av} < 2.0$ are observed at temperatures below 100 K.

The [4Fe–4S] clusters of most proteins have a ground state $S = 0$ in the oxidized ([4Fe–4S]$^{2+}$) state, and are reduced by one electron to a [4Fe–4S]$^+$ state with $S = \frac{1}{2}$. The less common *high-potential-iron–sulfur proteins* (HiPIPs) are also ferredoxins containing a similar [4Fe–4S]$^{2+}$ cluster, but they undergo oxidation to a [4Fe–4S]$^{3+}$ state, with $S = \frac{1}{2}$. As their name implies, they have considerably higher

midpoint potentials than the [4Fe–4S]$^{2+/1+}$ proteins, and they have completely different protein structures.

[3Fe–4S] clusters were first observed as relatively narrow $g = 2.01$ EPR signals in oxidized [4Fe–4S] proteins, and were assigned as HiPIP-type clusters; they were then shown to have only three iron atoms [27]. Some of these were then shown to be products of oxidative damage to [4Fe–4S] clusters in proteins such as aconitase, a soluble mitochondrial enzyme that is not a component of a respiratory chain [28]. It later emerged that [3Fe–4S] clusters are not always the result of oxidative damage, being natural constituents of various electron-transfer proteins, including mitochondrial complex II and nitrate reductase. In their stable reduced forms ([3Fe–4S]^0) they have an $S = 2$ ground state and on oxidation to the [3Fe–4S]$^+$ state they have $S = ½$ [29].

In some cases, bioinformatics analysis of the amino-acid sequence, from the gene sequence, can provide an indication of the types of cluster present. Each type of cluster may be bound by one of a number of characteristic protein sequence motifs; it may, however, be difficult to assign the ligands to some clusters. A useful approach is to substitute cysteine ligands in the sequence by site-directed mutagenesis and to examine the resulting variant protein by EMR spectroscopy. This is not a completely reliable criterion, however, as in some cases a modification of one part of a protein may prevent assembly of an Fe–S elsewhere in the protein; or removal of a cluster ligand may result in substitution of another amino-acid residue as a direct ligand, with minimal changes to the spectroscopic properties. An instructive, though unusual, example of the latter was provided by variant studies of the [2Fe–2S] ferredoxin from *Clostridium pasteurianum*. EPR spectroscopy revealed that even if two of the five potential cluster-binding cysteine ligands were substituted by alanine, a [2Fe–2S] cluster could still be formed, indicating that a different residue from the protein was being recruited to rescue the cluster. Even so, the ESEEM spectra of the reduced cluster were similar, showing couplings to peptide ^{14}N. The protein structure was finally solved by analogy with the crystal structure of a related protein from *Aquifex aeolicus* and variants of it [30]. Two of the cysteine ligands form a rigid core, which maintains the structure of the [2Fe–2S] cluster, while the other two are in a flexible loop, so that other residues can substitute for cysteine without disrupting the covalent structure of the cluster. Substitution by serine produced a high-spin state [31].

3. INFORMATION FROM ADVANCED EMR

The development and concomitant application to biological systems of advanced EMR techniques has expanded quite rapidly over the past two or three decades. On the one hand, the drive toward ever-higher magnetic fields and microwave frequencies (e.g. [32]) has established the idea of multifrequency EMR, whereby there are different optimal fields and frequencies for different applications. On the other hand, the further development of pulsed EMR into several dimensions has introduced the phenomena of correlation spectroscopy to EPR as well as the

application of a second frequency be it a microwave (PELDOR) or a radio frequency (pulsed ENDOR). Here we will briefly mention these methods in conjunction with the information they provide on Fe–S clusters

3.1. Relaxation Rates

The electron spin-lattice relaxation rates T_1 and T_2 may be measured by pulsed EPR sequences, such as saturation-recovery or inversion-recovery. The relaxation rate of isolated Fe–S clusters increases in general in the order [2Fe–2S] < [3Fe–4S] < [4Fe–4S]$^{3+}$ < ferredoxin-type [4Fe–4S]$^{1+}$; hence the temperature dependence of their EPR signals can in principle be used as a guide as to the type of cluster. However, it should be noted that spin–spin interactions between clusters can lead to an enhanced relaxation. An example of this is the interaction between the [2Fe–2S] cluster 1 and [4Fe–4S] cluster 2 in succinate:quinone oxidoreductase and quinol:fumarate reductase (see below).

3.2. Identification of Cluster Ligands

An important contribution of ENDOR to cluster ligand identification was the classic observation of the imidazole N$^\delta$-nitrogens of histidine as direct ligands to the Fe–S clusters in the Rieske-type protein phthalate dioxygenase [33,34]. ESEEM and HYSCORE were used to demonstrate the presence of histidine nitrogen in the Rieske dioxygenases proteins of mitochondrial and photosynthetic electron-transfer chains [35] and dioxygenases [36–38]. Recently HYSCORE has been extended to different states of the Rieske cluster, including the fully deprotonated form [39]. Analysis of the ^{14}N ESEEM and HYSCORE spectra of metal centers in proteins yields two useful parameters: the hyperfine coupling constant A and nuclear quadrupolar coupling κ (= $|e^2qQ/4h|$) [40, 41,132]. The first describes the coupling strength and can thus be used to estimate distances. The ESEEM effect arises principally from the dipolar interaction, so a nucleus that is observed does not necessarily have to be a direct ligand to the metal. The quadrupolar coupling is very characteristic of the type of ^{14}N nucleus involved, e.g., there is a distinct difference between the κ for peptide nitrogen and for nitrogen within the imidazole ring of histidine [107].

3.3. Interactions with Protons and Paramagnets

Although their presence may be inferred, protons are not observed in protein crystal structures. Protons near paramagnetic centers may be observed directly in ENDOR and ESEEM. These protons are important, because hydrogen bonds provide stabilization of particular oxidation states. Protonation also influences the electron-density distributions in the clusters. Cluster redox potentials, and the kinetics of oxidation–reduction reactions, are strongly dependent on compensation of electrostatic charge during oxidation–reduction, which can be provided by proton movements. Exchangeable protons or deuterons (hydrons) associated with Fe–S

clusters are of particular interest, and include peptide NH, cysteine –SH and serine –OH. Proton movements can be observed by EMR measurements of the protein at different pH values and in different oxidation states, in ^{1}H$_2$O and ^{2}H$_2$O. ^{14}N couplings to clusters in ESEEM and HYSCORE spectra provide evidence for NH–S hydrogen bonds to Fe–S clusters, as well as information about hydrogen-bonding networks, accessibility to solvent, and protein flexibility. Interactions of redox groups with protons are of particular interest in systems such as mitochondrial Complexes I and III, where ET between complexes is coupled to proton translocation across the membrane.

Interactions of Fe–S clusters with other paramagnetic centers within electron-transfer distances have also been observed using EMR techniques. In proteins of the xanthine oxidase family, interactions between the Fe–S cluster and the neighboring Mo(V) were observed [42,43], while in hydrogenase PELDOR spectroscopy was used to determine the individual spin-projection factors within n [Fe–4S] cluster through the dipolar interaction with the neighboring nickel [44].

3.4. Further Structural Information

The ideal situation is when the protein of interest can be obtained as a single crystal, which allows a full analysis of the electronic structure and hyperfine interactions, as for simple inorganic complexes. However, so far, only a few Fe–S proteins have produced crystals large enough for single-crystal EMR studies [45]. Even if the crystals are not large enough for EMR spectroscopy, the structure of the protein, from either X-ray crystallography or NMR, greatly assists interpretation of the EMR of the clusters.

For ET complexes in membranes, some degree of ordering in the EMR spectra can be provided by the use of oriented membrane bilayers. This is achieved by carefully drying down samples of membrane vesicles, or by magnetic ordering [46,47]. In this way, the organization of clusters relative to the membrane plane can be determined. For example, the alignment of the [4Fe–4S] clusters F$_A$ and F$_B$ in Photosystem I was estimated from an EPR study of oriented thylakoid membranes from the cyanobacterium *Synechocystis* [48]. This arrangement was later confirmed by X-ray crystallography [49].

3.5. Orientation-Selective ENDOR and ESEEM

The rhombic spectra of the Fe–S clusters allow the use of orientation selection to determine the orientation of the *g*-matrix relative to the protein molecular axes [34]. This has been determined in a few cases of [2Fe–2S] clusters, notably with the Rieske proteins [33]. Couplings of nonexchangeable β-CH$_2$ protons of the ligands to the [2Fe–2S] cluster were observed in 2D-ESEEM of [2Fe–2S] ferredoxin from *Porfira umbilicalis*, and assigned on the basis of the proton positions predicted from the crystal structure of a related ferredoxin [50]. The orientation-selective ^{1}H cw-ENDOR of the reduced [2Fe–2S] ferredoxin from the cyanobacte-

rium *Arthrospira platensis* was analyzed with reference to the X-ray crystal structure [51]. ENDOR spectra recorded across an EPR spectrum with an anisotropic *g*-tensor comprise all the information about the anisotropy of the hyperfine couplings. Generally, in order to resolve ambiguities in assignment of resonances, a complete determination of hyperfine couplings often requires some additional structural information, which may include selective chemical or isotopic substitution at particular residues [52], NMR, DFT calculations, or single-crystal EPR data [53,54]. For the analysis of *A. platensis* ferredoxin, a crucial piece of information was identification of the iron atom that is Fe^{2+}, from sequential NMR assignment [55]. The dipolar couplings to four protons around the cluster were assigned, from which it was possible to determine the orientation of the principal axes of the *g*-matrix in the molecular frame, as well as the spin density on the two iron atoms.

For such studies, measurements of ENDOR frequencies are required across the full width of the rhombic EPR spectrum, especially at the upper and lower field limits. The latter spectra are the least intense and thus difficult to measure, but they are critical, as they represent almost single orientations of the B_0 field relative to the axes of the *g*-matrix. Such information may be difficult to obtain from ET complexes where there are multiple overlapping spectra from paramagnets.

The utility of orientation-selective ^{14}N ESEEM and HYSCORE was demonstrated by a study of the ^{14}N quadrupole parameters for two hyperthermophilic Rieske-type proteins [38]. This showed that the proteins have significant differences in the nuclear quadrupolar coupling parameters but small differences in hyperfine couplings. The differences were interpreted in terms of rotation of the imidazole planes of the histidines, which left the binding to the iron relatively intact.

3.6. Studies of Intact Membrane-Bound Complexes

The ability of these protein complexes to perform their primary functions such as transmembrane proton pumping depends crucially on their intact structure. The behavior of the Fe–S clusters in membranes, when an electrochemical potential is operating, is different from that in isolated complexes. Therefore, although it is possible to learn much about composition and properties from studies of isolated components, a study of the intact complexes or even whole organelles or cells may be necessary for a complete understanding of their function. A recent study has examined the cw-EPR spectra of whole mitochondria from the yeast *Saccharomyces cerevisiae*, in which the oxidation state of a number of Fe–S clusters was observed while the mitochondria were actively respiring [56].

Interactions have also been observed between paramagnetic Fe–S clusters and radicals of flavin, quinones, and chlorophylls, which have been examined by advanced EMR. For example, an EPR signal that has only been observed in intact mitochondria has been attributed to a spin–spin interaction between two ubiquinone radicals, interacting with a fast-relaxing species suggested to be the [3Fe–4S] cluster S3, or possibly a heme, of Complex II. [57,58]. Another fast-relaxing EPR signal of a protein-bound semiquinone anion radical SQ_{Nf} is observed in energized membranes, but disappears when the transmembrane potential

is collapsed by an uncoupler [59]. This radical is spin-coupled to cluster N2, as shown by its rapid relaxation rate, and splitting [60,61]. These signals are important as indicators of the energized state of the membrane in mitochondrial Complex I.
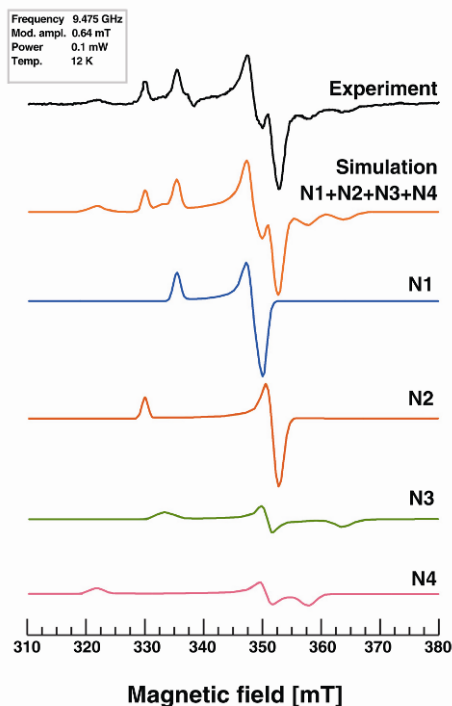
Figure 3. X-band cw-EPR spectrum of isolated Complex I from yeast (*Yarrowia lipolytica*) recorded at 12 K; microwave power of 0.1 mW (experiment). Prominent EPR signatures of individual clusters (N1–N4) are indicated. The simulation represents the result of addition of four individually simulated spectra of clusters N1–N4 in a 1:1 stoichiometry. The simulated spectrum of Complex I is the sum of four simulated spectra. Unpublished data kindly supplied by Klaus Zwicker and Uli Brandt, J.W. Goethe University Frankfurt, Germany. Please visit http://www.springer.com/978-1-4419-1138-4 to view a high-resolution full-color version of this illustration.

3.7. Methods of Isolating Spectra of Individual Components

As already noted, for membrane-bound ET proteins in mitochondrial or bacterial respiratory chains, the presence of several paramagnetic iron–sulfur clusters is the norm. When applying field-modulated EPR spectroscopy these species may be distinguished by their derivative features, but in fact their EPR are overlapping (Fig. 3). Since the expansion of the application of modern pulsed EPR methods to study such complex biological systems in much greater detail, spectral overlap has to be considered carefully. One important prerequisite for the analysis and assign-

ment of specific experimental observations in biological samples is the ability to study the contributions arising from specific species individually and directly.

In principle, such paramagnetic species can be distinguished in several ways. First, one can try to render all species EPR-silent except the one of interest, by adjustment of the redox potential. This is possible where the signal is the only one observable in the oxidized state, such as the [3Fe–4S] cluster of Complex II [62] or fumarate reductase [63]; or where it is the first one to be reduced, for example, the Rieske protein of Complex III [64]. If more than one component participates in the spectrum, progressive reduction, either by adjusting the redox potential or by adding specific substrates, can vary the relative amounts of each species [65]. The contributions of each component may then be extracted, in favorable cases, by spectral deconvolution.

Biological methods may produce a sample in which one paramagnet is the predominant species. The choice of mitochondria from thermogenic tissues of the lily *Arum maculatum* provided samples in which Complex II predominated over Complexes I and III [66]. This specialized tissue produces heat with a minimum production of ATP; Complex I is present at low levels, being substituted by an alternative NADH dehydrogenase that is devoid of Fe–S clusters [67]. It was then possible to apply ENDOR and ESEEM to measure the hyperfine and quadrupolar coupling parameters of the Fe–S clusters of Complex II in intact mitochondrial membranes. Although these methods are applied extensively, it may sometimes not be possible to remove certain contributions to the overall spectrum while maintaining the correct redox state for the species to be investigated by EPR. More flexibility is provide by the respiratory chains of microorganisms, which often are the counterparts of mitochondrial systems, and which allow manipulations by genetic engineering. It is possible to have cells of *E. coli*, for example, in which Complex II or fumarate reductase is the principal membrane-bound iron–sulfur complex. Over-expression of the genes can produce preparations that are more concentrated [68]. Site-directed mutagenesis, as already mentioned, can modify or remove particular paramagnetic centers, or prevent assembly of the entire protein.

One can also distinguish these species spectroscopically. If the paramagnetic species under study have different g-factors, multifrequency EPR experiments may separate them. High-Field EPR spectroscopy is now commonly used, since higher magnetic fields lead to a higher spectral resolution of the EPR spectrum, especially for organic radicals. If the overlapping species have different electronic spin quantum numbers S and m_s, they can be distinguished by their different Rabi oscillation (nutation) frequencies. The temperature dependence of the EPR spectra of the iron–sulfur clusters is strongly dependent on the population of multiple spin states of the spin-coupled systems. The cw-EPR spectra of Fe–S clusters are easily saturated with microwave power at low temperatures,, but less so as the temperature is raised, and relaxation times (T_{1e}) increase. Then the dominant relaxation process is the Orbach mechanism [22,69]. At higher temperatures, excited states of the spin-coupled systems become increasingly populated, so that signals from the $S = \frac{1}{2}$ ground states, particularly for the [4Fe–4S] clusters, disappear almost completely [70]. If the contribution of one component to the spectrum is different at different

temperatures, the properties of each may be determined by difference spectra. However, it should be borne in mind that the values of T_1 and T_2 may vary considerably across the EPR envelope, particularly where there is an interaction between two paramagnets.

Relaxation Filtered Hyperfine (REFINE) Spectroscopy is a technique that was recently introduced for the separation of different paramagnetic species by differences in their longitudinal relaxation times (T_{1e}) [71,72]. A pulse sequence is used that includes an inversion-recovery pulse applied together with a standard Hahn-echo detection sequence. The time between the inversion-recovery pulse and the detection sequence is varied and, depending on this so-called filter time (T_F), it is possible to selectively suppress one of two overlapping EPR species and thus record the individual EPR spectrum of a second species. Not only is it possible to record individual EPR spectra, but once these filter times have been determined one can perform other EMR experiments such as ESEEM [71] or even ENDOR and HYSCORE [72] selectively on each of the individual species within an overlapping EPR spectrum. The method was used to characterize the important Fe–S cluster N2 in Complex I [71]. It was not possible to study this Fe–S center individually in Complex I owing to spectral overlap, and so the advanced EMR technique was developed to address the question of the amino-acid coordination of this center in the protein.

In addition to separating EMR spectra of overlapping Fe–S signals, experiments such as REFINE and ESEEM can also be used for separating spectra from other classes of paramagnetic centers in proteins, e.g., from overlapping radical and Fe–S signals in Complex III (MacMillan, submitted, 2008).

3.8. Results from ^{14}N ESEEM

Three-pulse or stimulated-echo ESEEM of Fe–S clusters, at temperatures at or below 4.2 K, usually show interactions with ^{14}N of the protein. Two parameters relating to the hyperfine interaction with ^{14}N can be derived from the spectra: (a) hyperfine coupling, which is a measure of the strength of interaction and from which information may be derived about the distance between the nucleus and the unpaired spin; (b) quadrupolar coupling, which is indicative of the chemical state of the nitrogen atom and orientation. The contributions of nuclear hyperfine, quadrupolar, and nuclear Zeeman interactions can be distinguished by adjusting the microwave frequency and thus the resonant magnetic field. These parameters are usually interpreted by comparison with model compounds and/or other proteins, for example, NQR data for metal–peptide complexes. Software for analysis of such interactions is becoming increasingly powerful and accessible, such as EasySpin [73], but some insights into the interactions involved may be obtained by approximate treatments that apply in specific cases.

A situation where an approximate treatment gives good results is that of nearly exact cancellation between the nuclear Zeeman frequency (H_{NZ}) and the hyperfine frequency (H_{IS}) in one manifold (Fig. 4a). In this case the ESEEM experiment

gives deep modulations in the time-domain spectra, and the frequencies observed are the quadrupolar frequencies ν_+, ν_-, and ν_0 in that manifold:

$$\nu_0 = 2\kappa\eta; \quad \nu_- = \kappa(3-\eta); \quad \nu_+ = \kappa(3+\eta), \tag{1}$$

$$\kappa^2 = (e^2 qQ/4h)^2, \tag{2}$$

where $e^2 qQ/h$ is the quadrupolar coupling parameter, η the asymmetry parameter, and ν_i the nuclear Zeeman frequency. A fourth line corresponding to the so-called double-quantum ($\Delta M_I = 2$) frequency ν_{dq}^β for the other manifold can also be seen, but the other two frequencies are broadened due to anisotropy.

For ^{14}N coupled to the [2Fe–2S] ferredoxins at X-band frequency (9–10 GHz), the assumption of exact cancellation is a poor approximation (Fig. 4b), but at C-band (7 GHz) it is closer to exact cancellation. At this frequency good resolution of two ^{14}N was observed for the ferredoxin from *P umbilicalis* [74]. Spectra of this type commonly arise from interaction of Fe–S clusters with ^{14}N nuclei of the peptide backbone, consistent with a hydrogen bond to this peptide backbone N, as predicted by crystallography and NMR (see [55,75]). These hydrogen bonds are believed to have a role in the redox potentials of the clusters [76].

Another approximate method of analysis may be applied when the hyperfine coupling to the ^{14}N ligands is considerably greater than the nuclear Zeeman frequency (Fig. 5a,c), which often provides similar information to a full simulation [35,77–79]. In a sample of randomly oriented molecules, the distribution of ^{14}N quadrupolar couplings gives a sharp maximum for the $\Delta M_I = 2$ transition. The double-quantum transitions lead to prominent features in the frequency-domain spectrum. The NQR frequencies are given by

$$\nu_{dq\pm} = 2[(\nu_1 \pm a/2)^2 + \kappa^2(3+\eta^2)]^{1/2}. \tag{3}$$

Hence if there are two ^{14}N ligands, four lines are expected (see Fig. 5c). The value of η cannot be estimated without a full spectrum simulation, but values over the possible range (0–1) make only a minor uncertainty (about ±15%) in the estimation of the coupling parameters.

In summary, the parameters determined from ESEEM and HYSCORE experiments on [2Fe–2S] clusters allow us to define two categories (see Fig. 6) depending on the magnitude of the isotropic hyperfine coupling and the NQR parameters. Those centers bound to the protein through a ferredoxin-like motif, i.e., to a peptide nitrogen, are characterized by a smaller isotropic hyperfine coupling, whereas those bound through histidine, as are the Rieske class of centers, have a much larger isotropic hyperfine coupling. This classification may be used when studying systems where the Fe–S composition is unknown.

Relevant to the study of the [4Fe–4S] clusters are the pioneering ENDOR studies by Lamotte, Mouesca, and coworkers on the oxidized ($[4Fe–4S]^{3+}$) and reduced ($[4Fe–4S]^+$) sites in single crystals of synthetic model compounds of the
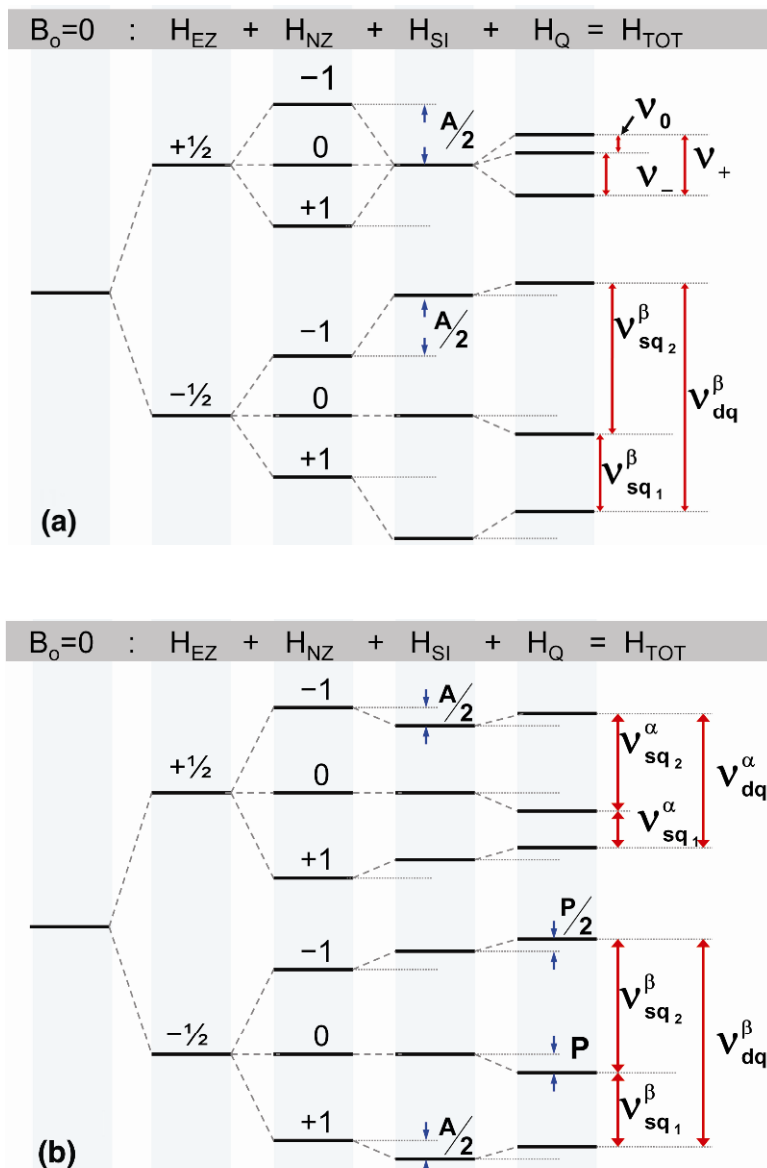
Figure 4. Energy levels for an electron–nitrogen system showing conditions for (a) exact cancellation between the nuclear hyperfine and Zeeman couplings and (b) weak hyperfine coupling. HEZ is the electron Zeeman term, HNZ is the nuclear Zeeman term, HSI is the hyperfine term, and HQ is the quadrupole term. Observable transitions are also indicated. Please visit http://www.springer.com/978-1-4419-1138-4 to view a high-resolution full-color version of this illustration.
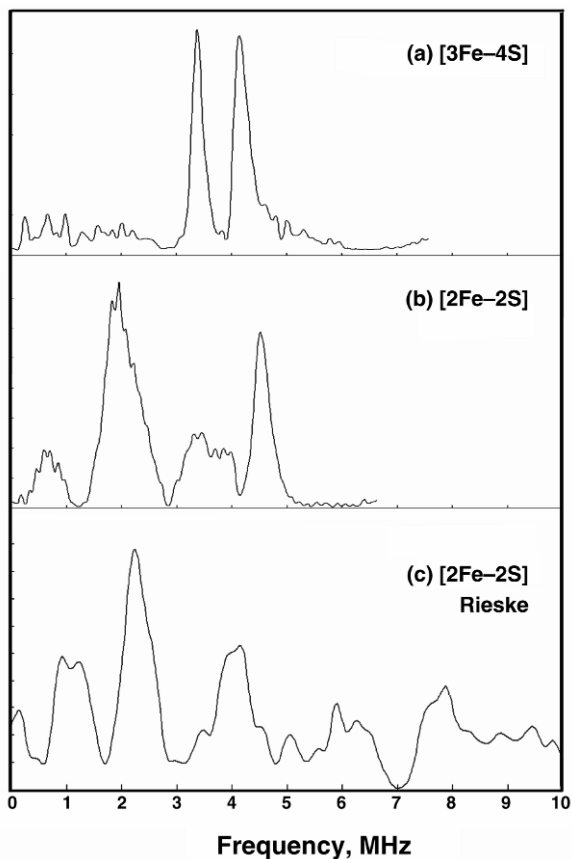
Figure 5. X-band ESEEM spectra of (a) the [3Fe–4S] cluster in fumarate reductase from *E. coli* [63]; (b) the [2Fe–2S] ferredoxin from *A. platensis* [66]; (c) the Rieske protein in bovine heart mitochondria [64].

type $[N(C_2H_5)_4]^{2-}[Fe_4S_4(SCH_2C_6H_5)_4]$ [80,81]. From analysis of the proton ENDOR [82] it was possible to identify couplings to the eight β-CH_2 protons, plus three from nearest neighbors. The results were interpreted with the help of DFT calculations, in terms of two classes of center — one resembling the clusters in reduced [4Fe–4S] ferredoxins, the other a [4Fe–4S] cluster with a unique iron atom resembling those in hydratases such as aconitase [83,84]. The electron density distribution in the former case has been described as two ferrous irons and two mixed-valence iron atoms, coupled to give a ground state with $S = \frac{1}{2}$. High-resolution ^{57}Fe ENDOR at Q-band [85] combined with DFT calculations indicated that the two ferrous ions have distinctly different hyperfine interactions.
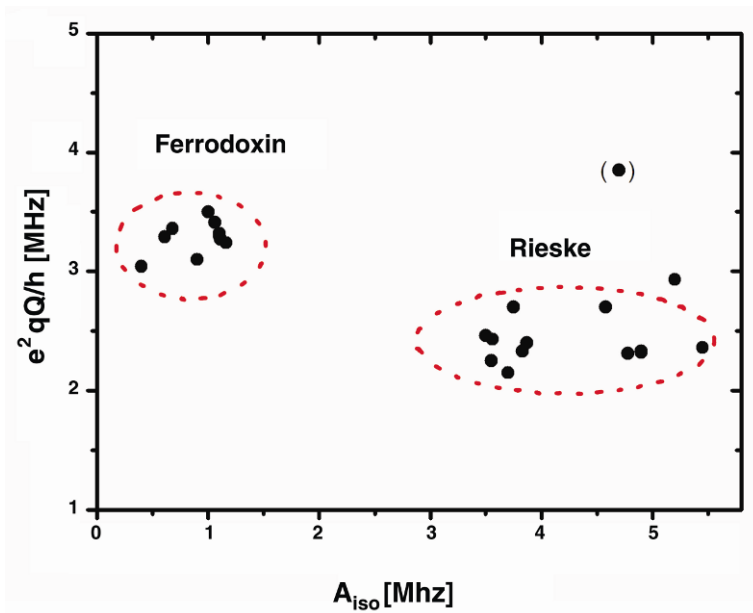
Figure 6. Plot of the couplings from different types of Fe–S clusters (e^2qQ/h vs. A_{iso}) with values taken from the references in Table 2. Please visit http://www.springer.com/978-1-4419-1138-4 to view a high-resolution full-color version of this illustration. Please visit http://www.springer.com/978-0-387-84855-6 to view a high-resolution full-color version of this illustration.

4. SELECTED EXAMPLES FROM ELECTRON-TRANSPORT CHAINS

4.1. Xanthine Dehydrogenase/Oxidase as a Model

Xanthine dehydrogenase is a membrane-associated enzyme involved in purine metabolism. It is present abundantly in milk, and so can be isolated in large quantities, so it was one of the first complex Fe–S proteins to be studied. There are a number of enzymes with similar structure but different substrate specificity, which have similar EMR properties, and it is an example of a number of oxidoreductases that involve an internal electron-transfer chain of Fe–S clusters. Specifically, these are the molybdopterin cofactor, at which the oxidation of xanthine occurs, two [2Fe–2S] clusters that transfer electrons, and a flavin (FAD) at which NAD becomes reduced. Extensive investigations of the protein were carried out in pioneering studies by Bray and colleagues, particularly on the molybdenum center. These were among the first to use rapid freezing to trap the enzyme in different stages of the catalytic cycle [86]. Two different EPR signals are observed from the Fe–S clusters in this and related proteins. One has an unusually high rhombicity, but

Table 2. Hyperfine couplings to ^{14}N determined by EMR

Center	A_{iso}, MHz	E^2qQ/h, MHz	Reference
Arthrospira ferredoxin [2Fe–2S]	1.0	3.5	[66]
Porfira umbilicalis ferredoxin	1.16	3.24	[74]
[2Fe–2S]	0.40	3.04	
Clostridium pasteurianum	0.61	3.29	[127]
[2Fe–2S] protein			
Fumarate reductase [2Fe–2S]	1.05	3.4	[68]
cluster 1			
[3Fe–4S] cluster 3	0.6	3.36	[128]
Arum maculatum succinate			
dehydrogenase			
[2Fe–2S] cluster 1	1.1	3.3	[66]
[3Fe–4S] cluster 3	0.82	3.24	
Xanthine oxidase reduced [2Fe–2S]	1.10	3.30	[87]
(both clusters similar)			
Rieske cluster in bovine heart			
mitochondrial membranes			
N^1	3.55	2.25	[64]
N^2	5.20	2.93	
Benzene dioxygenase Rieske-			
type [2Fe–2S] from HYSCORE			
N^1	3.56	2.33	[36]
N^2	4.78	2.46	
Benzene dioxygenase Rieske-type			
[2Fe–2S] ferredoxin from HYSCORE			
N^1	5.45	2.36	[129]
N^2	3.83	2.33	
Rieske cluster in cytochrome			
b_6f complex (spinach)			
N^1	4.58	2.70	[35]
N^2	3.75	2.70	
Burkholderia cepacia 2-halobenzoate		2.15	[130]
1,2-dioxygenase		3.85	
N^1	3.70		
N^2	4.70		
B. cepacia AC 1100 phthalate dioxy-			
genase from ENDOR N^1	4.3		[33]
N^2	5.5		
Rieske cluster in bovine heart mito-			
chondrial membranes N^1	3.55	2.25	[64]
N^2	5.20	2.93	
Rieske cluster in *Rhodobacter capsu-*			
ulatus bc$_1$ complex from ENDOR N^1	4.5		[112]
N^2	5.5		
Complex I cluster N1	0.9	3.1	[97]

after examination of the crystal structure of the protein it has emerged that this cluster is bound to a type 1 protein structure. ESEEM of the clusters in xanthine

oxidase showed that they were similar to those in typical [2Fe–2S] ferredoxins [87]. It appears that the lineshape of the cw-EPR spectra of Fe–S clusters is not a reliable indicator of the protein fold around the cluster.

4.2. Mitochondria and Aerobic Bacteria

An important achievement of the use of EPR in the study of mitochondria was the identification of a large number of Fe–S clusters [7,88,89]. The EPR signals were assigned by performing spectroscopy of isolated complexes. In many cases the overlapping spectra were only resolved by determining the temperature dependence of the constituent signals, which of course relates to the individual electron-spin relaxation times. Further resolution was achieved by selective reduction techniques, which in addition allowed their midpoint potentials to be determined. Potentiometric sample preparation methods made it possible to determine the midpoint redox potentials of the clusters [90].

4.3. Complex I (NADH:Ubiquinone Reductase)

Complex I is the least well understood of the major electron-transfer complexes of the mitochondrial respiratory chain. Similar proteins are observed in aerobic bacteria, plants, and yeast. It takes reducing equivalents from NADH on the matrix side of the membrane, and transfers them as electrons to ubiquinone, which is embedded in the membrane (Fig. 1). In the process it generates a proton gradient that leads to formation of ATP (for a recent review of Complex I see [91]). Complex I is the largest electron-transfer complex in the respiratory chain, and it also contains the greatest number of Fe–S clusters [90]. Originally they were designated clusters 1–6, on the basis of the temperature dependence of their EPR signals [88]. Subsequently the clusters were further subdivided on the basis of their redox potentials, and it was shown that the N_1 signals and N6 each represented two different species. The EPR signals of the clusters in reduced Complex I dominate the low-temperature spectra of mitochondria, and can be observed in samples of tissues such as heart and brain.

The recent crystallographic structure of the membrane-extrinsic portion of the enzyme from *Thermus thermophilus* has revealed the precise location of nine Fe–S clusters — N1a, N1b, N2, N3, N4, N5, N6a, N6b, and N7; the latter, however, however is only present in enzymes from some aerobic bacteria [92] (Fig. 1). N1a and N1b are [2Fe–2S] clusters, located near to the FMN, to take electrons from NADH. The other clusters are [4Fe–4S] and form a chain leading to cluster N2, located at the membrane surface. The assignment of clusters N4 and N5 has recently been disputed [93]. N2 is of particular interest because its redox potential is pH dependent, indicating that its reduction is linked to protonation and is probably related to proton translocation [94].

Figure 3 shows the cw-EPR spectrum of Complex I isolated from the yeast *Yarrowia lypolytica* at 12 K, revealing a complex overlapping pattern of at least

Fe–S clusters. Spectral simulation does allow a deconvolution of this spectrum to identify the g-tensors of each of the clusters; however, it is not possible to study individual clusters individually using advanced EMR. However, the recently introduced technique of Relaxation Filtered Hyperfine (REFINE) spectroscopy has been applied to Complex I to determine the amino-acid coordination of the N2 cluster [71]. It had been suggested that N2 has three coordinating cysteines and one histidine [95]. The experiments clearly excluded direct histidine coordination. Recently the 3D structure of the peripheral arm of Complex I (which contains all the Fe–S centers) has been solved [92,96] and confirms the assignments made from REFINE. More recent ESEEM and HYSCORE [97] confirmed the typical [2Fe–2S] ferredoxin-like structure, consistent with the crystal structure model [92]. Future work should elucidate the possible conformational changes suggested to occur during energy conservation in Complex I [98].

4.4. Complex II (Succinate:Quinone Reductase) and Quinol:Fumarate Reductase

Complex II, succinate:quinone reductase or succinate dehydrogenase, is an enzyme of the citric acid cycle, located in the mitochondrial membrane, which transfers electrons from succinate to ubiquinone. Quinol:fumarate reductase is a similar enzyme from bacteria such as *E. coli* grown under anaerobic conditions, and it catalyzes a similar ET reaction in the opposite direction, i.e., from a quinol to fumarate [99]. It is required for growth of the bacteria with fumarate as terminal electron acceptor. Although there are differences between the two enzymes in the redox potentials of their Fe–S clusters, they have many EPR characteristics in common. From EPR and MCD spectroscopy it was inferred that each enzyme comprises a [2Fe–2S], a [3Fe–4S] and a [4Fe–4S] cluster [100–102]. From the more recent crystal structures [103,104] it has emerged that the clusters are arranged in a chain from the flavin where succinate is oxidized, to the heme where quinones are reduced (Fig. 1).

The [3Fe–4S] cluster, called S3 in succinate:quinone reductase, has an $S = 1/2$ spin state when oxidized. Its signal dominates the EPR spectra of oxidized membranes of mitochondria and *E. coli*. On reduction by succinate it is reduced to an $S = 2$ state, so the narrow signal disappears. At a similar reduction potential, the [2Fe–2S] cluster S1 is reduced to an $S = 1/2$ state, which, together with the signal of Complex I cluster N1, gives rise to the origin of the "$g = 1.94$ signal" first observed by Beinert and Sands [3].

3-pulse ESEEM spectra were obtained of the reduced [2Fe–2S] cluster 1 of succinate dehydrogenase from beef heart [105], from *Arum maculatum* mitochondria [66], and *Escherichia coli* fumarate reductase [68]. In the latter case it was confirmed that this was due to interaction of the unpaired electron spin of the Fe–S cluster with a weakly coupled ^{14}N nucleus by measurements at different microwave frequencies. A three-pulse ESEEM experiment at $g = 1.94$ and an EPR frequency of 8.8 GHz yielded modulation frequencies at 0.9, 2.1, 3.0, and 4.2 MHz; at 11.4 GHz the components scaled with the magnetic field in a manner consistent with an

interaction with ^{14}N [68]. The very weak hyperfine coupling (about 1 MHz) indicated a coupling to a remote ^{14}N [63].

ESEEM spectra of the oxidized [3Fe–4S] clusters in fumarate reductase (Fig. 5a) were interpreted assuming that the two prominent lines are for the double-quantum ($\Delta m_S = 2$) transitions; this was found to be a good approximation for a similar weak coupling to the [3Fe–4S] cluster in *Thiocapsa roseopersicina* hydrogenase [106]. Simulation of the spectra of fumarate reductase using the density matrix formalism of Mims [99] indicated a nitrogen atom at a distance of 0.37 nm with $e^2qQ/h = 3.30$ MHz, consistent with peptide nitrogen [107]. Similar results have been obtained with succinate:quinone reductase from *Paracoccus denitrificans* [108]. Examination of the structure of the succinate dehydrogenase and fumarate reductase indicates that there are three potential peptide nitrogens within 0.4 nm of the [2Fe–2S] cluster. There is also the possibility of NH-S hydrogen bonds, as seen in the [2Fe–2S] ferredoxin [51]. The parameters are listed in Table 2.

Cluster S2 is a [4Fe–4S] cluster and is paramagnetic in the reduced state. There is a spin–spin interaction between reduced clusters 1 and 2, which increases the spin relaxation rate of S1 when S2 becomes reduced. The existence of S2 was first indicated indirectly by the increase of the $g = 1.94$ signal of cluster S1, measured under saturating microwave power, when S2 became reduced. The enhancement of the spin–spin relaxation rate of cluster S1 is readily detected by spin-echo EPR [63]. The signal of S2 itself is very broad, probably due to spin–spin interaction with the $S = 2$ reduced state of cluster S3, so that in the first-derivative cw-EPR spectra the signal is easily lost in the baseline. By using field-swept spin-echo-detected EPR, the spectrum of center 2 in fumarate reductase was observed, and ESEEM spectra were recorded [63].

[3Fe–4S] clusters appear in the EMR spectra of a number of complex iron–sulfur proteins such as succinate:quinone reductase, fumarate reductase, and nitrate reductase, in the oxidized state. Their EPR signals appear at temperatures below 100 K, with g-factors in the range 2.00–2.05. Initially these were assigned to the "HiPIP-type" [4Fe–4S]$^{3+}$ clusters (see below), but after the discovery of [3Fe–4S] clusters that give EPR signals in the same region [27], it became necessary to distinguish between the two types of clusters. Their magnetic circular dichroism (MCD) spectra were found to be distinct [109], and in particular the MCD magnetization curves of the reduced clusters were shown to be characteristic of the $S = 2$ ground state. Another method, developed by Bill Mims, the pioneer of a number of useful pulsed EPR techniques [110], is the linear electric field effect (LEFE). In this experiment the amplitude of the spin echo from either a 2- or 3-pulse spin-echo sequence is diminished by the application of a pulsed electrostatic field to the sample coincident with the second microwave pulse. The parameter σ, the electrostatic field required to reduce the echo amplitude by 50%, is plotted against applied magnetic field B (Fig. 7b). This method has been somewhat neglected in recent years, as it requires a pulsed electrostatic field source and a special cavity. However, it is quite rapid and diagnostic of noncentrosymmetric
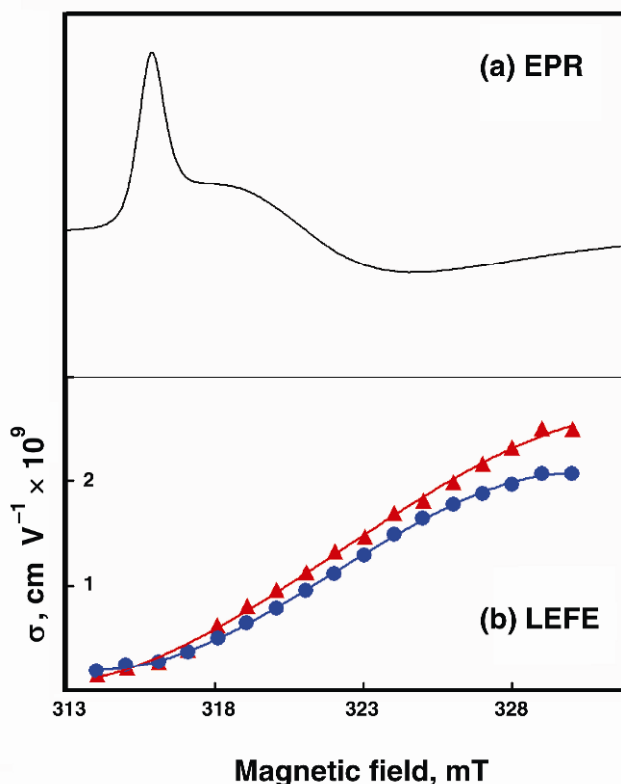
Figure 7. (a) Cw-EPR and (b) LEFE spectra of the oxidized [3Fe–4S] cluster in *E. coli* fumarate reductase. After [68]. Please visit http://www.springer.com/978-1-4419-1138-4 to view a high-resolution full-color version of this illustration.

paramagnetic centers. Thus it is an incisive way of distinguishing between the "HiPIP-type" $[4Fe–4S]^{3+}$ clusters and the [3Fe–4S] clusters in their oxidized states. Peisach et al. demonstrated that the LEFE pattern is characteristic for the cluster type [111], and used it to demonstrate that center 3 in succinate dehydrogenase is a [3Fe–4S] cluster [62]. An application to Cluster 3 of fumarate reductase is illustrated in Figure 7, showing a pattern characteristic of the [3Fe–4S] type, an assignment that has subsequently been verified by X-ray crystallography [103].

4.5. Complex III

Ubiquinol:cytochrome-c reductase (Complex III or bc_1 complex) comprises a Rieske [2Fe–2S] protein, three hemes, designated cytochromes b_{562}, b_{566} and c_1, and two quinone/quinol binding sites. Both ENDOR and ESEEM were used to determine that the Rieske cluster has two histidine residues as ligands to one iron

atom, the other one being bound by cysteines [35,112]. The existence of histidine nitrogen ligands to Rieske clusters was first proposed on the basis of Mössbauer spectroscopy [113], and this was further elucidated by orientation-selective ^{14}N ENDOR spectroscopy [34]. The high redox potential of Rieske clusters means that they can be reduced to the paramagnetic state under conditions where other types of clusters are oxidized, hence the EPR signals can be observed selectively. Pulsed-EPR and cw-ENDOR spectra were recorded of the Rieske cluster in bovine heart mitochondrial membranes, poised at a potential where the other clusters in the respiratory chain are oxidized [64]. Cluster S3 of Complex II was the only other cluster that was paramagnetic under these conditions. The Rieske cluster could be selected because of the wider range of g-factors, but the spectral overlap precluded a complete orientation-selection data set. Similar clusters are found in the "Rieske" dioxygenases [114], which use them as electron carriers to the nonheme iron active sites.

Movement of the Rieske cluster between two distinct sites in the complex is an important part of the Complex III Q-cycle mechanism by which the complex pumps protons across the membrane [115]. In one site, a histidine ligand is proposed to be hydrogen-bonded to a ubiquinone/ubiquinol. Changes in the hydrogen bonding can be observed as changes in the g-factors of the reduced Rieske cluster. Two inhibitors, myxothiazol and stigmatellin, which mimic the binding of ubiquinone and ubiquinol to the complex, have been suggested to maintain the Rieske protein in these two different positions, as has been observed previously by crystallography. This was demonstrated in the bc_1 complex of *Rhodobacter sphaeroides* using orientation-selective ESEEM [116]. Observed hyperfine and quadrupolar couplings suggested that when quinone is present in the site the interaction of the histidine atoms of the Rieske cluster is similar to that observed when stigmatellin is present, and is different from the configuration in the presence of myxothiazol [116]. This reorientation of the Rieske protein has been directly observed as a change in the g-tensor orientation of the reduced Rieske cluster in the cytochrome bc_1 complex from *Rhodovolum sulfidophilum* [117]. HYSCORE spectroscopy can be used to subtly probe the exact coordination and geometry of the coordinating histidines groups [38]. An example of the HYSCORE spectrum obtained from isolated yeast Complex III (*Saccharomyces cerevisiae*) containing myxothiazol is shown in Figure 8, revealing clearly the double quantum transitions (ν_{dq}^{N1} and ν_{dq}^{N2}) at [–2.7, 6.7] and [–3.5, 7.5] MHz, respectively, for each of the two coordinating histidine nitrogen (N_δ) atoms.

4.6. Microbial Anaerobic Respiration

4.6.1. Nitrate Reductase

Together with formate dehydrogenase, this molybdenum-containing Fe–S protein forms a system that pumps protons across the membrane of bacteria such as *E. coli* using a classic Mitchell loop mechanism [118]. The protein contains an Mo–pyranopterin group and five [4Fe–4S] clusters; the cluster nearest to the Mo cofac-

tor has one histidine ligand, and exists in an $S = 3/2$ state on reduction [119]. A stabilized semiquinone intermediate has been observed in *E. coli* nitrate reductase and studied by ENDOR [120].
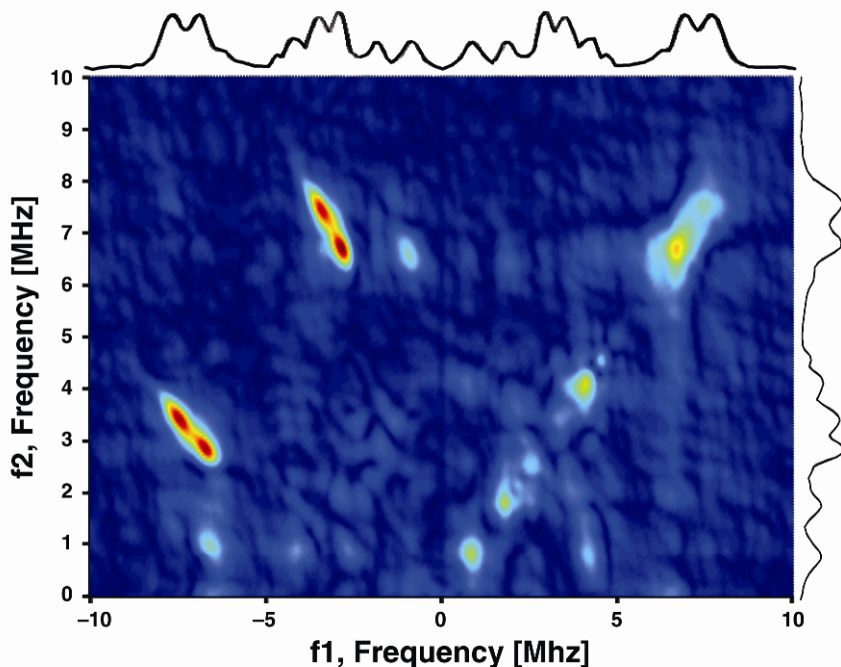
Figure 8. HYSCORE spectrum of Complex III from yeast (*Saccharomyces cerevisiae*) measured at $g_y = 1.91$ with $\tau = 132$ ns, showing both the (+,–) and (+,+) quadrants. F. Mac-Millan (UEA Norwich) and Carola Hunte (University of Leeds), unpublished data. Please visit http://www.springer.com/978-1-4419-1138-4 to view a high-resolution full-color version of this illustration.

4.6.2. Methanogenesis: Heterodisulfide Reductase

Heterodisulfide reductase is an Fe–S protein that catalyzes the reversible two-electron reduction of mixed disulfides to thiol coenzymes in a process termed disulfide respiration. This enzyme uses a [4Fe–4S] cluster to mediate this disulfide reduction. From [57]Fe and [33]S labeling, together with both cw-EPR and variable-temperature MCD spectroscopy [121], the mechanism was proposed to involve a novel substrate-bound [4Fe–4S][3+] cluster with two thiolate ligands at a unique Fe site. Recently compelling evidence for this structure was demonstrated by [57]Fe pulsed ENDOR spectroscopy at 9 and 94 GHz [122]. One interesting aspect of this work was the assignment information obtained from highly polarized patterns in

the W-band ENDOR spectra, which permit the sign of the observed hyperfine coupling to be determined. There had been prior evidence of pentacoordinated [4Fe–4S]$^{3+}$ clusters in ferredoxin:thioredoxin reductase, which also catalyzes disulfide cleavage [123]. A common C-terminal binding motif (designated CCG) has very recently been identified for this novel [4Fe–4S] cluster [124].

4.6.3. Photosynthetic Electron-Transport Chains

Fe–S clusters are electron acceptors in the photosynthetic ET chains of chloroplasts, cyanobacteria, and green photosynthetic bacteria. Their spectra have been observed by cw-EPR, but to date most studies using pulsed EPR have been directed at flash-induced kinetics of ET from P$_{700}$, the primary donor chlorophyll pair, through the secondary carrier chlorophyll A$_1$, to the Fe–S clusters. If ET beyond A$_1$ is blocked, a strong spin-polarized triplet is observed, due to the electron spin-polarized pair P-700^{+}/A$_1^{-}$ [125]. Electron-spin relaxation of the chlorophyll radicals has been measured by pulsed EPR, and the rates were enhanced in the presence of the Fe–S clusters when in their paramagnetic reduced states [126].

5. CONCLUSIONS

The practical application of pulsed EPR methods has developed along parallel paths to those of pulsed NMR, but leading to different outcomes. Multifrequency techniques, double and triple resonance, high-field EPR, and a plethora of other methods have all provided extra information about paramagnetic systems that would be difficult to obtain in other ways. Advanced EPR techniques are more powerful in the context of structural data from X-ray crystallography. Indeed they are complementary, in that they can observe transient states that cannot be crystallized, and observe interactions with protons, which are not detected in X-ray electron density maps. Many of the potential applications are tantalizingly close to the limits of detection for current instrumentation. In pilot studies, ESEEM and cw-ENDOR have been applied to more biological targets such as whole microbial cells and mitochondrial preparations. There are many possibilities for development in the biological preparation techniques. The use of selective mutant proteins, selective isotope substitution, and ultimately the growth of single crystals will greatly enhance the power of advanced EMR techniques. Improvements would allow the use of EMR to examine more about the structural changes related to the function of electron-transfer complexes. In summary, a wealth of new information awaits future exploration of multifrequency, multidimensional EMR techniques.

Reinhard Kappl, David Lowe, John McCracken, Jack Peisach, Bill Rutherford, Jas Shergill, and Joel Weiner.

ABBREVIATIONS

cw, continuous-wave
DFT, density-functional theory
EMR, electron magnetic resonance
ENDOR, electron-nuclear double resonance
EPR, electron paramagnetic resonance
ESEEM, electron spin-echo envelope modulation
ET, electron-transfer
Fe–S, iron–sulfur
HiPIP, high-potential iron–sulfur protein
HYSCORE, hyperfine sublevel correlation spectroscopy
MCD, magnetic circular dichroism
NQR, nuclear quadrupole resonance
PELDOR, pulsed electron-electron double resonance spectroscopy
REFINE, relaxation filtered hyperfine spectroscopy

NOTE

1. In this review we use the term EMR, electron magnetic resonance, to encompass all magnetic resonance techniques that examine paramagnetic systems, including multifrequency EPR, ENDOR, ELDOR, ESEEM, HYSCORE, etc.

REFERENCES

1.   Malkin R, Bearden AJ. 1971. Primary reactions of photosynthesis: photoreduction of a bound chloroplast ferredoxin at low temperature as detected by EPR spectroscopy. *Proc Natl Acad Sci USA* **68**:16–19.
2.   Evans MCW, Sihra CK, Bolton JR, Cammack R. 1975. Primary electron acceptor complex of Photosystem I in spinach chloroplasts, *Nature* **256**:668–670.
3.   Beinert H, Sands RH. 1960. Studies on succinic and DPNH dehydrogenase preparations by paramagnetic resonance (EPR) spectroscopy. *Biochem Biophys Res Commun* **3**:41–46.
4.   Beinert H, Lee W. 1961. Evidence for a new type of iron containing electron carrier in mitochondria. *Biochem Biophys Res Commun* **5**:40–45.
5.   Orme-Johnson NR, Orme-Johnson WH, Hansen RE, Beinert H, Hatefi Y. 1971. EPR-detectable electron acceptors in submitochondrial particles from beef heart with special reference to iron–sulfur components of DPNH–ubiquinone reductase. *Biochem Biophys Res Commun* **44**:446–452.

6.   Ohnishi T, Wilson DF, Chance B, Asakura T. 1972. Studies on iron–sulfur proteins in site I region of respiratory chain in pigeon heart mitochondria and submitochondrial particles. *Biochem Biophys Res Commun* **46**:1631–1638.

7.   Beinert H, Albracht SPJ. 1982. New insights, ideas and unanswered questions concerning iron–sulfur clusters in mitochondria. *Biochim Biophys Acta* **683**:245–277.

8.   Page CC, Moser CC, Chen XX, Dutton PL. 1999. Natural engineering principles of electron tunnelling in biological oxidation-reduction. *Nature* **402**:47–52.

9.   Gray HB, Winkler JR. 1996. Electron transfer in proteins. *Ann Rev Biochem* **65**:537–561.

10. Svistunenko DA, Davies N, Brealey D, Singer M, Cooper CE. 2006. Mitochondrial dysfunction in patients with severe sepsis: an EPR interrogation of individual respiratory chain components. *Biochim Biophys Acta Bioenerg* **1757**:262–272.

11. Atamna H, Walter PB, Ames BN. 2002. The role of heme and iron–sulfur clusters in mitochondrial biogenesis, maintenance, and decay with age. *Arch Biochem Biophys* **397**:345–353.

12. Brown GC. 1999. Nitric oxide and mitochondrial respiration. *Biochim Biophys Acta Bioenerg* **1411**:351–369.

13. Salerno JC, Blum H, Ohnishi T. 1979. Orientation of iron–sulfur clusters and a spin-coupled ubiquinone pair in the mitochondrial membrane. *Biochim Biophys Acta* **547**:270–281.

14. Blum H, Poole RK, Ohnishi. T. 1980. The orientation of iron–sulphur clusters in membrane multilayers prepared from aerobically-grown *Escherichia coli* K12 and a cytochrome-deficient mutant. *Biochem J* **190**:385–393.

15. Schweiger A, Jeschke G. 2001. *Principles of pulse electron paramagnetic resonance*. Oxford: Oxford UP.

16. Prisner T, Rohrer M, MacMillan F. 2001. Pulsed EPR spectroscopy: biological applications. *Annu Rev Phys Chem* **52**:279–313.

17. Bennati M, Prisner TF. 2005. New developments in high field electron paramagnetic resonance with applications in structural biology. *Rep Prog Phys* **68**:411–448.

18. Hagen WR. 1981. Dislocation strain broadening as a source of anisotropic linewidth and asymmetrical lineshape in EPR spectrum of metalloproteins and related systems. *J Magn Reson* **44**:447–469.

19. Beinert H, Holm RH, Münck E. 1997. Iron–sulfur clusters: nature's modular, multipurpose structures. *Science* **277**:653–659.

20. Cammack R. 1992. Iron–sulfur clusters in enzymes: themes and variations. *Adv Inorg Chem* **38**:281–322.

21. Meyer J. 2008. Iron–sulfur protein folds, iron–sulfur chemistry, and evolution. *J Biol Inorg Chem* **13**:157–170.

22. Gibson JF, Hall DO, Thornley JHM, Whatley FR. 1966. The iron complex in spinach ferredoxin. *Proc Natl Acad Sci USA* **56**:987–990.

23. Thornley JHM, Gibson JF, Whatley FR, Hall DO. 1966. Comment on a recent model of the iron complex in spinach ferredoxin. *Biochem Biophys Res Commun* **24**:877–879.

24. Tsibris JCM, Woody RW. 1970. Structural studies of iron–sulfur proteins. *Coord Chem Rev* **5**:417–458.

25. Dunham WR, Palmer G, Sands RH, Bearden AJ. 1971. On the structure of the iron–sulfur complex in the two-iron ferredoxins. *Biochim Biophys Acta* **253**:373–384.

26. Cammack R, Gay E, Shergill JK. 1999. Studies of hyperfine interactions in [2Fe–2S] proteins by EPR and double resonance spectroscopy. *Coord Chem Rev* **192**:1003–1022.

27. Beinert H, Thomson AJ. 1983. 3-iron clusters in iron–sulfur proteins. *Arch Biochem Biophys* **222**:333–361.

28. Ruzicka FJ, Beinert H. 1978. The soluble "high potential" type iron–sulfur protein from mitochondria is aconitase. *J Biol Chem* **253**:2514–2517.

29. Thomson AJ, Robinson AE, Johnson MK, Moura JJG, Moura I, Xavier AV, Legall J. 1981. The 3-iron cluster in a ferredoxin from *Desulfovibrio gigas*: a low-temperature magnetic circular-dichroism study. *Biochim Biophys Acta* **670**:93–100.

30. Meyer J. 2001. Ferredoxins of the third kind. *FEBS Lett* **509**:1–5.

31. Yeh AP, Ambroggio XI, Andrade SLA, Einsle O, Chatelet C, Meyer J, Rees DC. 2002. High resolution crystal structures of the wild type and Cys-55 → Ser and Cys-59 → Ser variants of the thioredoxin-like [2Fe–2S] ferredoxin from *Aquifex aeolicus*. *J Biol Chem* **277**:34499–34507.

32. Grinberg O, Berliner LJ, eds. 2004. *Very high frequency (VHF) ESR/EPR*, Vol. 22. New York: Plenum.

33. Gurbiel RJ, Batie CJ, Sivaraja M, True AE, Fee JA, Hoffman BM, Ballou DP. 1989. Electron nuclear double resonance spectroscopy of ^{15}N-enriched phthalate dioxygenase from *Pseudomonas cepacia* proves that 2 histidines are coordinated to the [2Fe–2S] Rieske-type clusters. *Biochemistry* **28**:4861–4871.

34. Hoffman BM, DeRose V, Doan PE, Gurbiel RJ, Houseman ALP, Telser J. 1993. Metalloenzyme active-site structure and function through multifrequency CW and pulsed ENDOR. In *Biological magnetic resonance: EMR of paramagnetic molecules*, pp. 151–218. Ed LJ Berliner, J Reuben. New York: Plenum.

35. Britt RD, Sauer K, Klein MP, Knaff DB, Kriauciunas A, Yu CA, Yu L, Malkin R. 1991. Electron-spin echo envelope modulation spectroscopy supports the suggested coordination of 2 histidine ligands to the Rieske Fe–S centers of the cytochrome–b_6f complex of spinach and the cytochrome–bc1 complexes of *Rhodospirillum rubrum*, *Rhodobacter sphaeroides* R-26, and Bovine Heart Mitochondria. *Biochemistry* **30**:1892–1901.

36. Shergill JK, Joannou C, Mason JR, Cammack R. 1995. Coordination of the Rieske-type [2Fe–2S] cluster of the terminal iron–sulfur protein of *Pseudomonas putida* benzene-1,2-dioxygenase, studied by 1D- and 2D-ESEEM spectroscopy. *Biochemistry* **34**: 16533–16542.

37. Iwasaki T, Kounosu A, Uzawa T, Samoilova RI, Dikanov SA. 2004. Orientation-selected ^{15}N-HYSCORE detection of weakly coupled nitrogens around the archaeal Rieske 2Fe–2S center. *J Am Chem Soc* **126**:13902–13903.

38. Dikanov SA, Shubin AA, Kounosu A, Iwasaki T, Samoilova RI. 2004. A comparative, two-dimensional ^{14}N ESEEM characterization of reduced 2Fe–2S clusters in hyper-thermophilic archaeal high- and low-potential Rieske-type proteins. *J Biol Inorg Chem* **9**:753–767.

39. Iwasaki T, Kounosu A, Samoilova RI, Dikanov SA. 2006. [15]N HYSCORE characterization of the fully deprotonated, reduced form of the archaeal Rieske 2Fe–2S center. *J Am Chem Soc* **128**:2170–2171.

40. Mims WB, Peisach J. 1981. Electron spin echo spectroscopy and the study of metalloproteins. in *Biological magnetic resonance*, pp. 213–263. Ed LJ Berliner, J Reuben. New York: Plenum.

41. Britt RD. 1993. Time-domain electron paramagnetic resonance spectroscopy. *Curr Opin Struct Biol* **3**:774–779.

42. Lowe DJ, Lynden-Bell RM, Bray RC. 1972. Spin–spin interaction beween molybdenum and one of the iron–sulphur systems of xanthine oxidase and its relevance to the enzymic mechanism. *Biochem J* **130**:239–249.

43. Barber MJ, Salerno JC, Siegel LM. 1982. Magnetic interactions in milk xanthine oxidase. *Biochemistry* **21**:1648–1656.

44. Elsasser C, Monien B, Haehnel W, Bittl R. 2005. Orientation of spin labels in de novo peptides. *Magn Reson Chem* **43**:S26–S33.

45. Bowman MK, Maryasov AG, Kim N, DeRose VJ. 2004. Visualization of distance distribution from pulsed double electron–electron resonance data. *Appl Magn Reson* **26**:23–39.

46. Blum H, Harmon HJ, Leigh JS, Salerno JC, Chance B. 1978. Orientation of a heme of cytochrome-c oxidase in submitochondrial particles. *Biochim Biophys Acta* **502**:1–10.

47. Seelig J, Borle F, Cross TA. 1985. Magnetic ordering of phospholipid membranes. *Biochim Biophys Acta* **814**:195–198.

48. Guigliarelli B, Guillaussier J, More C, Setif P, Bottin H, Bertrand P. 1993. Structural organization of the iron–sulfur centers in *Synechocystis*–6803 photosystem I: EPR study of oriented thylakoid membranes and analysis of the magnetic interactions. *J Biol Chem* **268**:900–908.

49. Jordan P, Fromme P, Witt HT, Klukas O, Saenger W, Krauss N. 2001. Three-dimensional structure of cyanobacterial photosystem I at 2.5 angstrom resolution. *Nature* **411**:909–917.

50. Dikanov SA, Bowman MK. 1998. Determination of ligand conformation in reduced [2Fe–2S] ferredoxin from cysteine beta-proton hyperfine couplings. *J Biol Inorg Chem* **3**:18–29.

51. Canne C, Ebelshauser M, Gay E, Shergill JK, Cammack R, Kappl R, Hüttermann J. 2000. Probing magnetic properties of the reduced [2Fe–2S] cluster of the ferredoxin from *Arthrospira platensis* by ^{1}H ENDOR spectroscopy. *J Biol Inorg Chem* **5**:514–526.

52. Muller A, Tscherny I, Kappl R, Hatchikian EC, Hüttermann J, Cammack R. 2002. Hydrogenases in the "active" state: determination of g-matrix axes and electron spin distribution at the active site by H-1 ENDOR spectroscopy. *J Biol Inorg Chem* **7**:177–194.

53. Foerster S, van Gastel M, Brecht M, Lubitz W. 2005. An orientation-selected ENDOR and HYSCORE study of the Ni–C active state of *Desulfovibrio vulgaris* Miyazaki F hydrogenase. *J Biol Inorg Chem* **10**:51–62.

54. Lubitz W, Reijerse E, van Gastel M. 2007. [NiFe] and [FeFe] hydrogenases studied by advanced magnetic resonance techniques. *Chem Rev* **107**:4331–4365.

55. Dugad LB, Lamar GN, Banci L, Bertini I. 1990. Identification of localized redox states in plant–type 2 iron ferredoxins using the nuclear Overhauser effect. *Biochemistry* **29**:2263–2271.

56. Hudder BN, Morales JG, Stubna A, Münck E, Hendrich MP, Lindahl PA. 2007. Electron paramagnetic resonance and Mössbauer spectroscopy of intact mitochondria from respiring *Saccharomyces cerevisiae*. *J Biol Inorg Chem* **12**:1029–1053.

57. Ruzicka FJ, Beinert H, Schepler KL, Dunham WR, Sands RH. 1975. Interaction of ubisemiquinone with a paramagnetic component in heart tissue. *Proc Natl Acad Sci USA* **72**:2886–2890.

58. Salerno JC, Ohnishi T, Lim J, Widger WR, King TE. 1977. Spin coupling between electron carriers in dehydrogenase segments of respiratory chain. *Biochem Biophys Res Commun* **75**:618–624.

59. Vinogradov AD, Sled VD, Burbaev DS, Grivennikova VG, Moroz IA, Ohnishi T. 1995. Energy-dependent complex I-associated ubisemiquinones in submitochondrial particles. *FEBS Lett* **370**:83–87.

60. van Belzen R, Kotlyar AB, Moon N, Dunham WR, Albracht SPJ. 1997. The iron–sulfur clusters 2 and ubisemiquinone radicals of NADH:ubiquinone oxidoreductase are involved in energy coupling in submitochondrial particles. *Biochemistry* **36**:886–893.

61. Yano T, Dunham WR, Ohnishi T. 2005. Characterization of the $\Delta\mu_{H+}$-sensitive ubisemiquinone species (SQ(Nf)) and the interaction with cluster N2: New insight into the energy-coupled electron transfer in complex I. *Biochemistry* **44**:1744–1754.

62. Ackrell B, Kearney E, Mims W, Peisach J, Beinert H. 1984. Iron–sulfur cluster 3 of beef heart succinate–ubiquinone oxidoreductase is a 3-iron cluster. *J Biol Chem* **259**:4015–4018.

63. Shergill JK, Cammack R, Weiner JH. 1991. Electron spin-echo envelope modulation and spin spin interaction studies of the iron sulfur clusters in fumarate reductase of *Escherichia coli. J Chem Soc Faraday* **87**:3199–3202.

64. Shergill JK, Cammack R. 1994. ESEEM and ENDOR studies of the Rieske iron–sulfur protein in bovine heart mitochondrial membranes. *Biochim Biophys Acta* **1185**:35–42.

65. Mileni M, MacMillan F, Tziatzios C, Zwicker K, Haas AH, Mantele W, Simon J, Lancaster CRD. 2006. Heterologous production in *Wolinella succinogenes* and characterization of the quinol:fumarate reductase enzymes from *Helicobacter pylori* and *Campylobacter jejuni. Biochem J* **395**:191–201.

66. Shergill JK, Cammack R. 1994. ESEEM studies of the iron–sulfur clusters of succinate dehydrogenase in *Arum maculatum* spadix mitochondrial membranes. *Biochim Biophys Acta Bioenerg* **1185**:43–49.

67. Cammack R, Palmer JM. 1977. Iron–sulphur centres in mitochondria from *Arum maculatum* spadix with very high rates of cyanide-resistant respiration. *Biochem J* **166**:347–355.

68. Cammack R, Chapman A, McCracken J, Cornelius JB, Peisach J, Weiner JH. 1988. Electron spin-echo spectroscopic studies of *Escherichia coli* fumarate reductase. *Biochim Biophys Acta* **956**:307–312.

69. Gayda J-P, Bertrand P, Deville A, More G, Gibson JF, Cammack R. 1979. Temperature dependence of the electronic spin-lattice relaxation time in a 2-iron–2-sulfur protein. *Biochim Biophys Acta* **581**:15–26.

70. Gayda J-P, Bertrand P, More C, LeGall J, Cammack R. 1981. Energy of the low-lying excited levels for some reduced [4Fe–4S] ferredoxins, from the relaxation broadening of the EPR signals. *Biochem Biophys Res Commun* **99**:1265–1270.

71. Maly T, MacMillan F, Zwicker K, Kashani-Poor N, Brandt U, Prisner TF. 2004. Relaxation filtered hyperfine (REFINE) spectroscopy: a novel tool for studying overlapping biological electron paramagnetic resonance signals applied to mitochondrial complex I. *Biochemistry* **43**:3969–3978.

72. Maly T, Prisner TF. 2004. Relaxation filtered hyperfine spectroscopy (REFINE). *J Magn Reson* **170**:88–96.

73. Stoll S, Schweiger A. 2006. EasySpin, a comprehensive software package for spectral simulation and analysis in EPR. *J Magn Reson* **178**:42–55.

74. Dikanov SA, Tyryshkin AM, Felli I, Reijerse EJ, Hüttermann J. 1995. C-band ESEEM of strongly-coupled peptide nitrogens in reduced two-iron ferredoxin. *J Magn Reson B* **108**:99–102.

75. Kappl R, Ebelshauser M, Hannemann F, Bernhardt R, Hüttermann J. 2006. Probing electronic and structural properties of the reduced [2Fe–2S] cluster by orientation-selective H-1 ENDOR spectroscopy: adrenodoxin versus Rieske iron–sulfur protein. *Appl Magn Reson* **30**:427–459.

76. Jensen GM, Warshel A, Stephens PJ. 1994. Calculation of the redox potentials of iron–sulfur proteins: the 2-/3- Couple of [Fe4s4·Cys(4)] clusters in *Peptococcus aerogenes* ferredoxin, *Azotobacter vinelandii* ferredoxin-I, and *Chromatium vinosum* high-potential iron protein. *Biochemistry* **33**:10911–10924.

77. Astashkin AV, Dikanov SA, Tsvetkov YD. 1984. Modulation effects from N-14 and N-15 nitrogen nuclei in the electron-spin echo of imidazoline nitroxyl radicals containing the 2-oximinoalkyl group. *J Struct Chem* **25**:45–55.

78. Reijerse EJ, Keijzers CP. 1987. Model calculations of frequency-domain ESEEM spectra of disordered-systems. *J Magn Reson* **71**:83–96.

79. Flanagan HL, Singel DJ. 1987. Analysis of N-14 ESEEM patterns of randomly oriented solids. *J Chem Phys* **87**:5606–5616.

80. LePape L, Lamotte B, Mouesca JM, Rius G. 1997. Paramagnetic states of four iron four sulfur clusters, 1: EPR single-crystal study of 3+ and 1+ clusters of an asymmetrical model compound and general model for the interpretation of the g-tensors of these two redox states. *J Am Chem Soc* **119**:9757–9770.

81. LePape L, Lamotte B, Mouesca JM, Rius G. 1997. Paramagnetic states of four iron four sulfur clusters, 2: proton ENDOR study of a 1+ state in an asymmetrical cluster. *J Am Chem Soc* **119**:9771–9781.

82. Moriaud F, Gambarelli S, Lamotte B, Mouesca JM. 2001. Detailed proton Q-band ENDOR study of the electron spin population distribution in the reduced [4Fe–4S](1+) state. *J Phys Chem B* **105**:9631–9642.

83. Werst MM, Kennedy MC, Houseman ALP, Beinert H, Hoffman BM. 1990. Characterization of the [4Fe–4S]$^+$ cluster at the active site of aconitase by Fe-57, S-33, and N-14 electron nuclear double resonance spectroscopy. *Biochemistry* **29**:10533–10540.

84. Werst MM, Kennedy MC, Beinert H, Hoffman BM. 1990. O-17, H-1, and H-2 electron nuclear double resonance characterization of solvent, substrate, and inhibitor binding to the [4Fe–4S]+ cluster of aconitase. *Biochemistry* **29**:10526–10532.

85. Moriaud F, Gambarelli S, Lamotte B, Mouesca JM. 2001. Single-crystal Fe-57 Q-band ENDOR study of the 4 iron–4 sulfur cluster in its reduced [4Fe–4S](1+) state. *J Magn Reson* **153**:238–245.

86. Bray RC. 1961. Chemistry of xanthine oxidase, 8: electron-spin-resonance measurements during enzymic reaction. *Biochem J* **81**:196–199.

87. Cammack R, Chapman A, McCracken J, Peisach J. 1991. Electron spin-echo spectroscopy of the iron sulfur clusters of xanthine-oxidase from milk. *J Chem Soc Faraday* **87**:3203–3206.

88. Orme-Johnson NR, Hansen RE, Beinert H. 1974. Electron-paramagnetic resonance-detectable electron-acceptors in beef heart mitochondria: reduced diphosphopyridine nucleotide ubiquinone reductase segment of electron-transfer system. *J Biol Chem* **249**:1922–1927.

89. Orme-Johnson NR, Hansen RE, Beinert H. 1974. Electron-paramagnetic resonance-detectable electron acceptors in beef heart mitochondria: ubihydroquinone–cytochrome-c reductase segment of electron-transfer system and complex mitochondrial fragments. *J Biol Chem* **249**:1928–1939.

90. Ohnishi T, Sled VD, Yano T, Yagi T, Burbaev DS, Vinogradov AD. 1998. Structure–function studies of iron–sulfur clusters and semiquinones in the NADH–Q oxidoreductase segment of the respiratory chain. *Biochim Biophys Acta Bioenerg* **1365**:301–308.

91. Brandt U. 2006. Energy converting NADH:quinone oxidoreductase (complex I). *Ann Rev Biochem* **75**:69–92.

92. Sazanov LA, Hinchliffe P. 2006. Structure of the hydrophilic domain of respiratory complex I from *Thermus thermophilus*. *Science* **311**:1430–1436.

93. Yakovlev G, Reda T, Hirst J. 2007. Reevaluating the relationship between EPR spectra and enzyme structure for the iron–sulfur clusters in NADH: quinone oxidoreductase. *Proc Natl Acad Sci USA* **104**:12720–12725.

94. Galkin A, Drose S, Brandt U. 2006. The proton pumping stoichiometry of purified mitochondrial complex I reconstituted into proteoliposomes. *Biochim Biophys Acta* **1757**:1575–1581.

95. Garofano A, Zwicker K, Kerscher S, Okun P, Brandt U. 2003. Two aspartic acid residues in the PSST-homologous NUKM subunit of complex I from *Yarrowia lipolytica* are essential for catalytic activity. *J Biol Chem* **278**:42435–42440.

96. Hinchliffe P, Sazanov LA. 2005. Organization of iron–sulfur clusters in respiratory complex I. *Science* **309**:771–774.

97. Maly T, Grgic L, Zwicker K, Zickermann V, Brandt U, Prisner T. 2006. Cluster N1 of complex I from *Yarrowia lipolytica* studied by pulsed EPR spectroscopy. *J Biol Inorg Chem* **11**:343–350.

98. Ohnishi T, Salerno JC. 2005. Conformation-driven and semiquinone-gated proton pump mechanism in the NADH–ubiquinone oxidoreductase (complex I). *FEBS Lett* **579**:4555–4561.

99. Cecchini G, Schroder I, Gunsalus RP, Maklashina E. 2002. Succinate dehydrogenase and fumarate reductase from *Escherichia coli*. *Biochim Biophys Acta Bioenerg* **1553**:140–157.

100. Johnson MK, Morningstar JE, Cecchini G, Ackrell BAC. 1985. Detection of a tetranuclear iron sulphur centre in fumarate reductase from *Escherichia coli* by EPR. *Arch Microbiol* **131**:756–762.

101. Johnson MK, Morningstar JE, Bennett DE, Ackrell BAC, Kearney EB. 1985. Magnetic circular dichroism studies of succinate dehydrogenase: evidence for [2Fe–2S], [3Fe–4S], and [4Fe–4S] centres in reconstitutively active enzyme. *J Biol Chem* **260**:7368–7379.

102. Cammack R, Patil DS, Weiner JH. 1986. Evidence that center-2 in *Escherichia coli* fumarate reductase is a [4Fe–4S] cluster. *Biochim Biophys Acta* **870**:545–551.

103. Iverson TM, Luna-Chavez C, Croal LR, Cecchini G, Rees DC. 2002. Crystallographic studies of the *Escherichia coli* quinol-fumarate reductase with inhibitors bound to the quinol-binding site. *J Biol Chem* **277**:16124–16130.

104. Yankovskaya V, Horsefield R, Tornroth S, Luna-Chavez C, Miyoshi H, Leger C, Byrne B, Cecchini G, Iwata S. 2003. Architecture of succinate dehydrogenase and reactive oxygen species generation. *Science* **299**:700–704.

105. Lobrutto R, Haley PE, Yu CA, Ohnishi T, Leigh JS. 1986. Electron-paramagnetic-resonance and electron-spin echo studies of iron–sulfur clusters-S-1 and clusters-S-2 in beef heart succinate dehydrogenase. *Biophys J* **49**:A327–A327.

106. Cammack R, Kovacs KL, McCracken J, Peisach J. 1989. Spectroscopic characterization of the nickel and iron–sulfur clusters of hydrogenase from the purple photosynthetic bacterium *Thiocapsa roseopersicina*, 2: electron spin-echo spectroscopy. *Eur J Biochem* **182**:363–366.

107. Edmonds DT, Speight PA. 1971. Nitrogen quadrupole resonance in amino acids. *Phys Lett A* **34**:325–326.

108. Hung SC, Grant CV, Peloquin JM, Waldeck AR, Britt RD, Chan SI. 2000. ESEEM studies of succinate:ubiquinone reductase from *Paracoccus denitrificans*. *J Biol Inorg Chem* **5**:593–602.

109. Thomson AJ, Robinson AE, Johnson MK, Cammack R, Rao KK, Hall DO. 1981. Low-temperature magnetic circular-dichroism evidence for the conversion of 4-iron–sulfur clusters in a ferredoxin from *Clostridium pasteurianum* into 3-iron–sulfur clusters. *Biochim Biophys Acta* **637**:423–432.

110. Mims WB. 1976. The linear electric field effect in paramagnetic resonance. Oxford: Oxford UP.

111. Peisach J, Beinert H, Emptage MH, Mims WB, Fee JA, Orme-Johnson WH, Rendina AR, Orme-Johnson NR. 1983. Characterization of 3-iron ferredoxins by means of the linear electric-field effect in electron-paramagnetic resonance. *J Biol Chem* **258**:13014–13016.

112. Gurbiel RJ, Ohnishi T, Robertson DE, Daldal F, Hoffman BM. 1991. Q-band ENDOR spectra of the Rieske protein from *Rhodobacter capsulatus* ubiquinol–cytochrome-c oxidoreductase show two histidines coordinated to the [2Fe–2S] cluster. *Biochemistry* **30**:11579–11584.

113. Fee JA, Findling KL, Yoshida T, Hille R, Tarr GE, Hearshen DO, Dunham WR, Day EP, Kent TA, Münck E. 1984. Purification and characterization of the Rieske iron–sulfur protein from *Thermus thermophilus*: evidence for a [2Fe–2S] cluster having non-cysteine ligands. *J Biol Chem* **259**:124–133.

114. Mason JR, Cammack R. 1992. The electron-transport proteins of hydroxylating bacterial dioxygenases. *Annu Rev Microbiol* **46**:277–305.

115. Samoilova RI, Kolling D, Uzawa T, Iwasaki T, Crofts AR, Dikanov SA. 2002. The interaction of the Rieske iron–sulfur protein with occupants of the Q(o)-site of the bc(1) complex, probed by electron spin echo envelope modulation. *J Biol Chem* **277**:4605–4608.

116. Milov AD, Samoilova RI, Tsvetkov YD, Gusev VA, Formaggio F, Crisma M, Toniolo C, Raap J. 2002. Spatial distribution of spin-labeled trichogin GA IV in the Gram-positive eubacterial cell membrane determined from PELDOR data. *Appl Magn Reson* **23**:81–95.

117. Brugna M, Rodgers S, Schricker A, Montoya G, Kazmeier M, Nitschke W, Sinning I. 2000. A spectroscopic method for observing the domain movement of the Rieske iron–sulfur protein. *Proc Natl Acad Sci USA* **97**:2069–2074.

118. Jormakka M, Tornroth S, Byrne B, Iwata S. 2002. Molecular basis of proton motive force generation: structure of formate dehydrogenase-N. *Science* **295**:1863–1868.

119. Rothery RA, Bertero MG, Cammack R, Palak M, Blasco F, Strynadka NCJ, Weiner JH. 2004. The catalytic subunit of Escherichia coli nitrate reductase A contains a novel 4Fe–4S cluster with a high-spin ground state. *Biochemistry* **43**:5324–5333.

120. Grimaldi S, Lanciano P, Bertrand P, Blasco F, Guigliarelli B. 2005. Evidence for an EPR-detectable semiquinone intermediate stabilized in the membrane-bound subunit NarI of nitrate reductase A (NarGHI) from *Escherichia coli*. *Biochemistry* **44**:1300–1308.

121. Duin EC, Madadi-Kahkesh S, Hedderich R, Clay MD, Johnson MK. 2002. Heterodisulfide reductase from *Methanothermobacter marburgensis* contains an active-site

[4Fe–4S] cluster that is directly involved in mediating heterodisulfide reduction. *FEBS Lett* **512**:263–268.

122. Bennati M, Weiden N, Dinse KP, Hedderich R. 2004. [57]Fe ENDOR spectroscopy on the iron–sulfur cluster involved in substrate reduction of heterodisulfide reductase. *J Am Chem Soc* **126**:8378–8379.

123. Staples CR, Gaymard E, Stritt-Etter AL, Telser J, Hoffman BM, Schurmann P, Knaff DB, Johnson MK. 1998. Role of the Fe4–S4 cluster in mediating disulfide reduction in spinach ferredoxin:thioredoxin reductase. *Biochemistry* **37**:4612–4620.

124. Hamann N, Mander GJ, Shokes JE, Scott RA, Bennati M, Hedderich R. 2007. A cysteine-rich CCG domain contains a novel [4Fe–4S] cluster binding motif as deduced from studies with subunit B of heterodisulfide reductase from *Methanothermobacter marburgensis*. *Biochemistry* **46**:12875–12885.

125. Moenne-Loccoz P, Heathcote P, Maclachlan DJ, Berry MC, Davis IH, Evans MCW. 1994. Path of electron-transfer in photosystem-1: direct evidence of forward electron-transfer from A(1) to Fe–SX. *Biochemistry* **33**:10037–10042.

126. Berry MC, Bratt PJ, Evans MCW. 1997. Relaxation properties of the photosystem 1 electron transfer components: indications of the relative positions of the electron transfer cofactors in photosystem 1. *Biochim Biophys Acta Bioenerg* **1319**:163–176.

127. Shergill JK, Golinelli MP, Cammack R, Meyer J. 1996. Coordination of the [2Fe–2S] cluster in wild type and molecular variants of *Clostridium pasteurianum* ferredoxin, investigated by ESEEM spectroscopy. *Biochemistry* **35**:12842–12848.

128. Shergill JK, Cammack R, Weiner JH. 1993. Electron spin-echo envelope modulation studies of the [3Fe–4S] cluster of *Escherichia coli* fumarate reductase. *J Chem Soc Faraday* **89**:3685–3689.

129. Unalkat P. 1996. The [2Fe–2S] ferredoxin from benzene dioxygenase in *Pseudomonas putida* ML2. PhD dissertation. King's College, University of London.

130. Riedel A, Fetzner S, Rampp M, Lingens F, Liebl U, Zimmermann JL, Nitschke W. 1995. EPR, electron spin echo envelope modulation, and electron nuclear double resonance studies of the 2Fe2S centers of the 2-halobenzoate 1,2-dioxygenase from *Burkholderia* (*Pseudomonas*) *cepacia* 2CBS. *J Biol Chem* **270**:30869–30873.

131. Sayle RA, Milner-White EJ. 1995. Rasmol: biomolecular graphics for all. *Trends Biochem Sci* **20**:374–376.

132. Deligiannakis Y, Louloudi M, Hadjiliadis N. 2000. Electron spin echo envelope modulation (ESEEM) spectroscopy as a tool to investigate the coordination environment of metal centers. *Coor. Che. Rev* **204**:1–112.

CATALYSIS AND GENE REGULATION

Helmut Beinert[†]

Institute for Enzyme Research, University of Wisconsin — Madison

This chapter deals with the border territory between protein and molecular biology. Nature has found use for the "corpse" of an enzyme that normally deals with energy transformation, for directing mRNA use in the cytoplasm: the iron-regulatory protein "IRP," which simply is cytoplasmic aconitase without the main constituent of its active site, the [4Fe–4S] cluster. The remaining protein, now known as "IRP1," shows affinity for up to ten mRNAs in animal cells. The first mRNA discovered to be targets for IRP1 binding were the two subunits of the iron storage protein ferritin and the mRNA encoding transferrin receptor 1 (TfR1), required for iron uptake by most animal cells. When the supply of iron is adequate, IRP1 is converted to c-aconitase and any excess iron can be stored in ferritin while uptake of iron by TfR1 is diminished; when however, the iron supply declines, the cluster in c-aconitase is disassembled and IRP1 now binds to ferritin and TfR mRNA, which decreases iron storage and increases cellular iron uptake. In what follows, we will provide more of the background on which the described processes are made possible. We then proceed to illustrate related control systems, such as the global microbial control system, based on the FNR protein, in which again a sensitive Fe–S cluster is the active control device. The cluster of FNR decays from the [4Fe–4S] to the [2Fe–2S] state in the presence of oxygen, which provides the signal for microbes to switch from using oxygen as oxidant to compounds such as fumarate and nitrate as, albeit less effective, oxidizing agents. Related systems, based on the sensitivity of Fe–S clusters, are also mentioned. The use of EPR in analysis of these regulatory systems will be referred to when relevant. The application of electron paramagnetic resonance (EPR) to analyzing regulatory proteins is based on the observation of EPR signals from the various cluster types containing [2Fe–2S], [3Fe–4S], or [4Fe–4S] and eventually superclusters, such as those occurring in nitrogen-fixing systems. The signals are found for the one-electron reduced states with [2Fe–2S] and [4Fe–4S] clusters and for the oxidized form of the [3Fe–4S] cluster and of high-potential Fe–S proteins.

[†] Deceased. Address all correspondence to the Editor, Graeme R. Hanson, Centre for Magnetic Resonance, The University of Queensland, St. Lucia, Queensland, 4072 Australia, +61 7-3365-3242, +61 7-3365-3833 (fax), <Graeme.Hanson@cmr.uq.edu.au>.

In the field under consideration here, the application and usefulness of EPR in the field of biological gene control, what one could call the "Big Bang," occurred in March 1991, when the almost simultaneous appearance of two notes, one in *Cell* by Rouault et al. [1] and the other by Hentze and Argos [2] in *Nucleic Acid Research* reported that "IRP," the Iron Regulatory Protein, which they had characterized, had striking similarities in its amino-acid sequence with the enzyme aconitase from mammalian mitochondria. By that time it had been established that aconitase is an Fe–S protein with an unusual [4Fe–4S] cluster, in which one Fe site had an OH instead of a cysteine ligand. This Fe is able to bind isocitrate and constitutes the swivel-point about which the substrate must swing to assume the citrate conformation. In view of the involvement of an Fe–S cluster in this reaction, a variety of spectroscopic methods became applicable and among them EPR and electron nuclear double resonance (ENDOR) [3].

But what is the relationship of all this to IRP? IRP is a cytosolic protein, while aconitase, whose sequence and structure were known, is a mitochondrial protein. However, in liver there also exists a cytosolic aconitase, and it became clear that IRP is in fact the cytoplasmic aconitase from which the Fe–S cluster has been removed. This applies to IRP1; there is also an IRP2 known, but this protein does not appear to be an Fe–S protein.

Since our previous work on aconitase and its indirect participation in gene regulation had been referred to and discussed, human cytoplasmic aconitase has been crystallized and its structure has determined by Dupuy et al. [4]. All aconitases thus far known are composed of four distinct domains that are combined in a similar sequence, and it was concluded from the crystal structure that when the protein part serves as IRP, i.e., has lost its Fe–S cluster, domain 4 moves distinctly away from the remaining domains, thus creating space for binding the RNA.

Finally, it may be of interest to report an instance where EPR has played the decisive role in clarifying a foggy area that had arisen concerning the sensitivity of the enzyme aconitase toward nitric oxide [5]. Since mitochondrial aconitase activity had long been known to be diminished when cells were exposed to NO [6,7], two groups determined if c-aconitase was also a target. These studies demonstrated significant loss of c-aconitase activity and generation of IRP1 RNA binding activity in cells stimulated to generate NO [8,9]. However, controversy arose concerning whether NO, or its metabolite peroxynitrite (ONOO$^-$), were responsible for loss of the Fe–S cluster from c-aconitase. There appeared papers from two different laboratories that stated that mitochondrial aconitase is not inactivated by NO [10,11], whereas we found that both the mitochondrial as well as the cytoplasmic aconitase were inactivated by NO at an easily measurable rate, depending on conditions [5]. We could show by EPR that both c- and m-aconitase readily formed the dinitrosyl iron complex, easily recognizable by its typical line at $g = 2.04$. We were even able to show that in the presence of histidine, a histidinyl dinitrosyl–iron–dithiol complex was formed. Our work has subsequently been confirmed and extended by Drapier and associates, who have shown that NO promotes removal of all four iron atoms from c-aconitase and generates IRP1 RNA binding activity in vitro [12,13]. The role of ONOO$^-$ in inactivating c-aconitase is well accepted, but

the extent to which this agent can generate functional IRP1 RNA binding activity remains controversial [12–15].

At about the same time that aconitase was shown to be converted to IRP1, there was another regulatory Fe–S protein discovered in *Escherichia coli*, called SoxR, which is involved in monitoring the intracellular superoxide level [16]. This protein is simply a [2Fe–2S] protein that under low levels of superoxide is in the inactive reduced $[2Fe–2S]^+$ state. When superoxide levels increase, the cluster becomes oxidized to the 2+ state, and SoxR triggers the production of defensive measures by upregulation of SoxS and its regulon, which includes enzymes attacking the excessive oxidizing species. EPR played a critical role in establishing the oxidation states of SoxR in both whole cells and in in-vitro studies. Thus, in the case of IRP1 it is the lack of cluster that determines its action, while in the case of SoxR it is the oxidation state of the cluster.

To date the most actively investigated example for the use of Fe–S clusters in the regulation of gene function is the FNR protein from *E. coli*. FNR stands for "fumarate and nitrate reduction," as this factor triggers the production of enzymes that allow the organism to carry out oxidative metabolism with fumarate and nitrate as oxidants in the absence of oxygen. The FNR protein is a [4Fe–4S] protein that stimulates the production of a host of enzymes for this purpose [17–20].

When the [4Fe–4S] cluster is intact, it allows the protein to dimerize, which is necessary for its DNA binding function [21–23]. In the presence of oxygen, however, the $[4Fe–4S]^{2+}$ cluster is readily converted to a $[2Fe–2S]^{2+}$ cluster apparently via the intermediate formation of a [3Fe–4S] cluster [24–26]. Since both the [4Fe–4S] and [2Fe–2S] clusters are in the 2+ oxidation state, they are not observable by EPR and the [4Fe–4S] cluster has too low a redox potential to readily form the reduced species that would be detectable by EPR. In addition, the $[4Fe–4S]^{2+}$ cluster is rebuilt from the $[2Fe–2S]^{2+}$ cluster when anaerobic conditions are established and a suitable reductant is present. In our work on FNR we found Mössbauer spectroscopy superior because the necessity for having the ^{57}Fe isotope in the compound studied allowed detection of all Fe species of FNR. It was even possible to observe the destruction and reformation of the [4Fe–4S] cluster in whole cells of *E. coli* by collecting cells through high-speed centrifugation and rapidly freezing the paste obtained [27]. Studies on the mechanism of cluster decay were reported by Crack et al. [24] and Sutton et al. [28].

In recent years much effort has been expended to study the mechanism of biosynthesis of Fe–S clusters. Much of this work was done in bacteria and in mitochondria, which are the primary site of Fe–S cluster formation in mammals and yeast. There is now rather extensive literature available internationally on this subject [29,30]. In some bacteria, the Isc (an acronym for Iron–sulfur cluster) system of proteins starts with IscS, which carries a sulfane sulfur (extracted from free cysteine) ready to be used for the sulfide constituents of the cluster to be formed. In the second step, the IscU protein provides a scaffold on which a [2Fe–2S] cluster is preliminarily assembled. The next component, IscA, is proposed to function as an alternative scaffold and/or in providing the Fe to be used for cluster assembly. In

the ensuing steps chaperone proteins, ATP, and a reducing enzyme come into play whose functions are not entirely understood. In yeast mitochondria, there is an equivalent system that functions in Fe–S biogenesis; however, Fe delivery seems to be provided by frataxin [31], which was originally discovered because defects in the gene encoding frataxin are responsible for the human genetic disease Friedreich's ataxia.

When the organization of the genes encoding the Isc biogenesis system was investigated in *E. coli*, it was observed that these genes were arranged in an operon with the first gene in the operon encoding an Fe–S protein, which turned out to repress expression of the Isc system [32]. Consequently it was named IscR as a "regulator" of the Isc biogenesis pathway. The observation that IscR was itself an Fe–S protein suggested a negative feedback mechanism by which the expression of the Isc pathway could be sensitive to the demands for cellular Fe–S biogenesis. If demand for cellular Fe–S biogenesis increases, then less of the Isc machinery would be available for formation of Fe–S–IscR, and, consequently, the levels of the active repressor would drop, increasing the production of the Isc proteins until the synthetic process could speed up and more Fe–S proteins — including the active repressor Fe–S IscR — would again be formed, which in turn would restore the *isc* operon to its repressed state. At this time these ideas have still to be considered as interesting hypotheses and the last word has not been heard yet. Application of EPR demonstrated that when isolated, IscR has primarily a $[2Fe–2S]^{1+}$ cluster that can be readily oxidized and reduced, although the role of oxidation states in controlling IscR activity, if any, has not been established.

There is a second, partially analogous system for Fe–S protein synthesis, which is thought to be called upon when oxidative stress arises. It is called the SUF system [33,34]. An interesting observation is that IscR controls expression of both of these operons; although IscR is a repressor of the *isc* operon, it is an activator of the *suf* operon [35]. While the mechanism remains to be established, oxidative stress increases expression of both *isc* and *suf* in part through changes in IscR function.

One typical sign of inefficient synthesis of Fe–S proteins is the accumulation of ferric iron in mitochondria. This phenomenon can easily be tested by EPR after adding a suitable chelator of ferric iron, which will produce the well known $g = 4.3$ signal [36].

A most interesting example of the direct involvement of an Fe–S cluster in DNA metabolism came out of the work of Sheila David on the excision glycosylase MutY of *E. coli* [37]. This enzyme serves in preventing mutations by removal of adenine from an adduct of adenine to 7,8-dihydro-8-oxo-2′-deoxyguanosine, which would create a mismatch in duplex DNA. It had been suggested previously that the [4Fe–4S] cluster might serve to create a favorable position of the reactants in the interactions of the components of the described reacting system and had been catalogued in the reviewing literature as a "structural role" of an Fe–S cluster. It has, however, since been shown in elegant work in collaboration with the laboratory of Jacqueline Barton [37,38] that the Fe–S cluster actually is taking part in a redox process.

In summary, in the last two decades EPR has often been called upon as a decisive method for providing critical information on the role of Fe–S clusters in controlling the activity of regulatory proteins both in vitro and in whole cells.

ACKNOWLEDGMENTS

REFERENCES

1. Rouault TA, Stout CD, Kaptain S, Harford JB, Klausner RD. 1991. Structural relationship between an iron-regulated RNA-binding protein (IRE–BP) and aconitase: functional implications. *Cell* **64**(5):881–883.
2. Hentze MW, Argos P. 1991. Homology between IRE–BP, a regulatory RNA-binding protein, aconitase, and isopropylmalate isomerase. *Nucleic Acids Res* **19**(8):1739–1740.
3. Beinert H, Kennedy MC, Stout CD. 1996. Aconitase as iron–sulfur protein, enzyme, and iron-regulatory protein. *Chem Rev* **96**(7):2335–2374.
4. Dupuy J, Volbeda A, Carpentier P, Darnault C, Moulis JM, Fontecilla-Camps JC. 2006. Crystal structure of human iron regulatory protein 1 as cytosolic aconitase. *Structure* **14**(1):129–139.
5. Kennedy MC, Antholine WE, Beinert H. 1997. An EPR investigation of the products of the reaction of cytosolic and mitochondrial aconitases with nitric oxide. *J Biol Chem* **272**(33):20340–20347.
6. Drapier JC, Hibbs JB, Jr. 1986. Murine cytotoxic activated macrophages inhibit aconitase in tumor cells: inhibition involves the iron-sulfur prosthetic group and is reversible. *J Clin Invest* **78**(3):790–797.
7. Drapier JC, Pellat C, Henry Y. 1991. Generation of EPR-detectable nitrosyl-iron complexes in tumor target cells cocultured with activated macrophages. *J Biol Chem* **266**(16):10162–10167.
8. Drapier JC, Hirling H, Wietzerbin J, Kaldy P, Kühn LC. 1993. Biosynthesis of nitric oxide activates iron regulatory factor in macrophages. *Embo J* **12**(9):3643–3649.
9. Weiss G, Goossen B, Doppler W, Fuchs D, Pantopoulos K, Werner-Felmayer G, Wachter H, Hentze MW. 1993. Translational regulation via iron-responsive elements by the nitric oxide/NO-synthase pathway. *Embo J* **12**(9):3651–3657.
10. Castro L, Rodriguez M, Radi R. 1994. Aconitase is readily inactivated by peroxynitrite, but not by its precursor, nitric oxide. *J Biol Chem* **269**(47):29409–29415.
11. Hausladen A, Fridovich I. 1994. Superoxide and peroxynitrite inactivate aconitases, but nitric oxide does not. *J Biol Chem* **269**(47):29405–29408.
12. Soum E, Brazzolotto X, Goussias C, Bouton C, Moulis JM, Mattioli TA, Drapier JC. 2003. Peroxynitrite and nitric oxide differently target the iron–sulfur cluster and amino acid residues of human iron regulatory protein 1. *Biochemistry* **42**(25):7648–7654.
13. Soum E, Drapier JC. 2003. Nitric oxide and peroxynitrite promote complete disruption of the [4Fe–4S] cluster of recombinant human iron regulatory protein 1. *J Biol Inorg Chem* **8**(1–2):226–232.

14. Bouton C, Hirling H, Drapier JC. 1997. Redox modulation of iron regulatory proteins by peroxynitrite. *J Biol Chem* **272**(32):19969–19975.

15. Cairo G, Ronchi R, Recalcati S, Campanella A, Minotti G. 2002. Nitric oxide and peroxynitrite activate the iron regulatory protein-1 of J774A.1 macrophages by direct disassembly of the Fe–S cluster of cytoplasmic aconitase. *Biochemistry* **41**(23):7435–7442.

16. Demple B, Ding H, Jorgensen M. 2002. *Escherichia coli* SoxR protein: sensor/transducer of oxidative stress and nitric oxide. *Methods Enzymol* **348**:355–364.

17. Green J, Scott C, Guest JR. 2001. Functional versatility in the CRP–FNR superfamily of transcription factors: FNR and FLP. *Adv Microb Physiol* **44**:1–34.

18. Kang Y, Weber KD, Qiu Y, Kiley PJ, Blattner FR. 2005. Genome-wide expression analysis indicates that FNR of *Escherichia coli* K-12 regulates a large number of genes of unknown function. *J Bacteriol* **187**(3):1135–1160.

19. Kiley PJ, Beinert H. 1998. Oxygen sensing by the global regulator, FNR: the role of the iron–sulfur cluster. *FEMS Microbiol Rev* **22**(5):341–352.

20. Kiley PJ, Beinert H. 2003. The role of Fe–S proteins in sensing and regulation in bacteria. *Curr Opin Microbiol* **6**(2):181–185.

21. Lazazzera BA, Bates DM, Kiley PJ. 1993. The activity of the *Escherichia coli* transcription factor FNR is regulated by a change in oligomeric state. *Genes Dev* **7**(10):1993–2005.

22. Lazazzera BA, Beinert H, Khoroshilova N, Kennedy MC, Kiley PJ. 1996. DNA binding and dimerization of the Fe–S-containing FNR protein from *Escherichia coli* are regulated by oxygen. *J Biol Chem* **271**(5):2762–2768.

23. Moore LJ, Kiley PJ. 2001. Characterization of the dimerization domain in the FNR transcription factor. *J Biol Chem* **276**(49):45744–45750.

24. Crack J, Green J, Thomson AJ. 2004. Mechanism of oxygen sensing by the bacterial transcription factor fumarate–nitrate reduction (FNR). *J Biol Chem* **279**(10):9278–9286.

25. Green J, Bennett B, Jordan P, Ralph ET, Thomson AJ, Guest JR. 1996. Reconstitution of the [4Fe–4S] cluster in FNR and demonstration of the aerobic–anaerobic transcription switch in vitro. *Biochem J* **316**(Pt 3):887–892.

26. Khoroshilova N, Popescu C, Münck E, Beinert H, Kiley PJ. 1997. Iron–sulfur cluster disassembly in the FNR protein of *Escherichia coli* by O_2: [4Fe–4S] to [2Fe–2S] conversion with loss of biological activity. *Proc Natl Acad Sci USA* **94**(12):6087–6092.

27. Popescu CV, Bates DM, Beinert H, Münck E, Kiley PJ. 1998. Mössbauer spectroscopy as a tool for the study of activation/inactivation of the transcription regulator FNR in whole cells of *Escherichia coli*. *Proc Natl Acad Sci USA* **95**(23):13431–13435.

28. Sutton VR, Mettert EL, Beinert H, Kiley PJ. 2004. Kinetic analysis of the oxidative conversion of the $[4Fe–4S]^{2+}$ cluster of FNR to a $[2Fe–2S]^{2+}$ cluster. *J Bacteriol* **186**(23):8018–8025.

29. Mühlenhoff U, Lill R. 2000. Biogenesis of iron–sulfur proteins in eukaryotes: a novel task of mitochondria that is inherited from bacteria. *Biochim Biophys Acta* **1459**(2–3):370–382.

30. Smith AD, Jameson GN, Dos Santos PC, Agar JN, Naik S, Krebs C, Frazzon J, Dean DR, Huynh BH, Johnson MK. 2005. NifS-mediated assembly of [4Fe–4S] clusters in the N- and C-terminal domains of the NifU scaffold protein. *Biochemistry* **44**(39):12955–12969.

31. Yoon T, Cowan JA. 2003. Iron–sulfur cluster biosynthesis: characterization of frataxin as an iron donor for assembly of [2Fe–2S] clusters in ISU-type proteins. *J Am Chem Soc* **125**(20):6078–6084.

32. Schwartz CJ, Giel JL, Patschkowski T, Luther C, Ruzicka FJ, Beinert H, Kiley PJ. 2001. IscR, an Fe–S cluster-containing transcription factor, represses expression of *Escherichia coli* genes encoding Fe–S cluster assembly proteins. *Proc Natl Acad Sci USA* **98**(26):14895–14900.

33. Nachin L, Loiseau L, Expert D, Barras F. 2003. SufC: an unorthodox cytoplasmic ABC/ATPase required for [Fe–S] biogenesis under oxidative stress. *Embo J* **22**(3):427–437.

34. Takahashi Y, Tokumoto U. 2002. A third bacterial system for the assembly of iron–sulfur clusters with homologs in archaea and plastids. *J Biol Chem* **277**(32):28380–28383.

35. Giel JL, Rodionov D, Liu M, Blattner FR, Kiley PJ. 2006. IscR-dependent gene expression links iron–sulphur cluster assembly to the control of O_2-regulated genes in *Escherichia coli*. *Mol Microbiol* **60**(4):1058–1075.

36. Woodmansee AN, Imlay JA. 2002. Quantitation of intracellular free iron by electron paramagnetic resonance spectroscopy. *Methods Enzymol* **349**:3–9.

37. Yavin E, Boal AK, Stemp ED, Boon EM, Livingston AL, O'Shea VL, David SS, Barton JK. 2005. Protein-DNA charge transport: redox activation of a DNA repair protein by guanine radical. *Proc Natl Acad Sci USA* **102**(10):3546–3551.

38. Yavin E, Stemp ED, O'Shea VL, David SS, Barton JK. 2006. Electron trap for DNA-bound repair enzymes: a strategy for DNA-mediated signaling. *Proc Natl Acad Sci USA* **103**(10):3610–3614.

IRON–SULFUR CLUSTERS IN "RADICAL SAM" ENZYMES: SPECTROSCOPY AND COORDINATION

Serge Gambarelli[1], Etienne Mulliez,[2] and Marc Fontecave[2]

[1]*Service de Chimie Inorganique et Biologique, UMR-E 3 CEA-UJF et FRE CNRS 3200, INAC/SCIB, CEA-Grenoble*; [2]*Laboratoire de Chimie et Biochimie des Métaux, CNRS-CEA-Université Joseph Fourier n° 5249, iRTSV/LCBM, CEA-Grenoble*

There is increasing evidence for the versatility of the coordination of iron–sulfur clusters in biology. In addition to cysteine residues as the most favored ligand and providing sulfur coordination, oxygen-based (aspartate, tyrosinate …) and nitrogen-based (histidine, arginine …) residues have also been observed as ligands to the clusters. Furthermore, low-molecular-weight substrates (citrate in the case of aconitase) and cofactors (S-adenosylmethionine, SAM, in the case of "Radical SAM" enzymes) have been shown to bind to one of the iron atoms of the [4Fe–4S] clusters where they are then activated. In this chapter we discuss the potential as well as the limitations of ENDOR and HYSCORE spectroscopy for characterizing metalloprotein coordination and, more specifically, the cluster–SAM complexes that are essential intermediates in pyruvate formate lyase-activating enzyme, lysine 2,3 aminomutase, and ribonucleotide reductase activating enzyme. These three systems are prototypes for the "Radical SAM" enzyme superfamily, whose chemistry seems to be extensively utilized in the metabolism of all living organisms.

1. INTRODUCTION

Iron–sulfur clusters are among the most structurally and functionally versatile cofactors in biology [1]. The most prevalent associations of iron and sulfur atoms are those found in proteins in the form of [2Fe–2S] and [4Fe–4S] clusters. They mainly take part in electron-transfer systems in important biological functions such as photosynthesis and respiration. In addition, these clusters have been shown to

Address all correspondence to Serge Gambarelli, Service de Chimie Inorganique et Biologique, INAC/SCIB, CEA-Grenoble, 17 rue des Martyrs, 38054 Grenoble cedex 9-France, <serge.gambarelli@cea.fr>.

play essential roles in: (i) gene regulation, as they can be used to sense changes in levels of iron, oxygen, and superoxide (e.g., [2]); (ii) nonredox catalysis as they display strong Lewis acid properties utilized for polarization of substrate bonds [3]; (iii) redox catalysis, as exemplified by the enzymes of the "Radical SAM" super-family extensively discussed in this chapter [4–6].

Obviously it is because these clusters can enjoy various redox states depending on their coordination environment, the electronic properties of the protein site where they are anchored, and their hydrogen bonding that they have been selected to participate in electron-transfer and redox reactions. An interesting property of the redox states is that they can be easily differentiated by spectroscopy. For example, the oxidized $[4Fe–4S]^{2+}$ state is $S = 0$, diamagnetic, and thus EPR-silent. In contrast, the corresponding reduced form $[4Fe–4S]^+$ is $S = 1/2$ in its ground state, paramagnetic, and displays characteristic EPR properties. This is the same for the $[2Fe–2S]^{2+/1+}$ redox couple.

Another interesting feature of the [Fe–S] clusters is the broad diversity of ligands that the iron atoms can accommodate. In the class of protein ligands, cysteine, providing sulfur coordination, is the most common coordinating amino-acid residue. However, there are several examples of nitrogen coordination, with histidine or arginine as the ligands [7–10], and oxygen coordination, with aspartate, glutamine, or tyrosine as the ligands [11–13]. There are also more and more examples of clusters coordinated by exogenous ligands, such as water, enzyme substrates (such as citrate in the case of aconitase), or enzyme cofactors (as S-adenosylmethionine in the case of "Radical SAM" enzymes) [3–6,10,14].

Spectroscopic analysis of reduced paramagnetic forms of the clusters — in particular electron paramagnetic resonance (EPR), electron-nuclear double resonance (ENDOR), and Hyperfine Sublevel Correlation spectroscopy (HYSCORE) — has been successfully used to identify the ligands to the iron atoms, thus providing important insights into the electronic and geometric properties of the clusters as well as into the mechanisms of a number of reactions catalyzed by those clusters. In this chapter we will discuss the case of the "Radical SAM" enzymes as a nice example illustrating the power of spectroscopy for elucidating the chemistry of [Fe–S] clusters. In fact it was EPR spectroscopy that first demonstrated the presence of [Fe–S] clusters in these enzymes, whereas it was ENDOR spectroscopy, which probes coupling between electronic and nuclear spins, which provided the first evidence for the coordination of SAM to the unique iron site of the [4Fe–4S] cluster [15]. This was further confirmed by x-ray crystallography [10,14,16,17]. HYSCORE has been more recently used in this context and has also proved very useful [18]. It is important to note that the vast majority of studies in this field were carried out by B.M. Hoffman and his group at Northwestern University.

2. "RADICAL SAM" IRON-SULFUR ENZYMES: AN EXAMPLE OF A LOW-MOLECULAR-WEIGHT LIGAND TO A [4Fe–4S] CLUSTER

There are few examples of biological catalytically relevant complexes between a protein-bound iron–sulfur ([Fe–S]) center and a low-molecular-weight compound

(a substrate or a cofactor). The first historically important example is that of the aconitase–citrate complex [19]. In the early 80s a new function for [Fe–S] clusters appeared with the discovery of aconitase, a central enzyme in the TCA cycle of cellular metabolism. This enzyme catalyzes the reversible conversion of citrate to isocitrate through aconitate using a special $[4Fe–4S]^{2+}$ center coordinated by only 3 cysteines of the polypeptide chain. Even though the reduced $[4Fe–4S]^{+}$ state of the enzyme is not the physiologically relevant one, ENDOR spectroscopy applied to that paramagnetic state proved to be an invaluable tool in revealing the structural details of this center in the presence or absence of substrate. Using ^{17}O, ^{1}H, and ^{2}H ENDOR spectroscopy at X- and Q-band microwave frequencies, B. Hoffman et al. identified the ligand to the fourth iron of the cluster as a solvent hydroxo group [20–22]. Moreover, they found that in the presence of the citrate substrate this hydroxo becomes protonated and citrate binds to the subsite iron by its α-hydroxycarboxylato moiety, leading to a hexacoordinated iron, in agreement with Mössbauer studies and the 3D structure of the enzyme [19].

Almost 20 years later, a new chapter in the rich history of the [Fe–S] proteins began with the discovery of the "Radical SAM" (SAM = S-adenosylmethionine) superfamily of enzymes [4–6]. The "Radical SAM" superfamily was recognized in 2001 by iterative profile searches of primary sequence databanks based on one unusual cysteine motif, CxxxCxxC, called the "cysteine triad" [23]. At that time the best-studied members of that enzyme family were lysine 2,3-aminomutase (LAM), pyruvate formate lyase activating enzyme (PFL-AE), and ribonucleotide reductase III activating enzyme (aRNR-AE) which are involved in completely different metabolic reactions [24–26] (Fig. 1).

In spite of their differences, these three systems share several characteristics: they use the universal methylating agent S-adenosylmethionine (SAM) (Fig. 1) as a cofactor in a new role since, in these reactions, it is reductively cleaved into the 5′-deoxyadenosyl radical and methionine; they proceed by radical chemistry; they contain a [4Fe–4S] center chelated by the three cysteines of the "cysteine triad," and, finally, both PFL-AE and aRNR-AE use the same low-potential electron donor system (NADPH:flavodoxin reductase:flavodoxin).

The extensive spectroscopic characterization of these systems (see below) has led to a consensus picture in which the function of the [Fe–S] center is twofold: it binds the SAM molecule, and, from the induced proximity, it reduces the sulfonium to yield the very reactive 5′-deoxyadenosyl radical (Ado°), leaving methionine as a byproduct. Even though the highly energetic Ado° radical has not been directly spectroscopically observed, several indirect lines of evidence strongly support its involvement in reactions catalyzed by "Radical SAM" enzymes. First, in the case of LAM, a stable Ado° allylic radical analog, 3′,4′-anhydro-5′-deoxyadenosin-5′-yl radical, could be directly detected by EPR spectroscopy when the reaction was carried out in the presence of a functional SAM analog, 3′-4′-anhydroadenosylmethionine [27]. Second, using ^{2}H(glycine)-labeled PFL and aRNR preparations, ^{2}H atom transfer to the Ado moiety coupled to glycyl radical
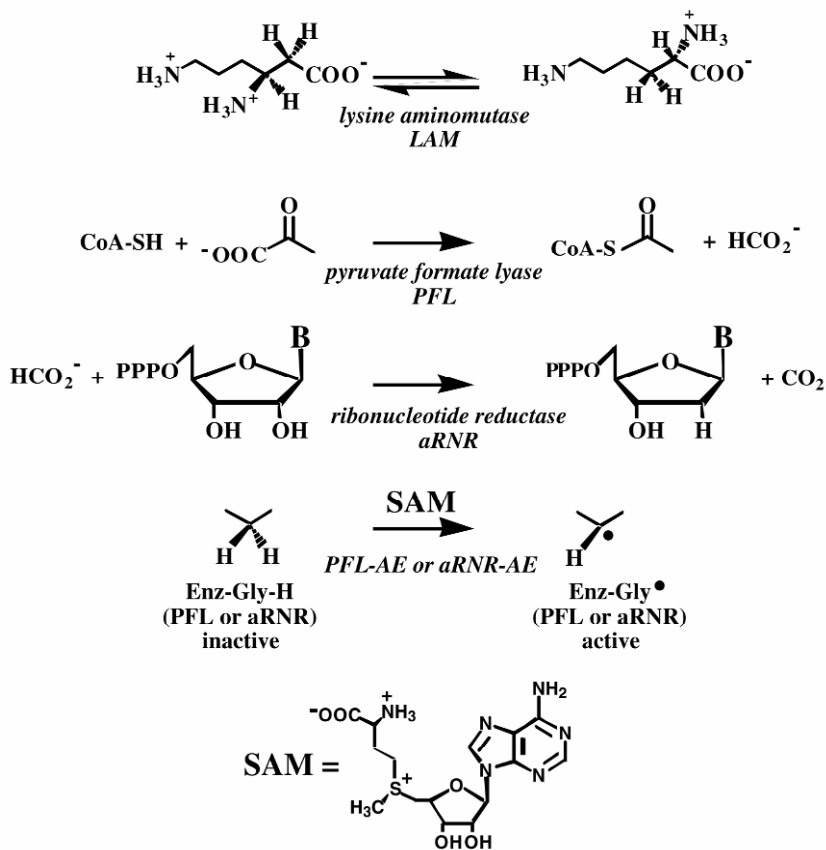
Figure 1. The reactions catalyzed by LAM, PFL, and aRNR.

formation was observed, in agreement with H atom abstraction by Ado° [18,28]. Third, the same approach in the case of LAM using a ^{3}H-labeled lysine substrate demonstrated ^{3}H atom transfer to the Ado moiety [29].

The inference of two key reaction intermediates — namely the [4Fe–4S]–SAM complex and the Ado° radical — allowed a general mechanism for the reactions catalyzed by "Radical SAM" enzymes to be proposed (Fig. 2).

The first step is common to all enzymes and consists in the reductolysis of SAM. This is achieved by: (i) binding of SAM to the reduced [4Fe–4S]$^+$ cluster; (ii) electron transfer from the cluster to SAM; (iii) homolytic cleavage of the S–C (adenosyl) bond to generate methionine and Ado°. In the second step of the reaction Ado° can be used in one of two ways. In one subclass of enzymes, Ado° is directly used to convert a nonprotein substrate into a substrate radical by H atom abstraction, and thus to activate it for conversion to the reaction product. This is the

step 1

step 2
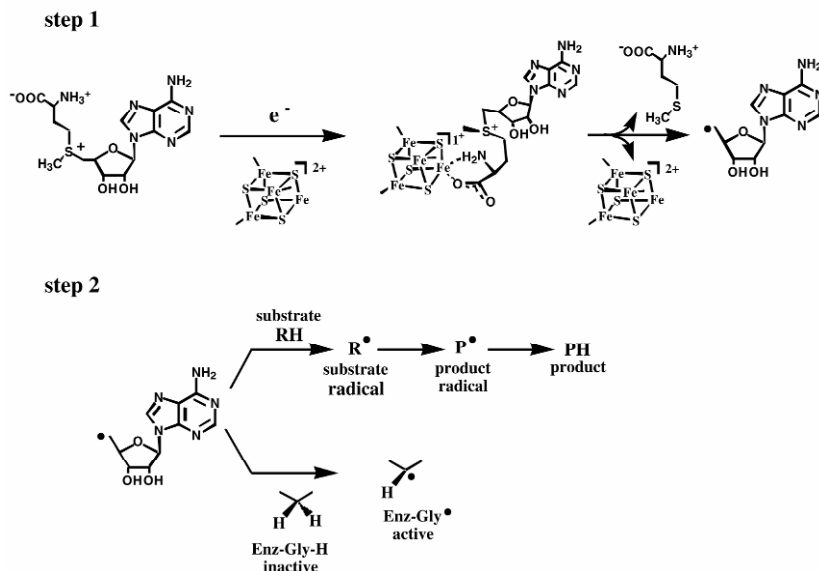
Figure 2. General mechanism proposed for the "Radical SAM" enzymes.

case, for example, for LAM or SPL [24,30]. In this case SAM functions catalytically. In the second subclass of enzymes Ado° serves for the formation of a glycyl radical on a target protein. This type of enzyme system is thus made up of two intimately associated components: an activase, the "Radical SAM" enzyme proper, and its specific protein target. The latter absolutely requires a glycyl radical in its active site for enzyme activity and thus depends on the activating enzyme for introduction of that radical. PFL-AE and aRNR-AE belong to this subclass [25,26]. In this case SAM is used stoichiometrically with regard to the target enzyme, which then acquires the ability to turn over. Even though the number of characterized "Radical SAM" enzymes has recently increased, PFL-AE, LAM, and aRNR-AE remain the best-studied systems both for their biochemical and spectroscopic properties and are briefly described in the following paragraphs.

2.1. The Pyruvate Formate Lyase System

In anaerobic microorganisms, part of the energy production occurs via glucose fermentation. The key reaction in this process, a thiolytic cleavage of pyruvate by CoA yielding acetyl-CoA and formate, is catalyzed by pyruvate formate lyase (PFL) (Fig. 1) [25]. PFL is a dimer (2×85 kDa) encoded by the gene *pflB*. The enzyme exists in two forms — inactive and active — and the latter was shown in 1984 to exhibit a very O_2-sensitive radical. By a series of labeling studies combined with EPR analysis, the radical was later shown to be located on the Gly734 residue of the 757-amino acid polypeptide [31]. Immediately downstream in the

operon, a second gene named *pflA* encodes a 28-kDa polypeptide that is essential for the formation of the glycyl radical. The pflA protein, referred to as PFL-AE, contains a [4Fe–4S] cluster bound to the protein via the 3 cysteines of the cysteine triad [32]. The Fe–S center of PFL-AE may be reduced in the absence of SAM to give an axial EPR signal at $g_{\parallel} = 2.029$ and $g_{\perp} = 1.925$. In the presence of SAM a new signal appears with g values at 2.009, 1.921, and 1.886, suggesting the formation of an SAM/PFL-AE complex [32]. It is only upon binding to PFL that this complex gives rise to the 5′-deoxyadenosyl radical, which selectively abstracts an H atom from the Gly734 residue of PFL [33]. Other reports have claimed that, as observed with LAM, the [Fe–S] center can be reduced only when SAM is present to give an almost axial signal with g values at 2.013, 1.889, and 1.878 [34]. More recently, however, Broderick et al. found that photoreduction in the absence of SAM leads to a rhombic signal with g values at 2.02, 1.94, and 1.88, which, in the presence of SAM, is converted into an axial species exhibiting the g values indicated above [35]. Evidently, minor changes in sample preparation have a strong impact on EPR parameters. An article recently published provides the first 3D structure of PFL-AE [104].

2.2. Lysine 2,3-Aminomutase

LAM catalyzes the reversible conversion of α-lysine into β-lysine (Fig. 1) [24]. It is a dimer enzyme arranged in a hexamer (287 kDa) using pyridoxal-phosphate (PLP) and SAM as cofactors. It contains two metal binding sites, one referred to as the cysteine triad, typical of "Radical SAM" enzymes, and a second cysteine-rich one that has recently been shown to accommodate a structural Zn atom [17]. The cysteine triad binds a labile [4Fe–4S] cluster whose reduction is strictly dependent on the presence of SAM or an SAM analog [36]. In this reduced state the LAM/SAM complex is stable and exhibits a rhombic X-band EPR spectrum with g values at 2.0, 1.9, and 1.85. Addition of the substrate triggers electron transfer from the reduced cluster to SAM, and the adenosyl radical resulting from the reductive cleavage of SAM converts the lysine substrate, engaged in a Schiff base with PLP, into a substrate radical. This primary radical is then converted to a product radical via a PLP aziridinyl intermediate [24]. Finally, the product radical is reduced by 5′-deoxyadenosine, and the resulting adenosyl radical reverts to SAM.

2.3. Anaerobic Ribonucleotide Reductase

All living cells depend on a balanced input of deoxyribonucleotides (dNTPs) for their genetic perenity. There is only one de novo biosynthetic pathway to dNTPs, and it proceeds by reduction of the corresponding ribonucleotides. This reaction is catalyzed by ribonucleotide reductases (Fig. 1) [37]. Three classes of these are known, of which only the class III (aRNR), found in strict or facultative anaerobes, is a "Radical SAM" enzyme [26]. Like PFL, aRNR (protein α) is a dimer (2 × 80 kDa) and a free radical enzyme. The active form of aRNR contains, in the C-terminal part of the 712-amino acid polypeptide, a glycyl radical located

on Gly681 and a structural Zn atom bound to four conserved cysteines and linked to the radical site (28 Å away) by a flexible loop [38]. aRNR-AE (protein β) is the "Radical SAM" part of the system and, although known to act catalytically in the introduction of the glycyl radical in aRNR, it does form a tight $\alpha_2\beta_2$ complex with aRNR [39]. It is a small protein of 17.5 kDa containing five cysteines, of which three are arranged in the familiar CxxxCxxC motif of all "Radical SAM" proteins. A double-mutant carrying only these three cysteines was shown to be fully active (unpublished results). The reduced activase exhibits a rhombic EPR signal at 2.03, 1.92, and 1.86 showing relaxation behavior typical of a $[4Fe–4S]^+$ center. During incubation with SAM this signal is replaced by an axial one with g values at $g_\parallel =$ 1.99 and $g_\perp = 1.91$, with little change in the relaxation behavior, again suggesting the formation of a complex with SAM [40].

aRNR-AE has the distinctive ability to catalyze the cleavage of SAM in the absence of its physiological partner, the reductase itself. However, the reaction of the reduced cluster of aRNR-AE with SAM is exceedingly slow. It was shown early on that the presence of thiols, and especially dithiothreitol (DTT), could dramatically increase the rate of the cleavage reaction (by more than 100-fold) [41]. Actually, DTT has a strong impact on the properties of the cluster. In the presence of DTT the rhombic signal of the reduced protein becomes axial ($g_\parallel = 2.03$ and $g_\perp = 1.92$), and its relaxation is now characteristic of a $[2Fe–2S]^+$ center (unpublished results). However, the temperature dependence of the signal closely follows that of typical $[4Fe–4S]^+$ centers. Using square wave electrochemistry it was found that DTT decreases the redox potential from –450 to –500 mV [42]. Finally, a Mössbauer study showed that the Fe^{2+} pair of the reduced cluster was strongly affected by the presence of DTT [40]. All these data were first interpreted as the signatures of DTT coordination to the subsite iron of the cluster, but, as shown below, this was dismissed by ENDOR and HYSCORE experiments.

Over the last five years, the characterization of several other members of the "Radical SAM" family has reinforced the idea that all of them proceed by the same radical chemistry. Table 1 gives a short overview of the currently recognized "Radical SAM" enzymes whose biochemical activity has been shown to depend on the presence of both a [Fe–S] center and SAM.

Biotin synthase (BioB) and lipoate synthase (LipA) catalyze a sulfur insertion into nonactivated C–H bonds during the final step in the biosynthesis of biotin and lipoic acid, respectively [43,44]. MiaB is involved in the thiomethylation of a specific adenine in tRNA [45]. MoaA is used for a GTP rearrangement leading to the precursor Z intermediate during molybdopterin biosynthesis [16]. The anaerobic coproporphyrinogen III oxidase (HemN) decarboxylates the A and B heme propionate groups to yield protoporphyrinogen IX [14,46]. Benzyl succinate synthase (BSS) catalyzes the coupling of toluene to fumarate in aromatic hydrocarbon anaerobic catabolism [47]. Anaerobic glycerol dehydratase (aGD) is involved in the metabolism of many anaerobic bacteria growing on glycerol to yield 3-hydroxypropionaldehyde, which is further reduced to 1,3-propanediol [48]. The

Table 1. "Radical SAM" Enzymes Whose Biochemical Activity Depends on
the Presence of Both an [Fe–S] center and SAM

Protein (a)	Accession no. (b)	Reaction type	Field	X-ray struct.	Ref.
LAM	AAD43134	Transposition	Lysine catabolism	+	24
PFL (AE)	P0A9N4	C–C cleavage	Anaerobic metabolism	–	25
aRNR (AE)	P0A9N8	C–OH reduction	Nucleotide reduction	–	26
BioB	P12996	Sulfur insertion	Cofactor biosynthesis	+	43,44
LipA	P60716	Sulfur insertion	Cofactor biosynthesis	–	43
MiaB	P77645	Sulfur insertion	tRNA modification	–	45
MoaA	P69848	Rearrangement	Cofactor biosynthesis	+	16
HemN	CP0977	Oxidative decarboxylation	Cofactor biosynthesis	+	14,46
BSS (AE)	CAA05050	C–C formation	Catabolism of aromatics	–	47
aGD (AE)	AAM54729	Dehydration	Anaerobic metabolism	–	48
Hpd (AE)	CAD65891	Decarboxylation	Catabolism of aromatics	–	49
SPL	P37956	C–C cleavage	DNA repair	–	50
AtsB	CAB40960	OH/SH oxidation	Sulfatase activation	–	51
HydE/G	AAS92601	?	[Fe–Fe] hydrogenase maturation	–	52

(a) In the case of AE proteins (activating enzymes), the reaction type and field refer to the activated protein.
(b) NCBI protein accession number.

decarboxylation of 4-hydroxyphenylacetate to p-cresol is catalyzed by 4-hydroxyphenylacetate decarboxylase (Hpd), actively participating in the anaerobic catabolism of aromatic derivatives [49]. Spore photoproduct lyase (SPL) is an enzyme repairing a specific photolesion in bacterial spores [50]. AtsB activates procaryotic sulfatases by oxidation of a particular serine or cysteine residues into a formyl derivative [51]. Both HydE and HydG are essential for the maturation of [Fe–Fe] hydrogenases but the nature of the enzymatic reactions is still unknown [52].

3. DETECTION OF HYPERFINE COUPLING INTERACTIONS IN METALLOPROTEINS

In EPR spectroscopy, one major source of structural information (number, nature, and geometry of ligands) regarding the paramagnetic metal center resides in the hyperfine coupling interactions between the paramagnetic electron and nearby nuclei with non-null spin (^1H, ^2H, ^{13}C, ^{14}N, ^{15}N, …). It is important to note that each hyperfine coupling interaction is independently observed, if we neglect nucleus–nucleus interactions, and that its tensor values can be easily analyzed using relatively simple local models (see below). On the contrary, global properties, reflected in Hamiltonian parameters such as g- and Zero Field Splitting D-tensors, are notoriously difficult to compute for metalloproteins as they require the complete electronic wave function to be taken into account [53–56].

In principle, hyperfine interactions can be seen directly in EPR spectra as they induce line splitting. In practice, when studying metalloprotein systems in a disor-

dered state in which a large number of hyperfine interactions exist, in the best cases one can only detect one or two of the most intense of these. In general the detectable interactions are produced between the nucleus and the electrons of the metal ion itself, as nicely illustrated by copper- and manganese-containing proteins [55,58–60]. There are three reasons for this phenomenon, summarized here:

- There are many nuclei with nuclear spins in the vicinity of the paramagnetic center. Since the *EPR transition* energy depends on the spin state of all nearby nuclei, the expected number of lines in an EPR spectrum due to hyperfine splitting increases roughly exponentially with the number of nuclei involved. Therefore, it is impossible to individually observe all these lines. As a consequence, the usual spectrum displays a broad *inhomogeneous* line.
- Hamiltonian parameters are in general anisotropic. In disordered state samples, a so-called "powder spectrum" is observed in which only very broad features subsist.
- There are other major sources of line broadening in these systems: structural disorder, due to the flexible nature of proteins in solution, leads to variations of spectroscopic parameters (*g*-strain, ZFS-strain, etc.) [61]. Inhomogeneity arising from these sources can be orders of magnitude greater than hyperfine splittings.

During the 1970s, several techniques — namely ENDOR and 1D and 2D electron spin echo envelope modulation (ESEEM) spectroscopy — were developed to efficiently measure hyperfine coupling in disordered systems. These techniques are, to a large extent, insensitive to the three major drawbacks listed above. Indeed they:

- can produce spectra in which (at least at first order for 1D and 2D ESEEM) the number of lines is roughly proportional to the number of nuclei involved. This is because these techniques detect *NMR transitions*. An NMR transition corresponding to a nucleus is independent (if we neglect the very weak nuclei–nuclei interaction) of the state of neighboring nuclei.
- produce their spectra from a subset of the molecules which all have similar orientations, thus generating a pseudomonocrystal spectrum. Due to their finite power, microwave pulses excite only a small fraction of molecules whose resonance field is within a narrow window around the applied field. Since in metalloproteins, the major source of anisotropy is the *g*-tensor anisotropy, it is possible to select a subset of proteins with the same *g* value. The classical interrogation fields used are the turning points in a dominant *g* tensor powder spectrum. If the g-tensor is rhombic, fields corresponding to g_{min} and g_{max} select molecules with only one orientation each. If the g-tensor is orthorhombic, only the field corresponding to $g_\parallel$ correspond to a pseudo-monocrystal selection. In all cases, this phenomenon greatly re-

duces the set of orientations of molecules contributing to the spectrum.

- are more or less insensitive to *g*-strain since they rely on NMR transitions that lie in one electron manifold.

On the other hand, the common major drawbacks of these techniques are their poor sensitivity compared to standard EPR and the technical difficulty of their implementation. Since these spectroscopic methods are well suited for investigating coordination of ligands to metal centers, for example, coordination of low-molecular-weight compounds to [4Fe–4S] clusters, the main topic of this chapter, it is worth briefly describing them in the following paragraphs.

3.1. ENDOR: Principles and General Considerations

ENDOR (Electron Nuclear Double Resonance) spectroscopy is used to detect small hyperfine coupling constants by combining the effect of two electromagnetic radiations that induce electronic and nuclear transitions. It can be described as NMR spectroscopy detected by EPR and is extensively used for studying biological systems [62–66]. It is implemented in two different ways: continuous wave (cw) ENDOR and pulse ENDOR. cw ENDOR is based on the partial desaturation of an EPR transition by a radiofrequency-driven nuclear transition. In solid-state samples, its major drawback is that the temperature range within which electron and nuclear relaxation times are favorable to the ENDOR phenomenon is sometimes narrow and difficult to determine. In pulsed ENDOR, the only limitation to the observation of an ENDOR effect is the relaxation time of the system during the pulse sequence. However, the choice between these techniques depends on the system studied [62]. Two main pulsed schemes are used: Davies and Mims sequences, based on a transfer of *polarization* between electron and nuclear transitions with radiofrequency (rf) pulses [65,67,68]. The Davies sequence is based on selective microwave pulses and is best adapted to the detection of large hyperfine coupling constants [65,69,70]. The Mims sequence, which is better adapted to the detection of small hyperfine coupling constants, will be discussed here. This sequence is based on the stimulated echo sequence ($\pi/2 - \tau - \pi/2 - T - \pi/2$), where a monochromatic radiofrequency π pulse is applied between the second and third microwave pulses (see Fig. 3). The change in echo intensity induced by the radiofrequency pulse is characterized by the ENDOR efficiency F, defined as follows:

$$F = \frac{1}{2}[V_{\text{off}} - V_{\text{on}}]/V_{\text{off}} , \tag{1}$$

where V_{off} is the echo amplitude without rf pulse and V_{on} is the echo amplitude with rf pulse. The echo intensity change induced by the rf pulse increases with F. An echo inversion corresponds to $F = 1$, while $F = 0$ corresponds to an absence of ENDOR effect.
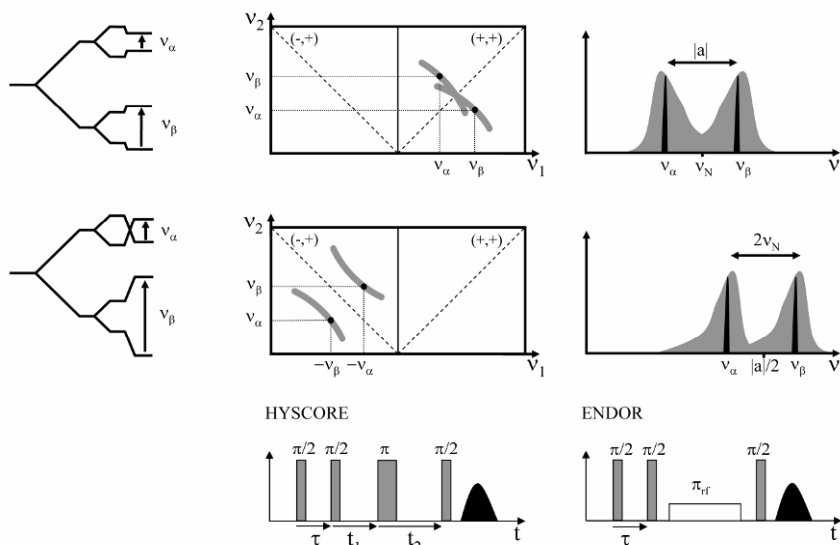
Figure 3. $I = 1/2$, $S = 1/2$ system for two different advanced EPR techniques. Upper panel: weak coupling case; lower panel: strong coupling case; left: energy level diagram; middle: HYSCORE peak pattern; right: ENDOR spectrum. In all cases, black circles or lines represent one orientation while gray patterns represent disordered system spectra.

The simplest case to investigate is an isotropic hyperfine interaction (a_{iso}) between an $I = 1/2$ nucleus and an $S = 1/2$ electronic spin (Fig. 3). There are two nuclear transitions: ν_α and ν_β. Thus,

$$F = 0 \text{ if rf frequency is different from } \nu_\alpha \text{ or } \nu_\beta, \tag{2a}$$

$$F = (1 - \cos 2\pi a_{iso}\tau)/4 \text{ if the rf frequency equals } \nu_\alpha \text{ or } \nu_\beta. \tag{2b}$$

For each nucleus, a pair of lines is detected at ν_α and ν_β. $|a_{iso}|/2 < \nu_N$ (ν_N being the nuclear Zeeman frequency) means that this doublet is centered on ν_N and separated by $|a_{iso}|$. This case is called "weak" coupling. "Strong" coupling is observed when $|a_{iso}|/2 > \nu_N$ and the doublet is centered on $|a_{iso}|/2$ and separated by $2\nu_N$. These rules stand true when an anisotropic hyperfine coupling is present. Under these conditions, a_{iso} is replaced by A, the hyperfine splitting for the actual molecular orientation. Spectra generated from $I > 1/2$ nuclei are more difficult to analyze due the presence of a quadrupolar tensor whose principal directions are, in general, noncolinear with those of the hyperfine tensor.

From an experimental point of view, it must be noted that the Mims sequence suffers from a "blind spot" phenomenon, as predicted from Eq. (2b). ENDOR efficiency F is exactly 0 for $A = n/\tau$, and for these hyperfine coupling values no signal can be detected [71]. It is thus important to carry out experiments at different τ values in order to ensure that all signals are detected. Another possible reason for

the nonobservation of lines is due to the poor ENDOR sensitivity of low NMR frequencies. Nuclei with a small gyromagnetic ratio and hyperfine coupling are not detected and the low-frequency line of a pair is sometimes very small or invisible [68,72]. To counteract this effect, the usual strategy is to increase the frequency of the EPR apparatus (Q or W band), thus shifting the interrogation field to a higher value and increasing the nuclear Zeeman effect. This last limitation is also observed for Davies ENDOR.

In an ordered system (single crystal) an ENDOR spectrum consists of a set of narrow symmetrical lines [73–75], whereas in a disordered state sample (most commonly found in biological samples) the lines are broader and acquire a complex shape [76]. This is due to the fact that each broad line is the sum of numerous individual narrow lines from molecules with a set of differing orientations. It is only for pseudomonocrystal orientations (see above) that the ENDOR spectrum is simple. In general, a series of ENDOR spectra for different magnetic fields and simulation of the lineshape is essential to obtain the principal values for the hyperfine tensor. This phenomenon is particularly troublesome for $I > 1/2$ nuclei and could undermine the ability to obtain the principal hyperfine tensor values. If this situation arises with ^{14}N nuclei, the simplest solution may be to isotopically label the protein with ^{15}N, whose nucleus has an $I = 1/2$ nuclear spin. Since ^{14}N and ^{15}N nuclei have a very small gyromagnetic ratio, it is necessary to operate at Q or W band. Another possibility is to use an ESEEM or HYSCORE sequence.

3.2. ESEEM and HYSCORE

1D and 2D ESEEM (Electron Spin Echo Envelope Modulation) methods can also be used to accurately determine hyperfine coupling constants. They are based on echo amplitude modulation when changing pulse delays [68]. Upon Fourier transformation, it produces the ESEEM spectrum in which each nuclear frequency appears. A 3-pulse ESEEM sequence ($\pi/2-\tau-\pi/2-T-\pi/2$–echo) can be very easily used to measure hyperfine constants in metalloproteins and models [75,78–80]. One of the major drawbacks of this sequence is due to "dead time" effects. In principle, it is possible to obtain an "ideal" spectrum if one acquires the whole echo intensity modulation as a function of time interval T between the second and third pulses. But the loss of the earliest points of this time evolution due to spectrometer "dead time" leads to signal distortion and disappearance of broad features. Signal processing may reduce this phenomenon without completely removing it.

HYSCORE (Hyperfine Sublevel Correlation) is a two-dimensional version of 3-pulse ESEEM in which hyperfine transitions in alpha and beta electron manifolds are correlated. This is achieved by introducing, in the 3-pulse ESEEM sequence, a microwave π pulse that transfers nuclear coherence between the two electronic manifolds. Echo intensity modulation is recorded for various values of t_1 and t_2 free evolution times, and a 2D Fourier transform is subsequently applied (Fig. 3). Information is displayed in four quadrants, called (+,+), (–,+), (+,–), and (–,–), with reference to the values of ν_1 and ν_2 frequency abscissa, either <0 or >0. It is symmetrical relative to 0; therefore, the traditional representation consists of only the two upper quadrants: (–,+) and (+,+). Originally developed by Höfer for the study

of single crystals, this sequence has become the standard 2D ESEEM technique for hyperfine coupling measurement in disordered systems [81–85]. It is particularly well adapted for this purpose since it is less prone to dead-time problems. On the contrary, it is prone to blind-spot phenomena (depending on the τ value), and therefore several HYSCORE spectra must be acquired with various τ values in order to detect all relevant spectral features. HYSCORE spectra correlate each nuclear transition $\nu_{\alpha i}$ in the alpha manifold with each nuclear transition $\nu_{\beta i}$ in the beta manifold. For each correlated couple $(\nu_{\alpha i}, \nu_{\beta i})$, a pair of cross-peaks is observed in the $(+,+)$ quadrant in symmetry with respect to the diagonal and another pair in the $(-,+)$ quadrant symmetric about the antidiagonal. In general these two pairs exhibit very different intensities and in most cases only one is visible: in the $(+,+)$ quadrant for a weakly coupled nucleus and in the $(-,+)$ quadrant for a strongly coupled nucleus. Their relative intensities can be computed using the density matrix formalism [68].
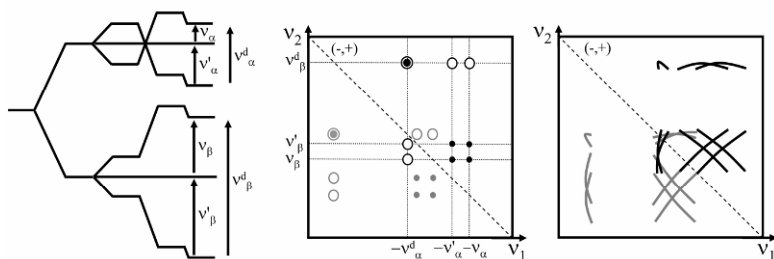

Figure 4. $I = 1$, $S = 1/2$ system in strong coupling case. Left, energy level diagram showing transitions in α and β manifolds. ν_{α}^{d} and ν_{β}^{d} represent double quanta transitions. Middle: HYSCORE peak pattern in the $(-,+)$ quadrant for a single orientation, showing the nine correlations peaks: one double quanta–double quanta peak (filled circle with halo), four double quanta–single quanta peaks (open circles), and four single quanta–single quanta peaks (filled circles). In addition to these nine peaks, nine other peaks symmetrical in the antidiagonal line are observed (shown in gray). Right: HYSCORE peak pattern in the $(-,+)$ quadrant for a disordered system. Each peak appears as a more or less elongated ridge. If the hyperfine tensor is mainly isotropic, the double quanta–double quanta correlation ridge is very short and is the dominant HYSCORE feature.

As a consequence, a HYSCORE spectrum of an $I = 1/2$ nucleus is composed of a pair of cross-peaks lying at $(\nu_{\alpha}, \nu_{\beta})$, $(\nu_{\beta}, \nu_{\alpha})$ in the weak coupling case and at $(-\nu_{\alpha}, \nu_{\beta})$ and $(-\nu_{\beta}, \nu_{\alpha})$ in the strong coupling case. If the sample is in a disordered state, cross-peaks arising from differently oriented systems produce elongated features, or "ridges." With an $I = 1$ nucleus, the spectrum becomes much more complicated since we can observe up to nine spots of pairs in a single quadrant. This number is easily explained since there are now three hyperfine transitions in each manifold: two of them are $\Delta m_I = 1$ or single (nuclear) quantum transitions, and the third is a $\Delta m_I = 2$ or double (nuclear) quantum transition. Conse-

quently, of these nine pairs, four correspond to single quantum–single quantum transition correlations, four correspond to single quantum–double quantum transition correlations, and one to a double quantum–double quantum transition correlation. Their relative disposition in a quadrant is characteristic and greatly simplifies the interpretation of such a spectrum (see Fig. 4). In the disordered state one must now deal with up to 18 ridges in a somewhat overcrowded quadrant! In the majority of cases, only a fraction of these 18 ridges is observed, but incompletely due to a poor signal-to-noise ratio. This is because the observation of a ridge is correlated not only with the intrinsic intensity of the cross-correlated pairs for each orientation but also with the ridge "frequency extension" in the (ν_1, ν_2) space. Indeed if the position of a pair changes little with molecular orientation, the corresponding ridge will be very "short" and its "linear intensity" will be important. On the contrary, an extended ridge will have a very small "linear intensity" regardless of its true intensity. This phenomenon is of prime importance in the case of a strongly coupled ^{14}N in close proximity with a paramagnetic center such that the hyperfine coupling is mainly isotropic. The double quantum–double quantum correlation peaks are, to the first order, insensitive to orientation and thus become the dominant and most easily attributed feature of the spectrum [83,86,87]. Their positions are given by the formula used to calculate hyperfine coupling constants and to roughly estimate quadrupolar coupling:

$$\nu_{dqdq} = 2[(\nu_N \pm a/2)^2 + K^2(3+\eta^2)]^{1/2}. \tag{3}$$

If a small anisotropic hyperfine interaction exists, this analysis stands true. It is possible now to repeat it for each turning point of a powder spectrum where g anisotropy is dominant to obtain the hyperfine coupling values for the three principal g-tensor directions. This rapid but crude analysis forms a good basis for a much more in-depth work involving numerical spectrum simulations based on a complete spin Hamiltonian with g-, A-, and Q-tensor values and relative orientations. The possibility to discriminate between hyperfine and quadrupolar coupling for $I > 1/2$ nuclei is a unique property of HYSCORE. It is especially useful in systems where several nuclei are present and display overlapping lines in ENDOR and 1D ESEEM spectra.

4. ANALYSIS OF LIGAND HYPERFINE COUPLING INTERACTIONS

Analysis of hyperfine coupling interactions can be made with several levels of refinement. A general statement is that an important hyperfine constant interaction is characteristic of a strongly "involved" atom: the isotropic part of the hyperfine tensor is characteristic of an electronic delocalization via orbital overlap (contact term), while the anisotropic (dipolar) part is correlated with the distance between the nucleus and the paramagnetic center. This simple analysis nevertheless allows some firm conclusions, for example, regarding the presence or not of a given atom in close proximity to the paramagnetic center. It is tempting to use the information

provided by the hyperfine coupling tensor to produce a description of the precise geometric/electronic properties of a system. However, it is necessary to understand that the robustness of the conclusions drawn from this analysis strongly depends on the accuracy of the hyperfine tensor determination (in contrast to the qualitative analysis, which requires only a rough estimate) and on the model/theoretical chemistry calculations used.

The basis of all these models is that, for a simple system (one electron in a spatial wave function ψ_0 and one nucleus):

    i.   the (contact) isotropic hyperfine constant a_{iso} is directly proportional to the probability of the presence of electron spin density at the nucleus:

$$a_{iso} = (2\mu_0/3)g_e\mu_B g_N\mu_N \left|\psi_0(0)\right|^2 ; \tag{4}$$

    ii. the dipolar hyperfine interaction can be described by a traceless symmetric tensor A:

$$A_{ij} = (\mu_0/4\pi)g_e\mu_B g_N\mu_N \left\langle \psi_0 \left|(3r_ir_j - \delta_jr^2)/r^5\right|\psi_0\right\rangle, \tag{5}$$

where r_i stands for the ith coordinate of the $\mathbf{r}$ vector connecting the electron and the nucleus. If the average distance R between the electron and nucleus is greater than electronic delocalization ($<1/r^3> = 1/R^3$), A becomes an axial tensor ($-a,-a,2a$), with $a = (\mu_0/4\pi)g_e\mu_B g_N\mu_N/R^3$, and with the axial principal direction parallel to the electron-nucleus direction.

For an [Fe–S] cluster system, a precise analysis is very difficult to carry out for several different reasons:

•   In exchange-coupled systems like an [Fe–S] cluster, it is impossible to model an $S = 1/2$ state as a single paramagnetic electron. On the contrary, each iron atom has a contribution whose general effect can be seen as a dipole only at very long distances. For shorter distances the individual contribution of each ion is not negligible and one must use a *local spin* description of the system [88,89]. The contribution of the ith iron depends on the coupling scheme and the magnetic state of the cluster and is characterized by a "spin coupling coefficient," K_i, which reflects the way the iron spin projects itself onto the total cluster spin. The four K_i values of a [4Fe–4S] cluster in the $S = 1/2$ state can be either positive or negative, and their sum is equal to 1. This local spin model implies that the through-space (nonlocal) dipolar hyperfine tensor between a nucleus and the paramagnetic cluster is now

$$A = \Sigma_i K_i A_i, \tag{6}$$

where A_i stands for the through-space dipolar hyperfine tensor corresponding to the *i*th iron.

This local spin model implies that this hyperfine tensor is now rhombic and that the simple law in $1/R^3$ for its principal values is no longer valid. The presence of K_i values of opposite signs can even lead to a "magic magnetic configuration" phenomenon for which the different dipolar contributions cancel each other at a finite distance [89,90]. Therefore, in all cases, a quantitative distance determination must use the correct set of K_i values. These values are, in general, difficult to obtain and show variation from one system to another depending on ligand nature, geometry and environment. Robust determinations of K_i in [4Fe–4S] model systems have been obtained in rare cases by single-crystal ENDOR studies and subsequent extensive analysis [75,91]. Hoffman et al. determined K_i values in the case of the substrate-bound [4Fe–4S] aconitase enzyme [69].

- The experimental anisotropic dipolar hyperfine tensor is in general not equal to the through-space dipolar hyperfine tensor. There is another contribution due to the dipolar interaction between the nucleus and the paramagnetic electron that is delocalized to some extent on orbitals centered on the nucleus itself. This last term is named the local dipolar contribution.

- The (contact) isotropic hyperfine constant is very difficult to evaluate. There is no obvious model capable of correlating the spin density on a ligand nucleus to simple geometric properties (distance, angle, ...) between the cluster and this atom. Quantum chemistry computations, in general based on DFT programs, must be used. But these computations involve the polarization of s orbitals by all the other orbitals, a phenomenon difficult to efficiently reproduce by such programs, especially when the atom hybridization is sp^2 or sp [92,93]. Knowledge of K_i values for each iron, and more particularly for the atom closest to the nucleus, is also necessary to correctly evaluate the isotropic coupling constant. In addition, there is an *orbital* contribution for both isotropic and anisotropic hyperfine tensors of the order of $\Delta g/R^3$ [94].

Since quantitative analysis of the isotropic hyperfine coupling constant for bonding atoms in order to obtain geometric/electronic prediction is very difficult, the quantitative results are generally derived from the analysis of more distant atoms where dipolar contributions predominate, as illustrated below in the case of PFL-AE.

5. APPLICATIONS TO METALLOPROTEINS

The general strategy to precisely understand the ligation in a [4Fe–4S] cluster system with three cysteine and a fourth exogenous ligand was developed by Hoffman et al. for the aconitase system in a series of seminal articles (see, e.g., [20–22,95]. While not being based on a "Radical SAM" enzyme, we think that these studies must be briefly discussed here since the same methods were employed later for the "Radical SAM" proteins [15,35]. Aconitase catalyzes the stereospecific interconversion of citrate and isocitrate. The active site contains a [4Fe–4S] iron–sulfur cluster with a labile iron. Water molecules, substrate (citrate, isocitrate, and cis-aconitate) and analogues (nitroisocitrate) can bind to this iron site. To study these ligations, the Hoffman group developed a method involving [17]O isotopic labeling of the oxygen atoms of solvent, substrates, and inhibitors (carboxylic and hydroxyl group) in different experiments [20–22]. They subsequently showed that for some labeled positions a strong [17]O hyperfine coupling interaction (9–15 MHz) was observed by using ENDOR, while for others no hyperfine coupling could be detected. An immediate and very robust interpretation of these results was that oxygen atoms for which a strong hyperfine coupling was observed were directly coordinated to the paramagnetic cluster. Further analysis showed that it was possible to distinguish between an oxygen hydroxyl coordination (with a nearly isotropic tensor of 9 MHz) and an oxygen carboxylate coordination (with a strongly anisotropic tensor of 13–15 MHz). Additional results were obtained using ^{1}H, ^{2}H, and ^{13}C ENDOR spectroscopy [21,22]. This powerful method of selective isotopic labeling of labile ligands was used successfully with two "Radical SAM" proteins, namely, PFL-AE and LAM.

5.1. Pyruvate Formate Lyase-Activating Enzyme (PFL-AE)

From initial spectroscopic and biochemical results, it was inferred that the SAM molecule was a labile fourth ligand of the reduced iron–sulfur cluster of PFL-AE (see introduction). This hypothesis was proved correct by selective [17]O and ^{13}C isotopic labeling of the SAM carboxylate group and Q-band pulsed ENDOR spectroscopic analysis of the reduced protein treated with labeled SAM [72]. Figure 5 presents 35-GHz pulsed ENDOR spectra of the [4Fe–4S]$^+$ SAM complex for samples in which the carboxyl group of the methionine moiety has been labeled with [17]O (top) and [13]C (center) and in which the amino group has been labeled with [15]N (bottom) [72]. The authors of this study found one [17]O hyperfine coupling constant of $\approx$12 MHz and a ^{13}C hyperfine coupling of 0.71 MHz along g_3 (= 1.87). These values are reminiscent of those found in the aconitase system for citrate/isocitrate directly bound via the carboxylate oxygen to the unique iron of the cluster. Another important result was the observation (Fig. 5, bottom) that a ^{14}N hyperfine coupling pattern on the ENDOR spectrum observed in the presence of ^{14}N SAM was replaced by a ^{15}N signal on the spectrum when ^{15}N-labeled SAM was used instead. This last isotopic labeling experiment result was important for two reasons. First of
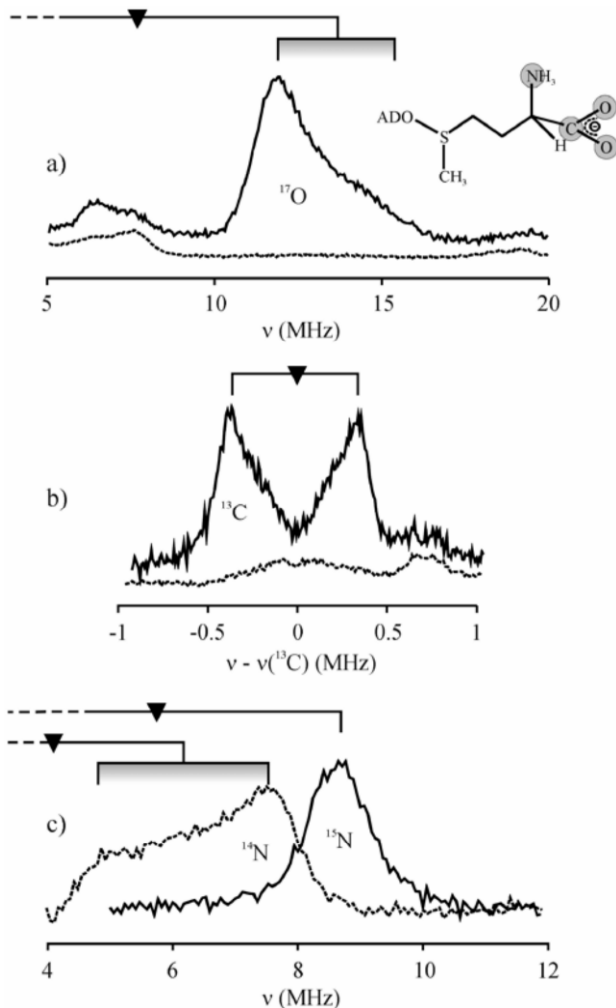
Figure 5. 35-GHz pulsed ENDOR spectra of PFL-AE with ^{17}O (a) and ^{13}C (b) carboxylato-labeled, and N-amino-labeled (c) AdoMet compared with data from an unlabeled sample, at $g_\perp$. **Conditions**: $T = 2$ K; $\nu_{MW} = 34.9$ GHz; rf pulse length = 60 μs. (a) ^{17}O-labeled, Davies ENDOR; MW pulse lengths = 80, 40, and 80 ns; number of averaged transients at each point: ^{17}O = 288, unlabeled = 200. (b) ^{13}C-labeled, Mims ENDOR; MW pulse lengths = 80 ns; $\tau = 552$ ns, number of averaged transients: ^{13}C-labeled = 144, unlabeled = 600. (c) ^{15}N-labeled, Davies ENDOR; MW pulse lengths = 80, 40, and 80 ns; number of averaged transients: ^{15}N-labeled = 80, unlabeled = 624. Reprinted with permission from [72]. Copyright © 2002, American Chemical Society.

all, it proved that the amino group was somehow involved in the ligation of SAM to the cluster. Second, it facilitated the analysis of the ENDOR nitrogen spectrum and permitted a robust estimation of the nearly isotropic hyperfine coupling con-

stant (5.8 and 6.4 MHz after refinement) [96]. This value is comparable to that of histidine nitrogen hyperfine coupling in Rieske protein as well as that of ACC (amino-cyclopropane carboxylate) nitrogen coupling to the mononuclear Fe of ACC oxidase [97,98]. Since x-ray crystallography demonstrated that, in the Rieske protein, the nitrogen atom was directly bound to Fe, this similarity implied that the amino group nitrogen of SAM is directly ligated to the unique iron of the PFL-AE cluster. It appears from these experiments that the iron–sulfur cluster anchors the SAM molecule by an oxygen/nitrogen bidentate coordination (Fig. 2). Even though no three-dimensional structure is available for PFL-AE as of yet, this mode of SAM binding was observed in 3D structures of all "Radical SAM" enzymes crystallographically resolved to date. The Hoffman group performed other studies with the same methodology by labeling substituents of the sulfonium center of SAM [71]. They succeeded in observing a hyperfine coupling interaction between the paramagnetic cluster and ^{13}C and ^{2}H atoms of the SAM methyl group. The maximum value observed for ^{2}H (1 MHz) corresponds to an equivalent ^{1}H hyperfine coupling of 6–7 MHz and must be due to an atom in the near vicinity. The same conclusion could be obtained from the ^{13}C hyperfine coupling constant.

To quantitatively analyze their results, Hoffman et al. first obtained the best possible estimation of the ^{13}C hyperfine tensor using the evolution of ENDOR spectra across the EPR spectrum to extract its principal values and principal directions. The ^{13}CH$_3$ tensor principal values were found to be equal to [–0.6 (1), +0.4 (1.5), –0.5(1)] MHz [71]. The authors subsequently analyzed this tensor as the sum of an isotropic contribution (–0.23 MHz) and of two purely anisotropic orthogonal tensors of the form (–a,–a,+$2a$). The isotropic part is attributed to the presence of spin density on the ^{13}C nucleus. This means that there is an orbital overlap between the cluster and the CH$_3$ group. Hoffman et al. suggested that this delocalization is indirect, passing through the sulfur atom of the sulfonium group [71]. The two anisotropic tensors are attributed to the nonlocal through-space dipolar interaction between the cluster and the ^{13}C nucleus and to a local dipolar interaction, respectively. Assuming that only the nearest iron atom contributes to the nonlocal dipolar tensor and taking a |K| value range from 0.86 to 1.78 (determined from the aconitase-bound cluster), the authors obtained a ^{13}C–Fe distance of between 4.0 and 5.0 Å.

The same analyses were performed on the carboxylate ^{13}C ENDOR spectra [99] and the ^{2}H ENDOR spectra of the deuterated methyl group [71]. The first analysis gives a distance between the anchoring iron and the carbon atom of 3.3 Å with a K value of 1.57, thus confirming the binding of carboxylate to the cluster. The second is trickier because (i) there are now three hyperfine tensors involved and (ii) the ^{2}H nuclear spin is equal to 1, implying that a (small) quadrupolar contribution is now present. Nevertheless, the authors managed to obtain distances between the closest ^{2}H atom and the iron compatible with those found with the ^{13}CH$_3$ experiment. Obviously, this methodology can be applied only to paramagnetic states. In order to check whether SAM was also a ligand to the cluster in the native [4Fe–4S]$^{2+}$, Hoffman et al. performed the same spectroscopic analysis on

cryoreduced frozen enzyme preparations of PFL-AE in the $[4Fe–4S]^{2+}$ state. Reduction of the frozen oxidized protein allows its conversion to the EPR-observable paramagnetic 1+ state while, because of the low temperature, retaining the 2+ state coordination and geometry. ENDOR spectra were essentially the same as those obtained with the nonfrozen reduced PFL-AE, demonstrating that SAM was bound to the cluster through the same coordination mode in oxidized and reduced enzyme.

The above analysis is based on a fundamental hypothesis: only the nearest iron atom of the cluster contributes to the hyperfine interaction and consequently it is possible to impose a $(–a,–a,+2a)$ axial form on the nonlocal through-space dipolar tensor. However, strictly speaking, contributions of the three other iron ions are not negligible, since they account for approximately 10% of the experimental anisotropic tensor. Therefore, it is impossible to decompose the experimental anisotropic tensor into local and nonlocal tensors as suggested by the authors. However, the breakdown of this hypothesis would not substantially change the distance calculated. This is because the neglected corrective term due to the three other iron ions are one order of magnitude smaller than the term from the closest iron. Since the distance is proportional to the inverse of the cubic root of hyperfine tensor principal values, a 10% uncertainty in the value of the hyperfine tensor would result in a 3% uncertainty on the calculated distance! But it must be noted that the authors' method, as presented here, is not necessarily better than a very crude distance estimation from the diagonalized unprocessed experimental anisotropic hyperfine tensor.

5.2. Lysine 2,3-Aminomutase (LAM)

LAM was studied by the Hoffman group in the same way as PFL-AE [99]. They found essentially the same results with a SAM coordination via an oxygen atom of the carboxylate group and the nitrogen of the amino group and a close proximity between the SAM methyl group and the iron–sulfur cluster. Hyperfine coupling tensors were nonetheless distinctly different from those obtained in the PFL-AE system, in particular for the ^{15}N amino group (9.1 MHz at g_2 vs. 6.4 MHz for PFL-AE) and the $^{13}CH_3$ methyl group (0.8 MHz at g_2 vs. 0.6 MHz). These results showed that the precise geometry of the cluster SAM complex is somewhat different in PFL-AE and in LAM. In particular, the authors pointed out that despite a greater ^{13}C hyperfine interaction with the cluster, there was a lack of spin density on this nucleus. This implies a closer proximity between the sulfonium group and the cluster without orbital overlap. The ^{17}O and ^{15}N hyperfine coupling differences were harder to analyze since the isotropic hyperfine contribution is dominant (see above). It is only when more proteins have been discovered that it will be possible to determine the meaning of these variations and to correlate them with other properties. So far, LAM is the only "Radical SAM system" for which both ENDOR analysis and three-dimensional structure determination have been performed. Spectra obtained with cryoreduced or standard samples were indistinguishable, thus indicating the same geometry in the two redox states [99].

5.3. Anaerobic Ribonucleotide Reductase Activating Enzyme (aRNR-AE)

To prove that SAM binds the iron–sulfur cluster of the aRNR activase, we decided to use HYSCORE spectroscopy with unlabelled SAM [18]. Figure 6 shows the HYSCORE spectra of anaerobically reduced aRNR-AE either in the absence (6A) or in the presence (6B) of an excess of SAM. Upon addition of SAM, the HYSCORE spectrum was dramatically modified and a complex spot pattern appeared, mainly in the (–,+) quadrant. By comparison with theoretical results [68,85] and HYSCORE spectra of Rieske proteins [86,100–102], it was possible to interpret this pattern as produced by a ^{14}N atom experiencing strong coupling. One easily observed feature, and probably the most characteristic and interesting one, is constituted by two peaks lying in the (–,+) quadrant and slightly elongated along the antidiagonal up to (–9.16,+5.25) and (–5.25,+9.16) MHz. They were attributed to a double quantum–double quantum correlation. As explained above, they are easily observed since a double quantum transition frequency does not depend, to first order, on the quadrupolar interaction. It is possible to obtain a good estimation of the hyperfine constant from the position of the double quantum–double quantum peaks using Eq. (3). The value obtained, when scaled according to $(\gamma^{15}N/\gamma^{14}N)$ gives a mainly isotropic constant of 8.9 MHz on $g_\perp$ in the range of the values obtained by ^{15}N ENDOR spectroscopy for LAM and PFL-AE. Strictly speaking, this experiment does not demonstrate that SAM is bound to the cluster since the ^{14}N atom might belong to the polypeptide chain and become a ligand to the cluster due to a conformational change induced by the addition of SAM itself. However, because of the similarities between hyperfine coupling values obtained with PFL-AE and LAM, we concluded that, in aRNR-AE, the amino group of SAM was a ligand to the cluster. The same experiment was carried out with aRNR-AE complexed to the G681A mutant aRNR protein α and gave exactly the same results, showing that the binding of SAM to the subsite Fe of the [Fe–S] center is not affected by complex formation of the activase to its target protein [18].

As mentioned in the introduction, DTT has a strong impact on the spectroscopic and biochemical properties of aRNR-AE. A possible explanation was that the changes seen upon DTT incubation were due to DTT binding to the [Fe–S] center. It is interesting to note that such a binding has been found in the crystal structure of the MoaA protein (a radical SAM protein carrying an additional [4Fe–4S] center) [16]. Several attempts were made to demonstrate a ligation between the DTT molecule and the cluster by actually observing the hyperfine coupling between the paramagnetic center and the DTT nuclei. cw X-band ENDOR of reduced aRNR-AE incubated with DTT and (d4)-DTT were carefully compared. They showed no differences in the ^{1}H region (apart from nearly distant protons) and appearance of a small broad featureless line in the ^{2}H zone [103]. Since X-band ENDOR is not adapted to efficiently detect a signal in such a low-frequency range, an X-band HYSCORE experiment was performed. The (d4)-DTT HYSCORE spectrum showed a strong signal in the ^{2}H frequency range mainly on the (+,+)
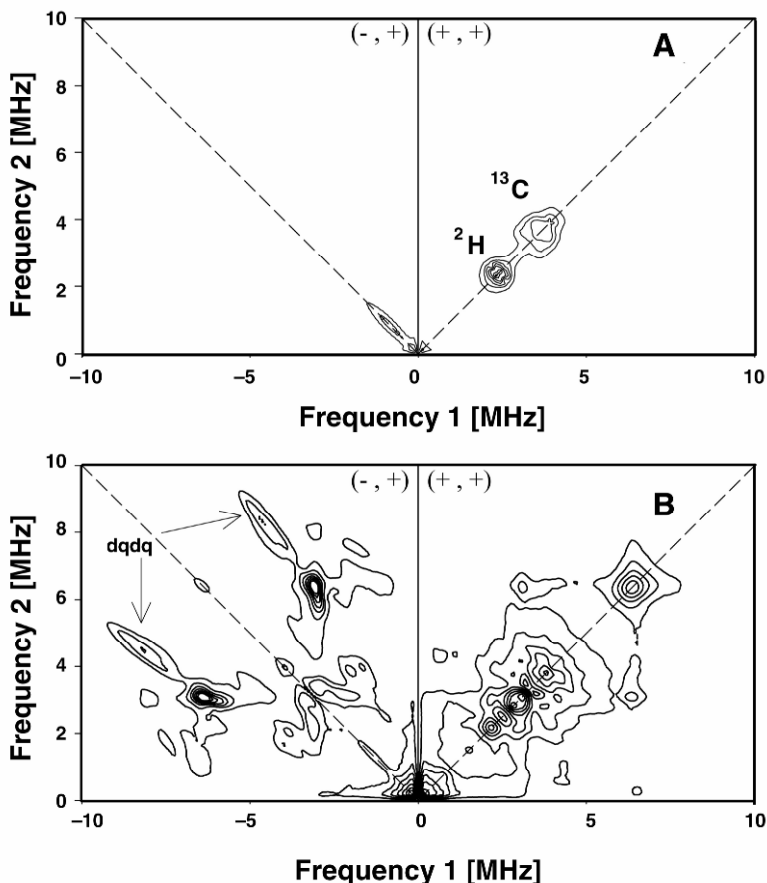
Figure 6. Low-frequency region of the X-band HYSCORE spectra of the activase (0.8 mM) reduced with sodium dithionite in the presence of DTT (5 mM) before (6A) and after (6B) addition of SAM (2 mM). In the (+,+) quadrant, spots due to distant ^{13}C and ^{2}H nuclei are indicated. In the (–,+) quadrant of Figure 6B, the peaks are characteristic of a strongly coupled ^{14}N nucleus, and those denoted dq are assigned to a pair of a double quanta correlation peak. The marked features (*) in Figure 6B are artefactual due to nonideal pulses. **Recording conditions**: frequency (GHz): without SAM, 9.75; with SAM, 9.68. Recording fields (mT): without SAM, 362; with SAM, 359. Temperature: 12 K. Sequence: $\pi/2–\tau–\pi/2–t_1–\pi–t_2–\pi/2$. $\pi/2 = 16$ ns, $\tau = 132$ ns, 4-step phase cycle. The experimental data set of 256×256 points (increment of t_1 and $t_2 = 24$ ns) was acquired on a Bruker Elexsys E-580 X-band pulsed spectrometer.

quadrant diagonal. Upon careful analysis, a small structure along the (+,+) quadrant diagonal could be detected and attributed to the ^{2}H quadrupolar interaction. Another attempt was made with (^{77}Se)-DTT. Upon addition to reduced aRNR-AE, this molecule caused changes to the EPR spectrum similar to those observed with

DTT (g tensor, relaxation properties). A careful analysis showed that no broadening due to a strong hyperfine coupling could be detected. Similarly, relaxation properties were found to be identical to the DTT system. Further analysis with HYSCORE experiments only showed a small signal occurring at ν^{77}Se along the (+,+) diagonal quadrant without any sizeable splitting characteristic of a hyperfine coupling constant [103]. The conclusions that could be drawn from these two experiments were compatible: DTT was not a cluster ligand.

6. CONCLUSION

Advanced EPR methods (ENDOR, HYSCORE) have demonstrated their great potential for providing detailed information on coordination of metal centers in metalloproteins. This is nicely illustrated by the studies on "Radical SAM" enzymes since, in this case, these EPR methods led to a model for the [4Fe–4S]–SAM complex that was proved to be exact by subsequent x-ray crystallographic studies. Drastic changes of the EPR spectrum of a [4Fe–4S]$^+$ cluster upon addition of a small molecule are not an unambiguous signature of complex formation, as generally assumed. ENDOR and HYSCORE spectroscopy studies on appropriately labeled compounds remain the best tool to firmly establish the existence of such complexes.

There is still a need to accumulate more spectroscopic and crystallographic data on more examples as well as to develop theoretical models in order to establish correlations between structure and hyperfine coupling interactions.

ACKNOWLEDGMENT

REFERENCES

1. Beinert H. 2000. Iron–sulfur proteins: ancient structures, still full of surprises. *J Biol Inorg Chem* **5**:2–15.
2. Green J, Paget MS. 2004. Bacterial redox sensors. *Nature Rev Microbiol* **2**:954–966.
3. Flint DH, Allen RM. 1996. Iron–sulfur proteins with nonredox functions. *Chem Rev* **96**:2315–2334.
4. Fontecave M, Mulliez E, Ollagnier-de Choudens S. 2001. Adenosylmethionine as a source of 5'-deoxyadenosyl radicals. *Curr Opin Chem Biol* **5**:506–511.
5. Cheek J, Broderick JB. 2001. Adenosylmethionine-dependent iron–sulfur enzymes: versatile clusters in a radical new role. *J Biol Inorg Chem* **6**:209–226.
6. Frey PA, Magnusson OT. 2003. S-adenosylmethionine: a wolf in sheep's clothing, or a rich man's adenosylcobalamin? *Chem Rev* **103**:2129–2148.

7. Volbeda A, Charon MH, Piras C, Hatchikian EC, Frey M, Fontecilla-Camps JC. 1995. Crystal structure of the nickel-iron hydrogenase from *Desulfovibrio gigas*. *Nature* **373**:580–587.

8. Nicolet Y, Piras C, Legrand P, Hatchikian CE, Fontecilla-Camps JC. 1999. *Desulfovibrio desulfuricans* iron hydrogenase: the structure shows unusual coordination to an active site Fe binuclear center. *Structure* **7**:13–23.

9. Peters JW, Lanzilotta WN, Lemon BJ, Seefeldt LC. 1998. X-ray crystal structure of the Fe-only hydrogenase (CpI) from *Clostridium pasteurianum* to 1.8 angstrom resolution. *Science* **282**:1853–1858.

10. Berkovitch F, Nicolet Y, Wan JT, Jarrett JT, Drennan CL. 2004. Crystal structure of biotin synthase, an S-adenosylmethionine-dependent radical enzyme. *Science* **303**:76–79.

11. Calzolai L, Gorst CM, Zhao ZH, Teng Q, Adams MW, La Mar GN. 1995. ^{1}H NMR investigation of the electronic and molecular structure of the four-iron cluster ferredoxin from the hyperthermophile *Pyrococcus furiosus*: identification of Asp 14 as a cluster ligand in each of the four redox states. *Biochemistry* **34**:11373–11384.

12. Dobritzsch D, Schneider G, Schnackerz, KD, Lindqvist Y. 2001. Crystal structure of dihydropyrimidine dehydrogenase, a major determinant of the pharmacokinetics of the anti-cancer drug 5-fluorouracil. *EMBO J* **20**:650–660.

13. Bückel W. Personal communication.

14. Layer G, Moser J, Heinz DW, Jahn D, Schubert W-D. 2003. Crystal structure of coproporphyrinogen III oxidase reveals cofactor geometry of Radical SAM enzymes. *EMBO J* **22**:6214–6224.

15. Walsby CJ, Ortillo D, Broderick WE, Broderick JB, Hoffman BM. 2002. An anchoring role for FeS clusters: chelation of the amino acid moiety of S-adenosylmethionine to the unique iron site of the [4Fe–4S] cluster of pyruvate formate-lyase activating enzyme. *J Am Chem Soc* **124**:11270–11271.

16. Hänzelmann P, Schindelin H. 2004. Crystal structure of the S-adenosylmethionine-dependent enzyme MoaA and its implications for molybdenum cofactor deficiency in humans. *Proc Natl Acad Sci USA* **10**:12870–12875.

17. Lepore BW, Ruzicka FJ, Frey PA Ringe D. 2005. The X-ray crystal structure of lysine-2,3-aminomutase from *Clostridium subterminale*. *Proc Natl Acad Sci USA* **102**:13819–13824.

18. Gambarelli S, Luttringer F, Padovani D, Mulliez E Fontecave M. 2005. Activation of the anaerobic ribonucleotide reductase by S-adenosylmethionine. *ChemBioChem* **6**:1–3.

19. Beinert H, Kennedy MC, Stout CD. 1996. Aconitase as iron–sulfur protein, enzyme, and iron-regulatory protein. *Chem Rev* **96**:2335–2374.

20. Werst MM, Kennedy MC, Beinert H, Hoffman BM. 1990. [17]O, ^{1}H, and ^{2}H electron nuclear double resonance characterization of solvent, substrate, and inhibitor binding to the [4Fe–4S]$^+$ cluster of aconitase. *Biochemistry* **29**:10526–10532.

21. Telser J, Emptage MH, Merkle H, Kennedy MC, Beinert H, Hoffman BM. 1986. [17]O electron nuclear double resonance characterization of substrate binding to the [4Fe–4S]$^{1+}$ cluster of reduced active aconitase. *J Biol Chem* **261**:4840–4846.

22. Kennedy MC, Werst M, Telser J, Emptage MH, Beinert H, Hoffman BM. 1987. Mode of substrate carboxyl binding to the [4Fe–4S]$^+$ cluster of reduced aconitase as studied by [17]O and ^{13}C electron-nuclear double resonance spectroscopy. *Proc Natl Acad Sci USA* **84**:8854–8858.

23. Sofia HJ, Chen G, Hetzler BG, Reyes-Spindola JF, Miller NE. 2001. Radical SAM, a novel protein superfamily linking unresolved steps in familiar biosynthetic pathways

with radical mechanisms: functional characterization using new analysis and information visualization methods. *Nucleic Acids Res* **29**:1097–1106.

24. Frey PA, Booker S. 1999. Radical intermediates in the reaction of lysine 2,3-aminomutase. In *Advances in Free Radical Chemistry*, 2:1–43. Ed Z Zard. Greenwich: JAI Press.

25. Buis JM, Broderick JB. 2005. Pyruvate formate-lyase activating enzyme: elucidation of a novel mechanism for glycyl radical formation. *Arch Biochem Biophys* **433**:288–296.

26. Fontecave M, Mulliez E, Logan DT. 2002. Deoxyribonucleotide synthesis in anaerobic microorganisms: the class III ribonucleotide reductase. In *Progress in Nucleic Acid Research and Molecular Biology*, 72:95–127. Ed K Moldave. San Diego: Elsevier Science.

27. Magnusson OT, Reed G Frey PA. 1999. Spectroscopic evidence for the participation of an allylic analogue of the 5'-deoxyadenosyl radical in the reaction of lysine 2,3-aminomutase. *J Am Chem Soc* **121**:9764–9765.

28. Frey M, Rothe M, Wagner AF, Knappe J. 1994. Adenosylmethionine-dependent synthesis of the glycyl radical in pyruvate formate-lyase by abstraction of the glycine C-2 pro-S hydrogen atom: studies of [^{2}H]-glycine-substituted enzyme and peptides homologous to the glycine 734 site. *J Biol Chem* **269**:12432–12437.

29. Kilgore JL, Aberhart DJ. 1991. Lysine 2,3-aminomutase: role of S-adenosyl-l-methionine in the mechanism: demonstration of tritium transfer from (2RS,3RS)-[3-^{3}H]lysine to S-adenosyl-L-methionine. *J Chem Soc Perkin Trans* **1**:79–84.

30. Cheek J, Broderick JB. 2002. Direct H atom abstraction from spore photoproduct C-6 initiates DNA repair in the reaction catalyzed by spore photoproduct lyase: evidence for a reversibly generated adenosyl radical intermediate. *J Am Chem Soc* **124**:2860–2861.

31. Wagner AF, Frey M, Neugebauer FA, Schafer W, Knappe J. 1992. The free radical in pyruvate formate-lyase is located on glycine-734. *Proc Natl Acad Sci USA* **89**:996–1000.

32. Kulzer R, Pils T, Kappl R, Huttermann J, Knappe J. 1998. Reconstitution and characterization of the polynuclear iron–sulfur cluster in pyruvate formate-lyase-activating enzyme: molecular properties of the holoenzyme form. *J Biol Chem* **273**:4897–4903.

33. Henshaw TF, Cheek J, Broderick JB. 2000. The [4Fe–4S]$^{1+}$ cluster of pyruvate formate-lyase activating enzyme generates the glycyl radical on pyruvate formate-lyase: EPR-detected single turnover. *J Am Chem Soc* **122**:8331–8332.

34. Broderick JB, Duderstadt RE, Fernandez DC, Wojtuszewski K, Henshaw TF, Johnson, MK. 1997. Pyruvate formate-lyase activating enzyme is an iron–sulfur protein. *J Am Chem Soc* **119**:7396–7397.

35. Walsby CJ, Hong W, Broderick WE, Cheek J, Ortillo D, Broderick JB, Hoffman BM. 2002. Electron-nuclear double resonance spectroscopic evidence that S-adenosylmethionine binds in contact with the catalytically active [4Fe–4S]$^+$ cluster of pyruvate formate-lyase activating enzyme. *J Am Chem Soc* **124**:3143–3151.

36. Lieder KW, Booker S, Ruzicka FJ, Beinert H, Reed GH, Frey PA. 1998. S-Adenosylmethionine-dependent reduction of lysine 2,3-aminomutase and observation of the catalytically functional iron–sulfur centers by electron paramagnetic resonance. *Biochemistry* **37**:2578–2585.

37. Jordan A, Reichard P. 1998. Ribonucleotide reductases. *Annu Rev Biochem* **67**:71–98.

38. Logan DT, Mulliez E, Larsson KM, Bodevin S, Atta M, Garnaud PE, Sjöberg B-M, Fontecave M. 2003. A metal binding site in the catalytic subunit of anaerobic ribonucleotide reductase. *Proc Natl Acad Sci USA* **100**:3826–3831.

39. Tamarit J, Mulliez E, Meier C, Trautwein A, Fontecave M. 1999. The anaerobic ribonucleotide reductase from *E. coli*: the small protein is an activating enzyme containing a [4Fe–4S]$^{2+}$ center. *J Biol Chem* **274**:31291–31296.

40. Padovani D, Thomas F, Trautwein AX, Mulliez E, Fontecave M. 2001, Activation of class III ribonucleotide reductase from *E. coli*: the electron transfer from the iron sulfur center to S-adenosyl methionine. *Biochemistry* **40**:6713–6719.

41. Ollagnier S, Mulliez E, Schmidt PP, Eliasson R, Gaillard J, Deronzier C, Bergman T, Graslund A, Reichard P, Fontecave M. 1997. Activation of the anaerobic ribonucleotide reductase from *Escherichia coli*: the essential role of the iron-sulfur center for S-adenosylmethionine reduction. *J Biol Chem* **272**:24216–24223.

42. Mulliez E, Padovani D, Atta M, Alcouffe C, Fontecave M. 2001. Activation of class III ribonucleotide reductase by flavodoxin: a protein radical-driven electron transfer to the iron–sulfur center. *Biochemistry* **40**:3730–3736.

43. Fontecave M, Ollagnier-de-Choudens S, Mulliez E. 2003. Biological radical sulfur insertion reactions. *Chem Rev* **103**:2149–2166.

44. Jarrett JT. 2005. The novel structure and chemistry of iron–sulfur clusters in the adenosylmethionine-dependent radical enzyme biotin synthase. *Arch Biochem Biophys* **433**:312–321.

45. Pierrel F, Douki T, Fontecave M, Atta M. 2004. MiaB protein is a bifunctional radical-S-adenosylmethionine enzyme involved in thiolation and methylation of tRNA. *J Biol Chem* **279**:47555–17563.

46. Layer G, Grage K, Teschner T, Schunemann V, Breckau D, Masoumi A, Jahn M, Heathcote P, Trautwein AX, Jahn D. 2005. Radical S-adenosylmethionine enzyme coproporphyrinogen III oxidase HemN: functional features of the [4Fe–4S] cluster and the two bound S-adenosyl-L-methionine. *J Biol Chem* **280**:29038–29046.

47. Leuthner B, Leutwein C, Schulz H, Horth P, Haehnel W, Schiltz E, Schagger H, Heider J. 1998. Biochemical and genetic characterization of benzylsuccinate synthase from *Thauera aromatica*: a new glycyl radical enzyme catalysing the first step in anaerobic toluene metabolism. *Mol Microbiol* **28**:615–628.

48. O'Brien JR, Raynaud C, Croux C, Girbal L, Soucaille P, Lanzilotta WN. 2004. Insight into the mechanism of the B12-independent glycerol dehydratase from *Clostridium butyricum*: preliminary biochemical and structural characterization. *Biochemistry* **43**:4635–4645.

49. Andrei PI, Pierik AJ, Zauner S, Andrei-Selmer LC, Selmer T. 2004. Subunit composition of the glycyl radical enzyme p-hydroxyphenylacetate decarboxylase: a small subunit, HpdC, is essential for catalytic activity. *Eur J Biochem* **271**:2225–2230.

50. Rebeil R, Sun Y, Chooback L, Pedraza-Reyes M, Kinsland C, Begley TP, Nicholson WL. 1998. Spore photoproduct lyase from *Bacillus subtilis* spores is a novel iron–sulfur DNA repair enzyme which shares features with proteins such as class III anaerobic ribonucleotide reductases and pyruvate–formate lyases. *J Bacteriol* **180**:4879–4885.

51. Fang Q, Peng J, Dierks T. 2004. Post-translational formylglycine modification of bacterial sulfatases by the radical S-adenosylmethionine protein AtsB. *J Biol Chem* **279**:14570–14578.

52. Rubach JK, Brazzolotto X, Gaillard J, Fontecave M. 2005. Biochemical characterization of the HydE and HydG iron-only hydrogenase maturation enzymes from *Thermatoga maritima*. *FEBS Lett* **579**:5055–5060.

53. van Lenthe E, van der Avoird A, Hagen WR, Reijerse EJ. 2000. Density functional calculations of g-tensors of low-spin iron(I) and iron(III) porphyrins. *J Phys Chem A* **104**:2070–2077.

54. Malkina OL, Vaara J, Schimmelpfenning B, Munzarova M, Malkin VG, Kaupp M. 2000. Density functional calculations of electronic g-tensors using spin-orbit pseudopotentials and mean-field all-electron spin-orbits operators. *J Am Chem Soc* **122**:9206–9218.

55. Vrajmasu VV, Bominaar EL, Meyer J, Münck E. 2002. Mössbauer study of reduced rubredoxin as purified and in whole cells: structural correlation analysis of spin hamiltonian parameters. *Inorg Chem* **41**:6358–6371.

56. Gambarelli S, Mouesca J-M. 2004. Correlation between the magnetic g tensors and the local cysteine geometries for a series of reduced [2Fe–2S*] protein clusters: a quantum chemical density functional theory and structural analysis. *Inorg Chem* **43**:1441–1451.

57. Solomon EI, Szilagyi RK, DeBeer George S, Basumallick L. 2004. Electronic structure of metal sites in proteins and models: contributions to function in blue copper proteins. *Chem Rev* **104**:419–458.

58. Hwang HJ, Nagraj N, Lu Y. 2006. Spectroscopic characterizations of bridging cysteine ligand variants of an engineered Cu2(Scys)2 CuA azurin. *Inorg Chem* **45**:102–107.

59. Schansker G, Goussias C, Petrouleas V, Rutherford AW. 2002. Reduction of the Mn cluster of the water-oxidizing enzyme by nitric oxide: formation of an S-2 state. *Biochemistry* **41**:3057–3064.

60. Wu AJ, Penner-Hahn JE, Pecoraro VL. 2004. Structural, spectroscopic, and reactivity models for the manganese catalases. *Chem Rev* **104**:903–938.

61. Hagen WR. 1989. *g*-strain: inhomogeneous broadening in metalloprotein EPR. In *Advanced EPR Applications in Biology and Biochemistry*, pp. 785–811. Ed AJ Hoff. Amsterdam: Elsevier.

62. Hoffman BM. 2003. ENDOR of metalloenzymes. *Acc Chem Res* **36**:522–529.

63. Hoffman BM. 2003. Electron-nuclear double resonance spectroscopy (and electron spin-echo envelope modulation spectroscopy) in bioinorganic chemistry. *Proc Natl Acad Sci USA* **100**:3575–3578.

64. Brecht M, Van Gastel M, Buhrke T, Friedrich B, Lubitz W. 2003. Direct detection of a hydrogen ligand in the [NiFe] center of the regulatory H$_2$-sensing hydrogenase from *Ralstonia eutropha* in its reduced state by HYSCORE and ENDOR spectroscopy. *J Am Chem Soc* **125**:13075–13083.

65. Walsby CJ, Krepkiy D, Petering DH, Hoffman BM. 2003. Cobalt-substituted zinc finger 3 of transcription factor IIIA: interactions with cognate DNA detected by ^{31}P ENDOR spectroscopy. *J Am Chem Soc* **125**:7502–7503.

66. Lendzian F. 2005. Structure and interactions of amino acid radicals in class I ribonucleotide reductase studied by ENDOR and high-field EPR spectroscopy. *Biochim Biophys Acta* **1707**:67–90.

67. Gemperle C, Schweiger A. 1991. Pulsed electron-nuclear double resonance methodology. *Chem Rev* **91**:1481–1505.

68. Schweiger A, Jeschke G. 2001. *Principles of pulsed electron paramagnetic resonance*. Oxford: Oxford UP.

69. Telser J, Huang H, Lee H-I, Adams MW, Hoffman BM. 1998. Site Valencies and Spin Coupling in the 3Fe and 4Fe (*S* = 1/2) clusters of *Pyrococcus furiosus* ferredoxin by [57]Fe ENDOR. *J Am Chem Soc* **120**:861–870.

70. Bennati M, Weiden N, Dinse KP, Hedderich R. 2004. ^{57}Fe ENDOR spectroscopy on the iron–sulfur cluster involved in substrate reduction of heterodisulfide reductase. *J Am Chem Soc* **126**:8378–8379.

71. Walsby CJ, Hong W, Broderick WE, Cheek J, Ortillo D, Broderick JB, Hoffman BM. 2002. Electron-nuclear double resonance spectroscopic evidence that S-adenosylmethionine binds in contact with the catalytically active [4Fe–4S]$^+$ cluster of pyruvate formate-lyase activating enzyme. *J Am Chem Soc* **124**:3143–3151.

72. Walsby C, Ortillo D, Broderick WE, Broderick JB, Hoffman BM. 2002. An anchoring role for FeS clusters: chelation of the amino acid moiety of S-adenosylmethionine to the unique iron site of the [4Fe–4S] cluster of pyruvate formate–lyase activating enzyme. *J Am Chem Soc* **124**:11270–11271.

73. Hole EO, Nelson WH, Sagstuen E, Close DM. 1998. Electron paramagnetic resonance and electron nuclear double resonance studies of x-irradiated crystals of cytosine hydrochloride, Part I: free radical formation at 10 K after high radiation doses. *Radiat Res* **149**:109–119.

74. Hole EO, Sagstuen E, Nelson WH, Close DM. 2000. Free radical formation in x-irradiated crystals of 2'-deoxycytidine hydrochloride: electron magnetic resonance studies at 10 K. *Radiat Res* **153**:823–834.

75. Moriaud F, Gambarelli S, Lamotte B, Mouesca J-M. 2001. Detailed proton Q-band ENDOR study of the electron spin population distribution in the reduced [4Fe–4S]$^{1+}$ state. *J Phys Chem B* **105**:9631–9642.

76. Hoffman BM, Martinsen J, Venters RA. 1984. General theory of polycrystalline ENDOR patterns: g and hyperfine tensors of arbitrary symmetry and relative orientation. *J Magn Reson* **59**:110–123.

77. Bender CJ, Rosenzweig AC, Lippard SJ, Peisach J. 1994. Nuclear hyperfine coupling of nitrogen in the coordination sphere of the diiron center of methane monooxygenase hydroxylase. *J Biol Chem* **269**:15993–15998.

78. Riedel A, Fetzner S, Rampp M, Lingens F, Liebl U, Zimmermann J-L, Nitschke W. 1995. EPR, electron spin echo modulation, and electron nuclear double resonance studies of the 2Fe–2S centers of the 2-halobenzoate 1,2-dioxygenase from *Burkholderia (Pseudomonas) cepacia* 2CBS. *J Biol Chem* **270**:30869–30873.

79. Lee HC, Scheuring E, Peisach J, Chance MR. 1997. Electron spin echo envelope modulation and extended x-ray absorption fine structure studies of active site models of oxygenated cobalt-substituted hemoproteins: correlating electron-nuclear couplings and metal–ligand bond lengths. *J Am Chem Soc* **119**:12201–12209.

80. Ke S-C, Warncke K. 1999. Interactions of substrate and product radicals with CoII in cobalamin and with the active site in ethanolamine deaminase, characterized by ESE-EPR and ^{14}N ESEEM spectroscopies. *J Am Chem Soc* **121**:9922–9927.

81. Kofman V, Farver O, Pecht I, Goldfarb D. 1996. Two-dimensional pulsed EPR spectroscopy of the copper protein azurin. *J Am Chem Soc* **118**:1201–1206.

82. Dikanov SA, Davydov RM, Gräslund A, Bowman MK. 1998. Two-dimensional ESEEM spectroscopy of nitrogen hyperfine couplings in methemerythrin and azidomethemerythrin. *J Am Chem Soc* **120**:6797–6805.

83. Tyryshkin AM, Dikanov SA, Reijerse EJ, Burgard C, Hüttermann J. 1999. Characterization of bimodal coordination structure in nitrosyl heme complexes through hyperfine couplings with pyrrole and protein nitrogens. *J Am Chem Soc* **121**:3396–3406.

84. Van Doorslaer S, Jeschke G, Epel B, Goldfarb D, Eichel R-A, Kräuther B, Schweiger A. 2003. Axial solvent coordination in "base-off" Cob(II)alamin and related Co(II)-corrinates revealed by 2D-EPR. *J Am Chem Soc* **125**:5915–5927.

85. Foerster S, van Gastel M, Brecht M, Lubitz W. 2005. An orientation-selected ENDOR and HYSCORE study of the Ni–C active state of *Desulfovibrio vulgaris* Miyazaki F hydrogenase. *J Biol Inorg Chem* **10**:51–62.

86. Dikanov SA, Xun L, Karpiel AB, Tyryshkin AM, Bowman MK. 1996. Orientationally-selected two-dimensional ESEEM spectroscopy of the Rieske-type iron–sulfur cluster in 2,4,5-trichlorophenoxyacetate monooxygenase from *Burkholderia cepacia* AC1100. *J Am Chem Soc* **118**:8408–8416.

87. Maryasov AG, Bowman MK. 2004. Hyperfine sublevel correlation (HYSCORE) spectra for paramagnetic centers with nuclear spin $I = 1$ having isotropic hyperfine interactions. *J Phys Chem B* **108**:9412–9420.

88. Middleton P, Dickson DPE, Johnson CE, Rush JD. 1978. Interpretation of the Mössbauer spectra of the four-iron ferredoxin from *Bacillus stearothermophilus*. *Eur J Biochem* **88**:135–141.

89. Bertrand P, More C, Guigliarelli B, Fournel A, Bennett B, Howes B. 1994. Biological polynuclear clusters coupled by magnetic interactions: from the point dipole approximation to a local spin model. *J Am Chem Soc* **116**:3078–3086.

90. Bertrand P, More C, Cammensuli P. 1995. Evidence for a magic magnetic configuration between FMN and the $[2Fe–2S]^+$ center of phthalate dioxygenase reductase of *Pseudomonas cepacia*. *J Am Chem Soc* **117**:1807–1809.

91. Moriaud F, Gambarelli S, Lamotte B, Mouesca J-M. 2001. Single-crystal ^{57}Fe Q-band ENDOR study of the 4 Iron–4 sulfur cluster in its reduced $[4Fe–4S]^{1+}$ state. *J Magn Reson* **153**:238–245.

92. Barone V, Bencini A, Cossi M, Di Matteo A, Mattesini M, Totti F. 1998. Assessment of a combined QM/MM approach for the study of large nitroxyde systems in vacuo and in condensed phases. *J Am Chem Soc* **120**:7069–7078.

93. Improta R, Barone V. 2004. Interplay of electronic, environnemental, and vibrational effects in determining the hyperfine coupling constants of organic free radicals. *Chem Rev* **104**:1231–1253.

94. Mouesca J-M, Rius G, Lamotte B. 1993. Single-crystal proton ENDOR studies of the $[Fe4S4]^{3+}$ cluster: determination of the spin population distribution and proposal of a model to interpret the ^{1}H NMR paramagnetic shifts in high-potential ferredoxins. *J Am Chem Soc* **115**:4714–4731.

95. Werst M, Kennedy MC, Houseman ALP, Beinert H, Hoffman BM. 1990. Characterization of the $[4Fe–4S]^+$ cluster at the active site of aconitase by ^{57}Fe, ^{33}S, and ^{14}N electron nuclear double resonance spectroscopy. *Biochemistry* **29**:10533–10540.

96. Walsby CJ, Ortillo D, Yang J, Mnyepi MR, Broderick WE, Hoffman BM, Broderick JB. 2005. Spectroscopic approaches to elucidating novel iron–sulfur chemistry in the "radical SAM" protein superfamily. *Inorg Chem* **44**:727–741.

97. Gurbiel RJ, Doan PE, Gassner GT, Macke TJ, Case DA, Ohnishi T, Fee JA, Ballou DP, Hoffman BM. 1996. Active site structure of Rieske-type proteins: electron nuclear double resonance studies of isotopically labeled phthalate dioxygenase from *Pseudomonas cepacia* and Rieske protein from *Rhodobacter capsulatus* and molecular modeling studies of a Rieske center. *Biochemistry* **35**:7834–7845.

98. Rocklin AM, Tierney DL, Kofman V, Brunhuber NMW, Hoffman BM, Christoffersen RE, Reich NO, Lipscomb JD, Que LJr. 1999. Role of the nonheme Fe(II) center in the biosynthesis of the plant hormone ethylene. *Proc Natl Acad Sci USA* **96**:7905–7909.

99. Chen D, Walsby C, Hoffman BM, Frey PA. 2003. Coordination and mechanism of reversible cleavage of S-adenosylmethionine by the [4Fe–4S] center in lysine 2,3-aminomutase. *J Am Chem Soc* **125**:11788–11789.

100. Shergill J, Joannou CL, Mason JR, Cammack R. 1995. Coordination of the Rieske-type [2Fe–2S] cluster of the terminal iron–sulfur protein of *Pseudomonas putida* benzene 1,2-dioxygenase, studied by one- and two-dimensional electron spin-echo envelope modulation spectroscopy. *Biochemistry* **34**:6533–16542.

101. Samoilova RI, Kolling D, Uzawa T, Iwasaki T, Crofts A, Dikanov SA. 2002. The interaction of the Rieske iron–sulfur protein with occupants of the Q_0-site of the bc1 complex, probed by electron spin echo envelope modulation. *J Biol Chem* **277**:4605–4608.

102. Iwasaki T, Kounosu A, Uzawa T, Samoilova RI, Dikanov SA. 2004. Orientation-selected ^{15}N-HYSCORE detection of weakly coupled nitrogens around the archaeal rieske [2Fe–2S] center. *J Am Chem Soc* **126**:13902–13903.

103. Gambarelli S, Mulliez E, Fontecave M. Unpublished results.

104. Vey JL, Yang J, Li M, Broderick WE, Broderick JB, Drennan CL. 2008. Structural basis for glycyl radical formation by pyruvate formate-lyase activating enzyme. *Proc Natl Acad Sci USA* **105**:16137–16141.

MONONUCLEAR MOLYBDENUM ENZYMES

Molybdenum was first discovered to be present in an enzyme in 1953, when Reichert et al. [1] reported that xanthine oxidase contained the metal. Molybdenum-containing enzymes, commonly called molybdoenzymes, have since been found to be utilized by all types of microbial, plant and animal life (Table 1) and are involved in extremely important life processes that include the natural cycles and metabolism of carbon, nitrogen, and sulfur [2]. These enzymes can be divided into two major classes, with classification depending upon the identity of the characteristic active center to which the molybdenum atom is bound (the iron–molybdenum cofactor, or the molybdenum cofactor) and hence the type of reaction that the molybdenum center catalyzes (Fig. 1) [2-5].

Table 1. Properties of Selected Molybdenum-Containing Enzymes

| Enzyme	Source	Mol. wt. (Daltons)	Prosthetic groups (per molecule)
Nitrogenase molybdo-ferredoxin	*Azotobacter vinelandii* [6,7]	220,000	FeMoco protein: $2 \times$ [Mo–3Fe–3S] and $4 \times$ [4Fe–4S] P-cluster (Fe protein): [8Fe–7S]
Xanthine dehydrogenase	Chicken liver [8]	300,000	$2 \times$ Moco, $2 \times$ [2Fe–2S], $2 \times$ FAD
Xanthine oxidase	Bovine milk [4]	283,000	$2 \times$ Moco, $4 \times$ [2Fe–2S], $2 \times$ FAD
Sulfite oxidase	Rat liver [9]	120,000	$2 \times$ Moco, $2 \times$ haem (cytochrome b_5)
Aldehyde oxidase	Rabbit liver [9]	346,000	$2 \times$ Moco, $2 \times$ [2Fe–2S], $2 \times$ FAD
Carbon monoxide oxidase	*Pseudomonas carboxydo-vorans* [10]	230,000	$2 \times$ Moco, $2 \times$ [2Fe–2S], $2 \times$ FAD
Formate dehydrogenase H	*Escherichia coli* [11]	608,000	Moco, selenocysteine, [4Fe–4S]
Assimilatory nitrate reductase	*Neurospora crassa* [12]	230,000	Moco, $2 \times$ cytochrome b_{557}, $2 \times$ cytochrome b_5, FAD
Dissimilatory nitrate reductase	*Thiosphaera pantotropha* [13,14]	880,000	Moco, [4Fe–4S], cytochrome c
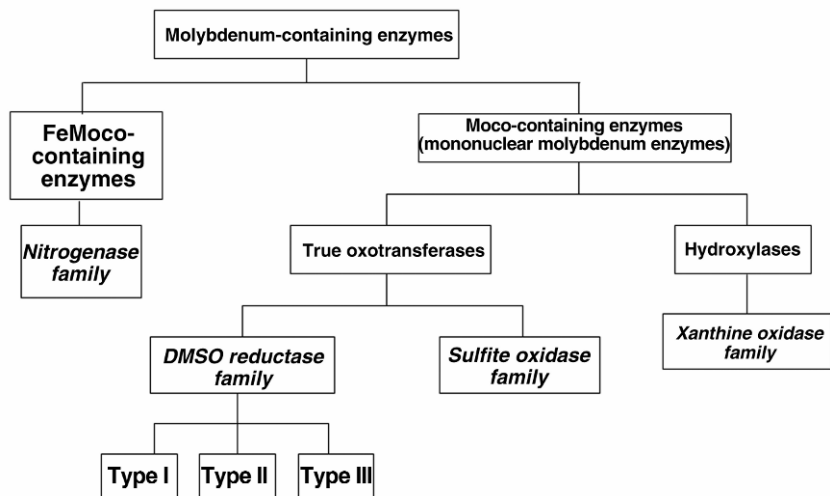
Figure 1. Classification of the molybdenum-containing enzymes.

The first class of the molybdoenzymes is found in certain bacteria (which usually form nodules in plant roots) and assorted blue-green algae. This class consists only of the protein known as nitrogenase. The active site of nitrogenase, termed the iron–molybdenum cofactor (FeMoco), is made up of two components. The first component consists of an [8Fe–7S] cluster known as the P-cluster (Fig. 2a) and the second an [Mo–X–3Fe–3S] moiety (where X is an interstitial atom) (Fig. 2b) known as the molybdenum–iron protein, which is thought to be the site of substrate reduction [6,7,15]. The elucidation of the high-resolution (1.16 Å) crystal structure of the nitrogenase MoFe protein from *Azobacter vinelandii* [9] has revealed that an interstitial atom (X), presumably nitrogen [17,18], resides in the center of the FeMo protein. These clusters are both linked by three non-protein-based ligands [5]. Nitrogenase plays a fundamental role in the nitrogen cycle of the earth, as it catalyzes the fixation of molecular nitrogen to ammonia. The ammonia so produced is then used for the synthesis of amino acids, nucleic acids, and other nitrogen-containing compounds [19,20]. Nitrogenase is able to catalyze the above reaction at ambient temperature and pressure; therefore. a fundamental understanding of the reaction mechanism would be of significant use to man, since ammonia and ammonia-based products remain one of the largest products of the chemical industry due to their use as fertilizers [3]. Although much recent research has centered around the mechanism of nitrogenase [21–26], we still do not fully understand how the molybdenum center catalyzes nitrogen fixation. Man has therefore devised alternative methods for the process. The Haber-Bosch process is an industrial
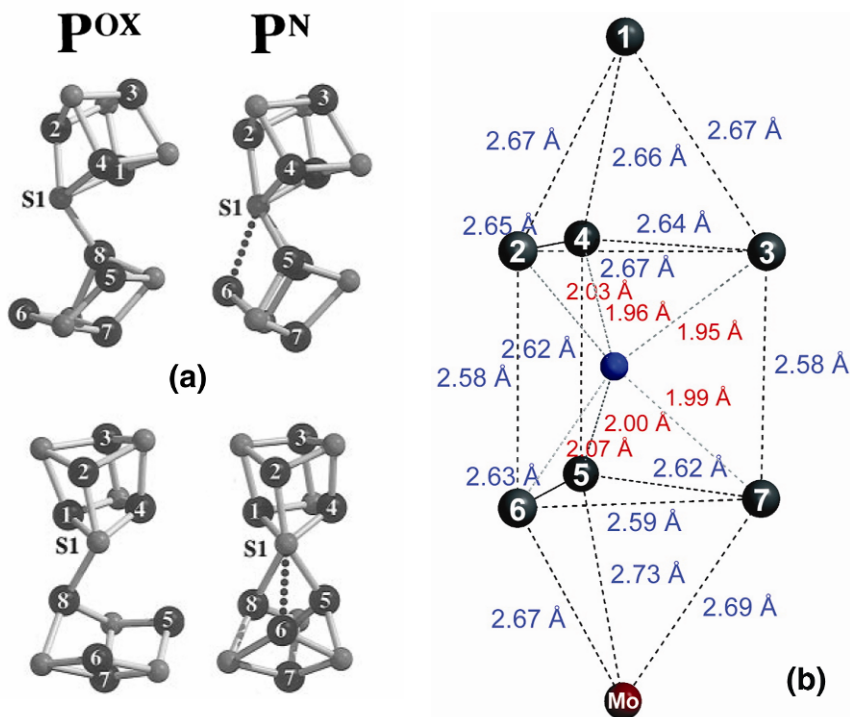
Figure 2. (a) Structure of the P-cluster of nitrogenase from *Azotobacter vinelandii* in oxidized and reduced forms. Iron atoms are numbered and appear black in color, sulfur atoms appear gray. Reprinted with permission from [7]. Copyright © 1997, American Chemical Society. (b) Structure of the iron–molybdenum cofactor from the same protein. The iron atoms are numbered and the interstitial atom (proposed to be nitrogen) is colored blue [16]. Please visit http://www.springer.com/978-1-4419-1138-4 to view a high-resolution full-color version of this illustration.

method for nitrogen fixation which directly combines N_2 and H_2 over an iron catalyst and requires temperatures of some 450°C, combined with a pressure of 270 atmospheres [27]. The fact that man is forced to use such extreme reaction conditions when nature can achieve the same result at ambient temperature and pressure provides an insight into the complexity of the mechanism that nature has evolved.

The second class of molybdoenzymes, collectively termed mononuclear molybdenum enzymes [4], can be subdivided into oxotransferases and hydroxylases (Fig. 1, Table 2). The latter group comprises the xanthine oxidase family of enzymes, and the application of EPR spectroscopy to the structural characterization of their molybdenum active sites is described in Chapter 5. The oxotransferase family (Fig. 1) can be further subdivided into the sulfite oxidase (discussed in

Table 2: Summary of the Oxygen Transfer Reactions of Molybdenum-Containing Enzymes

Enzyme	Reaction catalyzed
Xanthine oxidase	Xanthine + $H_2O \rightarrow$ uric acid + $2e^- + 2H^+$
Sulfite oxidase	$SO_3^{2-} + H_2O \rightarrow SO_4^{2-} + 2e^- + 2H^+$
Nitrate reductase	$NO_3^- + 2e^- + 2H^+ \rightarrow NO_2^- + H_2O$
DMSO* reductase	$(CH_3)_2SO + 2e^- + 2H^+ \rightarrow (CH_3)_2S + H_2O$
DMS* dehydrogenase	$(CH_3)_2S + H_2O \rightarrow (CH_3)_2SO + 2e^- + 2H^+$
Formate dehydrogenase	$HCOOH \rightarrow CO_2 + 2e^- + 2H^+$
CO* dehydrogenase	$CO + H_2O \rightarrow CO_2 + 2e^- + 2H^+$
TMAO* reductase	$(CH_3)_2NO + 2e^- + 2H^+ \rightarrow (CH_3)_2N + H_2O$

*DMSO: dimethylsulfoxide; DMS: dimethylsulfide; CO: carbon monoxide; TMAO: trimethylamine-N-oxide.

Chapter 6) and DMSO (dimethylsulfoxide) reductase (Chapter 7) families based upon the structure of their molybdenum cofactor and amino acid sequence homologies [28,29].

All mononuclear molybdenum enzymes contain a common molybdenum cofactor (Moco) made up of a single molybdenum atom bound to an organic, substituted pterin moiety. Accordingly, the cofactor is frequently referred to as the molybdenum pterin cofactor (MPT) (Fig. 3) [30]. This group of proteins catalyze a number of physiologically important processes, and a summary of these is presented in Table 2.

REFERENCES

1. Richert DA, Westerfeld WW. 1953. Isolation and identification of the xanthine oxidase factor as molybdenum. *J Biol Chem* **203**:915–923.
2. Enemark JH, Young CG. 1993. Bioinorganic chemistry of pterin-containing molybdenum and tungsten enzymes. *Adv Inorg Chem* **40**:1–88.
3. Kaim W, Schwederski B. 1994. *Bioinorganic chemistry: inorganic elements in the chemistry of life. an introduction and guide*. Chichester: John Wiley & Sons.
4. Hille R. 1996. The mononuclear molybdenum enzymes. *Chem Rev* **96**:2757–2816.
5. Moura JJG, Barata BAS. 1994. Aldehyde oxidoreductases and other molybdenum-containing enzymes. *Methods Enzymol* **243**:24–42.
6. Chan MK, Kim J, Rees DC. 1993. The nitrogenase FeMo-cofactor and P-cluster pair: 2.2 Å resolution structures. *Science* **260**:792–794.
7. Peters JW, Stowell MHB, Soltis SM, Finnegan MG, Johnson MK, Rees DC. 1997. Redox-dependent structural changes in the nitrogenase P-cluster *Biochemistry* **36**: 1181–1187.
8. Bray RC. 1975. Molybdenum iron–sulfur flavin hydroxylases and related enzymes. In *The enzymes*, Vol. 12, pp. 299–419. Ed PD Boyer. New York: Academic Press.
9. Hille R, Massey V. 1985. Molybdenum containing hydroxylases: xanthine oxidase, aldehyde oxidase, and sulfite oxidase. In *Molybdenum enzymes*, pp. 443–518. Ed TG Spiro. New York: John Wiley & Sons.
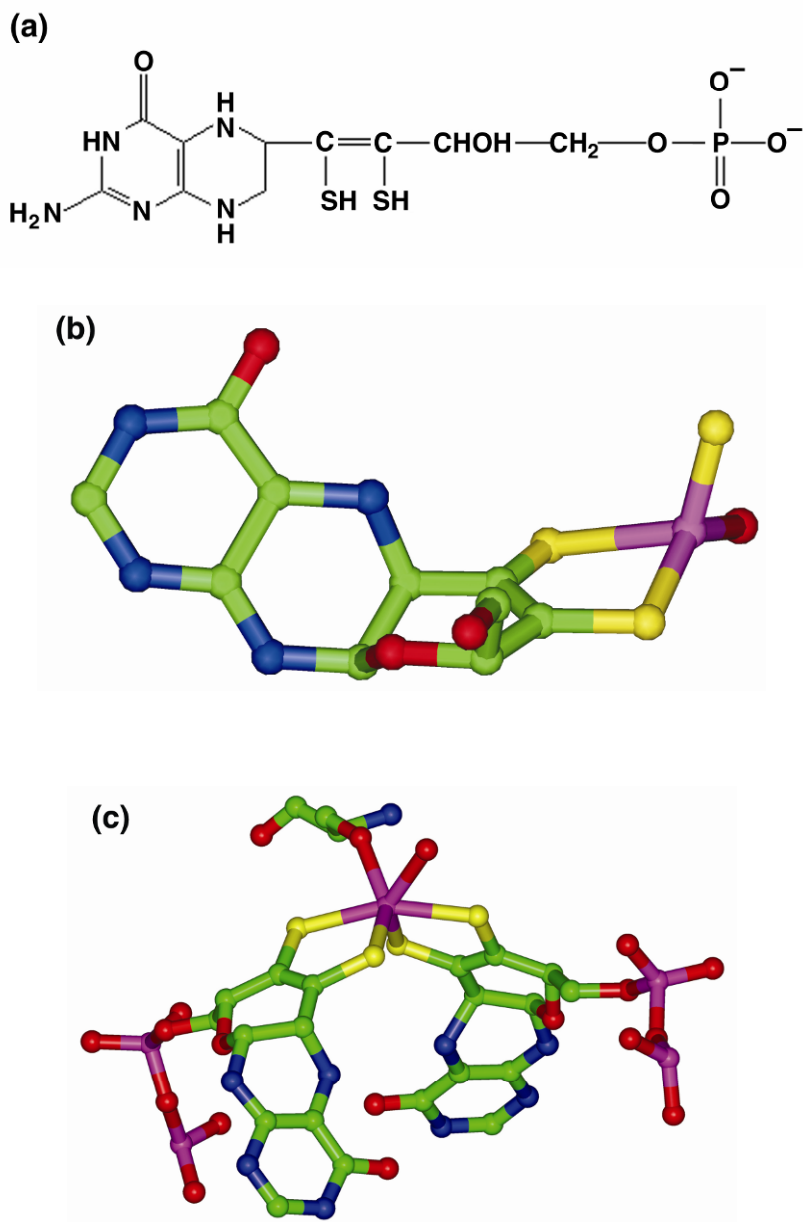
(a)

(b)

(c)

Figure 3. Structures of molybdenum cofactors. (a) Schematic structure of the molybdenum cofactor MPT and examples of the molybdenum cofactor in (b) xanthine oxidase and (c) dimethylsulfoxide reductase. Please visit http://www.springer.com/978-1-4419-1138-4 to view a high-resolution full-color version of this illustration.

10. Meyer O. 1982. Chemical and spectral properties of carbon monoxide: methylene blue oxidoreductase: the molybdenum-containing iron–sulfur flavoprotein from *Pseudomonas carboxydovorans*. *J Biol Chem* **257**:1333–1341.

11. Boyington JC, Gladyshev VN, Khangulov SV, Stadtman TC, Sun PD. 1997. Crystal structure of formate dehydrogenase H: catalysis involving Mo, molybdopterin, seleno-cysteine, and an Fe_4S_4 cluster. *Science* **275**:1305–1308.

12. Adams MWW, Mortenson LE. 1985. Mo reductases: nitrate reductase and formate dehydrogenase. In *Molybdenum enzymes*, pp. 519–593. Ed TG Spiro. New York: John Wiley & Sons.

13. Berks BC, Richardson DJ, Reilly A, Willis AC, Ferguson SJ. 1995. The napEDABC gene cluster encoding the periplasmic nitrate reductase system of *Thiosphaera pantotropha*. *Biochem J* **309**:983–992.

14. Breton J, Berks BC, Thomson AJ, Ferguson SJ, Richardson DJ. 1994. Characterization of the paramagnetic iron-containing redox centres of *Thiosphaera pantotropha* periplasmic nitrate reductase. *FEBS Lett* **345**:76–80.

15. Kim J, Rees DC. 1992. Structural models for the metal centers in the nitrogenase molybdenum–iron protein. *Science* **257**:1677–1682.

16. Einsle O, Tezcan FA, Andrade SLA, Schmidt B, Yoshida M, Howard JB, Rees DC. 2002. Nitrogenase MoFe-protein at 1.16 Å resolution: a central ligand in the FeMo-cofactor. *Science* **297**:1696–1700.

17. Lovell T, Liu T, Case DA, Noodleman L. 2003. Structural, spectroscopic, and redox consequences of a central ligand in the FeMoco of nitrogenase: a density functional theoretical study. *J Am Chem Soc* **125**:8377–8383.

18. Lukoyanov D, Pelmenschikov V, Maeser N, Laryukhin M, Yang TC, Noodleman L, Dean DR, Case DA, Seefeldt LC, Hoffman BM. 2007. Testing if the interstitial atom, X, of the nitrogenase molybdenum–iron cofactor is N or C: ENDOR, ESEEM, and DFT studies of the $S = 3/2$ resting state in multiple environments. *Inorg Chem* **46**: 11437–11449.

19. Bray RC. 1988. The inorganic biochemistry of molybdoenzymes. *Q Rev Biophys* **21**: 299–329.

20. Ueyama N, Nakamura A, Otsuka S. 1988. In *Metalloproteins: chemical properties and biological effects*, pp. 393–406. Ed S Otsuka, T Yamanaka. Tokyo: Elsevier.

21. Dance I. 1996. Theoretical investigations of the mechanism of biological nitrogen fixation at the FeMo cluster site. *J Biol Inorg Chem* **1**:581–586.

22. Pickett CJ. 1996. The Chatt cycle and the mechanism of enzymic reduction of molecular nitrogen. *J Biol Inorg Chem* **1**:601–606.

23. Coucouvanis DN. 1996. Functional analogs for the reduction of certain nitrogenase substrates: are multiple sites within the Fe/Mo/S active center involved in the $6e^-$ reduction of N_2? *J Biol Inorg Chem* **1**:594–600.

24. Sellmann D, Sutter J. 1996. Elementary reactions, structure–function relationships, and the potential relevance of low molecular weight metal–sulfur ligand complexes to biological N_2 fixation. *J Biol Inorg Chem* **1**:587–593.

25. Thorneley RNF, Lowe DJ. 1996. Nitrogenase: substrate binding and activation. *J Biol Inorg Chem* **1**:576–580.

26. Seefeldt LC, Dance I, Dean DR. 2004. Substrate interactions with nitrogenase: Fe versus Mo. *Biochemistry* **43**:1401–1409.

27. Shriver DF, Atkins PW, Langford CH. 1990. In *Inorganic chemistry*. Melbourne: Oxford UP.

28. Kisker C, Schindelin H, Rees DC. 1997. Molybdenum-cofactor-containing enzymes: structure and mechanism. *Annu Rev Biochem* **66**:233–267.
29. McDevitt CA, Hugenholtz P, Hanson GR, McEwan AG. 2002. Molecular analysis of dimethyl sulphide dehydrogenase from *Rhodovulum sulfidophilum*: its place in the dimethyl sulphoxide reductase family of microbial molybdopterin-containing enzymes. *Mol Microbiol* **44**:1575–1587.
30. Johnson JL, Hainline BE, Rajagopalan KV, Arison AH. 1984. The pterin component of the molybdenum cofactor: structural characterization of two fluorescent derivatives. *J Biol Chem* **259**:5414–5422.

EPR Studies of Xanthine Oxidoreductase and Other Molybdenum-Containing Hydroxylases

Russ Hille

Department of Biochemistry,
University of California Riverside

A summary is provided both of early work establishing the different types of EPR signals manifested by the molybdenum centers of enzymes such as xanthine oxidoreductase and of more recent studies, frequently employing more advanced EPR-related methods, which have contributed significantly to our understanding of the physical and electronic structures of the enzyme active site. Structures for the signal-giving species, frequently supported by independent x-ray crystallographic studies, are placed in a catalytic context.

1. INTRODUCTION

Electron paramagnetic resonance spectroscopy and related methods have been used to understand the structure and function of molybdenum-containing enzymes for many years (see [1] for a review of the early work). The present account constitutes a summary of both early work establishing the different types of EPR signal manifested by the active site of such enzymes as xanthine oxidoreductase (known as the oxidase or dehydrogenase, depending on whether the preferred oxidizing substrate for the specific form of the enzyme is O_2 or NAD^+ [2]), as well as more recent studies utilizing a variety of more advanced methods that have contributed significantly to our understanding of the physical and electronic structures of the various EPR-active centers of the enzyme and the manner in which they interact.

2. HISTORICAL CONTEXT

In 1966 Bray and Meriwether [3] published a study of bovine milk xanthine oxidoreductase with both the natural abundance of molybdenum isotopes and enzyme isolated from the milk of cows that had been injected with ^{95}Mo-molybdate

(I = 5/2) to enrich in this isotope. Two types of EPR signal were examined in the course of the reaction of enzyme with xanthine: a first that appeared and disappeared rapidly in the course of the reaction, and a second that accumulated more slowly and persisted longer. The first of these had g values of 2.025, 1.956, and 1.951 and showed no evidence of coupling to protons. The second had g values of 1.994, 1.977, and 1.966 and exhibited the characteristic doublet-of-doublets reflecting the presence of one more strongly and a second more weakly coupled proton. The spectral changes seen in this study as a result of the isotopic substitution demonstrated unambiguously not only that the observed EPR signals were in fact due to discrete Mo(V) species but that the molybdenum itself was an integral component of the enzyme active site that became reduced in the course of the reaction with xanthine. The work was a tour de force in the application of isotope enrichment to study the reaction mechanism of an enzyme from a (very large) eukaryote.

The two signals examined in this work had been discovered previously in a set of studies entailing one of the earliest applications of freeze-quench kinetics to a biological system [4,5]. The two signals, originally referred to as $\gamma\delta$ and $\alpha\beta$, were subsequently designated "very rapid" and "rapid, type 1" on the basis of the kinetics of their formation and decay in the course of the reaction of enzyme with xanthine [6]. The latter signal was termed "type 1" to distinguish it from a "type 2" signal that had similar g values but superhyperfine splitting due to two strongly coupled protons rather than one strongly and one weakly coupled one, affording a 1:2:1 pattern rather than a doublet of doublets [6–8]. Using this nomenclature, the principal Mo(V) EPR signals manifested by the active site of xanthine oxidoreductase under various conditions are shown in Figure 1.

Over the years, much advantage has been made of EPR to examine the kinetics and mechanism of the reaction of enzyme with the variety of aldehydes and heterocyclic compounds that serve (with varying degrees of effectiveness) as reducing substrates. The two signals that are the most directly relevant to catalysis are those indicated above: the "very rapid" and "rapid type 1" signals. The first of these is seen with xanthine and certain other substrates [9], and accumulates maximally at high pH. The apparent rate constants for its formation and decay are approximately 140 and 30 s^{-1} at pH 10 [5,10], which are each faster than turnover under the experimental conditions (~17 s^{-1}). At maximal accumulation, approximately 15% of the enzyme is present in the signal-giving form. The "rapid type 1" signal appears on approximately the same timescale as the "very rapid" signal disappears (with an apparent rate constant of 30 s^{-1}) and persists at the longest times examined at just under 5% of the total enzyme concentration. The structures of the various signal-giving species, as well as their relationship to one another in the catalytic sequence, can be understood in the context of the considerable amount of information that is available for xanthine oxidoreductase and related enzymes from studies utilizing x-ray absorption spectroscopy and protein crystallography, as discussed presently.

Figure 1. Representative Mo(V) EPR signals arising from different forms of xanthine oxidoreductase. From top to bottom, the "very rapid," "rapid type 1," "rapid type 2," "slow," "desulfo inhibited," and "arsenite-inhibited" signals.

3.   THE ACTIVE SITE STRUCTURE OF XANTHINE OXIDOREDUCTASE

The 2.1-Å resolution structure of oxidized bovine xanthine oxidoreductase [11] and the 1.9-Å resolution structure of the reduced enzyme in complex with the tight-binding inhibitor designated FYX-051 [12] (see below) are known. It is evident that the molybdenum center of the (oxidized) enzyme is best represented as having an LMoOS(OH) structure with a distorted square-pyramidal coordination geometry, as shown in Figure 2. Such a geometry had been seen previously in the crystal structure of the aldehyde oxidoreductase from *Desulfovibrio gigas*, a related molybdenum hydroxylase [13,14], and is a highly conserved feature in this family of enzymes. Here, L represents a bidentate enedithiolate ligand to the metal contributed by a pyranopterin cofactor having the structure shown in Figure 2, with the Mo=O group occupying the apical position of the coordination sphere; the enedi-

thiolate, Mo=S, and Mo-OH ligands constitute the four equatorial ligands. In the earliest structures of the molybdenum hydroxylases, the Mo=S was assigned the apical position, but it is evident in the crystal structure of the FYX-051 complex that the sulfur occupies the equatorial and the Mo=O apical position. This assignment is consistent with the observation of apical Mo=O groups in the active sites of two other molybdenum-containing enzymes bearing strong sequence and structural homologies to xanthine oxidoreductase: CO dehydrogenase from *Oligotropha carboxidovorans* [15,16] and quinoline-2-hyroxylase from *Pseudomonas putida* [17]. In both these cases, the assignment of an apical oxygen rather than sulfur is unambiguous. It is now generally recognized that this coordination geometry is likely shared by all members of the molybdenum hydroxylase family of enzymes.
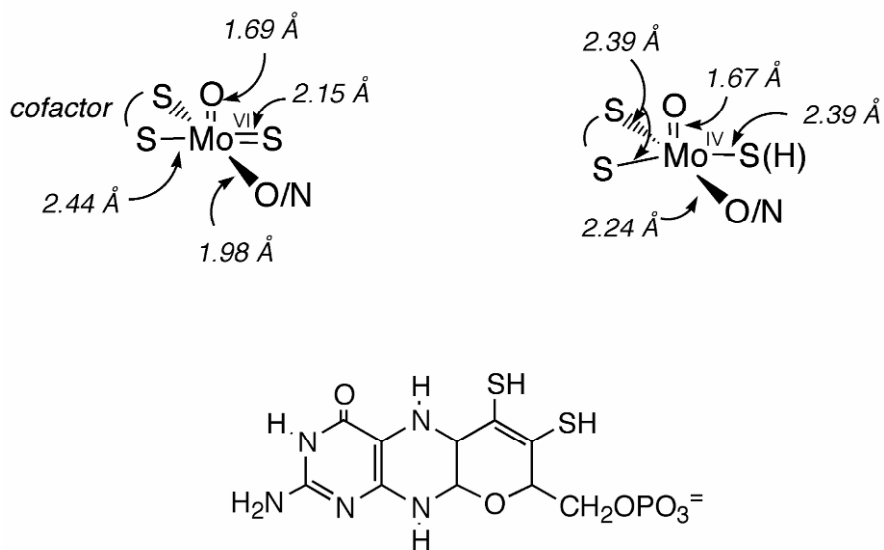
Figure 2. Schematic structures of the active site of xanthine oxidoreductase in its oxidized (**left**) and reduced (**right**) states. The structure of the pyranopterin cofactor that coordinates the metal via its dithiolene sidechain is shown at **bottom**.

Also shown in Figure 2 is a summary of the very precise metal–ligand distances obtained using x-ray absorption spectroscopy (XAS) from a number of laboratories [18–23]. Importantly, it has recently been shown using XAS that at 1.98 Å the Mo–OH ligand is unambiguously in the singly protonated state and represents a metal-bound hydroxide rather than water, even at low pH [24]. At pH 10, however, the Mo–O distance shortens significantly to 1.75 Å, reflecting deprotonation to Mo–O–/Mo=O. This is a significant mechanistic point, since at neutral pH (where the enzyme is most active) a deprotonated Mo–OH (yielding Mo–O–) is expected

to be a considerably better nucleophile in initiating catalysis than a deprotonated Mo–OH$_2$ (yielding a still-protonated Mo–OH) in initiating attack on substrate (see below).

The structure of the molybdenum center of xanthine oxidoreductase at the outset of catalysis is thus well established. The structure of the reduced molybdenum center at the completion of the reaction is similarly well characterized, the most significant aspect being that reduction of the molybdenum from the (VI) to the (IV) oxidation state results in the protonation of the Mo=S group of the oxidized enzyme to an Mo–SH group in the reduced state (Fig. 2). This is reflected in an increased Mo–S distance (from 2.15 to 2.39 Å) in the reduced enzyme, as established first by x-ray absorption spectroscopy [20,21] and subsequently verified crystallographically [11,12]. The uptake of protons by ligands in the molybdenum coordination sphere is a common property of even the simplest molybdenum complexes [25,26], and in the context of the enzyme is expected on the basis of the principle of charge neutrality: that the protein environment of the metal center favors a particular net charge on the cluster — uptake of protons concomitant with reduction minimizes the overall change in net charge upon reduction of the center.

The final structural aspect relevant to the catalytic mechanism is the structure of xanthine oxidoreductase in complex with the inhibitor FYX-051 alluded to previously [12]. FYX-051 is itself an aromatic heterocycle having the structure shown in Figure 3 and is in fact a very slow substrate for xanthine oxidoreductase [27], being hydroxylated at the position indicated in Figure 3. Like certain other substrates for the enzyme (most notably the pterin lumazine [28,29]) the E$_{red}$·P complex encountered in the course of the reaction (see below) exhibits long wavelength absorbance due to a low-energy metal–ligand charge-transfer transition. With both lumazine [28] and FYX-051 [27], kinetic studies have established that the long-wavelength absorbing species is an authentic catalytic intermediate, and the stability of the complex accounts for the observed inhibition. In the crystal structure of the E$_{red}$·(FYX-051) complex [12], product is coordinated to the molybdenum in the equatorial plane, facing into the solvent access channel with a bridging oxygen (representing the catalytically introduced hydroxyl group of product) occupying the position of the Mo–OH of the oxidized enzyme. The electron density associated with this bridging oxygen and the overall orientation of the heterocycle with respect to the molybdenum center make it clear from the crystallographic evidence that product is complexed to the molybdenum in a simple end-on fashion: Mo–O–P, with a bond angle of approximately 135°.

A variety of kinetic and mechanistic studies have led to a chemical reaction that proceeds as follows (as summarized in previous reviews [30–32]). An active site glutamate residue, Glu 1261 in the bovine enzyme, is thought to abstract a proton from the Mo–OH group of oxidized enzyme, which then undertakes nucleophilic attack on the carbon position to be hydroxylated. Such a role for this glutamate, which is universally conserved among the molybdenum hydroxylases, was first proposed by Huber et al. [14] on the basis of the crystal structure
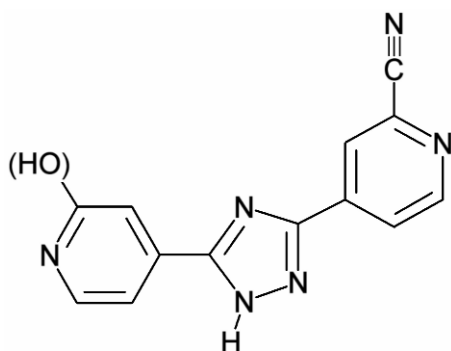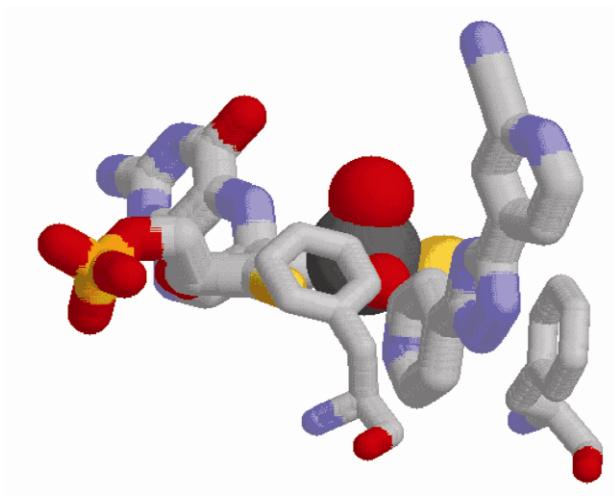
Figure 3. The structure of the inhibitor FYX-051 complexed to xanthine oxidoreductase. **Top**: the structure of the complexed molybdenum center (as reported by Okamoto et al. [12]). The inhibitor binds between Phe 1009 and Phe 914, coordinated to the molybdenum via the catalytically introduced hydroxyl group. The molybdenum is rendered *dark gray*, carbon *light gray*, oxygen *red*, and nitrogen *blue*. Bottom: the chemical structure of FYX-051, with the position that is hydroxylated by the enzyme indicated in parentheses. Please visit http://www.springer.com/978-1-4419-1138-4 to view a high-resolution full-color version of this illustration.

of the *D. gigas* aldehyde oxidoreductase, and is consistent with the pH dependence of catalysis toward both heterocycles [33] and aldehydes [34]. Subsequently, using the xanthine dehydrogenase from *Rhodobacter capsulatus* (for which an efficient recombinant expression system exists [35]), it has been shown that mutation of this glutamate to an alanine reduces catalytic activity by a factor of at least 10^7 [36]. A reaction mechanism predicated on nucleophilic attack on substrate had earlier been

suggested by Skibo et al. [37] on the basis of the observation of a strong Hammett correlation between catalysis and susceptibility to nucleophilic attack in a homologous series of substituted quinazoline substrates for the enzyme.

Concomitant with the proton abstraction from the Mo–OH group and nucleophilic attack on substrate at the carbon to become hydroxylated, hydride is transferred from the carbon to the Mo(VI)=S. This results in reduction of the molybdenum to yield E_{red}·P, an Mo(IV)–SH species that has product complexed to the molybdenum via the catalytically introduced hydroxyl group. All this chemistry takes place in the equatorial plane of the molybdenum center, normal to the plane of the substrate, which is positioned between two phenylalanine residues in the substrate binding site. At the completion of this first step of the reaction, the molybdenum has become reduced, the C–H bond of substrate cleaved, and the C–O bond of product formed, with product coordinated to the molybdenum as seen in the crystal structure of the FYX-051 complex. The outcome is consistent with the long-established observation that while the oxygen incorporated catalytically into product in the course of the reaction is ultimately derived from water [38], in the course of a single turnover the proximal donor of the oxygen atom is a catalytically labile site in the molybdenum center, which is subsequently regenerated with solvent water at the completion of the catalytic cycle [39]. Further, it has been shown that it is the equatorial Mo–OH that is exchanged with solvent under single turnover conditions [34], a further indication that the Mo–OH represents the catalytically labile site. This chemistry occurs via two-electron chemistry to yield the Mo(IV)·P complex directly [40], without the formation of a discrete Mo(V) intermediate. Formation of the Mo(V)·P species giving rise to the "very rapid" EPR signal occurs subsequently, and is an oxidative one-electron event [41], involving electron transfer to other redox-active centers in the enzyme.

Hydride transfer from substrate with reduction of the molybdenum is consistent with the observation that the C-8 proton of substrate is transiently transferred to the molybdenum center (prior to exchange with solvent) [42,43], and has been extensively corroborated by density functional calculations on models for the reaction [44–47]. In this step of the reaction, the Mo=S group is essential since its loss by reaction with cyanide (which results in the Mo=S group being replaced by an Mo=O) inactivates the enzyme ([48], see below). Computational studies [46] have demonstrated that substitution of Mo=O for Mo=S results in a significant increase in the free energy of the transition state for the hydroxylation reaction, and that the transition state occurs much earlier along the reaction coordinate. The result is consistent with the greater electronegativity of oxygen relative to sulfur, which is expected to render it less susceptible to hydride transfer, and the greater covalency of Mo–S relative to Mo–O bonds.

Once the E_{red}·P complex is formed, it breaks down by electron transfer to the other redox-active centers of the enzyme to reoxidize the molybdenum, along with displacement of product by hydroxide from solvent to release product. It is only when one-electron oxidation of the molybdenum precede displacement of product from the molybdenum coordination sphere that an Mo(V)·P complex affording the

"very rapid" EPR signal is formed. The Mo–SH of reduced enzyme must deprotonate upon one-electron oxidation, since there is no proton superhyperfine splitting evident in the "very rapid" EPR signal. That product remains bound in the signal-giving species is reflected in the long-noted demonstration that ^{13}C coupling is seen in the "very rapid" signal when 8-^{13}C-labeled substrate is used to generate the EPR signal [49].

The ^{13}C hyperfine coupling seen when 8-^{13}C-labeled substrate is used to generate the "very rapid" signal has been extensively analyzed with ENDOR spectroscopy by both Howes et al. [50], using xanthine as substrate, and Manikandan et al. [51], using 2-hydroxy-6-methylpurine as substrate (which affords significantly improved signal-to-noise since the signal-giving species accumulates to considerably greater degree [9,41]). The two ENDOR studies substantively agree as regards the basic experimental observation, with the anisotropic ^{13}C hyperfine tensor having $A_{1,2,3}$ = 10.2, 7.0, and 6.5 MHz in the better-characterized signal generated with 2-hydroxy-6-methylpurine (and 11.1, 7.6, and 7.6 MHz in the signal generated with xanthine), with the unique axis making an angle of 25° to g_2 (reported as 65° relative to g_1 in [51]). The interpretation of the data differ in the two studies, however, as to how the symmetric component of the tensor is used to arrive at an estimate of the Mo–C distance in the signal-giving species. Howes et al. [50] assumed sp hybridization of the C-8 carbon and on the basis of the observed degree of anisotropy in A estimated the Mo–C distance to be no longer than 2.4 Å, and likely considerably shorter. It was concluded that the signal-giving species possessed a direct Mo–C bond, with the C=O bond of product coordinated to molybdenum in a side-on η_2 fashion. The assumption of sp hybridization was taken to represent a worst-case scenario that would overestimate the Mo–C distance, an assumption based in turn on the belief that sp-hybridized carbon was less symmetric than sp^3-hybridized carbon (since the three p orbitals sum to spherical symmetry, and the s orbital is symmetric). In fact, however, a *given* sp^3-hybridized orbital is considerably *more* directed in space than a given sp-hybridized orbital, and the more asymmetric. The 2.4 Å distance obtained assuming sp hybridization thus represents a lower limit on the Mo–C distance, not an upper one. Using a more chemically realistic assumption of sp^2-hybridization, Manikandan et al. arrived at a distance of 2.8 Å, which is comparable to the distance seen crystallographically in the complex of enzyme with FYX-051 [12] and too long to reflect any significant direct Mo–C bond formation. Thus, from both the ENDOR and crystallographic work to date it is evident that product is bound to molybdenum in a simple end-on fashion, not in a side-on η_2 manner, and that there is no significant Mo–C bond character to the complex (nor, by inference, in intermediates preceding it in the catalytic sequence) [31,32,52].

The "very rapid" species has also been examined by pulsed EPR [53], utilizing the electron spin echo envelope modulation (ESEEM) approach to probe for magnetic interactions with nitrogen, phosphorus, and hydrogen nuclei. Strong ^{14}N modulation is observed in the "very rapid" EPR signal formed with 2-hydroxy-6-methylpurine substrate bound to molybdenum, interpreted as arising from nitrogens of the bound purine substrate. On the other hand, no modulation is observed

from nonexchangeable deuterons in experiments performed in D_2O, indicating that each of the substrate methyl group deuterons is greater than 4.9 Å from the molybdenum. Moderately deep deuteron modulation arises from exchangeable sites, including the N7 deuteron of substrate. On the basis of the strength of the modulation, this proton was estimated to be approximately 3.2 Å from the molybdenum, consistent with a coordination geometry involving simple end-on binding of nascent product to the molybdenum.

Finally, taking advantage of its paramagnetism, the "very rapid" species has also been examined by magnetic circular dichroism spectroscopy (MCD) [54]. The low-energy ($<\sim$30 000 cm^{-1}) C-term MCD that is observed for this paramagnetic intermediate is remarkably similar to that of the model compound LMoO(bdt) (L = hydrotris(3,5-dimethyl-1-pyrazolyl)borate; bdt = 1,2-benzenedithiolate), and the MCD bands have been assigned as dithiolate in-plane S_p to Mo d_{xy} and out-of-plane S_p to Mo $d_{xz,yz}$ LMCT transitions. These transitions require a coordination geometry in which the Mo=O bond is oriented *cis* to the benzenedithiolate ligand, as seen in the crystal structure of the model complex. Covalent π-bonding interactions between the redox-active d_{xy} orbital of the metal and the in-plane S_p orbitals of the benzenedithiolate are maximized when the oxo ligand is oriented *cis* to the dithiolate/molybdenum plane. The virtual identity of the MCD spectra seen with the model and the "very rapid" species strongly suggest that the two bear fundamentally similar structures and that the Mo=O group in the enzyme is also in the apical position (as borne out in subsequent crystallographic studies of the enzyme, as discussed above). The results underscore the importance of in-plane interactions between the ene-1,2-dithiolate portion of the pyranopterin with the molybdenum, which provide an efficient superexchange pathway for electron transfer out of the molybdenum center of the enzyme, once reduced by substrate.

Closely related to the "very rapid" EPR signal is that observed when reduced enzyme in complex with the mechanism-based inhibitor alloxanthine is reoxidized under controlled conditions [55]. This inhibitor, with the structure shown in Figure 4, is the product of enzyme action on the therapeutic agent allopurinol [56], and once hydroxylated forms an extremely tight complex with the reduced enzyme. The EPR signal of the partially reoxidized complex, with molybdenum in the Mo(V) oxidation state, exhibits g values virtually identical to those of the "very rapid" signal seen with xanthine, with $g_{1,2,3} = 2.0279$, 1.9593, and 1.9442. Like the "very rapid" signal, that seen with the alloxanthine complex also shows no proton superhyperfine coupling, but does exhibit weak superhyperfine coupling to a nitrogen nucleus with $A_{1,2,3} = 9.9$, 9.6, and 8.7 MHz [55], presumably that occupying the apical position of the pyrazole ring of the inhibitor, analogous to the C-8 position of xanthine that becomes hydroxylated. On the basis of the coupling to nitrogen, a structure for the signal-giving species was proposed with alloxanthine coordinated directly to the molybdenum via the apical nitrogen, as shown in Figure 5. This structure has quite recently been substantiated crystallographically in a study of the alloxanthine complex of the reduced xanthine dehydrogenase from *R. capsulatus*
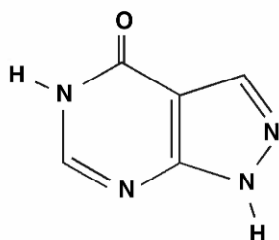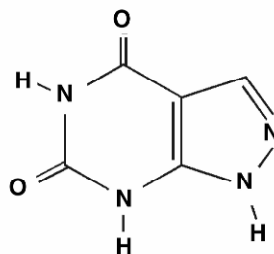
Figure 4. The chemical structures for allopurinol and alloxanthine. The former is hydroxylated to the latter by xanthine oxidoreductase, which forms a tight-binding inhibitor to the reduced form of the enzyme.
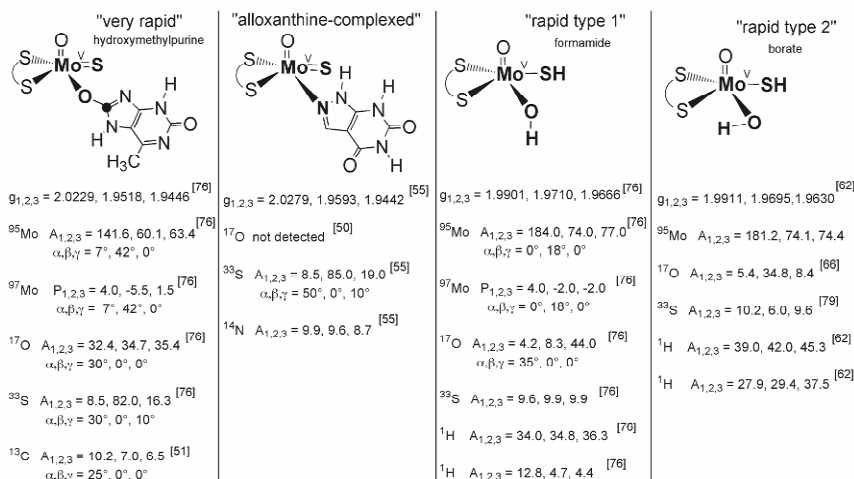

Figure 5. Structures and EPR parameters for various forms of the functional molybdenum center of xanthine oxidoreductase. From left to right, the "very rapid," "alloxanthine-complexed," "rapid type 1," and "rapid type 2" species. Specific nuclei giving rise to the superhyperfine coupling are indicated in *boldface*. In the "very rapid" species, the C-8 carbon that is labeled with ^{13}C to give the observed superhyperfine coupling is indicated by the heavy dot. Numbers in brackets refer to references in the text from which the values were taken (in some cases originally reported as superhyperfine splitting (in mT) or coupling (in cm^{-1}).

[57], where it is found that the bound inhibitor coordinates to the metal (via its N_2 nitrogen, as shown in Fig. 5) at the equatorial position otherwise occupied by the Mo–OH, facing into the solvent access channel to the active site.

Together, the available structural data are consistent with the structure shown in Figure 5 for the "very rapid" species, with the molybdenum coordination sphere best represented as LMoOS(OR), with *cis* Mo=O (apical) and Mo=S (equatorial) groups, L the bidentate enedithiolate ligand contributed by the pterin cofactor, and OR the now-hydroxylated product coordinated to the molybdenum in a simple end-on fashion as discussed above; both L and OR lie in the equatorial plane of the molybdenum coordination sphere. The structure shown is consistent with both the ^{13}C ENDOR and ^{1}H ESEEM results discussed above. The structure of the signal-giving species has recently been examined computationally [58], and the results substantively corroborate the structure shown (although a somewhat longer Mo–C distance of 3.18 Å is obtained, as compared to the 2.8–3.0 Å distance estimated from the ^{13}C-ENDOR work). The very similar alloxanthine-complexed signal arises from a structure akin to this, but with the pyrazolopyrimidine of inhibitor coordinated to the molybdenum directly via the N_2 nitrogen, as shown in Figure 5.

Considering next the "rapid type 1" signal, the species giving rise to it is best formulated as LMoO(SH)(OH), with the enedithiolate, protonated Mo–SH and Mo–OH ligands in the equatorial plane and an apical Mo=O group. Significantly, with no evidence of coupling to ^{13}C when labeled substrate is used, there is no evidence that the purine nucleus is directly coordinated to the molybdenum in the signal-giving species. The more strongly coupled proton seen in the "rapid type 1" signal is attributed to that of the Mo–SH group, and the more weakly coupled proton to the Mo–OH group.

The mechanistic relationship of the species giving rise to the "very rapid" and "rapid type 1" EPR signals deserves additional comment. It was initially thought that the former decayed directly to the latter on the basis of the similar kinetics of their decay and formation, respectively. More recently, however, it has been shown that this is not the case — instead, the species giving rise to the "rapid type 1" signal represents a nonproductive complex of substrate with partially reduced enzyme possessing Mo(V) [59]. The complex arises owing to the fact that, with a pair of [2Fe–2S] centers and flavin adenine dinucleotide (FAD) in addition to the molybdenum, it takes three equivalents of substrate to fully reduce the enzyme. The two- and four-electron reduced intermediates generated in the course of full reduction of enzyme by substrate all possess a certain fraction of Mo(V) based simply on the distribution of reducing equivalents in partially reduced enzyme [60], and the "rapid type 1" signal arises when substrate binds to enzyme possessing already partially reduced molybdenum. Although catalytically incompetent (the molybdenum must be in the Mo(VI) oxidation state to accept a pair of reducing equivalents from substrate), the signal-giving species in fact represents a paramagnetic analog of the $E_{ox} \cdot S$ Michaelis complex, and as such provides a unique opportunity to examine the electronic structure of this otherwise refractory (but critical) enzyme intermediate. On the basis of the observed kinetics, it was initially assumed that the

"rapid type 1" species lay downstream in the catalytic sequence from the "very rapid" species. It was clearly established by Tsopanakis et al. [61] that the "rapid" species could not be obtained simply by protonation of the "very rapid" species (or vice versa). Furthermore, although the "rapid" signal appears on a timescale comparable to that for the decay of the "very rapid" [5, 62], it has been shown that the species giving rise to it does not lie downstream from that yielding the "very rapid" signal. When, for example, fully oxidized enzyme is reacted with less than one equivalent of 2-hydroxy-6-methylpurine at high pH and 4°C, the "very rapid" signal accumulates slowly over the first ~30 sec of the reaction, with no subsequent generation of the "rapid type 1" signal appears as the "very rapid" signal disappears [41]. When, on the other, enzyme is first partially reduced with sodium dithionite and reacted with an excess of the substrate, the "rapid type 1" signal appears essentially instantaneously upon mixing with substrate and increases in intensity through the course of the reaction [59]. Since the "rapid type 1" signal is not seen in the breakdown of the "very rapid" signal under substoichiometric conditions and appears only under those circumstances when substrate is able to encounter already partially reduced enzyme in the course of the reaction, it can only be concluded that it represents a complex of Mo(V) with substrate rather than a product lying downstream from the "very rapid" species, as discussed above.

Although substrate is not thought to directly coordinate to the molybdenum in the species giving rise to the "rapid type 1" signal, it is well established that the signal does vary from one substrate to another, however, and that seen in the presence of substrate is distinct from the Mo(V) signal seen when enzyme is partially reduced by sodium dithionite in the absence of substrate. It is thus very likely that the "rapid type 1" species arises from a complex of substrate (not product) with partially reduced enzyme in which the molybdenum is partially reduced to the Mo(V) level (either by prior reduction with dithionite or during turnover by reaction with a prior molecule of substrate). Variations in the chemical nature and/or orientation of substrate in its binding site presumably account for the small differences in g-values, etc. among different types of "rapid type 1" signal.

By contrast, the difference between the "rapid type 1" and "type 2" families of signal (most importantly the number of strongly coupled protons in the signal-giving species) is rather more difficult to rationalize simply on the basis of differences in orientation of substrate in the binding site. Assuming that the Mo–SH proton is always strongly coupled, however, it is possible that the principal factor determining whether the Mo–OH proton is weakly ("type 1") or strongly ("type 2") coupled is the dihedral angle between the equatorial plane of the molybdenum coordination sphere and the plane of the Mo–O–H bond. Such a situation has been proposed to account for differences in Mo–OH coupling in a recent ESEEM study of the related system sulfite oxidase: upon going from low pH to high, the active site Mo–OH proton is proposed to rotate out of the equatorial plane, significantly weakening its interaction with the unpaired electron in the d_{xy} orbital [63]. The likely structures of the "rapid type 1" and "type 2" species are shown in Figure 5.

In addition to the "rapid" and "very rapid" EPR signals referred to already, a variety of other signals attributable to Mo(V) are manifested by the enzyme under

various conditions and which, while not directly catalytically relevant, nevertheless provide important structural information regarding the molybdenum center. The first of these to be considered is the "slow" Mo(V) signal [64] that arises from a partially reduced form of nonfunctional enzyme in which the Mo=S group of the functional active site is replaced by a second Mo=O group. This species represents 25–50% of the total enzyme in most preparations of the enzyme and forms spontaneously, if slowly, in aqueous solution [48]. Although originally thought that the labile sulfur identified from this work was the terminal sulfur of a persulfide, subsequent work has unambiguously established that it is the Mo=S of the molybdenum coordination sphere, as first proposed by Malthouse and Bray [65], and as discussed further below. Formation of the desulfo form of the enzyme can be accelerated by treatment of the enzyme with cyanide, which releases the catalytically essential sulfur as thiocyanate after displacement from the molybdenum coordination sphere by solvent hydroxide. This so-called desulfo form of the enzyme is catalytically inert but does react (sluggishly) with nonphysiological reductants such as sodium dithionite. In rapid kinetic experiments, reduction of the nonfunctional desulfo enzyme and accumulation of the "slow" Mo(V) signal occurs via (slow) intermolecular electron transfer from individual molecules of the rapidly reduced functional form of the enzyme to nonfunctional molecules in the reaction mix [60]. The "slow" signal has $g_{1,2,3}$ = 1.9719, 1.9671, and 1.9551 and exhibits strong coupling to two inequivalent protons ($A_{1,2,3}$ = 44.7, 44.4, and 42.6 MHz, and $A_{1,2,3}$ = 3.9, 4.5, and 6.3 MHz) [43, 67]. The structure of the signal-giving species is best represented as LMoO$_2$(OH), as indicated in Figure 6.
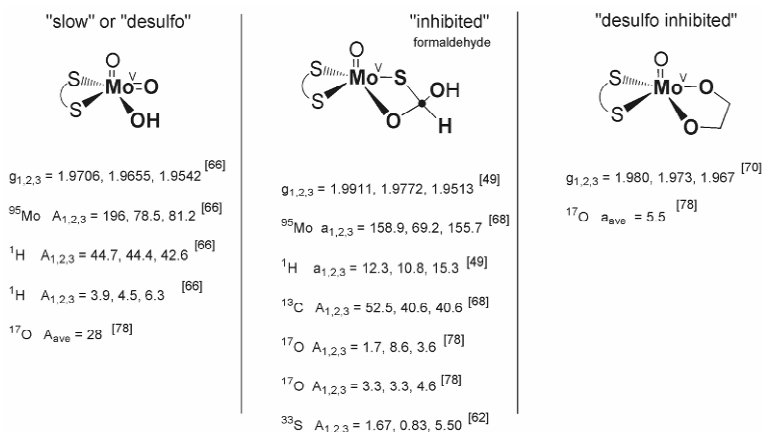
Figure 6. Structures and EPR parameters for various inactivated forms of xanthine oxidoreductase. From left to right, "slow," "inhibited," and "desulfo inhibited" enzyme. Specific nuclei giving rise to the superhyperfine coupling are indicated in *boldface*. In the "inhibited" species, the carbon that is labeled with ^{13}C gives rise to the observed superhyperfine coupling, as indicated by the heavy dot. Numbers in brackets refer to references in the text from which the values were taken (in some cases originally reported as superhyperfine splitting (in mT) or coupling (in cm^{-1}).

Treatment of functional xanthine oxidoreductase with methanol or formaldehyde generates an EPR signal termed "inhibited" [68]. The signal exhibits $g_{1,2,3}$ = 1.9911, 1.9772, and 1.9513 and exhibits coupling to one nonexchangeable proton (derived from the inhibitor itself) with $a_{1,2,3}$ = 0.44, 0.39, and 0.56 mT (equivalent to $A_{1,2,3}$ = 12.3, 10.8, and 15.3 MHz). When ^{13}C-labeled formaldehyde is used to generate the signal, strong coupling is seen with $A_{1,2,3}$ = 52.5, 40.6, and 40.6 MHz [50]. Although a short Mo–C distance was calculated from the degree of anisotropy evident in the ^{13}C coupling, for the same reasons as discussed above in the case of the "very rapid" signal it is likely that the distance is in fact considerably greater than this. Given this consideration, the most likely structure for the signal-giving species is that proposed by Howes et al. [69], with the formaldehyde unit coordinated in a bidentate fashion, as shown in Figure 6. A similar species, but lacking proton superhyperfine, is seen upon treatment of the inactive desulfo form of the enzyme with ethylene glycol [70]; this "desulfo inhibited" signal has $g_{1,2,3}$ = 1.980, 1.973, and 1.967 and is devoid of discernible coupling to protons. The signals have been interpreted as arising from a species designated LMoO(R), where R is a *gem* diol coordinated to the molybdenum, as indicated in Figure 6. It is unfortunate that ethylene glycol interacts with the molybdenum center of xanthine oxidoreductase, as it is a very commonly used low-temperature glassing agent for aqueous solutions employed in a variety of transmission spectrophotometric methods (such as MCD, as referred to above).

Another EPR signal arising from an inactivated form of xanthine oxidoreductase is that seen upon partial reduction of enzyme that has been treated with the thiol reagent *p*-chloromercuribenzoate (*p*CMB), which reacts with the Mo–SH group of the reduced, functional enzyme (the desulfo form of the molybdenum center does not react with *p*CMB) [71]. Reduction of enzyme by sodium dithionite in the presence of *p*CMB yields an Mo(V) EPR signal with $g_{1,2,3}$ = 1.9687, 1.9581, and 1.9434; there is no proton superhyperfine evident in the signal. When *p*CMB labeled with [199]Hg (I = 1/2; 13.2% natural abundance) is used to generate the signal, strong and anisotropic coupling is seen with $A_{1,2,3}$ = 443, 285, and 272 MHz, and Euler angles α, β, γ = 5, 7, and 8.6°. Strong and anisotropic coupling was found to both [17]O ($A_{1,2,3}$ = 4.1, 8.2, and 34 MHz) and [33]S ($A_{1,2,3}$ = 13.8, 7.4, and 8.7 MHz) when isotropically substituted enzyme was used [71]. When [201]Hg-labeled *p*CMB was used instead (I = 3/2 and Q = 0.39 b for [201]Hg; 13.2% natural abundance), in addition to the superhyperfine coupling, evidence of strong quadrupolar coupling to the [201]Hg nucleus was found, yielding $P_{1,2,3}$ = 166, –91, and –75 MHz. The **A** and **P** tensors were coincident. The proposed structure of the signal-giving species is shown in Figure 7, with the *p*CMB reacted with the Mo–SH of reduced enzyme as shown to give an Mo^V–S–Hg–pϕ–Cl moiety.

A final inhibited form of the enzyme that exhibits a most unique EPR signal is that formed on partial reduction of enzyme in the presence of arsenite [72,73]. Arsenite has long been known to be an inhibitor of xanthine oxidoreductase, but its effect on the EPR spectrum of the molybdenum center was not immediately recognized. The signal is exceptional for two reasons: (1) it exhibits not only
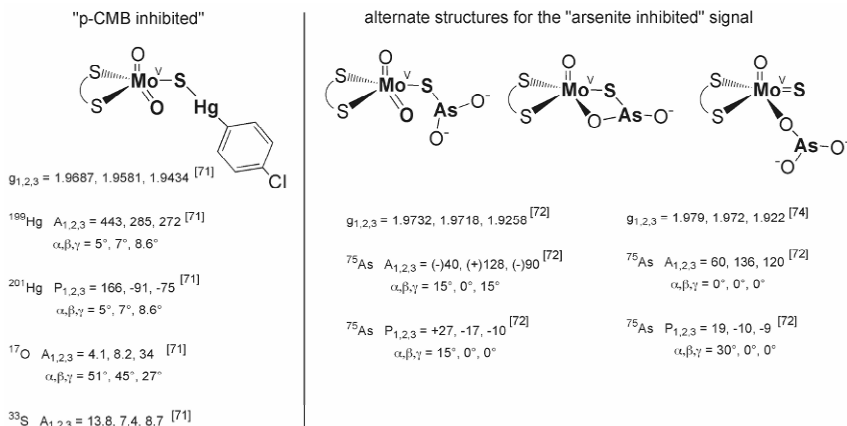
Figure 7. Structures and EPR parameters for the p-CMB- and arsenite-inhibited forms of xanthine oxidoreductase. Two alternate structures for the latter species are shown. Specific nuclei giving rise to the superhyperfine reported are indicated in *boldface*. Numbers in brackets refer to references in the text from which the values were taken (in some cases originally reported as superhyperfine splitting (in mT) or coupling (in cm^{-1})).

strong superhyperfine due to the $I = 3/2$ ^{75}As nucleus, but also strong quadrupolar coupling as well; and (2) the signal is significantly perturbed on binding either xanthine or salicylate, indicating that while arsenite inhibits the enzyme the latter remains able to bind substrates and substrate analogues. A reasonable fit over most of the observed spectrum for the signal seen in the absence of xanthine or salicylate was obtained using $g_{1,2,3} = 1.9732$, 1.9718, and 1.9258, with $A_{1,2,3} = -40$, 128, and -90 MHz, and $P_{1,2,3} = 27$, -17, and -10 MHz. In both studies [72,73] it was concluded that arsenite complexed to the molybdenum center via the Mo–SH of reduced enzyme, consistent with the known affinity of arsenite toward thiols. Subsequently, the EPR-active complex was analyzed by x-ray absorption spectroscopy [21] and, consistent with the proposed structure, an Mo–As distance of 3.02 Å was determined from the extended x-ray absorption fine structure (EXAFS) of both the Mo and As nuclei. The As EXAFS also showed 1–2 sulfurs at 2.41 Å (and possibly 2–1 oxygens at 1.78 Å). Combining Mo–S, As–S, and Mo–As distances of 2.39, 2.41, and 3.02 Å, a geometry for the complex with an Mo–S–As angle of 80° was obtained. It was also shown in this work that sulfur appeared in the As EXAFS only when enzyme was reduced to at least the Mo(V) state; in the complex of arsenite with oxidized enzyme, only oxygen was found within bonding distance to the arsenic atom. The signal-giving species was considered to have an Mo–S–AsO$_2$$^=$ structure, as shown in Figure 7, with the caveats that an additional sulfur may be bound to the arsenite (unlikely in light of the subsequently elucidated crystal structure) and that one of the As–O$^-$ groups might coordinate to the molybdenum at the position otherwise occupied by the equatorial Mo–OH (see further below). It is noteworthy that the geometry suggested by x-ray absorption spectroscopy (XAS) places the arsenic atom so as to maximally overlap with the redox-

active d_{xy} orbital in the equatorial plane of the molybdenum, accounting for the strong magnetic interaction seen in the signal.

The above interpretation regarding the structure of the signal-giving species has recently been called into question, however. Working with the aldehyde dehydrogenase from *D. gigas*, Boer et al. [74] observed an Mo(V) signal with arsenite-treated enzyme resembling that seen in the presence of xanthine with bovine xanthine oxidoreductase. A high-quality fit was obtained using $g_{1,2,3}$ = 1.979, 1.972, and 1.922, with $A_{1,2,3}$ = 60, 136, and 120 MHz, and $P_{1,2,3}$ = 19, –10, and –9 MHz. Significantly, the crystal structure of the arsenite complex was also determined, and it was found that the $AsO_3^=$ ion was complexed to the desulfo molybdenum center at the equatorial position facing into the solvent access channel, the position otherwise occupied by the catalytically labile Mo–OH group in native enzyme. Because the enzyme was in the inactive desulfo form, there was no possibility to form an As–S interaction, and yet the observed EPR signal resembled one of those seen with (presumably functional) xanthine oxidoreductase. It thus seems likely that at least one of the EPR signals seen with the arsenite-complexed bovine enzyme arises from the desulfo rather than functional form of the enzyme. Interestingly, the structure of the arsenite complex of the *D. gigas* enzyme seen crystallographically suggests that if an As–S bond does form with the functional enzyme (as strongly implicated by the As XAS of the bovine enzyme), then bidentate coordination of arsenite to the molybdenum is possible, if not likely.

4. ISOTOPIC SUBSTITUTION STUDIES

The above constitutes an introduction to the Mo(V) EPR signals exhibited by xanthine oxidoreductase, with the *g*-values and proton superhyperfine characteristics summarized in Figures 4 and 5. Beginning in the late 1970s, R.C. Bray began a series of now-classic studies of ^{95,97}Mo-, ^{17}O-, and ^{33}S-substituted xanthine oxidoreductase that has provided a wealth of information concerning the electronic structures of the several signal-giving species. This information has become even more significant as the physical structures of the signal-giving species have become increasingly well understood, permitting in best cases a detailed picture of the electronic as well as physical structure of the signal-giving species. These studies relied in turn on the equally elegant studies of small inorganic complexes of molybdenum in the Mo(V) valence state containing ^{17}O and ^{33}S, subsequently examined by Wedd, Pilbrow, Enemark, and others (as reviewed in [75]). The results of this impressive body of work are now considered in detail.

Carrying forward the work of Bray and Meriwether discussed above, George and Bray [76] have reexamined molybdenum hyperfine and quadrupolar coupling in the two most catalytically significant EPR-active states of xanthine oxidoreductase (those giving rise to the "very rapid" and "rapid type 1" signals), taking advantage of computer simulation methodologies not initially available in the original study. This work (as well as that preceding it) was facilitated by the fortuitous circumstance that nature provides in significant natural abundance isotopes of molybdenum that have no nuclear spin (each of the even isotopes ^{92}Mo, ^{94}Mo, ^{96}Mo,

^{98}Mo, and ^{100}Mo, in natural abundances totaling 74.8%), a nucleus with $I = 5/2$ but no significant nuclear quadrupole (^{95}Mo, 15.7% natural abundance), and an $I = 5/2$ nucleus with a strong nuclear quadrupole (^{97}Mo, 9.5% natural abundance). A comparison of the natural-abundance spectra (dominated by the $I = 0$ isotopes) with those seen with ^{95}Mo- and ^{97}Mo-enriched enzyme have provided a detailed picture of the magnitudes of the g-, A-, and P-tensors for the two signal-giving species, as well as the orientations of each of their principal axes with respect to one another. Data was obtained in this work at both X- and Q-band, resulting in a high level of confidence in the parameters obtained by fit. Beginning with the "very rapid" EPR signal, generated with the slow substrate 2-hydroxy-6-methylpurine (which affords much greater accumulation of the signal-giving species, and on a seconds rather than milliseconds timescale so that freeze-quench methods are not required), in addition to $g_{1,2,3}$ of 2.0229, 1.9518, and 1.9446 (comparable to $g_{1,2,3}$ of 2.0252, 1.9550, and 1.9494 seen for this signal when generated with xanthine), $A_{1,2,3}$ was found to be 141.6, 60.1, and 63.4 MHz with ^{95}Mo-enriched enzyme [76]. Furthermore, simulation indicated that none of the principal axes for the g- and A-tensors were coincident, with Euler angles $\alpha = 7$, $\beta = 42°$, and $\gamma = 0°$. When enzyme substituted with ^{97}Mo was used, in addition to the hyperfine A-tensor (obtained after correction for the ratio of the nuclear magnetons of the two isotopes), simulation gave $P_{1,2,3} = 4.0$, -5.5, and 1.5 MHz. The A- and P-tensors were coincident. Interestingly, in the case of the signal from ^{97}Mo-enriched enzyme, it proved possible by simulation to establish the specific contributions of the formally forbidden $\Delta M_I = \pm 1, \pm 2, \pm 3, \pm 4$, and ± 5 transitions (made possible due to d-orbital mixing resulting from the nuclear quadrupole) to the EPR signal [76]. The highly anisotropic nature of $\mathbf{P}$, with P_{yy} as the largest principal axis, was taken as most likely arising from an MoOS structure for the signal-giving species, with *cis* Mo=O and Mo=S bonds (although other possible structures were considered). As discussed above, this interpretation is fully consistent with our present understanding of the structure for this reaction intermediate.

For the "rapid type 1" signal generated with formamide as substrate (so as to avoid complications due to generation of other types of Mo(V) signal) in addition to $g_{1,2,3} = 1.9901$, 1.9710, and 1.9666 — and $A_{1,2,3} = 34.0$, 34.8, and 36.3 MHz for the more strongly coupled proton and $A_{1,2,3} = 12.8$, 4.7, and 4.4 MHz for the more weakly coupled one — fits to the data gave $A_{1,2,3} = 184$, 74, and 77 MHz for ^{95}Mo-enriched enzyme, and $P_{1,2,3} = 4.0$, -2.0, and -2.0 for ^{97}Mo-enriched enzyme [76]. Again, the A- and P-tensors were colinear with Euler angles α, β, and γ of 0, 18, and 0°, respectively, relative to the principal axis system for the g-tensor. Unlike the parameters yielding the best fit for the "very rapid" signal, those for the "rapid type 1" signal were similar to those seen subsequently for model complexes possessing an MoO(SH) core [66,67], supporting the interpretation that the signal-giving species possessed a similar core, consistent with the structure shown in Figure 5.

Considering ^{17}O-enrichment of the enzyme, the first species to be examined was that giving rise to the "very rapid" EPR signal [77]. When the "very rapid"

signal was generated by reaction of enzyme with xanthine at pH 10.2 in [17]O-enriched water, there was clear evidence of strong coupling of [17]O in the observed signal. Although quantitative analysis was complicated by the fact that the [17]O-labeled water was (and remains) available at enrichments no greater than ~50%, it proved possible using computer simulation of the signal to establish that the observed spectral perturbation was due to the presence of a single [17]O nucleus that was strongly and approximately isotropically coupled with $a_{1,2,3}$ = 1.34, 1.40, and 1.36 mT (reported as $A_{1,2,3}$ = 38.0, 38.3, and 37.1 MHz, in George and Bray [76], subsequently refined by ENDOR [50] as $A_{1,2,3}$ = 32.4, 34.7, and 35.4 MHz, with Euler angles α, β, and γ of 30°, 0°, and 0°, respectively). It was also shown that incorporation of [17]O into the molybdenum center of the enzyme occurred rapidly only under turnover conditions [77]. On the basis of the essentially isotropic nature of the hyperfine coupling, it was concluded that the signal-giving species most likely possessed a labeled Mo–[17]O–C unit rather than Mo=O (known to be present in the molybdenum coordination sphere from earlier x-ray absorption spectroscopic studies [18,19]). The carbon in this moiety again represents the hydroxylated C-8 position of substrate (this on the basis of the observed ^{13}C superhyperfine seen when 8-^{13}C-labeled substrate was used to generate the signal, as discussed above). This work has subsequently been substantiated in an ENDOR study which demonstrated that no second, more weakly coupled oxygen site in the enzyme (e.g., Mo=O) could be identified under the experimental conditions [50].

More recent work, again taking advantage of software advances that made it possible to more sensitively assess the effects of [17]O substitution using difference techniques, has confirmed the above results with the "very rapid" signal and extended the approach to several of the other EPR signals exhibited by the molybdenum center of xanthine oxidoreductase, notably the "inhibited," "slow," and both "rapid type 1" and "rapid type 2" signals [76,78]. For the "rapid type 1" signal generated with purine as substrate, the results indicate a single strongly coupled [17]O nucleus, with a_{ave} = 1.4 mT (A_{ave} = 39 MHz for g_{ave} = 1.979). A more comprehensive analysis of the "rapid type 1" signal seen with formamide has yielded $A_{1,2,3}$ = 4.2, 8.3, and 44.0 MHz, with Euler angles α, β, and γ of 35, 0, and 0°, respectively [76]. Although the strong anisotropy of the [17]O coupling was initially interpreted as reflecting the presence of an Mo=O group, subsequent model compound studies [79] have concluded (correctly) that the strong, anisotropic coupling arises from an Mo–OH group in a ligand field that includes a second Mo=O group present in the enzyme that is not labeled under the experimental conditions. Greenwood et al. [79] specifically suggested a reaction mechanism in which the strongly coupled Mo–OH represented the catalytically labile oxygen site that had previously been demonstrated [39]. As indicated above, this has subsequently been demonstrated to be the case with the enzyme: when enzyme is reacted with substrate under single-turnover conditions in [17]O-labeled water, oxygen is incorporated into a site in the molybdenum center that is strongly and anisotropically coupled to the unpaired electron spin in the "rapid type 1" species that is generated at the end of the reaction [34], i.e., the equatorial Mo–OH.

Other signals for which the [17]O coupling has been examined include the "rapid type 2" signal generated in the presence of borate, with an $a_{ave} \sim 1.0$ mT initially reported [78] subsequently refined to $A_{1,2,3} = 5.4$, 34.5, and 3.0 MHz [79], with $g_{1,2,3} = 1.9911$, 1.968, and 1.967 [67]; the "slow" signal with $a_{ave} \sim 1$ mT (or $A_{ave} \sim 28$ MHz) [78] and the "desulfo inhibited signal, with $a_{ave} \sim 0.3$ mT (or $A_{ave} \sim 5.5$ MHz) [78]. For each of these latter two signals it was concluded that two coupled oxygen nuclei were present in the signal-giving species.

Turning now to work involving xanthine oxidoreductase labeled with [33]S, we again consider the "very rapid" signal first. Malthouse and Bray [65] first demonstrated that [33]S coupling in this signal (from labeled enzyme prepared by treatment of the inactive, reduced, desulfo form of the enzyme with [33]S–Na$_2$S under controlled conditions) was strong and anisotropic; later this same group [62] reported $a_{1,2,3} = 0.3$, 2.8, and 0.7 mT (or $A_{1,2,3} = 8.5$, 82.0, and 16.3 MHz, as subsequently reported by George and Bray [76], with Euler angles α, β, and γ of 30, 0, and 10°, respectively). The strength and anisotropy of the coupling was interpreted as reflecting the presence of an Mo=S group in the signal-giving species. This conclusion was also consistent with XAS studies of xanthine oxidoreductase that provided independent evidence in support of an Mo=S group in oxidized enzyme [19]. The magnitude of the [33]S anisotropy in the "very rapid" signal has been used to estimate some 38% localization of the unpaired electron spin on the sulfur in the signal-giving species [76].

In the case of the "rapid type 1" signal generated using the substrate 1-methylxanthine, the strong and anisotropic coupling seen in the "very rapid" signal collapsed to a smaller and more isotropic coupling, with $a_{1,2,3} = 0.34$, 0.36, and 0.36 mT [62]; subsequently, $A_{1,2,3} = 9.5$, 9.9, and 9.9 MHz was reported for coupling in the "rapid type 1" signal generated with formamide [76], in good agreement with the results using 1-methylxanthine as substrate. The highly isotropic coupling reflects little unpaired spin delocalization on the Mo–SH in the signal-giving species, a result that contrasts with the case of the "very rapid" species where there is significant spin delocalization onto the Mo=S group. This work was subsequently corroborated and extended by Wilson et al. [67] to the "rapid type 2" (generated in the presence of borate) and alloxanthine-complexed signals, finding $A_{1,2,3} = 10.2$, 6.0, and 9.6 MHz and $A_{1,2,3} = 8.4$, 85.2, and 19.2 MHz, respectively. The latter values compared favorably with those seen for [33]S coupling in the "very rapid" EPR signal, given above.

The relative energy levels for a d[1] system in a distorted octahedral field are shown in Figure 8, along with the spin–orbit coupling operators that mix specific pairs of d orbitals when the externally applied magnetic field is oriented along the x, y, or z axes of the coordinate system for **g**. From g-tensor theory, it can be shown that the three principal g values are given (to first-order) by [80]

$$g_1 = g_e - 8\zeta/\Delta_1,$$

$$g_2 = g_e - 2\zeta/\Delta_2,$$

$$g_3 = g_e - 2\zeta/\Delta_3,$$
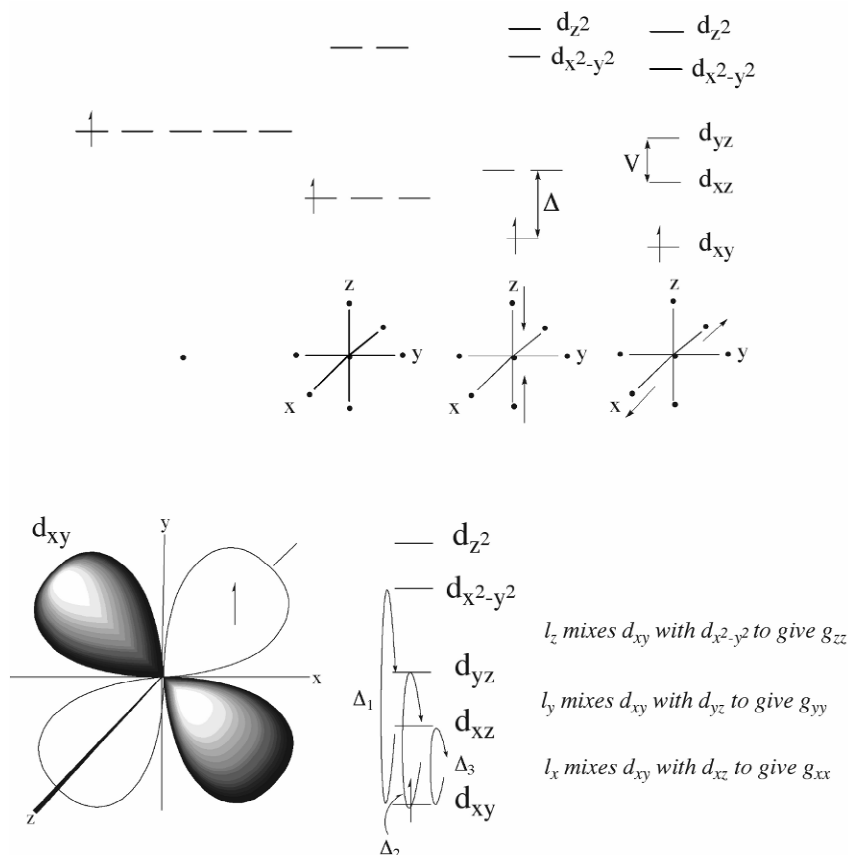
Figure 8. Ligand field parameters relevant to xanthine oxidoreductase. **Top**: the relative energies of the several d orbitals for a metal ion in a distorted octahedral ligand field. **Bottom**: the mixing of specific d orbitals that occurs as a result of spin–orbit coupling in an octahedral ligand field, with the externally applied magnetic field oriented along each of the three principal axes of the g tensor for the system.

with Δ_1, Δ_2 and Δ_3 defined as indicated in Figure 8, and ζ being the spin–orbit coupling constant for the system — 1030 cm^{-1} in the case of Mo(V). With these equations it is possible to calculate the energy separation of the various d orbitals from the g values for a given paramagnetic center, albeit with the significant caveat that spin delocalization onto sulfur (as much as 38% in the case of the "very rapid" species, on the basis of the anisotropy of the ^{33}S A tensor [76]) renders the crystal field treatment less rigorous. More rigorous density functional approaches have been used to understand the g-values of certain molybdenum complexes [81], but as yet an analysis has not been extended to models including Mo=S groups such as are likely to exhibit extensive spin delocalization. These considerations notwithstanding, the results of such calculations are qualitatively informative. Starting

with the "rapid Type 1" signal seen with formamide, $g_{1,2,3}$ = 1.9901, 1.9710, and 1.9666 yield Δ_1, Δ_2, and Δ_3 of 6.6×10^5 cm^{-1}, 6.6×10^4 cm^{-1}, and 5.8×10^4 cm^{-1}, respectively. It is evident that the octahedral distortion along the z axis is significantly greater than in the xy plane, as expected given the structure of the signal-giving species, with a strong-field apical Mo=O group. The situation is more complicated in the case of the "very rapid" signal" since its lowest-field (largest) g value, 2.0229 for the signal seen with 2-hydroxy-6-methylpurine, is actually greater than that for the free electron as 2.0023 (undoubtedly the result of the significant degree of spin delocalization onto sulfur, as referred to above). Nevertheless, the same qualitative conclusion can be drawn, namely that the distortion along the z axis is considerably greater than that in the xy plane. For the "slow" signal, $g_{1,2,3}$ = 1.9901, 1.9710, and 1.9666 yield Δ_1, Δ_2, and Δ_3 of 2.6×10^5 cm^{-1}, 5.6×10^4 cm^{-1}, and 4.3×10^4 cm^{-1}, respectively — while distortion along z is still the greatest, the ligand field is no longer as dramatically asymmetric as in the case with the functional forms of the enzyme. Presumably the presence of an equatorial Mo=O in the signal-giving species weakens the apical Mo=O, a phenomenon related to the "spectator oxo" effect described by Rappé and Goddard [82]. Consistent with this, upon removal of the equatorial Mo=O in the desulfo enzyme upon formation of the "desulfo inhibited" species with $g_{1,2,3}$ = 1.9901, 1.9710, and 1.9666 and $\Delta_{1,2,3}$ = 3.4×10^5 cm^{-1}, 6.5×10^4 cm^{-1}, and 5.4×10^4 cm^{-1}, the predominance of distortion along the z axis as defined by the Mo=O bond is at least partially restored.

5. MAGNETIC INTERACTIONS BETWEEN CENTERS IN XANTHINE OXIDOREDUCTASE

Xanthine oxidoreductase possesses two [2Fe–2S] clusters of the spinach ferredoxin variety and one equivalent of FAD in addition to the molybdenum center, and electron transfer from the molybdenum to the flavin (which is the site of the oxidative half of the catalytic cycle in which O_2 becomes reduced to peroxide or superoxide) is mediated by the intervening iron–sulfur centers and is an integral aspect of catalysis. A variety of studies have shown that electron transfer occurs rapidly compared to catalysis [83–86]. Although very similar to one another from a spectroscopic standpoint, in their reduced states the two iron–sulfur centers are $S = 1/2$ and can be distinguished by their EPR signals in the reduced state. The signal designated Fe/S I has $g_{1,2,3}$ = 2.022, 1.932, and 1.894 [86, 87], and can be seen at even liquid nitrogen temperatures. In linewidth and temperature dependence, this signal is very similar to that exhibited by spinach ferredoxin. The signal designated Fe/S II, on the other hand, is unusual. It has $g_{1,2,3}$ = 2.110, 1.991, and 1.902 [86,87], and is atypical of [2Fe–2S] clusters in having greater g anisotropy. In addition, it is seen only below 20 K and has unusually broad linewidths, both properties reflecting an unusually fast rate of spin-relaxation in the signal-giving species. With the determination of the x-ray crystal structure of first the aldehyde oxidoreductase from *D. gigas* (which also has two [2Fe–2S] clusters and exhibits similar Fe/S EPR signals [88]) and then xanthine oxidoreductase, the question arose as to the assignment of the two EPR signals to the two [2Fe–2S] centers in

the enzyme. With one of the iron–sulfur domains having a typical ferredoxin-like fold and the other unusual in having a fold that is principally α-helical rather than β-sheet, it would have seemed very likely that the "normal" EPR signal would have arisen from the [2Fe–2S] cluster in the "normal" fold, and that with the more unusual EPR features from the cluster in the domain with the unique fold. In fact, however, the evidence to date indicates clearly that the Fe/S I EPR signal arises from the cluster in the domain with the α-helical fold, while the Fe/S II EPR signal arises from the cluster in the domain with the ferredoxin fold. In the rat enzyme, for example, when Cys 115 (a ligand to the [2Fe–2S] cluster in the helical domain) is mutated to a serine, it is the Fe/S I signal that is perturbed in the reduced enzyme. Conversely, when Cys 51 in the ferredoxin-like domain is mutated to serine, it is Fe/S II that is perturbed. The same conclusion has been drawn from detailed EPR analyses of mutants of the aldehyde oxidoreductases from *D. gigas* [88] and *D. alaskensis* [89], and CO dehydrogenase from *O. carboxidovorans* [90]. The spatial orientation of the molybdenum center and Fe/S I within the polypeptide is shown in Figure 9. The unusual features of the Fe/S II signal appear to be due to an unusually high degree of solvent accessibility, which increases the spin–lattice relaxation rate of the paramagnetic cluster.
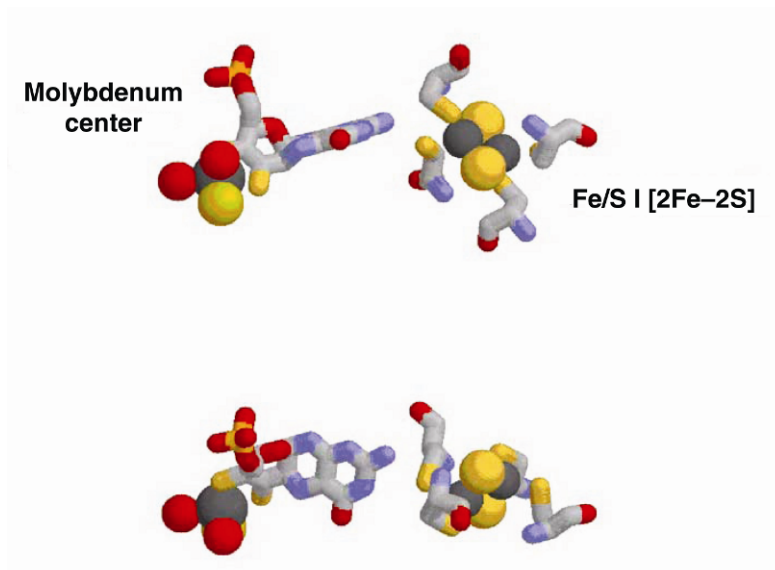
Figure 9. The spatial orientation of the molybdenum center and Fe/S I in xanthine oxidoreductase. The orientation at bottom is rotated 90° about the horizontal relative to that at the top. The metal ions are shown in *dark gray*, carbon *light gray*, oxygen *red*, nitrogen *blue*, and sulfur *yellow*. The four cysteines coordinated the [2Fe–2S] iron–sulfur cluster are also shown. Please visit http://www.springer.com/978-1-4419-1138-4 to view a high-resolution full-color version of this illustration.

The initial report of a magnetic interaction between the molybdenum center of xanthine oxidoreductase and Fe/S I was by Lowe et al. [91]. These workers found that at ~40 K the molybdenum center in the normal "slow" and "rapid type 1" Mo(V) forms exhibited spin–spin coupling of 1.1 mT with the [2Fe–2S] cluster giving rise to the Fe/S I EPR signal and, as discussed above present in the nearer, α-helical domain to the molybdenum center. Subsequent ELDOR studies [92] demonstrated unambiguously that the splitting of the "slow" Mo(V) signal was approximately isotropic and due to interaction with a single other paramagnetic center interconverting between two states (corresponding to its $M_S = \pm 1/2$ states) at a rate (31 MHz) comparable to that for the spin–lattice relaxation rate of Fe/S I. In later work focusing on the extremely stable "glycol inhibited" Mo(V) signal, the coupling to Fe/S I was found to be even larger, ca. 2.4 mT, and again approximately isotropic [92]. The temperature dependence of the interaction demonstrated that the lower-field feature of the ELDOR doublet for each g value was enhanced at lower temperature (~4.2 K) to the degree expected for the increased ground-state population of the Fe/S I signal at the lower temperature, indicating that the coupling was ferromagnetic and the same sign at all g values [91]. The magnitude of the coupling did vary with the type of Mo(V) EPR signal, ranging from 0.7 mT for the "rapid" signals to 2.4 mT for the "glycol inhibited" signal. Comparable magnetic interactions are seen between Mo(V) and Fe/S I in avian and bacterial xanthine dehydrogenases [93] and in the *D. gigas* aldehyde oxidoreductase [94], as well as bacterial members of the molybdenum hydroxylase family such as quinoline 2- oxidoreductase [95,96]. It is evident that the phenomenon is a general one in this family of enzymes.

An examination of the crystal structure of the bovine enzyme [11] indicates that the molybdenum atom is 14.7 Å from the nearer iron atom of Fe/S I, with the pterin ring of the cofactor intervening — the distal amino group of the pterin cofactor is near the sulfur of Cys 150 (in the crystal structure of the *D. gigas* aldehyde oxidoreductase, it is considered to be hydrogen-bonded to the corresponding cysteine residue in this protein [13]). This distance is remarkably close to the distance of ≤14 Å calculated by Coffman and Buettner [97] on the basis of the small amount of dipolar (anisotropic) contribution to the spin–spin interaction between the two centers (particularly bearing in mind the fact that the cysteine sulfur itself is properly considered a part of the cluster, shortening the effective distance between the two centers). The approximately isotropic nature of the observed coupling notwithstanding, these workers demonstrate convincingly that coupling is principally dipolar rather than superexchange in nature.

In addition to characterizing the nature of the interaction between the molybdenum and Fe/S I centers of xanthine oxidoreductase, EPR has been used to establish which of the two iron atoms in each of the two [2Fe–2S] clusters is redox-active. Unlike [4Fe–4S] clusters, which are substantively valence-delocalized, [2Fe–2S] clusters are valence-localized and only one of the two participating iron atoms becomes formally reduced upon addition of one electron. Studies of a variety of ferredoxins and ferredoxin-like systems have consistently indicated that it is

the iron atom coordinated to the more N-terminal pair of cysteine residues in the protein fold that is redox-active, and this is also seen to be the case in the aldehyde oxidoreductase from *D. gigas*, a member of the xanthine oxidoreductase family of enzymes, on the basis of a detailed EPR analysis of the magnetic interactions between the redox-active centers [94]. This being the case, it is the iron coordinated to Cys 43 and 48 (rather than the one coordinated to Cys 51 and 73) in the bovine xanthine oxidoreductase that is redox-active. This is the iron that lies closer to Fe/S I (interestingly, the two irons of Fe/S II are approximately equidistant from the FAD of the enzyme). Consistent with this assignment of the redox-active iron in the N-terminal ferredoxin domain, mutation of Cys 51 to Ser in the rat xanthine dehydrogenase does not greatly alter either the EPR signal or its reduction potential of Fe/S II, whereas mutation of Cys 43 to Ser does [98].

For Fe/S I, in the α-helical domain, one of the iron atoms in the bovine enzyme is coordinated by Cys 113 and 150, and the other by Cys 116 and 148. Again in the case of the rat enzyme, mutation of Cys 115 (analogous to Cys 116 in the bovine sequence) results in only a very modest perturbation of the Fe/S I EPR signal, implying that it is the other iron, coordinated to Cys 113 and 150 in the bovine enzyme, that is the redox-active iron. This is the nearer iron to the molybdenum center, the one coordinated to Cys 150. Significantly, it is the homologous Cys 139 in the *D. gigas* enzyme to which the distal amino group of the pterin cofactor is hydrogen-bonded. The orientation of the Fe/S I cluster in the polypeptide is such that one of the bridging sulfur atoms is nearest to the distal Fe/S II. Fully consistent with this interpretation, in the case of the *D. gigas* aldehyde oxidoreductase, fits to the observed spectra manifesting significant spin–spin interaction that included both exchange and dipolar terms in the Hamiltonian best reproduced the observed spectra when the iron coordinated to Cys 100 and 139 (equivalent to the bovine Cys 113 and 150) was the redox-active iron — that is, it is the iron lying closer to the molybdenum center that is redox-active [94].

6. CONCLUDING COMMENTS

The application of electron paramagnetic resonance and related spectroscopic techniques has provided a wealth of detailed information concerning the structures of reaction intermediates encountered in the course of substrate hydroxylation by xanthine oxidoreductase. In conjunction with comparable studies of model compounds developed over the years that are increasingly faithful mimics of the active site structure, this work has contributed enormously to our understanding of the specific chemical pathway by which substrate hydroxylation occurs. Structural methods such as x-ray crystallography and x-ray absorption spectroscopy have provided a clear context in which to understand the spectroscopic properties of the various signal-giving species, and computational approaches have begun to shed light on the overall reaction coordinate for the reaction as well as the transition states that separate specific intermediates. Most recently, a better understanding of the manner in which the other centers in the enzyme interact magnetically, as

manifested in their EPR spectra, has provided important information regarding the orientation of the centers and their internal electronic structure.

REFERENCES

1. Bray RC. 1975. Molybdenum iron–sulfur flavin hydroxylases and related enzymes. In *The Enzymes*, Vol. 12 3rd ed, pp. 299–419. Ed Boyer PD. New York: Academic Press.
2. Hille R, Nishino T. 1995. Xanthine oxidase and xanthine dehydrogenase. *FASEB J* **9**:995–1003.
3. Bray RC, Meriwether LS. 1966. Electron spin resonance of xanthine oxidase substituted with molybdenum–95. Nature 212(506):467-469.
4. Palmer G, Bray RC, Beinerrt H. 1964. Direct studies on the electron transfer sequence in xanthine oxidase by electron paramagnetic resonance spectroscopy, I: techniques and description of spectra. *J Biol Chem* **239**(8):2657–2666.
5. Bray RC, Palmer G, Beinert H. 1964. Direct studies on the electron transfer sequence in xanthine oxidase by electron paramagnetic resonance spectroscopy, II: kinetic studies employing rapid freezing. *J Biol Chem* **239**(8):2667–2676.
6. Bray RC, Vänngård T. 1969. "Rapidly appearing" molybdenum electron-paramagnetic-resonance signals from reduced xanthine oxidase. *Biochem J* **114**(1):725–734.
7. Pick, FM, Bray RC. 1969. Complex formation between reduced xanthine oxidase and purine substrates demonstrated by electron paramagnetic resonance. *Biochem J* **114(3)**:735–742.
8. Bray RC, Barber MJ, Lowe DJ. 1978. Electron paramagnetic resonance spectroscopy of complexes of xanthine oxidase with xanthine and uric acid. *Biochem J* **171**(3):653–658.
9. Bray RC, George GN. 1985. Electron paramagnetic resonance studies using pre-steady-state kinetics and substitution with stable isotopes on the mechanism of action of molybdoenzymes. *Biochem Soc Trans* **13**(3):560–567.
10. Edmondson DE, Ballou D, van Heuvelen A, Palmer G, Massey V. 1973. Kinetic studies on the substrate reduction of xanthine oxidase. *J Biol Chem* **248**(17):6135–6144.
11. Enroth C, Eger BT, Okamoto K, Nishino T, Nishino T, Pai EF. 2000. Crystal structures of bovine milk xanthine dehydrogenase and xanthine oxidase: structure-based mechanism of conversion. *Proc Natl Acad Sci USA* **97**(20):10723–10728.
12. Okamoto K, Matsumoto K, Hille R, Eger BT, Pai EF, Nishino T. 2004. The crystal structure of xanthine oxidoreductase during catalysis: implications for reaction mechanism and enzyme inhibition. *Proc Natl Acad Sci USA* **101**(21):7931–7936.
13. Romão MJ, Archer M, Moura I, Moura JJG, LeGall J, Engh R, Schneider M, Hof P, Huber R. 1995. Crystal structure of the xanthine oxidase-related aldehyde oxidoreductase from *D. gigas*. *Science* **270**(5239):1170–1176.
14. Huber R, Hof P, Duarte RO, Moura JJG, Moura I, LeGall J, Hille R, Archer M, Romão M. 1996. A structure-based catalytic mechanism for the xanthine oxidase family of molybdenum enzymes. *Proc Natl Acad Sci USA* **93**(17):8846–8851.
15. Dobbek H, Gremer L, Meyer O, Huber R. 1999. Crystal structure and mechanism of CO dehydrogenase, a molybdo iron–sulfur flavoprotein containing selanylcysteine. *Proc Natl Acad Sci USA* **96**(16):8884–8889.

16. Dobbek H, Gremer L, Kiefersauer R, Huber R, Meyer O. 2002. Catalysis at a dinuclear [CuSMo(O)OH] cluster in a CO dehydrogenase resolved at 1.1-angstrom resolution. *Proc Natl Acad Sci USA* **99**(25):15971–15976

17. Bonin I, Martins BM, Purvanov V, Fetzner S, Huber R, Dobbek H. 2004. Active site geometry and substrate recognition of the molybdenum hydroxylase quinoline 2-oxidoreductase. *Structure* **12**(8):1425–1435.

18. Tullius TD, Kurtz DM Jr, Conradson SD, Hodgson KO. 1979. The molybdenum site of xanthine oxidase: structural evidence from X-ray absorption spectroscopy. *J Am Chem Soc* **101**(10):2776–2779.

19. Bordas J, Bray RC, Garner CD, Gutteridge S, Hasnain S. 1980. X-ray absorption spectroscopy of xanthine oxidase: the molybdenum centres of the functional and the desulpho forms. *Biochem J* **191**(2):499.

20. Cramer SP, Wahl R, Rajagopalan KV. 1981. Molybdenum sites of sulfite oxidase and xanthine dehydrogenase: a comparison by EXAFS. *J Am Chem Soc* **103**(26):7721–7727.

21. Cramer SP, Hille, R. 1985. Arsenite-inhibited xanthine oxidase: determination of the molybdenum–sulfur–arsenic geometry by EXAFS. *J Am Chem Soc* **107**(26):8164–8169.

22. Hille R, George GN, Eidsness MK, Cramer SP. 1989. EXAFS of xanthine oxidase complexes with alloxanthine, violapterin, and 6-pteridylaldehyde. *Inorg Chem* **28**(21):4018–4022.

23. Turner NA, Bray RC, Diakun GP. 1989. Information from e.x.a.f.s. spectroscopy on the structures of different forms of molybdenum in xanthine oxidase and the catalytic mechanism of the enzyme. *Biochem J* **260**(2):563–571.

24. Doonan, CJ, Stockert, AL, Hille R, George GN. 2005. Nature of the catalytically labile oxygen in the active site of xanthine oxidase. *J Am Chem Soc* **127**(12):4518–4522.

25. Stiefel EI. 1973. Proposed molecular mechanism for the action of molybdenum in enzymes: coupled proton and electron transfer. *Proc Natl Acad Sci USA* **70**(4):988–992.

26. Stiefel EI. 1977. The coordination and bioinorganic chemistry of molybdenum. *Prog Inorg Chem* **21**(1):1–223.

27. Okamoto K, Eger BT, Nishino T, Kondo S, Pai EF, Nishino T. 2003. An extremely potent inhibitor of xanthine oxidoreductase. *J Biol Chem* **278**(3):1848–1855.

28. Davis MD, Olson JS, Palmer G. 1982. Charge-transfer complexes between pteridine substrates and the active-center molybdenum of xanthine oxidase. *J Biol Chem* **259**(24):4630–4737.

29. Davis MD, Olson JS, Palmer G. 1984. The reaction of xanthine oxidase with lumazine: characterization of the reductive half-reaction. *J Biol Chem* **259**(6):3526–3533.

30. Hille, R. 1996. The mononuclear molybdenum enzymes, *Chem Rev* **96**(7):2757–2816.

31. Hille, R. 2002. Molybdenum and tungsten in biology. *Trends Biochem Sci* **27**(7):360–367.

32. Hille R. 2005. Molybdenum-containing hydroxylases. *Arch Biochem Biophys* **433**(1):107–116.

33. Kim JH, Ryan MG, Knaut H, Hille R. 1996. The reductive half-reaction of xanthine oxidase: a pH dependence and solvent kinetic isotope effect study. *J Biol Chem* **271**(12):6771–6780.

34. Xia M, Dempski R, Hille R. 1999. The reaction of xanthine oxidase with aldehyde substrates. *J Biol Chem* **274**(6):3323–3330.

35. Leimkühler S, Hodson R, George GN, Rajagopalan KV. 2003. Recombinant Rhodobacter capsulatus xanthine dehydrogenase, a useful model system for the characteriza-

tion of protein variants leading to xanthinuria in humans. *J Biol Chem* **278**(23):20802–20811.

36. Leimkühler S, Stockert AL, Igarashi K, Nishino T, Hille R. 2004. The role of active site glutamate residues in catalysis of Rhodobacter capsulatus xanthine dehydrogenase. *J Biol Chem* **279**(39):40437–40444.

37. Skibo EB, Gilchrist JH, Lee C-H. 1987. Electronic probes of the mechanism of substrate oxidation by buttermilk xanthine oxidase: role of the active-site nucleophile in oxidation. *Biochemistry* **26**(11):3032–3037.

38. Murray KN, Watson JG, Chaykin S. 1965. Catalysis of the direct transfer of oxygen from nicotinamide N-oxide to xanthine by xanthine oxidase. *J Biol Chem* **241**(20):4798–4801.

39. Hille R, Sprecher H. 1987. On the mechanism of action of xanthine oxidase. *J Biol Chem* **262**(23):10914–10917.

40. Stockert AL, Shinde S, Anderson RF, Hille R. 2002. The reaction mechanism of xanthine oxidase: evidence for two-electron chemistry rather than sequential one-electron steps. *J Am Chem Soc* **124**(49):14554–14555.

41. McWhirter RB, Hille R. 1991. The reductive half-reaction of xanthine oxidase: spectral intermediates in the hydroxylation of 2-hydroxy-6-methylpurine. *J Biol Chem* **266**(35):23724–23731.

42. Bray RC, Knowles PF. 1968. Electron spin resonance in enzyme chemistry: the mechanism of action of xanthine oxidase. *Proc Roy Soc (London) A* **302**(1474):351–353.

43. Gutteridge S, Tanner SJ, Bray RC. 1978. The molybdenum centre of native xanthine oxidase: evidence to proton transfer from substrates to the centre and for existence of an anion binding site. *Biochem J* **175**(3):869–878.

44. Voityuk AA, Albert K, Kostlmeier S, Nasluzov VA, Neyman KM, Hof P, Huber R, Romão MJ, Rosch N. 1997. Prediction of alternative structures of the molybdenum site in the xanthine oxidase-related aldehyde oxide reductase. *J Am Chem Soc* **119**(13):3159–3160.

45. Ilich P, Hille R. 1999. The mechanism of formamide hydroxylation catalyzed by a molybdenum–dithiolene complex: a model for xanthine oxidase reactivity. *J Phys Chem B* **103**(25):5406–5412

46. Ilich P, Hille R. 2002. Reactivity of oxo, selenido and tellurido Mo–dithiolene: understanding the reactivity of xanthine oxidase. *J Am Chem Soc* **124**(24):6796–6797.

47. Zhang X-H, Wu Y-D. 2005. As theoretical study on the mechanism of the reductive half-reaction of xanthine oxidase. *Inorg Chem* **44**(5):1466–1471.

48. Massey V, Edmondson D. 1970. On the mechanism of inactivation of xanthine oxidase by cyanide. *J Biol Chem* **245**(24):6595–6598.

49. Tanner S, Bray RC, Bergmann F. 1978. [13]C hyperfine splitting of some molybdenum electron paramagnetic resonance signals of xanthine oxidase. *Biochem Soc Trans* **6**(8):1328–1330.

50. Howes BD, Bray RC, Richards RL, Turner NA, Bennett B, Lowe DJ. 1996. Evidence favoring molybdenum-carbon bond formation in xanthine oxidase action: [17]O- and ^{13}C-ENDOR and kinetic studies. *Biochemistry* **35**(5):1432–1443.

51. Manikandan P, Choi E-Y, Hille R, Hoffman BM. 2001. 35 GHz ENDOR characterization of the "very rapid" signal of xanthine oxidase reacted with 2-hydroxy-6-methylpurine ([13]C8): evidence against direct Mo–C interaction. *J Am Chem Soc* **123**(11):2658–2663.

52. Lowe DJ. 2002. Enzymes of the xanthine oxidase family: the role of molybdenum and tungsten: their roles in biological processes. In *Metal ions in biological systems*, Vol. 39, pp. 455–479. Ed A Sigel, H Sigel. New York: Marcel Dekker.

53. Lorigan GA, Britt RD, Kim JH, Hille R. 1994. Electron spin echo envelope modulation spectroscopy of the molybdenum center of xanthine oxidase. *Biochim Biophys Acta* **1185**(3):284–294.

54. Jones RM, Inscore FE, Hille R, Kirk ML. 1999. Freeze-quench difference magnetic circular dichroism study of a xanthine oxidase intermediate. *Inorg Chem* **38**(22):4963–4970.

55. Hawkes, TR, George GN, Bray RC. 1984. The structure of the inhibitory complex of alloxanthine (1*H*-pyrazolo[3,4-*d*]pyrimidine-4,6-diol) with the molybdenum centre of xanthine oxidase from electron paramagnetic resonance spectroscopy. *Biochem J* **218**(3):961–968.

56. Massey V, Komai H, Palmer G, Elion GB. 1970. On the mechanism of inactivation of xanthine oxidase by allopurinol and other pyrazolo[3,4-*d*]pyrimidines. *J Biol Chem* **246**(11):2837–2844.

57. Truglio JJ, Theis K, Leimkühler S, Rappa R, Rajagopalan KV, Kisker C. 2002. Crystal structures of the active and alloxanthine-inhibited forms of xanthine dehydrogenase from *Rhodobacter capsulatus*. *Structure* **10**(1):115–126.

58. Bayse CA. 2006. Theoretical characterization of the "very rapid" Mo(V) species generated in the oxidation of xanthine oxidase. *Inorg Chem* **45**(5):2199–2202.

59. Hille R, Kim JH, Hemann C. 1993. Reductive half-reaction of xanthine oxidase: mechanistic role of the species giving rise to the "rapid" MoV EPR signal. *Biochemistry* **32**(15):3973–3980.

60. Olson JS, Ballou DP, Palmer G, Massey V. 1974. The mechanism of action of xanthine oxidase. *J Biol Chem* **249**(14):4363–4382.

61. Tsopanakis A, Tanner SJ, Bray RC. 1978. pH-jump studies at sub-zero temperatures on an intermediate in the reaction of xanthine oxidase with xanthine. *Biochem J* **175**(3):879–885.

62. Malthouse JPG, George GN, Lowe DJ, Bray RC. 1981. Coupling of [³³S] sulphur to molybdenum(V) in different reduced forms of xanthine oxidase. *Biochem J* **199**(3):629–637.

63. Astashkin AV, Mader ML, Pacheco A, Enemark JH, Raitsimring AM. 2000. Direct detection of the proton-containing group coordinated to Mo(V) in the high pH form of chicken sulfite oxidase by refocused primary ESEEM spectroscopy: structural and mechanistic implications. *J Am Chem Soc* **122**(22):5294–5302.

64. Bray RC, Knowles PF, Pick FM, Vänngård T. 1968. Electron spin resonance evidence for interaction of protons with Mo(V) in reduced forms of xanthine oxidase. *Biochem J* **107**(2):601–602.

65. Malthouse JPG, Bray RC. 1980. The nature of the sulphur liberated from xanthine oxidase by cyanide. *Biochem J* **191**(1):265–267.

66. Wilson GL, Kony M, Tiekink ERT, Pilbrow JR, Spence JT, Wedd AG. 1988. O-17 and Mo-95 coupling in spectroscopic models of molybdoenzymes. *J Am Chem Soc* **110**(20):6923–6925.

67. Wilson GL, Greenwood RJ, Pilbrow JR, Spence JT, Wedd AG. 1991. Molybdenum(V) sites in xanthine oxidase and relevant analog complexes: comparison of Mo-95 and S-33 hyperfine coupling. *J Am Chem Soc* **113**(18):6803–6812.

68. FM, McGartoll MA, Bray RC. 1971. Reaction of formaldehyde and of methanol with xanthine oxidase. *Eur J Biochem* **18**(1):65–72.

69. Howes BD, Pinhal NM, Turner NA, Bray RC, Anger G, Ehrenberg A, Raynor JB, Lowe DJ. 1990. Proton electron-nuclear double-resonance spectra of molybdenum(V) in different reduced forms of xanthine oxidase. *Biochemistry* **29**(26):6120–6127.

70. Lowe DJ, Barber MJ, Pawlik RT, Bray RC. 1976. A new non-functional form of milk xanthine oxidase containing stable quinquivalent molybdenum. *Biochem J* **155**(1):81–85.

71. George GN, Bray RC. 1983. Formation of the inhibitory complex of *p*-chloromercuribenzoate with xanthine oxidase, evaluation of hyperfine and quadrupole couplings of mercury to molybdenum(V) from the electron paramagnetic resonance spectrum, and the structure of the complex. *Biochemistry* **22**(23):5443–5452.

72. George GN, Bray RC. 1983. Reaction of arsenite ions with the molybdenum center of milk xanthine oxidase. *Biochemistry* **22**(5):1013–1021.

73. Hille R, Stewart RC, Fee JA, Massey V. 1983. The interaction of arsenite with xanthine oxidase. *J Biol Chem* **258**(8):4849–4856.

74. Boer DR, Thapper A, Brondino CD, Romão MJ, Moura JJG. 2004. X-ray crystal structure and EPR spectra of "arsenite-inhibited" *Desulfovibrio gigas* aldehyde dehydrogenase: a member of the xanthine oxidase family. *J Am Chem Soc* **126**(28):8614–8615.

75. Enemark JH, Cooney, JJA, Wang J-J, Holm RH. 2004. Synthetic analogs and reaction systems relevant to the molybdenum and tungsten oxotransferases. *Chem Rev* **104**(2):1175–1200.

76. George GN, Bray RC. 1988. Studies by electron paramagnetic resonance spectroscopy of xanthine oxidase enriched with molybdenum-95 and with molybdenum-97. *Biochemistry* **27**(10):3603–3609.

77. Gutteridge S, Bray RC. 1980. Oxygen-17 splitting of the very rapid molybdenum(V) e.p.r. signal from xanthine oxidase. *Biochem J* **189**(3):615–623.

78. Bray RC, Gutteridge S. 1982. Numbers and exchangeability of oxygen-17 atoms coupled to molybdenum(V) in different reduced forms of xanthine oxidase. *Biochemistry* **21**(23):5992–5999.

79. Greenwood RJ, Wilson GL, Pilbrow JR, Wedd AG. 1993. Molybdenum(V) sites in xanthine oxidase and relevant analog complexes: comparison of O-17 hyperfine coupling. *J Am Chem Soc* **115**(13):5385–5392.

80. Abragam A, Bleaney B. 1970. *Electron paramagnetic resonance of transition ions*. Oxford: Oxford UP.

81. Swann J, Westmoreland TD. 1997. Density functional calculations of *g* values and molybdenum hyperfine coupling constants for a series of molybdenum(V) oxyhalide anions. *Inorg Chem* **36**(23):5348–5357.

82. Rappé, AK, Goddard III WA. 1980. Bivalent spectator oxo bonds in metathesis and epoxidation of alkenes. *Nature* **285**(5763):311–312.

83. Hille R, Massey V. 1986. The equilibration of reducing equivalents within milk xanthine oxidase. *J Biol Chem* **261**(3):1241–1247.

84. Hille R, Anderson RF. 1991. Electron transfer in milk xanthine oxidase as studied by pulse radiolysis. *J Biol Chem* **266**(9):5608–5615.

85. Hille R, Anderson RF. 2001. Coupled electron transfer and protonation/deprotonation in complex flavoproteins: solvent kinetic isotope effect studies of electron transfer in xanthine oxidase and trimethylamine dehydrogenase. *J Biol Chem* **276**(33):31193–31201.

86. Palmer G, Massey V. 1969. Electron paramagnetic resonance and circular dichroism studies of milk xanthine oxidase. *J Biol Chem* **244**(10):2614–2620.

87. Hille R, Hagen WR, Dunham, WR. 1985. Spectroscopic studies of the iron–sulfur centers in xanthine oxidase. *J Biol Chem* **260**(19):10569–10575.

88. Caldeira J, Belle V, Asso M, Guigliarelli B, Moura I, Moura JJG, Bertrand P. 2000. Analysis of the electron paramagnetic resonance properties of the [2Fe–2S](1+) centers in molybdenum enzymes of the xanthine oxidase family: assignment of signals I and II. *Biochemistry* **39**(10):2700–2707.

89. Andrade SLA, Brondino CD, Feio MJ, Moura I, Moura JJG. 2000. Aldehyde oxidoreductase activity in *Desulfovibrio alaskensis* NCIMB 13491: EPR assignment of the proximal [2Fe–2S] cluster to the Mo site. *Eur J Biochem* **267**(7):2054–2061.

90. Gremer L, Kellner S, Dobbek H, Huber R, Meyer O. 2000. Binding of flavin adenine dinucleotide to molybdenum-containing carbon monoxide dehydrogenase from *Oligotropha carboxidovorans*: structural and functional analysis of a carbon monoxide dehydrogenase species in which the native flavoprotein has been replaced by its recombinant counterpart produced in *Escherichia coli*. *J Biol Chem* **275**(3):1864–1872.

91. Lowe DJ, Lynden-Bell RM, Bray RC. 1972. Spin–spin interaction between molybdenum and one of the iron–sulphur systems of xanthine oxidase and its relevance to the enzymic mechanism. *Biochem J* **130**(1):239–249.

92. Lowe DJ, Hyde JS. 1975. Electron–electron double resonance measurements on xanthine oxidase. *Biochim Biophys Acta* **377**(1):205–210.

93. Lowe DJ, Bray RC. 1978. Magnetic coupling of the molybdenum and iron–sulphur centres in xanthine oxidase and xanthine dehydrogenases. *Biochem J* **169**(2):471–479.

94. More C, Asso M, Roger G, Guigliarelli B, Caldeira J, Moura J, Bertrand P. 2005. Study of the spin-spin interactions between the metal centers of *Desulfovibrio gigas* aldehyde oxidoreductase: identification of the reducible sites of the [2Fe–2S](1+2) clusters. *Biochemistry* **44**(34):11628–11635.

95. Canne C, Stephan I, Finsterbusch J, Lingens F, Kappl R, Fetzner S, Hüttermann J. 1997. Comparative EPR and redox studies of three prokaryotic enzymes of the xanthine oxidase family: quinoline 2-oxidoreductase, quinaldine 4-oxidase, and isoquinoline 1-oxidoreductase. *Biochemistry* **36**(32):9780–9790.

96. Canne C, Lowe DJ, Fetzner S, Adams B, Smith AT, Kappl R, Bray RC, Hüttermann J. 1999. Kinetics and interactions of molybdenum and iron–sulfur centers in bacterial enzymes of the xanthine oxidase family: mechanistic implications. *Biochemistry* **38**(42):14077–14087.

97. Coffman RE, Buettner GR. 1979. General magnetic dipolar interaction of spin–spin coupled molecular dimers: application to an EPR spectrum of xanthine oxidase. *J Phys Chem* **83**(18):2392–2399.

98. Iwasaki T, Okamoto K, Nishino T, Mizushima J, Hori H, Nishino T. 2000. Sequence motif-specific assignment of two 2Fe–2S clusters in rat xanthine oxidoreductase studied by site-directed mutagenesis. *J Biochem* **127**(5):771–778.

HIGH-RESOLUTION EPR SPECTROSCOPY OF MO ENZYMES. SULFITE OXIDASES: STRUCTURAL AND FUNCTIONAL IMPLICATIONS

John H. Enemark, A.V. Astashkin, and A.M. Raitsimring

Department of Chemistry,University of Arizona, Tucson

Sulfite oxidases (SOs) are physiologically vital Mo-containing enzymes that occur in animals, plants, and bacteria and which catalyze the oxidation of sulfite to sulfate, the terminal reaction in the oxidative degradation of sulfur-containing compounds. X-ray structure determinations of SOs from several species show nearly identical coordination structures of the molybdenum active center, and a common catalytic mechanism has been proposed that involves the generation of a transient paramagnetic Mo(V) state through a series of coupled electron–proton transfer steps. This chapter describes the use of pulsed electron-nuclear double resonance (ENDOR) and electron spin echo envelope modulation (ESEEM) spectroscopic techniques to obtain information about the structure of this Mo(V) species from the hyperfine interactions (*hfi*) and nuclear quadrupole interactions (*nqi*) of nearby magnetic nuclei. Variable frequency instrumentation is essential to optimize the experimental conditions for measuring the couplings of different types of nuclei (e.g., ^{1}H, ^{2}H, ^{31}P, and ^{17}O). The theoretical background necessary for understanding the ESEEM and ENDOR spectra of the Mo(V) centers of SOs is outlined, and examples of the use of advanced pulsed EPR methods (RP-ESEEM, HYSCORE, integrated four-pulse ESEEM) for structure determination are presented. The analysis of variable-frequency pulsed EPR data from SOs is aided by parallel studies of model compounds that contain key functional groups or that are isotopically labeled and thus provide benchmark data for enzymes. Enormous progress has been made on the use of high-resolution variable-frequency pulsed EPR methods to investigate the structures and mechanisms of SOs during the past ~15 years, and the future is bright for the continued development and application of this technology to SOs, other molybdenum enzymes, and other problems in metallobiochemistry.

Address all correspondence to John H. Enemark, Department of Chemistry, 1306 E. University Boulevard, University of Arizona, Tucson, Arizona 85721-0041 USA, +1 520 621-2245, +1 520 626-8065 (fax), <jenemark@u.arizona.edu>.

1. INTRODUCTION AND STRUCTURES FROM
    X-RAY CRYSTALLOGRAPHY

Sulfite oxidases (SOs) are physiologically vital Mo-containing enzymes encountered in numerous organisms: humans, avians, plants and bacteria. These enzymes catalyze the oxidation of sulfite to sulfate, coupled, at least in vertebrates, with the subsequent reduction of two equivalents of ferricytochrome c (cyt c)$_{ox}$ to ferrocytochrome c (cyt c)$_{red}$ [1,2]:

$$SO_3^{2-} + H_2O + 2(cyt\ c)_{ox} \leftrightarrow SO_4^{2-} + 2(cyt\ c)_{red} + 2H^+ .$$
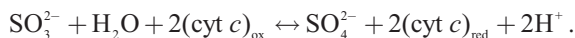
This is the terminal reaction in the oxidative degradation of sulfur-containing compounds and is physiologically essential.

The vertebrate SOs consist of two identical subunits [3–8], each with a molecular weight of ~51.5 kDa. Each subunit in turn has two functionally distinct domains. The smaller N-terminal domain (~10 kDa) contains a b_5-type heme center, with the heme Fe being in oxidation state III in the resting enzyme. The larger C-terminal domain (~42 kDa) contains an Mo atom with a resting oxidation state of VI (see Fig. 1).
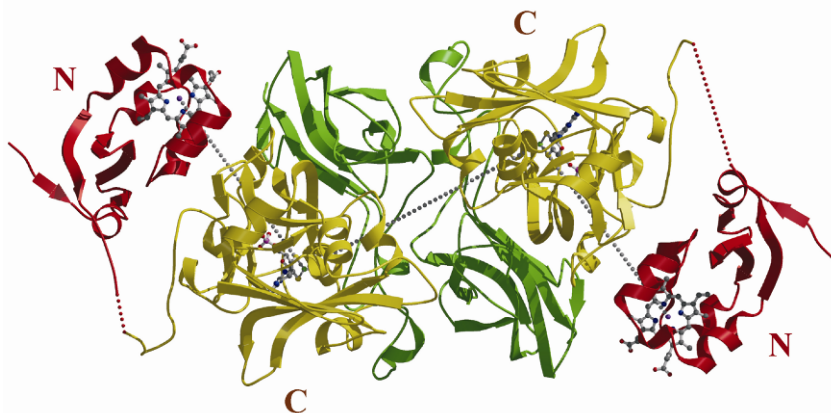
Figure 1. X-ray structure of CSO from PDB 1sox [4]. Please visit http://www.springer.com/978-1-4419-1138-4 to view a high-resolution full-color version of this illustration.

The two-electron oxidation of SO_3^{2-} occurs at the Mo center to give a formally Mo^{IV} state that is then reoxidized to Mo^{VI} by sequential one-electron transfers to the b_5-type heme center. After each Mo → Fe one-electron-transfer step, the b_5 center is reoxidized by exogenous (cyt c)$_{ox}$, resulting in the catalytic turnover cycle shown in Scheme 1. While vertebrate SOs contain Mo and heme domains in each subunit, the dimeric SO found in plants (*pl*-SO) [9,10] contains only an Mo domain in each subunit and lacks an Fe domain. The Mo domain of *pl*-SO is highly homologous to that of a vertebrate SO, and the structure of *pl*-SO from *Arabidopsis thaliana* is presented in Figure 2.
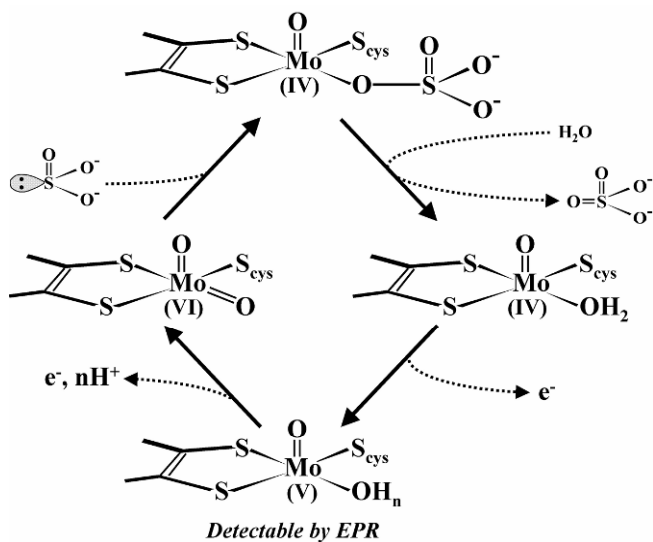
Scheme 1. Proposed catalytic cycle of sulfite oxidase of vertebrates.
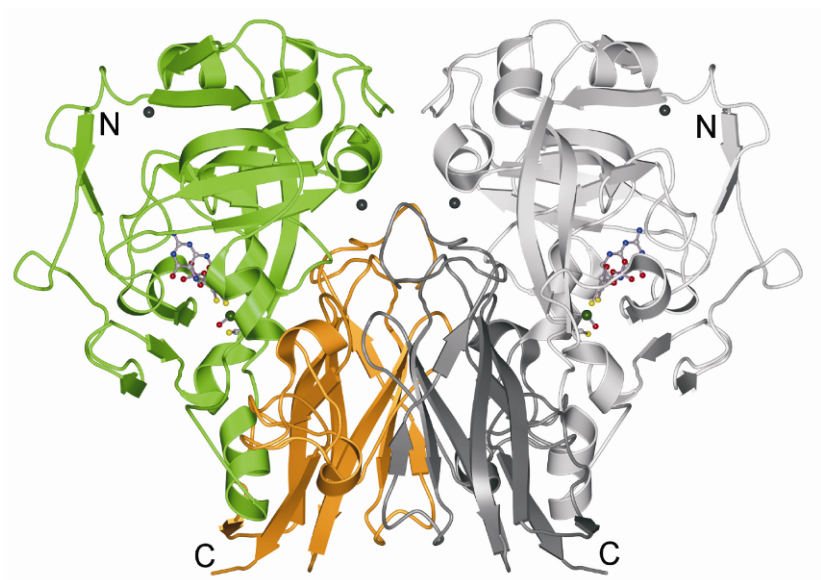
Figure 2. The crystal structure of plant sulfite oxidase. Reprinted with permission from [9]. Copyright © 2003, Elsevier. Please visit http://www.springer.com/978-1-4419-1138-4 to view a high-resolution full-color version of this illustration.

The SO found in bacteria (*b*-SO) differs from the SOs of vertebrates and plants [11–13]. Bacterial SO is a heterodimer consisting of a 40.6-kDa subunit containing an Mo cofactor and an 8.8-kDa subunit containing a single *c*-type heme. The two subunits of *b*-SO are tightly associated (Fig. 3), and the Fe···Mo distance (~16 Å) is much smaller than that seen in the crystal structure of chicken SO (CSO) .
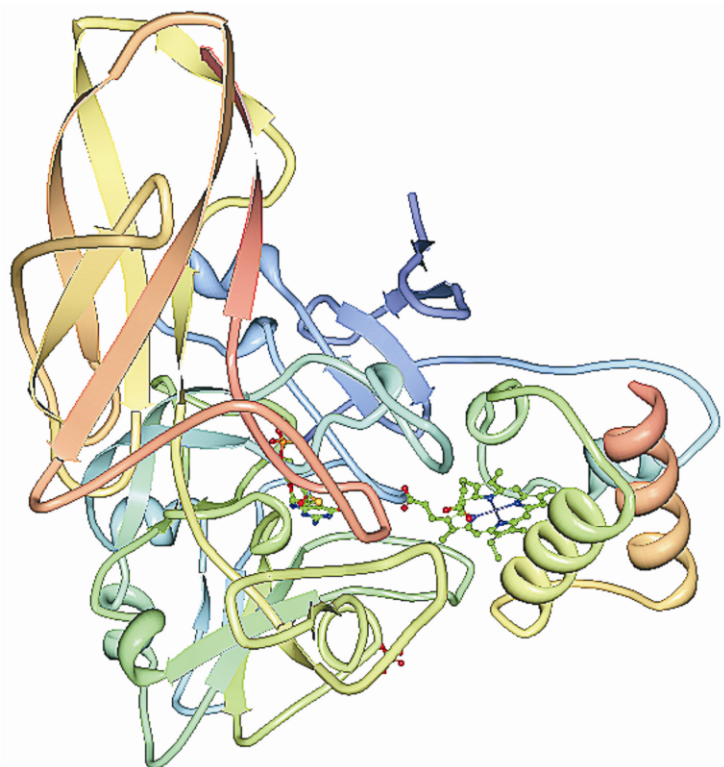
Figure 3. High-resolution structure of the heterodimeric complex of the catalytic molybdopterin subunit and the *c*-type cytochrome subunit from *Starkeya novella* from PDB 2blf [11]. Please visit http://www.springer.com/978-1-4419-1138-4 to view a high-resolution full-color version of this illustration.

The geometry of the Mo center (which is well conserved in all the SOs) [14,15], as revealed by x-ray crystallography and shown in Figure 4, is approximately square pyramidal, with an oxo group occupying the apical position. The equatorial positions are occupied by a second oxygen and by three sulfurs, one of which is supplied by a cysteine sidechain, while the other two come from the ene-dithiolate group of the molybdopterin. For CSO the crystal structure reveals that the equatorial oxygen ligand is accessible to the solvent, whereas the apical one is

more shielded by the surrounding protein. During the proposed catalytic cycle (Scheme 1), the Mo center of SOs passes through the formal Mo(V) oxidation state. The immediate environment of this paramagnetic d^1 electron configuration can be investigated by electron paramagnetic resonance (EPR) techniques.
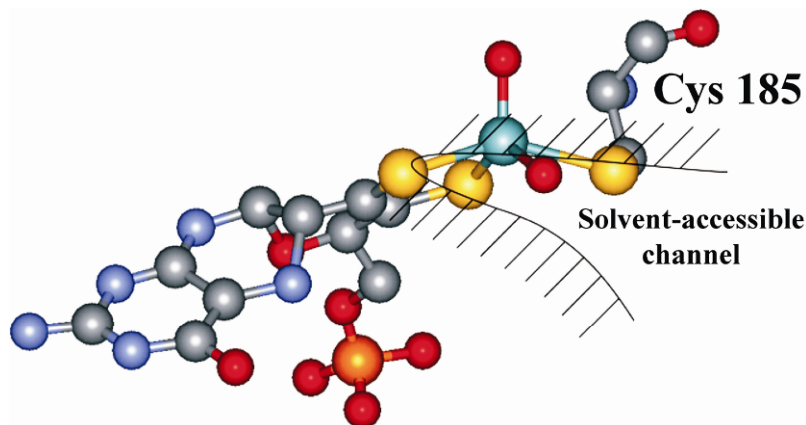
Figure 4. The detailed structure of the molybdenum active site of CSO [4]. Please visit http://www.springer.com/978-1-4419-1138-4 to view a high-resolution full-color version of this illustration.

2. EARLIER CW EPR INVESTIGATIONS

Extensive continuous wave (cw) EPR investigations of CSO during the late 1970s and early 1980s, carried out primarily by Cramer, Bray, and others (see, e.g., [16–20]), demonstrated that CSO has an EPR spectrum characterized by a general rhombic g-factor anisotropy (Fig. 5). Three distinct forms having different sets of principal g-values were observed depending upon pH and anions in the medium. In high-pH buffers (pH 9–9.5) containing low anion concentrations one form was obtained exclusively, whereas the other two were observed in buffers of ~pH 7 containing high concentrations of anions such as Cl⁻ or phosphate. At intermediate pH values a mixture of the species was observed. The particular form observed at low pH depended upon whether phosphate was present in the buffer, and so these two forms have become known as the low-pH (*lpH*) form and the phosphate inhibited (*Pi*) form. Similarly, the species observable at high pH has become known as the high-pH (*hpH*) form.

The EPR spectrum of the *lpH* form clearly shows well-resolved doublet splittings at the g_z and g_x positions (Fig. 5), which disappear in D_2O buffer. This finding allowed Bray and coworkers to conclude that the observed splitting is caused by a hyperfine interaction (*hfi*) of Mo(V) with a single exchangeable proton, most

probably belonging to an Mo–OH group [7]. From numerical simulations of the cw-EPR spectrum Bray and coworkers obtained the *hfi* tensor associated with this proton [7]. However, the intrinsically low resolution of the cw-EPR experiments precluded obtaining such important structural information as the orientation of the OH ligand with respect to the rest of the Mo complex.
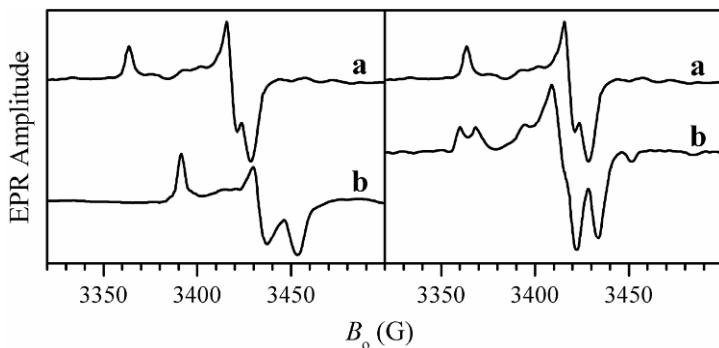
Figure 5. Left panel: cw X-band EPR spectra of low- (a) and high-pH (b) forms of CSO in D_2O buffer. This panel demonstrates the variation of *g*-values with pH. Right panel: cw-EPR spectra of *lpH* form of CSO in D_2O (a) and H_2O (b) buffers. In the latter the proton-related splittings are clearly visible.

    No proton splittings were observed in the EPR spectra of either the *Pi* or *hpH* forms of the enzyme. In the case of the *Pi* form, cw-EPR experiments using [17]O-substituted PO_4^{3-} [17] provided early evidence that a phosphate group coordinates to the Mo(V) center, displacing OH. For the *hpH* form, the lack of observation of an exchangeable proton in the cw spectra was initially believed to reflect deprotonation of the putative Mo–OH group of the *lpH* form. Later, however, George proposed that an Mo–OH moiety was also present at high pH [21]. This suggestion was supported by earlier [17]O studies which showed that, unlike the *Pi* form, both the *hpH* and *lpH* forms have a water-exchangeable oxygen-containing ligand [17]. An OH moiety would be a likely candidate for this ligand, and George suggested a possible mechanism involving pH-dependent coordination changes that might explain the transition from the *lpH* to the *hpH* form without invoking the loss of Mo–OH [21].

    Generally, the features of the EPR spectra of vertebrate SOs are independent of whether the Mo center is reduced by sulfite (a common practice), photochemically, or by titanium(III) citrate. However, when reduction of CSO was carried out in 4-morpholine-ethanesulfonic acid (Mes) buffer (pH 6.0), cw-EPR difference spectra gave evidence for a form of SO with principal *g*-values similar to those of *lpH* SO, but lacking the characteristic splittings from an exchangeable proton. This atypical form of SO was tentatively attributed to excess sulfite binding to the

Mo(V) center, thereby blocking water access [19]. No additional studies of this atypical form of SO have been described.

When the investigations were expanded from vertebrate SO to plant, bacterial, and mutant SOs, it became evident that the classification derived from the initial EPR investigation of vertebrate SO**s** is far from complete. For instance, for *pl*-SO the EPR spectrum of the form obtained by sulfite reduction at low pH does not show any proton-related splittings, and is similar to the atypical low-pH spectrum previously observed for vertebrates [19]. However, reduction of *pl*-SO by sulfite at high pH results in EPR spectra that are indistinguishable from those for wild-type chicken and human SO. For *b*-SO the EPR spectrum was found to be independent of pH and the presence of anions in solution, and resembled the EPR spectrum of the *hpH* form of vertebrates under all conditions.

The increasingly diverse cw-EPR results for SO proteins emphasized the need for the application of high-resolution pulsed EPR techniques that could provide intimate structural details for the Mo(V) centers of different organisms under various conditions. Such studies have been a primary focus of our research during the last decade. The structural information in these investigations was derived from *hfi* and nuclear quadrupole interactions (*nqi*) evaluated from pulsed electron-nuclear double resonance (ENDOR) or electron spin echo (ESE) envelope modulation (ESEEM) spectra. The spectra obtained by these pulsed EPR techniques contain the lines at fundamental nuclear transition frequencies. In addition, some of the ESEEM techniques display lines at frequencies that are linear combinations (usually, simple sums and differences) of the fundamental ones.

The appearance of the ESEEM spectra strongly depends on the specific technique, operational microwave (mw) frequency, and the *hfi* and *nqi* parameters of the studied nuclei. As a result, in order to determine the nuclear *hfi* and *nqi* parameters, one often needs to perform several experiments employing different pulsed EPR techniques at different mw frequencies. In the following section we briefly describe the relationship between the spectral line positions and magnetic resonance parameters, and discuss the optimal conditions for detection and interpretation of ESEEM and pulsed ENDOR spectra.

3. FREQUENCIES OBSERVED IN PULSED EPR FOR A SYSTEM OF ELECTRON SPIN $S = 1/2$ AND ARBITRARY NUCLEAR SPIN IN WEAK INTERACTION LIMIT

Most of the practical EPR studies of biological systems, including SOs, are performed on frozen solutions in which protein molecules do not have any preferential orientations. Depending on the magnetic properties of these paramagnetic centers, two spectroscopically different situations may arise. The first is where the anisotropy of the electron spin interactions (e.g., *g*-factor anisotropy) is not very strong and the anisotropic broadening is much smaller than the effective width of the mw excitation. In this case the paramagnetic centers contributing to the EPR or ESE signal form an ensemble of complete orientational disorder. The ESEEM or ENDOR spectra in such a nonselective situation provide information about the

magnitudes of the nuclear hyperfine and quadrupole interactions and about the relative orientations of the *hfi* and *nqi* tensors.

The second situation arises when the anisotropic broadening dominates the EPR spectrum and is much greater than the mw excitation width. In this case the EPR or ESE signal is contributed by paramagnetic centers that have a limited set of orientations with respect to the magnetic field vector, $\mathbf{B}_0$. Depending on the measurement position within the EPR spectrum (which, for a given mw frequency, ν_{mw}, is selected by choosing the strength of the resonance magnetic field, B_0), different sets of orientations can be made to contribute to the ENDOR or ESEEM spectra. Tracing the dependence of these spectra on the EPR position allows one to obtain information about the magnitudes of *hfi* and *nqi* and about the orientations of the *hfi* and *nqi* tensors with respect to the major magnetic tensor (e.g., the *g*-tensor) that determines the EPR anisotropy.

The ENDOR and ESEEM results obtained for both orientation-selective and nonselective situations can ultimately be interpreted in terms of the orientations of the nuclear interaction tensors with respect to the molecular coordinate frame. Whether this last step in the interpretation can only be done using rigorous quantum chemical computations, or simple qualitative considerations will suffice, depends on the complexity of the situation (primarily, on the symmetry).

Below we will outline the theoretical background necessary for understanding the ESEEM and ENDOR spectra of an Mo(V) center of SO. In this specific case we will be dealing with orientation-selective experiments. The orientation selection will be determined by the *g*-factor anisotropy that is not very large (the principal *g*-values are within the range from about 2.0 to 1.95), but sufficient to broaden the EPR spectrum to tens of Gauss even in C-band ($\nu_{mw} \sim 5$ GHz), significantly greater than the mw excitation width, ~10 G. The nuclear spin Hamiltonian appropriate for a system consisting of an electron spin $S = 1/2$ and a nuclear spin $I \neq 0$ in strong magnetic field is

$$H = -\nu_I I_Z + (a_{iso} + T_{ZZ})S_Z I_Z + T_{ZX} S_Z I_X + T_{ZY} S_Z I_Y + k(3I_{Z'}^2 + \eta(I_{X'}^2 - I_{Y'}^2)) . \quad (1)$$

where $\nu_I = g_n \beta_n B_0$ is the nuclear Zeeman frequency (g_n is the nuclear *g*-factor and β_n is the nuclear magneton), a_{iso} is the isotropic *hfi* constant, and T_{Zj} ($j = X, Y, Z$) are the components of the anisotropic *hfi* tensor. The parameter k is related to the quadrupole coupling constant, e^2Qq, as $k = e^2Qq/4I(2I-1)h$ (Q is the quadrupole moment, q is the largest component of the electric field gradient tensor on the nucleus, h is Planck's constant), while η is the asymmetry parameter of the electric field gradient tensor. X, Y, and Z are the axes of the laboratory coordinate frame, with $\mathbf{B}_0$ // Z. X', Y', and Z' are the principal axes of the *nqi*. The electronic *g*-factor is assumed to be not very anisotropic, so that the electron spin quantization axis is reasonably aligned with $\mathbf{B}_0$ // Z, and the electron spin projection on $\mathbf{B}_0$, m_S ($m_S \equiv \langle S_Z \rangle$), assumes the values $-1/2$ and $1/2$. The strong magnetic field condition mentioned above implies that the electron Zeeman interaction is much stronger than any of the interactions accounted for by Eq. (1).

Let us consider first the simplest case of $I = 1/2$, when the quadrupole interaction is absent. In this situation the nuclear transition frequencies (so called fundamental frequencies) are:

$$\nu_{\alpha,\beta} = \sqrt{\left(\nu_I \mp \frac{a_{\text{iso}} + T_{ZZ}}{2}\right)^2 + \frac{T_{ZX}^2 + T_{ZY}^2}{4}} \approx \tag{2a}$$

$$\approx \nu_I \mp \frac{(a_{\text{iso}} + T_{ZZ})}{2} + \frac{T_{ZX}^2 + T_{ZY}^2}{8\nu_I \mp 4(a_{\text{iso}} + T_{ZZ})} \approx \tag{2b}$$

$$\approx \nu_I \mp \frac{(a_{\text{iso}} + T_{ZZ})}{2}, \tag{2c}$$

where subscripts α and β denote, respectively, the electron spin projections $m_S = 1/2$ and $-1/2$. Equation (2a) represents the exact solution for the spin Hamiltonian Eq. (1), while Eqs. (2b) and (2c) are approximations for $|\nu_I \pm (a_{\text{iso}} + T_{ZZ})/2| >> (T_{ZX}^2 + T_{ZY}^2)/4$. The simplest Eq. (2c) is usually sufficient to understand the positions and shapes of the fundamental lines.

A typical purpose of the ENDOR/ESEEM spectroscopic investigation is to obtain separate estimates of the isotropic and anisotropic *hfi* parameters. In a system where the orientation selective experiments are possible (like SO) these estimates can in principle be obtained from the dependence of the shapes and positions of the fundamental lines on the EPR position. This approach, however, may sometimes become difficult to use because of possible overlaps of spectral lines from several different nuclei, or when broad statistical distributions of the *hfi* parameters obscure the lineshape details. In spite of these limitations, this is the only approach available in ENDOR experiments. In ESEEM, however, there are additional possibilities related to the fact that the ESEEM spectra may contain combination lines [22]. The most useful of these combination lines is the sum-combination $\nu_\sigma = \nu_\alpha + \nu_\beta$. From Eq. (2b) it follows that in the limit of weak *hfi*, $\nu_I >> |a_{\text{iso}} + T_{ZZ}|/2$, the sum-combination frequency is

$$\nu_\sigma = \nu_\alpha + \nu_\beta \approx 2\nu_I + \frac{T_{ZX}^2 + T_{ZY}^2}{4\nu_I}. \tag{3}$$

One can see that the sum-combination line is upshifted from $2\nu_I$, to higher frequencies by the value $\Delta\nu_\sigma$ proportional to the square of the anisotropic *hfi* constant. In a specific situation of complete orientational disorder and an axially symmetric anisotropic *hfi* tensor a good practical estimate of the sum-combination line shift is [22]

$$\Delta\nu_\sigma \approx \frac{9T_\perp^2}{16\nu_I}, \tag{4}$$

where $T_\perp$ is the perpendicular component of the anisotropic *hfi* tensor. Conversely, from the position of the sum-combination line, using Eq. (4), it is easy to estimate the anisotropic *hfi* constant. Then one can use this estimate and obtain from the fundamental line positions the isotropic *hfi* constant a_{iso}.

Of course, in practice the weak *hfi* condition $v_I \gg |a_{iso} + T_{ZZ}|/2$ may not be rigorously satisfied, the anisotropic *hfi* tensor may be (and often is) rhombic rather than axial, and, in addition, in orientation-selective experiments the set of orientations contributing to the ESEEM spectrum may be restricted. Still, Eq. (4) is used even in these situations to obtain an estimate of the anisotropic *hfi* that can be then used as a starting approximation in rigorous numerical simulations of the ESEEM spectra. All in all, using the sum-combination line shift to separately estimate the anisotropic *hfi* represents an extremely powerful approach that has been successfully used in numerous ESEEM studies of SO and other systems described below.

Let us now consider nuclei with $I > 1/2$. The examples of such nuclei that we were dealing with in our investigations of SO are ^{2}H (deuteron, $I = 1$) and ^{17}O ($I = 5/2$). For both of these nuclei an ESEEM or ENDOR experiment can be set up (by choosing the appropriate B_0 and v_{mw}) to provide the situation of weak *nqi*, $v_I \pm (a_{iso} + T_{ZZ})/2 \gg k$, which permits the most easy observation and interpretation of the *nqi* effects in the ESEEM and ENDOR spectra. When this condition of weak *nqi* is satisfied, the condition of weak *hfi*, $v_I > |a_{iso} + T_{ZZ}|/2$, is obviously also fulfilled. Under these weak interaction conditions the approximate expressions for the nuclear transition frequencies can be obtained from the simplified spin-Hamiltonian

$$H = -v_I I_z + m_s (a_{iso} + T_{zz}) I_z + \tilde{Q} I_z^2 ,\tag{5}$$

where $\tilde{Q} = \dfrac{3}{2} k[3b_{Z'Z}^2 - 1 + \eta(b_{X'Z}^2 - b_{Y'Z}^2)]$, and $b_{X'Z}$, $b_{Y'Z}$, and $b_{Z'Z}$ are the direction cosines of the Z axis in the XYZ' frame.

For $I = 1/2$ there is only one nuclear transition within each electron spin manifold. For $I > 1/2$, however, we have to consider the total of $I(2I + 1)$ transitions within each of the electron spin manifolds. We will denote the transition frequencies between the nuclear spin projections m_I and $m_I + \Delta m_I$ ($m_I \equiv \langle I_Z \rangle$) within the α and β electron spin manifolds as $v_\alpha^{\Delta m_I}(m_I)$ and $v_\beta^{\Delta m_I}(m_I)$. It is easy to see from Eq. (5) that these frequencies are given by [23]

$$v_{\alpha,\beta}^{\Delta m_I}(m_I) = \left| [-v_I \mp (a_{iso} + T_{ZZ})/2 + \tilde{Q}(2m_I + \Delta m_I)] \cdot \Delta m_I \right| .\tag{6}$$

In particular, for the $\Delta m_I = 1$ transition one obtains:

$$v_{\alpha,\beta}^1(m_I) = \left| -v_I \mp (a_{iso} + T_{ZZ})/2 + \tilde{Q}(2m_I + 1) \right| .\tag{7}$$

In the case of weak *nqi*, obviously, $v_{\alpha,\beta}^{\Delta m_I}(m_I) \approx |\Delta m_I| \cdot v_{\alpha,\beta}^1(m_I)$.

From Eq. (6) one can see that each of the fundamental frequencies $v_\alpha^{\Delta m_I}$ and $v_\beta^{\Delta m_I}$ splits into $2I + 1 - \Delta m_I$ different frequencies that depend on the specific m_I values involved in the nuclear transition. The splitting between the spectral lines $v_{\alpha,\beta}^{\Delta m_I}(m_I)$ corresponding to the nuclear transitions $m_I \leftrightarrow m_I + \Delta m_I$ and the lines $v_{\alpha,\beta}^{\Delta m_I}(m_I + 1)$ corresponding to $m_I + 1 \leftrightarrow m_I + 1 + \Delta m_I$, as obtained from Eq. (7), is equal to

$$\Delta v_{\alpha,\beta}^{\Delta m_I} = \left| v_{\alpha,\beta}^{\Delta m_I}(m_I + 1) - v_{\alpha,\beta}^{\Delta m_I}(m_I) \right| = 2 \left| \tilde{Q} \Delta m_I \right| .\tag{8}$$
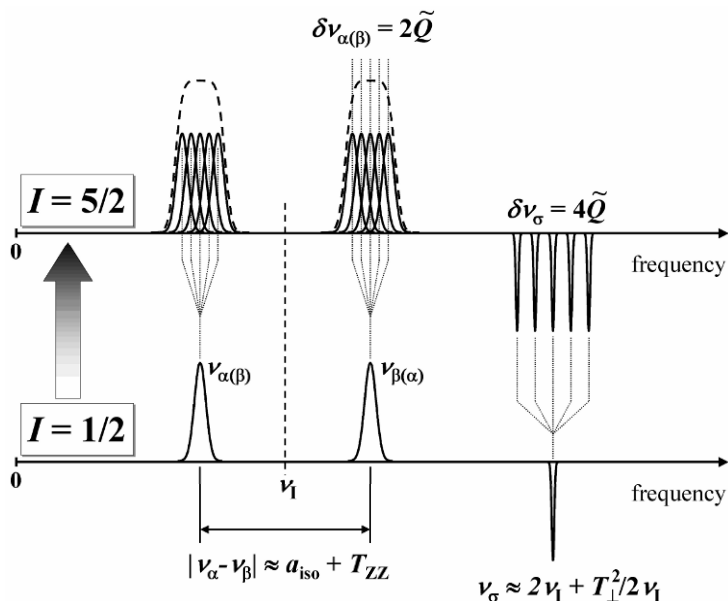
Figure 6. Schematic representation of the ESEEM spectra for a system with $S = 1/2$ and $I = 5/2$ in a disordered situation having weak *hfi* and *nqi*. The quadrupole-related splittings are not resolved in fundamental lines (ν_α and ν_β) but are resolved in the sum-combination line, ν_σ. The figure shows only the "generic" sum-combination line for $I = 5/2$ (see text).

One can see that under the weak interaction conditions the splitting is purely due to the *nqi*. In most cases, however, Eq. (8) cannot be used to determine the *nqi* parameters from the one-dimensional (1D) experimental ENDOR or ESEEM spectra because the *hfi* distribution, whether purely statistical or because of the *hfi* anisotropy, will broaden the individual $\nu_{\alpha,\beta}^{\Delta m_I}(m_I)$ lines to the extent that small quadrupolar splittings cannot be resolved. This situation is schematically shown in Figure 6. The two-dimensional (2D) spectra (e.g., 2D Mims ENDOR [24], hyperfine-correlated ENDOR (HYEND) [25] or hyperfine sublevel correlation spectroscopy (HYSCORE) [26]) can resolve the quadrupole splitting, but often only at the expense of unacceptably long data acquisition times needed to achieve sufficient spectral resolution.

We have seen that for $I = 1/2$ the sum-combination line is not affected by the *hfi* to first order (see Eq. (3)). For $I > 1/2$ the situation is similar if one considers the sum of ν_α and ν_β that correspond to the same Δm_I. Such sum-combination frequency $\nu_\sigma^{\Delta m_I}$ does not contain contributions linear in *hfi* but retains the contributions linear in *nqi*. This provides for a possibility to determine the *nqi* parameters from 1D ESEEM spectra. In the following we will be mostly interested in the sum-combination line ν_σ^1 that corresponds to $\Delta m_I = 1$ because this line is broadened by the *nqi* (and the second-order *hfi* effects) to the least extent, has the largest ampli-

tude of all of the sum-combination lines, and is therefore most easily detectable in the experimental spectra. The explicit expression for ν_σ^1 is

$$\nu_\sigma^1(m_I) = \nu_\alpha^1(m_I) + \nu_\beta^1(m_I) = -2\nu_I + 2\tilde{Q}(2m_I + 1). \tag{9}$$

As follows from Eq. (9), the generic sum-combination harmonic ν_σ^1 splits into $2I$ subharmonics corresponding to different transitions $m_I \leftrightarrow m_I + 1$. The splitting between the frequencies of these subharmonics,

$$\Delta\nu_\sigma^1 = \left|\nu_\sigma^1(m_I + 1) - \nu_\sigma^1(m_I)\right| = 4\left|\tilde{Q}\right|, \tag{10}$$

is twice as large as that between the fundamental subharmonics (see Eq. (8)). Taken together with the lack of the first order of *hfi* broadening, this substantially increases chances for observation of the quadrupole splittings in a 1D ESEEM experiment, and indeed this technique was successfully used to determine the ^{2}H and ^{17}O *nqi* of SO, as described in section 7.

The key phrase of the above theoretical discussion was "weak interaction," meaning the *hfi* and *nqi* being weak compared to the nuclear Zeeman interaction. While the former two interactions represent a function of the composition and structure of the paramagnetic center, the Zeeman interaction is proportional to the magnetic field, B_0, and is completely under the control of the experimentalist. Thus, in order to organize the weak interaction conditions, one simply has to select B_0 that would provide $\nu_I > |a_{iso} + T_{ZZ}|/2$ and $\nu_I \pm (a_{iso} + T_{ZZ})/2 >> k$. This selection of B_0 has to be accompanied by the corresponding selection of the mw frequency that would satisfy the resonance conditions for the electron spin (e.g., $\nu_{mw} = g\beta B_0/h$). Since at present pulsed EPR spectrometers are available that operate at ν_{mw} from ~2 GHz (S-band) to 130 GHz (D-band), the weak interaction conditions can be achieved for an extremely broad range of *hfi* and *nqi* parameters.

It might seem that the higher the B_0 used in an experiment, the better. While this is certainly true from the point of view of the ease of interpretation of the spectra, some words have to be said about their detection. It is commonly recognized that (pulsed) ENDOR usually gains in sensitivity with increasing B_0 and ν_{mw} (at least, for paramagnetic centers with $S = 1/2$). In ESEEM, however, the situation is different. As we will see in the next section, the ESEEM amplitude in the weak interaction case decreases as ν_I increases, and if the observed B_0 is too high, the ESEEM may simply become unobservable. In addition, the shift of the sum-combination line is inversely proportional to ν_I (see Eqs. (3) and (4)), and at very strong B_0 the ν_σ line becomes useless as far as the anisotropic *hfi* measurements are concerned. Therefore, in ESEEM experiments there always exists a range of B_0 (and ν_{mw}) values that provide a compromise between the best conditions for the observation of the ESEEM spectra and the best conditions for their interpretation. The optimal B_0 and ν_{mw} values depend on the *hfi* and *nqi* parameters of the studied nuclei and, to some extent, on the specific pulsed sequence used in experiment. In the following sections we will demonstrate the application of the theoretical results and considerations presented here to obtain the *hfi* and *nqi* parameters of different nuclei that belong to the ligands of the Mo(V) center of SO.

4. PULSED EPR TECHNIQUES USED IN THIS WORK

4.1. ENDOR

The ENDOR spectra contain only fundamental lines. As we mentioned before, for a nucleus with $I > 1/2$ the fundamental lines may overlap to a considerable degree, which makes ENDOR difficult to use for measurement of weak *nqi*, unless a good orientational selectivity is available or the characteristic width of the statistical distribution of *hfi* parameters is much smaller than the *nqi* splittings. However, as a frequency domain technique, ENDOR is suitable for detection of broad fundamental lines that are hard to detect by ESEEM due to fast damping of the modulation (see below). Of course, in order to detect very broad lines, the baseline distortions in the ENDOR spectra usually should be suppressed by randomizing the radiofrequency (RF) sweeps [27].

In this work we mainly used 1D pulsed ENDOR techniques such as Mims ENDOR [26], Davies ENDOR [29], and refocused Mims ENDOR [30]. The reasons for using this or that technique in each particular spectroscopic situation are well known [25], and we will not reiterate them here. Instead, we provide some details on a more exotic 2D Mims ENDOR technique [24] that we used to assess the full range of the ^{1}H fundamental lines in complex and overlapping ENDOR spectra.

2D Mims ENDOR is a combination of time domain and frequency domain techniques. It consists in measuring the Mims ENDOR spectrum as a function of the time interval τ between the first two mw pulses of the three-pulse (stimulated) ESE pulse sequence used in this technique. The refocused Mims ENDOR pulse sequence (consisting of four mw pulses) can be used with equal success in such measurements. The RF pulse in both techniques is applied during the time interval T between the second and third mw pulses. The Mims ENDOR response (which is the difference between the stimulated ESE amplitudes with and without the RF pulse) is an oscillating function of τ:

$$\Delta V(\nu_{RF}, \tau) \propto [1 - \cos(2\pi\nu_\delta\tau)] \cdot [\delta(\nu_{RF} - \nu_\alpha) + \delta(\nu_{RF} - \nu_\beta)], \qquad (11)$$

where ν_{RF} is the radiofrequency, ν_α and ν_β are the fundamental frequencies, and $\nu_\delta = |\nu_\alpha - \nu_\beta|$. The Fourier transformation (FT) of the τ-dependence results in a 2D Mims ENDOR spectrum:

$$\Delta V(\nu_{RF}, \tau) \propto \delta(\nu_\tau - \nu_\delta)] \cdot [\delta(\nu_{RF} - \nu_\alpha) + \delta(\nu_{RF} - \nu_\beta)], \qquad (12)$$

where ν_τ is the frequency corresponding to time interval τ. Thus, in a 2D spectrum of an oriented system the nuclear transitions will appear as peaks located at (ν_α, ν_δ) and (ν_β, ν_δ). In a disordered situation, the spectrum of a nucleus with $I = 1/2$ consists of ridges that are spread as far as $\max(a_{iso} + T_{ZZ})$ in the ν_τ direction and $\nu_I \pm \max(a_{iso} + T_{ZZ})/2$ in the ν_{RF} direction (see Fig. 7). An example of the application of this technique will be shown in section 7.1.1.
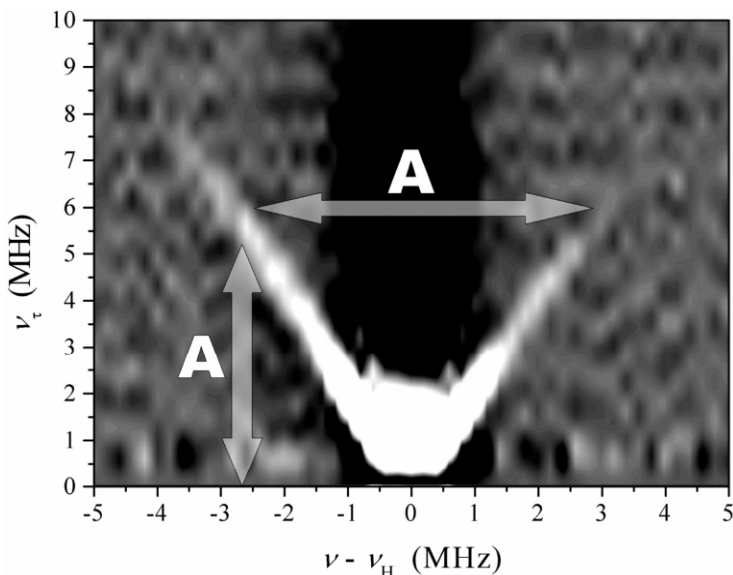
Figure 7. Example of ^{1}H 2D Mims ENDOR spectrum of b-SO in H_2O. Spectrum collected at v_{mw} = 9.4196 GHz and B_0 = 3423 G (at g_Y), which corresponds to the most nonselective field position. The vertical arrow shows that the spread of ridges in the v_τ direction is $\mathbf{A} \approx \max(a_{iso} + T_{ZZ})$. In the v_{RF} (horizontal) direction this spread is $v_I \pm \mathbf{A}/2$. Therefore, the maximum hfi constant, $\mathbf{A}$, evaluated from the spread is 7.5–8 MHz.

4.2. ESEEM Techniques

As we already mentioned, the sum-combination lines in the ESEEM spectra can provide useful information about the anisotropic hfi and nqi tensors. In order to observe these lines one usually employs two-pulse or four-pulse techniques. For example, the two-pulse ESEEM for a system with S = 1/2 and I = 1/2 is described by

$$V_{1/2}(\tau) = 1 - \frac{k_m}{2}(1 - \cos 2\pi v_a \tau - \cos 2\pi v_\beta \tau + \frac{1}{2}\cos 2\pi v_\delta \tau + \frac{1}{2}\cos 2\pi v_\sigma \tau), \qquad (13)$$

where the modulation amplitude factor k_m is

$$k_m = \frac{v_I^2(T_{ZX}^2 + T_{ZY}^2)}{v_a^2 v_\beta^2}. \qquad (14)$$

The fundamental and combination lines are readily recognizable in the cosine FT spectrum of this ESEEM by the sign of their amplitude: positive for the former and negative for the latter.

For a higher nuclear spin the expressions describing the ESEEM become more complicated. For example, the two-pulse ESEEM for I = 5/2, assuming zero nqi, is [22]

$$V_{5/2}(\tau) = \frac{1}{3}\left[16V_{1/2}^{5}(\tau) - 16V_{1/2}^{3}(\tau) + 3V_{1/2}(\tau)\right], \tag{15}$$

and its spectrum contains a total of $2I(2I + 1) = 30$ fundamental lines, as well as numerous combination lines. From Eq. (15) it follows that the fundamental harmonics $\nu_{\alpha,\beta}^{\Delta m_I}$ (in the case of zero nqi $\nu_{\alpha,\beta}^{\Delta m_I} = \Delta m_I \cdot \nu_{\alpha,\beta}^{1}$; see above) will have relative amplitudes $\propto (k_m)^{\Delta m_I}$. In the weak hfi limit ($\nu_I \gg |a_{iso}+T_{ZZ}|/2$) k_m is approximately

$$k_m = \frac{(T_{ZX}^2 + T_{ZY}^2)}{\nu_I^2}, \tag{16}$$

and the amplitude of the ESEEM harmonics rapidly decreases with increasing Δm_I. The fundamental and combination lines of $\Delta m_I = 1$ transitions in such ESEEM spectra will have the largest amplitude compared to all other lines. It is also seen from Eq. (16) that the ESEEM amplitude decreases in proportion with B_0^2 and becomes unobservable if the magnetic field is sufficiently strong.

Since the ESEEM techniques work in the time domain, they have two intrinsic problems that result in distortion of the observed spectra. One such problem is mostly related to the fact that the mw pulses used in ESEEM experiments are usually very powerful, and the power dissipation in the mw resonator down to the levels safe for the receiver typically takes from several tens up to ~200 nanoseconds. Therefore, one cannot detect the ESEEM at time intervals between the mw pulses shorter than a certain minimal interval t_d called the dead time. This may cause difficulties in detecting broad (usually fundamental) lines for which the modulation decays within the dead time. To deal with this problem, one can use an approach where the ESE signal generated within the dead time and unobservable directly is refocused by an additional 180° mw pulse that is positioned in such a way as to make the refocused signal observable. One such technique, refocused primary (RP) ESEEM [31], was used by us to detect a broad and featureless sum-combination line from an OH$_{(2)}$ ligand proton in hpH SO (see §7.1.1).

The second problem is related to the finite time duration, Δt, of the recorded ESEEM that results in line broadening (~$1/\Delta t$) and loss of resolution in FT spectra. The time interval Δt is usually limited either by the electron spin relaxation time, or by the total time one wants to spend on data acquisition. The first situation is rather typical for the two-pulse (primary) and RP ESEEM techniques, where ESE signal decay is governed by phase relaxation with a characteristic time T_2 (typically, <2–4 μs in frozen solutions). The second situation typically arises in HYSCORE. Here the ESE signal decay is governed by the longitudinal relaxation that has a characteristic time $T_1 \gg T_2$, which creates a potential for achieving the spectral resolution on the order of $1/T_1$. However, since HYSCORE is a 2D technique, it is rather time consuming, and therefore one usually deliberately limits the detection intervals in both time dimensions so as to provide an acceptable overall data acquisition time.

In section 3 we discussed the use of sum-combination lines to determine the anisotropic hfi and nqi parameters. The simplest technique where the sum-

combination line is observed is two-pulse (primary) ESEEM. As we just mentioned, this technique suffers from both a relatively long dead time ($t_d \sim 100$ ns) and a short detection interval ($\Delta t \sim T_2$). In order to increase Δt while still being able to generate the ν_σ line, one can employ the four-pulse ESEEM sequence [32]. The ESE signal in this technique decays with a characteristic time T_1 (usually $>>T_2$) as a function of the time interval between the second and third mw pulses, T. This allows one to increase Δt to tens of microseconds and obtain a frequency resolution better than 0.1 MHz. However, because the ESEEM amplitudes and phases in the four-pulse sequence depend on the time interval τ between the first and second pulses, it is advantageous to perform the four-pulse measurements in a 2D format, T vs. τ. The 1D FTs along the high-resolution T coordinate spectrum, correspond-ing to different τ values, are then simply added together. As a result, one obtains a high-resolution 1D spectrum of what is called integrated (over τ) four-pulse ESEEM that has a virtually zero dead time (because the minimal time interval T in this technique is only determined by the finite duration of the mw pulses) and can therefore be easily phased to provide the fundamental lines of positive amplitude and combination lines of negative amplitude.

The 2D spectra of fundamental lines obtained by HYSCORE can also provide the spectral resolution necessary for detecting quadrupole interactions, although, as we mentioned, at the expense of a relatively long data acquisition time. In HYSCORE spectra the line splittings and shifts caused by *hfi* and *nqi* occur in mu-tually perpendicular directions (see Fig. 8), which makes the observation of *nqi* splittings possible even if the fundamental lines are broadened by the anisotropy and statistical distribution of the *hfi*. Employing HYSCORE one can also disentan-gle the *nqi* splittings due to distant matrix nuclei from those related to ligand nuclei that have an appreciable *hfi*, as is shown in Figure 8.

In the simplest cases of two- or three-pulse ESEEM and $I = 1/2$ the ampli-tudes of fundamental and combination lines are simply proportional to k_m (see, e.g., Eq. (13)). In more complex techniques the amplitudes of some or all of the ESEEM harmonics may depend on k_m in nonlinear fashion. For example, in integrated (over the time interval T between the primary ESE signal and the refocusing (third) pulse) RP ESEEM spectra of a system with $I = 1/2$ and weak *hfi*, the amplitude of the sum combination line ν_σ is proportional to [31]

$$A(\nu_\sigma) \propto k_m (1 - \sqrt{1 - k_m}) . \tag{17}$$

From Eqs. (14) and (17) one can see that if $k_m << 1$, which corresponds to very weak anisotropic *hfi* (e.g., for matrix nuclei), then $A(\nu_\sigma) \propto (k_m)^2$. On the other hand, if the Zeeman and anisotropic *hfi* become comparable, and especially if $|a_{iso} + T_{ZZ}|$ approaches $2\nu_I$ at least for some of the orientations, then $k_m \sim 1$ and $A(\nu_\sigma) \propto k_m$. These properties allow the integrated RP ESEEM to be used for suppressing the sum-combination line from distant matrix nuclei in order to facilitate the detection
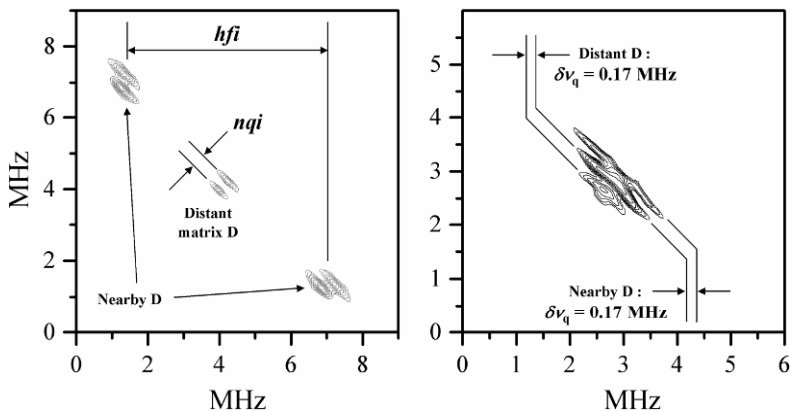
Figure 8. Examples of *hfi/nqi* resolution by HYSCORE spectroscopy. Left panel: spectrum of *pl*-SO, *lpH* form reduced by Ti citrate in D_2O buffer, collected at ν_{mw} = 17.283 GHz and B_0 = 6252 G, which corresponds to the most nonselective field position near g_Y. In this particular case the isotropic *hfi* for the deuteron of the directly ligated (–OD) group is rather large and the fundamental lines in the spectrum are well separated from each other as well as from the distant "matrix" deuterons. The fundamental lines also show well-resolved quadrupole splittings. Right panel: spectrum of *b*-SO in D_2O buffer, collected at ν_{mw} = 11.320 GHz and B_0 = 4120 G, which corresponds to the most nonselective field position near g_Y. In this particular case the isotropic *hfi* for the deuteron of the directly ligated (–OD) group is close to zero, but due to rather large anisotropic *hfi*, the lines of the latter and lines of matrix deuterons are still well disentangled. In both situations the observed quadrupole splittings are typical for a hydroxyl deuteron. Reprinted from [43].

of the sum-combination lines from more strongly magnetically coupled nuclei. In contrast, in the spectrum of integrated four-pulse ESEEM of I = 1/2 under the weak *hfi* conditions [32]:

$$A(\nu_\sigma) \propto k_m(1+\sqrt{1-k_m}), \tag{18}$$

which, being expanded into a power series, always contains the term linear in k_m, irrespective of the strength of the anisotropic *hfi*.

The above review of various pulsed EPR techniques suggests a suitable strategy for determining the *hfi* and *nqi* parameters under weak interaction conditions. Since the measurements have to be performed at several B_0 values corresponding to different positions in the *g*-anisotropic EPR spectrum of Mo(V), the entire experiment becomes quite time consuming, even if only 1D techniques are employed. Using 2D techniques increases the necessary experimental time dramatically. Therefore, our usual approach in such investigations is to start with 1D techniques (two-pulse ESEEM, Mims or Davies ENDOR), and utilize 2D methods (HYSCORE, RP ESEEM, 2D Mims ENDOR) mainly to resolve ambiguous situations.

5. GENERAL PROBLEMS IN EXTRACTION OF STRUCTURAL
PARAMETERS FROM MAGNETIC RESONANCE PARAMETERS

As mentioned, the orientation-selective pulsed EPR measurements allow one to determine the orientation of the *hfi* and *nqi* tensors of the studied magnetic nuclei with respect to the *g*-tensor coordinate frame (*g*-frame). However, these parameters almost never represent a final product of the investigation, and one is usually interested in extracting from them some information about the geometrical structure, i.e., distances and directions to nearby nuclei from Mo(V). Solving this problem may encounter two difficulties.

The first difficulty is related to the fact that, while the electron spin is mainly situated on the Mo(V) ion, it is also distributed to some degree (~20%) over the ligand atoms. Whether this distribution is to be taken into account when interpreting the anisotropic tensor *hfi* of a given nucleus depends on how far this nucleus is located from the Mo ion. The contribution of the Mo(V) electron spin population, ρ_{Mo}, to the anisotropic *hfi* is with good accuracy axial, with the principal components ($T_\perp$, $T_\perp$, $-2T_\perp$), and the anisotropic *hfi* constant $T_\perp$ is given by

$$T_\perp = -\frac{g\beta g_n \beta_n}{hR^3} \cdot \rho_{Mo}, \qquad (19)$$

where R is the distance between the Mo and the nucleus. While the spin population ρ_{Mo} in SOs is actually about 0.8, for very distant nuclei ($R \gg 2$ Å) one can formally take $\rho_{Mo} = 1$ to calculate the total anisotropic *hfi* constant, which will include the spin population transferred to the ligands.

For nearby nuclei the anisotropic *hfi* tensor also includes intrinsic contributions from the spin population transferred to the ligand orbitals that are comparable with the "through-space" interaction with ρ_{Mo}. For example, for an Mo–OH moiety, the oxygen spin population of ~5% will result in comparable characteristic values of the proton anisotropic *hfi* tensor components for Mo···H and O···H dipolar interactions [33]. Deconvolution of the experimental *hfi* tensor into the various contributions is complicated and, at present, often ambiguous. Therefore, accurate geometrical predictions based on the *hfi* data for nearby nuclei will generally require an extensive use of quantum chemical calculations. As we will show below, however, for some important qualitative comparative conclusions on the enzyme structures such a deconvolution may not be required.

The structural interpretation of the *nqi* may sometimes be more straightforward than that of the *hfi*. For example, the *nqi* tensor of the deuteron of a hydroxyl ligand is practically axial, with the main axis coinciding with the direction of the OD bond. Therefore, the direction of the main *nqi* axis of the deuteron established in an ESEEM or ENDOR experiment immediately gives one the direction of the OD bond with respect to the *g*-frame. Similarly, the main axis of the [17]O *nqi* tensor of a terminal [17]O oxo group is usually directed along the Mo-[17]O bond.

The second difficulty in structural interpretation of the *hfi* and *nqi* parameters is created by rather limited knowledge about the relationship between the *g*- and

molecular coordinate frames. Of course, we have a qualitative idea about the directions of the *g*-tensor axes, but the departures of the complex structure from the ideal square pyramid result in uncertainties in the direction of *g*-axes on the order of tens of degrees [34]. Therefore, establishing the direction of an Mo-nucleus radius vector with respect to the *g*-frame does not automatically establish its direction with respect to the molecular frame.

Experimentally, this problem can be solved if the system has some nucleus whose position within the molecular frame is known with good accuracy and whose *hfi* and/or *nqi* tensor axes have a well-established direction with respect to the local structural elements. Studying such a marker nucleus by pulsed EPR, one can determine the orientation of the *g*-frame relative to the molecular frame. This orientation can then be used to transform the *g*-frame coordinates of all other nuclei back into the molecular frame.

Using a single marker nucleus may not result in complete and sufficiently accurate knowledge of the relative orientations of the *g*- and molecular coordinate systems, and therefore increasing the number of studied markers improves the accuracy of structural predictions. Two of the markers used in our investigations were the deuteron of the equatorial OD ligand and the ^{17}O oxo group mentioned above. To some degree, the proton of the equatorial OH ligand whose isotropic *hfi* constant is sensitive to the dihedral angle between the MoOH plane and the plane of the d_{xy} orbital, and the C_α proton of the cysteine ligand that we identified in the ENDOR spectra and which has the largest possible anisotropic *hfi* among the non-exchangeable protons, could also serve as a markers.

6. SAMPLE PREPARATION AND INSTRUMENTATION

The results presented below were obtained for a variety of SOs. The *pl*-SO was recombinant wild-type *Arabidopsis thaliana* sulfite oxidase that was expressed and purified as described [35]. For sulfite-reduced *pl*-SO, the protein was reduced with a 30-fold excess of sodium sulfite and then reoxidized by about 1/2 equivalent of ferricyanide (per enzyme) to maximize the Mo(V) signal. Reduction of *pl*-SO by a stoichiometric amount of Ti(III) citrate [36] produced the Mo(V) form of *pl*-SO directly. The *b*-SO, which is sulfite dehydrogenase from *Starkeya novella*, was expressed and purified as described [37]. The protein was reduced with a 20-fold excess of sodium sulfite. His-tagged recombinant human SO was purified from TP1000 cells containing pTG718 [38]. The protein was reduced with a 20-fold excess of sodium sulfite. Highly purified CSO was prepared as described [39]. As we discussed in the theoretical sections, different types of pulsed EPR experiments and different *hfi/nqi* parameters of the studied nuclei require different optimal magnetic fields and mw frequencies. This consideration does not only refer to the Mo enzymes, but to any paramagnetic centers. Therefore, we took effort to construct over the years a series of broadband pulsed EPR spectrometers continuously covering the range of mw frequencies from 2 to 18 GHz (corresponding to S, C, X and K_u bands) and from 26.5 to 42 GHz (K_a band) [40–42]. The flexible hard- and soft-

ware design of these spectrometers allows one to run virtually any kind of ESEEM or pulsed ENDOR experiment. The success of many of our investigations of SOs can be attributed to the possibility of mw frequency optimization provided by this equipment. The typical measurement temperature was 20 K.

7. HIGH-RESOLUTION PULSED EPR SPECTRA, MAGNETIC RESONANCE PARAMETERS, AND STRUCTURAL IMPLICATIONS FOR VARIOUS FORMS OF SO

7.1. Exchangeable Protons: Similarities and Differences in SOs from Different Organisms

7.1.1. High-pH Forms

The x-ray structures of the various forms of SO show that the equatorial oxygen ligand in all forms has access to water (see Fig. 4). Therefore, it was expected that they would have exchangeable water or –OH ligands. For the *lpH* form of CSO, human SO and *pl*-SO (Ti(III) reduction), the presence of such a group was confirmed in cw-EPR investigations where *hfi* for an exchangeable proton coupled to Mo(V) was directly observed. (The cw-EPR spectrum of *b*-SO, as already mentioned in §2, does not depend on pH and resembles the *hpH* form of vertebrates.) The situation was more complicated for *hpH* forms (pH ~ 9). The cw-EPR spectra of wild-type SO**s** from all organisms are similar in H_2O buffer and do not show any features that can be attributed to nearby exchangeable protons. Furthermore, changing the buffer from H_2O to D_2O does not alter the cw-EPR spectrum. The only indication of the possible presence of an exchangeable H_2O related group was the observation of an Mo–^{17}O *hfi* in $H_2^{17}O$-enriched solution [20]. These earlier cw-EPR findings resulted in a number of tentative proposals about the nature of the exchangeable ligand(s) in the *hpH* form [21]. To finally prove the presence of OH or H_2O ligand, a direct observation of the ligand proton was still necessary, and we therefore undertook ESEEM investigations of *hpH* SO from various organisms.

Our reasoning, which defined the strategy for the ESEEM experiments, was as follows. With an Mo–O distance of about 2.25 Å [4], the distance to the OH proton should be about 2.7 Å (if an sp^3 hybridization of oxygen orbitals is assumed). The contribution of $\rho_{Mo} \sim 0.8$ to the proton anisotropic *hfi* (Eq. (19)) can be estimated as $|T_\perp| \sim 3.2$ MHz. In addition to this, however, a significant contribution is also to be expected from the spin population transferred to the hydroxyl oxygen. However, taking 3.2 MHz as a minimum possible characteristic anisotropic *hfi* constant, we can estimate, using Eq. (4), the minimal expected shift of the ^1H sum-combination line from the $2\nu_I$ position. For an X-band experiment this shift amounts to $\Delta\nu_\sigma \sim$ 0.4 MHz and should be easily resolvable, at least in a four-pulse ESEEM experiment.

The primary ESEEM spectra of *b*-SO in the H_2O buffer [43] immediately revealed the shifted sum-combination feature (see Fig. 9). To additionally confirm
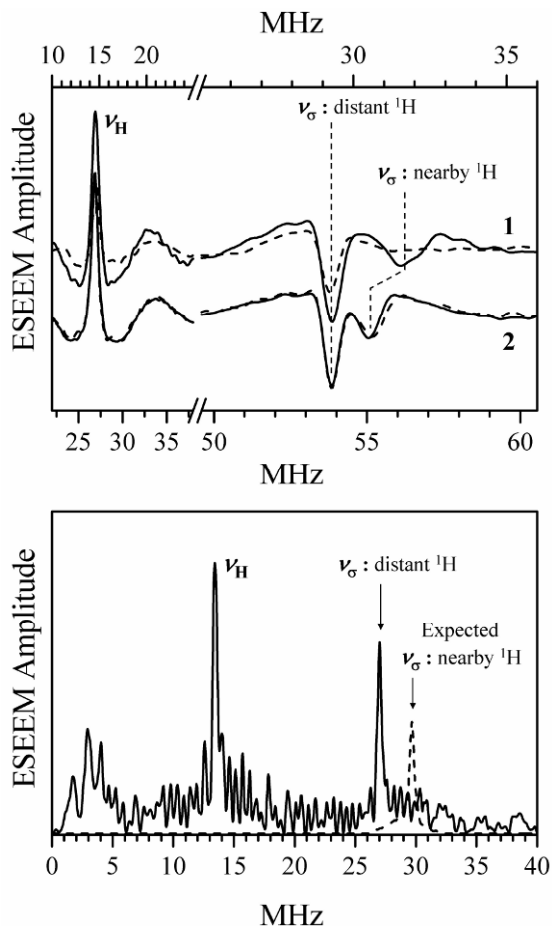
Figure 9. Top panel: Primary ESEEM spectra forms of *b*-SO. Solid and dashed traces 1, in H_2O and D_2O buffers, respectively, at pH 7; ν_{mw} = 9.4196 GHz; B_0 = 3423 G (at g_Y); T = 20 K. Solid and dashed traces 2: in H_2O buffer at pH 7 and 9.5, respectively; ν_{mw} = 17.334 GHz; B_0 = 6297 G (at g_Y); T = 20 K. Bottom panel: Primary ESEEM spectra of the *hpH* form of CSO in H_2O buffer; ν_{mw} = 8.702 GHz; B_0 = 3170 G (at g_Y). The expected position and amplitude of the sum-combination line (rescaled from top panel) of the nearby proton is shown by a dashed line. Reprinted from [43].

this assignment, experiments were performed in a D_2O solution, where the shifted ν_σ line disappeared (see Fig. 9, top panel). In addition, the measurements at a higher mw frequency resulted in a decrease of the shift, as predicted by Eq. (4). The assignment thus confirmed that one can estimate the anisotropic *hfi* constant as $T_\perp \sim -8$ MHz. This $T_\perp$ is substantially larger than that estimated above for the "through-space" interaction with ρ_{Mo}. This discrepancy, as we mentioned, is caused by the dipole interaction of the hydroxyl proton with the electron spin population,

ρ_O, delocalized to the hydroxyl oxygen atom. The contribution of ρ_O to the proton anisotropic *hfi* depends on the way that ρ_O is distributed over the oxygen orbitals. Therefore, the proton anisotropic *hfi* tensor, even though accurately determined (in the *g*-frame), is essentially useless for quantitative structural predictions until independent investigation of the distribution of ρ_O over the oxygen orbitals is performed and the contribution of ρ_O to the total anisotropic *hfi* tensor can be evaluated. Nonetheless, the studies of *hpH* SO are important because they allow one to directly observe the exchangeable protons of the equatorial ligand that could not be detected by cw EPR. This information is essential for developing reasonable hypotheses for the catalytic cycle of the SO enzymes.
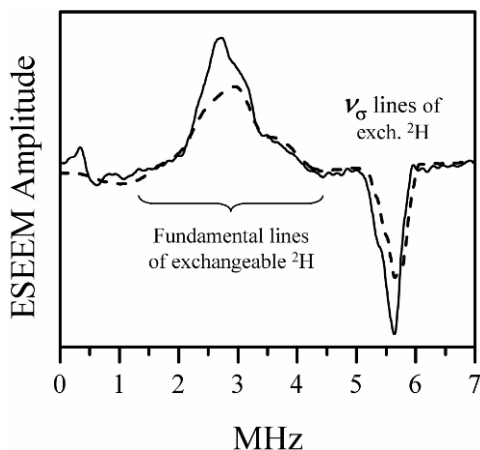
Figure 10. Solid trace: sum of integrated four-pulse ESEEM spectra of *b*-SO in D_2O at pH 7 obtained at $B_0 = 4072$ G (near g_z), 4120 G (near g_y), and 4140 G (near g_x). Experimental conditions: microwave frequency, 11.320 GHz; pulse sequence, 20 ns (90°)–τ–20 ns (90°)–T–15 ns (180°)–T–20 ns (90°)–τ–echo; temperature, 20 K. Dashed trace: a simulation for a nonselective excitation of the entire EPR spectrum. Simulation parameters: nucleus, ^{2}H; $a_{iso} = 0.2$ MHz; $T_\perp$ is uniformly distributed from –1.1 to –1.5 MHz; nuclear quadrupole coupling constant, $e^2Qq/h = 0.23$ MHz. Reprinted from [43].

The large magnitude of the anisotropic *hfi* explains the absence of the fundamental lines in the ESEEM spectra presented in Fig. 9 because the time domain oscillations corresponding to such broad lines decay within the dead time. To recover the fundamental lines and determine the isotropic *hfi* one can use some zero dead time ESEEM techniques (e.g., RP ESEEM) or ENDOR. Another approach is to perform experiments in D_2O solution. Exchange of ^{1}H by ^{2}H decreases the *hfi* by a factor of about 6.51. The anisotropic *hfi* will thus decrease from ~8 to ~1.3 MHz, which is substantially smaller than the inverse dead time. The ESEEM spectrum shown in Fig. 10 immediately revealed the fundamental lines, as well as the sum-combination line. As can be seen from Fig. 10, the fundamental lines arising from

the α and β electron spin manifolds overlap and form a single feature centered at the ^{2}H Zeeman frequency, which indicates that a_{iso} is small and does not exceed $T_\perp$.

Knowing the anisotropic *hfi* it is possible to estimate a_{iso} from numerical simulations of the fundamental lines in the ESEEM spectra. These simulations, however, should also include the ^{2}H *nqi*, which somewhat complicates the problem because the hydroxyl/water ^{2}H quadrupole coupling constant may vary somewhat as a result of hydrogen bonding. In addition, the direction of the *nqi* tensor axis with respect to the *g*-frame is not known in advance.

We discussed above that the information about *nqi* can in principle be obtained from the sum-combination line splittings in the (integrated) four-pulse ESEEM spectra or from the splittings of fundamental lines in 2D HYSCORE spectra. Figure 10 shows that for this particular case in the experimental integrated four-pulse ESEEM spectra the quadrupole splittings are not well resolved because the spectra of the nearby and distant (protein backbone, matrix water) deuterons are overlapping. In HYSCORE spectra, on the other hand, the spectral lines of distant and nearby deuteron(s) were separated (see Fig. 8) and $e^2Qq/h \approx 0.23$ MHz could easily be determined. This quadrupole coupling constant is typical for a ^{2}H that belongs to a hydroxyl or a water molecule.

Using this quadrupole coupling constant we have performed numerical simulations of the integrated four-pulse ESEEM spectra for various trial values of a_{iso} and angles between the main axes of *hfi* and *nqi*. These simulations resulted in $a_{iso} \approx$ 0.2 MHz (~ 1.3 MHz as recalculated for ^{1}H; see the simulated spectrum in Fig. 10). In spite of the concerns stated above, the a_{iso} estimate was not sensitive to the details of *nqi* because a distribution of *hfi* had to be introduced in order to reproduce the smooth experimental lineshapes.

Additional experiments aimed at estimating a_{iso} included pulsed ENDOR performed in protonated and deuterated buffers (see Fig. 11) and 2D Mims ENDOR (see Fig. 7). All the measurements confirmed that a_{iso} for ^{1}H does not exceed 2 MHz. From the literature on the d^1 systems (to which Mo(V) belongs) it is well known that the isotropic *hfi* constant for the equatorial OH ligand proton strongly depends on the dihedral angle between the plane of the SOMO (d_{xy}) and the Mo–OH plane (see [33] and the references therein). The maximal isotropic constant observed in model compounds for a dihedral angle of ~0° is ~45 MHz. Therefore, the experimental $a_{iso} < 2$ MHz serves as a clear indication that the O–H bond is substantially out of the equatorial plane of the complex. The qualitative reconstruction of the Mo–OH$_{(n)}$ coordination geometry in *b*-SO based on the described *hfi* and *nqi* data is shown as Structure 1.

Unlike *b*-SO, the *hpH* form of CSO did not show any clear lines attributable to nearby exchangeable protons (see Fig. 9) in similar primary ESEEM experiments. The reason for this was understood after the RP ESEEM technique [31] was applied at $\nu_{mw} \sim 5.4$ MHz. At this mw frequency the ESEEM amplitude factor $k_m \sim 1$ for the nearby protons was achieved and their observation conditions were thus optimized. The ESEEM amplitude for the distant protons, however, was still reasonably small.
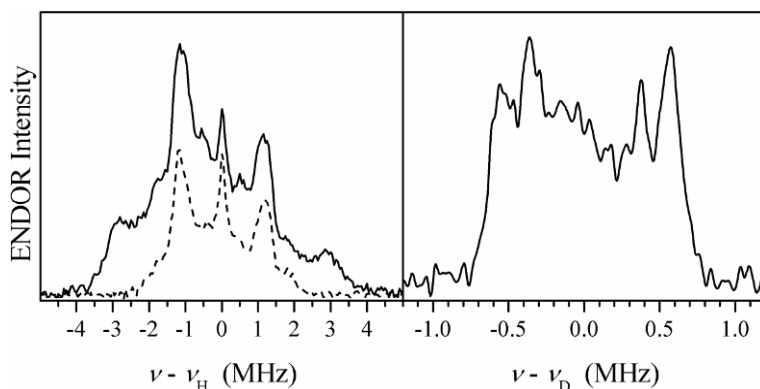
Figure 11. ENDOR spectra of b-SO: $\nu_{mw} = 9.4196$ GHz; $B_0 = 3385$ G (at g_z). Left panel: [1]H Davies ENDOR in H_2O (solid line) and D_2O (dashed line) buffers. Comparison of these two spectra shows that the external shoulders belong to exchangeable protons with *hfi* up to 7 MHz. Right panel: [2]H Mims ENDOR in D_2O buffer. The spectrum presents only exchangeable deuterons. The maximal *hfi* (rescaled to protons) is ~7–7.5 MHz, in agreement with the spectra shown in the left panel.

hpH **form of SO :**
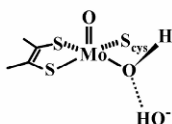
Equatorial OH ligand with the OH bond significantly out of the molybdenum d_{xy} orbital plane. For *wt* bacterial SDH this from is also observed at low pH.

Phosphate-inhibited (Pi) **form of SO :**
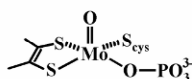
Observed at low pH when phosphate is present in the buffer. Equatorial ligand is a phospate.
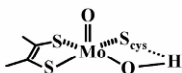
lpH **form of SO :**

Equatorial OH ligand with the OH bond almost parallel to the molybdenum d_{xy} orbital plane.

Atypical low-pH **form of SO :**
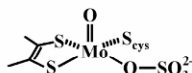
Observed at low pH for sulfite-reduced plant SO. Equatorial ligand is a sulfate.

Structure 1. Qualitative structures for different forms of SOs based on pulsed EPR results.

In the integrated RP ESEEM spectrum (Fig. 12) the ν_σ line of the nearby protons is readily observable. This line is quite broad (~5 MHz), suggesting that the *hfi* parameters are distributed over wide limits, and thus explaining the absence of the clear ν_σ line in the primary ESEEM spectra by the damping of the corresponding oscillations within the dead time. Numerical simulations of the RP ESEEM spectra (Fig. 12) revealed that the anisotropic *hfi* constant was indeed distributed over very

broad limits, from $T_\perp \approx -4.1$ MHz to $T_\perp \approx -7.3$ MHz. Depending on the model of *hfi* distribution, the ligand may contain either one or two protons. Experiments performed in ^{2}H buffer allowed estimation of the isotropic *hfi* (0–2 MHz), which is in the same range as for *b*-SO.
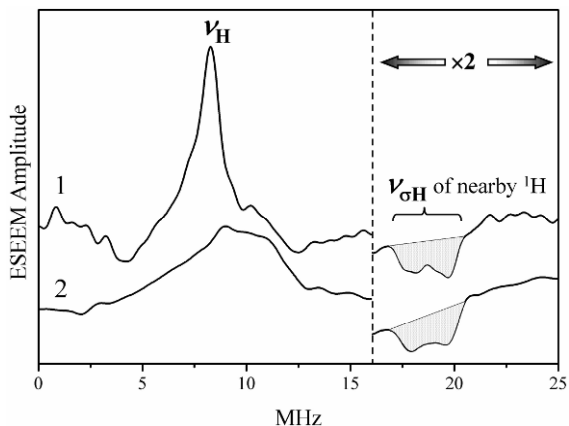
Figure 12. Trace 1, cosine FT of integrated RP ESEEM of *hpH* form of CSO in H_2O detected at $\nu_{mw} = 5.404$ GHz, $B_0 = 1970$ G (near g_y). Trace 2, simulated for two nearby protons with $a_{iso} = 0$ and distributed anisotropic *hfi*: $T_\perp = -4.1 - 3.2 \cos^2 \gamma$, where γ is defined as the angle between the plane of the Mo(V) d_{xy} orbital and the Mo–O–H plane. A planar Mo–OH$_2$ unit was assumed with the second proton being situated at a dihedral angle of $\gamma + 180°$.

Thus, the *hpH* form of CSO is generally similar to *b*-SO. Both forms have a directly coordinated –OH$_{(n)}$ group in the equatorial position, and the proton(s) of this group are substantially out of the d$_{xy}$ plane (based on the small magnitude of the isotropic *hfi*). However, the distribution of anisotropic interactions in CSO is apparently broader than that in *b*-SO (which follows from observation of the ν_σ line in the primary ESEEM spectra of *b*-SO). This anisotropic *hfi* distribution provides a clear indication that the geometry of the Mo–OH$_{(n)}$ in CSO is distributed over more broad limits than in *b*-SO. These structural variations can change the oxygen position relative to the equatorial plane of the complex, which may affect the distribution of ρ_O over the oxygen orbitals and modulate the O–H part of the dipolar interaction. In addition, some variation of Mo–H distances cannot be excluded. Therefore, as in the case of *b*-SO, we cannot quantitatively use the *hfi* to directly predict the structures of the Mo–OH$_{(n)}$ fragment, and such a situation will persist until a complete picture of the spin density transfer to oxygen can be investigated. Nevertheless, the qualitative outcome and implications for the SO active sites are quite clear.

Two more *hpH* forms of SO, human and plant [35,45], were investigated by pulsed EPR. It was found that the Mo(V) centers in these SOs certainly contain an equatorial OH$_{(n)}$ ligand. The spectroscopic, and thus structural, situation for this

ligand was found to be more similar to that of CSO than of *b*-SO in that it shows a pronounced distribution of the anisotropic *hfi* constants. At present the factors that cause the structural differences between *b*-SO and *hpH* SOs from other organisms are not exactly clear, although plausible speculations are presented in section 8.

7.1.2. The lpH forms of CSO, HSO, and Ti(III) Citrate-Reduced pl-SO

The cw-EPR spectra of *lpH* forms of CSO, human SO, and Ti(III) citrate-reduced *pl*-SO show EPR splittings attributable to a neighboring exchangeable proton, and the approximate *hfi* parameters for this proton have been obtained from EPR simulations. More accurate estimates of the *hfi* parameters were later obtained from pulsed EPR experiments that included two- and integrated four-pulse ESEEM for samples in a buffered D_2O solution, and pulsed ENDOR for H_2O and D_2O solutions. Some examples of pulsed EPR spectra are shown in Figures 8 and 13.
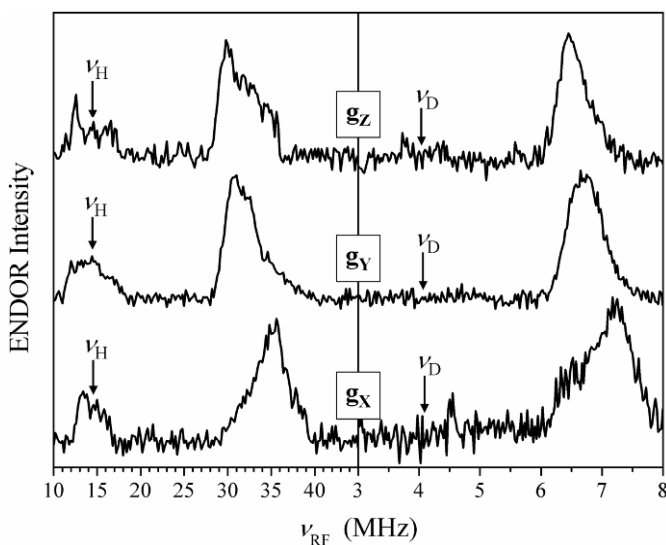
Figure 13. Example of detection of magnetically strongly coupled proton in the *lpH* form of *pl*-SO from titanium(III) citrate reduction. Left panel: Pulsed Davies ENDOR spectra in H_2O buffer; $v_{mw} = 9.4315$ GHz. Right panel: ReMims ENDOR; D_2O buffer; $v_{mw} = 17.283$ GHz. For both panels spectra were collected at three field positions that correspond to g_x, g_y, and g_z. Only one of the two fundamental lines (high-frequency lines) is shown in each spectrum.

The proton a_{iso} in these *lpH* samples was found to be within the range 25–36 MHz (see Table 1), depending on the source organism, which is close to the highest $a_{iso} \sim 45$ MHz ever observed for equatorial OH ligands in Mo complexes [45a]. This provided an indication that the OH ligand in *lpH* SO is oriented in such a way that the Mo–OH plane is close to the plane of the Mo(V) d_{xy} orbital and the equatorial plane of the complex.

Table 1. Parameters of *hfi* and ^{2}H *nqi* Tensors, Found from Pulsed EPR
Experiments for Exchangeable Ligands in *lpH* Forms
(orientations of *hfi* and *nqi* tensors are relative to *g*-frames)

| | ^{1}H | | | ^{2}H | | |
A_{iso} MHz	Anisotropic principal values, MHz	Euler angles $\theta_h \, \varphi_h \, \psi_h$	e^2Qq/h, MHz	Euler angles $\theta_q, \, \phi_q$	Organism	Ref.
26	10.4, –5.2, –5.2	79°, 45°, NA	0.225	90–95°, 24– 26°	CSO	[39]
26.5	16.2, –7, –9.2	80°, 0°, 40–120°			CSO	[44]
26.2	14.6, –6.7, –7.9	80°, 0°, 40–120°			human SO	[45]
35.5 ± 4	10, –5, –5	70°, 20°			*pl*-SO	[35]
	10, –4, –6	70°, 20°, 30°	0.25	85°, 38°		

For instance, according to numerical simulations of the ENDOR spectra of *pl*-SO, the isotropic *hfi* constant is distributed around the central value of 35.5 MHz, with the distribution width between the maximal slope points of $\Delta a_{iso} \sim 4$ MHz. Assuming the dependence of a_{iso} on the dihedral angle θ_{MoOH} between the MoOH plane and the plane of the d_{xy} orbital to be $a_{iso} \sim (45$ MHz$) \times \cos^2 \theta_{MoOH}$ [33], one can estimate a variation of θ_{MoOH} with a width of about 10°, which gives an idea about the structural freedom for the Mo–OH fragment. Similar ranges of dihedral angle variations can be obtained for CSO and human SOs .

The anisotropic *hfi* was described by a rhombic *hfi* tensor (for details see Table 1) whose largest component was in the range 10–15 MHz. As in the case of *hpH* SO, the experimentally found anisotropic *hfi* tensor has contributions from spin populations on molybdenum and oxygen. The latter contribution is clearly evident from the fact that the angle between the main axes of the *nqi* and *hfi* tensors, θ_{hq}, (as estimated from data shown in Table 1) is found to be about 20°, which is significantly smaller than the ~50° expected for the normal geometry of an Mo–O–H fragment.

Semiquantitatively, the experimental θ_{hq} can be reproduced if one assumes the oxygen spin population $\rho_O \sim 0.035$ localized in the center of the oxygen atom. While this picture certainly serves qualitative purposes, it is overly simplistic in that it does not take into account the distribution of ρ_O over the oxygen orbitals. Therefore, it is difficult to use the proton anisotropic *hfi* data for quantitative structural conclusions without performing rigorous quantum chemical calculations.

Investigation of the orientation dependence of the *nqi* of ^{2}H was more promising. Such experiments were performed for CSO and Ti(III) citrate-reduced *pl*-SO, and *nqi* was determined from the splitting of the sum-combination line in four-pulse ESEEM spectra and from the splitting of the fundamental lines in

HYSCORE spectra. The dependence of *nqi*-related splitting on the EPR position for CSO is presented in Figure 14. It is clear from this illustration that the direction of the O–D bond is close to the *X*-axis of the *g*-frame because the quadrupole splitting approximately doubles when the measurement position varies from g_Z to g_X. This conclusion confirms that the OH(D) bond is about parallel to the equatorial plane of the Mo complex [39].
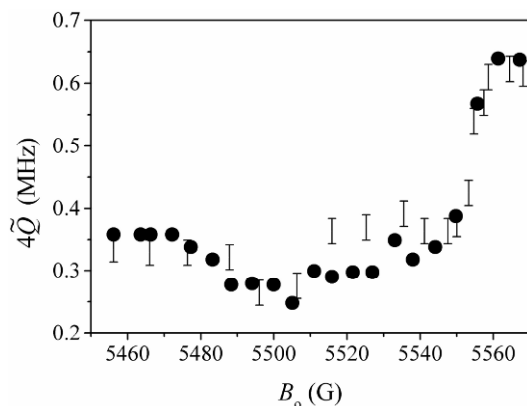
Figure 14. Experimental (bars) and simulated (circles) dependence of the quadrupole splitting of the sum-combination line of *lpH* CSO (in D_2O) on the magnetic field. The simulations lead to a nuclear quadrupole coupling constant of 0.225 MHz and direction of the main axis of quadrupole tensor Z_q in the *g*-frame as {0.903, –0.42, –0.087}, which corresponds to Euler angles $\theta = 95^0$ and $|\varphi| = 25^0$.

Numerical simulations showed that the polar (θ_q) and azimuthal (φ_q) angles of the *nqi* tensor axis relative to the *g*-frame were about 90 and 25°, respectively. Similar angles, about 95 and 38°, were found for *pl*-SO. The absolute value of $e^2Qq/h \approx 0.23$ MHz found from these simulations represents a typical quadrupole coupling constant for a hydroxyl deuteron. Thus, these data unambiguously identify a hydroxyl group as a ligand coordinated to Mo(V) in the *lpH* forms of SO and show that the Mo–OH plane is close to the *XY*-plane of the *g*-frame, as shown in Structure 1.

7.2. Groups Blocking Water Access to Mo(V)

7.2.1. Pi-Form of CSO [46]

The direct ligation of $-PO_4$ to Mo(V) in CSO was inferred from the observation of Mo(V)–^{17}O *hfi* in the cw-EPR spectrum in ^{17}O-enriched phosphate buffer [17]. However, the *hfi* of Mo(V) with ^{31}P itself was never directly detected in the cw-EPR spectra. The absence of an observable Mo···P *hfi* in the cw-EPR spectra was not quite understandable since the isotropic constant for ^{31}P is about an order

of magnitude greater than that of a proton and *hfi* related splittings for the latter (as was discussed above) were readily observable. In pulsed EPR spectra (primary ESEEM) the presence of a P-containing ligand was observed immediately. The spectrum of Figure 15 shows only the ν_σ line related to ^{31}P; no fundamental lines related to a ^{31}P interaction were observed. Such a situation resembled that observed for the proton of an –OH group in *b*-SO at *hpH* (see above). However, the measurements for the *Pi* form of CSO, performed over a wide range of operational frequencies (~9 to ~15.5 GHz) and corresponding magnetic fields, demonstrated that this $\nu_{P\sigma}$ line was always located near $2\nu_I$ of ^{31}P and, depending on operational frequency, was either upshifted or appeared to be downshifted from $2\nu_I$, indicating the presence of "strong" *hfi* at some ν_{mw}'s. In addition, the normalized intensity of the $\nu_{P\sigma}$ line was small (if one assumed that the *hfi* was only due to the Mo···P dipolar interaction) and only slightly varied with ν_{mw}, in disagreement with Eq. (13). All these features indicated that the $\nu_{P\sigma}$ line originates from a ^{31}P nucleus that has an appreciable and predominantly isotropic *hfi* with the Mo(V) center that is distributed over a broad range of magnitudes.
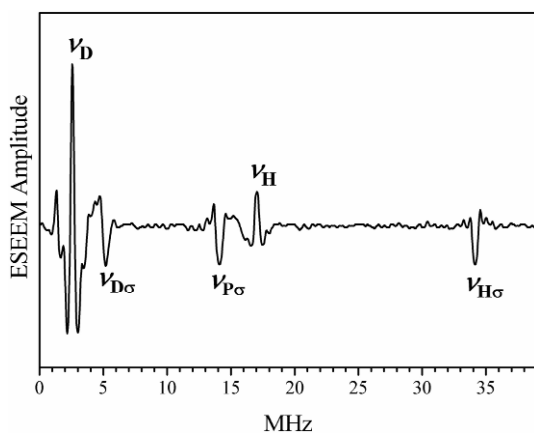
Figure 15. Cosine Fourier transform of the primary ESEEM of *Pi* CSO in phosphate buffer in D$_2$O, recorded at ν_{mw} = 11.001 GHz, B_0 = 4000 G (near g_X = 1.965). The labels near the spectral lines indicate their assignment to fundamental (ν_H, ν_D) or sum-combination ($\nu_{H\sigma}$, $\nu_{D\sigma}$, $\nu_{P\sigma}$) lines of ^{1}H, D, and ^{31}P. Reprinted from [46].

Numerical simulations of the experimental ESEEM spectra confirmed this conclusion and resulted in the estimated range of a_{iso} distribution from ~0 to ~20 MHz. *hfi* constants that large can only be expected for ^{31}P that belongs to the equatorial ligand, and thus this investigation has unequivocally confirmed the PO$_4^{3-}$ coordination to the Mo center in SO. The range of a_{iso} variation estimated for the *Pi* form of CSO is close to that observed in a similar d^1 system having a d$_{xy}$ ground state, a vanadyl complex coordinated by PO$_4^{3-}$ groups [47–49].

The observed distribution of a_{iso} signifies that the orientation of the PO_4^{3-} ligand relative to the plane of the Mo(V) d_{xy} orbital is not well defined but is distributed within certain limits (see Structure 1). This leads to a variation of the π-overlap between the d_{xy} orbital and the orbital of the O–P bond, and to the changes in spin delocalization to the O–P bond orbital, as was discussed for the phosphate ligand in a vanadyl complex (see comment to [47]).
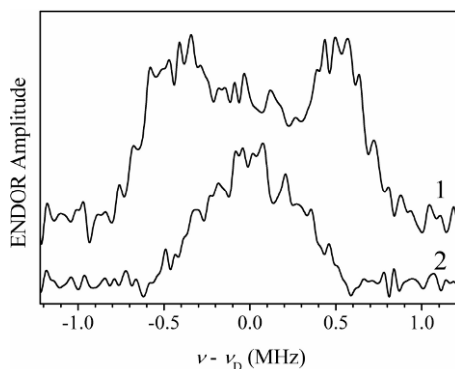
Figure 16. Trace 1, ^{2}H Mims ENDOR spectrum of *pl*-SO (pH 9.5) in D_2O recorded at $B_0 =$ 5320 G (near g_Y). Experimental conditions: $\nu_{mw} = 14.800$ GHz; mw pulses, 3×10 ns; interval τ between the first and second mw pulses, 400 ns; interval between the second and third mw pulses, 100 μs; RF pulse duration, 60 μs; temperature, ~20 K. Trace 2, ^{2}H Mims ENDOR spectrum of *pl*-SO (pH 6) in D_2O recorded at $B_0 = 3410$ G (near g_Y). $\nu_{mw} = 9.410$ GHz. Other experimental conditions are the same as for trace 1. Reprinted from [35].

7.2.2. pl-SO, Tentative Observation of –SO_4^{2-} Ligation to Mo(V) [35]

As mentioned in section 2, the features of the EPR spectra of vertebrate SOs are apparently independent of the method of reduction. For *pl*-SO, unlike SO of vertebrates, however, we found that reduction of the Mo center by sulfite at low pH produces an Mo(V) EPR signal distinctly different from that generated by reduction using titanium(III) citrate at low pH. The cw-EPR spectrum of sulfite-reduced *pl*-SO at low pH does not show any proton splittings and is similar to the atypical low-pH spectrum observed for CSO in Mes buffer [19]. The lack of some features in the cw-EPR spectra does not, however, prove that certain ligands are absent from the Mo(V) coordination, as we already observed in a case of the *hpH* form of SO. Numerous pulsed EPR techniques were applied to this *pl*-SO reduced by sulfite, and none showed any evidence of a proton-containing group directly ligated to Mo(V) [35]. As an example, trace 2 in Figure 16 shows the ^{2}H ENDOR spectrum of *pl*-SO recorded at g_Y. This spectrum is considerably narrower than that of *hpH* *pl*-SO (trace 1 in the same figure), which tells us that in the sulfite-reduced *pl*-SO at low pH the OH ligand is most likely missing from the Mo(V) coordination sphere. This conclusion is supported by a detailed analysis of the ENDOR and

ESEEM data. The minimum Mo···H distance evaluated from these data is about 3.3–3.4 Å, much larger than the 2.8 Å expected for protons of Mo–OH$_2$ or Mo–OH groups (Structure 1). The most reasonable explanation for the absence of a proton-containing ligand is to assume that the equatorial ligand is sulfate that is trapped by the "closed" structure of *pl*-SO at high pH [35]. This explanation is similar to that suggested earlier for the atypical CSO spectrum [19]. We regard this explanation as highly likely, although a final conclusion will only be possible when an experiment with ^{33}S-enriched sulfite is performed. The biological implications of these findings are discussed in section 8.

7.3. Nonexchangeable Protons [50]

The nearby nonexchangeable protons in the Mo site of SO belong to several neighboring amino-acid residues. For example, in CSO the C$_\alpha$ and C$_\beta$ protons of Cys185, C$_\gamma$ proton of Arg138 and C$_\varepsilon$ proton of Tyr322, depending on possible conformations of these residues, could be within 3.5 Å from Mo(V), as follows from the x-ray structure reported in [4]. Most of these protons belong to amino-acid residues other than the cysteine residue coordinated to the Mo ion, and therefore their isotropic *hfi* constants are completely negligible. Also, the C$_\alpha$ and C$_\beta$ protons of the cysteine ligand are far from the sulfur atom that is directly bonded to Mo(V), and rather far from Mo(V) itself. It is therefore unlikely for these protons to have any appreciable isotropic *hfi*. Since the *hfi* of these "second sphere" protons are rather small, they are not resolved in cw-EPR spectra. In pulsed EPR experiments these protons are certainly detectable, but the overlapping spectra of several of them usually make the assignment of spectral features to specific protons very difficult or completely impossible even in the orientation-selective experiments. One can still use the pulsed EPR spectra to make comparisons between samples of different origin and/or preparation (e.g., differing in pH). Without assigning at least some of the spectral features to individual protons, however, these comparisons will invariably result in vague conclusions that the spectra, and thus the overall proton surroundings, are similar, or that they are different. In the latter case it is rather difficult to tell what structural rearrangements brought about the observed spectral change.

The only situation that can potentially result in positive assignments is when the pulsed EPR (e.g., ENDOR) spectrum has features that stand out from the overlapped spectral region, and there is an x-ray map of the site that allows one to assign these features with small degree of uncertainty. To illustrate such a situation we present examples of the Davies ENDOR spectra of nonexchangeable protons of *lpH* and *hpH* SO (Fig. 17). In both cases the spectra consist of multiple overlapping lines, and their appearance depends on the observation magnetic field. The spectral shapes and overall spectral widths for the *lpH* and *hpH* SO are different, irrespective of which EPR positions are compared. Apart from this general observation, one feature is immediately obvious: in the ENDOR spectra of *lpH* SO the largest
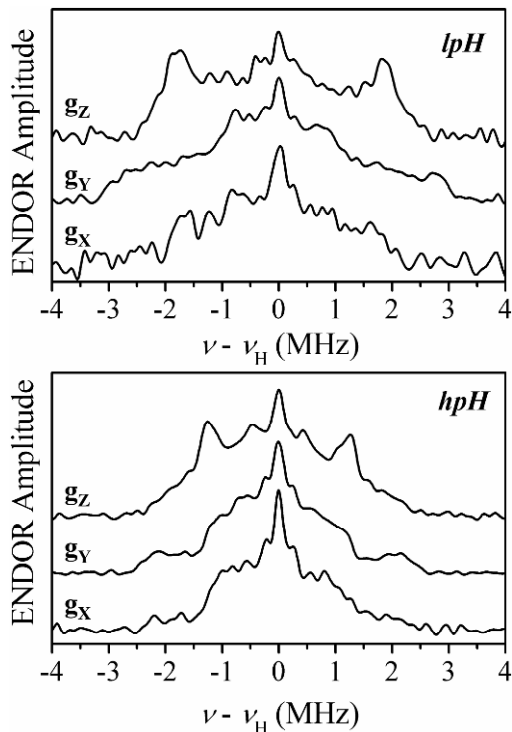
Figure 17. Davies ^{1}H ENDOR spectra of *lpH* CSO (top) and *hpH* CSO (bottom) in D_2O buffer recorded at the EPR turning points. Experimental conditions: ν_{mw} = 9.449 GHz; mw pulse durations, 120, 60, and 120 ns.

observed splitting is about 6 MHz, while in the spectrum of *hpH* SO it is only about 4.4 MHz. These observations can be interpreted as pH-induced conformation changes that result in a change of distance between Mo and the closest nonexchangeable proton of the protein surroundings [50].

In addition to the general conclusion made above, we can discuss the 6-MHz splitting in the *lpH* SO spectrum in some detail. Since this is the largest splitting in the set of ENDOR spectra taken at various EPR positions, it has to be assigned to the largest *hfi* tensor component. As we discussed above, for the second sphere protons it is a good approximation to assume the *hfi* tensor to be axial, with $a_{iso} \approx 0$ MHz and $T_{\parallel} = -2T_{\perp} \approx 6$ MHz. Although from the ENDOR data it was impossible to tell just how small a_{iso} really is, the measurement of the ν_{σ} line shift in the four-pulse ESEEM spectra performed at the mw frequency of 4.75 GHz resulted in $T_{\perp} = -3.2$ MHz. Combining this with the maximum ENDOR splitting of about 6 MHz, we immediately find that $|a_{iso}|$ does not exceed 0.5 MHz.

Now we can estimate the distance to the proton responsible for the 6 MHz feature, and the direction to this proton relative to the *g*-frame. In doing so we will reasonably assume that the anisotropic *hfi* is largely determined by the "through-

space" Mo–H dipole interaction given by Eq. (19). The Mo–H distance estimated this way is about 2.8 Å [50]. To assign this distance to a specific nearby proton, we used the x-ray crystal structure for CSO. The best candidate for the evaluated distance was the C_α-proton of the coordinated cysteine residue.
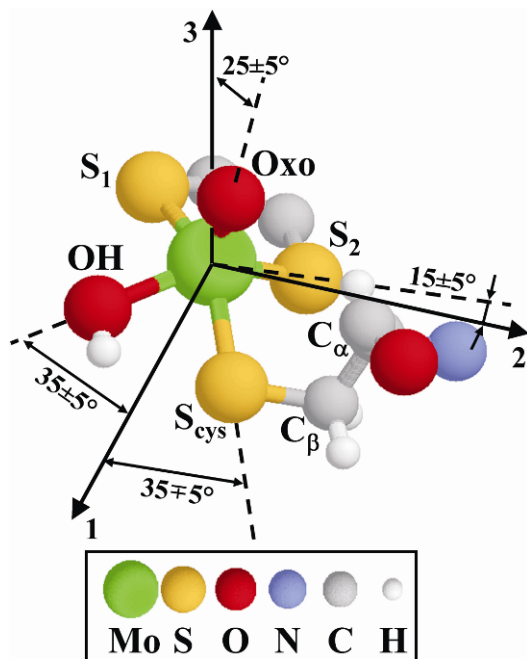
Figure 18. Composite structure of *lpH* forms of SOs based on pulsed EPR results obtained for the OH ligand proton, cysteine C_α-proton, and ^{17}O-exchanged oxo ligand (see data below). 1, 2, and 3 denote the *g*-frame axes. Reprinted from [64]. Please visit http://www.springer.com/978-1-4419-1138-4 to view a high-resolution full-color version of this illustration.

The decrease of the maximal splitting in the ENDOR spectra of *hpH* SO was then attributed to the slight variations of the conformation of the cysteine residue with pH, which consisted of two consecutive 15° rotations around the C_α–C_β and C_β–S_γ bonds. (Figure 18, which depicts the composite structure of SO obtained from all pulsed EPR experiments, gives an idea about the mentioned rotations.) This conformational change might reflect the overall change of the protein geometry with pH. To get more definitive information on the geometry of the coordinated cysteine residue will require preparation of SO enzyme in which the cysteine protons are selectively substituted by deuterons.

7.4. Exchangeable Oxygen Ligands

7.4.1. Equatorial Oxygen Ligand

The importance of detailed knowledge of spin delocalization on the equatorial oxygen ligand has been repeatedly emphasized in this chapter because it is a key element in reconstructing the Mo–H anisotropic *hfi* tensor for the hydroxyl proton. It has long been known from cw-EPR that the –OH$_{(n)}$ moiety in SO is easily exchangeable in H$_2$^{17}O buffer, and that the equatorial ^{17}O *hfi* is strong (~25–30 MHz), and readily detectable [16,17,20]. A similar situation was observed in related enzymes and model compounds [51–54]. However, the cw EPR only gives general information on the magnitude of the *hfi*, from which it is impossible to extract the details of spin density distribution and the parameters of the quadrupole interaction. Investigation of equatorial oxygen ligands by pulsed EPR is potentially able to provide much more detailed information, but it is quite difficult because of the combination of strong *hfi* (tens of MHz) and the low magnetic moment of the ^{17}O nucleus. As a result, the strong *hfi* condition ($\nu_I < |a_{iso} + T_{ZZ}|/2$) is satisfied for the equatorial ^{17}O up to $B_0 \sim 20$ kG, which corresponds to $\nu_{mw} \sim 60$ GHz. In K$_a$-band (~ 30 GHz), the highest mw band currently available for our ESEEM measurements, the ^{17}O ESEEM was only observable for *lpH* SO, which has somewhat weaker ^{17}O *hfi* (~25 MHz), while the *hpH* SO did not show any ^{17}O ESEEM in K$_a$ band. The situation with such measurements is expected to improve when the construction of a high-power (1 W) W-band ESEEM spectrometer (which is in progress [55]) is completed. However, even in that case the spectra will only be possible to detect under the conditions close to Zeeman-*hfi* cancellation, $\nu_I \sim |a_{iso} + T_{ZZ}|/2$, which may complicate their interpretation because of *nqi*. At present we can only show the results of initial K$_a$-band experiments (see Fig. 19) that have helped to understand the experimental conditions necessary to optimize the ESEEM measurements for equatorial ^{17}O in SO.

7.4.2. Axial Oxygen Ligand (oxo group)

Even though the situation with observing the equatorial ^{17}O still remains complicated, it is at present completely resolved for the axial oxygen ligand that has been detected in both high- and low-pH forms of SO from various organisms [56]. To facilitate understanding of the spectral features for the axial oxygen ligand in the ESEEM spectra of SO, we will first describe the data obtained for a well-characterized model system, [Mo^{17}O(SPh)$_4$]$^-$ [57–61]. This compound has a well-defined geometry and is highly symmetrical (C_4), with the symmetry axis coinciding with the Mo≡O bond. Accordingly, its EPR spectrum is characterized by axial *g*-anisotropy, with the principal *g*-values $g_\parallel$ and $g_\perp$ corresponding, respectively, to parallel and perpendicular orientations of the main *g*-tensor axis, *Z*, with respect to **B**$_0$. The *Z* axis for this symmetric compound obviously coincides with the direction of the Mo≡O bond. The pulsed EPR measurements performed at an EPR position characterized by some *g*-value between $g_\parallel$ and $g_\perp$ select the complexes whose *Z* axis is oriented at a certain angle with respect to **B**$_0$. This angle, θ, is defined by

$$\cos^2 \theta = \frac{g^2 - g_\perp^2}{g_\parallel^2 - g_\perp^2} .$$

(20)

The orientational selectivity in an axial spectrum is quite high and limited by either the intrinsic linewidth of the EPR spectrum or the spectral width of the mw pulses (whichever is larger).
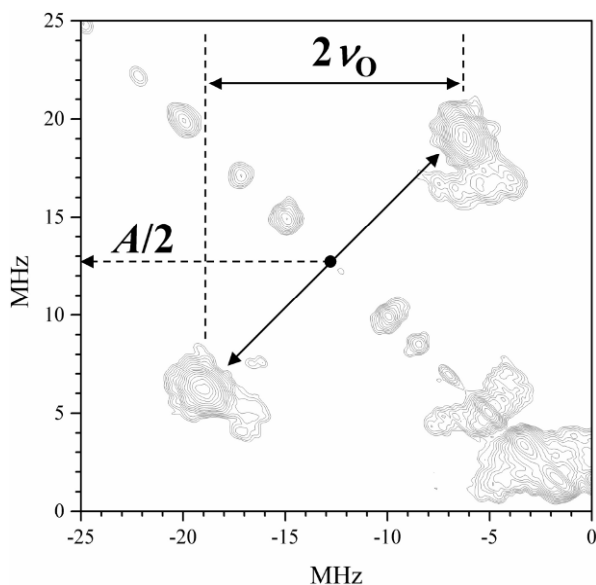
Figure 19. (–,+) quadrant of the HYSCORE spectrum of Mo(V) center in the *lpH* form of CSO in $H_2{}^{17}O$ buffer. The observed correlation lines are due to the strongly magnetically coupled equatorial ^{17}OH ligand. They are located at $A/2 \pm \nu_O$, where A is the *hfi* constant and ν_O is the Zeeman frequency of ^{17}O. Experimental conditions: $\nu_{mw} = 32.02$ GHz; $B_0 = 1.1599$ T (near g_Y); mw pulses, 10, 10, 11(π), and 10 ns; time interval between the first and second mw pulses, $\tau = 200$ ns; temperature, 20 K. Reprinted from [42].

Investigations using cw EPR of this compound in liquid solution allowed one to estimate the axial ^{17}O $a_{iso} \sim 6.5$ MHz [52,53]. To improve the accuracy of a_{iso}, as well as to measure the anisotropic *hfi* and *nqi* tensors, ESEEM measurements in a frozen solution were performed. From the cw-EPR a_{iso} estimate we calculated that the weak *hfi* condition for this system can be reached at $\nu_{mw} \geq 20$ GHz. Thus, our ESEEM measurements were performed at $\nu_{mw} \approx 29$ GHz, which is one of the frequencies we routinely use in our K_a-band experiments. After some experimenting we found that all the information we were interested in could most conveniently be obtained from basic two-pulse and integrated four-pulse ESEEM spectra. Due to high orientational selectivity, good mw excitation conditions and weak *hfi* conditions provided by our choice of the mw frequency, the primary ESEEM spectra

were, as seen from an example presented in Figure 20, textbook illustrations of Eq. (12). The spectra of Figure 20 show the four generic lines (two fundamental and two combination) that would be observed in a system with $I = 1/2$, and their numerous combinations that are recognizable by their amplitude, phase, and position.
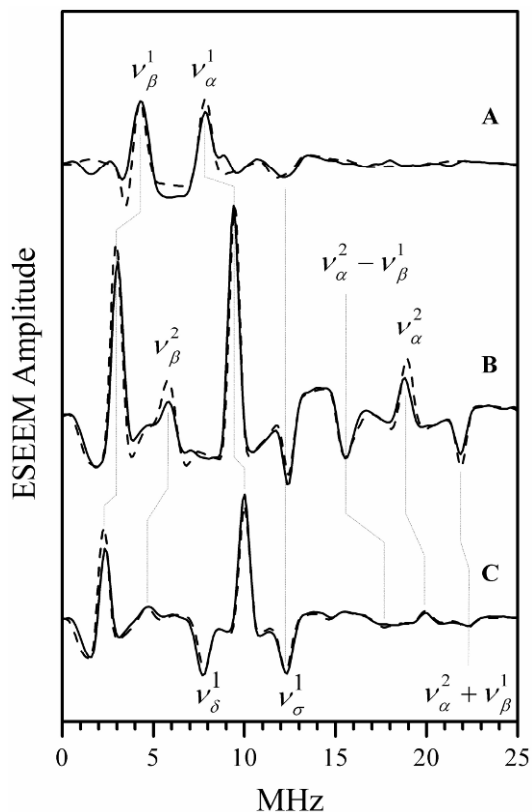
Figure 20. Solid traces A, B, and C, cosine Fourier transforms (low-frequency part) of the primary ESEEM of $[Mo^{17}O(SPh)_4]^-$ obtained at various positions of the EPR spectrum: (A) $B_0 = 1040$ mT, $g_\perp$; (C) $B_0 = 1058.3$ mT, $g_\parallel$; and intermediate position (B) $B_0 = 1053.5$ mT. Experimental conditions: mw frequency, 29.372 GHz, $T = 20$ K. Dashed traces show the corresponding simulated primary (2-pulse) ESEEM spectra. The simulation parameters were as follows: nucleus, ^{17}O; isotropic *hfi* constant, $a_{iso} = 6.5$ MHz; axial anisotropic *hfi* tensor with $T_\perp = 1.6$ MHz; axial *nqi* tensor with the quadrupole coupling constant (e^2Qq/h) = 1.45 MHz. The axes of the *hfi*, *nqi*, and *g*-tensors were coincident. The assignments of the clearly visible lines are indicated. Reprinted from [57].

The ν_σ line in the two-pulse ESEEM spectra does not clearly show the ^{17}O *nqi*-related splittings, but in the integrated four-pulse ESEEM these splittings are well resolved (see Fig. 21). The dependence of the *nqi* splitting on angle θ (see Eq. (20))
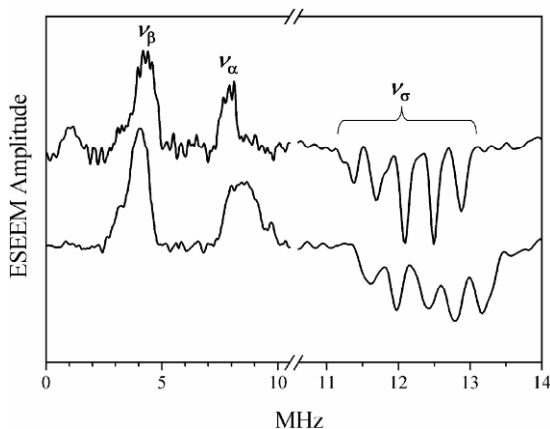
Figure 21. Cosine FT of integrated four-pulse ESEEM. Upper trace: [Mo^{17}O(SPh)$_4$]$^-$, B_0 = 10400 G, ($g_{\parallel}$), ν_{mw} = 29.372 GHz. Low trace: *hpH* CSO; B_0 =10550 G (g_Z), ν_{mw} = 29.34 GHz. In both experiments: mw pulses, 14, 14, 17, and 14 ns; dead time, T_d = 20 ns. T = 20 K. Reprinted from [64].

was measured by performing the ESEEM experiments at several EPR positions. This dependence is presented in Figure 22a, and it shows that the *nqi* tensor is axial and its main axis with good accuracy coincides with the *Z* axis of the *g*-frame and thus with the Mo≡O bond direction. The quadrupole coupling constant calculated from this dependence is $e^2Qq/h \approx 1.45$ MHz. The *hfi* tensor was also measured in the same experiments. As one can see from Figure 22b, the *hfi* tensor is also axial and its main axis is also parallel to the *g*-tensor axis *Z*. From the *hfi* orientation dependence, $a_{iso} \approx 6.5$ MHz and $T_{\perp} \approx 1.6$ MHz were determined, the isotropic part being close to that found earlier from cw-EPR measurements [56]. As for the oxo-^{17}O *nqi*, this, to our knowledge, was the first such measurement for an oxo group in a metal complex. It is important that e^2Qq/h of the oxo–^{17}O is about four times smaller than that of ^{17}O in water. Such a dramatic difference certainly allows one to unambiguously distinguish between ≡O and –OH$_n$ types of ligands. The well-defined geometry of this model compound allowed reliable DFT calculations to be performed that gave information about the electronic and spin populations of the oxygen orbitals. From these calculations it was instructional to learn that the s-character in the –oxo bond is nearly zero, and all three oxygen p-orbitals carry similar spin populations of about –0.017 per orbital. As a consequence, the total contribution of these spin populations to the anisotropic *hfi* is close to zero, and the experimental anisotropic *hfi* is thus mostly determined by the Mo–O dipolar interaction. Therefore, the model system investigations yielded detailed characterization of the *hfi* and *nqi* parameters of an oxo group.

In CSO and *b*-SO prepared in H$_2$^{17}O-enriched buffer, very similar ^{17}O *hfi* and *nqi* parameters were observed indicating that the oxo group of these compounds is
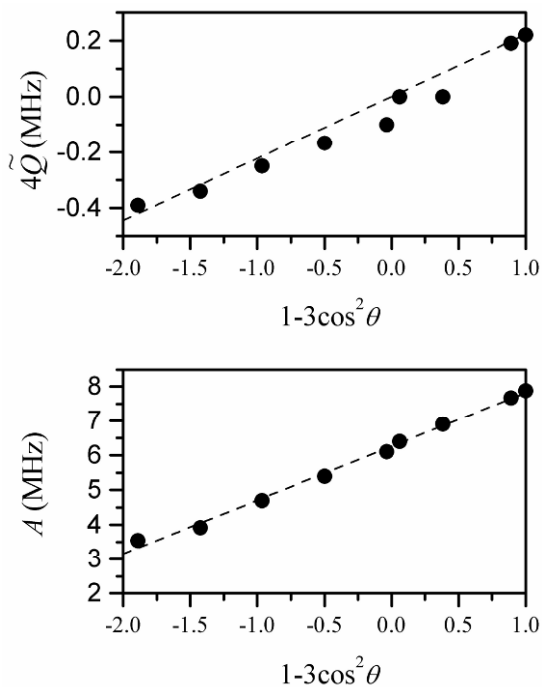
Figure 22. The dependences of the quadrupole (top panel) and dipolar (bottom panel) split-tings on $(1 - 3 \cos^2 \theta)$, where θ is the angle between the $g_{\parallel}$ axis (direction to the oxo group) and $\mathbf{B}_0$. The quadrupole splitting was determined as the separation between the adjacent component lines of the v_σ quintet, and hfi as a frequency difference between fundamental lines, as shown in Fig. 21. Reprinted from [57].

exchangeable. As an example, Figure 23 presents the HYSCORE spectrum of the *hpH* form of CSO, which clearly demonstrates a ^{17}O-related spectrum with an *hfi* constant of about 4–6 MHz, substantially less than that observed for an equatorial ^{17}O. The HYSCORE spectra did not show resolved quadrupole splittings, indicat-ing that quadrupole splittings are small. To resolve the quadrupole splittings, we have obtained the integrated four-pulse ESEEM spectra, in which these splittings were nicely resolved (see Fig. 21). It is obvious from Figure 21 that the quadrupole splittings in the model complex and in SO are similar. Numerical simulations of the spectra resulted in $e^2 Qq/h \approx 1.5$ MHz, $a_{iso} \approx 6.3$ MHz, and $|T_{\parallel}/2| \approx 1.7$ MHz (see Table 2). The similarity in all parameters between the model system and SO unam-biguously confirmed that the oxygen of the oxo ligand of CSO and *b*-SO is ex-changeable. Some possible mechanisms of oxo group exchange are discussed in section 8.
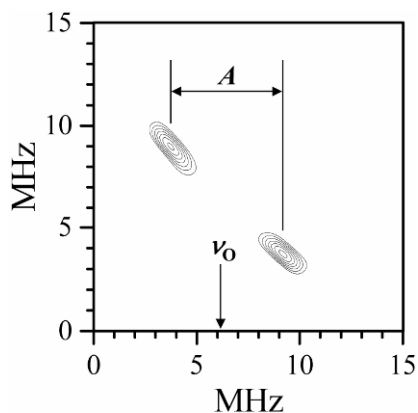
Figure 23. (+,+) quadrant of the ^{17}O HYSCORE spectrum of *hpH* CSO in H$_2$^{17}O obtained at the g_Y position of the EPR spectrum. Experimental conditions: mw frequency, 29.252 GHz; Bo = 1063.2 mT; mw pulses, 4 × 15 ns; time interval τ between the first and second mw pulses, 200 ns; measurement temperature, 20 K; The value of the ^{17}O Zeeman frequency ν_O is indicated by an arrow. Reprinted from [56].

Table 2. *hfi* and *nqi* Parameters of ^{17}O in [Mo^{17}O(SPh)$_4$]$^-$
and the Mo(V) Center of *hpH* CSO in H$_2$^{17}O (orientations
of *hfi* and *nqi* tensors relative to *g*-frames)

System	[Mo^{17}O(SPh)$_4$]$^-$	*hpH* CSO
a_{iso} (MHz)	6.5	6.3
(T_{11}, T_{22}, T_{33}) (MHz)	(1.6, 1.6, –3.2)	(2.4, 1, –3.4)
$(\theta_h, \varphi_h, \psi_h)$	(0°, NA, NA)	(20°, 55°, –10°)
e^2Qq/h (MHz)	1.45	1.5
η	0	1
$(\theta_q, \varphi_q, \psi_q)$	(0°, NA, NA)	(20°, 55°, 0°)

8. BIOLOGICAL IMPLICATIONS.

X-ray structure determinations of CSO, *pl*-SO, and *b*-SO show nearly identical coordination about the molybdenum atom. A common chemical mechanism has been proposed for SOs involving the Mo(VI/V/IV) oxidation states, as shown in Scheme 1. A key feature of the catalytic mechanism is the generation of a transient paramagnetic Mo(V) state through a series of coupled electron–proton transfer steps. Consequently, detailed knowledge of the nearby proton environment of the Mo(V) states is essential for evaluating Scheme 1. Particularly important are the effects of changes in pH, anions in the medium, and mutations on the reactivities of SOs. X-ray crystallography cannot detect the hydrogen atoms in these complex, but similar, structures; however, pulsed EPR methods provide an extremely sensitive

probe of protons that are close to the paramagnetic Mo(V) center. Addition of D$_2$O enables exchangeable and nonexchangeable protons to be distinguished from one another. The above sections have reviewed the experimental procedures for investigation of the Mo(V) active site structures of SOs by high-resolution variable frequency pulsed EPR. These EPR studies show substantial structural diversity of the Mo(V) sites, particularly the arrangement of nearby exchangeable protons, even though the coordinates of the non-hydrogen atoms, as determined from x-ray crystallography, are very similar for all SOs.

Two examples illustrate the structural diversity of the Mo(V) sites of SOs that is beginning to be recognized. The dimeric *pl*-SO contains no prosthetic groups other than the molybdenum cofactor. The EPR spectra of this *pl*-SO depend upon the mode of reduction as well as pH. The signal resulting from reduction by sulfite at low pH shows no coupling to nearby exchangeable protons, even with careful pulsed experiments. However, reduction at low pH by Ti(III) citrate shows clear splitting from a single nearby exchangeable proton that is in the equatorial plane of the Mo(V) center and hydrogen bonded to the sulfur atom of the coordinated cysteine residue. Reduction of *pl*-SO by sulfite at high pH results in pulsed EPR spectra with couplings to nearby exchangeable protons, similar to the spectra of other SOs at high pH. Scheme 2 shows the postulated active site species that are consistent with these results. These unusual EPR properties of *pl*-SO are proposed to be directly related to the "open" and "closed" forms of the active site modulated by conformations of the active site arginine (Arg374) in combination with a more restricted substrate and water access to the active site of the plant enzyme than that found in vertebrate Sos [35].

A second example illustrates the sensitivity of the Mo(V) site to perturbations of the hydrogen bonding environment through mutations of hydrogen bonding groups near the active site. All SOs have a conserved active site tyrosine that is hydrogen bonded to the equatorial oxygen ligand. In *b*-SO, mutation of this residue to phenylalanine (Tyr236Phe) substantially changes the EPR spectrum even though x-ray crystallography shows that the overall structure of the residues near the Mo active site is little changed [62]. In the wild-type *b*-SO enzyme the EPR spectrum is independent of pH [13,43], and pulsed EPR shows a nearby exchangeable proton (Figs. 9–11). However, for the Tyr236Phe mutant the EPR spectrum shows a strong pH dependence that closely resembles wild-type vertebrate enzymes, indicating that the hydrogen bonding network near the active site has been altered. This mutant also has reduced catalytic activity and does not undergo intramolecular electron transfer from Fe(II) to Mo(VI) [62]. At this point it is clear that high-resolution pulsed EPR methods can provide a detailed view of changes in the proton environment of the active site arising from mutations of nearby residues, especially those that disrupt the hydrogen bonding network that involves the oxo/hydroxo/aquo ligands of the Mo active site. However, direct information about the oxygen atoms of these coordinated oxo/hydroxo/aquo ligands of the Mo(V) center is essential for critically assessing the generally accepted mechanism proposed in Scheme 1.
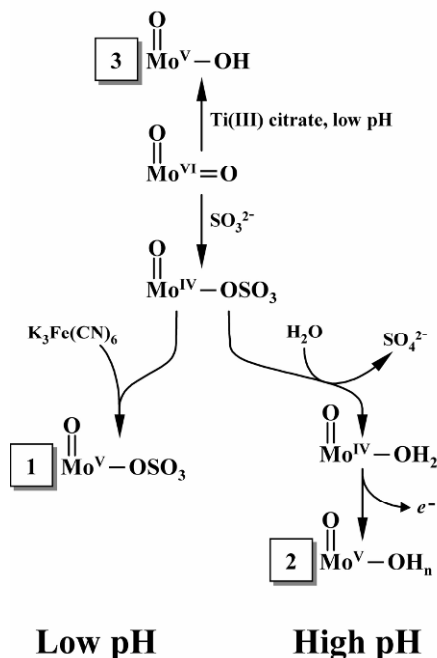
Scheme 2. Proposed reactions for formation of the Mo(V) forms of *pl*-SO observed by EPR. (1) *pl*-SO species formed by sulfite reduction at low pH that shows no exchangeable protons; (2) *hpH* species formed in both *pl*-SO and vertebrate SO; (3) *lpH* species formed in both *pl*-SO and vertebrate SO by direct reduction of the Mo(VI) center.

SOs and other molybdenum enzymes use water as the source or sink of the oxygen atoms in the redox reactions of substrates. The mechanism for SOs shown in Scheme 1 involves hydrolysis of the Mo(IV)–SO_4 complex by water (or OH^-) followed by one-electron oxidation to give species that contain the $Mo^VO(OH_n)$ fragment. In the proposed mechanism of Scheme 1, the equatorial oxo ligand that is in a solvent exposed pocket exchanges with $H_2{}^{17}O$ to become an equatorial Mo–OH_n unit. Support for this view comes from the large ^{17}O hyperfine interactions originally observed for the *hpH* and *lpH* forms of CSO in $H_2{}^{17}O$ enriched solution. However, our high-resolution pulsed EPR studies of several SOs at K_a band (~30 GHz) have clearly shown that the axial Mo=O group of SOs also exchanges with $H_2{}^{17}O$, from the unambiguous *hfi* and *nqi* interactions for an axial Mo^V=O moiety. This result raises the intriguing possibility that the axial oxo group plays a more active role in the catalytic cycle of these enzymes than previously thought. Additional studies in $H_2{}^{17}O$ enriched systems, especially of mutant proteins and other molybdenum enzymes, will be needed to assess alternatives to the general mechanism for SOs of Scheme 1.

9. CONCLUSION

The technique of cw-EPR spectroscopy has been used to characterize SOs since 1971 [63]. This chapter demonstrates that structures of the transient Mo(V) states of SOs can be investigated by high-resolution pulsed EPR studies of the *hfi* and *nqi* of magnetic nuclei, such as ^{1}H, ^{2}H, ^{31}P, and ^{17}O. However, variable frequency instrumentation is essential to obtain the optimum experimental conditions for measuring the couplings of each type of nucleus; moreover, the optimum frequency may also depend upon the chemical nature of the ligand, e.g., Mo≡O, Mo–OH or Mo–OH$_2$. Thus, ESEEM measurements at K$_a$ band (~30 GHz) have enabled the first determination of the ^{17}O *hfi* and *nqi* parameters for a terminal oxo ligand (Mo≡O), and the *nqi* parameters have clearly demonstrated that Mo≡O, Mo–OH, and Mo–OH$_2$ can be distinguished from one another by their *nqi* signatures. The analysis of variable-frequency pulsed EPR data from SOs is aided by parallel studies of model compounds that contain key functional groups or which are isotopically labeled and thus provide benchmark data for enzymes, e.g., [Mo^{17}O(SPh)$_4$]$^-$. These well-characterized Mo(V) centers are also amenable to high-level theoretical calculations of the spin density of the individual magnetic nuclei for direct comparison with experiment. Investigation of ^{17}O-labeled systems has also required the development of simulation software and protocols for pulsed EPR spectra of magnetic nuclei with $I > ½$. An additional complication for analyzing the spectra of many types of ligands, e.g., –OH, –OH$_2$, and –OPO$_3^{3-}$ results from their distributed orientations. Nonetheless, enormous progress has been made on the use of high-resolution variable frequency pulsed EPR methods to investigate the structures (Fig. 18 and Structure 1) and mechanisms (Schemes 1 and 2) of SOs during the past ~15 years [64], and the future is bright for the continued development and application of this technology to SOs, other molybdenum enzymes, and other problems in metallobiochemistry.

For Sos, some specific immediate challenges are: (1) synthesize model compounds with an Mo–^{17}OH ligand to obtain reliable *hfi* and *nqi* parameters for this group; (2) synthesize model compounds labeled with ^{33}S to obtain *hfi* and *nqi* parameters and spin densities for various types of S-containing ligands; (3) expand the library of mutants with compromised function and relate function to the hydrogen bonding structure of the active site; and (4) use pulsed electron–electron double resonance (ELDOR) to determine the Mo⋯Fe distance in CSO and *b*-SO.

NOTE ADDED IN PROOF

Several important developments have occurred since this chapter was submitted for publication. (i) The proposal that reduction of *pl*-SO with sulfite at low pH results in an equatorial sulfate ligand that blocks the active site [35] (see §7.22) has been proved by direct ESEEM detection of ^{33}S ($I = 3/2$) with nonzero isotropic *hfi*, following reduction of *pl*-SO with ^{33}S-labeled sulfite [65]. A similar *blocked* form has also been detected for the Y343F mutant of HSO [66], where the active site

tyrosine is replaced by phenylalanine (similar to the Y236F mutation in *b*-SO [62]). Somewhat different *blocked* forms were detected for the fatal R160Q mutant of human SO [67] and for the analogous R55Q mutant of sulfite dehydrogenase (*b*-SO) [68]. Since the *blocked* form represents a catalytic dead end, its formation in R160Q human SO at physiological pH might be a contributing factor in the lethality of this mutation. (ii) Variable-frequency pulsed EPR studies of the *lpH* form of SO in the presence of ^{35}Cl$^-$ and ^{37}Cl$^-$ (both $I = 3/2$) yielded a Cl *hfi* constant that indicates that the Cl$^-$ ion is close to the Mo(V) center. Extensive density functional calculations strongly favor a structure in which the Cl$^-$ is hydrogen-bonded to the equatorial Mo–OH unit, rather than directly coordinated to the Mo(V) [69]. It was suggested that the physiological role of Cl$^-$ is to adjust the *local* pH [70]. (iii) The ^{17}O quadrupole coupling constant for the axial oxo ligand in the *blocked* form of R160Q HSO is substantially larger than that found for other sulfite-oxidizing enzymes. The stronger *nqi* is proposed to result from coordination of an oxygen from glutamine (Q160) to the (sixth) axial position of the Mo center, *trans* to the oxo ligand [67,71]. If correct, then the ^{17}O *nqi* of oxo ligands will provide an easy experimental way to distinguish between five- and six-coordinate Mo(V) centers in enzymes. (iv) Finally, the construction of the high-power (ESEEM-enabled) W-band instrument mentioned in section 7.4.1 has been completed [72], and the equatorial ^{17}O ligand was observed in preliminary experiments. The *hfi* and *nqi* of the equatorial ^{17}O ligands obtained from the W-band ESEEM measurements will provide additional useful markers for determination of the structures of Mo(V) enzyme sites.

ACKNOWLEDGMENTS

REFERENCES

1. Hille R. 1996. The mononuclear molybdenum enzymes. *Chem Rev* **96**:2757–2816.
2. Hille R. 1996. Structure and function of mononuclear molybdenum enzymes. *J Biol Inorg Chem* **1**:397–404.
3. George GN, Kipke CA, Prince RC, Sunde RA, Enemark JH, Cramer SP. 1989. Structure of the active site of sulfite oxidase: x-ray absorption spectroscopy of the Mo(IV), Mo(V), and Mo(VI) oxidation states. *Biochemistry* **28**:5075–5080.
4. Kisker C, Schindelin H, Pacheco A, Wehbi WA, Garrett RM, Rajagopalan KV, Enemark JH, Rees DC. 1997. Molecular basis of sulfite oxidase deficiency from the structure of sulfite oxidase. *Cell* **91**:973–983.
5. Kisker C, Schindelin H, Rees DC. 1997. Molybdenum-cofactor-containing enzymes: structure and mechanism. *Ann Rev Biochem* **66**:233–267.

6.   Karakas E, Wilson HL, Graf TN, Xiang S, Jaramillo-Busquets S, Rajagopalan KV, Kisker C. 2005. Structural insights into sulfite oxidase deficiency. *J Biol Chem* **280**(39):33506–33515.

7.   Bray RC. 1988. The inorganic biochemistry of molybdoenzymes. *Q Rev Biophys* **21**:299–329.

8.   George GN, Garrett RM, Prince RC, Rajagopalan KV. 1996. The molybdenum site of sulfite oxidase: a comparison of wild-type and the cysteine 207 to serine mutant using x-ray absorption spectroscopy. *J Am Chem Soc* **118**:8588–8592.

9.   Schrader N, Fischer K. Theis K, Mendel RR, Schwarz G, Kisker C. 2003. The crystal structure of plant sulfite oxidase provides insights into sulfite oxidation in plants and animals. *Structure* **11**:1251–1263.

10. Eilers T, Schwarz G, Brinkmann H, Witt C, Richter T, Nieder J, Koch B, Hille R, Hänsch R, Mendel RR. 2001. Identification and biochemical characterization of *Arabidopsis thaliana* sulfite oxidase a new player in plant sulfur metabolism. *J Biol Chem* **276**:46989–46994.

11. Kappler, U, Bailey S. 2005. Molecular basis of intramolecular electron transfer in sulfite-oxidizing enzymes is revealed by high resolution structure of a heterodimeric complex of the catalytic molybdopterin subunit and a c-type cytochrome subunit. *J Biol Chem* **280**:24999–25007.

12. Toghrol F, Southerland, WM. 1983. Purification of *Thiobacillus novellus* sulfite oxidase: evidence for the presence of heme and molybdenum. *J Biol Chem* **258**:6762–6766.

13. Kappler U, Bennett B, Rethmeieri J, Schwarz G, Deutzmann R, McEwan AG, Dahl C. 2000. Sulfite:cytochrome *c* oxidoreductase from *Thiobacillus novellu*. *J Biol Chem* **275**:13202–13212.

14. Barber MJ, Neame PJ. 1990. A conserved cysteine in molybdenum oxotransferases. *J Biol Chem* **265**:20912–20915.

15. Garton SG, Garrett RM, Rajagopalan KV, Johnson MK. 1997. Resonance Raman characterization of the molybdenum center in sulfite oxidase: identification of Mo=O stretching modes. *J Am Chem Soc* **119**:2590–2591.

16. Lamy MT, S. Gutteridge S, Bray RC. 1980. Electron-paramagnetic-resonance parameters of molybdenum(V) in sulphite oxidase from chicken liver. *Biochem J* **185**:397–403.

17. Gutteridge S, Lamy MT, Bray RC. 1980. The nature of the phosphate inhibitor complex of sulphite oxidase from electron-paramagnetic-resonance studies using oxygen-17. *Biochem J* **191**:285–288.

18. Bray RC, Gutteridge S, Lamy MT, Wilkinson T. 1983. Equilibria amongst different molybdenum(V)-containing species from sulphite oxidase: evidence for a halide ligand of molybdenum in the low-pH species. *Biochem J* **211**:227–236.

19. Bray RC, Gutteridge S, Lamy MT, Wilkinson T. 1982. Evidence from electron-paramagnetic-resonance spectroscopy for a complex of sulphite ions with the molybdenum centre of sulphite oxidase. *Biochem J* **201**:241–243.

20. Cramer SP, Johnson JL, Rajagopalan KV, Sorrell TS. 1979. Observation of [17]O effects on Mo[V] EPR spectra in sulfite oxidase; xanthine dehydrogenase, and $MoO(SC_6H_5)_4$. *Biochem Biophys Res Commun* **91**:434–439.

21. George GN. 1985. The proton spin-flip lines of Mo(V) EPR signals from sulfite oxidase and xanthine oxidase. *J Magn Reson* **64**:384–394.

22. Dikanov SA, Tsvetkov Yu.D. 1992. *Electron spin-echo envelope modulation (ESEEM) spectroscopy*. Boca Raton, FL: CRC Press.

23. Raitsimring AM, Astashkin AV, Baute D, Goldfarb D, Caravan P. 2004. W-band 17O pulsed electron nuclear double resonance study of gadolinium complexes with water. *J Phys Chem A* **108**:7318–7323.

24. Liao PF, Hartmann SR. 1973. Determination of Cr–Al hyperfine and electric quadrupole interaction parameters in ruby using spin-echo electron-nuclear double resonance. *Phys Rev B* **8**:69–80.

25. Schweiger A, Jeschke G. 2001. *Principles of pulse electron paramagnetic resonance*. Oxford: Oxford UP.

26. Höfer P, Grupp A, Nebenfüher H, Mehring M. 1986. Hyperfine sublevel correlation (HYSCORE) spectroscopy: a 2D ESR investigation of the squaric acid radical. *Chem Phys Lett* **132**:279–282.

27. Epel B, Arieli D, Baute D, Goldfarb D. 2003. Improving W-band pulsed ENDOR sensitivity—random acquisition and pulsed special TRIPLE. *J Magn Reson* **164**:78–83.

28. Mims WB. 1965. Pulsed ENDOR experiment. *Proc Roy Soc* **283A**:452–457.

29. Davies ER. 1974. A new pulse ENDOR technique. *Phys Lett A* **47**:1–2.

30. Doan PE, Hoffman BM. 1997. Making hyperfine selection in Mims ENDOR independent of deadtime. *Chem Phys Lett* **269**:208–214.

31. Astashkin AV, Raitsimring AM. 2000. Refocused primary echo: a zero dead time detection of the ESEEM. *J Magn Reson* **143**:280–291.

32. Van Doorslaer S, Schweiger A. 1997. A two-dimensional sum combination frequency pulse EPR experiment. *Chem Phys Lett* **281**:297–305.

33. Raitsimring A, Astashkin AV, Feng C, Enemark JH, Nelson K, Rajagopalan KV. 2003. Pulsed EPR studies of the exchangeable proton at the molybdenum center of dimethyl sulfoxide reductase. *J Biol Inorg Chem* **8**:95–104.

34. Cosper M, Neese F, Astashkin AV, Carducci MD, Raitsimring A, Enemark JH. 2005. Determination of the g-tensors and their orientations for cis,trans-(L–N_2S_2)Mo^{V}OX (X = Cl, SCH$_2$Ph) by single-crystal EPR spectroscopy and molecular orbital calculations. *Inorg Chem* **44**:1290–1301.

35. Astashkin AV, Hood BL, Feng C, Hille R, Mendel RR, Raitsimring AM, Enemark JH. 2005. Structures of the Mo(V) forms of sulfite oxidase from *Arabidopsis thaliana* by pulsed EPR spectroscopy. *Biochemistry* **44**:13274–13281.

36. Codd R, Astashkin AV, Pacheco A, Raitsimring AM, Enemark JH 2002. Pulsed ELDOR spectroscopy of the Mo(V)/Fe(III) state of sulfite oxidase prepared by one–electron reduction with Ti(III) citrate. *J Biol Inorg Chem* **7**:338–350.

37. Kappler U, McEwan AG. 2002. A system for the heterologous expression of complex redox proteins in *Rhodobacter capsulatus*: characterization of recombinant sulphite:cytochrome c oxidoreductase from *Starkeya novella*. *FEBS Lett* **529**:208–214.

38. Temple CA, Graf TN, Rajagopalan KV. 2000. Optimization of expression of human sulfite oxidase and its molybdenum domain. *Arch Biochem Biophys* **383**:281–287.

39. Raitsimring AM, Pacheco A, Enemark JH. 1998. ESEEM investigation of the high and low pH forms of chicken liver Sulfite Oxidase. *J Am Chem Soc* **120**:11263–11273.

40. Borbat P, Raitsimring A. 1994. A new pulse EPR spectrometer at the University of Arizona. In *Abstracts of 36th Rocky Mountain Conference on Analytical Chemistry*, Denver, CO, July 31–Aug 5, 1994, p. 94.

41. Astashkin AV, Raitsimring A, Walker FA. 1999. Two- and four-pulse ESEEM studies of the heme binding center of a low spin ferriheme proteine: the importance of a multi-frequency approach. *Chem Phys Lett* **306**:9–17.

42. Astashkin AV, Raitsimring A, Enemark JH. 2006. 26.5–40 GHz K_a-band pulsed EPR spectrometer. *Conc Magn Reson B (Magn Reson Engineering)* **29B**:125–136.

43. Raitsimring A, Kappler U, Feng C, Astashkin AV, Enemark JH. 2005. Pulsed EPR studies of a bacterial sulfite-oxidizing enzyme with pH-invariant hyperfine interactions from exchangeable protons. *Inorg Chem* **44**:7283–7285.

44. Astashkin A, Mader ML, Pacheco A, Enemark JH, Raitsimring A. 2000. Direct detection of the proton-containing group coordinated to Mo(V) in high-pH form of chicken liver sulfite oxidase. *J Am Chem Soc* **122**:5294–5302.

45. Astashkin AV, Raitsimring AM, Feng C, Johnson JL, Rajagopalan KV, Enemark JH. 2002. The Mo–OH proton of the low-pH form of sulfite oxidase: comparison of the hyperfine interactions obtained from pulsed ENDOR, CW-EPR and ESEEM measurements. *Appl Magn Reson* **22**:421–430.

45a. Wilson GL, Greenwood RJ, Pilbrow JR, Spence JT, Wedd AG. 1991. Molybdenum(V) sites in xanthine oxidase and relevant analog complexes: comparison of molybdenum–95 and sulfur-33 hyperfine coupling. *J Am Chem Soc* **113**:6803–6812.

46. Pacheco A, Basu P, Borbat P, Raitsimring AM, Enemark JH. 1996. Multi-frequency ESEEM spectroscopy of sulfite oxidase in phosphate buffer: direct evidence for coordinated phosphate. *Inorg Chem* **35**:7001–7006.

47. Dikanov SA, Liboiron BD, Thompson KH, Violet EV, Yuen G, McNeill JH, Orvig C. 1999. *In vivo* electron spin-echo envelope modulation (ESEEM) spectroscopy: first observation of vanadyl coordination to phosphate in bone. *J Am Chem Soc* **121**:11004–11005 [see comment as ref. [20] therein: Variation of the *hf* couplings for three P atoms can be attributed to different O–V–O(–P) angles. The isotropic constant is proportional to the unpaired 3s spin density and the coefficient 13306 MHz computed for a unit 3s electron. The anisotropic coupling results from dipole–dipole interaction (mainly from the V–P distance), and indirect spin transfer on a 3p orbital of P. A V–P distance of 3.44 Å for a V–O–P fragment in ADP complexes corresponds to $T = 0.79$ MHz for point dipoles; computed T for a unit 3p electron is 367 MHz. Thus, the isotropic coupling should be far more sensitive to structural variations than the anisotropic coupling.]

48. Buy C, Matsui T, Andrianambininstoa S, Sigalat C, Girault G, Zimmerman J-L. 1996. Binding sites for Mg(II) in H^+-ATPase from *Bacillus PS3* and in the subcomplex studied by one-dimensional ESEEM and two-dimensional HYSCORE spectroscopy of oxovanadium(IV) complexes: a possible role for -His-324. *Biochemistry* **35**:14281–14293.

49. Mustafi D, Telser J, Makinen MW. 1992. Molecular geometry of vanadyl–adenine nucleotide complexes determined by EPR, ENDOR, and molecular modeling. *J Am Chem Soc* **114**:6219–6226.

50. Astashkin AV, Raitsimring AM, Feng C, Johnson JL, Rajagopalan KV, Enemark JH. 2002. Pulsed EPR studies of nonexchangeable protons near the Mo(V) center of sulfite oxidase: direct detection of the α-proton of the coordinated cysteinyl residue and structural implications for the active site. *J Am Chem Soc* **124**:6109–6118.

51. Greenwood RJ, Wilson GL, Pilbrow JR, Wedd AG. 1993. Molybdenum(V) sites in xanthine oxidase and relevant analog complexes: comparison of oxygen-17 hyperfine coupling. *J Am Chem Soc* **115**:5385–5392.

52. Hanson GR, Wilson GL, Bailey TD, Pilbrow JR, Wedd AG. 1987. Multifrequency electron spin resonance of molybdenum(V) and tungsten(V) compounds. *J Am Chem Soc* **109**:2609–2626.

53. Hanson GR, Brunette AA, McDonell AC, Murray KS, Wedd AG. 1981. Electronic properties of thiolate compounds of oxomolybdenum(V) and their tungsten and selenium analogs: effects of oxygen-17, molybdenum-98, and molybdenum-95 isotope substitution upon ESR spectra. *J Am Chem Soc* **103**:1953–1959.

54. Boyd IW, Dance IG, Murray KS, Wedd AG. 1978. Mononuclear oxo-thiolato compounds of molybdenum(V). *Aust J Chem* **31**:279–284.

55. D. Goldfarb, private communication. (New W-band spectrometer which is scheduled to be completed in 2007 will be able generate a 15 ns π-pulse providing >30 MHz of B_1.)

56. Astashkin AV, Feng C, Raitsimring AM, Enemark JH. 2005. [17]O ESEEM evidence for exchange of the axial oxo ligand in the molybdenum center of the high pH form of sulfite oxidase. *J Am Chem Soc* **127**:502–503.

57. Astashkin AV, Neese F, Raitsimring AM, Cooney JJA, Bultman E, Enemark JH. 2005. Pulsed EPR investigations of systems modeling molybdenum enzymes: hyperfine and quadrupole parameters of Oxo–[17]O in $[Mo^{17}O(SPh)_4]^-$. *J Am Chem Soc* **127**:16713–16723.

58. Dance IG, Wedd AG, Boyd IW. 1978. The formation and molecular structure of the di-μ-oxo-di[di(benzenethiolato)oxomolybdate(V)] dianion. *Aust J Chem* **31**:519–526.

59. Bradbury JR, Mackay MF, Wedd AG. 1978. The crystal and molecular structure of tetraphenylarsonium tetrakis(benzenethiolato)oxomolybdate(V). *Aust J Chem* **31**:2423–2430.

60. Boyd W, Dance IG, Landers AE, Wedd AG. 1979. Triply bridged binuclear thiolate complexes of oxomolybdenum(V): synthesis of $[Mo_2O_2(SR)_6Z]^-$ (Z = OR', SR', NR'$_2$) and crystal structures of $(Et_4N)[Mo_2O_2(SCH_2CH_2O)_2Cl_3$, (Et_4N) $[Mo_2O_2(SCH_2CH_2O)_3Cl]$ and $(Pr_3NH)[Mo_2O_2(SCH_2CH_2O)_3(SCH_2CH_2OH)]$. *Inorg Chem* **18**:1875–1885.

61. Cleland Jr WE, Barnhart KM, Yamanouchi K, Collison D, Mabbs FE, Ortega RB, Enemark JH. 1987. Syntheses, structures, and spectroscopic properties of six-coordinate mononuclear oxo-molybdenum(V) complexes stabilized by the hydrotris(3,5-dimethyl-1-pyrazolyl)borate ligand. *Inorg Chem* **26**:1017–1025.

62. Kappler U, Bailey S, Feng C, Honeychurch M, Hanson GR, Bernhardt PV, Tollin G, Enemark JH. 2006. Kinetic and structural evidence for the importance of Tyr236 for the integrity of the Mo-active site in a bacterial sulfite dehydrogenase. *Biochemistry* **45**:9696–9705.

63. Cohen HJ, Fridovich I, Rajagopalan KV. 1971. Hepatic sulfite oxidase: a functional role for molybdenum. *J Biol Chem* **246**(2):374–382.

64. Enemark JH, Astashkin AV, Raitsimring AM. 2006. Investigation of the coordination structures of the molybdenum(V) sites of sulfite oxidizing enzymes by pulsed EPR spectroscopy. *Dalton Trans* **29**:3501–3514.

65. Astashkin AV, Johnson-Winters K, Klein EL, Byrne RS, Hille R, Raitsimring AM, Enemark JH. 2007. Direct demonstration of the presence of coordinated sulfate in the reaction pathway of *Arabidopsis thaliana* sulfite oxidase using [33]S labeling and ESEEM spectroscopy. *J Am Chem Soc* **129**:14800–14810.

66. Raitsimring AM, Astashkin AV, Feng C, Wilson HL, Rajagopalan KV, Enemark JH. 2008. Studies of the Mo(V) center of the Y343F mutant of human sulfite oxidase by variable frequency pulsed EPR spectroscopy. *Inorg Chim Acta* **361**:941–946.

67. Astashkin AV, Johnson-Winters K, Klein EL, Feng C, Wilson HL, Rajagopalan KV, Raitsimring AM, Enemark JH. 2008. Structural studies of the molybdenum center of

the pathogenic R160Q mutant of human sulfite oxidase by pulsed EPR spectroscopy and [17]O and [33]S labeling. *J Am Chem Soc* **130**:8471–8480.

68. Rapson TD, Ashtashkin AV, Johnson-Winters K, Kappler U, Raitsimring AM, Enemark JH. Pulsed EPR investigations of the Mo(V) centers of the R55Q and R55M variants of sulfite dehydrogenase from *Starkeya novella*. Manuscript in preparation.

69. Klein EL, Astashkin, AV, Ganyushin D, Riplinger C, Johnson-Winters K, Neese F, Enemark JH. 2009. Direct detection and characterization of chloride in the active site of the low-pH form of sulfite oxidase using electron spin echo envelope modulation spectroscopy, isotopic labeling, and density functional theory calculations. *Inorg Chem* **48**: 4743–4752.

70. Enemark JH, Astashkin AV, Raitsimring AM. 2008. Structures and reaction pathways of the molybdenum centres of sulfite-oxidizing enzymes by pulsed EPR spectroscopy. *Biochem Soc Trans* **36**:1129–1133.

71. Doonan CJ, Wilson HL, Rajagopalan KV, Garrett RM, Bennett B, Prince RC, George GN. 2007. Modified active site coordination in a clinical mutant of sulfite oxidase. *J Am Chem Soc* **129**:9421.

72. Goldfarb D, Lipkin Y, Potapov A, Gorodetsky Y, Epel B, Raitsimring AM, Radoul M, Kaminker I. 2008. HYSCORE and DEER with an upgraded 95 GHz pulse EPR spectrometer. *J Magn Reson* **194**:8–15.

DIMETHYLSULFOXIDE (DMSO) REDUCTASE, A MEMBER OF THE DMSO REDUCTASE FAMILY OF MOLYBDENUM ENZYMES

Graeme R. Hanson and Ian Lane

*Center for Magnetic Resonance, The
University of Queensland, St. Lucia,
Queensland, Australia*

NOTE: The reader should kindly note that all the figures and tables for this chapter do not appear in the text; however, they can be viewed in PDF format at <http://www.springer.com/978-1-4419-1138-4>.

Herein we describe the application of continuous wave (CW) and pulsed EPR spectroscopy to the structural (geometric and electronic) characterization of the Mo(V) active site within dimethylsulfoxide (DMSO) reductase and where appropriate, model molybdenum(V) complexes. Specifically, the electronic and geometric structure of the Low-g and High-g EPR signals and their relevance to the enzymes' catalytic cycle are described. CW and pulsed EPR studies of a dithionite-reduced sample of DMSO reductase reveal the presence of a sulfur-centered radical localized on the molybdenum cofactor.

1. INTRODUCTION

Molybdenum enzymes (other than nitrogenase) form a diverse but coherent family known as the molybdenum oxotransferases and hydroxylases [1–6]. Most of these enzymes catalyze an oxygen atom transfer to or from a substrate in a reaction that is linked to a two-electron redox reaction involving molybdenum cycling between the oxidation states of +6 to +4 or vice versa.

Address all correspondence to Graeme R. Hanson, Centre for Magnetic Resonance, The University of Queensland, St. Lucia, Queensland 4072, Australia, +61 7-3365-3242, +61 7-3365-3833 (fax), <Graeme.Hanson@cmr.uq.edu.au>.

Three distinct families of mononuclear molybdoenzymes (xanthine oxidase, sulfite oxidase/nitrate reductase, and dimethylsulfoxide (DMSO) reductase) have been identified on the basis of their sequence homology and structure of the active site molybdenum cofactor [1–6]. The molybdenum cofactor in all of these enzymes contains an organic component known as molybdopterin (MPT), which is a modified pterin providing an ene-dithiolene sidechain responsible for ligating the Mo [1,2,7–10]. The xanthine oxidase family of enzymes (Chapter 5) contains an active site molybdenum ion coordinated by a single MPT moiety, an oxo, a sulfido, and either an aqua or hydroxide ligand [11–13], whilst the sulfite oxidase/nitrate reductase family of enzymes (Chapter 6) contain a single MPT ligated to the molybdenum atom, with one or two oxo groups and a cysteinyl sulfur ligand completing the coordination sphere [14]. In contrast, the DMSO reductase family of enzymes contain two MPT ligands linked to a dinucleotide (in DMSO reductase this dinucleotide is guanidine and the MPT is referred to as MGD), a single oxo group, and an amino acid ligand such as Ser, Thr, Cys, or SeCys [1,6,15]. A phylogenetic study [16] has further subdivided the DMSO reductase family of enzymes into three clades (Types I, II, and III) based upon whether (I and II) or not (III) they contain an N-terminus cysteine-rich region and, second, whether (I) or not (II) a [4Fe–4S] cluster is present.

Type I: assimilatory nitrate reductase (NasA), periplasmic nitrate reductase (NapA), formate dehydrogenase (Fdh), thiosulfate reductase/polysulfide reductase (PhsA/PsrA)

Type II: dimethylsulfoxide reductase (periplasmic) (DmsA), dimethylsulfide dehydrogenase (Ddha), selenate reductase (SerA), ethylbenzene dehydrogenase(Ebda), nitrate reductase (NarGHI)

Type III: trimethylamine-*N*-oxide reductase (TorA), dimethylsulfoxide reductase (membrane bound) (DorA), biotin sulfoxide reductase (BisC)

The active site of dissimilatory nitrate reductase (NAP) is representative of this group of enzymes. In the structure of oxidized NAP from *Desulfovibrio desulfuricans* [17] (Fig. 1a), the molybdenum atom is ligated by four sulfur atoms of two asymmetrically bound molybdopterin guanine dinucleotide (MGD) forms of Moco, a single hydroxo/water group, and the oxygen atom of a cysteine sidechain (Fig. 1b). Unlike DMSO reductase, NAP also contains a [4Fe–4S] cluster as part of its electron-transfer pathway. In this chapter, we have limited the discussion concerning the role of EPR spectroscopy in characterizing the Mo(V) active sites in these enzymes, to a single example, namely, DMSO reductase. However, the information concerning this enzyme's active site and catalytic mechanism may well be relevant to other members of the DMSO reductase family [1,2].

Dimethylsulfoxide (DMSO) reductase purified from the photosynthetic anaerobe *Rhodobacter capsulatus* catalyzes the conversion of DMSO to DMS with an accompanying two-electron and proton transfer and has proved to be invaluable in

probing the catalytic pathway of the DMSO reductase family of mononuclear molybdenum enzymes. This is due to the fact that the molybdenum cofactor (Moco) is the only redox center that occurs within this enzyme. In the absence of additional redox chromophores, the molybdenum center can be freely observed by spectroscopic techniques without interference from centers such as hemes, iron–sulfur clusters, and flavins that tend to be strongly absorbing and can hence mask those signals from the weaker molybdenum chromophore [1,2,19–22].

The elucidation of the high-resolution (1.3 Å) crystal structure of DMSO reductase from *R. sphaeroides* in the resting Mo(VI) state [23] and that of the structure of DMSO reductase from *R. capsulatus* bound to substrate in the Mo(IV) oxidation state [24] have provided us with two crucial points of reference within the catalytic cycle of this enzyme. However, to fully determine the catalytic mechanism of this enzyme, we must also determine the paramagnetic Mo(V) intermediates generated transiently during the single-electron reductions/oxidations that are proposed to make up the enzyme's redox cycle [1,25]. Electron paramagnetic resonance (EPR) has proven to be a powerful tool for the structural characterization of Mo(V) centers in molybdoenzymes [1,26–32]. This is a consequence of the spin Hamiltonian parameters determined by EPR spectroscopy being extremely sensitive to minute changes in the coordination sphere of the paramagnetic Mo(V) species under study. A brief introduction to Mo(V) EPR spectroscopy is given as background material in order for the reader to appreciate the subsequent discussion of the EPR spectra from DMSO reductase [33,34].

2. EPR STUDIES OF MO(V) SPECIES

EPR spectra of mononuclear molybdenum complexes or metalloenzymes can be interpreted with the aid of a spin Hamiltonian [33–36]:

$$H = \beta B \cdot g \cdot S + S \cdot A \cdot I + I \cdot P \cdot I - \gamma_n B \cdot I , \tag{1}$$

where terms (interactions) from left to right correspond to the electron Zeeman, Hyperfine, Quadrupole, and nuclear Zeeman interactions, and S and I are the electron and nuclear spin operators, respectively, g and A are the electron Zeeman and hyperfine coupling matrices, respectively, P the quadrupole tensor, γ_n the nuclear gyromagnetic ratio, β the Bohr magneton, and B the applied magnetic field. Additional Hyperfine and Quadrupole terms will be required when the magnetic moment of the unpaired electron interacts with the magnetic moment of ligand nuclei possessing a nonzero nuclear spin, such as ^1H, ^2H, ^{17}O, and ^{33}S. For further information, the reader is referred to Chapters 4 and 5 in Volume 28 of this series [35,36].

Naturally abundant molybdenum occurs as seven isotopes: $^{92, 94, 95, 96, 97, 98,}$ ^{100}Mo [37]. The ^{95}Mo and ^{97}Mo isotopes account for 25.5% of the mass of naturally abundant Mo (Table 1) and possess a nuclear spin of 5/2. The other five isotopes have no nuclear spin. When Mo is present in molecules in a paramagnetic state (i.e.,

Mo(III) or Mo(V)), the room temperature EPR spectrum[1] will consist of a major resonance with an intensity representing 74.53% of the Mo atoms containing no nuclear spin that is in the center of, and flanked by, six minor resonances with intensities (4.245%), representing the 25.47% of Mo atoms with a nuclear spin of 5/2 [38,39]. These six minor resonances arise though hyperfine coupling of the nuclear spin of the Mo atom with the unpaired electron spin. This type of spectrum (Fig. 2) is indicative of a solution of an axially coordinated complex at ambient temperature, where the molecules are able to tumble freely, averaging out any *g*- or *A*-anisotropy present in the system. However, EPR spectra of Mo(V) species exhibiting low symmetries and measured at low temperature produce complicated spectral line shapes (Fig. 2) as a consequence of the coordination geometry and symmetry of the metal ion, the ligands coordinating to the metal ion, and the extent of delocalization of the unpaired electron onto the ligands [38–42]. Interpretation of these spectra is thus nontrivial as a consequence of overlapping resonances, and therefore one or more of the following approaches is required for a complete analysis of the spectra. These approaches involve:

- Multifrequency EPR, which exploits *g*-value resolution, state mixing, and distributions of parameters to improve spectral resolution [38,39],
- High-resolution CW and pulsed techniques such as electron nuclear double resonance (ENDOR), electron spin echo envelope modulation (ESEEM), and hyperfine sublevel correlation spectroscopy (HYSCORE) for identifying coupled nuclei in the first and second coordination spheres of metal ions [43–50],
- Isotope enrichment [1,28,31,32,44,48–50],
- Computer simulation to extract spin Hamiltonian parameters [35,51], and
- Manipulation of experimental spectra using computational techniques such as deconvolution of lineshapes and difference spectra [3].

Each approach has been utilized in the analysis of EPR spectra of Mo(V) species.

3. EPR STUDIES OF DMSO REDUCTASE

The following sections not only describe the early biochemical studies of DMSO reductase incorporating Mo(V) EPR spectroscopy [19,21,22,52], but also present new insights into the electronic structure of the molybdenum(V) catalytic intermediates. The terminology of Bennett et al. [22] used to identify Mo(V) species of DMSO reductase by way of their g_{iso} values will be used throughout this chapter. High-g species are those with g_{iso} values that approximate 1.98, while Low-g species are those with g_{iso} values that approximate 1.96. Within this nomen-

clature scheme, the High-g and Low-g signals are further categorized as Type 1 or 2 depending on their appearance. Additionally, the terms "split" and "unsplit" refer to the presence or absence of superhyperfine coupling to one or more protons in the continuous wave EPR spectra. Readers interested in the EPR spectroscopic characterization of the catalytically active tungsten-containing DMSO reductase are referred to the reviews on bioinorganic chemistry of tungsten [53,54].

3.1. Respiratory DMSO Reductase

DMSO reductase extracted from *E. coli* (termed DmsABC) is a membrane-bound enzyme and is made up of three subunits comprising a catalytic molybdenum center in the form of *bis*(MGD)Mo (DmsA), a subunit containing four [4Fe–4S] clusters (DmsB), and a hydrophobic polypeptide membrane anchor unit (DmsC) that secures DmsB to the membrane [55,56]. Respiratory DMSO reductase is a terminal reductase able to reduce DMSO as well as a number of *S*- and *N*-oxides and pyridine *N*-oxide substrates, while menaquinol is oxidized to menaquinone, causing a proton gradient across the inner bacterial membrane [1,57,58]. An Mo(V)-centered EPR signal [$g_1 = 1.987$, $g_2 = 1.976$, $g_3 = 1.960$ ($g_{av} = 1.974$)] similar to the High-pH form exhibited by *E. coli* nitrate reductase was produced by fully oxidized resting membranes isolated from DMSO reductase enriched cells [56]. This signal, present in preparations from pH 5.0 to 9.0, slowly disappeared upon reduction to ~100 mV and did not reappear when the enzyme was reoxidized at this stage. If the enzyme was further reduced, however, the signal intensity increased once again, reaching a maximum at around –55 to –75 mV before disappearing completely. The process was found to be reversible in this range of potentials. The maximum Mo(V) signal intensity was found to occur at the potential corresponding to the average of the Mo(VI)/Mo(V) and Mo(V)/Mo(IV) couples for this enzyme [56].

By mutating the molybdenum ligand Ser-176 in *E. coli* DMSO reductase with a number of different amino acids, a variety of new EPR signals were obtained, indicating the involvement of Ser-176 as a ligand in the molybdenum ions' coordination sphere of *E. coli* DMSO reductase [59].

3.2. Periplasmic DMSO Reductase

DMSO reductase extracted from the periplasm of *R. capsulatus* and *R. sphaeroides* contains no prosthetic group other than the active site molybdenum cofactor, making it an ideal model enzyme system to study the catalytic mechanism. In addition to being able to utilize DMSO as substrate, this enzyme can also catalyze the reduction of a number of *S*-oxide, *N*-oxide, and pyridine *N*-oxide substrates with an accompanying two-electron transfer [1,2].

Three independent X-ray crystal structures (Table 2) of native (resting, Mo(VI)) DMSO reductase purified from *R. sphaeroides* [60] and *R. capsulatus* [61,62] were published by the end of 1997. However, there was no consensus re-

garding the number and identity of the ligands coordinated to the molybdenum ion within these structures. One major discrepancy between all three structures was the Mo–S distances of the Q-MGD moiety. Although the structure of McAlpine et al. [62] showed that both the P- and Q-MGD moieties were bound to the molybdenum atom, the structure of the *R. sphaeroides* enzyme displayed a Q-MGD Mo–S2 distance of 3.1 Å [60], while the structures of Schneider et al. [61] and McAlpine et al. [62] revealed that the dithiolene sulfurs of Q-MGD were not coordinated to the molybdenum ion. The Mo–S distances of the dithiolene Q-MGD sulfurs were in this case determined to be 3.5 and 3.9 Å to S1 and S2, respectively. Additionally, the dithiolene sulfur atoms of the displaced Q-MGD moiety were found to interact, with a reported S1–S2 distance of 2.5 Å [61]. In contrast, the dithiolene sulfurs of the P-MGD moiety were found to be well within the coordination sphere of the molybdenum ion in all three structures, with Mo–S distances ranging between 2.3 and 2.5 Å [60-62].

There has also been considerable debate regarding the nature of the remaining ligands coordinated to molybdenum in the oxidized crystal structures of DMSO reductase. While it is accepted that the molybdenum atom is bound to the O of Serine-147 in all three structures, the X-ray structures of the enzyme originating from *R. capsulatus* (McAlpine et al. [62] and Schneider et al. [61]) indicated the presence of two oxo groups, while that of the *R. sphaeroides* enzyme (Schindelin et al. [60]) indicated only a single oxo group. Supporting spectroscopic evidence for these structural differences came from EXAFS [63,64], while resonance Raman spectroscopy of DMSO reductase purified from *R. sphaeroides* supported the view that a single oxo group is present in the resting enzyme [65,66].

The debate regarding the structure of the molybdenum active site of DMSO reductase was finally resolved when a high-resolution (1.3 Å) crystal structure of oxidized DMSO reductase from *R. sphaeroides* was published [23]. This revealed that the molybdenum ion's coordination sphere in the structure of DMSO reductase was discretely disordered, occurring as hexa- and pentacoordinate sites (Table 2, Fig. 3b,c) [23]. The hexacoordinate molybdenum structure (Fig. 3b) shows the Mo ion is ligated by the four sulfur atoms of the P- and Q-MGD moieties, with an average Mo–S bond length of 2.43 Å. The remaining ligands consist of a single oxo group at 1.76 Å and the oxygen atom from a Serine-147 sidechain at 1.84 Å. The pentacoordinate molybdenum structure (Fig. 3c) has only the P-MGD moiety within the coordination sphere of the molybdenum atom, with Mo–S bond lengths of 2.50 and 2.45 Å to S1 and S2, respectively. The Q-MGD Mo–S bond lengths of 3.62 and 4.53 Å for S1 and S2, respectively, mean that the Q-MGD is no longer considered a ligand of Mo. The other ligands of Mo in this structure were determined to be two oxo groups at 1.75 and 1.71 Å for O1 and O2, respectively (O1 is common between the hexa- and pentacoordinate forms) and the oxygen atom of Serine-147 at 1.92 Å. The major difference between these two structures was found to be the displacement of the molybdenum atom by 1.6 Å [23], and it was proposed that this discrete disorder was responsible for the different crystal structures originally elucidated for DMSO reductase [23].

3.2.1. Mo(V) EPR Signals from Periplasmic DMSO Reductase

Molybdenum(V) EPR signals from dimethylsulfoxide reductase extracted from the bacterial sources *R. capsulatus* and *R. sphaeroides* have been previously reported [19,22,52]. These have revealed a remarkable flexibility about the molybdenum center of the enzyme, with Bennett et al. reporting four major signal types from the *R. capsulatus*-derived protein [22]. The Mo(V) EPR signals from these two bacterial types display similar lineshapes and parameters under similar conditions. The signals have been shown to change only slightly with changes in pH and buffer related anions [19,22].

3.2.1.1. Low-g Mo(V) EPR active species

Dithionite reduction of DMSO reductase in Bicine (N,N-bis(2-hydroxyethyl) glycine) buffer, pH 8.2, produces Mo(V) EPR signals with g_{av} values of approximately 1.96 (Fig. 4a) [22,69,95]. Computer simulation [51] of this spectrum with an orthorhombic spin Hamiltonian (Eq. (1)) and the parameters in Table 3 revealed that the majority of resonances are attributable to an Mo(V)-centered signal (Fig. 4b) previously described and designated the Low-g Type-1 signal [22]. Since the magnitude of Δg ($\Delta g = g_i - 2.00232$; $i = x,y,z$) decreases as the number of sulfur atoms coordinated to the molybdenum ion increases [39,41,42], a consequence of spin–orbit coupling from sulfur, the Low-g Mo(V) species are expected to have a reduced number of sulfur atoms ligated to the Mo(V) center. A comparison of the spin Hamiltonian parameters for the Mo(V) Low-g Type-1 signal seen in the dithionite-reduced DMSO reductase with other Mo(V) enzyme-based EPR signals indicates that it is very similar to that of the Slow (nitrate) signal from desulfo xanthine oxidase (XO) (Table 3) [13,22,67,68]. The similarity between the *g*-matrices for the two signals implies that the species responsible for both signals must possess similar Mo coordination spheres [22,69,95], as these parameters are highly sensitive to changes in geometry and ligation. Since the xanthine oxidase family of enzymes contains only one molecule of MPT (Fig. 3a) [1–3,11,12], it is highly likely that the DMSO reductase Low-g Type-1 species has one molecule of MGD coordinated (through the dithiolene S atoms) to the molybdenum ion. As discussed above, X-ray crystallographic data for the five-coordinate structure of DMSO reductase reveals that the dithiolene sulfurs from the P-MGD remain coordinated to the molybdenum ion while the dithiolene sulfurs of the Q-MGD are outside the molybdenum coordination sphere [61].

The presence of an anion in the coordination sphere of the species responsible for the Slow (nitrate) signal of desulfo XO was suggested by EPR [67,68]. Bennett et al. [22] proposed that an anionic ligand is also present in the DMSO reductase Low-g Type-1 signal-giving species. This anion must presumably originate from the buffer solution, as the Low-g Type-1 signal was only observed using DMSO reductase samples that had been dialyzed into Bicine pH 8.0 buffer prior to anaerobic reduction with dithionite. Hepes (4-(2-hydroxyethyl)-1-piperazineethanesul-

fonic acid) has been shown crystallographically to bind at the active site of DMSO reductase [61].

^{95}Mo enrichment of DMSO reductase has enabled the determination of the ground-state molecular orbital and allowed a comparison of the ^{95}Mo hyperfine matrix for the enzyme with model Mo(V) complexes and other molybdoenzymes, in order to gain insights into the structure of the Low-g Type-1 center [69,95]. Reduction of ^{95}Mo-enriched DMSO reductase with sodium dithionite produced the spectrum shown in Figure 5a, attributable to the Low-g Type-1 Mo(V) species. The three resonances at $B = 330.7$, 336.7, and 340.0 mT (labeled with vertical lines) correspond to a sulfur-centered radical (§3.2.1.2). Computer simulation [51] of the spectrum with an orthorhombic spin Hamiltonian (Eq. (1)) failed to reproduce the resonant field positions and the spectral lineshape. However, lowering the symmetry to triclinic and employing the spin Hamiltonian parameters listed in Table 3 produced the spectrum shown in Figure 5b. The orientation of the principal ^{95}Mo hyperfine components (Euler angles χ, ρ, and τ) with respect to the g-matrix [51], whose components are assumed to lie along the x, y, and z axes, are shown in Figure 5c. A comparison of the ^{95}Mo hyperfine matrices (Table 3) for the Low-g Type-1 and desulfo xanthine oxidase Mo(V) center reveals very similar principal ^{95}Mo hyperfine components, though the largest value (66.3×10^{-4} cm^{-1}) is associated with a different g-value, and the orientation (Euler angles) of the components is different (Table 3). While the symmetry for the Slow Mo(V) center in desulfo xanthine oxidase approximates monoclinic (C_s), with a vertical plane of symmetry bisecting the Mo–S and Mo–O bonds (Fig. 3a) [12], the symmetry for the Low-g Type-1 Mo(V) species in DMSO reductase is lower and triclinic (C_1), a consequence of the five-coordinate distorted geometry (Fig. 3c) [23]. In the Low-g Type-1 Mo(V) species, there is an approximate vertical plane of symmetry that runs through the Mo=O bond to the oxygen atom of the ethoxy group of the Bicine molecule positioned near, or coordinated to, the molybdenum atom. This plane bisects the dithiolene moiety and the angle formed by the Mo–OH and Mo–O (Ser) bonds (Fig. 3c). Assuming a C_s symmetric site with the x and y axes placed between the metal–ligand bonds, the molecular orbitals can be written as [39,70]

$$\Psi^{a'*}_{X^2-Y^2} = \alpha\,[a_1 d_{X^2-Y^2} + b_1 d_{XZ} + c_1 d_{Z^2}],$$
$$\Psi^{a'*}_{XZ} = \beta\,[a_2 d_{XZ} + b_2 d_{X^2-Y^2} + c_2 d_{Z^2}],$$
$$\Psi^{a'*}_{Z^2} = \gamma\,[a_3 d_{Z^2} + b_3 d_{X^2Y^2} + c_3 d_{XZ}], \qquad\qquad (2)$$
$$\Psi^{a''*}_{XY} = \delta\,[a_4 d_{XY} + b_4 d_{YZ}],$$
$$\Psi^{a''*}_{YZ} = \varepsilon\,[a_5 d_{YZ} + b_5 d_{XY}],$$

where, by definition, $a_q > b_q$, c_q ($q = 1,2,...$). Here covalency appears only implicitly through the metal-centered orbital coefficients α, ..., ε. Since the molecular X and Y axes are placed between the metal–ligand bonds (Fig. 6), the ground-state wavefunction is $\Psi^{a'*}_{X^2-Y^2}$ (SOMO = singly occupied molecular orbital). The ground-state

molecular orbital $\left(\Psi_{x^2-y^2}\right)$ involves an admixture of the $d_{x^2-y^2}$ orbital with the d_{xz} and d_{z^2} orbitals and for the Slow Mo(V) center in desulfo xanthine oxidase, $a_1 > b_1$ and $c_1 \sim 0$, i.e.. the admixture of the d_{xz} into $d_{x^2-y^2}$ results in a rotation of the $d_{x^2-y^2}$ orbital about the y axis [39,42].

A multifrequency EPR study (Fig. 6) of the Mo(V) C_s symmetric complexes Tp*MoS(cat) and Tp*MoO(cat) (Tp* = hydrotris(3,5-dimethylpyrazol-1-yl)borate, cat = catechol) also reveals that $g_{zz} < g_{yy} < g_{xx} < g_e$ and $A_{z'z'} > A_{x'x'} \approx A_{y'y'}$, and a non-coincidence angle of $\beta = 33°$ (Table 3) [39]. Multifrequency EPR, especially at S-band, was found to be particularly valuable in the unambiguous assignment of the spin Hamiltonian parameters in these low-symmetry complexes. The weaker π-donor terminal sulfido ligand yields a smaller SOMO–LUMO gap, and reduced g-values for the thiomolybdenyl complexes compared with molybdenyl analogues supports existing crystallographic and EPR data for an equatorially coordinated oxo group in the active site of xanthine oxidase. In a subsequent paper [42], Drew and Hanson employed density functional theory (ORCA) [36] to calculate the principal components of the g and ^{95}Mo (A) matrices and their relative orientations and found that the ground state singly occupied molecular orbital was indeed $d_{x^2-y^2}$ based and the orientation of the A matrix is directly related to the orientation of this orbital (rotated about the y axis through mixing of the d_{xz} as predicted from simple crystal field theory). The largest single contribution to the orientation of the g-matrix arises from spin–orbit coupling of the d_{YZ}-based lowest-unoccupied molecular orbital into the ground state. A number of smaller, cumulative charge transfer contributions augment the d–d contributions. Employing Tp*MoO(bdt) as a model system, Drew and Hanson also showed that the a non-coincidence angle β was directly related to the dithiolene fold angle and that a twisting of the dithiolene unit could lead to triclinic symmetry, as is observed for Low-g Type-1 species and found crystallographically in the pentacoordinate oxidized enzyme structure [71].

3.2.1.2. Observation of a novel sulfur-centered radical signal

In addition to the Low-g Type-1 Mo(V) EPR spectrum produced upon reduction of DMSO reductase with dithionite, a spectrum consisting of three resonances with principal g-values all greater than or equal to 2.000 (Table 3) was observed (Fig. 4a) [69,95]. A similar spectrum (Fig. 5a) was observed when the molybdenum ion in DMSO reductase was enriched with ^{95}Mo, indicating that the unpaired electron is not located on the molybdenum ion. Computer simulation [51] of this spectrum with an orthorhombic spin Hamiltonian (Eq. (1)) and the parameters $g_x = 1.9999$, $g_y = 2.0182$, $g_z = 2.0545$, and $A_2(^{95}$Mo$) = 5.0 \times 10^{-4}$ cm^{-1} yields the spectrum shown in Figure 4c. A computer simulation of the experimental spectrum (Fig. 4a) is obtained by adding Figures 4b and 4c (multiplied by 0.938) to obtain the spectrum in Figure 4d. The large g-anisotropy, long T_1, and very small ^{95}Mo hyperfine coupling indicate that the unpaired electron is centered on a dithiolene sulfur atom. A comparison of the g-matrices for this radical with those from an Ni(II)

dithiolene radical complex [72], a transient perthiyl (R–S–S·⁻) radical of ribonu-cleoside-diphosphate reductase [73], and low-temperature EPR studies of protein thiyl radicals [74,75] (Table 3) also indicate that the orthorhombic EPR spectrum can be attributed to a sulfur-centered dithiolene radical and not to a carbon-, nitro-gen-, or oxygen-centered radical. Mössbauer studies of [Au(II)(bpy)(L₁)] and its one-electron oxidized complex ([Au(III)(bpy)(L₁·)]) demonstrated that the addi-tional electron was ligand- (sulfur-) rather than metal-centered [79]. A comparison of the g-matrices of the sulfur-centered radical with the series of dithiolene com-plexes ([Co(III)(L₃·)], [Pd(II)(bpy)(L₁·)], and [Au(III)(bpy)(L₁·)]) reveals that they are very similar, and thus the unpaired electron must be located on a dithiolene sulfur. The g- and A-anisotropy (Table 3) are also inconsistent with an SO_2^- radical [76]. A comparison of the experimental (Fig. 4a) and simulated (Fig. 4d) spectra reveals that there are at least two resonances (labeled ∗ in Fig. 4a) that do not arise from either the Low-g Type-1 Mo(V) species or the sulfur radical. A comparison of the EPR spectra from naturally abundant molybdenum (Fig. 4a) and [95]Mo-enriched (Fig. 5a) Low-g Type-1 Mo(V) species indicates that these resonances do not arise from molybdenum hyperfine coupling. However, it is possible that these resonances arise from a dipole–dipole coupled ($S = 1$) center involving both the Low-g Type-1 Mo(V) center and the sulfur-centered radical [69,95].

3-pulse electron spin echo envelope modulation (ESEEM) [80,81] spectra of [95]Mo-enriched samples of dithionite-reduced DMSO reductase in 50 mM Bicine, pH 8.0, were measured at three different magnetic fields ($B = 337.0$, 341.4, and 345.0 mT, corresponding to the g-values ($g_z = 2.0545$, $g_y = 2.0182$, and $g_x = 1.9999$) for the sulfur-centered radical), and revealed several overlapping peaks between 1 and 6 MHz and a peak corresponding to the proton Larmor frequency between 14 and 15 MHz. The latter peak at the three different orientations exhibits slight broadening, indicating weak coupling (<1 MHz) to one or more protons. The peaks between 1 and 6 MHz arise from ^{14}N hyperfine coupling but cannot be easily assigned. HYSCORE [80–82], a two-dimensional technique, correlates the transi-tions from the $M_S = -1/2$ manifold, with those from the $M_S = +1/2$ manifold, sim-plifying the analysis [80–82]. The HYSCORE spectra measured at the three orien-tations (Fig. 7a, 342.2 mT; Fig. 7b, 337.1 mT, and Fig. 7c, 345.0 mT) reveal strong ridges in the (−+) and (+−) quadrants and a number of cross peaks (2–5 MHz, 2–5 MHz) in the (++) quadrant that arise from ^{14}N hyperfine coupling. The weak pro-ton coupling was also evident in the HYSCORE spectra. The notation of Dikanov et al. [83] was employed to identify the features in the HYSCORE spectrum. For example, the ridges centered at (∓5.0, ±9.2) MHz refer to ridges centered at (−5.0, +9.2) MHz and (−9.2, +5.0) MHz.

Of the features in the HYSCORE spectra that are attributable to ^{14}N hyperfine coupling, only the well-resolved pair of ridges at (∓5.5, ±9.2) MHz can be defini-tively assigned. These peaks arise from correlations between the double quantum transitions in the two-electron spin manifolds. These peaks are typically well re-solved in powder HYSCORE spectra, as the frequencies of these transitions are only weakly dependent on the anisotropic terms in the spin Hamiltonian. The other peaks in the HYSCORE spectra are attributed to correlations between single quan-

tum transitions but cannot be easily assigned without more knowledge of the field dependence of the frequencies.

The double quantum peaks in the HYSCORE spectra at the three orientation-selective field positions can be used to estimate the diagonal elements of the nitrogen hyperfine matrix in the g-matrix coordinate system [84]. Using Eq. (5.1) given by Dikanov et al. [84] and the center of the ridges at the three field positions, we obtain the values ($A_x = 6.33$, $A_y = 6.36$, and $A_z = 6.08$ MHz). It is likely that the principal axes of the g- and nitrogen hyperfine matrices are not colinear. The anisotropic contribution to the nitrogen hyperfine interaction will therefore be slightly larger. This is supported by the elongation of the double quantum ridges at each of these field positions.

The frequencies of the double quantum cross peaks (compare Figs. 7a–c with Fig. 7d) were reproduced with the following spin Hamiltonian [33–35]:

$$H = \sum_{i=x,y,z} (\beta B_i \cdot g_i \cdot S_i + S_i \cdot A_{iN} \cdot I_{iN})$$
$$+ P_N (I_{z,N}^2 - \tfrac{1}{3} I_N (I_N + 1)) + \eta (I_{x,N}^2 - I_{y,N}^2) - \gamma_N B \cdot I_N , \qquad (4)$$

and the spin Hamiltonian parameters $P_N = -1$ MHz, $\eta = 0$, $A_{iso} = 6.7$ MHz, $A_x = 7.5$ MHz, $A_y = 6.5$ MHz, and $A_z = 6.08$ MHz. Although the anisotropy in the hyperfine interaction cannot be accurately defined from these experiments, its magnitude is relatively small ($A'_i = 0.8, -0.2, -0.7$ MHz, where $A'_i = A_i - A_{iso}$, $i = x,y,z$). This set of parameters can also explain the origin of the other peaks in the (–+) and (++) quadrants (Fig. 7).

These results are consistent with the X-ray structures determined by Schindelin et al. [60], Schneider et al. [61], and Li et al. [22], where the longer Mo–S2 (Q-MGD) distance of 3.1 Å in the structure of Schindelin et al. indicates a species in which the molybdenum ion is in the process of moving away from the Q-MGD, while the pentacoordinate structures [22,61] describe a species where the Q-MGD is fully removed from the coordination sphere of the molybdenum atom. With these observations in mind, the dithiolene S of the Q-MGD moiety is an excellent candidate for the sulfur-centered radical.

3.2.1.3. Mechanism of formation of the low-g type-1 species and the sulfur-centered radical

A plausible mechanism for the reduction of Mo(VI) to Mo(IV) involving proton-coupled electron transfer has been established from extensive studies of oxomolybdenum enzymes, especially the xanthine oxidase family of enzymes and their synthetic analogues [1–3,30–32,38–41]. By analogy with the desulfo form of xanthine oxidase, a mechanism involving successive proton-coupled electron transfer for the reduction of the five-coordinate dioxo Mo(VI) form of DMSO reductase has been proposed (Fig. 8a). The Mo(V) species (Species 2) corresponds to the Low-g Type-1, which has an unpaired electron in the ground-state molecular orbital $\Psi_1 = a[a_1 \, d_{x^2-y^2} + b_1 \, d_{XZ} + c_1 \, d_{z^2}]$ and strongly interacts with a proton, as-

sumed to arise from the protonation of the equatorial oxo group. A similar mechanism can be derived for the six-coordinate Mo center (Fig. 8b), in which successive one-electron reduction of the native (Mo(VI)) enzyme (Species 4) to the hexacoordinate Mo(V) species (Species 5) and then to the pentacoordinate Mo(IV) species (Species 6) occur. However, Species 5 corresponds to the High-g Split Mo(V) species observed by Bennett et. al. and not the Low-g Type-1 species [22].

An alternative reductive pathway (Fig. 8b) involves intramolecular electron transfer of the (native, Mo(VI)) enzyme (Species 4) to give Species 5, which can subsequently undergo protonation of the oxo group to give Species 10. Interestingly, the reduction of Species 4 to Species 10 also involves coupled proton–electron transfer. One electron reduction of Species 10 can yield the Mo(IV)–sulfur-centered radical (Species 11) or the Low-g Type-1 Mo(V) species (Species 12), in which one of the dithiolene moieties is no longer coordinated to the molybdenum ion. The sulfur-centered radical (Species 11) may also be formed via intramolecular electron transfer of the High-g Split Mo(V) species (Species 5).

Resonance delocalization of the unpaired electron on the sulfur atom (Species 11) onto the pyranopterin ring system (Fig. 9) would undoubtedly enhance the stability of this species. Importantly, this resonance delocalization predicts hyperfine coupling to a single nitrogen atom (N8), which was found experimentally from the HYSCORE spectra. The magnitude of A_{iso} (^{14}N), 6.7 MHz, indicates that the highest occupied molecular orbital has 0.4% s-character and, assuming $A_{aniso} = 1$ MHz, 1.8% p-character. This is inconsistent with dipole–dipole coupling to the nitrogen(s) of His-643, Trp-116, and N(5), which are between 3.4 and 5.9 Å away from the sulfur atom containing the unpaired electron and would only be expected to contribute less than 0.14 MHz to the anisotropy of the ^{14}N hyperfine matrix.

Both Species 8 and 10 formerly contained two unpaired electrons (one on each of the molybdenum and sulfur atoms), and it would be expected they would be either exchange or dipole–dipole coupled. The resonances identified by an asterisk in Figure 4a may indeed arise from dipole–dipole coupling of these two unpaired electrons.

The formation of the sulfur-centered radical in the native (resting, Mo(VI)) enzyme may occur through oxidation of Species 10 to yield Species 9, or alternatively, through a one-electron oxidation of Species 7 and subsequent protonation, to yield Species 9. The lack of resonances attributable to a dipole–dipole coupled center (compare Figs. 4a and 5a) indicates that the oxidation state of the molybdenum ion is either +4 or +6, with the latter more likely, as proposed by Species 9. Resonance stabilization of Species 12 is also likely to increase the lifetime of the sulfur-centered radical. The presence of a small proportion of Species 9 in the native enzyme suggests that the two species (4 and 9) are in equilibrium, and perhaps the dissociation of the dithiolene sulfurs represents the first step in the reductive half of the reaction cycle.

X-ray crystallographic data of oxidized DMSO reductase shows that the pyran ring deviates from the plane of the pyrazine ring by 30° in the P-MGD and 50° in the Q-MGD moiety, suggesting that they are not identical [1]. In support of this, a study of the oxidation state of the modified pterin in the extracted cofactor of

DMSO reductase from *R. capsulatus* revealed that it is possible that each of the two MGD moieties are in different redox states [85]. This was achieved by comparing the absorption spectrum of the extracted cofactor with pterin standards of known redox state and measuring the extent of reduction of 2,6-dichlorophenolindophenol (DCPIP) by the pterins. The absorption spectrum of the extracted cofactor is also consistent with the presence of both dihydro- and fully reduced tetrahydro-pterin species. The results of treatment with DCPIP indicated the presence of an MGD moiety containing a pyrazine ring at the oxidation level of a dihydropterin and an MGD species containing a pyrazine ring at the oxidation level of a fully aromatic pteridine. From the above results, the P-MGD was presumed to be in the unreactive, fully oxidized state whilst the Q-MGD was proposed to be in the saturated, reactive dihydro state, as reflected in the labile nature of the Mo–S bonds in the Q-MGD determined by X-ray crystallography [60,61].

A study by Luykx et al. [86] reported a molybdopterin-based $S = \frac{1}{2}$ radical signal appearing in the EPR spectra of oxidized aldehyde dehydrogenases from *Comamonas testosteroni* and *Amycolatopis methanolica*. Hyperfine coupling constants (Table 3) were consistent with the presence of an Mo(VI)–trihydropyranopterin radical, with the N5 atom (pterin nomenclature) of the pterin moiety hydrogen bonding to two locations in the protein structure. It was proposed in this study that the molybdopterin cofactor could behave as a dinuclear redox center, due to the electron spin density being present at the molybdenum atom and/or around the N5 atom of the pterin. The role in electron transfer of the pterin ring system in these enzymes is proposed to be that of a one-electron carrier, capable of transferring electrons to a nearby $[2Fe–2S]^{2+/1+}$ cluster as it cycles between trihydropyranopterin and tetrahydropyranopterin redox states. The presence of a pterin-based radical in aldehyde dehydrogenases and a sulfur-centered radical in DMSO reductase strongly support the involvement of the pterin moiety in electron transfer between the native electron donor of each enzyme (DorC in the case of DMSO reductase) [87,88] and the molybdenum active site.

Another study [89] that utilized gas-phase photoelectron spectroscopy (PES) probed the covalency of Mo–S dithiolene interactions through the use of model Mo(VI) complexes in which a dithiolene group is ligated to the molybdenum ion. The stabilizing nature of the Mo–S interaction was proposed to be the principal function of the dithiolene moiety and was termed the "electronic buffer" effect, since it would dampen the effects of change in metal ion oxidation state and oxygen atom transfer during the catalytic cycle of molybdoenzymes. These findings seem to indicate that, even if the pterin moiety is not directly involved in formal electron transfer that takes place during the catalytic cycle of these enzymes, it is most likely involved in dissipating charge after electronic changes around the metal center, such as the loss or gain of an axial ligand (e.g., an oxo group in DMSO reductase). Indeed, in a review of protein-based radicals in metalloproteins, it was suggested that the primary function of these radicals was to neutralize the charge on the accompanying metal centers [90], which could be important in stabilizing

reaction intermediates following coordination of DMSO to the molybdenum center during catalysis.

The crystal structure of aldehyde oxidoreductase (Mop) from *Desulfovibrio gigas* [1,91] exhibits attributes that imply that DMSO reductase is not the only molybdoenzyme to possess facile dithiolene binding. The structure of oxidized Mop contains a dithiolene S–S distance of 3.0 Å, compared with 3.5 Å in the structure of the reduced species. The presence of a partial disulfide bond in the oxidized enzyme, which is broken upon formation of the reduced species, is proposed to represent evidence pointing to the pterin moiety having been incorporated into the structure of molybdoenzymes to modulate the redox potential of the molybdenum atom.

3.2.1.4. The borohydride signal

The Borohydride Signal is produced by treating DMSO reductase with benzyl viologen (BV$^{\cdot+}$) in the presence of sodium borohydride (NaBH$_4$), but is unable to be generated using any other reductant [22]. Formation of this species results in an approximately 40% loss of enzyme activity. The species responsible for the signal has been shown to contain anywhere from 2 to 30% Mo(V) and is resistant to oxidation; however, it is abolished upon prolonged dialysis. Treatment of the sample displaying the borohydride signal with dithionite results in replacement of this signal with transient Mo(V) signals that have not been well studied; however, reoxidation of these samples with oxygen has been shown to regenerate the borohydride signal.

3.2.1.5. High-g unsplit type-1 and type-2

Room-temperature EPR potentiometry was used to directly monitor the appearance and disappearance of the paramagnetic (S = 1/2) Mo(V) species during reduction of the Mo(VI) species to Mo(IV) and its reoxidation [19,56,92–94]. EPR spectra observed in a typical titration in the reductive direction are shown in Figure 10 [94,95]. A plot of the integrated intensity or the relative amplitude of the g_z resonance was plotted against the applied potential (Fig. 11a) [92,94]. This was fitted with the Nernst equation and a biphasic reduction to produce the results listed in Table 4. A comparison of the Mo(VI/V) midpoint potentials at pH 6.0 and 8.0 (Table 4) indicates that the Mo(VI/V) redox couple is pH dependent, involving a single proton. Interestingly, whilst this redox couple involves protonation, the continuous wave EPR spectrum of the Mo(V) species (High-g Unsplit Type-2, Fig. 10) does not show any hyperfine coupling from strongly coupled protons. Following reduction of the enzyme to Mo(IV), an oxidative titration was performed and Figure 11b shows that the redox-integrated signal intensity of Mo(V) at a given redox potential species was similar to that of the Mo(V) species during reductive titration [92,94]. However, a notable difference was that, upon reoxidation, the Mo(V) species generated was the High-g Split form of DMSO reductase (Fig. 11c). The hyperfine coupling in this signal-giving species has been demonstrated to arise from a strongly coupled proton [22,96]. In order to characterize the High-g Unsplit species

further, [95]Mo isotope enrichment was undertaken in conjunction with CW-EPR spectroscopy of the Mo(V) species and also undertook high-resolution pulsed EPR studies of the native enzyme [94,95].

Reduction of DMSO reductase by dimethylsulfide (DMS) has been shown crystallographically and spectroscopically to produce a "pink" form of the enzyme in which the Mo ion is in the +4 oxidation state [24]. Furthermore, DMS coordinates through the terminal oxo ligand in the oxidized enzyme to yield a coordinated DMSO molecule. Anaerobic oxidation of this "pink" form of the enzyme with half an equivalent of the oxidant DCPIP yields the spectrum shown in Figure 12a [94,95]. Solvent exchange into ^2H_2O yields the spectrum shown in Figure 12b. Whilst the greater spectral resolution (narrower linewidths) in Figures 12b versus that of 12a (^1H_2O) may at first glance suggest the presence of proton hyperfine coupling, the correct interpretation is that the lineshape differences and the appearance of additional resonances (at high field) result from different proportions of the High-g Unsplit Type-1 and Type-2 species in these samples [94,95]. Addition of phenazine ethosulfate (PES) in conjunction with 2,6-dichlorophenolindophenol (DCPIP) produces an EPR spectrum (Fig. 12c) arising from a single species, the High-g Unsplit Type-2 species [94,95]. Clearly, PES facilitates electron transfer to the Mo center, pushing the equilibrium involving the High-g Unsplit Type-1 and -2 Mo(V) species to the High-g Unsplit Type-2 species, and this is consistent with the requirement for PES for rapid turnover of the enzyme when DMS is used as a reductant [97]. Computer simulation [51] of the High-g Unsplit Type-1 and Type-2 species (Mo ($I = 0$) resonances) using an orthorhombic spin Hamiltonian (Eq. (1)) and the spin Hamiltonian parameters in Table 5 produced spectra for the High-g Unsplit Type-1 (Fig. 12d) and Type-2 species (Fig. 12e) [94,95].

Isotopic enrichment with ^{95}Mo ($I = 5/2$) to 96.8% increases the intensity of the hyperfine resonances and, in conjunction with computer simulation, allows determination of the A(^{95}Mo) hyperfine matrix and the identity of the ground-state molecular orbital containing the unpaired electron. An X-band EPR spectrum of ^{95}Mo-enriched DMSO reductase reduced anaerobically with DMS and subsequently oxidized with DCPIP, but without PES, is shown in Figure 13c [94,95]. A comparison of Figures 13a and 13c reveals that the predominant species giving rise to the EPR spectrum in Figure 13c is the High-g Unsplit Type-2 species, though there is a significant amount of the High-g Unsplit Type-1 species present. Computer simulation of the spectrum arising from the High-g Unsplit Type-2 species (Fig. 13c) employed an orthorhombic spin Hamiltonian (Eq. (1)) and the spin Hamiltonian parameters listed in Table 5 [51,94,95]. Whilst the resonant field positions for the simulated spectrum (Fig. 13d) are accurate, the intensities in the low-field region do not accurately reproduce those observed experimentally, a consequence of the presence of the High-g Unsplit Type-1 species.

While the redox potentiometric titrations [92] indicated that the Mo(VI/V) couple was pH dependent, in agreement with that obtained from cyclic voltammetry [93], the continuous wave EPR spectrum of the High-g Unsplit Type-2 species did not resolve any strongly coupled proton hyperfine coupling [94,95]. High-

resolution pulsed EPR spectroscopy was employed to probe the origin of the pH dependence of the Mo(VI/V) redox couple. A pulsed field-swept EPR spectrum (Fig. 14a) of the High-g Unsplit Type-2 species was generated by reducing DMSO reductase with DMS and subsequently oxidizing the enzyme with DCPIP in the presence of PES [94,95]. HYSCORE spectra (Figs. 14b,c) were measured along the perpendicular ($B_\perp$ = 349.2 mT) and parallel ($B_\parallel$ = 352.2 mT) directions of g, respectively. The positive quadrant of the HYSCORE spectrum along the perpendicular region reveals cross peaks at 12.7, 17.3 and 17.3, 12.7 MHz attributable to ^{1}H hyperfine coupling and a peak along the diagonal at 2.99 MHz corresponding to the Larmor frequency for ^{14}N at 349.2 mT. The signal-to-noise is not sufficient (after scanning for 100 scans (30 shots per loop)) to accurately determine the ^{14}N hyperfine coupling at this magnetic field. The *tau* values were optimized to eliminate the blind spots for the nitrogen hyperfine couplings, which produces nodes in the proton cross peaks (Fig. 14b) [94,95].

Reduction of DMSO reductase with sodium dithionite and then poising the potential at +56 mV with potassium ferricyanide yields an EPR spectrum consisting of the High-g Unsplit Type-2 and High-g Split Mo(V) species (Fig. 15a). Subsequent addition of DMSO to the sample results in an EPR spectrum of the High-g Unsplit Type-2 Mo(V) species (Fig. 15b). The signal lost upon addition of DMSO (utilizing difference spectra) was the pure High-g Split signal (Fig. 15c). This indicates that the High-g Split Mo(V) species is involved in the oxidative half reaction [92,94].

In agreement with previous observations, the High-g Unsplit Type-2 signal-producing species is formed either upon reductive treatment of DMSO reductase [19,59,97] or following incubation of the DMS-reduced form of DMSO reductase with PES/DCPIP [94,95,98]. The High-g Unsplit Type-2 Mo(V) species was named because there was no evidence from the CW X-band EPR spectrum for hyperfine coupling associated with an exchangeable proton close to the molybdenum. However, 3-pulse ESEEM and HYSCORE studies revealed weak ^{14}N and ^{1}H hyperfine coupling whose origin will be described below [94,95].

The spin Hamiltonian parameters determined for the High-g Unsplit Type-2 species (Table 5) show that $g_\perp > g_\parallel$, which is unusual for oxomolybdenum(V) complexes that normally have an unpaired electron in a $d_{x^2-y^2}$ ground-state molecular orbital (x and y principal axes lie between the metal ligand bonds), leading to $g_\parallel$ being greater than $g_\perp$ [38–40]. However, for non-oxo molybdenum(V) complexes such as $[Mo(abt)_3]^-$ [30,38] (abtH$_2$ = o-aminobenzenethiol) and $[Mo(S_2C_2H_2)_3]^-$ [99,100], which have a trigonal prismatic geometry (D$_{3h}$ symmetry), the unpaired electron is located in a 4a1' molecular orbital (see Fig. 2 in [32]), which involves the overlap of the Mo d_{z^2} atomic orbital with a set of ligand p$_Z$ atomic orbitals [100]. The net result from an EPR perspective is that $g_\perp$ is greater than $g_\parallel$, as observed experimentally for $[Mo(abt)_3]^-$ (Table 5) [30,38]. $g_\perp$ is also greater than $g_\parallel$ for the molybdenum(V) analogue of amavadin [101,102] and the molybdenum (V) complexes [39,42] Tp*MoO(cat) and Tp*MoS(cat) (Table 3). However, the catecholate complexes exhibit monoclinic C$_s$ symmetry, producing a ground-state molecular orbital that involves an admixture of the $d_{x^2-y^2}$ orbital with

the d_{XZ} orbital. This results in a rotation of the $d_{x^2-y^2}$ -based orbital about the Y axis and the presence of a noncoincident angle, β, between the g_Z, A_Z and g_X, A_X principal axes [42]. Computer simulation of the High-g Unsplit Type-2 spectrum (Table 5) did not require inclusion of a noncoincident angle, indicating that the unpaired electron is in a d_{z^2} -based molecular orbital [94,95].

Further insights into the structure of the High-g Unsplit Type-2 Mo(V) species can be obtained from the high-resolution X-ray crystal structure of DMSO reductase. The magnitude of the g- and A-values and the observed g-anisotropy (Table 5) [41,42] indicate that both the P-MGD and Q-MGD dithiolenes are coordinated to the molybdenum atom and that the geometrical arrangement of the ligating atoms is trigonal prismatic [23]. In addition, the lack of strong proton hyperfine coupling indicates that the oxo group is not protonated. Consequently, the six-coordinate geometry of the Mo(VI) species (Fig. 3a) is retained upon reduction of the resting enzyme to Mo(V) and the desoxo Mo(IV) species. Closer examination of the X-ray crystal structure [23] reveals that the indole nitrogen of Trp-116 is hydrogen bonded to the oxo group (Fig. 1a), which may explain the origin of the ^{14}N and ^{1}H hyperfine coupling observed in the ESEEM and HYSCORE spectra since the unpaired electron is in a d_{z^2} -based ground state with the z axis lying along the Mo=O triple bond.

Small quantities of the High-g Unsplit Type-1 Mo(V) species were also observed in the resting form of DMSO reductase and as a minor Mo(V) species formed during DMS reduction of DMSO reductase and subsequent reoxidation of the enzyme with DCPIP [94,95]. In comparison with EPR signals generated by other oxomolybdenum enzyme species (Table 5), the High-g Unsplit Type-1 signal shows most similarity to the High-pH signal from *E. coli* nitrate reductase [22,103,104]. However, the species responsible for the High-pH signal shows weak superhyperfine coupling to a single exchangeable proton [103]. Since the g- and ^{95}Mo hyperfine matrices for the High-g Unsplit Type-1 and Type-2 species are similar, they are expected to be structurally similar. It has been previously observed that the buffer solution used to measure the EPR spectra of different Mo(V) signals from DMSO reductase affects the lineshape (g-values) of the High-g Unsplit Type-1 spectrum. It was proposed that the binding of a buffer anion to the molybdenum atom was the cause of these observations [22]. Binding of a buffer ion to the trigonally prismatic molybdenum atom in the High-g Unsplit Type-1 Mo(V) species is therefore proposed to cause the difference seen between this signal and that generated by the High-g Unsplit Type-2 species. Hepes has been found to bind close to the Mo atom in the five-coordinate structure of DMSO reductase.

Since the High-g Unsplit Type-1 signal is not generated during EPR potentiometric titrations, this species is expected to be kinetically unfavorable, interconverting to the catalytically competent High-g Unsplit Type-2 species by loss of a buffer ion. This proposal is supported by the observation that treatment of the DMS-reduced form of DMSOR with DCPIP in the presence of PES forms only the High-g Unsplit Type-2 species. Clearly, PES facilitates electron transfer to the Mo center, pushing the equilibrium set up between the two High-g Unsplit species to-

ward formation of the High-g Unsplit Type-2 species. These data are consistent with the conclusion that the High-g Unsplit Type-1, present in small quantities in the oxidized resting enzyme, represents a dead-end form of the enzyme that is recalcitrant toward oxidative treatment with oxygen or DMSO but can be "redox cycled" using the one-electron carrier PES [97].

In the catalytic cycle of DMSO reductase, the conversion of DMSO reductase from an Mo(VI) to an Mo(IV) species is considered to proceed via an Mo(V) form. It has been assumed that this Mo(V) species was defined spectroscopically as giving the High-g Split EPR signal. This species exhibits proton superhyperfine coupling due to the presence of a hydroxyl ligand formed by protonation of an Mo-oxo group upon reduction of the enzyme [19,22,98]. However, we note that there is no direct kinetic evidence for the formation of this species during the reaction cycle, since there is no rapid freeze data for the observation of the Mo(V) species formed using the native biological electron donor cytochrome-DorC [87,88]. We note that the High-g Split EPR signal is easily generated by reduction of the Mo center in DMSO reductase to its Mo(IV) state followed by partial oxidation by oxygen or ferrocyanide during the oxidative half of a redox titration. In contrast, the High-g Unsplit Type-2 species is generated during a reductive redox titration (Fig. 10), although upon oxidation it forms the High-g Split species.

Although the conversion of an Mo(VI)-oxo species to an Mo(IV)-desoxo species without the formation of an Mo(V)-hydroxo form is not intuitively the most obvious catalytic route, there are reasons why such a route might be beneficial during catalysis. It is interesting to note that the more distantly related DMSO reductase from *E. coli* (DmsABC) exhibits a High-g Unsplit Type-2 EPR signal that does not undergo a pH-dependent conversion to a High-g Split form across a pH range of 5–9 [56]. In this case, there is no evidence that formation of an Mo(V)-OH species has any role in catalysis. More recent protein film voltammetry studies of DmsABC [105] have shown that there is a striking correlation between the region of optimal catalytic activity and the redox potential for maximal formation of the Mo(V) species as measured using EPR spectroscopy. This observation, as well as the pH dependence of catalytic turnover (as measured using cyclic voltammetry), indicates that the optimal reaction pathway involves conversion of Mo(VI) to an Mo(IV)-H$^+$ state. If electron transfer is too rapid relative to proton transfer, this results in formation of an Mo(IV) state that is catalytically incompetent. The conclusion of Armstrong et al. [105] is that crucial steps in the reaction mechanism are directed through the Mo(V) state, where rearrangement of the active site can occur.

Since the High-g Unsplit Type-2, the High-g Split, and the Mo(IV) species are in equilibrium (Figs. 15 and 16), removal of the Mo(IV) will readjust the equilibrium according to Le Chatelier's principle. Since k_4 is greater than k_3 (Fig. 16), the High-g Split species is lost from the equilibrium (Fig. 16; Mo(V)-OH, bolded). This is consistent with the observation that the High-g Split EPR signal is observed upon oxidation (air, Fe(CN)$_6$, NO$_2^-$) of reduced Mo(IV) DMSO reductase and is clearly not involved in the reductive side of the catalytic mechanism [94,95].

Recent density functional theory calculations [106] have shown that the oxygen atom transfer reaction of DMSO reductase with dimethylsulfoxide more than likely occurs by way of an associative mechanism, with the oxygen atom of DMSO forming a bond with the molybdenum atom of DMSO reductase. This form is then converted to a transition state, which transfers the oxygen atom of DMSO to the molybdenum atom, while severing the S–O bond. Importantly, the calculations suggested that, unlike molybdenum model complexes that have octahedral geometry about the molybdenum center, the active site of DMSO reductase maintains a trigonal prismatic geometry upon reduction of the Mo(VI) enzyme to Mo(V) and then to Mo(IV). The rigidity of the active site structure imposed by the dithiolene ligands causes the enzyme to remain in a transition-like state throughout the reaction cycle, predisposing the reaction. In this way, the active site of DMSO reductase is truly an example of the entatic state [107,108]. The continuous wave and pulsed EPR results described above provide experimental evidence supporting this, in that the High-g Unsplit Type-2 species maintains a trigonal prismatic geometry with the unpaired electron present in a d_{z^2}-based ground-state molecular orbital [94,95]. In addition, the weak ^{1}H and ^{14}N coupling in the HYSCORE spectrum reflects delocalization of the unpaired electron spin onto the N–H moiety in Trp-116, where the proton is hydrogen bonded to the oxo group.

Webster and Hall [106] suggested that the role of the bis-MGD ligands was to maintain the coordination geometry around the molybdenum ion during the catalytic cycle. The poor π-donor abilities of the dithiolene ligand may also help adjust the potential at the active site to perform different catalytic reactions [1,54]. The observation of sulfur-centered radicals upon reduction of the Mo(VI) enzyme [69,95] and upon the addition of DMSO to the reduced enzyme suggests that the pterin ligand (Q-MGD) may not be innocent and may play an important role in electron transfer.

3.2.1.4. The high-g split signal

The High-g Split Mo(V) EPR signal has previously been suggested to be the catalytically relevant Mo(V) species on the reductive side of the catalytic cycle and consequently has been extensively studied [19,22,96]. The High-g Split species displays a rhombic EPR spectrum with strong hyperfine coupling to a single solvent exchangeable proton, as shown by exchange with ^{2}H$_2$O buffer (Fig. 11c, Table 5) [19,22]. Pulsed EPR (ESEEM and HYSCORE) techniques found that the proton hyperfine coupling constant is variable, and dependent upon the orientation of the O–H bond, which can vary over a 30° wide distribution about the Mo–O bond [96].

The High-g Split signal (Table 5) can be generated under a number of different conditions, including partial reduction of DMSO reductase with electrochemically reduced benzyl viologen (BV·$^+$), dithionite, and by over-reduction of DMSO reductase, followed by partial reoxidation with pure oxygen or air [22,95]. The EPR parameters of this signal are slightly altered in different buffer solutions, indicating that a buffer molecule or anion either coordinates to the Mo(V) ion or is present in the second coordination sphere [22,95]. This is consistent with the X-ray structure

of the oxidized pentacoordinate DMSO reductase (Fig. 3c), which shows a Hepes molecule close to the molybdenum ion [23]. The relevance of this binding site to the physiological form of the enzyme in vivo remains unclear.

Potentiometric titrations of DMSO reductase (§3.2.1.5) showed that the High-g Split signal was not generated during the reductive half reaction [Mo(VI) → Mo(V) → Mo(IV)] of DMSO reductase as previously thought, but that it is generated during the oxidative half reaction [Mo(IV) → Mo(V) → Mo(VI)] of the redox cycle. While the g- and proton hyperfine coupling matrices have been accurately determined through computer simulation of the High-g Split signal (Table 5), there is no information on the ^{95}Mo hyperfine matrix and hence the ground-state molecular orbital remains unknown. The proposed structure of this species involves a six-coordinate molybdenum center in which the four sulfur atoms of the bis(MGD) and the Ser ligand coordinate to the molybdenum centre. The strong proton superhyperfine coupling is thought to arise from a hydroxide ligand perpendicular to the Mo–O–Ser bond [94,95].

3.3. Catalytic Mechanism

As discussed in earlier sections of this chapter, there was much debate in the literature concerning the number and identity of molybdenum ligands in the active site of DMSO reductase [23,60–62]. However, even though we are now armed with high-resolution structures of a large number of molybdopterin-containing enzymes, the exact chemical nature of the catalytic pathway by which these enzymes function is not yet fully understood, as the structures of intermediates generated during the reactions of these enzymes are as yet only postulated. Additionally, the question of whether or not the cofactor, especially the dithiolene moiety, plays any part in facilitating electron transfer during these reactions remains unanswered. The research described herein is an effort to bridge this important gap in molybdoenzyme chemistry by way of characterizing the Mo(V) transient species that lie between the now well-established structures of the oxidized and reduced molybdenum species in the catalytic pathway. The structural similarities between the active sites of molybdopterin-containing enzymes are such that a fundamental understanding of the reaction mechanism of catalysis for DMSO reductase will provide a basis for understanding the catalytic mechanism for all the molybdopterin enzymes in the DMSO reductase family.

A recent publication by Armstrong et al. described the electrochemistry of the catalytic cycle of DMSO reductase from *E. coli* using results of protein film voltammetry [105]. These workers presented a possible catalytic pathway for DMSO reductase (Fig. 16, sections in black and blue print), incorporating the notion of "switches" (single-electron oxidations or reductions proposed to occur from groups within the protein during catalysis), which reflect the catalytic mechanism. This switch was reported to disappear as pH was decreased. It was suggested that the catalytic mechanism of *E. coli* DMSO reductase occurred over only a narrow potential range, within which these reactions were optimized. At the borders of this potential range were one-electron processes. Interestingly, by employing EPR, it

was determined that this potential range encompasses a region in which the Mo(V) oxidation state is stabilized. Accordingly, the authors concluded that the DMSO reductase reaction pathway is mediated through the Mo(V) state and that all crucial steps of catalysis are performed in this oxidation state.

Figure 16 reveals a modification of the principal features of the aforementioned catalytic mechanism (sections in red print), based on results presented within section 3.2.1 of this chapter and incorporating experimental results presented below. These species and their redox interconversions are shown in Figure 17. The hexacoordinate Mo(VI) species (Fig. 16: Mo(VI) form; Figure 17: Species 7, in red), with ligands of molybdenum consisting of four sulfurs from two MGD moieties, a single oxo group, and the oxygen of a Serine-147 sidechain, is now ubiquitously acknowledged as that of the catalytically relevant oxidized species of DMSO reductase and is at the starting point for an explanation of the mechanism of catalysis.

Reductive potentiometric titration of the oxidized Mo(VI) form of DMSO reductase (§§3.2.1.5 and 3.2.1.6) has revealed that the High-g Unsplit Type-2 species (Fig. 16: Mo(V)-H$^+$; Figure 17: Species 8, in green) is formed during the one-electron Mo(VI) reduction to the Mo(V) state [92]. Electrochemistry has shown that this reductive step is pH dependent [93,105]. HYSCORE spectroscopy data presented in section 3.2.1.6 reveals the molybdenum atom is weakly coupled to both a proton and a nitrogen nucleus in the High-g Unsplit Type-2 species. CW-EPR spectroscopy in conjunction with ^{95}Mo isotope enrichment and computer simulation enabled determination of the spin Hamiltonian parameters, which showed that the unpaired electron was in a $\left| d_{z^2} \right\rangle$-based molecular orbital. Examination of the 1.3 Å hexacoordinate crystal structure [23] reveals the origin of the ^{14}N and ^{1}H coupling as the nitrogen of Trp-116 hydrogen bonded to the oxo group of the molybdenum active site. A further one-electron reduction of the High-g Unsplit Type-2 species leads to the removal of water to form a *des* oxo Mo(IV) form (Fig. 16: Mo(IV)-H$^+$; Fig. 17: Species 3, in pink). This is the form of the enzyme in which substrate binds and then undergoes oxygen atom transfer to produce the resting Mo(VI) enzyme and DMS.

A recent density functional calculation study has shown that the oxygen atom transfer reaction of DMSO reductase with dimethylsulfoxide more than likely occurs by way of an associative mechanism, with the oxygen molecule of DMSO forming a bond with the molybdenum atom of DMSO reductase [106]. This form is then converted to a transition state that transfers the oxygen atom of DMSO to the molybdenum atom, while severing the S–O bond. Importantly, the calculations suggested that, unlike molybdenum model complexes that have octahedral geometry about the molybdenum center, the active site of DMSO reductase maintains a trigonal prismatic geometry upon reduction of the Mo(VI) enzyme to Mo(V) and then to Mo(IV). The rigidity of the active site structure imposed by the dithiolene ligands causes the enzyme to remain in a transition-like state throughout the reaction cycle, predisposing the reaction. In this way, the active site of DMSO reductase is truly an example of the entatic state [107,108]. The continuous wave and

pulsed EPR results presented in section 3.2.1.5 provide experimental evidence supporting this, i.e., the High-g Unsplit Type-2 species contains an electron in the $\left| d_{z^2} \right\rangle$ ground state and shows weak ^{1}H and ^{14}N coupling to the nitrogen in Trp-116 and the proton involved in hydrogen bonding between the N–H of Trp-116 and the Mo=O moiety.

Webster and Hall [106] suggested that the role of the bis-MGD ligands was to maintain the coordination geometry around the molybdenum ion during the catalytic cycle. The poor π-donor abilities of the dithiolene ligand may also help adjust the potential at the active site to perform different catalytic reactions [1,54]. The observation of sulfur-centered radicals upon reduction of the Mo(VI) enzyme and upon the addition of DMSO to the reduced enzyme suggests that the pterin ligand (Q-MGD) may not be innocent and may play an important role in electron transfer. Whilst the sulfur-centered radicals probably result from dead-end complexes, they nevertheless demonstrate that they can be involved in electron transfer. Definitive evidence for their involvement awaits studies involving DMSO reductase and the native electron donor DorC.

Benson [92,94] demonstrated that both the High-g Unsplit Type-2 and High-g Split (Fig. 17: Species 5, in blue) signals could be formed by reducing DMSO reductase with sodium dithionite and then poising the potential at +56 mV using potassium ferricyanide (Fig. 15a). DMSO was subsequently added to the sample, and the resultant EPR signal generated was purely that of the High-g Unsplit Type-2 species (Fig. 15b). The signal lost upon addition of DMSO (utilizing difference spectra) was the pure High-g Split signal. Since the High-g Unsplit Type-2, the High-g Split, and the Mo(IV) species are in equilibrium, removal of the Mo(IV) will readjust the equilibrium according to Le Chatelier's principle. Since k_4 is greater than k_3, the High-g Split species is lost from the equilibrium (Fig. 16: Mo(V)-OH, in red). This is consistent with the observation that the High-g Split EPR signal is observed upon oxidation (air, Fe(CN)$_6$, NO$_2^-$) of reduced Mo(IV) DMSO reductase and is clearly not involved in the reductive side of the catalytic mechanism.

In the absence of redox buffering, addition of DMSO to dithionite-reduced DMSO reductase produces an EPR spectrum shown in Figure 18. The EPR spectrum (Fig. 18a) consists of the Mo(V) High-g Split and Low-g Type-1 species and an orthorhombic EPR signal to lower field that can be attributed to a sulfur-centered radical (see Fig. 18d). Upon oxidation of the sample, the EPR spectrum (Fig. 18b,c) reveals that the Low-g Type-1 signal is lost. As can be seen in Figure 4, the sulfur-centered radical (Species 15, in blue) can be formed by intramolecular electron transfer of the High-g Split species.

The High-g Unsplit Type-1 Mo(V) signal-giving species (not shown in the catalytic pathway) is proposed to be formed by addition of a buffer ion to the anion binding site of the molybdenum atom in the High-g Unsplit Type-2 Mo(V) species. This explains why only a relatively small percentage of Mo(V) EPR signal is due to the Type-1 species in samples of resting enzyme and DMS/DCPIP-treated DMSO reductase. The High-g Unsplit Type-1 species is expected to share essentially the same structure as the High-g Unsplit Type-2 species in all other respects

and retains the $\left|d_{z^2}\right\rangle$ ground state. The presence of an anion similar to a buffer species is not expected to be present in vivo; therefore, the High-g Unsplit Type-1 species is proposed to be catalytically irrelevant.

Whilst the High-g Split and High-g Unsplit EPR signals generated by DMSO reductase have been found to be similar to those of bacterial dissimilatory nitrate reductases, the Low-g Type-1 signal of DMSO reductase was noted to be similar to that of the "Slow" (nitrate) signal generated by the reduction of desulfo xanthine oxidase in the presence of nitrate [22].

Formation of the Low-g Type-1 species involves intramolecular electron transfer of the (native, Mo(VI)) enzyme (Fig. 17: Species 7 in red) to give Species 11, which can subsequently undergo protonation of the oxo group to give Species 14. Interestingly, the reduction of Species 7 to Species 14 also involves coupled proton–electron transfer. One electron reduction of Species 14 can yield the Mo(IV)–sulfur-centered radical (Fig. 17: Species 15 in blue) or the Low-g Type-1 Mo(V) species (Fig. 17: Species 17) in which one of the dithiolene moieties is no longer coordinated to the molybdenum ion. The sulfur-centered radical (Fig. 17: Species 15) may also be formed via intramolecular electron transfer of the High-g Split Mo(V) species (Fig. 17: Species 5). X-ray crystallography has also shown the presence of an anion binding site (Mes; 2-(N-morpholino)ethanesulfonic acid) at the molybdenum center.

Interestingly, the hexacoordinate Mo(VI) center (Fig. 17: Species 7 in red) may be converted to the pentacoordinate dioxo Mo(IV) species (Fig. 8: Species 3) by deprotonating Species 18 (Fig. 17). X-ray crystallography has also shown that the sulfonic acid group of a buffer molecule in which the enzyme is immersed may bind at the molybdenum active site of DMSO reductase and enable the conversion of the hexacoordinate form to the pentacoordinate form [23].

The considerable debate in the literature [23,60–62] regarding the number and identity of molybdenum ligands in the active site of DMSO reductase complex is not surprising given the complex interconversions of the Mo(VI), Mo(V), and Mo(IV) species (Fig. 17). Whilst it is recognized that the hexacoordinate site is the active species and the pentacoordinate dioxo site is inactive in converting DMSO to DMS, the ability to interconvert between these species may present an auto-regulatory mechanism in vivo.

Presently, in consideration of all available evidence collected on DMSO reductase, the catalytically relevant Mo(V) species of DMSO reductase is the High-g Unsplit Type-2 formed by reduction of the oxidized hexacoordinate Mo(VI) form of DMSO reductase. A further one-electron reduction of the High-g Unsplit Type-2 species leads to the removal of water to form a *des*oxo Mo(IV) form (Fig. 16: Mo(IV)-H$^+$; Fig. 17: Species 3, in pink). This is the form of the enzyme in which substrate binds and then undergoes oxygen atom transfer to produce the resting Mo(VI) enzyme and DMS.

4. CONCLUSIONS

Combining the results of CW and pulsed EPR studies of naturally abundant and [95]Mo-enriched molybdenum-containing DMSO reductase with those from X-ray crystallography has enabled the structures of the various transient Mo(V) species generated during the catalytic cycle of this enzyme to be determined.

EPR studies of naturally abundant and [95]Mo-enriched DMSO reductase reduced with sodium dithionite revealed the presence of the Low-g Type-1 species and a sulfur-centered radical in which the unpaired electron was located on one of the sulfur atoms of the Q-MGD dithiolene ligand that was no longer coordinated to the molybdenum ion. Computer simulation of the Low-g Type-1 EPR spectrum revealed that the ground-state molecular orbital was $d_{x^2-y^2}$, with the x and y axes placed between the metal–ligand bonds. A mechanism involving intramolecular electron transfer was proposed to account for the formation of both species.

Upon reduction (potentiometric titrations) of Mo(VI) to Mo(V), the High-g Unsplit Type-2 species is formed in which the oxo group is still present and hydrogen bonded to the indole nitrogen of Trp-116, accounting for the pH dependence of the redox process and the nitrogen hyperfine coupling in the ESEEM and HY-SCORE spectra. Further reduction produces Mo(IV), substrate binds, and oxygen atom transfer occurs, producing the native enzyme and DMS. Importantly, the trigonal prismatic geometry of the molybdenum center is retained for the Mo(VI), Mo(V) (unpaired electron located in the d_{z^2} orbital), and Mo(IV) species in the reductive half of the catalytic cycle. These results provide experimental evidence that the active site in DMSO reductase is an example of an entatic state. The Mo(V) High-g Split species was shown to be involved in the oxidative half of the catalytic cycle.

NOTE

1. Some complexes of molybdenum, specifically Mo(III) complexes, are unable to be studied at room temperature as the spin lattice relaxation time, T_1, is too short.

REFERENCES

1.   Hille R. 1996. The mononuclear molybdenum enzymes. *Chem Rev* **96:**2757–2816.
2.   Kisker C, Schindelin H, Rees DC. 1997. Molybdenum cofactor-containing enzymes: structure and mechanism. *Annu Rev Biochem* **66:**233–267.
3.   Bray RC 1988. The inorganic biochemistry of molybdoenzymes. *Q Rev Biophys* **21:**299–329.
4.   Enemark JH, Young CG. 1993. Bioinorganic chemistry of of pterin-containing molybdenum and tungsten enzymes. *Adv Inorg Chem* **40:**1–88.
5.   Romao MJ, Huber R. 1998. Structure and function of the xanthine-oxidase family of molybdenum enzymes. *Struct Bonding* **90:**69–95.

6. Hille R. 2004. Molybdenum and tungsten in biology. *Trends Biochem Sci* **27:**360–367.

7. Rajagopalan KV, Johnson JL. 1992. The pterin molybdenum cofactors. *J Biol Chem* **267:**10199–10202.

8. Rajagopalan KV. 1991. Novel aspects of the biochemistry of the molybdenum cofactor. *Adv Enzymol Relat Subj Biochem* **64:**215–290.

9. Johnson JL. 1980. The molybdenum cofactor common to nitrate reductase, xanthine dehydrogenase and sulfite oxidase. In *Molybdenum and molybdenum-containing enzymes*, pp. 345–383. Ed MP Coughlan. New York: Pergamon Press.

10. Kramer SP, Johnson JL, Ribeiro AA, Millington DS, Rajagopalan KV. 1987. The structure of molybdenum cofactor. *J Biol Chem* **262:**16357–16363.

11. Romao MJ, Archer M, Moura I, Moura JJG, LeGall J, Engh R, Schneider M, Hof P, Huber R. 1995. Crystal structure of the xanthine oxidase-related aldehyde oxidoreductase from *D. gigas*. *Science* **270:**1170–1176.

12. Enroth C, Eger BT, Okamoto K, Nishino T, Nishino T, Pai EF. 2000. Crystal structures of bovine milk xanthine dehydrogenase and xanthine oxidase: structure-based mechanism of conversion. *Proc Natl Acad Sci USA* 97:10723–10728.

13. Huber R, Hof P, Duarte RO, Moura JJG, Liu M, LeGall J, Hille R, Archer M, Romao MJ. 1996. A structure-based catalytic mechanism for the xanthine oxidase family of molybdenum enzymes. *Proc Natl Acad Sci USA* **93:**8846–8851.

14. Kisker C, Schindelin H, Pacheco A, Wehbi WA, Garret RM, Rajagopalan KV, Enemark JH, Rees DC. 1997. Molecular basis of sulfite oxidase deficiency from the structure of sulfite oxidase. *Cell* **91:**973–983.

15. Hille R. 1996. Structure and function of mononuclear molybdenum Enzymes. *J Biol Inorg Chem* **1:**397–404.

16. McDevitt CA, Hugenholtz P, Hanson GR, McEwan AG. 2002. Molecular analysis of dimethyl sulphide dehydrogenase from *Rhodovulum sulfidophilum*: its place in the dimethyl sulphoxide reductase family of microbial molybdopterin-containing enzymes. *Mol Microbiol* **44**:1575–1587.

17. Dias JM, Than ME, Humm A, Huber R, Bourenkov GP, Bartunik HD, Bursakov S, Calvete J, Caldeira J, Caneiro C, Moura JJG, Moura I, Romao MJ. 1999. Crystal structure of the first dissimilatory nitrate reductase at 1.9 Å solved by MAD methods. *Struct Folding Design* **7:**65–79.

18. The RCSB protein databank can be accessed through the following web address: <http://www.rcsb.org/pdb/home/home.do>.

19. Bastian NR, Kay CJ, Barber MJ, Rajagopalan KV. 1991. Spectroscopic studies of the molybdenum-containing dimethyl sulfoxide reductase from *Rhodobacter sphaeroides* f.sp. *denitrificans*. *J Biol Chem* **266:**45–51.

20. Benson N, McEwan AG, Farra JA, Thompson AJ. 1992. Detection of the optical bands of molybdenum(V) in DMSO reductase (*Rhodobacter capsulatus*) by low-temperature MCD spectroscopy. *FEBS Lett* **307:**169–172.

21. Finnegan MG, Hilton J, Rajagopalan KV, Johnson MK. 1993. Optical transitions of molybdenum(V) in glycerol-inhibited DMSO reductase from *Rhodobacter sphaeroides*. *Inorg Chem* **32**:2616–2617.

22. Bennett B, Benson N, McEwan AG, Bray RC. 1994. Multiple states of the molybdenum centre of DMSO reductase from *Rhodobacter capsulatus* revealed by EPR spectroscopy. *Eur J Biochem* **225:**321–331.

23. Li H-K, Temple C, Rajagopalan KV, Schindelin H. 2000. The 1.3 Å crystal structure of *Rhodobacter sphaeroides* dimethylsulfoxide reductase reveals two distinct molybdenum coordination environments. *J Am Chem Soc* **122:**7673–7680.

24. McAlpine AS, McEwan AG, Bailey S. 1998. The high resolution crystal structure of DMSO reductase in complex with DMSO. *J Mol Biol* **275:**613–623.

25. Steifel EI. 1997. Chemical keys to molybdenum enzymes. *J Chem Soc Dalton Trans* 3915–3923.

26. Gutteridge S, Bray RC. 1980. Studies by electron paramagnetic resonance on the nature and reactions of the molybdenum centre of xanthine oxidase. In *Molybdenum and molybdenum-containing enzymes*, pp. 221–239. Ed MP Coughlan. New York: Pergamon Press.

27. Bray RC. 1980. EPR of molybdenum containing enzymes. In *Biological magnetic resonance*, Vol. 2, pp. 45–84. Ed J Reuben, LJ Berliner. New York: Plenum Press.

28. Bray RC 1961. The chemistry of xanthine oxidase: electron-spin-resonance measurements during the enzymic reaction. *Biochem J* **81:**196–199.

29. Palmer G, Bray RC, Beinert H. 1964. Direct studies on the electron transfer sequence in xanthine oxidase by electron paramagnetic resonance spectroscopy: techniques and description of spectra. *J Biol Chem* **239:**2657–2665.

30. Wilson GL. 1988. Multifrequency electron paramagnetic resonance of xanthine oxidase and relevant analogue complexes. PhD Thesis, LaTrobe University, Melbourne, Australia.

31. Wilson GL, Greenwood RJ, Pilbrow JR, Spence JT, Wedd AG. 1991. Molybdenum(V) sites in xanthine oxidase and relevant analog complexes: comparison of molybdenum-95 and sulfur-33 hyperfine coupling. *J Am Chem Soc* **113:**6803–6812.

32. Wilson GL, Kony M, Tiekink ERT, Pilbrow JR, Spence JT, Wedd AG. 1988. Oxygen-17 and molybdenum-95 coupling in spectroscopic models of molybdoenzymes. *J Am Chem Soc* **110:**6923–6925.

33. Weil JA, Bolton JR, Wertz JE. 2007. *Electron paramagnetic resonance, elementary theory and practical applications*. Weinheim: Wiley Interscience.

34. Pilbrow JR 1990. *Transition ion paramagnetic resonance*. New York: Oxford UP.

35. Hanson GR, Noble CJ, Benson S. 2009. Molecular Sophe, an integrated approach to the structural characterization of metalloproteins, the next generation of computer simulation software. In *Biological magnetic resonance*, Vol. 28, pp. 105–174. Ed GR Hanson, LJ Berliner. New York: Springer.

36. Neese F. 2009. Spin-Hamiltonian parameters from first principle calculations: theory and application. In *Biological magnetic resonance*, Vol. 28, pp. 175–229. GR Hanson, LJ Berliner. New York: Springer.

37. Holden NE. 1998. In *CRC Handbook of chemistry and physics*, pp. 42–146. Ed DR Lide, HPR Frederikse. New York: CRC Press.

38. Hanson GR, Wilson GL, Bailey TD, Pilbrow JR, Wedd AG. 1987. Multifrequency electron spin resonance of molybdenum(V) and tungsten(V) compounds. *J Am Chem Soc* **109:**2609–2616.

39. Drew SC, Hill JP, Lane I, Hanson GR, Gable RW, Young CG. 2007. Synthesis, structural characterization and multifrequency electron paramagnetic resonance studies of mononuclear thiomolybdenyl complexes. *Inorg Chem* **46:**2373–2387.

40. Dowerah D, Spence JT, Singh R, Wedd AG, Wilson GL, Farchione F, Enemark JH, Kristofzski J, Bruck M. 1987. Molybdenum(VI) and molybdenum(V) complexes with N,N′-dimethyl-N,N′-bis(2-mercaptophenyl) ethylenediamine: electrochemical and

electron paramagnetic resonance models for the molybdenum(VI/V) centers of the molybdenum hydroxylases and related enzymes. *J Am Chem Soc* **109**:5655–5665.

41. Hanson GR, Brunette AA, McDonnell AC, Murray KS, Wedd AG. 1981. Electronic properties of thiolate compounds of oxomolybdenum(V) and their tungsten and selenium analogues: effects of [17]O, [98]Mo, and [95]Mo isotope substitution upon ESR spectra. *J Am Chem Soc* **103**:1953–1959.

42. Drew SC, Young CG, Hanson GR. 2007. A density functional study of the electronic structure and spin Hamiltonian parameters of mononuclear thiomolybdenyl complexes. *Inorg Chem* **46**: 2388–2397.

43. Enemark JH, Astashkin AV, Raitsimring AM. 2008. Structures and reaction pathways of the molybdenum centers of sulfite oxidizing enzymes by pulsed EPR spectroscopy. *Biochem Soc Trans* **36**:1129–1133.

44. Astashkin AV, Johnson-Winters K, Klein EL, Byrne RS, Hille R, Raitsimring AM, Enemark JH. 2007. Direct demonstration of the presence of coordinated sulfate in the reaction pathway of *Arabidopsis thaliana* sulfite oxidase using [33]S labeling and ESEEM spectroscopy. *J Am Chem Soc* **129**:14800–14810.

45. Feng C, Tollin G, Enemark JH. 2007. Sulfite oxidizing enzymes. *Biochim Biophys Acta* **1774**:527–539.

46. Enemark JH, Astashkin AV, Raitsimring AM. 2006. Investigation of the coordination structures of the molybdenum(V) sites of sulfite oxidizing enzymes by pulsed EPR spectroscopy. *Dalton Trans* 3501–3514.

47. Lorigan GA, Britt RD, Kim JH, Hille R. 1994. Electron spin echo envelope modulation spectroscopy of the molybdenum center of xanthine oxidase. *Biochim Biophys Acta* **1185**:284–294.

48. Howes BD, Bray RC, Richards RL, Turner NA, Bennett B, Lowe DJ. 1996. Evidence favoring molybdenum-carbon bond formation in xanthine oxidase action: [17]O- and ^{13}C-ENDOR and kinetic studies. *Biochemistry* **35**:1432–1443.

49. Manikandan P, Choi E-Y, Hille R, Hoffman BM. 2001. 35-GHz ENDOR investigation of the "very rapid" signal of xanthine oxidase reacted with 8-[^{13}C]-2-hydroxy-6-methylpurine. *J Am Chem Soc* **123**:2658–2663.

50. Astashkin AV, Johnson-Winters K, Klein EL, Feng C, Wilson HL, Rajagopalan KV, Raitsimring AM, Enemark JH. 2008. Structural studies of the molybdenum center of the pathogenic R160Q mutant of human sulfite oxidase by pulsed EPR spectroscopy and [17]O and [33]S labeling. *J Am Chem Soc* **130**:8471–8480.

51. Hanson GR, Gates KE, Noble C, Griffin M, Mitchell A, Benson S. 2004. Xsophe–Sophe–XeprView: a computer simulation software suite (v. 1.1.3) for the analysis of continuous wave EPR spectra. *J Inorg Biochem* **98**:903–916.

52. Bennett B, Benson N, McEwan AG, Bray RC. 1994. EPR characterisation of the molybdenum centre of *Rhodobacter capsulatus* dimethyl sulfoxide reductase: new signals on reduction with $Na_2S_2O_4$. *Biochem Soc Trans* **22**:285S.

53. Beversa LE, Hagedoorna P-L, Hagen WR. 2009. The bioinorganic chemistry of tungsten. *Coord Chem Rev* **253**:269–290.

54. Johnson MK, Rees DC, Adams MWW. 1996. Tungstoenzymes. *Chem Rev* **96**:2817–2839.

55. Simala-Grant JL, Weiner JH. 1998. Modulation of the substrtate specificity of *Escherichia coli* dimethylsulfoxide reductase. *Eur J Biochem.* **251**:510–515.

56. Cammack R, Weiner JH. 1990. electron paramagnetic resonance spectroscopic charac-
     terization of dimethyl sulfoxide reductase of *Escherichia coli*. *Biochemistry* **29:**8410–
     8416.

57. Simala-Grant JL, Weiner JH. 1996. Kinetic analysis and substrate specificity of *Es-
     cherichia coli* dimethyl sulfoxide reductase. *Microbiology* **142:**3231–3239.

58. Zhao Z, Weiner JH. 1998. Interaction of 2-*n*-heptyl-4-hydroxyquinoline-*N*-oxide with
     dimethylsulfoxide reductase of *Escherichia coli*. *J Biol Chem* **273:**20758–20763.

59. Trieber CA, Rothery RA, Weiner JH. 1996. Consequences of removal of a molybde-
     num ligand (DmsA-Ser-176) of *Escherichia coli* dimethylsulfoxide reductase. *J Biol
     Chem* **271:**27339–27345.

60. Schindelin H, Kisker C, Hilton J, Rajagopalan KV, Rees DC. 1996. Crystal structure
     of DMSO reductase: redox-linked changes in molybdopterin coordination. *Science*
     272:1615–1621.

61. Schneider F, Lowe J, Huber R, Schindelin H, Kisker C, Knablein J. 1996. Crystal
     structure of dimethyl sulfoxide reductase from *Rhodobacter capsulatus* at 1.88 ang-
     strom resolution. *J Mol Biol* **263:**53–69.

62. McAlpine AS, McEwan AG, Shaw AL, Bailey S. 1997. Molybdenum active centre of
     DMSO reductase from *Rhodobacter capsulatus*: crystal structure of the oxidised en-
     zyme at 1.82 Å resolution and the dithionite-reduced enzyme at 2.8 Å resolution. *J
     Biol Inorg Chem* **2:**690–701.

63. George GN, Hilton J, Rajagopalan KV. 1996. X-ray absorption spectroscopy of di-
     methyl sulfoxide reductase from *Rhodobacter sphaeroides. J Am Chem Soc* **118**:1113–
     1117.

64. Baugh PE, Garner CD, Charnock JM, Collison D, Davies ES, McAlpine AS, Bailey S,
     Lane I, Hanson GR, McEwan AG. 1997. X-ray absorption spectroscopy of dimethyl-
     sulfoxide reductase from *Rhodobacter capsulatus*. *J Biol Inorg Chem* **2:**634–643.

65. Kilpatrick L, Rajagopalan KV, Hilton J, Bastian NR, Stiefel EI, Pilato RS, Spiro TG.
     1995. Resonance raman spectroscopic characterization of the molybdopterin active site
     of DMSO reductase. *Biochemistry* **34**:3032–3039.

66. Garton SD, Hilton J, Oku H, Crouse BR, Rajagopalan KV, Johnson JL 1997. Active
     site structures and catalytic mechanism of *Rhodobacter sphaeroides* dimethyl sulfox-
     ide reductase as revealed by resonance Raman spectroscopy. *J Am Chem Soc* **119**:
     12906–12916.

67. Bray RC, Knowles PF, Pick FM, Vänngård T. 1968. Electron-spin-resonance evidence
     for interaction of protons with Mo(V) in reduced forms of xanthine oxidase. *Biochem J*
     107:601–602.

68. Gutteridge S, Tanner SJ, Bray RC. 1978. Comparison of the centres of native and
     desulpho xanthine oxidase: the nature of the cyanide-labile sulphur atom and the pro-
     ton-accepting group. *Biochem J* **175:**887–897.

69. Lane I, Drew SC, Noble CJ, McEwan AG, Pilbrow JR, Hanson GR. 2009. EPR studies
     of sulfur centered radicals and the Low-g Type-I Mo(V) Species in dimethylsulfoxide
     reductase: implications for catalysis and electron transfer. Submitted.

70. Mabbs FE, Collison D. 1992. *Electron paramagnetic resonance of d transition metal
     cvompounds*. Amsterdam: Elsevier.

71. Drew SC, Hanson GR. 2009. Determination of the metal–dithiolate fold angle in
     mononuclear molybdenum(V) centers by EPR spectroscopy. *Inorg Chem* **48**:2224–
     2232.

72. Ohitani M, Ohkishi S, Kajitani M, Akiyama T, Sugimori A, Yamauchi S, Ohba Y,
     Iwaizumi M. 1992. Direct observations of the intermediate species in the photodisso-

ciation of bis(S-benzyl-1,2-diphenyl-1,2-ethylenedithiolato) nickel by time-resolved EPR and UV-visible absorption spectroscopy. *Inorg Chem* **31**:3873–3874.

73. Coves J, Le Hir de Fallois L, Le Pape L, Decout J-L, Fontecave M. 1996. Inactivation of *Escherichia coli* ribonucleotide reductase by 2′-deoxy-2′-mercaptouridine 5′-diphosphate. electron paramagnetic resonance evidence for a transient protein perthiyl radical. *Biochemistry* **35**:8595–8602.

74. Kolberg M, Bleifuss G, Gräslund A, Sjoberg B-M, Lubitz W, Lendzian F, Lassaman G. 2002. Protein thiyl radicals directly observed by EPR spectroscopy. *Arch Biochem Biophys* **403**:141–144.

75. Lassmann G, Kolberg M, Bleifuss G, Graslund A, Sjoberg B-M, Lubitz W. 2003. Protein thiyl radicals in disordered systems: a comparative EPR study at low temperature. *Phys Chem Chem Phys* **5:**2442–2453.

76. Fauth J-M, Schweiger A, Branschweiler L, Forrer J, Ernst RR. 1986. Elimination of unwanted echoes and reduction of dead time in three-pulse electron spin-echo spectroscopy. *J Magn Reson* **66**:74–85.

77. Kimura S, Bill E, Bothe E, Weyhermuller T, Weighardt K. 2001. Phenylthiyl radical complexes of Gallium(III), Iron(III), and Cobalt(III) and comparison with their phenoxyl analogues. *J Am Chem Soc* **123**:6025–6039.

78. Ghosh P, Begum A, Herebian D, Bothe E, Hildenbrand K, Weyhermuller T, Weighardt K. 2003. Coordinated o-dithio- and o-iminothiobenzosemiquinonate(1-) π radicals in [MII(bpy)(L·)](PF$_6$) complexes. *Angew Chem Int Ed* **42**:563–567.

79. Ray K, Weyhermuller T, Goossens A, Craje MW, Weighardt K. 2003. Do S,S′-coordinated o-dithiobenzosemiquinonate(1−) radicals exist in coordination compounds? The [AuIII(1,2-C$_6$H$_4$S$_2$)$_2$]$^{1-/0}$ couple. *Inorg Chem* **42**:4082–4087.

80. Schweiger A, Jeschke, G. 2001. *Principles of pulse electron paramagnetic resonance*. Oxford: Oxford UP.

81. Harmer J, Mitrikas G, Schweiger A. 2009. Advanced pulse EPR methods for the characterization of metalloproteins. In *Biological magnetic resonance*, Vol. 28, pp. 13–61. Ed GR Hanson, LJ Berliner. New York: Springer.

82. Höfer P, Grupp A, Nebenfuhr H, Mehring M. 1986. Hyperfine sublevel correlation (HYSCORE) spectroscopy: a 2D ESR investigation of the squaric acid radical. *Chem Phys Lett* **132:**279–282.

83. Dikanov SA, Davydov RM, Graslund A, Bowman MK. 1998. Two-dimensional ESEEM spectroscopy of nitrogen hyperfine couplings in methemerythrin and azidomethemerythrin. *J Am Chem Soc* **120**:6797–6805.

84. Dikanov SA, Tyryshkin AM, Huttermann J, Bogumil R, Witzel H. 1995. Characterization of histidine coordination in VO^{2+}-substituted D-xylose isomerase by orientationally-selected electron spin-echo envelope modulation spectroscopy. *J Am Chem Soc* **117:**4976–4986.

85. Solomon PS, Lane I, Hanson GR, McEwan AG. 1997. Characterisation of the pterin molybdenum cofactor in dimethylsulfoxide reductase of *Rhodobacter capsulatus*. *Eur J Biochem* **246:**200–203.

86. Luykx DMAM, Duine JA, de Vries S. 1998. Molybdopterin radical in bacterial aldehyde dehydrogenases. *Biochemistry* **37**:11366–11375.

87. McEwan AG, Richardson DJ, Hudig H, Ferguson SJ, Jackson JB. 1989. Identification of cytochromes involved in electron transport to trimethylamine N-oxide/dimethyl-sulphoxide reductase in *Rhodobacter capsulatus*. *Biochim Biophys Acta* **973**:308–314.

88. Shaw AL, Hochkoeppler A, Bonora P, Zannoni D, Hanson GR, McEwan AG. 1999. Characterization of DorC from *Rhodobacter capsulatus*, a c-type cytochrome involved in electron transfer to dimethyl sulfoxide reductase. *J Biol Chem* **274**:9911–9914.

89. Westcott BL, Gruhn NE, Enemark JH. 1998. Evaluation of molybdenum-sulfur interactions in molybdoenzyme model complexes by gas-phase photoelectron spectroscopy: the "electronic buffer" effect. *J Am Chem Soc* **120**:3382–3386.

90. Stubbe J, van der Donk WA. 1998. Protein radicals in enzyme catalysis. *Chem Rev* **98**:705–762.

91. Rebelo JM, Dias JM, Huber R, Moura JJG, Romao MJ. 2001. Structure refinement of the aldehyde oxidoreductase from *Desulfovibrio gigas* (MOP) at 1.28 Å. *J Biol Inorg Chem* **6**:791–800.

92. Benson N. 1994. Biochemical and spectroscopic studies of dimethylsulfoxide reductase from *Rhodobacter capsulatus*. PhD Thesis. University of East Anglia, United Kingdom.

93. Aguey-Zinsou K-F, Bernhardt PV, McEwan AG, Ridge JP. 2002. The first non-turnover voltammetric response from a molybdenum enzyme: direct electrochemistry of dimethylsulfoxide reductase from *Rhodobacter capsulatus. J Biol Inorg Chem* **7**: 879–883.

94. Lane I, Noble CJ, Ridge J, Benson N, McEwan AG, Hanson GR. 2009. Structural characterisation of the Mo(V) high-g unsplit species from *Rhodobacter capsulatus* dimethylsulfoxide reductase. In preparation.

95. Lane I. 2004. Electron paramagnetic resonance studies of *Rhodobacter capsulatus* dimethylsulfoxide reductase, model Mo(V) and W(V) complexes and metallotolyporphyrins. PhD Thesis. The University of Queensland, Brisbane, Australia.

96. Raitsimring AM, Astanshkin AV, Feng C, Enemark JH, Nelson KJ, Rajagopalan KV. 2003. Pulsed EPR studies of the exchangeable proton at the molybdenum center of dimethylsulfoxide reductase. *J Biol Inorg Chem* **8**:95–104.

97. Adams B, Smith AT, Bailey S, McEwan AG, Bray RC. 1999. Reactions of dimethylsulfoxide reductase from *Rhodobacter capsulatus* with dimethyl sulfide and with dimethyl sulfoxide: complexities revealed by conventional and stopped-flow spectrophotometry. *Biochemistry* **38**:8501–8511.

98. Bray RC, Adams B, Smith AT, Richards RL, Lowe DJ, Bailey S. 2001. Reactions of dimethylsulfoxide reductase in the presence of dimethyl sulfide and the structure of the dimethyl sulfide-modified enzyme. *Biochemistry* **40**:9810–9820.

99. Steifek EI, Eisenberg R, Rosenberg RC, Gray HB. 1966. Characterization and electronic structures of six-coordinate trigonal-prismatic complexes. *J Am Chem Soc* **88**: 2956–2966.

100. Cervilla A, Llopis E, Marco D, Pérez F. 2001. X-ray structure of (Bun$_4$N)[Mo(1,2-benzenedithiolate)$_3$]. trigonal-prismatic versus octahedral coordination in Tris(1,2-benzenedithiolate) complexes. *Inorg Chem* **40**:6525–6528.

101. Smith PD, Cooney JA, McInnes EJL, Beddoes RL, Collison D, Harben SM, Helliwell M, Mabbs FE, Mandel A, Powell AK, Garner CD. 2001. New molybdenum(V) analogues of amavadin and their redox properties. *J Chem Soc Dalton Trans* 3108–3114.

102. Yadav HS, Armstrong EM, Beddoes RL, Collison D, Garner CD. 1994.The molybdenum analogue of amavadin. *J Chem Soc Chem Commun* **5**:605–606.

103. George GN, Bray RC, Morpeth FF, Boxer DH. 1985. Complexes with halide and other anions of the molybdenum centre of nitrate reductase from *Escherichia coli*. *Biochem J* **227**:925–931.

104. George GN, Turner NA, Bray RC, Morpeth FF, Boxer DH, Cramer SP. 1989. X-ray-absorption and electron-paramagnetic-resonance spectroscopic studies of the environment of molybdenum in high-pH and low-pH forms of *Escherichia coli* nitrate reductase. *Biochem J* **259**:693–700.

105. Heffron K, Legr C, Rothery RA, Weiner JH, Armstrong FA. 2001. Determination of an optimal potential window for catalysis by *E. coli* dimethyl sulfoxide reductase and hypothesis on the role of Mo(V) in the reaction pathway. *Biochemistry* **40**:3117–3126.

106. Webster CE, Hall MB. 2001. The theoretical transition state structure of a model complex bears a striking resemblance to the active site structure of DMSO reductase. *J Am Chem Soc* **123**:5820–5821.

107. Vallee BL, William RJP. 1968. Metalloenzymes: the entatic nature of their active sites. *Proc Natl Acad Sci USA* **59**:498-505.

108. Williams RJP. 1995. Energised (entatic) states of groups and of secondary structures in proteins and metalloproteins. *Eur J Biochem* **234**:363–381.

MANGANESE-CONTAINING

ENZYMES

THE MANGANESE-CALCIUM CLUSTER OF THE OXYGEN-EVOLVING SYSTEM: SYNTHETIC MODELS, EPR STUDIES, AND ELECTRONIC STRUCTURE CALCULATIONS

Marcin Brynda and R. David Britt

Department of Chemistry, University of California Davis

1. INTRODUCTION

Manganese plays a variety of roles in enzymes [1], such as for example arginase, which catalyzes the hydrolysis of arginine, forming urea and ornithine as products [2–4]. Given the biological accessibility of at least three oxidation states — Mn^{II}, Mn^{III}, and Mn^{IV} — it is not surprising that manganese is also involved in important redox reactions [5]. Beside the well-known manganese superoxide dismutase and manganese catalase enzymes where Mn plays a role that can also be served by Fe or other metals, manganese exclusively acts as an oxidizer of water in the pentanuclear Mn_4Ca cluster of Photosystem II. This cluster carries out the four-electron oxidation of two H_2O molecules to O_2, providing nearly all of the free molecular oxygen in our atmosphere.

Photosystem II is a large transmembrane protein/cofactor complex with approximate C_2 symmetry that utilizes light energy to oxidize water to molecular oxygen and to reduce membrane diffusible plastoquinone. Two tyrosines called Y_D and Y_Z are sidechains of two polypeptides D1 and D2, positioned on both sides of the symmetry axis. Four successive photons are absorbed by the chlorophyll (Chl) pigment P_{680}; pheophytin (Ph) and two plastoquinones, Q_A and Q_B, participate in the electron transfer, while the pentanuclear Mn_4Ca moiety is used to build charges necessary for a subsequent electron transfer.

Address all correspondence to R. David Britt, Department of Chemistry, University of California Davis, One Shields Avenue, Davis, CA 95695, USA, 530 752-6377, 530 752-8995 (fax), <rdbritt@ucdavis.edu>.
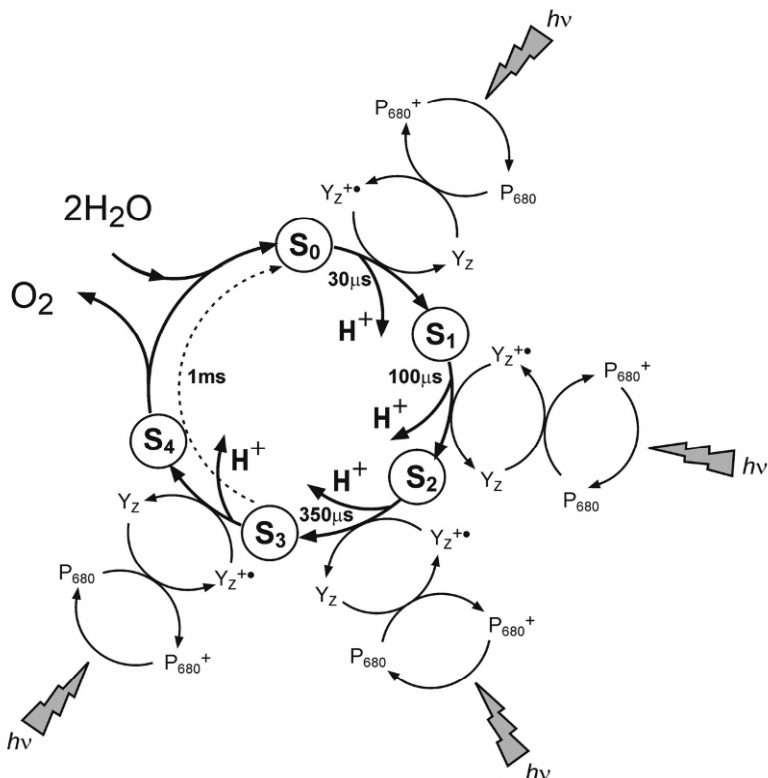
Figure 1. Kok cycle explaining the 4-step mechanism in which the OEC center accumulates four positive charges, then produces O_2 and returns to the ground state.

The near C_2 symmetry is completely broken at the level of the Mn cluster, which is located well off-axis near the Y_Z tyrosine and forms the catalytic water splitting assembly that is most often termed the oxygen-evolving complex (OEC). Along with the tetranuclear Mn moiety, there are required Ca^{2+} and Cl^- cofactors [6–8], which form the inorganic core of the OEC, and several ligands including the tyrosine Y_Z. The Mn cluster acts as a central element of the OEC in storing intermediate oxidation equivalents, and presumably it also acts to correctly position and catalytically activate the substrate water molecules to facilitate the formation of the O_2 double bond in the final oxidation step. Specifically, after a total of four oxidation equivalents are sequentially extracted from the OEC by way of the P_{680}-centered, single-electron photochemistry, O_2 is released, and the OEC resets to its most reduced state [9,10]. Details of this oxygen evolving cycle were first accurately described by Kok et al. [11], with a cycle involving five so-called S-state intermediates (displayed in Fig. 1), alternately termed the Kok or S-state cycle. The oxidations of Y_Z by P^+_{680}, shown on the periphery of the cycle, occur on the 50–

250 ns timescale, with the faster transfers associated with the more reduced states of the OEC [12]. The S-state transitions are coupled to the subsequent re-reductions of the $Y_Z^\bullet$ radical, and these occur on the 30–1000 μs timescale, as shown in the figure. Oxygen formation from the transient S_4 state occurs with the same 1000-μs time constant as the final $Y_Z^\bullet$ re-reduction.

Recent X-ray crystal structures [13–17] and X-ray spectroscopy studies [18] shed new light on the architecture of OEC. But even with these structural high-lights and despite numerous spectroscopic efforts, the exact topology of the Mn cluster, the nature of the terminal amino-acid ligands involved in the coordination of the Mn cations [19], and its exact role in water oxidation remain unknown. However, since its early discovery, constant efforts were devoted to understand the catalytic role of this multinuclear Mn moiety, using various spectroscopic tech-niques and synthetic models of increasing complexity. Recently, advanced mag-netic resonance results pertaining to the OEC as well as modern water oxidation mechanistic proposals were reviewed in depth in two contributions from our group [20,21]. To complement these reviews, in this chapter we present the related syn-thetic models and theoretical electronic structure calculations. In the following sections, we focus on the milestones provided by synthetic chemists that helped in the elucidation of the structural and mechanistic aspects of the OEC, via a panoply of synthetic manganese complexes. These important compounds are presented with emphasis on their EPR spectral signatures, discussed in the context of the EPR spectroscopy of OEC. We also briefly present the theoretical basis for the quantum mechanical calculations that helped to evaluate the electronic structure of these Mn complexes and present the latest theoretical advances on the computational front that target the structural and mechanistic aspects of the catalytic water splitting in PSII.

2. THEORETICAL BACKGROUND FOR THE POLYNUCLEAR MANGANESE CLUSTERS

2.1. Introduction to the Spin Physics of Exchange-Coupled Manganese Complexes

The first EPR spectrum of laser-flash illuminated PSII containing spinach chloroplasts was similar to the spectral patterns of binuclear mixed-valence Mn complexes (Fig. 2). This result pointed toward Mn as being an integral part of the OEC [22]. The finding from several, subsequent EPR and other spectroscopic stud-ies [23–28], suggested that the catalytic center consists of four manganese atoms, which are, most probably, oxygen bridged and couple magnetically to give a net electronic spin of $S = 1/2$ for the S_0 state, $S = 1$ for the S_1 state, and $S = 1/2$ for the S_2 state.

Polynuclear metal clusters, such as the [Fe_4S_4] cubane cofactors employed by numerous enzymes and electron transfer proteins [29–32], can be homogenous
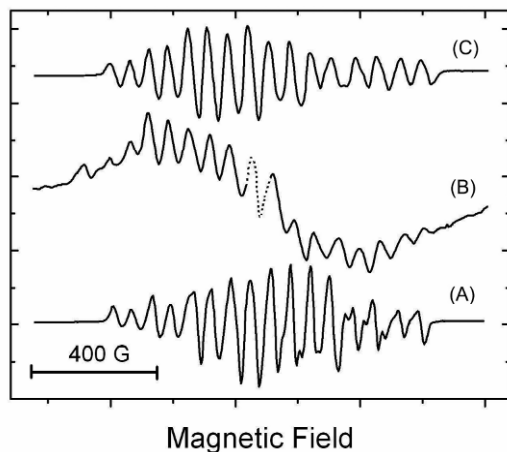
Figure 2. EPR signal obtained with a synthetic mixed valence dinuclear $Mn^{III}Mn^{IV}$ complex $[(bipy)_2Mn^{III}O_2Mn^{IV}(bipy)_2]^{3+}$ (A) compared to the EPR multiline signal of the PSII chloroplasts (B). Simulated spectrum of $[(bipy)_2Mn^{III}O_2Mn^{IV}(bipy)_2]^{3+}$ is shown in (C). Adapted from [23].

with respect to the identity of the metal centers or can contain mixed-metal cores such as the CuZn dimer found in superoxide dismutase [33], the nickel–iron dimer in NiFe-hydrogenase [34], or the pentanuclear Mn_4Ca cluster of Photosystem II [13]. Furthermore, multinuclear metal clusters within proteins are typically redox-active. Changes in oxidation states directly influence their functionality and, importantly, in the context of this chapter, their magnetic properties. They can modulate their ground spin state using both antiferromagnetic and ferromagnetic exchange coupling mechanisms, that induce unpaired electrons localized on individual nuclei to align either parallel or antiparallel to neighboring spins, yielding a higher or lower total electronic spin, respectively. The magnitude of the coupling between metal centers is characterized by the exchange coupling constant J, which is usually given in units of cm^{-1}. According to the most common convention, the magnitude of J is defined by the phenomenological Heisenberg-Dirac-van Vleck (HDvV) Hamiltonian, which in its isotropic form reads:[1]

$$\hat{H}_{HDvV} = -2\sum_{i,j} J_{ij}\hat{S}_i \cdot \hat{S}_j \qquad (1)$$

Antiferromagnetic coupling is characterized by negative J values, while positive J values signify a ferromagnetic coupling. J can be estimated by fitting variable-temperature magnetic susceptibility data using a modified van Vleck equation [35]. The derivation of this equation requires construction of a spin energy level diagram that takes into account the proper spin coupling scheme, as well as zero-field splitting (ZFS) and g anisotropy. The magnitude of the coupling will depend on the

distance, the local geometry, and the nature of the bridging ligand between the metal centers. Short distances or direct metal–metal bonding will lead to a very strong coupling, while more distant centers will exhibit moderate to weak coupling.

The simplest examples of EPR active exchange-coupled systems are homonuclear metallic dimers, in which the metal centers possess different oxidation states. Such compounds are termed mixed-valence species. The mixed-valence species were classified by Day and Robins into three distinct classes [36]. Class I consists of valence localized systems, in which the metal centers act independently one of another. Class III dimers are the opposite in that the odd electron is completely delocalized over both metal centers, yielding spectroscopically and crystallographically identical atoms. Examples of multinuclear manganese compounds belonging to either class I or III are rare. Most of the known mixed-valence manganese dimers possess crystallographically distinguishable metal centers yet also exhibit some valence delocalization. These characteristics define class II mixed-valence dimers.

As an example, let us consider the mixed-valence case of a manganese dimer with two different oxidation states for two distinct metal centers, Mn^{II} (d^5, $S_A = 5/2$) and Mn^{III} (d^4, $S_B = 2$). In such a dimeric unit with an $Mn^{II}Mn^{III}$ core, the "parallel" combination of the electronic spins leads to a ground spin state $S = 9/2$ high-spin configuration, while "antiparallel" pairing leads to a ground spin state $S = 1/2$ low-spin species. This latter case is achieved when the sign of J is negative. The parallel and antiparallel combinations of spins can be extended to higher nuclearity clusters such as trimers or tetramers; the corresponding magnetic properties of such clusters differ from those of the mononuclear constituents. The extent of the deviation from the characteristics typical for the mononuclear form (such as hyperfine constants, A or g-tensors) provides useful information toward the elucidation of the coupling mechanism. Most mononuclear Mn complexes are high-spin species, with the exception of those with a very strong ligand field [37] such as $[Mn^{II}(CN)_6]^{4-}$ or $[Mn^{III}(CN)_5NO_3]^{3-}$. The configuration of the d-electrons is in this context an important factor, which will differ for each oxidation state; therefore, different oxidation states will have certain preferences for specific coordination geometry. For example, Mn^{II} (d^5) adopts tetrahedral or octahedral complexes to minimize the ligand–ligand repulsions. In contrast, Mn^{IV} (d^3) compounds are stabilized by six-coordinate octahedral or pseudo-octahedral species. Complexes containing Mn^{III} (d^4) are the least selective due to the single unpaired electron in doubly degenerate antibonding orbitals in octahedral symmetry. As noticed by Pecoraro, a consequence of this lack of geometrical preference for Mn^{III} usually results in major structural changes, when sequential oxidation of the manganese compound from Mn^{II} to Mn^{IV} via Mn^{III} occurs [38].

The sign and magnitude of J are determined by a combination of several (sometimes competing) effects. Therefore understanding the nature of J is important to obtain insight into the geometric and chemical environment of the metal centers, the electronic structure of the complex, and for the elucidation of the mechanism of electron transfer [38,40]. In exchange-coupled clusters containing

metal centers, several, different exchange mechanisms have been identified and defined as follows:

Direct exchange is a ferromagnetic exchange interaction between two (or more) sites with no possible charge transfer, characterized by the lowest energy of the parallel spins in orthogonal orbitals. For non-orthogonal orbitals, or equivalently with configuration mixing (when two or more electronic configurations are contributing significantly to the ground state), direct exchange is one term in a sum of Heisenberg-type[2] terms (and other higher-order terms in spin coupling) [41,42].

Superexchange is a Heisenberg-type antiferromagnetic interaction that acts through the overlap of the molecular orbitals of the metal centers containing the opposite spins. The superexchange mechanism explains, for example, why two metals connected by an oxo bridge should have oppositely aligned spins. The shape of the oxygen p-orbital consists of two lobes. When this orbital is occupied by two electrons, then the electron spin on opposite sides of the oxygen must be anti parallel. The orientation of these spins forces the orientation of the partially occupied d-orbitals in the metal atom to be aligned in an anti-parallel manner. The efficiency of the superexchange mechanism will depend on the metal–oxygen–metal angle, and will decrease with deviation of this angle from 180° [43,44].

A *crossed superexchange mechanism* is a ferromagnetic analogue of the superexchange interaction and was observed in high oxidation state dinuclear and polynuclear Mn complexes. It consists of a ferromagnetic, Heisenberg-type interaction between a filled d-orbital on one high-spin metal site with an empty metal d-orbital on another site [45,46].

The *double exchange mechanism* is characteristic of mixed-valence species, and it is related to the conduction phenomenon with the electron "jumping" between two metal centers. If the bridging atoms are oxygens (as in majority of the mixed-valence Mn species), their p-orbitals are doubly occupied. Since the oxygen atom can not end up with a lack of electrons, there must be a simultaneous jump of both electrons: one jumping from the metal center to oxygen, and the other leaving oxygen to jump on the other metal center. In order to perform such a "double" jump, both electrons have to be in parallel spin configuration. The requirement of two parallel spins for the jumping electrons will force the metal center spins to also adopt the parallel alignment of spins [47–50]. This interaction that can be also seen as a form of "resonance delocalization" is the dominant mechanism for class II Robin and Day compounds [36].

In addition to these exchange mechanisms, the interaction with ligands and subsequent spin polarization (which can be ferromagnetic or antiferromagnetic) can be an important contribution to the observed net magnetic effect that in turn
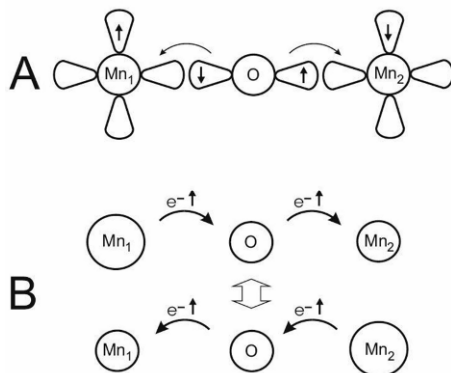
Figure 3. Schematic representation of the superexchange (A) and double-exchange (B) mechanisms resulting in, respectively, antiferromagnetic or ferromagnetic alignment of spins on metals centers. Note that for the double-exchange mechanism bigger and smaller circles schematically indicate the differences in ionic radius of the metal centers with different oxidation states. Adapted from [51].

dictates the final ground state [52,53]. For the dinuclear Mn mixed-valence compounds, the most important exchange mechanisms are the double-exchange and the superexchange ones (Fig. 3), this latter dictating the antiferromagnetic nature of these species. However, in manganese clusters of higher nuclearity, the resultant ground state is influenced by competition between superexchange, crossed-superexchange, and the ligand spin polarization.

Manganese atoms found in common oxidation states typical for the inorganic Mn complexes (Mn^{II}, Mn^{III} and Mn^{IV}) usually do not exhibit direct metal–metal bonding. For these molecules, a more effective mechanism for magnetic interaction is the superexchange pathway. The magnitude of the superexchange contribution to the total J value depends primarily on the metal and ligand type, which in turn dictate the bonding distances and geometry of the metal core. A sufficient overlap between the metal and bridging ligand atomic orbitals is necessary in order to assure an efficient delocalization of the spin over the metal center, through the resulting molecular metal–ligand orbital [38].

2.2. EPR Theory for Exchange Coupled Systems.

Interactions of interest for EPR spectroscopy are contained in the general, phenomenological spin Hamiltonian based on the concept developed by Pryce and Abragam [54,55]. For the exchange-coupled systems with n metal centers, this Hamiltonian in the most common form reads

$$\hat{H} = -2\sum_{i,j}^{N}\hat{S}_i \cdot J_{ij} \cdot \hat{S}_j + \sum_{i=1}^{N}\mu_B B \cdot g_i \cdot \hat{S}_i + \sum_{i=1}^{N}\hat{S}_i \cdot D_i \cdot \hat{S}_i + \sum_{k=1}^{n}\mu_n g_{n,k} B \cdot \hat{I}_k$$
$$+ \sum_{i=1}^{N}\sum_{k=1}^{n}\hat{S}_i \cdot A_k^i \cdot \hat{I}_k + \sum_{k=1}^{n}\hat{I}_k \cdot P_k \cdot \hat{I}_k.$$

$$(2)$$

The terms in the Hamiltonian have the following meaning:

$-2\sum\limits_{i,j}^{N}\hat{S}_i \cdot J_{ij} \cdot \hat{S}_j$ — exchange interaction between electrons;

$\sum\limits_{i=1}^{N}\mu_B B \cdot g_i \cdot \hat{S}_i$ — electronic Zeeman interaction, represents the interaction between the magnetic moment of the effective electron spin and the magnetic field (μ_B = Bohr magneton, B = magnetic field, g_i = electronic g-tensor, $\hat{S}_i$ = electron spin angular momentum operator)

$\sum\limits_{k=1}^{n}\mu_n g_{n,k} B \cdot \hat{I}_k$ — nuclear Zeeman interaction, represents the interaction between the magnetic moment of the nuclear spin and the magnetic field (μ_N = nuclear magneton, $g_{n,k}$ = nuclear g-factor, $\hat{I}_k$ = nuclear spin angular momentum operator);

$\sum\limits_{i=1}^{N}\sum\limits_{k=1}^{n}\hat{S}_i \cdot A_k^i \cdot \hat{I}_k$ — represents the hyperfine interaction, the interaction between the magnetic moment of the nuclear spin and the magnetic moment of the electron spin (A_i^i = hyperfine tensor);

$\sum\limits_{k=1}^{n}\hat{I}_k \cdot P_k \cdot \hat{I}_k$ — nuclear quadrupolar interaction, results from the interaction between the quadrupolar electric moment of the nucleus with the electric field gradient created by the surrounding electrons and nuclei (P_k = quadrupole tensor);

$\sum\limits_{i=1}^{N}\hat{S}_i \cdot D_i \cdot \hat{S}_i$ — Zero-Field Splitting term, results from spin–orbit and magnetic dipole–dipole interactions, resulting in a term similar to that for the nuclear quadrupolar interaction. It is only applicable for $S > \frac{1}{2}$ (D_i = ZFS matrix).

The energy levels of the system are obtained by diagonalization of the Hamiltonian matrix, whose elements are calculated starting from the Hamiltonian described above, and of the associated wavefunctions of the electronic and nuclear spins.

The simulation and interpretation of EPR spectra arising from magnetically coupled metal clusters requires a theoretical model accounting for the exchange-coupling scheme between the different metal centers. Due to the complexity of such systems (e.g., multiple overlapping hyperfine transitions), an in-depth discussion of the theory for EPR spectra of multinuclear systems (e.g., more than two metal centers) lies well beyond the scope of this short chapter.[3] However, the interested reader is directed to the seminal text on exchange-coupled systems by Bencini and Gatteschi [57]. We choose, instead, to focus on the analysis of the spectral properties of mixed-valence $Mn^{III}Mn^{IV}$ model complexes relevant to the Mn cluster in the OEC. The EPR spectra of such dimers arise from a combination of the spec-

tral patterns obtained for the individual ions, and will be governed by the coupling between the two mononuclear metal centers. It is worth noting that, in contrast to such a "coupled" spectral pattern, the EPR spectrum obtained for a class I Day and Robin dimer will be (at first approximation) simply the sum of the individual spectra for each noninteracting spin site perturbed only by the dipolar interaction with the adjacent metal ion.

2.2.1. Dimeric Species

The quantum mechanical description of the EPR spectra of the exchange-coupled species is based on the phenomenological spin Hamiltonian given in Eq. (2). Although the exchange is a purely quantum mechanical effect, it is useful to employ a classical description of the spins to represent this concept, and a pictorial representation of the interacting mononuclear spin systems is given in Figure 4.
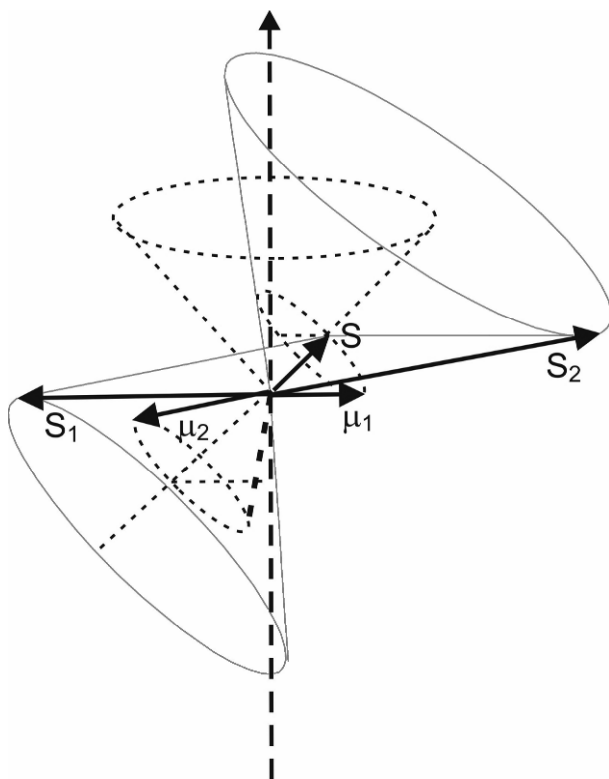
Figure 4. Pictorial representation of the classical description of two interacting metallic centers, M_1 and M_2, bearing the corresponding mononuclear spins: M_1 (Mn^{IV}) with $S_1 = 3/2$ and M_2 (Mn^{III}) with $S_2 = 2$. The total spin S will precess at high frequency around the total spin vector $S = 1/2$. Adapted [58].

The possible spin states (S) of this dimer are defined by addition of the individual site spin vectors (S_1 and S_2) abiding the angular momentum addition rules:

$$\left|S_1 - S_2\right| < S < \left|S_1 + S_2\right| \tag{3}$$

For an $Mn^{III}Mn^{IV}$ dimer, S can take all the values from 1/2 to 7/2 in increments of one: 1/2, 3/2, 5/2 and 7/2. In the external magnetic field the specific spins of the two metal centers M_1 (Mn^{IV}) with $S_1 = 3/2$ and M_2 (Mn^{III}) with $S_2 = 2$, will precess at high frequency around the total spin vector $S = 1/2$. As can be seen from Figure 4, the direction of the projection of S_1 on S is opposite to that of S. This results in the change of the sign of the effective hyperfine field at the M_1 Mn^{IV} site, while the projection of S_2 is in the same direction as S and will remain positive.

For most of the manganese dimeric complexes the exchange interactions are important. We can thus make the assumption that we are in the strong exchange limit, so that the electronic Zeeman, hyperfine, and quadrupolar interactions are much smaller than the exchange interaction. In such a system, the interaction between two spins can be simply described by the Heisenberg-Dirac-van Vleck (HDvV) Hamiltonian (1) (sometimes called, for short, the Heisenberg or Exchange Hamiltonian) introduced earlier. However, this form is merely an approximation, and the dominant interaction between two spins S_1 and S_2 is generally described as

$$\hat{H} = \hat{S}_1 \cdot J_{12} \cdot \hat{S}_2 , \tag{4}$$

with J_{12} defining an effective exchange tensor possessing an isotropic and an anisotropic part. Moreover, we can make one more simplification assuming that for most of the systems presented here only the isotropic part of the exchange term of the Hamiltonian is to be considered and J remains a scalar value.[4]

Let us now have a closer look at the phenomenological spin Hamiltonian for two magnetically coupled centers. For any exchange-coupled dimer, the general spin Hamiltonian (2) can be rewritten for two spin centers ($N = n = 2$) in the uncoupled basis[5] (where the subscript "ub" relates to the uncoupled basis representation) using the isotropic exchange term:

$$\hat{H}_{ub} = -2J_{12}\hat{S}_1\hat{S}_2 + \sum_{i=1}^{2}\hat{S}_i D_i \hat{S}_i + \sum_{i=1}^{2}\mu_B \mathbf{B} g_i \hat{S}_i - \sum_{k=1}^{2}\mu_n g_{n,k}\mathbf{B}\hat{I}_k \tag{5}$$
$$+ \sum_{i=1}^{2}\sum_{k=1}^{2}\hat{S}_i A_k^i \hat{I}_k + \sum_{k=1}^{2}\hat{I}_k P_k \hat{I}_k .$$

Since $|J| \gg \mu_B \mathbf{B}\cdot g$ and $|J| \gg |D|$, such strongly coupled systems dimers can be regarded as a ladder of well-separated spin manifolds (Fig. 5) with the separation between the ground-spin and the higher-spin manifolds much larger than the EPR microwave energies at classical EPR frequencies (X- and Q-band).

In such a case, each spin manifold can be treated independently. The interacting mononuclear spins can be coupled by the addition of the individual site spin vectors following the angular momentum addition rules, yielding an effective spin
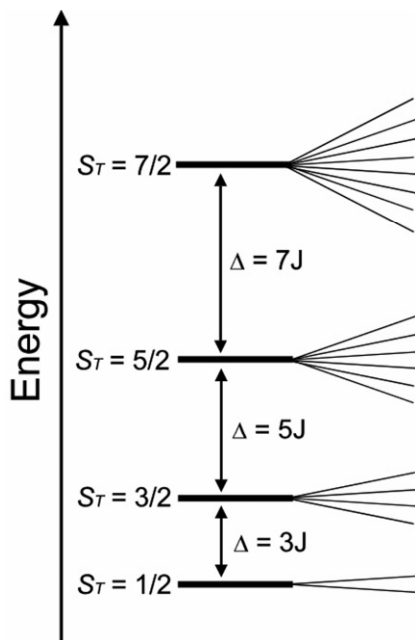
Figure 5. Schematic representation of spin energy levels for a typical mixed-valence $Mn^{III}Mn^{IV}$ complex. Adapted from [59].

for the coupled system in the individual spin manifold. The EPR spin Hamiltonian (5) in an uncoupled basis can then be expressed in terms of this effective spin in the so-called coupled basis. The transformation of the uncoupled basis to the coupled basis is done using the Wigner-Eckardt theorem. The new Hamiltonian in the coupled basis becomes (where the subscript "cb" relates to the coupled basis representation):

$$\hat{H}_{cb} = \hat{S} \cdot D^{eff} \cdot \hat{S} + \mu_B \mathbf{B} \cdot g^{eff} \hat{S} - \sum_{k=1}^{2} \mu_n g_{n,k} \mathbf{B} \cdot \hat{I}_k + \sum_{i=1}^{2}\sum_{k=1}^{2} \hat{S} \cdot_i A_k^i \cdot \hat{I}_k$$
$$+ \sum_{k=1}^{2} \hat{I} \cdot_k P_k \cdot \hat{I}_k. \tag{6}$$

The ZFS term D_i, the hyperfine term A_i and the g-tensor g_i are now defined as D^{eff}, A^{eff}, and g^{eff}, respectively in the coupled basis representation.

Keeping the usual notation S for the total spin of coupled S_1 and S_2 spins, one can, in principle, apply the spin projection technique, which relies on the so-called Kambe vector model of coupling spins [60], when the spin vectors are treated in a classical way and can be projected following simple vector algebra rules. Using the spin projected factors for two coupled metal centers:

$$c_1 = \frac{S_1(S_1+1) - S_2(S_2+1) + S(S+1)}{2S(S+1)}, \tag{7}$$

$$c_2 = \frac{S_2(S_2+1) - S_1(S_1+1) + S(S+1)}{2S(S+1)}. \tag{8}$$

The effective g-tensor (g^{eff}) for the coupled metallic dimer with two metal centers M_1 and M_2 is defined as:

$$g^{\text{eff}} = c_1 g_1 + c_2 g_2. \tag{9}$$

The analogous formulation can be used to express the effective hyperfine coupling observed for sites M_1 and M_2:

$$A_1^{\text{eff}} = c_1 A_1 \tag{10}$$

$$A_2^{\text{eff}} = c_2 A_2 \tag{11}$$

Equations (11) and (12) can also be applied to the ligand hyperfine couplings, allowing to analyze the effective ligand hyperfine $A_{\text{ligand}}^{\text{eff}}$, and in this way to determine the oxidation state of the coordinating metal center. In the case of the $Mn^{III}Mn^{IV}$ dimers, $c_1 = 2$ (for Mn^{III}) and $c_2 = -1$ (for Mn^{IV}).

The above-presented formulation assumes that the contribution of the mixed metal site ZFS terms D is neglected. This is indeed true for the strongly coupled dimeric species. Nevertheless, for the more weakly coupled dimers, one needs to account for this interaction. In this case the formulation for g^{eff} can be derived based on Eq. (9) yielding [61]:

$$g^{\text{eff}} = c_1 g_1 + c_2 g_2 + \frac{c_1 c_2 (g_1 - g_2)(b_1 D_1 - b_2 D_2)}{5J}, \tag{12}$$

where $b_1 = 3c_1 + 1$ and $b_2 = 3c_2 + 1$.

In an analogous way, the equations including the ZFS term for the hyperfine couplings can be obtained:

$$A_1^{\text{eff}} = c_1 a_1 - \frac{c_1 c_2 a_1 (b_1 D_1 - b_2 D_2)}{5J}, \tag{13}$$

$$A_2^{\text{eff}} = c_2 a_2 - \frac{c_1 c_2 a_2 (b_1 D_1 - b_2 D_2)}{5J}. \tag{14}$$

For the antiferromagnetically coupled manganese dimer $Mn^{IV}Mn^{III}$ there are two interacting spins — $S_1 = 2$ and $S_2 = 3/2$ — with the total coupled spin of $S = 1/2$. After substitution of the proper spin values S_1, S_2, and S, the effective g^{eff} term and the hyperfine couplings become

$$g^{\text{eff}} = 2g_1^{\text{Mn}^{\text{III}}} - g_2^{\text{Mn}^{\text{IV}}} - \frac{2(g_1^{\text{Mn}^{\text{III}}} - g_2^{\text{Mn}^{\text{IV}}})(7D_1^{\text{Mn}^{\text{III}}} + 2D_2^{\text{Mn}^{\text{IV}}})}{5J}, \tag{15}$$

$$A_1^{\text{eff(Mn}^{\text{III}})} = 2A_1^{\text{Mn}^{\text{III}}} + \frac{2A_1^{\text{Mn}^{\text{III}}}(7D_1^{\text{Mn}^{\text{III}}} + 2D_2^{\text{Mn}^{\text{IV}}})}{5J}, \tag{16}$$

$$A_2^{\text{eff(Mn}^{\text{IV}})} = -A_2^{\text{Mn}^{\text{IV}}} + \frac{2A_2^{\text{Mn}^{\text{IV}}}(7D_1^{\text{Mn}^{\text{III}}} + 2D_2^{\text{Mn}^{\text{IV}}})}{5J}. \tag{17}$$

If the contribution from the ZFS term is small, and the exchange term J is greater than the corresponding hyperfine and ZFS terms, the second part of the equation vanishes and the previous equations are reduced to:

$$g^{\text{eff}} = 2g_1^{\text{Mn}^{\text{III}}} - g_2^{\text{Mn}^{\text{IV}}}, \tag{18}$$

$$A_1^{\text{eff(Mn}^{\text{III}})} = 2A_1^{\text{Mn}^{\text{III}}}, \tag{19}$$

$$A_2^{\text{eff(Mn}^{\text{IV}})} = -A_2^{\text{Mn}^{\text{IV}}}. \tag{20}$$

g^{eff} and A^{eff}_i can be derived for other valence manganese dimers (e.g., $Mn^{\text{II}}Mn^{\text{III}}$). The corresponding values for several exchange-coupled dimers are reported in Table 1. In this context it is important to recall that the J values of $Mn^{\text{II}}Mn^{\text{III}}$ dimers are usually an order of magnitude smaller than these of the $Mn^{\text{III}}Mn^{\text{IV}}$ species, thus placing often the former in the $|J| \approx |D|$ regime. In such a situation, the correction terms in Eqs. (13) and (14) have a large impact on the coupled EPR parameters, leading to important differences in the hyperfine parameters.

2.2.2. Clusters of Higher Nuclearity

The methodology presented above can be, in principle, applied for multinuclear manganese clusters, and in simple cases the Kambe vector model of coupling spins can be used in a straightforward manner. However, with each additional exchange-coupled nucleus, the spin projection equations become rapidly more complicated. Unfortunately, the Kambe model is only solvable for some selected cases where the coupling scheme can be easily reduced to a simple form based on symmetry considerations. In the nonsymmetrical manganese clusters, the differences in the exchange parameters between different metal centers result in the mixing of the intermediate spin states. A direct consequence of such changes is manifested by differences in the magnetic properties of the cluster, which translate to changes in the hyperfine couplings and g-tensors of the resulting EPR spectra.

Several models were developed to describe the magnetic properties of the multinuclear manganese cluster of PSII and the most popular (besides the dimeric species described above) are the models including four manganese atoms, because of the same manganese nuclearity as observed in the native enzyme. However, it is to

Table 1. Calculated Values of A_{eff} Coefficients for Several Dimeric and Tetrameric Mixed-Valence Manganese Clusters

Hyperfine coupling coefficient	A1	A2	A3	A4
Dimers				
(III)(IV) $\lvert 1/2; 2; 3/2 \rangle$	2A1′	–A2′	–	–
(II)(III) $\lvert 1/2; 5/2; 2 \rangle$	7/3A1′	–4/3A2′	–	–
Tetramers				
(IV)(IV)(IV)(III) $\lvert 1/2; 0; 1/2 \rangle$	0	0	2A3′	–A4′
(IV)(IV)(IV)(III) $\lvert 1/2; 3; 7/2 \rangle$	–A1′	–A2′	9/7A3′	12/7A4′
(III)(III)(III)(IV) $\lvert 1/2; 0; 1/2 \rangle$	0	0	2A3′	–A4′
(III)(III)(III)(IV) $\lvert 1/2; 4; 7/2 \rangle$	5/3A1′	5/3A2′	–4/3A3′	–A4′
(III)(III)(III)(II) $\lvert 1/2; 0; 1/2 \rangle$	0	0	7/3A3′	–4/3A4′
(III)(III)(III)(II) $\lvert 1/2; 4; 9/2 \rangle$	4/3A1′	4/3A2′	–55/27A3′	–44/27A4′
(II)(II)(II)(III) $\lvert 1/2; 0; 1/2 \rangle$	0	0	7/3A3′	–4/3A4′
(II)(II)(II)(III) 2A1′ $\lvert 1/2; 5; 9/2 \rangle$	2A2′	–5/3A3′	–4/3A2′	

notice that some models with three atoms were also probed. Most of these trinu-clear clusters exhibit an $S = 3/2$ ground state and exhibit the so-called spin-frustration (see §3.2.).

For symmetrical tetranuclear clusters such as the "dimer-of-dimers" model, the Kambe model can still be applied, in the assumption that several J couplings are of the same magnitude. For example, if one considers a hypothetical, highly symmet-ric (C_{2v}) tetramer with four manganese atoms, such as that schematically depicted in Figure 6B, then of the six possible pairwise exchange interactions, four will be equivalent ($J_{12} = J_{23} = J_{34} = J_{14}$), and the two others will different from the previous values: $J_{13} \neq J_{24} \neq J_{12}$. By using the Kambe projection technique, one can project the individual spins S_i on the total spin S, in a way analogous to that used in Sec-tion 2.2.1 for the $Mn^{III}Mn^{IV}$ and $Mn^{II}Mn^{III}$ dimers. However, with the number of
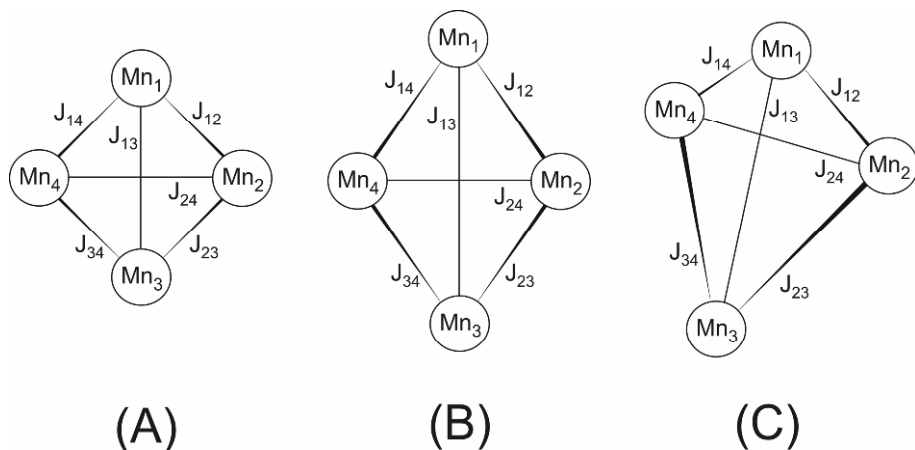
Figure 6. Schematic representations of the spin-coupling parameters between four manganese centers: (A) full symmetry T_d, (B) high symmetry C_{2v}, and (C) asymmetric model.

metal centers exceeding two, an additional complication occurs, such that several different coupling schemes are possible [62]. For example, in the above-mentioned symmetrical tetramer, the coupling of spins between centers Mn_1 and Mn_3 and between centers Mn_2 and Mn_4 resulting in two values (S_{13} and S_{24}) is only one of the three possible combinations for the coupling scheme. To obtain the projection of the total spin, one must first project S_i on its quantized resultant S_{ij}, which in turn must be projected on the total spin S (Fig. 7). Equations for the hyperfine couplings analogous to those obtained for the dimers can be derived, e.g.,

$$A_i = \frac{\vec{S}_i \cdot \vec{S}_{ij}}{\vec{S}_{ij}^2} \times \frac{\vec{S}_{ij} \cdot \vec{S}}{\vec{S}^2} \times A_i' . \tag{21}$$

For several exchange-coupled dimers and tetramers the coefficients c in Eqs. (10) and (11) have been calculated and reported in Table 1. The equations for A_i in the trinuclear and tetranuclear species based on expansion of Eq. (21) are reported in the Appendix. By defining the intermediate spin states S_i (or S_{ij}) that are projected on total spin vector S, one can use the simplified spin state notation for the dimers and higher nuclearity clusters exemplified in the following notation:

Dimers: $\left| S; S_1; S_2 \right\rangle$,   Trimers: $\left| S; S_{13}; S_2 \right\rangle$,   Tetramers: $\left| S; S_{13}; S_{24} \right\rangle$,

where S is the total spin, and S_i, S_{ij} are the respective "site" spin values (e.g., S_{13} is the value of the S_1–S_3 pair).

The situation is much more complicated if one wants to obtain the projection factors for the less symmetrical cluster topologies. This requires the use of numerical methods such as those described by Bencini and Gatteschi [57] or by Belinskii
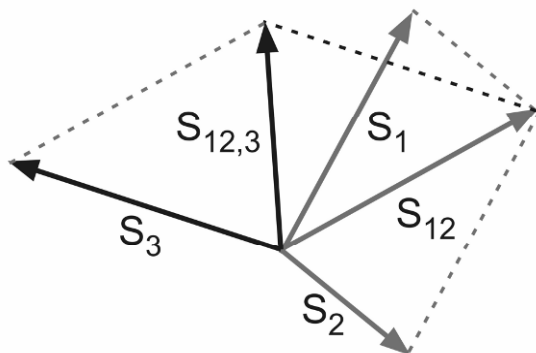
Figure 7. Schematic representations of the spin-coupling scheme for a three-spin system. First the S_1 is coupled with S_2, and the coupled S_{12} is finally coupled to the third spin S_3.

[63], who devoted several papers to the description of the coupling schemes for many symmetric and asymmetric tetranuclear Mn architectures; the reader can find the details of the useful equations in these theoretical works [63,64]. Several spin coupling models were also developed based on symmetry considerations and various spin coupling schemes [39,65–68].

2.3. Computational Methods for Magnetically Coupled Homonuclear Metal Clusters

Although quantum mechanical (QM) calculations on mononuclear transition metal complexes are commonplace in the literature, analogous computations on higher-nuclearity biologically active sites or synthetic multinuclear clusters are still very scarce [69,70]. Theoretical studies of such systems suffer from several difficulties, the most important including the correct treatment of the electronic correlation and the multiconfigurational character of metal–metal interactions. Hence, related computational tasks are usually difficult and very time consuming. These problems have been somewhat mitigated recently owing to the development of the faster optimization algorithms and increased capabilities of computer hardware. Improvements of these factors have led to faster calculations on more realistic model systems.

Despite the many current challenges, a major boon of quantum mechanical calculations applied to oligonuclear transition metal complexes is the possibility of combining advanced theory and experiment to elucidate their geometric and electronic structures. In order to relate results from spectroscopic studies to the structural or functional properties, a systematic and detailed interpretation of the spectroscopic parameters is necessary. As recently observed by Neese [71], such interpretation, based on a comparison between calculated and measured spectroscopic

data, hinges on the ability to calculate as many observables as possible with a high degree of accuracy.

In a way analogous to the efforts toward developing synthetic model compounds, the computational studies relevant to the manganese cluster of OEC focus on several distinctive aspects. The most important include the structural, closely related to, still unknown, structure of the OEC, and the functional one, targeting the mechanism of electron–proton transfer and the ultimate oxidation mechanism of water to dioxygen. Most of the early theoretical studies of the exchange-coupled multinuclear metal species targeted the mechanism of magnetic coupling and the possible exchange pathways, with particular focus on computation of the exchange parameters J. Elucidation of the exchange pathways in manganese dimers is, for example, important in relation to the ongoing discussion as to whether the bridges in the Mn_4 OEC unit are oxo or hydroxo, and if carboxylate functionalities of ligating amino acids are mono or bidentate. Historically, the first attempts to computationally probe coupled manganese clusters dates back to 1992, when Noodleman provided the theoretical description of an $Mn^{III}_3Mn^{IV}$ tetramer $[Mn^{IV}Mn^{III}_3O_3Cl_7(O_2CCH_3)_3]^{3-}$, a potential model for the S_0 state of the OEC using the so-called broken-symmetry approach, presented in more detail in the following section.

2.3.1. Broken-Symmetry Approach

Exchange-coupled systems constitute an area in which many theoretical approaches are still in *statu nascendi*. This is almost exclusively related to the fact that in these species the individual spins of two (or more) magnetic metal centers are coupled to a number of energetically close-lying electronic levels. For such strongly correlated entities, the monodeterminental post Hartree-Fock methods (e.g., Density Functional Theory) are only of limited usefulness. Systems involving multiple metals with strongly correlated electrons to be properly described require the use of multideterminental methods,[6] which, unfortunately, when applied to such large molecules are currently not feasible.

However, the calculation of magnetic properties, geometries, and exchange pathways are accessible using Density Functional Theory (DFT) in the so-called Broken-Symmetry DFT approach (BS-DFT), formulated by Noodleman [72–78]. In BS-DFT calculations, the true multideterminental character of antiferromagnetically coupled systems is approximated using a singledeterminental Kohn-Sham equivalent of wavefunction Ψ, with unpaired α and β electrons (α = spin-up, β = spin-down) partially localized at different metal sites. This procedure "breaks" the symmetry of the spin part of Ψ and implies that the energies, spin expectation values, and spin densities calculated in this manner are not the same as the ones that would be obtained from the truly multideterminental treatment. Nevertheless, using the Wigner-Eckart theorem [58,79,80] and the appropriate spin projection procedures [81] as described in Section 2.2.2, the exchange-coupling constants, hyperfine coupling constants, and g-tensor corresponding to the antiferromagnetic state can be easily obtained.

The basics of the BS-DFT approach can be defined in terms of a few important assumptions and postulates. The central point is that the ground state and low excited states of a coupled system are in principle multireference in character, which implies that they are not pure eigenstates of the total spin operator M_s, but rather a mixture of different states. The correct evaluation of their energy is therefore not possible using a single determinant; only the ferromagnetically coupled high-spin (HS) state has a single determinental representation. In the presence of strong antiferromagnetic coupling, however, the single-determinental wavefunction is close to the true ground state. In the presence of more weakly coupled systems, the problem can be solved by calculating an intermediate state lying between the high- and low-spin eigenstates, the so-called broken-symmetry (BS) state. This state is obtained by breaking the spin symmetry of the HOMO and LUMO orbitals and lowering a spatial symmetry of the orbitals containing the α and β spins. Therefore, the BS state is not a pure spin state but rather an "assymetrized" state of mixed spin symmetry and lower spatial symmetry. The second important point in the BS approach is that calculation of a broken symmetry state in DFT is straightforward. The DFT calculated BS state (S_{BS}) is an admixture of excited configurations to the given pure total spin state S, which, along with direct exchange, govern the effective spin coupling interactions [82]. On the other hand, the proper Heisenberg spin Hamiltonian can be derived from second-order perturbation theory, assuming that each interacting metal site has a well-defined net spin.

For a polynuclear complex, the Heisenberg Hamiltonian can be written as a sum of pairwise interaction terms. With the energies of the broken symmetry states in hand, one can relate it to those of pure spin eigenstates through the use of Clebsch-Gordon algebra rules. By evaluating all the $(S;S_j)$ terms for each broken symmetry state and multiplying by $-2J_{ii}$, a set of linear equations is obtained, from which the J parameters can be easily determined. The knowledge of the J values allows in turn determination of the energies of the pure spin states [83]..

If we consider once again the simple dinuclear $Mn^{III}Mn^{IV}$ system, the possible spin states can be schematically represented as in Figure 8. In order to access the magnitude of the exchange coupling, one wants to extract the wavefunctions of two different states: the high-spin (HS) and the broken-symmetry (BS) states. As can be seen from Figure 8, the true antiferromagnetic (AF) state lies below the BS state, but by using proper procedures the energy of this state can be obtained. The high-spin state is accurately represented in DFT, as the $S = 7/2$ wavefunction arises from only a single electron configuration, where both $S_1 = 2$ and $S_2 = 3/2$ are ferromagnetically coupled, whereas the antiferromagnetic state ($S = 1/2$) has contributions from all configurations containing $m_S = 1/2$. Fortunately, the BS state, while not physically relevant, is mathematically related to the energy of the HS and AF states by the exchange-coupling parameters and allows one to extrapolate the energy of the true antiferromagnetic state. This methodology and the related spin-projection techniques (see §2.2.) can be extended to multinuclear metal clusters. The details of the formulation of the BS-DFT can be found in pioneering work by Noodleman [72] and in several papers devoted to the use of the BS approach for calculation of magnetic properties [82–92].
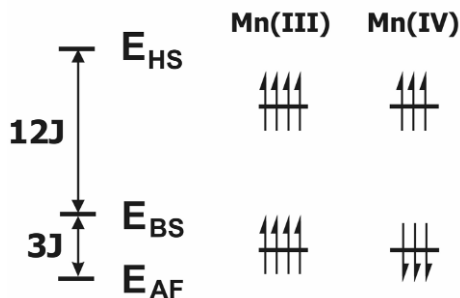
Figure 8. Schematic representation of the high- and low-spin states for the exchange-coupled manganese $Mn^{III}Mn^{IV}$ complex together with the broken-symmetry state obtained from the QM calculations.

2.3.2. *Calculations of EPR Parameters*

Modern quantum chemistry offers not only a large compendium of tools for elucidation of the structural and electronic aspects of the investigated systems but is also able to predict many valuable observables, which can be directly compared to experimental data from both biological samples and synthetic model compounds. In the case of EPR techniques, those properties include the *g*-tensor, as well as hyperfine and quadrupolar interactions; computational strategies exist also to simulate, for example, EXAFS spectra or to compute vibrational IR modes or the UV transitions.

With respect to the OEC, recent papers have shown that the same methodology is also capable of predicting qualitative trends for *g*- and hyperfine tensors in several exchange-coupled Mn dimers. Before highlighting important results from the available theoretical studies, several comments have to be made about the ability of DFT to yield accurate information about the magnetic parameters of such systems. Dipolar coupling (anisotropic part of the hyperfine tensor) calculated for different oxidation states of manganese are relatively close to the experimental values. Contrastingly, computed A_{iso} values are usually underestimated, due to the inability of most quantum mechanical methods to properly predict unpaired electron density at the nucleus (Fermi contact) [7] and the spin polarization phenomena. A critical validation of the use of DFT for such calculations was recently presented by Munzarova and Kaupp [93]. Additional topics, intrinsic to coupled metal centers, include the calculation of ZFS values [94], which are known to influence hyperfine coupling values for weakly coupled mixed-valence $Mn^{III}Mn^{IV}$ clusters. As ZFS results from spin–orbit coupling between excited electronic states, *E* and *D* parameters can only be accurately computed using a full-configuration interaction (CI) approach,[8] although recent implementation of the ZFS calculations based on the spin–orbit operators (SOOs) in the DFT code ORCA by Nesse are very promising. Some of the important results from these studies are summarized later in this chapter.

3.   SYNTHETIC MODELS FOR MANGANESE CLUSTER OF THE OEC

3.1. Current Structural Proposals for the Pentanuclear Mn_4Ca Cluster of the OEC

After it became apparent that a magnetically coupled manganese moiety is at the heart of the OEC, numerous studies were initiated to understand its architecture and the electronic structure related to the spectroscopically distinct signatures from consecutive S states of the Kok cycle. However, even with the recent publication of several modest resolution crystallographic X-ray structures and high-resolution X-ray absorption studies of PSII [14–17], the exact topology of the manganese cluster in the OEC remains unknown. Despite abundant experimental and theoretical investigations that have narrowed the range of its possible structural characteristics, due to the complexity of the system and impediments from the experimental techniques (e.g., crystal damage or possible changes in the cluster topology during exposition to X-ray radiation [95,96]), the exact architecture of Mn_4 remains a challenging goal.

Despite these issues, X-ray crystallographic and absorption experiments have provided together with spectroscopic techniques (EPR, IR) the most insight into the structural features of the tetranuclear Mn cluster of OEC. Briefly, results from these studies suggest that the manganese core of the OEC complex should incorporate four manganese atoms, interconnected by μ-oxo or di-μ-oxo bridges, with Ca^{2+} and Cl^- cofactors, of which the exact position is still to be determined. Internuclear distances determined from EXAFS studies suggest that the four manganese atoms adopt 3 + 1 arrangement, in which three Mn atoms are separated by about 2.7 Å and the fourth Mn lays farther out, at about 3.3 Å. It is worth noting that the bond lengths and bond angles in several synthetic di-μ-oxo Mn complexes are consistent with a required Mn–Mn distance of about 2.7 Å, while for a singly μ-oxo bridged Mn dimer this distance lies in the range 2.9–3.3 Å, depending on the bending angle of the Mn–O–Mn unit (see Table 2A).

Despite the lack of precise structural data for the OEC, numerous structures for the tetranuclear manganese moiety (and more recently for the pentanuclear Mn_4Ca cluster) have been proposed. In general they can be divided into two distinct structural categories: (i) the "dimer-of-dimers," with two dimeric, connected subunits; and (ii) the so-called "3+1 Dangler" model, with a trinuclear subunit connected to a more distant single manganese nucleus (dangling manganese). The recent X-ray crystallographic studies resulted in several proposed architectures for the four manganese centers and the calcium ion; all of them, however, postulate a "3+1 Dangler" arrangement consistent with the EXAFS studies. The common motif of most of the proposed structures is the so-called "cubane" fragment, in which three of the manganese atoms and calcium ion form a distorted cube, which is in turn connected to the more distant, fourth manganese. Based on a recent single crystal X-ray absorption studies by Yano et al. [99,100], an alternative model was proposed where the calcium ion is not a part of the "cubane," and the

Table 2. (A) Possible Oxidation States of Manganese Ions in the Tetranuclear Mn Cluster Together with the Corresponding Mn–Mn Distances and (B) Some Characteristic EPR Signals for Each S State of the Kok Cycle

A

Kok state	A	B	C	Possible Mn–Mn distances
S_0	$Mn^{II}_3Mn^{III}$	$Mn^{II}Mn^{III}_3$	$Mn^{III}_3Mn^{IV}$	$2 \times 2.69, 2.87, 3.3$ Å
S_1	$Mn^{II}_2Mn^{III}_2$	Mn^{III}_4	$Mn^{III}_2Mn^{IV}_2$	2 or $3 \times 2.7, > 3.3$ Å
S_2	$Mn^{II}Mn^{III}_3$	$Mn^{III}_3Mn^{IV}$	$Mn^{III}Mn^{IV}_3$	2 or $3 \times 2.7, > 3.3$ Å
S_3	Mn^{III}_4	$Mn^{III}_2Mn^{IV}_2$	Mn^{IV}_4	1 or $2 \times 2.8, 2.95, 3.3–3.5$ Å

B

Kok state	Characteristic EPR signals
S_0	Multiline signal with 24–26 peaks centered at $g \approx 2$
S_1	Parallel mode EPR broad signal at $g \approx 4.8$, multiline with 18 peaks at $g \approx 12$
S_2	Multiline signal with 19–21 peaks centered at $g \approx 2$, broad signal $g \approx 4.1$
S_3	Broad signal at $g \approx 6.7$, broad signals at $g \approx 12$ and at $g \approx 8$

Adapted from [97] and [98].

dangling manganese is connected via two oxo bridges. Several examples from each of these classes are presented schematically in Figure 9 (with the most recent proposed structures at the bottom), and the latest structural proposals for Mn_4Ca are discussed in [13].

Over the last three decades, EPR spectroscopic characterization of the different S states of the OEC have yielded spectral signatures for nearly each state of the Kok cycle (see Table 2B). Recent reviews devoted to the related EPR spectroscopic studies can be found in. [21,56]. In particular, spectroscopic studies of the native Mn_4 cluster in the OEC have focused on elucidation of the structure–functional relationship of the PSII active site. Parallel to these efforts, numerous investigations of much simpler Mn-containing models strived to aid in the interpretation of the spectroscopic data from the enzyme. Small synthetic moieties are often designed to model such particular characteristics of large metalloproteins as active site structure, catalytic/enzymatic function, and spectroscopic signature. With respect to PSII, the intense interest in designing simple, synthetic inorganic complexes that could model the structural and magnetic/spectroscopic properties observed for different S states of the OEC [101–103] is intimately related to the ultimate quest for a synthetic molecule capable of oxidizing water to dioxygen [104,105]. While to date no compounds exists that replicate all of these properties
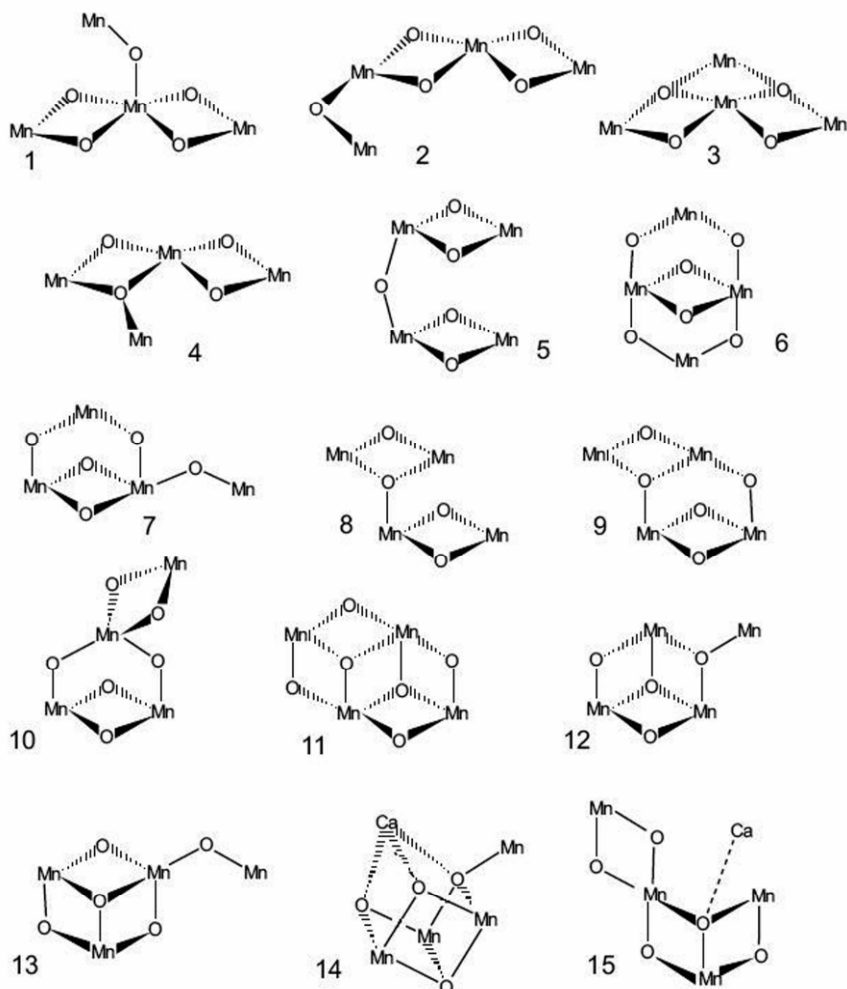
Figure 9. Schematic representation of the models proposed for the tetranuclear manganese cluster of the OEC. Adapted from [123].

simultaneously, considerable progress has been made in mimicking structural aspects of the Mn_4 core of the OEC determined by both X-ray crystallography and X-ray absorption techniques, such as XANES or EXAFS [106–115].

The high-valent μ-oxo or di-μ-oxo-bridged Mn units in the synthetic manganese clusters are most often stabilized by electron-rich ligands. The most popular bidentate ligands include bipyrydine (bipy), phenanthroline (phen), and salophene (salpn). However, other ligands can be used to this aim and some of these are reported in Table 3. Despite the fact that multiple homovalent and mixed-valence dimanganese complexes containing such stabilizing ligands were prepared and
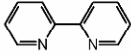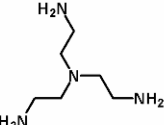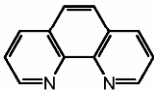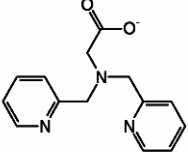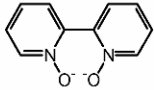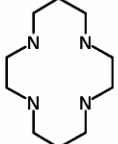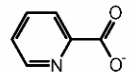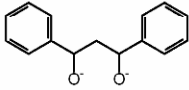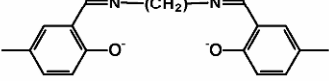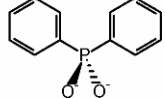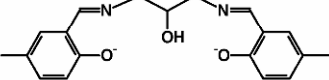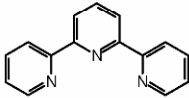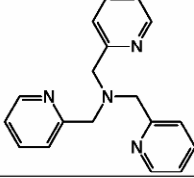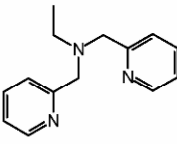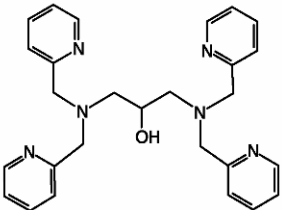
characterized (the reader can find an excellent compilation of their structural and spectroscopic characteristics in recent reviews by Vrettos and Brudvig [116] or by Mullins and Pecoraro [117]), to date, only some of the molecular architectures believed to be present in the OEC have been synthesized. Examples of these structural synthetic motifs relevant to OEC are reported in Figure 9. Despite the apparent abundance of the synthetic model species, it was very quickly realized that such molecular moieties could act as structural or functional models for OEC only to a very limited extent. Nevertheless, they have provided many useful insights into the electronic origin of the characteristic spectroscopic signals of the native enzyme and greatly helped in the elucidation of the structural and functional roles of the Mn_4 moiety of OEC. A complete coverage of the synthetic efforts in this field exceeds the scope of this chapter, and the avid reader is invited to consult several excellent reviews devoted to this area of research [98,118–122]. In the following sections, the most important models that contributed to the understanding of the OEC (classified into three distinct categories: dimers, trimers, and tetramers) are presented. These models (Table 4 contains selected synthetic Mn complexes with relevance to OEC, with their characteristic spectral EPR signatures), as well as those that remain compatible with the current knowledge of the Mn cluster topology, are discussed in more detail, with a focus on the corresponding magnetic resonance data and related computational studies.
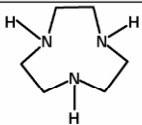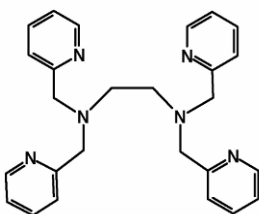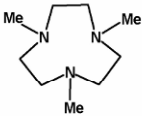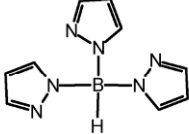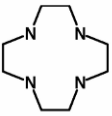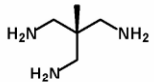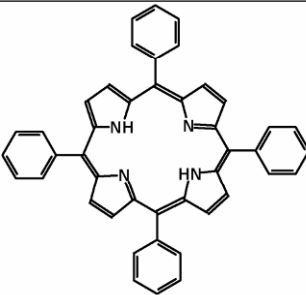
3.2. EPR Characteristics of the Manganese Cluster of the OEC

Before presenting the synthetic compounds that contributed to an understanding of the nature of the manganese moiety of OEC, it is important to briefly remind the reader of its EPR characteristics, essential in the context of this section. A complete coverage of this topic is provided in [21,56]. The hyperfine interaction resulting from the coupling of the unpaired electron spin to the nuclear spin of ^{55}Mn ($I = 5/2$) splits the Zeeman levels of the electronic α and β manifolds into an additional six nondegenerate levels. The corresponding allowed transitions ($\Delta M_S = \pm 1$) give rise to 6 distinct EPR lines that can be observed in the classical perpendicular-mode ($B_0 \perp B_1$) EPR experiment. According to the multiplicity rule ($N_L = 2I + 1$; N_L being the number of the EPR lines), the dimeric, trimeric, and tetrameric Mn moieties coupled to the unpaired electron would result in 36, 216, or 1296 lines respectively. However, many of these transitions will overlap and/or be obscured by the spectral linewidth, leading to a reduction in the total number of observed EPR lines.

One of the characteristic features of the Mn_4 cluster in PSII is the existence of two distinct X-band EPR spectral signatures observed for the OEC trapped in the S_2 state of the Kok cycle [102]. The first is a $g = 2.0$ signal with 16 to 19 visible ^{55}Mn hyperfine components (also known as the multiline signal) attributed to an $S = \frac{1}{2}$ ground state. The second is a broad transition centered at $g = 4.1$ with at least 16 hyperfine components observable only in the NH_3-treated and oriented membrane sample [124] and with the intermediate spin state of $S = 5/2$. Depending on

Table 3. Several Popular Ligands Used for Stabilizations of the Synthetic μ-Oxo-Bridged Mn Clusters with Their Common Abbreviations

Abbr.	Structure	Abbr.	Structure
bipy		tren	
phen		N₃O-py	
biphe		cyclam	
pic		*bis*pyzen	
dbm		salen / salpn	
dpp		2-OH-salpn	
terpy		tmpa	
bpea		tphpn	

Abbr.	Structure	Abbr.	Structure
tacn		tpen	
tmtacn			
HB(pz)₃		cyclen	
tame		tpp	

[a] bipy = 2,2'-bipyridine, phen = 1,10-phenantroline; biphe = 2,2'-biphenolate; pic = picolinate; dbm = dibenzoylmethane; dpp = diphenylphosphonate; terpy = 2,2':6,2''-terpyridine; bpea = *N,N-bis*(2-pyridyl-methyl)ethylamine; tacn = 1,4,7-triaza*cyclo*nonane; tmtacn = 1,4,7-trimethyl-1,4,7-triaza*cyclo*nonane; HB(pz)₃ = hydro*tris*(pyrazol-1-yl)borate; tame = 1,1,1,-*tris*(aminomethyl)ethane; tren = *tris*(2-amino-ethyl)amine; N₃O-py = *N,N-bis*(2-pyridylmethyl)glycine; cyclam = 1,4,8,11-tetraaza*cyclo*tetra-decane; *bis*pyzen = *N,N-bis*(pyrazinylmethyl)-1,2-ethanediamine; salen = *N,N*-disalicylidene-1,2-ethylene-diamine; salpn = *N,N-bis*(salicylidene)-1,3-propanediamine; 2-OH-salpn = *N,N*-disalicylidene-2-hydroxy-1,3-propanediamine; tmpa = *tris*(2-pyridylmethyl)amine; tphpn = *N,N,N',N'*-tetrakis(2-pyri-dylmethyl)-2-hydroxy-1,3-propanediamine; tpen = *N,N,N',N'*-tetrakis(2-pyridylmethyl)ethylenediamine; cyclen = 1,4,7,10-tetraaza*cyclo*dodecane; tpp = tetraphenylporphyrin.

the preparation conditions, freezing procedures, and the nature of the solvent [28,125–127], the intensity will shift from $g = 4.1$ signal to the $g = 2.0$ multiline signal, suggesting that the two signals arise from different spin states of the same manganese cluster. Several studies pointed out that such a "double EPR behavior" for a single manganese cluster must be associated with two distinct conformations of the polynuclear Mn aggregate, giving rise to the two different spin ground states. The $g = 2.0$ signal is associated with $S = 1/2$, while the $g = 4.1$ has a higher total spin of $S = 5/2$.

Table 4. Characteristic EPR Signals Obtained for Several Synthetic
Manganese Clusters Relevant to the OEC

Mn complex	EPR signals (ML = multiline)	References
$[Mn^{III}Mn^{IV}(\mu\text{-}O)_2(bipy)_4]^{3+}$	X-band: ML with 16 peaks centered at $g = 2$, 6.6 K ML with ~24 peaks centered at $g = 2$, 10 K Q-band: ML with ~16 peaks centered at $g = 2$, 40 K W-band: ML with ~18 peaks centered at $g = 2$, 20 K	[22–24, 128,129]
$[Mn^{III}Mn^{IV}(\mu\text{-}O)_2(phen)_4]^{3+}$	X-band: ML w/ 16 peaks centered at $g = 2$, 6.6–18 K Q-band: ML with 16 peaks centered at $g = 2$, 50 K	[128,130–133]
$[(2\text{-}OH\text{-}3,5\text{-}Cl_2\text{-}salpn)_2Mn^{III}Mn^{VI}]$	X-band: ML with 11 peaks centered at $g = 2$, 4-20 K, broad signal at $g = 4.6$, 110 K	[134,135]
$[(CH_3)_4(dtne)Mn^{III}Mn^{IV}(\mu\text{-}O)$ $(\mu\text{-}OAc)](BPh_4)_2$	X-band: ML with 16 peaks centered at $g = 2$, 2.4 K Q-band: ML with ~18 peaks centered at $g = 2$, 50 K	[132]
$[(tacn)_2Mn^{III}Mn^{IV}(\mu\text{-}O)$ $(\mu\text{-}OAc)](BPh_4)_2$	X-band: ML with 16 peaks centered at $g = 2$, 2.4 K ML with 16 peaks centered at $g = 2$, 20 K Q-band: ML with ~18 peaks centered at $g = 2$, 50 K W-band: ML with ~18 peaks centered at $g = 2$, 20 K	[129,136]
$[Mn^{III}Mn^{IV}(\mu\text{-}O)(tpp)_2]^{-1}$	X-band: ML with 16 peaks centered at $g = 2$, 10 K	[137]
$Mn^{III}Mn^{II}Mn^{III}(5\text{-}Cl\text{-}hsaladhp)_2$ $(sal)_4$	X-band: ML with 16 peaks centered at $g = 2$, broad signal at $g = 3.6$ and 4.1, 10 K	[138]
$Mn^{III}Mn^{II}Mn^{III}(hsaladhp)_2(hsal)_4$	X-band: ML with 16 peaks centered at $g = 2$, 4 K	[139]
$[Mn_3O_4(bipy)_4(OH_2)_2]^{4+}$	X-band: ML with 35 peaks centered at $g = 1.96$, 4 K	[140]
$[Mn_3O_4(bipy)_4(Cl)_2]^{4+}$	X-band: ML with 35 peaks centered at $g = 2$, 4 K	[141]
$[Mn_4(\mu\text{-}O)_3(\mu_3\text{-}Cl)]^{6+}$	X-band: ML with 16 peaks centered at $g = 2$, broad signal at $g = 5.2$ and 12, 10 K	[142]
$[Mn_4O_3Cl_6(OAc)_3(HIm)]$	X-band: ML with 16 peaks centered at $g = 2$, broad signal at $g = 5.2$ and 12, 10 K	[143]

3.3. Synthetic Models

3.3.1. Dimeric Species

Dimeric mixed-valence Mn complexes have played a historic role in elucidation of the nature of the Mn_4 core of the OEC. Upon its discovery, the above-mentioned multiline signal (total width of ~1900 G and hyperfine couplings of 85–90 G) associated with the $S = \frac{1}{2}$ form of the OEC trapped in the S_2 state of the Kok cycle was immediately compared to EPR spectra of mixed-valence dinuclear Mn complexes. A di-μ-oxo-bridged Mn dimer was first targeted as a potential mimic for the magnetic properties of the OEC, as the EPR spectrum of $[(bipy)_2Mn^{III}O_2Mn^{IV}(bipy)_2]^{3+}$, a low-spin ($S = 1/2$) exchange-coupled mixed-valence complex, exhibits a 16-line spectral pattern centered at $g = 2$, which is reminiscent of that obtained for the above-mentioned S_2 state of the OEC. Due to the larger overall spectral width of the PSII multiline signal, the possibility that this
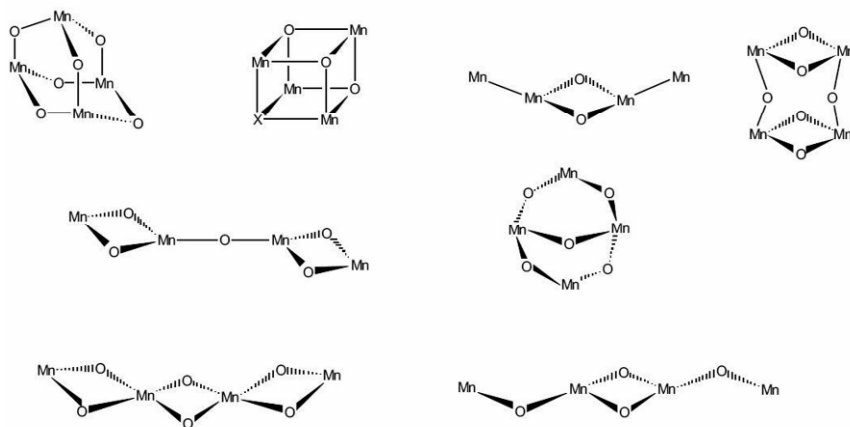
Figure 10. Different types of Mn–oxo bridged motifs that model the tetranuclear manganese cluster of the OEC and have been synthesized so far. Adapted from [123].
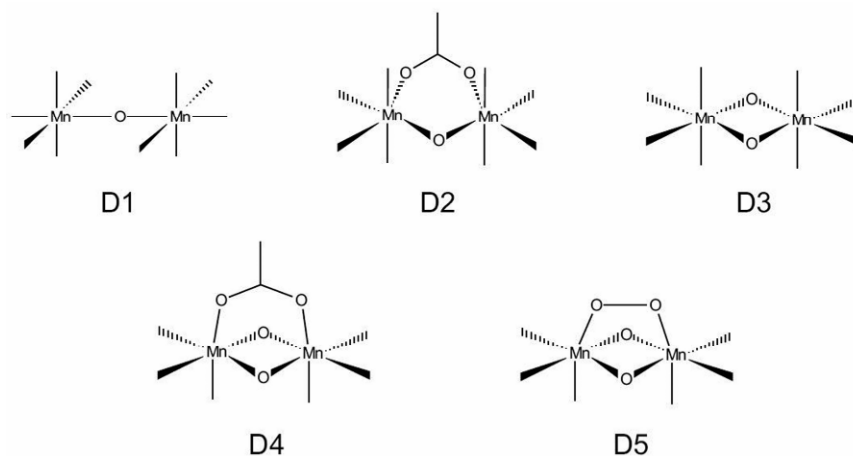
Figure 11. Schematic representations of the metal–metal core in several μ-oxo- or di-μ-oxo-bridged dimeric Mn clusters serving as synthetic models for the architecture of the Mn_4 cluster in the OEC.

signal arises from an $Mn^{II}Mn^{III}$ exchange-coupled dimer was also taken into account. The $Mn^{II}Mn^{III}$ dimers, due to the larger hyperfine couplings of Mn^{II} and higher projection factors for g (see §2.2.) also exhibit larger overall spectral width.

A comparative study by Dismukes and Siderer [23] emphasized these similarities and compelled others to synthesize a panoply of oxo-bridged mixed-valence Mn dimers, exhibiting a wide variety of structural and EPR characteristics. Typical

Magnetic Field
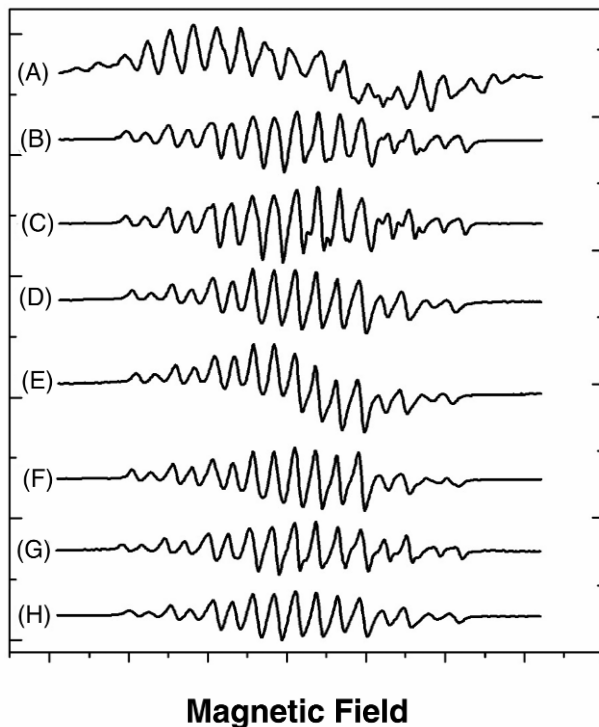
Figure 12. Characteristic EPR multiline signals from several synthetic manganese dimeric species together with the multiline signal form the S_2 state of the native PSII. (A) Multiline EPR signal from native OEC. Multiline signals from the mixed-valence $Mn^{III}Mn^{IV}$ dimeric species with following ligands: (B) bipy, (C) phen, (D) bpea, (E) tacn, (F) tpen, (G) bispicen and (H) salpn. Adapted from [59].

EPR patterns of some of these dimeric manganese complexes are presented in Figure 12. It is straightforward to notice that, despite the fact that none of these EPR spectral signatures reproduce exactly the EPR signal of the native enzyme, all of them exhibit striking resemblances with the multiline EPR signal of PSII in the S_2 state of the Kok cycle. In a recent review, Mukhopadhay et al. listed almost one hundred different Mn dimers with some relevance to the Mn cluster in OEC [98]. Some of the most relevant Mn–oxo core structures in these compounds are shown in Figure 11.

Like $[(tpp)Mn^{III}OMn^{IV}(tpp)]^-$ reported by Dismukes[137] or the $[(bipy)_2Mn^{III}O_2Mn^{IV}(bipy)_2]^{3+}$ dimer discussed above [144], most of the $Mn^{III}Mn^{IV}$ mixed-valence complexes exhibited the characteristic 16–18 line pattern (Fig. 11) in the EPR spectra [131,145–148], which was relatively simple to simulate using a variety of g- and A-tensors (e.g., for $[(bipy)_2Mn^{III}O_2Mn^{IV}(bipy)_2]^{3+}$ these values are: $g\perp$ = 1.995, $g_\parallel$ = 1.998, $A\perp(Mn^{III})$ = –480 MHz, $A_\parallel(Mn^{III})$ = –360 MHz, $A\perp(Mn^{IV})$ =

212 MHz, $A_{\parallel}(Mn^{IV})$ = 230 MHz. For exact g and A values for the other complexes, see p. 314 of [59]). At that time, however, it was unclear how the ^{55}Mn hyperfine coupling constant for the distinct metal centers (for the individual Mn ions $A_{\perp}(Mn^{III})$ = –230 MHz, $A_{\parallel}(Mn^{III})$ = –150 MHz, $D(Mn^{III})$ = –4 cm^{-1}, and $A_{\perp}(Mn^{IV})$ = $A_{\parallel}(Mn^{IV})$ = –230 MHz, $D(Mn^{IV}) \approx 0$). From [149], we would influence the spectral shape of this signal containing multiple transitions. The differences between the multiline EPR signal from the native protein and those of the dinuclear Mn model compound were attributed by some authors to exceedingly large nuclear quadrupolar couplings as well as larger hyperfine anisotropy for the two ^{55}Mn nuclei. Unfortunately, EPR techniques alone are not able to clarify this problem. To obtain precise information about the hyperfine couplings, a double resonance technique, such as ENDOR, which can yield detailed information about the nuclear spin, has to be used.

The importance of the combined EPR and ENDOR approach was fully demonstrated by Randall et al., who, using complete ENDOR analysis of a model dimeric $Mn^{III}Mn^{IV}$ compound, concluded that the same methodology could also be applied to explore the electronic structure of the OEC. It was only when Davies ENDOR was applied for the study of $[(bipy)_2Mn^{III}O_2Mn^{IV}(bipy)_2]^{3+}$ that an unambiguous assignment of the nuclear spin transitions for ^{55}Mn nuclei of both the Mn^{III} and Mn^{IV} ions was possible [150]. By constraining the simulations of EPR spectra based on effective ^{55}Mn hyperfine parameters derived from ENDOR experiments, the exact contribution of the 36 EPR transitions (see Fig. 13) to the significant spectral overlap giving rise to a "reduced" 16-line EPR spectrum for this bipyridine complex was resolved. This successful simulation of the EPR spectrum of $[(bipy)_2Mn^{III}O_2Mn^{IV}(bipy)_2]^{3+}$ dimer with a set of parameters, which completely failed to simulate the ^{55}Mn ENDOR spectrum of the multiline EPR signal of the native enzyme, allowed easily ruling out the dimeric origin of the multiline signal obtained for PSII. In contrast, the ^{55}Mn hyperfine couplings included into a tetranuclear model spin Hamiltonian provided a good simulation of both the EPR spectrum and the ^{55}Mn ENDOR spectrum of the PSII multiline.

A complementary work by the same authors on $[(bipy)_2Mn^{III}O_2Mn^{IV}(bipy)_2]^{3+}$ and $[(phen)_2Mn^{III}O_2Mn^{IV}(phen)_2]^{3+}$ complexes demonstrated that the observed ENDOR spectrum is governed by the effect of m_I and orientation selection, which depend on the position in the EPR envelope chosen for the ENDOR experiment [128]. Thus, by proper selection of the multiple m_I values across the EPR envelope (ENDOR experiments performed at different magnetic fields), it is possible to sort out different parameter trends. Based on an analysis of the influence of the quadrupole interactions on the ENDOR spectra, it was suggested that it is important to include the quadrupolar interaction, especially for the Mn^{III} ion, to properly describe the ENDOR spectra, in contrast to an analysis that neglected the quadrupolar contribution provided previously by Lubitz et al. [136].

Additional spectroscopic information can also be gathered from the simultaneous use of EPR spectroscopy at different microwave radiation frequencies. This
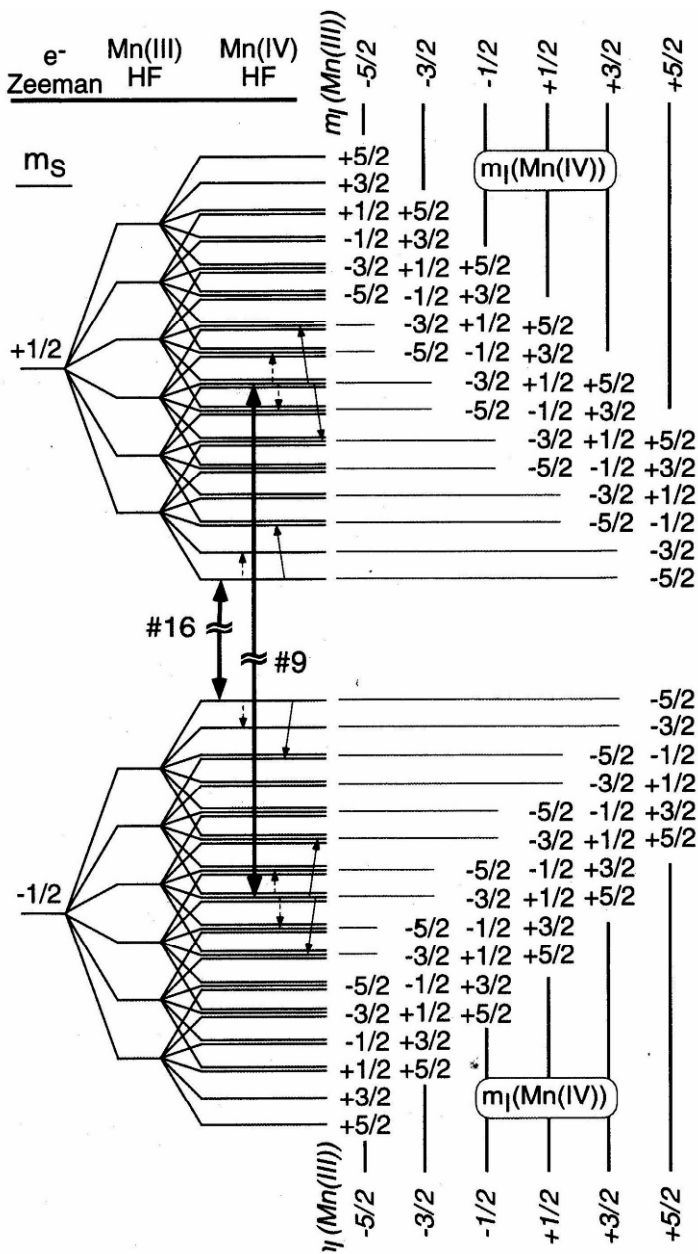
Figure 13. Energy diagram for the exchange-coupled $Mn^{III}Mn^{IV}$ dimer with all possible ENDOR transitions. Adapted from [128].

multifrequency approach has the clear advantage of being able to yield a precise determination of the g-tensor from high-field/frequency and hyperfine couplings from low-frequency EPR spectra. Using multifrequency EPR and ENDOR at X- and Q- band (35 GHz), Lubitz and coworkers [132,136] obtained enhanced g- and A-tensors on several complexes with either two μ-oxo bridges or two μ-oxo and an additional μ-aceto bridge such as [(tacn)Mn^{III}O(μ-CH$_3$CO$_2$)(μ-O)$_2$Mn^{IV}(tacn)] (BPh$_4$)$_2$ (D3 and D4 in Fig. 11). Precise determination of the orientation of the g- and ^{55}Mn HF tensors confirmed that these complexes containing tacn ligands are characterized by rhombic tensors, with the isotropic part much smaller than those of the bipy-type complexes. A similar study was extended by Schäfer to different EPR frequencies (X-, Q-, and W-band) [129]. At high frequencies (94 GHz and above) the g-tensor components were determined with much higher precision, which enabled improved simulation of the spectra at lower frequencies and yielded a high-precision dataset for g- and ^{55}Mn hyperfine tensors.

Although most of the dinuclear Mn complexes exhibit a quite similar Mn–O$_2$–Mn core, even small variations of the bridging geometry can lead to differences in g- and ^{55}Mn hyperfine values. The complexes containing dtne and mdtn ligands feature an additional geometric strain, while bipy and phen complexes lack the carboxylato bridging ligand. The other ligands seem to play a less important role, although they are responsible for some smaller differences. Very recently, Lubitz and coworkers have shown that the influence of even very subtle structural changes (e.g., small differences in the planarity of the Mn–(μ-O)$_2$–Mn core) could be detected with modern EPR techniques in the mixed-valence Mn^{III}Mn^{IV} and Mn^{II}Mn^{III} compounds with $S = 1/2$ ground state [151,152]. Similar multifrequency EPR studies (9, 95, 285 GHz) on di-μ-oxo Mn^{III}Mn^{IV} dimers with ligands containing nitrogen including bipy- and phen-containing species were also conducted by Un and coworkers [147] and showed that most of the anisotropy of the g-tensor originated from the Mn^{III} metal center.

Use of the non-oriented or partially oriented samples for the EPR studies preclude (in the majority of cases) direct access to information contained in the spectral patterns of the totally oriented systems. By studying model Mn complexes in single-crystal form, precise information about the magnetic tensors and their relative orientation can be directly obtained. Multifrequency (X- and Q-band) EPR studies of single crystals of [Mn^{III}Mn^{IV}O$_2$(phen)$_4$](PF$_6$)$_3$·CH$_3$CN, with a bulky PF$_6$ group, introduced to increase the distance between the adjacent metal centers [133], showed distinctly resolved ^{55}Mn hyperfine lines in all crystal orientations, unlike single-crystal EPR spectra of other Mn^{III}Mn^{IV} di-μ-oxo-bridged complexes where broad lines were attributed to dipolar interaction of the adjacent metal ions. Highly resolved hyperfine lines significantly simplified simulation of single-crystal spectra in the three principal directions, allowing assignment of the magnetic g- and A-tensors of the molecule with a high degree of reliability. These parameters were subsequently used to generate the solution EPR spectra at both X- and Q-band with excellent agreement.

Although failure to simulate the S_2 state multiline with merely two Mn ions demonstrated that simple dimeric Mn species cannot be considered as complete models for the manganese cluster of PSII, there is an advantage to such simplicity. Molecules with only two manganese ions can be instructive in accessing the exchange coupling between two metal ions (which is much simpler than in the analogous trimeric or tetrameric complexes) or the extent of the ZFS. As mentioned previously, the changes in the geometry of the Mn–Mn core can have a profound impact on the J values and consequently affect the exchange pathways. For example, inclusion of sterically hindered ligands increases the Mn–Mn distance and reduces the J value. Moreover, the influence of the bridging ligand (e.g., oxo versus hydroxo or halogen) on the exchange pathways and thus on the observed J values is of primary importance for the mechanistic aspect of water oxidation. Similarly, investigation of dimeric species with distinct geometrical features can help in understanding the topology of the Mn_4 cluster in PSII in respect to Mn–X–Mn connectivity. For example, incorporation of the bridging acetate groups can approximate the binding motif of carboxylate residues in the Mn-binding site of PSII. In addition, the exchange pathway is much less covalent, precluding efficient double exchange and superexchange.

Most of the symmetric di-μ-oxo mixed-valence $Mn^{III}Mn^{IV}$ dimers exhibit J values in the range of –100 to –400 cm^{-1} [38]. Representative examples of such intermediate-to-strong antiferomagnetic coupling are the previously mentioned di-μ-oxo- and di-μ-oxo-μ-aceto-bridged (D3 and D4 in Fig. 11) complexes studied by Lubitz and coworkers [132,136] ($J = -110$ cm^{-1} for di-μ-oxo-μ-acetato, $J = -150$ cm^{-1} for di-μ-oxo). However, a larger (as compared to the di-μ-oxo-bridged species) distance between the Mn atoms leads to a smaller extent of the exchange coupling and therefore to more weakly coupled dimers. A significant decrease in the J values is also observed upon successive protonation of the two μ-oxo bridges (from –92, –48, to –6 cm^{-1}, respectively) as noticed by Baldwin and Pecorarro [153,154], who reported magnetic studies on dimeric $Mn^{IV}Mn^{IV}$ species $[Mn^{IV}(salpn)(\mu-O)]_2$, $[Mn^{IV}(salpn)(\mu-O)(\mu-OH)]_2(CF_3SO_3)_2$, and $[Mn^{IV}(salpn)(\mu-OH)]_2(CF_3SO_3)_2$.

The highly asymmetric complex $[Mn(2-OH-3,5-Cl_2-salpn)]_2(thf)ClO_4$, in which the manganese centers are bridged by two chlorine atoms, exhibits a low-temperature X-band EPR spectrum [134] with 12 peaks (Fig. 14), which clearly differs from the usual 16-line pattern observed for most of the Mn di-μ-oxo-bridged dimers. A direct consequence of the different bridging ligand and different geometry of the Mn–Mn core (much longer Mn–Mn separation) is nearly an order of magnitude reduction in the exchange-coupling constant, ($J = -10$ cm^{-1}) as compared to that observed in complexes containing the μ-oxo or μ-acetato bridges, which exhibits J values close to –100 cm^{-1}. In this context it is worth noticing that the S_2 state of the OEC has negative J values of –20, –100, and –100 cm^{-1} [103] (alternative values of –125, –130, –170, and –225 cm^{-1} were derived by Charlot et al. in [66]), which may suggest that an additional bridging ligand, such as acetate, might be necessary to bring down the value of J.
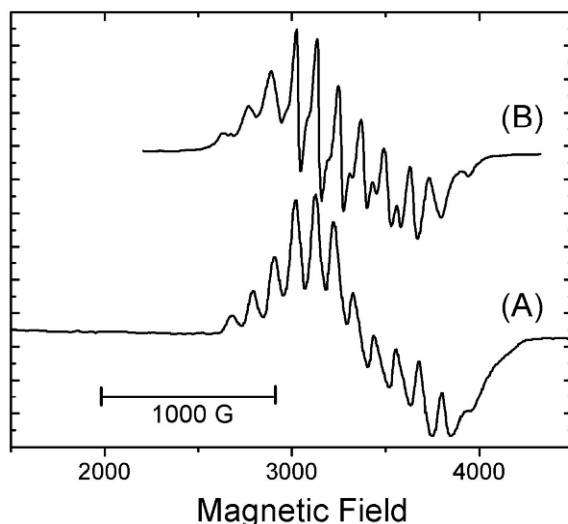
Figure 14. The 12-line EPR multiline pattern obtained at 4 K with a frozen solution of {[Mn(2-OH-3,5-Cl$_2$-salpn)]$_2$(thf)}ClO$_4$ (A) (adapted from [134]) and the corresponding simulation (B) (adapted from [149].

The small J value is responsible for a strongly temperature-dependent EPR spectra of [Mn(2-OH-3,5-Cl$_2$-salpn)]$_2$(thf)ClO$_4$, exhibiting a 12-line EPR pattern at $g = 2$, at 4 K. It is interesting to notice that this chloride-bridged complex showed the previously described "double EPR behavior" by yielding spectroscopic features attributed to the thermally populated excited spin states observed at higher g values ($g = 5$) with increasing temperature. The salpn complex was the first model reproducing such behavior and simultaneously mimicking the $g = 2$ multiline and $g = 4.1$ signals of the OEC.

Theoretical studies addressing the precise superexchange pathways in the mixed-valence Mn^{III}Mn^{IV} dimers were conducted by McGrady and Stranger on simple model complexes Mn(μ-O)$_2$Mn(NH$_3$)$_8{}^{3+}$ with ammonia ligands. This theoretical study showed that the spin delocalization involves essentially the crossed $J_{x^2-y^2/z^2}$ pathway, and hence might be regarded as a transfer of charge from the majority spin d$_{x^2}$ orbital on Mn^{III} to the minority spin d$_{x^2-y^2}$ orbital on Mn^{IV}. Optimized geometry was in accordance with a valence-trapped system, exhibiting two distinct Mn sites differing by the significantly longer (2.459 Å) Mn–N bond to axial nitrogen at the Mn^{III} nucleus as compared to an analogous bond at the Mn^{IV} nucleus (2.117 Å) [155]. In similar calculations on [Mn(μ-O)$_2$Mn(NH$_3$)$_8$]$^{n+}$ species extended to various degrees of metal oxidation (n = +2 to +5), Barone et al. showed that the computed J values are about three times bigger for the Mn^{III}Mn^{IV} species than for the corresponding Mn^{II}Mn^{III} analogues [156]. An examination of electron delocalization in these mixed-valence species allowed their classification as Class II compounds in the Robin-Day classification scheme [36].

The influence of the metal-bridging atom–metal geometry on the exchange pathways was more rigorously addressed by Delfs and Stranger [157], who showed that for the model $[Mn_2(\mu\text{-}O)_3(NH_3)_6]^{2+}$ complex exhibiting a very short Mn–Mn distance (2.3 Å), the large antiferromagnetic coupling $J = -390$ cm^{-1} is dominated by superexchange mechanism via the μ-oxo bridges, and that direct Mn–Mn interaction is very small. Similar calculations [158] on mixed oxo- and carboxylato-bridged Mn dimers confirmed that the magnetic coupling is profoundly affected by changes in both the bridging ligands and Mn oxidation state. Jahn-Teller distortion, observed for the Mn^{III} centers in the Mn^{III}Mn^{IV} dimers, was attributed to the changes in the bridging di-μ-oxo structure. The corresponding crossed exchange $J_{x^2-y^2/z^2}$ pathway was also responsible for a significant delocalization of the odd electron, which partially converts the Mn^{IV} ion into low-spin Mn^{III}. Therefore, the magnetic exchange in the ground state can be considered to arise from two interacting spin ladders, one the result of coupling between Mn^{IV} ($S = 3/2$) and high-spin Mn^{III} ($S = 2$), and the other the result of coupling between Mn^{IV} ($S = 3/2$) and low-spin Mn^{III} ($S = 1$). Similarly, the importance of strong exchange pathways via short Mn–Mn and Mn–oxo distances was pointed out by Noodleman and coworkers, who have provided BS-DFT calculations for triply bridged Mn–oxo dimers with terminal tacn ligands [53].

As explained in Section 2.2., ZFS can significantly contribute to both g-values and hyperfine tensors of exchange-coupled Mn dimer only when $|D/J| \leq 1$. This condition is satisfied in the above case of $[Mn(2\text{-OH-}3,5\text{-Cl}_2\text{-salpn})]_2$, which exhibit the "unusual" 12-line spectral pattern. A theoretical description of this phenomenon was provided by Zheng et al. [148], who showed that the usually neglected but important contribution of ZFS to Eqs. (13)–(17) (see §2.2.1.) cannot be omitted in the weak-coupling case, where the D/J ratio is much bigger than in a typical strong coupling case ($|D/J| \ll 1$). By using the appropriate D parameters in Eqs. (15)–(17) the 12-line spectrum of Figure 14 was successfully simulated.

Several Mn dimers with lower oxidation states exhibiting distinctive EPR signals were also synthesized [159,160], yet their relevance for the OEC is questionable.

Theoretical prediction of the EPR parameter by performing calculations on the strongly exchange-coupled dimers, for which a considerable amount of experimental data is available, such as $[bipy_2Mn^{III}(\mu\text{-}O)_2Mn^{IV}bipy_2]$ and $[phen_2Mn^{III}(\mu\text{-}O)_2Mn^{IV}phen_2]$, is a useful example of the utility of the BS approach. In our research group, we have performed several benchmark calculations on these dinuclear species and on simple mononuclear Mn complexes, with particular emphasis on characterizing the intrinsic DFT error coming from the inability of the current density functional methods to properly calculate the Fermi contact term in the hyperfine interaction tensor. As can be seen from Table 5, the computed isotropic part of the hyperfine interaction is underestimated by a factor of ca. 1.5–1.7, in accordance with recent studies conducted by Neese et al. [151,161,162]. It is also important to point out that the calculated Heisenberg exchange-coupling constants J using the same BS methodology are typically overestimated by a factor of 2–3.

Table 5. Computed Values of the Hyperfine Interactions for Mn[III] and Mn[IV] Centers for Several Mononuclear and Dinuclear Model Compounds Using Broken-Symmetry Approach

Mn complexes	A_{iso}	A_{11}	A_{22}	A_{33}	Mulliken spin density	Ref.
Mononuclear complexes						
Mn[III]						
[Mn(acac)$_3$]	−133					
	(−156)					
Mn[IV]						
[Mn(porph)(OCH$_3$)$_2$]	−133	−202				
[Mn(salahe)$_2$]	−128	−216				
[Mn(bmdmp)$_2$]	−128	−208				
Dinuclear mixed-valence complexes						
[bipy$_2$Mn[III](μ-O)$_2$Mn[IV]bipy$_2$]						
Experimental						
Mn[III]	−454	−502	−479	−376		a
Mn[IV]	219	210	216	233		a
Broken symmetry $S = 1/2$						
Mn[III]	−415	−502	−485	−259	3.60	
Mn[IV]	285	263	293	301	−2.39	
μ-O/1	3.1	40	19	−50	−0.19	
μ-O/2	3.4	41	20	−50	−0.19	
[phen$_2$Mn[III](μ-O)$_2$Mn[IV]phen$_2$]						
Experimental						
Mn[III]	−451	−502	−479	−373		a
Mn[IV]	221	213	216	233		a
Broken symmetry $S = 1/2$						
Mn[III]	−422	−509	−488	−268	3.55	
Mn[IV]	295	276	294	315	−2.36	
μ-O/1	1.7	36	16	−47	−0.17	
μ-O/2	0.9	38	15	−50	−0.18	

[a]Experimental values taken from [59]. Adapted from [170].

As it is the case for mononuclear and dinuclear complexes, the isotropic part of the hyperfine coupling calculated for the higher-nuclearity clusters will suffer from the same underestimation. Therefore, computed hyperfine coupling constants for exchange-coupled systems must first be deconvoluted into intrinsic sites-values according to the projection techniques described in Section 2.2. Then the isotropic component of the site HF tensor must be scaled by the empirically determined 1.5–1.7 factor. The intrinsic sites-values can then be compared to the available experimental data (e.g., Mn in Mn[III] and Mn[IV] oxidation states [163–166]), as well as to the HF values determined at the same level of theory on the mononuclear sites of the corresponding oxidation number.

Two recent interesting studies using BS-DFT by Neese and coworkers highlight the suitability of BS methodology for calculation of exchange couplings J, ligand and metal hyperfine couplings, as well as quadrupolar interactions and g-tensors in the mixed-valence $Mn^{III}Mn^{IV}$ systems. The investigation of the $[Mn^{III}Mn^{IV}(\mu\text{-}O)_2(\mu\text{-}OAc)dtne]^{2+}$ complex, clearly showed distinctly different Mn^{III} and Mn^{IV} sites for the high-spin and broken symmetry states, in agreement with experimental results [162]. Noticeable changes in the calculated geometrical and spectroscopic parameters for the manganese catalase, which possesses an exchange-coupled active site in its superoxidized Mn^{III}/Mn^{IV} state [167–169], were also highlighted using BS-DFT on simplified model species. The possible protonation of a μ-oxo bridge (although unlikely for the higher oxidation states of transition-metal centers) was easily ruled out by comparing the calculated and experimental spectroscopic parameters [151].

One of the most exciting developments in EPR and related techniques is the possibility to probe the nature of the ligands bound to the metal centers by accessing their hyperfine couplings via advanced ENDOR or ESEEM magnetic resonance techniques. Such studies are, for example, important in the context of determining the precise oxidation state of a given manganese atom in the Mn_4 center of the OEC via interaction with the neighboring ligand. Possible binding of H_2O or small molecules to the Mn cluster of OEC is another point of interest, in the context of water activation before its oxidation to O_2. In this respect, an excellent spectroscopic model for probing water binding to the Mn_4 cluster in OEC was precisely obtained using the $[(phen)_2Mn^{III}O_2Mn^{IV}(phen)_2]^{3+}$ dimer in different polar solvents , such as water, THF, and methanol [135]. ENDOR and ESEEM experiments showed that a solvent molecule is bound directly to the Mn^{III} of the dinuclear complex; however, solvent protons bound to Mn^{III} were found to have inequivalent axial dipolar hyperfine interactions. Their orientations and radial distances were determined using a model where the proton experiences a point–dipole interaction with each Mn ion.

Specific deuteration of the proton sites combined with ENDOR on structurally different complexes allowed correlating the experimentally observed HF tensors with precise protons of the surrounding ligands (dtne and tacn) in the multifrequency EPR and ENDOR study by Lubitz and coworkers [132,136]. In addition, a net decrease in the electric field gradient upon binding to the metal was evidenced by ^{14}N ENDOR spectroscopy, which showed smaller ^{14}N nuclear quadrupole parameters of the ligand nitrogens, as compared to the bipy- or phen-type ligands. These experiments were able to differentiate the axial ligand nitrogens directly bound to Mn^{III} from several more weakly coupled ^{14}N nuclei. These latter were studied with ESEEM spectroscopy and were assigned to be the equatorially bound nitrogens in close proximity to Mn^{III}. Thus, study of these parameters on the model species can provide a sensitive tool for ligand identification and can yield precise information about the local electronic structure via the electric field gradient.

3.3.2. Trimeric Species

For the synthetic species with a manganese nuclearity higher than two, an additional problem arises that is related to so-called "spin-frustration." Spin frustration can be easily explained on a model containing three spins being positioned on the vertices of an equilateral triangle. If two neighboring spins are antiferromagnetically coupled, the third spin is unable to couple antiferromagnetically with both adjacent spins simultaneously. Thus, this third spin is experiencing "spin-frustration." Spin frustration is an essential ingredient for a variety of magnetic phenomena, and is also present in the Mn clusters of higher nuclearity [171]. Its importance is manifested through the facile accessibility of multiple intermediate spin states observed in multinuclear manganese clusters. The role of the topology of the cluster on the magnetic properties of the asymmetric Mn trimers was highlighted in a theoretical study conducted by Gomez-Garcia et al. [172]. Inspection of Figure 9 reveals that the trimeric Mn motif pervades in several of the tetrameric Mn models of the OEC. In such models, the Mn ions occupy three vertices of a cube and are bridged by four oxo groups. This "cubane" Mn_3O_4 core is of interest, because there is strong body of evidence [13,18,117] that the Mn cluster of OEC exists in a $3 + 1$ type geometry, in which a trinuclear cluster is coupled to a single manganese ion.

The first EPR signal from a trinuclear Mn_3O_4 core with direct relevance to the OEC was obtained independently in 1990 by Sarneski et al. [140] and by Auger and colleagues [141], who synthesized almost identical trinuclear Mn complexes, $[Mn_3O_4(bipy)_4(H_2O)_2]^{4+}$ and $[Mn_3O_4(bipy)_4Cl_2]^{2+}$, bearing two single μ-oxo and one di-μ-oxo bridge between the adjacent metal centers. A well-resolved 35-line pattern with 23 G splittings in the $g = 2.0$ region (Fig. 15) was visible in the EPR spectra of both species, which were characterized by a fairly strong antiferromagnetic coupling between the metal centers ($J = 182$ cm^{-1} across the di-μ-oxo bridge and 98 cm^{-1} across single μ-oxo bridges).

Simulation of the EPR multiline was performed based on a simplified model, assuming two of the three Mn^{IV} manganese atoms to be equivalent (see §2.2.). Calculated energy levels revealed an $S = 3/2$ excited state adjacent to the $S = 1/2$ ground state that highlighted the importance of such a model for OEC, since adjacent $S = 1/2$, $S = 3/2$, and $S = 5/2$ states have been invoked to explain how the two EPR signals of the S_2 state of PSII could arise from the same Mn cluster. It is interesting to notice that a well-resolved multiline signal similar to the one reported above was also recorded at 12 K after the chemical oxidation of $[(bipy)_2Mn^{III}O_2Mn^{IV}(bipy)_2]^{3+}(ClO_4)_3·2H_2O$. This spectral pattern was likely wrongly assigned by the authors to be consistent with a superoxidized Mn^{IV}Mn^{IV} form of this complex, which is believed to correspond to the S_4 state of the Mn OEC cluster [173], as demonstrated later by Sarneski et al. [140]. With the aim to model the higher-spin ground states of the OEC, Mn_3O_4 cores of slightly different type were prepared: $([(Mn^{IV}_3O_4(OH)\text{-}(tpen)(p\text{-}tpen)](ClO_4)_6·4H_2O)[174]$ and $[(Mn^{IV}_3O_4(OH)(bpea)_3](ClO_4)$ [175]. Both species exhibited an EPR signal
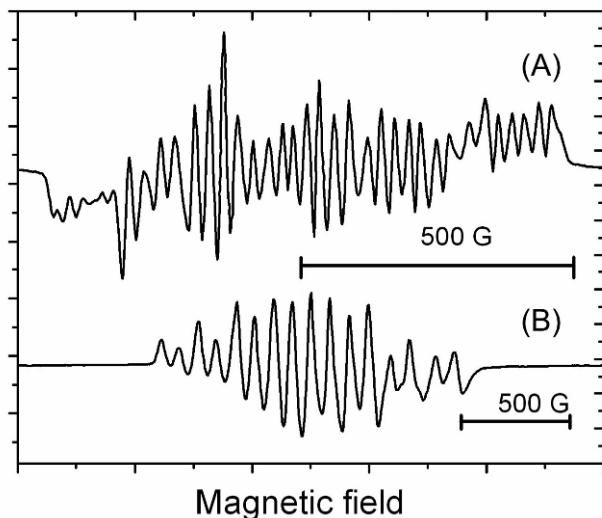
Figure 15. The EPR multiline with 35-line pattern obtained with the frozen solution of a tri-nuclear $[Mn_3O_4(bipy)_4(H_2O)_2]^{4+}$ complex at 4 K (A). For comparison, EPR spectrum of a di-nuclear mixed-valence complex $[(bipy)_2Mn^{III}O_2Mn^{IV}(bipy)_2](ClO_4)_3$ is depicted in (B). Adapted from [140].

corresponding to the ground state of $S = 3/2$ with either a complex pattern of four broad peaks or a single broad line centered at $g = 4.0$, respectively. In both cases, the ratio of the exchange couplings between the two equivalent manganese atoms and the third one is responsible for the ground state of the molecule: for $J'/J \sim 0.4$ $S = \frac{1}{2}$ and $S = 3/2$ are degenerate, for $J'/J = 0.54$ $S = \frac{1}{2}$ is the ground state, while for $J'/J = 0.14$ the $S = 3/2$ is the ground state.

Pronounced interest in a theoretical description of the mechanism of the magnetic coupling and the possible exchange pathways characterized most of the early computational studies of the exchange-coupled multinuclear metal species, with particular focus on the computation of exchange parameters J. Theoretical description of the exchange pathways in manganese clusters is, for example, important in relation to the ongoing discussion as to whether the bridges in the Mn_4 OEC moiety are oxo or hydroxo, and if carboxylate functionalities of ligating amino acids are mono or bidentate. Historically, the first computational study of a manganese cluster targeted an $Mn^{III}_3Mn^{IV}$ tetramer $[Mn^{IV}Mn^{III}_3O_3Cl_7(O_2CCH_3)_3]^{3-}$ considered as a potential model for the S_0 state of the OEC. This theoretical work (which initiated the use of the broken-symmetry approach for the study of the coupled manganese clusters) dates back to 1992, when Noodleman introduced such calculations using LCAO $X\alpha$ density functional method, the precursor of the modern DFT. The computed exchange parameters values for the ferromagnetic $Mn^{III}Mn^{III}$ and antiferromagnetic $Mn^{III}Mn^{IV}$ interactions were calculated to be 19.3 and -46.6 cm^{-1}, respectively, and yielded a total $S = 9/2$ ground state.

Another class of the manganese trimers with relevance to the Mn_4 cluster of OEC includes the homovalent $Mn^{II}Mn^{II}Mn^{II}$ and the mixed-valence $Mn^{III}Mn^{II}Mn^{III}$ linear cores, in which the three manganese atoms are bridged by a single μ-oxo bridge with additional acetate type ligands [176]. A variable-temperature EPR study of $[Mn^{III}Mn^{II}Mn^{III}(Hsaladhp)_2(AcO)_2(5\text{-}Cl\text{-}salpn)_2(thf)_2]$ in the range 4–10 K showed a poorly resolved multiline centered at $g = 2$, consistent with an $S = 3/2$ ground state. A similar $Mn^{II}Mn^{II}Mn^{II}(AcO)_6\text{-}(pybim)_2$ exhibits a broad signal at $g = 2.0$ with a weak feature at $g = 4.5$ and $g = 6.5$ and a ground state of $S = 5/2$. Several other $Mn^{II}Mn^{III}Mn^{II}$ complexes containing the N-glycoside ligands are characterized by a $g = 2.0$ centered sextet similar to that observed for the free Mn^{2+} ion [177].
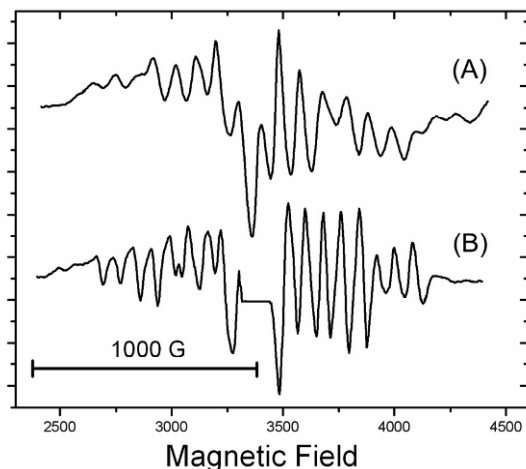
Figure 16. (A) The EPR multiline with 19 distinctive peaks similar to the EPR signal characteristic of the S_2 state of the Kok cycle in PSII, obtained with the frozen solution of the trinuclear $[Mn^{III}Mn^{II}Mn^{III}(Hsaladhp)_2(sal)_4\cdot 2CH_3CN]$ compound at 4 K. (B) Multiline signal form the native S_2 state of PSII enriched membranes illuminated at 200 K. Adapted from [139].

In 2000, Tangoulis reported a mixed-valence $Mn^{III}Mn^{II}Mn^{III}$ trinuclear complex of stoichiometry $[Mn^{III}Mn^{II}Mn^{III}(Hsaladhp)_2(sal)_4\cdot 2CH_3CN]$, characterized by a very small antiferromagnetic J coupling of ~6 cm^{-1}. Interestingly, the EPR spectrum obtained at 4 K was characterized by a 19-line signal centered at $g = 2.0$ (Fig. 16), similar to that observed for the S_2 state of the OEC [139]. In addition, a low-field EPR signal arising from a superposition of two peaks, one centered around $g = 3.6$ and the other, for which ^{55}Mn hyperfine structure is observed, centered around $g = 4.1$, was indicative of an $S = 3/2$ ground state in a way similar to the "double EPR behavior" of the native enzyme, exhibiting simultaneous $g = 2$ and $g = 4.1$ signals.

An interesting compound relevant to the "dimer-of-dimers" model was re-ported by Christou and coworkers with a core containing three Mn atoms con-nected by two di-μ-oxo bridges and exhibiting very weak antiferromagnetic and ferromagnetic couplings (-25 and 8 cm^{-1}) [178]. The ground state of the complex was assigned to be $S = 3/2$, with the first, degenerate excited state corresponding to $S = 1/2$ and $S = 5/2$ lying 123 cm^{-1} above the ground state. Importantly, small simi-lar values of J couplings were evoked to explain that such a situation, where the ground state is very sensitive to the relative strength of the competing antiferro-magnetic exchange interactions, could explain different spin states for the S_2 state of the OEC. Homo- and mixed-valence EPR active trinuclear Mn complexes were recently reviewed by Kessissoglou [138].

As in the case of the dinuclear Mn species, single-crystal studies were also performed on manganese trimers. Magnetic susceptibility and single-crystal EPR studies of an Mn_3 cluster, $Mn^{III}_2Mn^{II}(O)(O_2C-C_6F_5)_6(py)_3 \cdot CH_2Cl_2$, with six fluori-nated carboxylates that are relevant as mimics for possible binding acetate ligands in the Mn_4 moiety of OEC, indicated an $S = 3/2$ ground state, with antiferromag-netic coupling between Mn^{III} and Mn^{II} ions [179]. The negative J values (-5.4 and -3.4 cm^{-1} for Mn^{II}/Mn^{III} and Mn^{III}/Mn^{III} interactions, respectively) identified both of these exchange interactions as being antiferromagnetic, with a stronger anti-ferromagnetic coupling between Mn^{II} and Mn^{III} ions.

Since the exchange couplings J are small, and $|J| \approx |D|$, any small changes in the ratio of the J values will have a pronounced effect on the final ground state. It is interesting to examine this situation in the above-mentioned $Mn^{II}Mn^{III}$ dimer as exemplified by Figure 17, where the energies total spin ground states were plotted as a function of the J/J' ratio (J being the $Mn^{II}Mn^{III}$ and J' being the $Mn^{III}Mn^{III}$ interactions). It is straightforward to notice that in a J/J' range of 0.2 to 1.2, four
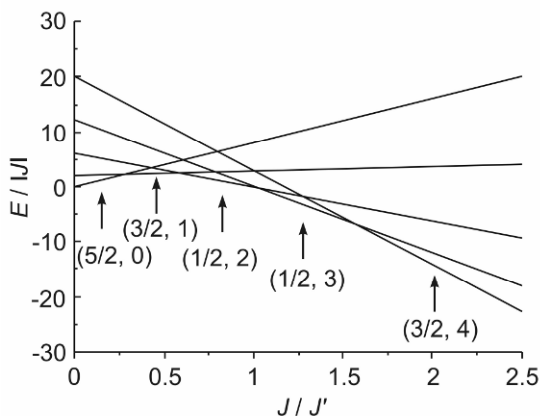
Figure 17. Plots of the eigenstates of total ground spin states S_T with the corresponding in-termediate states S_A from coupling of the spins of the two Mn^{III} ions. The states are labeled as (S_T, S_A) and are plotted against the J/J' ratio, where J is the $Mn^{II}Mn^{III}$ and J' the $Mn^{III}Mn^{III}$ exchange interaction. Adapted from [179].

different ground states with an overall $S_T = 0$ to 3 are lying very close to each other. This type of situation is also encountered in the polynuclear Mn cluster with higher oxidation states, and is of relevance for possible changes in the ground state of the manganese cluster of OEC.

Manganese trinuclear complexes found also an interesting application as models for the electron-transfer mechanism in PSII [180,181] By attaching the photosensitizing $Ru^{II}(bpy)_3$ type moieties (that can be easily oxidized to Ru^{III} upon photon absorption) to several Mn multinuclear species linked to electron-reach phenol groups, mixed Mn–Ru complexes of formula $Mn_3^{II}[Ru^{II}(bipy)_3ArO]_6$ (Ar = substituted phenol groups) were prepared. Transient $Ru^{III}(bipy)_3$ species, obtained using light energy, undergo the electron transfer from the trinuclear Mn_3^{II} cluster with simultaneous oxidation of one of the metal centers from Mn^{II} to Mn^{III}. Such behavior can be considered as a useful model for reaction PSII centers P_{680} since they can undergo analogous light-energy–induced charge separation.

3.3.3. Tetrameric Species

The first models of Mn tetramers with relevance to the OEC appeared in 1987, with the report of a synthetic Mn_4O_2 core [182] followed by the related "double-pivot" mechanism that was proposed for water oxidation [183]. In this mechanism, two Mn atoms, each carrying a water molecule, are attached to a di-μ-oxo-bridged Mn dimer via μ-O_3 bridges. This pseudo-linear arrangement of Mn atoms was proposed to recombine to a cubane-type structure after concomitant deprotonation of H_2O, through a pivot movement around each of the connecting μ-O_3 bridges, before the subsequent formation of an O–O bond and final O_2 release. The tetrameric structure was characterized by small J values of –7.6 and –22.5 cm^{-1}. Bashkin et al. [142] reported the same year an $Mn^{III}_3Mn^{IV}$ species with an imidazole ring bound to one of the Mn atoms and three acetate-bridging groups. The interesting structural feature with possible relevance for the OEC architecture is the "cubane-like" structure with four manganese atoms occupying the corners of the distorted cube. The Mn atoms are bridged by the three oxygens and a Cl$^-$ ion occupying the remaining vertex. The first solid-state magnetochemistry and EPR studies of this complex revealed similarities to the $Mn^{IV}Mn^{III}_3$ dimer-of-dimers model proposed by de Paula [27] for the native S_2 state, where the $Mn^{IV}Mn^{III}$ pair is strongly antiferromagnetically coupled to give an $S = 1/2$ state, which is in turn ferromagnetically coupled to the $Mn^{III}Mn^{III}$ pair, the latter exhibiting weak antiferromagnetic coupling between two Mn centers.

Low-temperature X-band EPR spectra (3.8-90 K) of this complex are characterized by two sets of signals (Fig. 18): a broad peak at $g = 6.0$ with a sharper motif at $g = 4.0$ plus a well-resolved 16 lines with manganese hyperfine structure centered at $g = 2.0$ corresponding to an $S = 1/2$ ground state. This complex is a trimeric example of the "double EPR behavior" observed previously in the dimeric species and relevant to the $g = 2$ and $g = 4$ signals of the S_2 state.
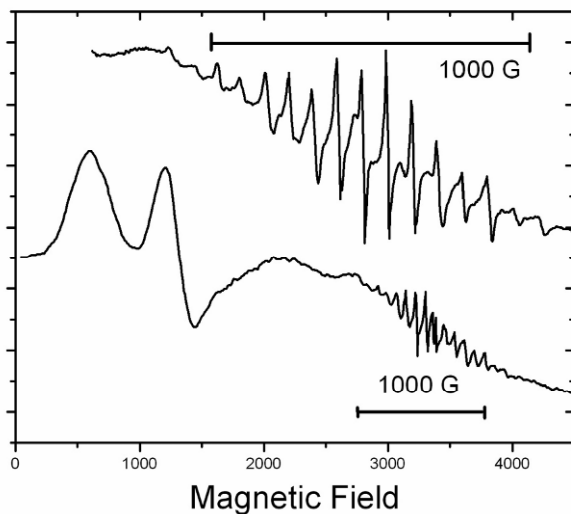
Figure 18. The EPR multiline with 16 peaks centered at $g = 2$ and a broad signal at $g = 4$ obtained from the frozen solution of $(H_2Im)_2[Mn_4O_3Cl_6(HIm)(OAc)_3]_{1.5}MeCN$. The expansion of the $g = 2$ signal is shown in the upper part of the figure. Adapted from [142].
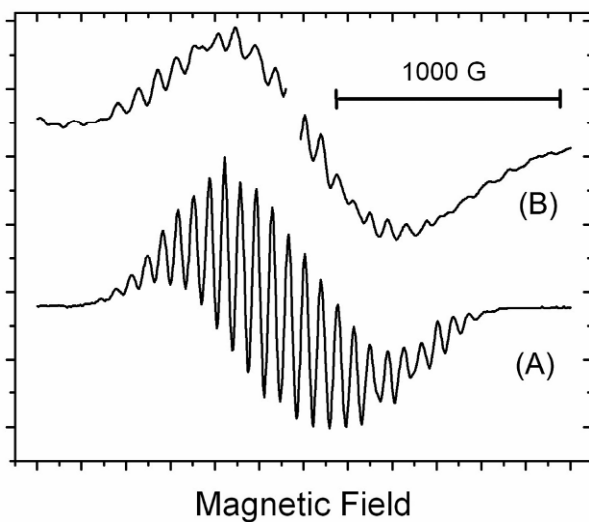
Figure 19. The EPR multiline with well-resolved 24 peaks centered at $g = 2$ obtained with frozen solution of $[\{(Mn^{III}Mn^{IV}_3)(\mu\text{-}O)_4(tphpn)\}_4]^{3+}$ (A). Multiline EPR signal of the PSII S_0 state shown for comparison in (B). Adapted from [189].

Three Mn_4O_2 "butterfly" core-type complexes with successive oxidation states $Mn^{II}{}_2Mn^{III}{}_2$, $Mn^{II}Mn^{III}{}_3$, and $Mn^{III}{}_4$ were synthesized by Vincent et al. [184] and were suggested to be consistent with the model for the S_{-1}, S_0, and S_1 states of OEC. Introduction of two additional oxo bridges into the tetranuclear unit resulted in synthesis of an Mn_4O_6 core [185]. An analogous model compound with one of the oxo bridges protonated was synthesized by the same authors, who suggested that the structure was relevant to the "adamantane-shaped" core proposed earlier by Brudvig [186].

Chan et al. [187] reported a complex relevant to the "dimer-of-dimers" model, with an $Mn^{III}Mn^{IV}Mn^{III}Mn^{IV}$ oxidation state, by coupling two Mn dimers together with a spanning polydentate ligand. Although no EPR signal was detectable at X-band in perpendicular mode, its parallel polarization EPR spectrum revealed a signal at $g = 6.0$ that bears a strong resemblance to the S_1 state OEC parallel polarization EPR spectrum [188]. This spectral evidence suggested that the manganese cluster in PSII in the S_1 state has an electronic structure similar to the "dimer-of-dimers" as observed in this synthetic compound. Another complex, formulated as $[\{(Mn^{III}Mn^{IV})_2(\mu\text{-}O)_2(tphpn)\}_2]^{4+}$, was also recently reported by Mukhopady et al. [189]. Its reduced rearrangement product obtained in solution, $[\{(Mn^{III}Mn^{IV}{}_3)(\mu\text{-}O)_4(tphpn)\}_4]^{3+}$, which bears a formal $Mn^{III}{}_3Mn^{IV}$ oxidation state, exhibits a very well-resolved 24-line EPR signal (Fig. 19) similar to the EPR signal of the PSII S_0 state.

Several interesting tetranuclear Mn models with the cubane-like architecture (four Mn atoms on the apices of a symmetric or distorted cube linked by oxo bridges) were reported by Dismukes and collaborators, as possible models for the oxygen evolution mechanism mediated by the manganese cluster of the OEC. The first of a series, reported in 1997 and formulated as $Mn_4O_4(O_2PPh_2)_6$, incorporates an $Mn_2{}^{III}Mn_2{}^{IV}O_4$ mixed-valence cubic core ligated by six phosphinate ligands [190,181]. These complexes were shown to undergo oxygen release with simultaneous loss of one of the phosphinate ligands in gas phase, while in solution the reduction by phenothiazine resulted in release of one water molecule [192,193]. The model was further extended by a slight modification of the ligand (replacement of PPh_2 by $P(PhMe)_2$ or $P(PhOMe)_2$. The $Mn_4O_4(O_2P(PhMe)_2)_6$ species were shown to undergo photodissociation in gas phase to a phosphinate ligand, a dioxygen molecule, and an $Mn_4O_2(O_2PPh_2)_5{}^+$ butterfly type core. However, in condensed phase (in solution) a release of two water molecules accompanied by simultaneous loss of two bridging oxygens from the cubane structure was observed [194,195]. Such reaction was also observed for the parent $Mn_4O_4(O_2P(PhOMe)_2)_6$. Recent photodissociation studies in gas phase have yielded similar results and were presented for $Mn_4O_4(O_2P(PhOMe)_2)_6$ and for the ionic form of previously reported $Mn_4O_4(O_2P(Ph)_2)_6$ [196,197].

As mentioned for the trinuclear Mn models, spin frustration is also observed in Mn aggregates of higher nuclearity [171]. Hendrickson reported the EPR spectra of tetranuclear cubane clusters with a spin ground state of $S = 9/2$ exhibiting important spin frustration [143]. The well-isolated spin ground state of $S = 9/2$ in these

distorted cubane $Mn^{IV}_3Mn^{III}O_3Cl$ complexes was described as resulting from anti-ferromagnetic $Mn^{IV}Mn^{III}$ interactions ($J = -20.8$ to -30.3 cm^{-1}) combined with weak ferromagnetic $Mn^{III}Mn^{III}$ coupling ($J = 8.6$ to 11.3 cm^{-1}). In relation to the "double EPR behavior" of the OEC, an interesting study was presented on very similar complexes exhibiting the same S = 9/2 ground state by Wang [198]. By presenting the theoretically derived dependence of the ground state on the J/J' ratio (J corresponding to the MnIIIMnIII and J' to the MnIIIMnIV interactions), the authors emphasized that the S = 3/2 and S = ½ ground states for this complex would be accessible with relatively small changes in the value of J. Such subtle changes could be induced by only very minor structural modifications (e.g., change in the bridging μ-oxo ligand from O to OH or O_2^-).

The first example of the high oxidation state synthetic complex $[Mn_4O_6(bipy)_6]^{4+}$, containing a homovalent Mn^{IV}_4 unit reported by Blondin [130] immediately gained high relevance to the OEC, since under irradiation of its frozen solution the reduced $Mn^{IV}_3Mn^{III}$ form $[Mn_4O_6(bipy)_6]^{3+}$ with ground state S = ½ was obtained.
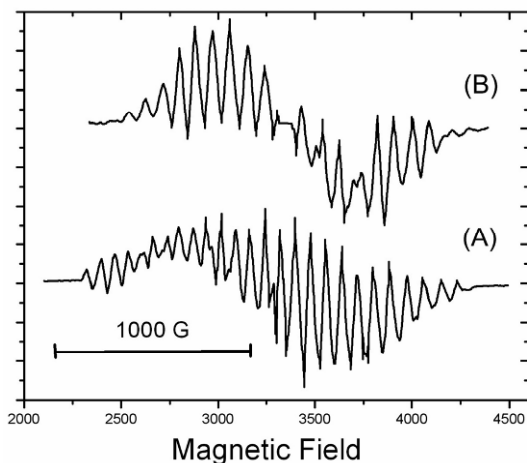
Figure 20. The EPR signal obtained with the frozen solution of $Mn^{IV}_3Mn^{III}$ form of the complex $[Mn_4O_6(bipy)_6]^{3+}$ showing a well-resolved multiline with 18 peaks plus an additional peak centered at $g = 2$ (A). A multiline of the S_2 state of the OEC is shown for comparison in (B). Adapted from [130].

This compound in its reduced form is believed to mimic the S_2 state of the OEC (Fig. 20). Its multiline X-band signal is composed of 18 well-resolved lines plus one in the center of the spectrum, with some additional poorly resolved features on both wings. The complex reported by Blondin served also as an excellent "benchmark compound" for simulation of the EPR multiline signal of the OEC. Based on simulation attempts, the striking difference between the parameters ob-

tained by other authors for an OEC Mn cluster [199,200] and those deduced for $[Mn_4O_6(bipy)_6]^{3+}$ is the presence of a large hyperfine value ($A = 450$ MHz) in the latter. This was suggested by the authors to arise from a difference in the redox states between the reduced form of the complex and the OEC or by the subtle structural differences between the reduced form of the synthetic complex and the OEC, which drastically affect the spectrum.
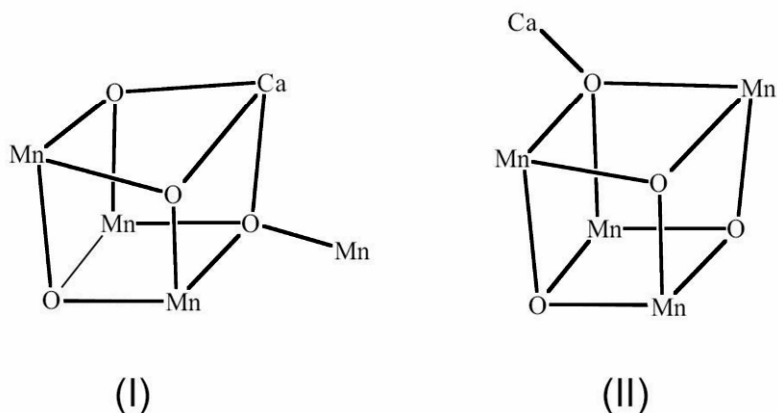
Figure 21. Two Mn_3CaO_4 distorted-cubane-type sites present in the $Mn_{13}Ca_2$ compound of [201]. Structure II was recently ruled out as a possible model for the OEC, based on EXAFS studies of the single crystal of PSII [18,99].

A recent report of X-ray crystallographic data for the Mn cluster of the OEC at higher resolution restimulated synthetic efforts toward cubane-type manganese models. Christou reported the first multinuclear cubane Mn cluster with Ca ion incorporated into an Mn_3-cube, with strong antiferromagnetic exchange interactions based on a solid-state dc magnetic susceptibility study [201]. Although this complex — $Mn_{13}Ca_2$ — exhibits a high nuclearity (as compared to the one found in the biological site, Mn_4Ca), two Mn_3CaO_4 distorted cubane-type sites are present in this compound (Fig. 21). The Ca–Mn distances are in the range 3.5–3.9 Å, slightly longer that the ones observed in the OEC.

Other interesting Mn tetramers showing distinct EPR signals include $[Mn_4O_6(bpea)_4]^{3+}$, reported by Dubé et al. [202], and the cubane-like complex $[Mn_4O_3Cl(OAc)_3(dbm)_3]^{3+}$ incorporating a chlorine atom reported by Christou and coworkers [203].

4. COMPUTATIONAL STUDIES OF THE OEC

4.1. Calculations on the Mechanistic Aspects of the Water Oxidation with DFT

Computational studies that attempt to discern the mechanism of water oxidation are intrinsically difficult due to the complexity of the OEC. An additional difficulty arises from a current lack of precise structural information about the topology of the Mn cluster and the surrounding proteinaceous ligands. Early attempts to rationalize this mechanism in OEC targeted generally small, drastically simplified models. Blomberg and Sieghban employed DFT using the functional hybrid B3LYP (the capabilities and limitations of this popular functional for studies of mixed-valence oxo–manganese compounds were recently reviewed by Batista and coworkers [204]), to study the geometries of high-spin manganese $Mn(OH)_n(H_2O)_{6-n}$ complexes [205]. The energetics of the O–H bond dissociation and structural rearrangements were probed by DFT in several model molecules containing manganese [206]. The models were built based on water molecules bound to the manganese ions or manganese clusters of increasing complexity. For each step of the reaction (H^+ translocation and e^- delivery), the initial geometry was re-optimized and the energy of the H–O bond in the coordinated substrate water molecule was monitored.
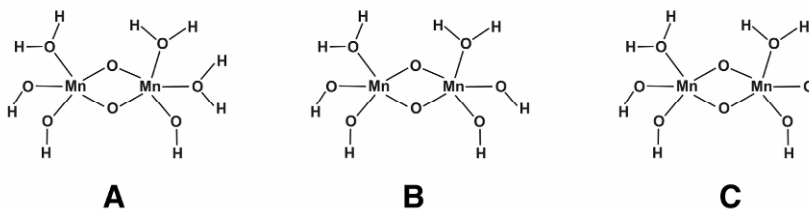
Figure 22. Dimeric Mn models used for theoretical studies of water extraction.

This methodology has since been employed to study increasingly complex models of the OEC active abstraction site. One of the simplest computational models (Fig. 22) uses an antiferromagnetically coupled $Mn^{III}Mn^{IV}$ dimer, with a single water molecule bound to the Mn ion. Two successive extractions of the H$^\bullet$ from the water substrate change the formal valence states of the Mn atoms — $Mn^{III}/Mn^{IV} \rightarrow Mn^{IV}/Mn^{IV} \rightarrow Mn^{IV}/Mn^{V}$ — leaving a terminal Mn^V oxo ready for O–O bond formation with another equivalent of this activated species. The computed OH bond energies are very close: 84.9 kcal/mole for the first hydrogen abstraction and 85.8 kcal/mole for the second [207].

A mononuclear Mn model including a calcium cofactor was also used to examine the pathway to possible O–O bond formation, through breaking of the OH bond with a barrier of formation of the O–O bond of 9.9 kcal/mole. The authors concluded that to lower the barrier of O–O formation a high-spin oxyl Mn^{IV}–$O^{\bullet}$ state is necessary [208]. Extending this approach to higher-nuclearity assemblies, the tetranuclear model, which incorporates three Mn atoms and Ca ion [209], revealed the strong chelating role that this cofactor plays, as the calculated Mn–Ca distance decreases from 3.60 to 3.25 Å for the S_1-to-S_2 transition. The calcium cofactor was proposed to significantly lower the energy necessary to reach the Mn^{IV}–$O^{\bullet}$ oxyl state by acting as a chelating ligand to the pentacoordinated manganese through an oxyl moiety, introducing an additional Mn–OH–Ca bond, thus inducing a hexacoordinated environment for the manganese atom.

Ultimately, the most important result of these theoretical studies is that the oxygen radical must be generated prior to O–O bond formation. Though this reactive intermediate forms at only one Mn atom, the position of the other three manganese atoms was proven to be critical, since the geometry optimizations showed a net elongation of both short Mn–Mn distances in the S_2-to-S_3 transition. Therefore, the possibility that an oxygen radical in the S_3 state might be present was proven to be energetically possible.

The possible presence of the oxyl radical, as an intermediate in the water oxidation mechanism was further reinforced by studies of the Mn^V oxidation state, which can lead to formation of an Mn^{IV}–oxyl radical. DFT calculations on a model complex, $[(terpy)(H_2O)Mn^{IV}(\mu\text{-}O)_2Mn^{III}H_2O\ (terpy)]^{3+}$, showed that it functions as a synthetic Mn catalyst capable of oxidizing water to O_2, with a barrier for O–O bond formation of only 23 kcal/mol [210]. Furthermore, these computational studies confirm experimental results, which show that the Mn^V–oxo form of this complex is inactive, suggesting that a radical step is required for O_2 formation [211]. An interesting finding derived from theoretical DFT studies is that formation of the oxyl radical could proceed through a transition between two spin surfaces (low spin corresponding to the Mn^{IV}–$O^{\bullet}$ with total spin $S = 1$ and the high-spin corresponding to the Mn^{IV}–$O^{\bullet}$ with total spin $S = 2$), without a significant thermodynamic penalty. This suggests that a similar spin transition in the OEC would have a limited effect on the reaction rate in that system.

Using an architecture for the OEC based on the recent Barber and coworkers crystallographic structure, a theoretical study of Mn_3Ca–Mn cubane proved that oxidation to a high-valent Mn–oxo species is not energetically feasible [212]. Instead, tentative proposals of the S_2–S_3 transition, involving structural rearrangements, in which an additional short Mn–Mn distance was obtained, were made, in line with suggestions based on EXAFS studies [213,214]. This study revealed another important observation: the oxidation in the suggested S_2–S_3 transition was centered on manganese and not on the ligand.

The utility of the DFT approach to address the mechanistic and energetic aspects of water oxidation is demonstrated in recent studies performed by Sieghban
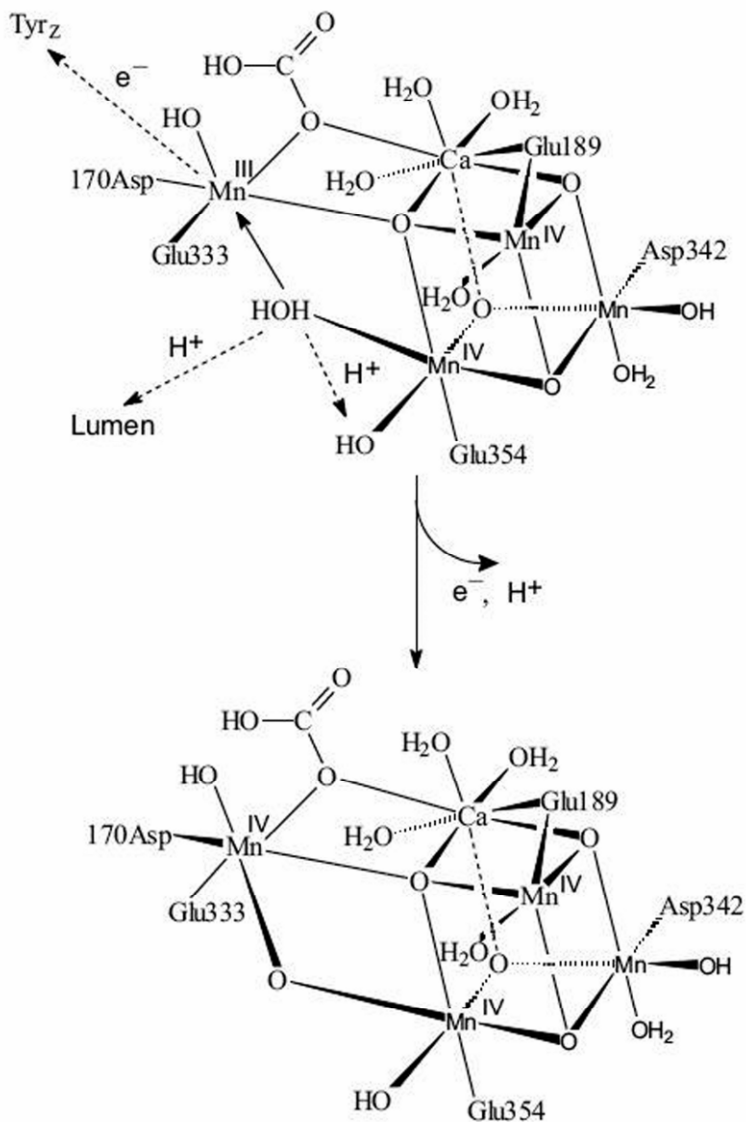
Figure 23. The mechanism for the S_2-to-S_3 transition incorporating an oxyl radical created in S_3 state, stabilized by a weak trans effect to a bridging oxygen based on DFT computations. An additional oxo bridge is formed between the dangling manganese and one of the manganese in the cube. Adapted from [215].

[215], which strongly suggested a key intermediate in the water oxidation being an oxyl radical created in the S_3 state. Based on extensive computations, this radical is believed to be stabilized by a weak trans-effect to a bridging oxygen atom in the

cubane-like moiety. To reach this radical state, a structural rearrangement appears necessary, in which one additional oxo bridge is formed between the dangling manganese and one of the manganese in the cube. Although the energetics computed for this reaction are not fully consistent with a correct mechanism (Fig. 23), the overall obtained energy balance is quite reasonable (Fig. 24). The authors attributed these energetic discrepancies to possible inaccuracies in the structure used for the QM calculations. They have emphasized that the bicarbonate, which appears in the X-ray structure proposed by Ferreira, might not be correct. In the recently presented model where the bicarbonate was replaced by hydroxide, the correct energy diagram was obtained [216].
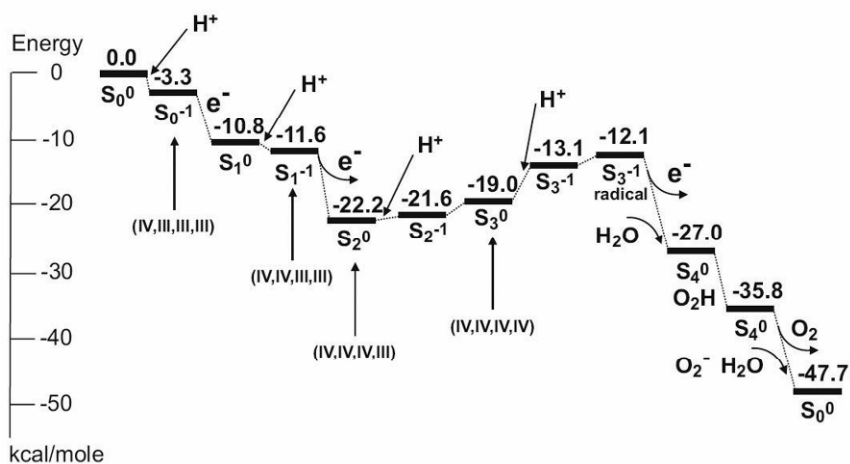
Figure 24. Energy diagram computed for the full Kok cycle (S_n states). The lower index designates the S-state, while the upper one is the charge of the model complex. Adapted from [215].

Another possibility, that the oxygen-evolution step in the OEC could proceed through intramolecular coupling of two bridging μ-oxo atoms, was also addressed theoretically. Redox-induced formation of an O–O bond was described recently in a model peroxo-bridged $Mn^{IV}Mn^{IV}$ dimer, $Mn_2(\mu\text{-}O)_2(\mu\text{-}O)_2(NH_3)_6^{2+}$ [217], and the dioxygen formation from a di-μ-oxo-bridged model compound with similar structure, $[Mn_2(\mu\text{-}O)_2(NH_3)_6(H_2O)_2]^{n+}$ ($n = 2$–5), was also recently investigated [46].

A DFT study on these latter models indicated that one-electron oxidation of the $[Mn_2(\mu\text{-}O)_2(NH_3)_6(H_2O)_2]^{4+}$ complex mostly affects the oxygen atoms, precluding oxidation of an Mn to an Mn^V state [218]. However, O–O bond formation following the third electron transfer leads to dissociation of dioxygen and generation of an $Mn^{II}Mn^{III}$ species, which could be stabilized by the surrounding protein cage. The water molecules in the environment could easily bond to the coordinatively

unsaturated Mn centers formed, thus regenerating the initial redox-active $Mn^{II}Mn^{III}$ dinuclear unit in S_0. These results suggest that the oxygen-evolution step in the OEC could proceed through intramolecular coupling of two bridging oxygen atoms, accompanied by oxygen-to-metal electron transfer. Contrary results studying the same models but with more sophisticated QM methods (incorporating possible solvent effects via inclusion of dielectric constant in COSMO solvent-field-corrected model), were obtained by Stranger, who found that O_2 release from the two bridging oxygen atoms is hindered by an important energy barrier (~70 to ~130 kJ mole^{-1} for dielectric constant of $\varepsilon = 4$ and 78.4, respectively) and is therefore highly unfavorable [46].

4.2. Mixed Molecular Mechanics/Quantum Mechanics Studies of Water Oxidation

As previously highlighted, the size of the OEC precludes computational studies in which the whole system including the manganese cluster, substantial cofactors, and the surrounding protein could be described at the quantum mechanical level. However, hybrid methods, in which the core of the system is described at the Quantum Mechanical (QM) level, while the surrounding protein is treated at the Molecular Mechanics (MM) level, are nowadays available. Such QM/MM methods were recently implemented in several commercial codes and are known as the ONIOM approach [219,220]. ONIOM methodology is currently successfully applied to molecular systems of increasing size up to several thousands atoms. Despite some incompleteness of the recent X-ray structures of the OEC, the new era of high-resolution X-ray diffraction promotes advanced computational methodologies to a previously unreachable level. The QM methods benefit from valuable structural information not only for the individual pieces of the complicated puzzle but for the overall system with the surrounding protein.

Recently, Batista and coworkers performed in-depth theoretical investigations of the OEC using QM/MM methodology on the architecture built from the Fereira X-ray structure [221]. To date, this work constitutes the most complete computational model including the Mn_4 cluster, Ca^{2+}, Cl^-, H_2O, and hydroxide cofactors, and complete proteinaceous ligation by amino-acid residues with overall 2×10^3 atoms (Fig. 25). The use of a model with such a degree of sophistication allowed computing the subtle structural changes intrinsic to advancement through each of the S states of the Kok cycle. Moreover, it made possible the simultaneous assignment of the corresponding oxidation states of all the Mn atoms in the Mn_4 moiety, and consequently allowed for a revised mechanistic proposal for water splitting to dioxygen based on first principles (Fig. 26). The validation of its subsequent steps was performed through the comparison of the computationally derived EXAFS peaks and computed vibrational modes with available experimental data.

Several conclusions of this work are deserving of being highlighted. First, only minor structural rearrangements occur in the model when the surrounding protein is replaced with a simplified set of amino-acid residues, suggesting that the manganese cluster including Ca, water, hydroxide, and chloride is a stable entity even in
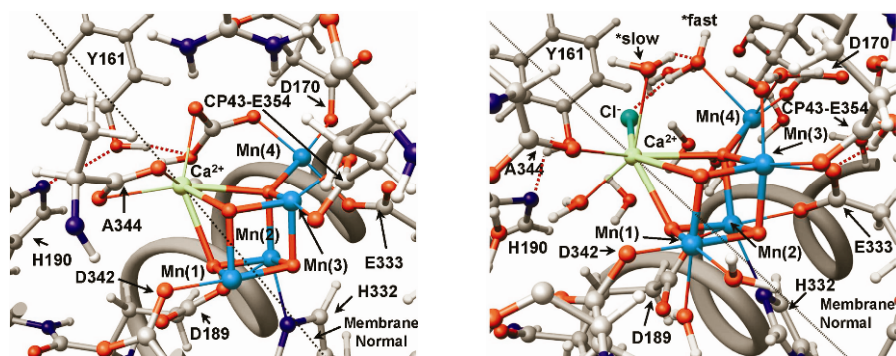
Figure 25. Structural details of the OEC obtained form QM/MM computations by Batista and coworkers showing the geometry of the tetranuclear Mn core and the binding acetate and water molecules. By courtesy of Prof. Victor Batista. Please visit http://www.springer.com/978-1-4419-1138-4 to view a high-resolution full-color version of this illustration.

the absence of the surrounding protein environment. More importantly, the ultimate S_4–S_0 transition, which carries the water oxidation, was once again reinforced as possibly proceeding through an Mn–oxo radical based on the DFT calculations (see Fig. 26).

Finally, it is worth noting that the possibility of simultaneous computational handling of the whole OEC opens new avenues for QM methods, and allows in-depth probing of such advanced topics as, for example, the still-unknown proton exit channel, which previously could only be hypothesized based on structural information [222–224].

5. CONCLUSIONS AND PROSPECTIVES

Recently, several high-resolution structures of the OEC have been brought to light. But even with the highest current X-ray resolution the exact architecture of one of its most important components, the pentanuclear Mn_4Ca cluster, cannot be fully resolved. Based on the crystallographic studies and the available spectroscopic data including X-ray absorption studies, there is now general agreement that the pentanuclear Mn_4Ca moiety includes a cubane-type core with three μ-oxo-bridged Mn atoms, the fourth one being attached to either a Ca cofactor or to one of the Mn atoms on its edge through an oxygen linker.

On the synthetic models front, the complex magnetic behavior of the multinuclear Mn clusters that directly translates into the complexity of the spectral patterns obtained in the magnetic resonance studies certainly does not make the interpretive task simple. On the other hand, the richness of the multiple distinct hyperfine parameters, combined with possible translocation of the oxidation states between
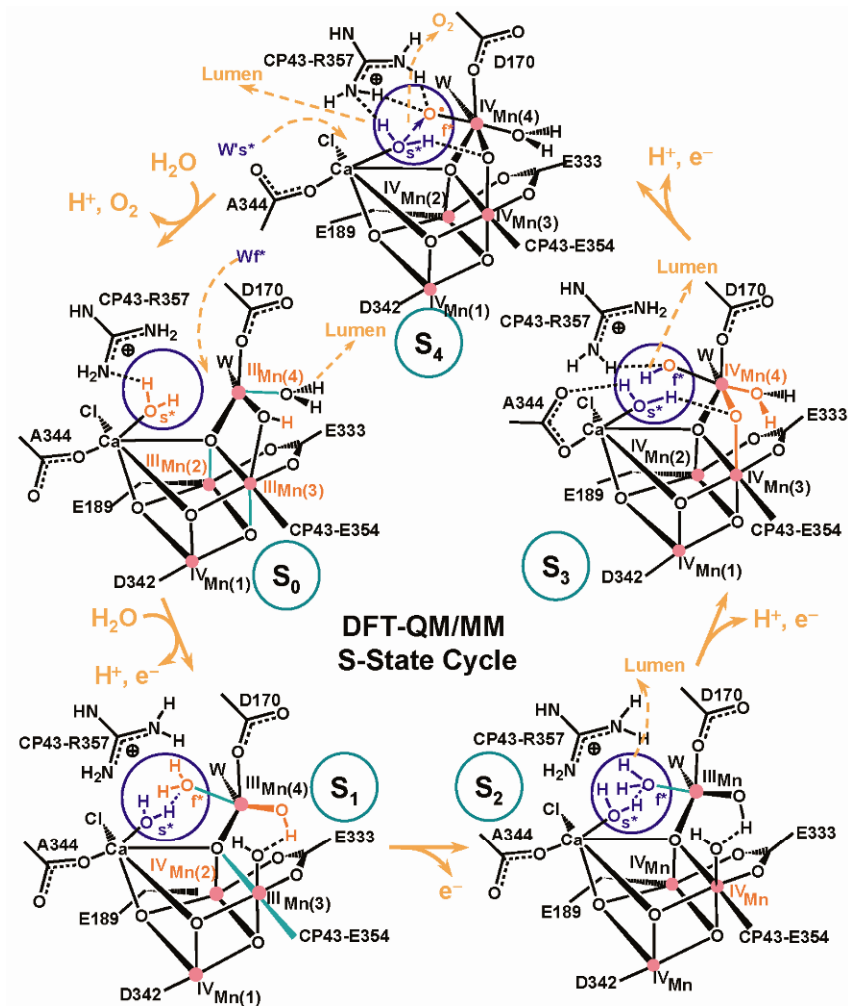
Figure 26. Schematic representation of the complete mechanism of water oxidation by the OEC as obtained from QM/MM computations by Batista and coworkers. By courtesy of Prof. Victor Batista. Please visit http://www.springer.com/978-1-4419-1138-4 to view a high-resolution full-color version of this illustration.

different Mn sites and the corresponding subtle structural changes of the metal environment in the synthetic complexes, offers a unique possibility of matching the spectroscopic data from such systems onto the complicated patterns obtained in the OEC. To understand such complex behavior, as well as the differences in the *J* coupling parameters in the OEC and in the synthetic species, new model com-

plexes, which will certainly help to answer many pertinent questions, will be valuable synthetic targets.

However, even if the exact structure of the manganese cluster was to be determined in the near future, this does not mean that the mechanism of water oxidation will be immediately understood. There are several important pieces of the puzzle that remain unresolved. First, as highlighted by recent theoretical studies, the low energetic barrier between quite different geometries of the cluster might render difficult precise assignment of the experimentally obtained crystal structure to the given S state and to relate it to the precise oxidation states of the Mn atoms. Along the same line comes the high sensitivity of the OEC structure to radiation damage. These factors, together with the still unknown nature of the proteinaceous ligation to Mn_4Ca through the S state cycle, preclude (at least for the moment) a unique compelling proposal for the water-splitting mechanism. The ultimate experimental evidence as to the exact nature of the recently observed [9,213] final intermediate preceding O_2 release during the S_4–S_0 transition would surely help in elucidation of the overall mechanism, but as for now such evidence is not available.

As underlined in the last section, the mechanistic clues as to water splitting to O_2 also begin to emerge from the high-level electronic structure calculations, which can now benefit form the abundance of structural and spectroscopic information. In this context hybrid QM/MM methods and the new formulations of DFT theory, such as frozen density embedding, which allow obtaining extremely accurate spectroscopic observables on systems comporting several thousands atoms, will surely find useful applications for the OEC. Most likely, in the future we will see even more synergy between highly accurate theoretical methods and advanced spectroscopic techniques. This tandem approach will surely bring to light the long-kept secret of photosynthesis.

ACKNOWLEDGMENTS

APPENDIX

Trinuclear:

$$A_1 = \frac{A_1'}{3} \times \left(\frac{S_{13}(S_{13}+1) + S_1(S_1+1) - S_3(S_3+1)}{S_{13}(S_{13}+1)} \right)$$

$$\times \left(\frac{S(S+1) + S_{13}(S_{13}+1) - S_2(S_2+1)}{S(S+1)} \right),$$

(22)

$$A_3 = \frac{A_3'}{3} \times \left(\frac{S_{13}(S_{13}+1) + S_3(S_3+1) - S_1(S_1+1)}{S_{13}(S_{13}+1)} \right)$$

$$\times \left(\frac{S(S+1) + S_{13}(S_{13}+1) - S_2(S_2+1)}{S(S+1)} \right), \qquad (23)$$

$$A_2 = \frac{A_2'}{3} \times \left(\frac{S(S+1) + S_2(S_2+1) - S_{13}(S_{13}+1)}{S(S+1)} \right). \qquad (24)$$

Tetranuclear:

$$A_1 = \frac{A_1'}{4} \times \left(\frac{S_{13}(S_{13}+1) + S_1(S_1+1) - S_3(S_3+1)}{S_{13}(S_{13}+1)} \right)$$

$$\times \left(\frac{S(S+1) + S_{13}(S_{13}+1) - S_{24}(S_{24}+1)}{S(S+1)} \right), \qquad (25)$$

$$A_2 = \frac{A_2'}{4} \times \left(\frac{S_{24}(S_{24}+1) + S_2(S_2+1) - S_4(S_4+1)}{S_{24}(S_{24}+1)} \right)$$

$$\times \left(\frac{S(S+1) + S_{24}(S_{24}+1) - S_{13}(S_{13}+1)}{S(S+1)} \right), \qquad (26)$$

$$A_3 = \frac{A_3'}{4} \times \left(\frac{S_{13}(S_{13}+1) + S_3(S_3+1) - S_1(S_1+1)}{S_{13}(S_{13}+1)} \right)$$

$$\times \left(\frac{S(S+1) + S_{13}(S_{13}+1) - S_{24}(S_{24}+1)}{S(S+1)} \right), \qquad (27)$$

$$A_4 = \frac{A_4'}{4} \times \left(\frac{S_{24}(S_{24}+1) + S_4(S_4+1) - S_2(S_2+1)}{S_{24}(S_{24}+1)} \right)$$

$$\times \left(\frac{S(S+1) + S_{24}(S_{24}+1) - S_{13}(S_{13}+1)}{S(S+1)} \right). \qquad (28)$$

NOTES

1. The interaction of spins described by this Hamiltonian is of purely quantum mechanical nature and is made under the assumption that S_i and S_j are the true spins and not the effective spins. For $S > 1/2$, this equation may only be the leading term of a series expansion, in which higher terms such as $(S_i S_j)^2$ occur. More de-

tailed discussion follows in §2.2.2. Note that other notations found in the literature use the prefactor J or $-J$ instead of $-2J$.

2. Heisenberg-type interactions are the spin interactions defined in the Heisenberg model based on the quantum mechanical concept of exchange, which does not have any classical analogue. This interaction is a direct consequence of the Pauli exclusion principle. The term Heisenberg-type usually concerns the isotropic interaction defined in the Heisenberg exchange Hamiltonian, as opposed to the simplified "semi-classical" Ising or XY model of interacting spins.

3. For the detailed review of the EPR and related advanced electron paramagnetic resonance studies relevant to the manganese cluster in the Oxygen-Evolving System of PSII, the reader is invited to consult several reviews recently published on this topic [21,56].

4. However, the overall exchange Hamiltonian (the "ex" subscript differentiate this Hamiltonian from the HDvV isotropic spin Hamiltonian) includes the anisotropic part of the exchange interaction:

$$\hat{H}_{ex} = J_{12}\hat{S}_1 \cdot \hat{S}_2 + d_{12} \cdot \hat{S}_1 \times \hat{S}_2 + \hat{S}_1 \cdot D_{12} \cdot \hat{S}_2 .$$

5. In the case of the exchange-coupled metal dimers, the uncoupled basis relates to the individual spin values on the metal centers. The proper basis set functions have to be used when constructing the corresponding matrix.

6. In the common wavefunction- or density functional theory-based calculations, the electronic state of the molecule is described by a wavefunction constructed from the occupied molecular orbitals as a single Slater determinant. This monodeterminental technique completely neglects all correlation between electrons. Molecular systems, in which the electron correlation is very strong, are usually said to be of "multideterminental character," since they cannot be described by the monodeterminental techniques, but have to be treated using multiconfiguration methods. The multiconfiguration techniques consists of simultaneous optimization of both the shapes of molecular orbitals and contributions from different electronic configurations using the variational method. The actual total electronic wavefunction is expanded in terms of Slater determinants, which describe singly-, doubly-, and multiply excited electronic configurations.

7. The isotropic part of the hyperfine coupling (Fermi contact), unlike most other electronic properties such as dipole moments or polarizabilities, is determined by the amplitude of the calculated wavefunction at a single point in space. Since the wavefunction is found by optimization based on the variational principle with a global energy criterion, a good wavefunction may have significant error at some particular point in space. This local character of the Fermi contact makes the calculations very sensitive to the quality and size of the atomic basis set.

8. Configuration interaction (CI) is a variational method that includes electronic correlation in many-electron systems. The coefficients of the linear combination of Slater determinants used for the wavefunction by mixing (thus interacting) different electronic configurations are solved simultaneously. CI suffers from the rapid increase in the number of molecular orbital integrals and the number of con-

figurations with an increase in the number of atoms, and can be generally used only for small molecules.

REFERENCES

1. Frausto da Silva JJR, Williams RJP. 2001. *The biological chemistry of the elements*, 2nd ed. Oxford UP.
2. Ash DE, Cox JD, Christianson DW. 2000. Arginase: a binuclear manganese metalloenzyme. *Met Ions Biol Sys* **37**:407–428.
3. Christianson DW. 2005. Arginase: structure, mechanism, and physiological role in male and female sexual arousal. *Acc Chem Res* **38**:191–201.
4. Dismukes GC. 1996. Manganese enzymes with binuclear active sites. *Chem Rev* **96**:2909–2926.
5. Pecoraro VL, ed. 1992. *Manganese redox enzymes*. New York: VCH.
6. Dasgupta J, Ananyev GM, Dismukes GC. 2008. Photoassembly of the water-oxidizing complex in photosystem II. *Coord Chem Rev* **252**:347–360.
7. Yocum CF. 1992. The calcium and chloride requirements for photosynthetic water oxidation. *Manganese Redox Enzymes*, pp. 71–83.
8. Yocum CF. 2008. The calcium and chloride requirements of the O_2 evolving complex. *Coord Chem Rev* **252**:296–305.
9. Dau H, Haumann M. 2008. The manganese complex of photosystem II in its reaction cycle: basic framework and possible realization at the atomic level. *Coord Chem Rev* **252**:273–295.
10. Rappaport F, Diner BA. 2008. Primary photochemistry and energetics leading to the oxidation of the $(Mn)_4Ca$ cluster and to the evolution of molecular oxygen in Photosystem II. *Coord Chem Rev* **252**:259–272.
11. Kok B, Forbush B, McGloin M. 1970. Cooperation of charges in photosynthetic oxygen evolution, I: a linear four step mechanism. *Photochem Photobiol* **11**:457–475.
12. Rutherford AW. 1989. Photosystem II, the water-splitting enzyme. *Trends Biochem Sci* **14**:227–232.
13. Barber J, Murray JW. 2008. Revealing the structure of the Mn-cluster of photosystem II by X-ray crystallography. *Coord Chem Rev* **252**:233–243.
14. Biesiadka J, Loll B, Kern J, Irrgang K-D, Zouni A. 2004. Crystal structure of cyanobacterial photosystem II at 3.2-Å resolution: a closer look at the Mn cluster. *Phys Chem Chem Phys* **6**:4733–4736.
15. Ferreira KN, Iverson TM, Maghlaoui K, Barber J, Iwata S. 2004. Architecture of the photosynthetic oxygen-evolving center. *Science* **303**:1831–1838.
16. Kamiya N, Shen J-R. 2003. Crystal structure of oxygen-evolving photosystem II from Thermosynechococcus vulcanus at 3.7-Å resolution. *Proc Natl Acad Sci USA* **100**:98–103.
17. Zouni A, Witt H-T, Kern J, Fromme P, Krauss N, Saenger W, Orth P. 2001. Crystal structure of photosystem II from Synechococcus elongatus at 3.8-Å resolution. *Nature* **409**:739–743.
18. Sauer K, Yano J, Yachandra VK. 2008. X-ray spectroscopy of the photosynthetic oxygen-evolving complex. *Coord Chem Rev* **252**:318–335.
19. Debus RJ. 2008. Protein ligation of the photosynthetic oxygen-evolving center. *Coord Chem Rev* **252**:244–258.

20. McCarrick RM, Britt RD. 2008. Current models and mechanism of water splitting. In *Photosynthetic protein complexes*, pp. 107–136. Ed P Fromme. New York: Wiley-VCH.

21. Stich TA, McCarrick RM, Britt RD. 2008. Advanced electron paramagnetic resonance studies of the oxygen evolving complex. *Coord Chem Rev*. In press.

22. Dismukes GC, Siderer Y. 1980. EPR spectroscopic observations of a manganese center associated with water oxidation in spinach chloroplasts. *FEBS Lett* **121**:78–80.

23. Dismukes GC, Siderer Y. 1981. Intermediates of a polynuclear manganese center involved in photosynthetic oxidation of water. *Proc Natl Acad Sci USA* **78**:274–278.

24. Dismukes GC, Ferris K, Watnick P. 1982. EPR spectroscopic evidence for a tetranuclear manganese cluster as the site for photosynthetic oxygen evolution. *Photobiochem Photobiophys* **3**:243–256.

25. Critchley C, Sargeson AM. 1984. A manganese–chloride cluster as the functional center of the oxygen evolving enzyme in photosynthetic systems. *FEBS Lett* **177**:2–5.

26. De Paula JC, Brudvig GW. 1985. Magnetic properties of manganese in the photosynthetic oxygen-evolving complex. *J Am Chem Soc* **107**:2643–2648.

27. De Paula JC, Beck WF, Brudvig GW. 1986. Magnetic properties of manganese in the photosynthetic O$_2$-evolving complex, 2: evidence for a manganese tetramer. *J Am Chem Soc* **108**:4002–4009.

28. Zimmermann JL, Rutherford AW. 1986. Electron paramagnetic resonance properties of the S2 state of the oxygen-evolving complex of photosystem II. *Biochemistry* **25**:4609–4615.

29. Armstrong FA. 2004. Hydrogenases: active site puzzles and progress. *Curr Opin Chem Biol* **8**:133–140.

30. Evans DJ, Pickett CJ. 2003. Chemistry and the hydrogenases. *Chem Soc Rev* **32**:268–275.

31. Sieker LC, Adman ET. 2001. The 2[4Fe–4S] ferredoxins. In *Handbook of metalloproteins*, Vol 1, pp. 574–592. Ed VL Pecoraro. New York: VCH.

32. Messerschmidt A. 2001. Ascorbate oxidase. In *Handbook of metalloproteins*, Vol. 2, pp. 1345–1358. Ed VL Pecoraro. New York: VCH.

33. Lyons TJ, Gralla EB, Valentine JS. 1999. Biological chemistry of copper–zinc superoxide dismutase and its link to amyotrophic lateral sclerosis. *Met Ions Biol Sys* **36**:125–177.

34. de Lacey AL, Fernandez VM, Rousset M. 2005. Native and mutant nickel–iron hydrogenases: Unraveling structure and function. *Coord Chem Rev* **249**:1596–1608.

35. van Vleck JH. 1932. The theory of electric and magnetic susceptibilities. Oxford: Clarendon.

36. Robin MB, Day P. 1967. Mixed valence chemistry: a survey and classification. *Adv Inorg Chem Radiochem* **10**:247–422.

37. Cotton FA, Geoffrey W. 1988. *Advanced inorganic chemistry*, 5th ed., pp. 699–709. New York: John Wiley & Sons.

38. Pecoraro VL. 1988. Structural proposals for the manganese centers of the oxygen evolving complex: an inorganic chemist's perspective. *Photochem Photobiol* **48**:249–264.

39. Blondin G, Girerd JJ. 1990. Interplay of electron exchange and electron transfer in metal polynuclear complexes in proteins or chemical models. *Chem Rev* **90**:1359–1376.

40. Thorp HH, Sarneski JE, Brudvig GW, Crabtree RH. 1989. Proton-coupled electron transfer in manganese complex [(bpy)$_2$Mn(O)$_2$Mn(bpy)$_2$]$^{3+}$. *J Am Chem Soc* **111**: 9249–9250.

41. Curély J. 2005. Magnetic Orbitals and Mechanisms of Exchange I. Direct Exchange. *Monatsh Chem* **136**:987–1011.

42. Van Vleck JH. 1953. Models of exchange coupling in ferromagnetic media. *Rev Mod Phys* **25**:220–227.

43. Curély J. 2005. Magnetic orbitals and mechanisms of exchange, II: superexchange. *Monatsh Chem* **136**:1013–1036.

44. Curély J, Barbara B. 2006. General theory of superexchange in molecules. *Struct Bond* **122**:207–250.

45. Hotzelmann R, Wieghardt K, Flörke U, Haup H-J, Weatherburn DC, Bonvoisin J, Blondin G, Girerd J-J. 1992. Spin exchange coupling in asymmetric heterodinuclear complexes containing the π-oxo-bis(p-acetato)dimetal core. *J Am Chem Soc* **114**:1681–1696.

46. Petrie S, Stranger R. 2004. On the mechanism of dioxygen formation from a di-μ-oxo-bridged manganese dinuclear complex. *Inorg Chem* **43**:5237–5244.

47. Anderson PW, Hasegawa H. 1955. Considerations on double exchange. *Phys Rev* **100**:675–681.

48. Bominaar EL, Hu Z, Münck E, Girerd J-J, Borshchs SA. 1995. Double exchange and vibronic coupling in mixed-valence systems: electronic structure of exchange coupled siroheme–(Fe$_4$S$_4$)$^{2+}$ chromophore in oxidized *E. coli* sulfite reductase. *J Am Chem Soc* **117**:6976–6989.

49. De Gennes P-G. 1960. Effects of double exchange in magnetic crystals. *Phys Rev* **118**:141–187.

50. Zener C, Heikes RR. 1953. Exchange interactions. *Rev Mod Phys* **25**:191–198.

51. Tilley RJD. 2004. *Understanding solids: the science of materials*. Chichester: John Wiley.

52. Ravi N, Bominaar EL. 1995. Exchange coupling approach to the radical disposition of an intermediate in *Escherichia coli* ribonucleotide reductase. *Inorg Chem* **34**:1040–1043.

53. Zhao XG, Richardson WH, Chen JL, Li J, Noodleman L, Tsai HL, Hendrickson DN. 1997. Density functional calculations of electronic structure, charge distribution, and spin coupling in manganese-oxo dimer complexes. *Inorg Chem* **36**:1198–1217.

54. Abragam A, Pryce MHL. 1951. Theory of the nuclear hyperfine structure of paramagnetic resonance spectra in crystals. *Proc Roy Soc* **A205**:135–153.

55. Pryce MHL. 1950. Spin–spin interaction within paramagnetic ions. *Phys Rev* **80**:1107–1108.

56. Haddy A. 2007. EPR spectroscopy of the manganese cluster of photosystem II. *Photosynth Res* **92**:357–368.

57. Bencini A, Gatteschi D. 1990. *Electron paramagnetic resonance of exchange coupled systems*. Berlin and Heidelberg: Springer-Verlag.

58. Sands RH, Durham WR. 1975. Spectroscopic studies on two-iron ferredoxins. *Q Rev Biophys* **7**:443–504.

59. Randall DW. 1997. Pulsed EPR studies of tyrosyl radicals and manganese complexes: insights into photosynthetic oxygen evolution. PhD thesis. University of California Davis.

60. Kambe K. 1950. Paramagnetic susceptibilities of some polynuclear complex salts. *J Phys Soc Jpn* **5**:48–51.

61. Sage JT, Xia YM, Debrunner PG, Keough DT, De Jersey J, Zerner B. 1989. Möss-bauer analysis of the binuclear iron site in purple acid phosphatase from pig allantoic fluid. *J Am Chem Soc* **111**:7239–7247.

62. Christmas C, Vincent JB, Chang HR, Huffman JC, Christou G, Hendrickson DN. 1988. Nonanuclear oxide-bridged manganese complex: preparation, structure, and magnetic properties of $[Mn_9O_4(O_2CPh)_8(sal)_4(salH)_2(pyr)_4]$ ($salH_2$ = salicylic acid; pyr = pyridine). *J Am Chem Soc* **110**:823–830.

63. Belinskii MI. 1994. Heisenberg model of tetrameric manganese cluster of S2 center of Photosystem II. *Chem Phys* **179**:1–22.

64. Belinskii MI. 1994. Exchange variation of hyperfine characteristics of tetrameric $[Mn_3(III)Mn(IV)]$ and $[Mn_3(IV)Mn(III)]$ clusters. *Chem Phys* **189**:451–465.

65. Borras-Almenar JJ, Clemente-Juan JM, Coronado E, Tsukerblat BS. 1999. High-nuclearity magnetic clusters: generalized spin Hamiltonian and its use for the calculation of the energy levels, bulk magnetic properties, and inelastic neutron scattering spectra. *Inorg Chem* **38**:6081–6088.

66. Charlot M-F, Boussac A, Blondin G. 2005. Towards a spin coupling model for the Mn_4 cluster in Photosystem II. *Biochim Biophys Acta* **1708**:120–132.

67. Hasegawa K, Ono T-A, Inoue Y, Kusunoki M. 1999. Spin-exchange interactions in the S2-state manganese tetramer in photosynthetic oxygen-evolving complex deduced from g = 2 multiline EPR signal. *Chem Phys Lett* **300**:9–19.

68. Isobe H, Shoji M, Koizumi K, Kitagawa Y, Yamanaka S, Kuramitsu S, Yamaguchi K. 2005. Electronic and spin structures of manganese clusters in the photosynthesis II system. *Polyhedron* **24**:2767–2777.

69. Siegbahn PEM, Blomberg MRA. 1999. Density functional theory of biologically relevant metal centers. *Ann Rev Phys Chem* **50**:221–249.

70. Siegbahn PEM, Blomberg MRA. 2000. Transition-metal systems in biochemistry studied by high-accuracy quantum chemical methods. *Chem Rev* **100**:421–437.

71. Neese F. 2004. Application of EPR parameter calculations in bioinorganic chemistry: application of epr parameter calculations in bioinorganic chemistry. In *Calculation of NMR and EPR parameters theory and applications*, pp. 581–591. Ed M Kaupp, M Bühl, V Malkin. New York: Wiley-VCH.

72. Noodleman L. 1981. Valence bond description of antiferromagnetic coupling in transition metal dimers. *J Chem Phys* **74**:5737–5743.

73. Noodleman L, Baerends EJ. 1984. Electronic structure, magnetic properties, ESR, and optical spectra for 2-iron ferredoxin models by LCAO-Xα valence bond theory. *J Am Chem Soc* **106**:2316–2327.

74. Noodleman L, Case DA. 1992. Density-functional theory of spin polarization and spin coupling in iron-sulfur clusters. *Adv Inorg Chem* **38**:423–470.

75. Noodleman L, Davidson ER. 1986. Ligand spin polarization and antiferromagnetic coupling in transition metal dimers. *Chem Phys* **109**:131–143.

76. Noodleman L, Norman JG, Jr. 1979. The Xα valence bond theory of weak electronic coupling: application to the low-lying states of octachlorodimolybdate. *J Chem Phys* **70**:4903–4906.

77. Noodleman L, Peng CY, Case DA, Mouesca JM. 1995. Orbital interactions, electron delocalization and spin coupling in iron–sulfur clusters. *Coord Chem Rev* **144**:199–244.

78. Schmitt EA, Noodleman L, Baerends EJ, Hendrickson DN. 1992. LCAO Xα calculation of the magnetic exchange interactions in a manganese MnIVMn₃III cubane com-

plex: relevance to the water oxidation center of photosystem II. *J Am Chem Soc* **114**:6109–6119.

79. Brink DM, Satchler GR. 1968. *Angular momentum*. Oxford UP.

80. Merzbacher E. 1970. *Quantum mechanics*, pp. 389–404. New York: Wiley.

81. Griffith JS. 1972. General theory of magnetic susceptibilities of polynuclear transition metal compounds: systems with two or three spins. *Struct Bond* **10**:87–126.

82. Ruiz E, Cano J, Alvarez S, Alemany P. 1999. Broken symmetry approach to calculation of exchange coupling constants for homobinuclear and heterobinuclear transition metal complexes. *J Comput Chem* **20**:1391–1400.

83. Ruiz E, Rodriguez-Fortea A, Cano J, Alvarez S, Alemany P. 2003. About the calculation of exchange coupling constants in polynuclear transition metal complexes. *J Comput Chem* **24**:982–989.

84. Adamo C, Barone V, Bencini A, Broer R, Filatov M, Harrison NM, Illas F, Malrieu JP, de Moreira I, Ruiz E, Cano J, Alvarez S, Polo V. 2006. Comment on "About the calculation of exchange coupling constants using density-functional theory: the role of the self-interaction error" (*J Chem Phys* **123**:164110, 2005). *J Chem Phys* **124**: 107101/107101–107101/107103.

85. Bi S, Liu C, Zhang C. 2002. Structural modeling and magnetostructural correlations for heterobinuclear Cu(II)–Ni(II) complex. *Int J Quantum Chem* **88**:347–354.

86. Caballol R, Castell O, Illas F, de Moreira I, Malrieu JP. 1997. Remarks on the proper use of the broken symmetry approach to magnetic coupling. *J Phys Chem A* **101**:7860–7866.

87. Harju A, Raesaenen E, Saarikoski H, Puska MJ, Nieminen RM, Niemelae K. 2004. Broken symmetry in density-functional theory: analysis and cure. *Phys Rev B: Condens Matter* **69**:153101/153101–153101/153104.

88. Hart JR, Rappe AK, Gorun SM, Upton TH. 1992. Estimation of magnetic exchange coupling constants in bridged dimer complexes. *J Phys Chem* **96**:6264–6269.

89. Illas F, de Moreira I, Malrieu PR, De Graaf C, Barone V. 2000. Magnetic coupling in biradicals, binuclear complexes and wide-gap insulators: a survey of ab initio wave function and density functional theory approaches. *Theor Chem Acc* **104**:265–272.

90. Liu C, Hu H, Yang X. 2001. A practicable parameter describing magnetic interactions. *Chem Phys Lett* **349**:89–94.

91. de Moreira I, Malrieu PR, Illas F. 2006. A unified view of the theoretical description of magnetic coupling in molecular chemistry and solid state physics. *Phys Chem Chem Phys* **8**:1645–1659.

92. Ciofini I, Daul CA. 2003. DFT calculations of molecular magnetic properties of coordination compounds. *Coord Chem Rev* **238-239**:187–209.

93. Munzarova M, Kaupp M. 1999. A critical validation of density functional and coupled-cluster approaches for the calculation of EPR hyperfine coupling constants in transition metal complexes. *J Phys Chem A* **103**:9966–9983.

94. Kaupp M, Bühl M, Malkin VG, ed. 2004. *Calculation of NMR and EPR parameters—theory and applications*. Weinheim: Wiley-VCH.

95. Tyystjaervi E. 2008. Photoinhibition of Photosystem II and photodamage of the oxygen evolving manganese cluster. *Coord Chem Rev* **252**:361–376.

96. Yano J, Kern J, Irrgang K-D, Latimer MJ, Bergmann U, Glatzel P, Pushkar Y, Biesiadka J, Loll B, Sauer K, Messinger J, Zouni A, Yachandra VK. 2005. X-ray damage to the Mn_4Ca complex in single crystals of photosystem II: a case study for metalloprotein crystallography. *Proc Natl Acad Sci USA* **102**:12047–12052.

97. Vincent JB, Christou G. 1989. Higher oxidation state manganese biomolecules. *Adv Inorg Chem* **33**:197–257.

98. Mukhopadhyay S, Mandal SK, Bhaduri S, Armstrong WH. 2004. Manganese clusters with relevance to Photosystem II. *Chem Rev* **104**:3981–4026.

99. Yano J, Kern J, Sauer K, Latimer MJ, Pushkar Y, Biesiadka J, Loll B, Saenger W, Messinger J, Zouni A, Yachandra VK. 2006. Where water is oxidized to dioxygen: structure of the photosynthetic Mn_4Ca cluster. *Science* **314**:821–825.

100. Yano J, Pushkar Y, Glatzel P, Lewis A, Sauer K, Messinger J, Bergmann U, Yachandra V. 2005. High-resolution Mn EXAFS of the oxygen-evolving complex in Photosystem II: structural implications for the Mn_4Ca cluster. *J Am Chem Soc* **127**:14974–14975.

101. Sivaraja M, Philo JS, Lary J, Dismukes GC. 1989. Photosynthetic oxygen evolution: changes in magnetism of the water-oxidizing enzyme. *J Am Chem Soc* **111**:3221–3225.

102. Rutherford AW, Boussac A, Zimmermann JL. 1991. EPR studies of the oxygen evolving enzyme. *New J Chem* **15**:491–500.

103. Peloquin JM, Campbell KA, Randall DW, Evanchik MA, Pecoraro VL, Armstrong WH, Britt RD. 2000. 55Mn ENDOR of the S2-State multiline EPR signal of Photosystem II: implications on the structure of the tetranuclear Mn cluster. *J Am Chem Soc* **122**:10926–10942.

104. Cady CW, Crabtree RH, Brudvig GW. 2008. Functional models for the oxygen-evolving complex of photosystem II. *Coord Chem Rev* **252**:444–455.

105. Herrero C, Lassalle-Kaiser B, Leibl W, Rutherford AW, Aukauloo A. 2008. Artificial systems related to light driven electron transfer processes in PSII. *Coord Chem Rev* **252**:456–468.

106. Bergmann U, Grush MM, Horne CR, DeMarois P, Penner-Hahn JE, Yocum CF, Wright DW, Dube CE, Armstrong WH, Christou G, Eppley HJ, Cramer SP. 1998. Characterization of the Mn oxidation states in photosystem II by Kb X-ray fluorescence spectroscopy. *J Phys Chem B* **102**:8350–8352.

107. Cinco RM, Holman KLM, Robblee JH, Yano J, Pizarro SA, Bellacchio E, Sauer K, Yachandra VK. 2002. Calcium EXAFS establishes the Mn–Ca cluster in the oxygen-evolving complex of Photosystem II. *Biochemistry* **41**:12928–12933.

108. Cinco RM, Robblee JH, Rompel A, Fernandez C, Yachandra VK, Sauer K, Klein MP. 1998. Strontium EXAFS reveals the proximity of calcium to the manganese cluster of oxygen-evolving Photosystem II. *J Phys Chem B* **102**:8248–8256.

109. Cinco RM, Rompel A, Visser H, Aromi G, Christou G, Sauer K, Klein MP, Yachandra VK. 1999. Comparison of the manganese cluster in oxygen-evolving Photosystem II with distorted cubane manganese compounds through X-ray absorption spectroscopy. *Inorg Chem* **38**:5988–5998.

110. DeRose VJ, Mukerji I, Latimer MJ, Yachandra VK, Sauer K, Klein MP. 1994. Comparison of the manganese oxygen-evolving complex in Photosystem II of spinach and Synechococcus sp. with multinuclear manganese model compounds by X-ray absorption spectroscopy. *J Am Chem Soc* **116**:5239–5249.

111. Glatzel P, Bergmann U, Yano J, Visser H, Robblee JH, Gu W, De Groot FMF, Christou G, Pecoraro VL, Cramer SP, Yachandra VK. 2004. The electronic structure of Mn in oxides, coordination complexes, and the oxygen-evolving complex of photosystem II studied by resonant inelastic X-ray scattering. *J Am Chem Soc* **126**:9946–9959.

112. Pizarro SA, Glatzel P, Visser H, Robblee JH, Christou G, Bergmann U, Yachandra VK. 2004. Mn oxidation states in tri- and tetra-nuclear Mn compounds structurally

relevant to photosystem II: Mn K-edge X-ray absorption and Kb X-ray emission spectroscopy studies. *Phys Chem Chem Phys* **6**:4864–4870.

113. Rompel A, Andrews JC, Cinco RM, Wemple MW, Christou G, Law NA, Pecoraro VL, Sauer K, Yachandra VK, Klein MP. 1997. Chlorine K-edge X-ray absorption spectroscopy as a probe of chlorine–manganese bonding: model systems with relevance to the oxygen evolving complex in Photosystem II. *J Am Chem Soc* **119**:4465–4470.

114. Yachandra VK, DeRose VJ, Latimer MJ, Mukerji I, Sauer K, Klein MP. 1993. Where plants make oxygen: a structural model for the photosynthetic oxygen-evolving manganese cluster. *Science* **260**:675–679.

115. Yachandra VK, Guiles RD, McDermott AE, Cole JL, DeRose VJ, Zimmermann JL, Sauer K, Klein MP. 1989. X-ray absorption spectroscopy of manganese in the photosynthetic apparatus. *Physica B* **158**:78–80.

116. Vrettos JS, Brudvig GW. 2004. Oxygen evolution. *Compr Coord Chem II* **8**:507–547.

117. Mullins CS, Pecoraro VL. 2008. Reflections on small molecule manganese models that seek to mimic photosynthetic water oxidation chemistry. *Coord Chem Rev* **252**: 416–443.

118. Brudvig GW, Crabtree RH. 1989. Bioinorganic chemistry of manganese related to photosynthetic oxygen evolution. *Prog Inorg Chem* **37**:99–142.

119. Thorp HH, Brudvig GW. 1991. The physical inorganic chemistry of manganese relevant to photosynthetic oxygen evolution. *New J Chem* **15**:479–490.

120. Osawa M, Morooka Y, Kitajima N. 1993. Manganese complexes modeling the active sites of manganese proteins. *Yuki Gosei Kagaku Kyokaishi* **51**:921–930.

121. Dave BC, Czernuszewicz RS. 1994. Coordination chemistry of manganese with 2,2'-bipyridine: synthetic access to high-valent polynuclear oxomanganese complexes of biological relevance. *New J Chem* **18**:149–155.

122. Hsieh W-Y, Campbell Kristy A, Gregor W, David Britt R, Yoder Derek W, Penner-Hahn James E, Pecoraro VL. 2004. The first spectroscopic model for the S1 state multiline signal of the OEC. *Biochim Biophys Acta* **1655**:149–157.

123. Chen H, Collomb M-N, Duboc C, Blondin G, Riviere E, Faller JW, Crabtree RH, Brudvig GW. 2005. New linear high-valent tetranuclear manganese-oxo cluster relevant to the oxygen-evolving complex of Photosystem II with oxo, hydroxo, and aqua coordinated to a single Mn(IV). *Inorg Chem* **44**:9567–9573.

124. Kim DH, Britt RD, Klein MP, Sauer K. 1992. The manganese site of the photosynthetic oxygen-evolving complex probed by EPR spectroscopy of oriented photosystem II membranes: the $g = 4$ and $g = 2$ multiline signals. *Biochemistry* **31**:541–547.

125. Ono T, Inoue Y. 1988. Abnormal S-state turnovers in ammonia-binding manganese centers of photosynthetic oxygen evolving system. *Arch Biochem Biophys* **264**:82–92.

126. Pace RJ, Smith P, Bramley R, Stehlik D. 1991. EPR saturation and temperature dependence studies on signals from the oxygen-evolving center of photosystem II. *Biochim Biophys Acta* **1058**:161–170.

127. van Vliet P, Rutherford AW. 1996. Properties of the chloride-depleted oxygen-evolving complex of Photosystem II studied by electron paramagnetic resonance. *Biochemistry* **35**:1829–1839.

128. Randall DW, Chan MK, Armstrong WH, Britt RD. 1998. Pulsed ^{1}H and [55]Mn ENDOR studies of dinuclear Mn(III)Mn(IV) model complexes. *Mol Phys* **95**:1283–1294.

129. Schaefer KO, Bittl R, Lendzian F, Barynin V, Weyhermueller T, Wieghardt K, Lubitz W. 2003. Multifrequency EPR investigation of dimanganese catalase and related Mn(III)Mn(IV) complexes. *J Phys Chem B* **107**:1242–1250.

130. Blondin G, Davydov R, Philouze C, Charlot M-F, Styring T, Akermark B, Girerd J-J, Boussac A. 1997. Electron paramagnetic resonance study of the $S = 1/2$ ground state of a radiolysis-generated manganese(III)–trimanganese(IV) form of [MnIV$_4$O$_6$ (bipy)$_6$]$^{4+}$ (bipy = 2,2'-bipyridine): comparison with the photosynthetic oxygen evolving complex. *J Chem Soc, Dalton Trans*, pp. 4069–4074.

131. Cooper SR, Dismukes GC, Klein MP, Calvin M. 1978. Mixed valence interactions in di-μ-oxo bridged manganese complexes: electron paramagnetic resonance and magnetic susceptibility studies. *J Am Chem Soc* **100**:7248–7252.

132. Schaefer K-O, Bittl R, Zweygart W, Lendzian F, Haselhorst G, Weyhermueller T, Wieghardt K, Lubitz W. 1998. Electronic structure of antiferromagnetically coupled dinuclear manganese (MnIIIMnIV) complexes studied by magnetic resonance techniques. *J Am Chem Soc* **120**:13104–13120.

133. Yano J, Sauer K, Girerd J-J, Yachandra VK. 2004. Single-crystal X- and Q-band EPR spectroscopy of a binuclear Mn$_2$(III,IV) complex relevant to the oxygen-evolving complex of Photosystem II. *J Am Chem Soc* **126**:7486–7495.

134. Larson E, Haddy A, Kirk ML, Sands RH, Hatfield WE, Pecoraro VL. 1992. Asymmetric mixed-valent complex {[Mn(2-OH-3,5-Cl$_2$-SALPN)]$_2$(THF)}ClO$_4$ shows a temperature-dependent interconversion between $g = 2$ multiline and low-field EPR signals. *J Am Chem Soc* **114**:6263–6265.

135. Randall DW, Gelasco A, Caudle MT, Pecoraro VL, Britt RD. 1997. ESE-ENDOR and ESEEM characterization of water and methanol ligation to a dinuclear Mn(III)Mn(IV) complex. *J Am Chem Soc* **119**:4481–4491.

136. Zweygart W, Bittl R, Wieghardt K, Lubitz W. 1996. EPR and ^{55}Mn cw-ENDOR study of an antiferromagnetically coupled dinuclear manganese (MnIIIMnIV) complex. *Chem Phys Lett* **261**:272–276.

137. Dismukes GC, Sheats JE, Smegal JA. 1987. Mn^{2+}/Mn^{3+} and Mn^{3+}/Mn^{4+} mixed valence binuclear manganese complexes of biological interest. *J Am Chem Soc* **109**:7202–7203.

138. Kessissoglou DP. 1999. Homo- and mixed-valence EPR-active trinuclear manganese complexes. *Coord Chem Rev* **185–186**:837–858.

139. Tangoulis V, Malamatari DA, Spyroulias GA, Raptopoulou CP, Terzis A, Kessissoglou DP. 2000. An EPR and ^{1}H NMR active mixed-valence manganese (III/II/III) trinuclear compound. *Inorg Chem* **39**:2621–2630.

140. Sarneski JE, Thorp HH, Brudvig GW, Crabtree RH, Schulte GK. 1990. Assembly of high-valent oxomanganese clusters in aqueous solution: redox equilibrium of water-stable Mn$_3$O$_4{}^{4+}$ and Mn$_2$O$_2{}^{3+}$ complexes. *J Am Chem Soc* **112**:7255–7260.

141. Auger N, Girerd JJ, Corbella M, Gleizes A, Zimmermann JL. 1990. Synthesis, structure, and magnetic properties of the stable triangular [Mn(IV)$_3$O$_4$]$^{4+}$ core. *J Am Chem Soc* **112**:448–450.

142. Bashkin JS, Chang HR, Streib WE, Huffman JC, Hendrickson DN, Christou G. 1987. Modelling the photosynthetic water oxidation center: preparation and physical properties of a tetranuclear oxide bridged manganese complex corresponding to the native S2 state. *J Am Chem Soc* **109**:6502–6504.

143. Hendrickson DN, Christou G, Schmitt EA, Libby E, Bashkin JS, Wang S, Tsai HL, Vincent JB, Boyd PDW. 1992. Photosynthetic water oxidation center: spin frustration in distorted cubane MnIVMnIII$_3$ model complexes. *J Am Chem Soc* **114**:2455–2471.

144. Bashkin JS, Schake AR, Vincent JB, Chang HR, Li Q, Huffman JC, Christou G, Hendrickson DN. 1988. Mixed valence manganese(II, III) and -(III, IV) dinuclear complexes: preparation, structure, magnetochemistry, and ESR spectra of

Mn$_2$(biphen)$_2$(biphenH)(bpy)$_2$ and Mn$_2$O$_2$Cl$_2$(OAc)(bpy)$_2$ (biphenH$_2$ = 2,2'-biphenol, bpy = 2,2'-bipyridine). *J Chem Soc, Chem Commun* **11**:700–702.

145. Frapart Y-M, Boussac A, Albach R, Anxolabehere-Mallart E, Delroisse M, Verlhac J-B, Blondin G, Girerd J-J, Guilhem J, Cesario M, Rutherford W, Lexa D. 1996. Chemical modeling of the oxygen-evolving center in plants: synthesis, structure, and electronic and redox properties of a new mixed valence Mn-oxo cluster: [Mn$_2$III,IVO$_2$(bisimMe$_2$en)$_2$]$^{3+}$ (bisimMe$_2$en = N,N'-dimethyl-N,N'-bis(imidazol-4-yl-methyl)ethane-1,2-diamine). EPR detection of an imidazole radical induced by uv irradiation at low temperature. *J Am Chem Soc* **118**:2669–2678.

146. Larson EJ, Pecoraro VL. 1992. Introduction to manganese enzymes. *Manganese Redox Enzymes*, pp. 1–28.

147. Policar C, Knuepling M, Frapart Y-M, Un S. 1998. Multifrequency high-field EPR study of binuclear Mn(III)Mn(IV) complexes. *J Phys Chem B* **102**:10391–10398.

148. Tan XL, Gultneh Y, Sarneski JE, Scholes CP. 1991. EPR-ENDOR of the electronic structure from two nitrogenously ligated bis(μ-oxo)-manganese(III)-manganese(IV) model complexes spectroscopically relevant to the multi-manganese center of photosystem II. *J Am Chem Soc* **113**:7853–7858.

149. Zheng M, Khangulov SV, Dismukes GC, Barynin VV. 1994. Electronic structure of dimanganese(II,III) and dimanganese(III,IV) complexes and dimanganese catalase enzyme: a general EPR spectral simulation approach. *Inorg Chem* **33**:382–387.

150. Randall DW, Sturgeon BE, Ball JA, Lorigan GA, Chan MK, Klein MP, Armstrong WH, Britt RD. 1995. ^{55}Mn ESE-ENDOR of a mixed valence Mn(III)Mn(IV) complex: comparison with the Mn cluster of the photosynthetic oxygen-evolving complex. *J Am Chem Soc* **117**:11780–11789.

151. Sinnecker S, Neese F, Lubitz W. 2005. Dimanganese catalase-spectroscopic parameters from broken-symmetry density functional theory of the superoxidized MnIII/MnIV state. *J Biol Inorg Chem* **10**:231–238.

152. Teutloff C, Schaefer K-O, Sinnecker S, Barynin V, Bittl R, Wieghardt K, Lendzian F, Lubitz W. 2005. High-field EPR investigations of MnIIIMnIV and MnIIMnIII states of dimanganese catalase and related model systems. *Magn Reson Chem* **43**:S51–S64.

153. Baldwin MJ, Gelasco A, Pecoraro VL. 1993. The effect of protonation on [Mn(IV)(μ2-O)]^2 complexes. *Photosynth Res* **38**:303–308.

154. Baldwin MJ, Stemmler TL, Riggs-Gelasco PJ, Kirk ML, Penner-Hahn JE, Pecoraro VL. 1994. structural and magnetic effects of successive protonations of oxo bridges in high-valent manganese dimers. *J Am Chem Soc* **116**:11349–11356.

155. McGrady JE, Stranger R. 1997. Redox-induced changes in the geometry and electronic structure of di-μ-oxo-bridged manganese dimers. *J Am Chem Soc* **119**:8512–8522.

156. Barone V, Bencini A, Gatteschi D, Totti F. 2002. DFT description of the magnetic properties and electron localization in dinuclear di-μ-oxo-bridged manganese complexes. *Chem Eur J* **8**:5019–5027.

157. Delfs CD, Stranger R. 2000. Magnetic exchange in [Mn$_2$(μ-O)$_3$(tmtacn)$_2$]$^{2+}$: metal–metal bonding or superexchange? *Inorg Chem* **39**:491–495.

158. Delfs CD, Stranger R. 2001. Oxidation state dependence of the geometry, electronic structure, and magnetic coupling in mixed oxo- and carboxylato-bridged manganese dimers. *Inorg Chem* **40**:3061–3076.

159. Howard T, Telser J, DeRose VJ. 2000. An electron paramagnetic resonance study of Mn$_2$(H$_2$O)(OAc)$_4$(tmeda)$_2$ (tmeda = N,N,N',N'-tetramethylethylenediamine): a model for dinuclear manganese enzyme active sites. *Inorg Chem* **39**:3379–3385.

160. Schake AR, Schmitt EA, Conti AJ, Streib WE, Huffman JC, Hendrickson DN, Christou G. 1991. Preparation and properties of mononuclear and ferromagnetically coupled dinuclear manganese complexes with 2,2'-biphenoxide. *Inorg Chem* **30**:3192–3199.

161. Sinnecker S, Rajendran A, Klamt A, Diedenhofen M, Neese F. 2006. Calculation of solvent shifts on electronic *g*-tensors with the conductor-like screening model (COSMO) and its self-consistent generalization to real solvents (Direct COSMO-RS). *J Phys Chem A* **110**:2235–2245.

162. Sinnecker S, Neese F, Noodleman L, Lubitz W. 2004. Calculating the electron paramagnetic resonance parameters of exchange coupled transition metal complexes using broken symmetry density functional theory: application to a MnIII/MnIV model compound. *J Am Chem Soc* **126**:2613–2622.

163. Campbell KA, Lashley MR, Wyatt JK, Nantz MH, Britt RD. 2001. Dual-mode EPR study of Mn(III) salen and the Mn(III) salen-catalyzed epoxidation of cis-beta-methylstyrene. *J Am Chem Soc* **123**:5710–5719.

164. Krivokapic I, Noble C, Klitgaard S, Tregenna-Piggott P, Weihe H, Barra A-L. 2005. Anisotropic hyperfine interaction in the manganese(III) hexaaqua ion. *Angew Chem, Int Ed* **44**:3613–3616.

165. Krzystek J, Yeagle GJ, Park J-H, Britt RD, Meisel MW, Brunel L-C, Telser J. 2003. High-frequency and -field EPR spectroscopy of tris(2,4-pentanedionato)manganese(III): investigation of solid-state versus solution Jahn-Teller effects. *Inorg Chem* **42**:4610–4618.

166. Weyhermuller T, Paine TK, Bothe E, Bill E, Chaudhuri P. 2002. Complexes of an aminebis(phenolate) [O,N,O] donor ligand and EPR studies of isoelectronic, isostructural Cr(III) and Mn(IV) complexes. *Inorg Chim Acta* **337**:344–356.

167. Brunold TC, Gamelin DR, Stemmler TL, Mandal SK, Armstrong WH, Penner-Hahn JE, Solomon EI. 1998. Spectroscopic studies of oxidized manganese catalase and μ-oxo-bridged dimanganese(III) model complexes: electronic structure of the active site and its relation to catalysis. *J Am Chem Soc* **120**:8724–8738.

168. Gamelin DR, Kirk ML, Stemmler TL, Pal S, Armstrong WH, Penner-Hahn JE, Solomon EI. 1994. electronic structure and spectroscopy of manganese catalase and di-μ-oxo [MnIIIMnIV] model complexes. *J Am Chem Soc* **116**:2392–2399.

169. Ivancich A, Barynin VV, Zimmermann J-L. 1995. Pulsed EPR studies of the binuclear Mn(III)Mn(IV) center in catalase from *Thermus thermophilus*. *Biochemistry* **34**:6628–6639.

170. Stich TA. Unpublished results.

171. Libby E, McCusker JK, Schmitt EA, Folting K, Hendrickson DN, Christou G. 1991. Preparation and properties of models for the photosynthetic water oxidation center: spin frustration in the manganese [Mn$_4$O$_2$(O$_2$CR)$_7$(pic)$_2$]-anion. *Inorg Chem* **30**:3486–3495.

172. Gomez-Garcia CJ, Coronado E, Georges R, Pourroy G. 1992. Role of the topology on the magnetic properties of mixed-valence trinuclear manganese clusters. *Physica B* **182**:18–26.

173. Khangulov SV, Goldfeld MG, Kirpichnikova NP, Dobryakov SN, Ilyasova VB. 1989. ESR of an oxidized manganese binuclear cluster: a possible model of the highest oxidized state of the oxygen-evolving complex of photosynthesis. *J Chem Soc, Chem Commun* ,1755–1756.

174. Pal S, Armstrong WH. 1992. Products from reactions of manganese oxo complex [Mn$_2$O$_2$(O$_2$CCH$_3$)(tpen)]$^{2+}$ in acidic and neutral aqueous media: [Mn$_2$(μ-O)$_2$(μ-

$O_2CCH_3)(tpen)]^{3+}$ and $[\{Mn_3(\mu\text{-}O)_4(OH)(tpen)\}_2(\mu\text{-}tpen)]^{6+}$. *Inorg Chem* **31**:5417–5423.

175. Pal S, Chan MK, Armstrong WH. 1992. Ground spin state variability in manganese oxo aggregates: demonstration of an $S = 3/2$ ground state for $[Mn_3O_4(OH)(bpea)_3]$ $(ClO_4)_3$. *J Am Chem Soc* **114**:6398–6406.

176. Tangoulis V, Malamatari DA, Soulti K, Stergiou V, Raptopoulou CP, Terzis A, Kabanos TA, Kessissoglou DP. 1996. Manganese(II/II/II) and manganese(III/II/III) trinuclear compounds: structure and solid and solution behavior. *Inorg Chem* **35**:4974–4983.

177. Tanase T, Tamakoshi S, Doi M, Mikuriya M, Sakurai H, Yano S. 2000. Novel MnIIMnIIIMnII trinuclear complexes with carbohydrate bridges derived from seven-coordinate manganese(II) complexes with N-glycoside. *Inorg Chem* **39**:692–704.

178. Bhaduri S, Pink M, Christou G. 2002. Towards a synthetic model of the photosynthetic water oxidizing complex: $[Mn_3O_4(O_2CMe)_4(bpy)_2]$ containing the $[MnIV3(\mu\text{-}O)_4]^{4+}$ core. *Chem Commun*, pp. 2352–2353.

179. Ito M, Onaka S, Ebisu H, Arakawa M, Yamada Y, Yoshida T. 2003. Single crystal ESR study on $[Mn_3(O)(O_2CC6F5)_6(py)_3]\cdot CH_2Cl_2$. *Inorg Chim Acta* **353**:51–58.

180. Burdinski D, Bothe E, Wieghardt K. 2000. Synthesis and characterization of tris(bipyridyl)ruthenium(II)-modified mono-, di-, and trinuclear manganese complexes as electron-transfer models for Photosystem II. *Inorg Chem* **39**:105–116.

181. Burdinski D, Wieghardt K, Steenken S. 1999. Intramolecular electron transfer from Mn or ligand phenolate to photochemically generated ruiii in multinuclear Ru/Mn complexes: laser flash photolysis and EPR studies on Photosystem II models. *J Am Chem Soc* **121**:10781–10787.

182. Vincent JB, Christmas C, Huffman JC, Christou G, Chang HR, Hendrickson DN. 1987. Modeling the photosynthetic water oxidation center: synthesis, structure, and magnetic properties of $[Mn_4O_2(OAc)_7(bipy)_2](ClO_4)\cdot 3H_2O$ (bipy = 2,2'-bipyridine). *J Chem Soc, Chem Commun*, pp. 236–238.

183. Vincent JB, Christou G. 1987. A molecular double-pivot mechanism for water oxidation. *Inorg Chim Acta* **136**:L41–L43.

184. Vincent JB, Christmas C, Chang HR, Li Q, Boyd PDW, Huffman JC, Hendrickson DN, Christou G. 1989. Modeling the photosynthetic water oxidation center:preparation and properties of tetranuclear manganese complexes containing $[Mn_4O_2]^{6+}$, $^{7+}$, $^{8+}$ cores, and the crystal structures of $Mn_4O_2(O_2CMe)_6(bipy)_2$ and $[Mn_4O_2(O_2CMe)_7(bipy)_2](ClO_4)$. J Am Chem Soc 111: 2086–2097.

185. Hagen KS, Westmoreland TD, Scott MJ, Armstrong WH. 1989. Structural and electronic consequences of protonation in $\{Mn_4O_6\}^{4+}$ cores: pH dependent properties of oxo-bridged manganese complexes. *J Am Chem Soc* **111**:1907–1909.

186. Brudvig GW, Crabtree RH. 1986. Mechanism for photosynthetic oxygen evolution. *Proc Natl Acad Sci USA* **83**:4586–4588.

187. Chan MK, Armstrong WH. 1991. Support for a dimer of di-μ-oxo dimers model for the photosystem II manganese aggregate: synthesis and properties of $[(Mn_2O_2)_2(tphpn)_2](ClO_4)_4$. *J Am Chem Soc* **113**:5055–5057.

188. Dexheimer SL, Klein MP. 1992. Detection of a paramagnetic intermediate in the S1 state of the photosynthetic oxygen-evolving complex. *J Am Chem Soc* **114**:2821–2826.

189. Mukhopadhyay S, Mok HJ, Staples RJ, Armstrong WH. 2004. Shape-shifting tetranuclear oxo-bridged manganese cluster: relevance to Photosystem II water oxidase active site. *J Am Chem Soc* **126**:9202–9204.

190. Ruettinger WF, Campana C, Dismukes GC. 1997. Synthesis and characterization of Mn_4O_4L6 complexes with cubane-like core structure: a new class of models of the active site of the photosynthetic water oxidase. *J Am Chem Soc* **119**:6670–6671.

191. Ruettinger WF, Ho DM, Dismukes GC. 1999. Protonation and dehydration reactions of the Mn_4O_4L6 cubane and synthesis and crystal structure of the oxidized cubane $[Mn_4O_4L6]^+$: a model for the photosynthetic water oxidizing complex. *Inorg Chem* **38**:1036–1037.

192. Ruettinger W, Yagi M, Wolf K, Bernasek S, Dismukes GC. 2000. O_2 evolution from the manganese-oxo cubane core $Mn_4O_4^{6+}$: a molecular mimic of the photosynthetic water oxidation enzyme? *J Am Chem Soc* **122**:10353–10357.

193. Ruettinger WF, Dismukes GC. 2000. Conversion of core oxos to water molecules by $4e^-/4H^+$ reductive dehydration of the $Mn_4O_2^{6+}$ core in the manganese-oxo cubane complex $Mn_4O_4(Ph_2PO_2)_6$: a partial model for photosynthetic water binding and activation. *Inorg Chem* **39**:1021–1027.

194. Maneiro M, Ruettinger WF, Bourles E, McLendon GL, Dismukes GC. 2003. Kinetics of proton-coupled electron-transfer reactions to the manganese-oxo "cubane" complexes containing the $Mn4O_6^{+4}$ and $Mn_4O_7^{+4}$ core types. *Proc Natl Acad Sci USA* **100**:3707–3712.

195. Yagi M, Wolf KV, Baesjou PJ, Bernasek SL, Dismukes GC. 2001. Selective photoproduction of O_2 from the Mn_4O_4 cubane core: a structural and functional model for the photosynthetic water-oxidizing complex. *Angew Chem, Int Ed* **40**:2925–2928.

196. Wu J-Z, De Angelis F, Carrell TG, Yap GPA, Sheats J, Car R, Dismukes GC. 2006. Tuning the photoinduced O_2-evolving reactivity of $Mn_4O_4^{7+}$, $Mn_4O_4^{6+}$, and $Mn_4O_3(OH)^{6+}$ manganese–oxo cubane complexes. *Inorg Chem* **45**:189–195.

197. Wu J-Z, Sellitto E, Yap GPA, Sheats J, Dismukes GC. 2004. Trapping an elusive intermediate in manganese-oxo cubane chemistry. *Inorg Chem* **43**:5795–5797.

198. Wang S, Tsai H-L, Hagen KS, Hendrickson DN, Christou G. 1994. New structural type in manganese carboxylate chemistry via coupled oxidation/oxide incorporation: potential insights into photosynthetic water oxidation. *J Am Chem Soc* **116**:8376–8377.

199. Kusunoki M. 1992. A new paramagnetic hyperfine structure effect in manganese tetramers: the origin of "multiline" EPR signals from an S2 state of a photosynthetic water-splitting enzyme. *Chem Phys Lett* **197**:108–116.

200. Zheng M, Dismukes GC. 1996. Orbital configuration of the valence electrons, ligand field symmetry, and manganese oxidation states of the photosynthetic water oxidizing complex: analysis of the S2 state multiline EPR signals. *Inorg Chem* **35**:3307–3319.

201. Mishra A, Wernsdorfer W, Abboud KA, Christou G. 2005. The first high oxidation state manganese-calcium cluster: relevance to the water oxidizing complex of photosynthesis. *Chem Commun* **1**:54–56.

202. Dube CE, Sessoli R, Hendrich MP, Gatteschi D, Armstrong WH. 1999. A spin topological model for the g = 4.1 S2 State Photosystem II water oxidase manganese aggregate. *J Am Chem Soc* **121**:3537–3538.

203. Wang S, Tsai H-L, Libby E, Folting K, Streib WE, Hendrickson DN, Christou G. 1996. Modeling the photosynthetic water oxidation center: chloride/bromide incorporation and reversible redox processes in the complexes $Mn_4O_3X(OAc)_3(dbm)_3$ (X = Cl, Br), and $(pyH)_3[Mn_4O_3Cl_7(OAc)_3]$. *Inorg Chem* **35**:7578–7589.

204. Sproviero EM, Gascón JA, McEvoy JP, Brudvig GW, Batista VS. 2006. Characterization of synthetic oxomanganese complexes and the inorganic core of the O_2-evolving

complex in photosystem II: evaluation of the DFT/B3LYP level of theory. *J Inorg Biochem* **100**:786–800.

205. Blomberg MRA, Siegbahn PEM. 1997. A comparative study of high-spin manganese and iron complexes. *Theor Chem Acc* **97**:72–80.

206. Lundberg M, Siegbahn PEM. 2005. Agreement between experiment and hybrid DFT calculations for O–H bond dissociation enthalpies in manganese complexes. *J Comput Chem* **26**:661–667.

207. Blomberg MRA, Siegbahn PEM, Styring S, Babcock GT, Aakermark B, Korall P. 1997. A quantum chemical study of hydrogen abstraction from manganese-coordinated water by a tyrosyl radical: a model for water oxidation in photosystem II. *J Am Chem Soc* **119**:8285–8292.

208. Siegbahn PEM, Crabtree RH. 1999. Manganese oxyl radical intermediates and O–O bond formation in photosynthetic oxygen evolution and a proposed role for the calcium cofactor in Photosystem II. *J Am Chem Soc* **121**:117–127.

209. Siegbahn PE. 2000. Theoretical models for the oxygen radical mechanism of water oxidation and of the water oxidizing complex of Photosystem II. *Inorg Chem* **39**: 2923–2935.

210. Lundberg M, Siegbahn PEM. 2005. Minimum energy spin crossings for an O–O bond formation reaction. *Chem Phys Lett* **401**:347–351.

211. Lundberg M, Blomberg Margareta RA, Siegbahn Per EM. 2004. Oxyl radical required for O–O bond formation in synthetic Mn-catalyst. *Inorg Chem* **43**:264–274.

212. Lundberg M, Siegbahn PEM. 2004. Theoretical investigations of structure and mechanism of the oxygen-evolving complex in PSII. *Phys Chem Chem Phys* **6**:4772–4780.

213. Haumann M, Liebisch P, Mueller C, Barra M, Grabolle M, Dau H. 2005. Photosynthetic O_2 formation tracked by time-resolved X-ray experiments. *Science* **310**:1019–1021.

214. Haumann M, Mueller C, Liebisch P, Iuzzolino L, Dittmer J, Grabolle M, Neisius T, Meyer-Klaucke W, Dau H. 2005. Structural and oxidation state changes of the Photosystem II manganese complex in four transitions of the water oxidation cycle ($S_0 \rightarrow S_1$, $S_1 \rightarrow S_2$, $S_2 \rightarrow S_3$, and $S_{3,4} \rightarrow S_0$) characterized by X-ray absorption spectroscopy at 20 k and room temperature. *Biochemistry* **44**:1894–1908.

215. Siegbahn PEM, Lundberg M. 2005. The mechanism for dioxygen formation in PSII studied by quantum chemical methods. *Photochem Photobiol Sci* **4**:1035–1043.

216. Siegbahn PEM, Lundberg M. 2006. Hydroxide instead of bicarbonate in the structure of the oxygen evolving complex. *J Inorg Biochem* **100**:1035–1040.

217. McGrady JE, Stranger R. 1999. Redox-induced formation and cleavage of O–O s and p bonds in a peroxo-bridged manganese dimer: a density functional study. *Inorg Chem* **38**:550–558.

218. Aullon G, Ruiz E, Alvarez S. 2002. Theoretical clues to the mechanism of dioxygen formation at the oxygen-evolving complex of photosystem II. *Chem Eur J* **8**:2508–2515.

219. Humbel S, Sieber S, Morokuma K. 1996. The IMOMO (integrated MO MO) method: integration of different levels of molecular orbital approximations for geometry optimization of large systems: test for n-butane conformation and SN2 reaction: RCl + Cl. *J Chem Phys* **105**:1959–1967.

220. Svensson M, Humbel S, Froese RDJ, Matsubara T, Sieber S, Morokuma K. 1996. ONIOM: a multi-layered integrated MO + MM method for geometry optimizations and single point energy predictions: a test for Diels-Alder reactions and Pt(P(τ-Bu)₃)₂ + H_2 oxidative addition. *J Phys Chem* **100**:19357–19363.

221. Sproviero EM, Gascón JA, McEvoy JP, Brudvig GW, Batista VS. 2008. QM/MM models of the O_2-evolving complex of Photosystem II. *Phil Trans R Soc Lond B Biol Sci* **1494**:1149–1156.

222. Barber J, Ferreira K, Maghlaoui K, Iwata S. 2004. Structural model of the oxygen-evolving centre of photosystem II with mechanistic implications. *Phys Chem Chem Phys* **6**:4737–4742.

223. Haumann M, Junge W. 1999. Photosynthetic water oxidation: a simplex-scheme of its partial reactions. *Biochim Biophys Acta* **1411**:86–91.

224. Ishikita H, Saenger W, Loll B, Biesiadka J, Knapp E-W. 2006. Energetics of a possible proton exit pathway for water oxidation in photosystem II. *Biochemistry* **45**:2063–2071.

Manganese Metalloproteins

Sarah J. Smith,[1] Kieran S. Hadler,[1] Gerhard Schenk,[1]
Graeme R. Hanson,[2] and Nataša Mitić[1]

[1]*School of Chemistry and Molecular Biosciences and*
[2]*Center for Magnetic Resonance, The University*
of Queensland, Brisbane, Australia

While manganese has been successfully exploited as a spectroscopic probe of EPR silent centers (Zn, Ca, Mg) in metalloenzymes, it was only during the last decade that manganese-containing metalloenzymes were investigated in great detail. Indeed, in some biological systems it remains unclear whether iron and/or manganese is required for catalytic competency. Binuclear manganese enzymes are a small group of enzymes that catalyze a variety of chemical reactions and are involved in numerous metabolic functions. In this review the structural and biochemical properties of these enzymes are described. The contributions of electron paramagnetic resonance-related techniques to our understanding of the structure and reactivity of binuclear manganese enzymes are discussed and, where appropriate, supported by data obtained from complementary spectroscopic methods. This article is intended as a guide to illustrate the usefulness of electron paramagnetic resonance-related techniques in the study of these enzymes.

1. INTRODUCTION

In a recent article in this book series we reviewed biochemical, structural, and spectroscopic (in particular electron paramagnetic resonance (EPR) related) properties of the large group of binuclear non-heme iron enzymes [1]. Several of these enzymes are also functional in the presence of manganese, for example, ribonucleotide reductase [2,3] and a purple acid phosphatase isolated from sweet potato, which contains a catalytically relevant heterobinuclear μ-oxo bridged

Address all correspondence to Nataša Mitić, School of Chemistry and Molecular Biosciences, The University of Queensland, St. Lucia 4072, Australia, +61 7-3365 4040, +61 7-3365 4273 (fax), <n.mitic@uq.edu.au>.

Table 1. Selected Binuclear Manganese Enzymes and Their Catalytic Function
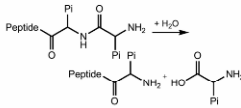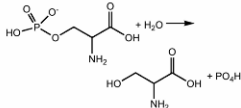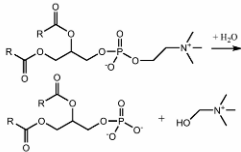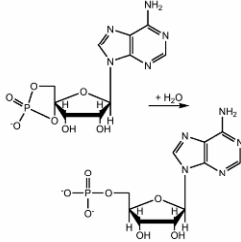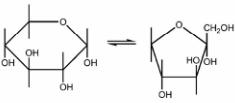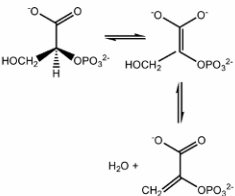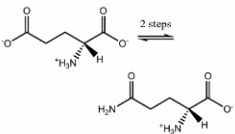
Enzyme	Reaction class	Catalytic reaction	Metabolic roles
Catalase	Oxidoreductase	$2H_2O_2 \longrightarrow 2H_2O + O_2$	Disproportionation of hydrogen peroxide
Ribonucleotide reductase (*Chlamydia trachomatis*)[*]	Oxidoreductase	$Mn^{II}Fe^{II} \xrightarrow{+ O_2} Mn^{IV}Fe^{IV} \xrightarrow{e^-} Mn^{IV}Fe^{III}$	Biosynthesis of DNA precursors
Arginase	Hydrolase	L-arginine $\rightarrow$ L-ornithine + urea	regulation of arginine/ornithine concentration; sexual function
Phosphotriesterase	Hydrolase	$PO_4R_3 + H_2O \longrightarrow PO_4R_2^- + ROH$	breakdown of phosphotriesters found in insecticides/herbicides/nerve gases
Aminopeptidase	Hydrolase		processing peptide chains
Exonucleases	Hydrolase	hydrolysis of nucleotides from nucleic acid molecules	DNA replication and repair
SoxB	Hydrolase	$SoxY\text{-}S\text{-}SO_3^- + H_2O \longrightarrow SoxY\text{-}S^- + H_2SO_4^-$	sulfur oxidation
Bacteriophage λ protein phosphatase	Hydrolase		signal transduction
Phospholipase D[*]	Hydrolase		signal transduction
Rv0805[*]	Hydrolase		signal transduction

Table 1, cont'd

Sweet potato purple acid phosphatase*	Hydrolase	$PO_4HR^- + H_2O \longrightarrow PO_4H_2^- + ROH$	mobilization of organic phosphate esters
Xylose isomerase	Isomerase		xylose metabolism in microorganisms
Enolase	Isomerase		ATP synthesis
Manganese transport regulator	Metalloregulator	Mn^{2+} binding	manganese homeostasis
Glutamine synthetase	Ligase		regulation of metabolism of cellular nitrogen
Aminoacyl-tRNA synthetase	Ligase	amino acid + tRNA + ATP $\longrightarrow$ aminoacyl-tRNA + AMP + PPi	first step of protein synthesis

*Heterobinuclear iron-manganese active site

Fe(III)Mn(II) center, the first example of such a center in biology [1,4]. In contrast, some enzymes have evolved a specific requirement for manganese, including catalases and arginase [5,6]. Here we discuss selectively advances in the study of the structure/function relationship of binuclear manganese-dependent enzymes. Similar to our review on binuclear non-heme systems [1], the biochemical and structural properties of the selected enzyme systems are described, followed by a summary of spectroscopic achievements, focusing on the contributions from EPR-related techniques. Where possible, a brief description of mechanistic features follows.

Reactions catalyzed by binuclear manganese-dependent enzymes include peroxidations and numerous hydrolytic reactions. Physiological functions range from signal transduction and protein biosynthesis to reactive oxygen species (ROS) metabolism and sulfur oxidations. Table 1 provides a list of representative enzyme systems, together with the reactions they catalyze, and their proposed biological functions.

It is not our aim to cover binuclear manganese enzymes comprehensively, but instead provide illustrative examples covering the breadth of the different classes

and chemical reactions within this group of enzymes. It is envisioned that the article may serve as a reference to gain easy access to the topic for the interested researcher. Furthermore, it is anticipated that the expert may find the discussion stimulating for his/her research aims.

2. MANGANESE CATALASES

2.1. Biochemical and Structural Characterization

Catalases (E.C. 1.11.1.6) catalyze the disproportionation of hydrogen peroxide, a toxic oxygen metabolite, into molecular oxygen and water before it further reacts to generate deleterious hydroxyl radicals [6]:

$$2H_2O_2 \rightarrow 2H_2O + O_2. \tag{1}$$

Although this reaction is spontaneous, significant kinetic barriers exist for the direct uncatalyzed reaction; catalases function by uncoupling the two half reactions and store electrons and protons between the two redox steps [7]:

$$H_2O_2 \rightleftharpoons O_2 + 2e^- + 2H^+,$$

$$H_2O_2 + 2e^- + 2H^+ \rightleftharpoons 2H_2O. \tag{2}$$

Although most catalases are haem enzymes, a class of manganese-containing catalases (MnCATs) have been identified in several bacterial organisms (*Lactobacillus plantarum* [7], *Thermus thermophilus* [8], *Salmonella enteric* [9], *Thermus* sp. YS 8-13 [10], and *Thermoleophilum album* NM [11]) and a hyperthermophilic archeon (*Pyrobaculum calidifontis* VA1 [12]). Both classes of catalases dismute hydrogen peroxide very rapidly, approaching the rate of a diffusion-limited reaction [13].

As isolated, the binuclear active center of MnCAT from *L. plantarum* exists as a mixture of oxidation states, including Mn(II)$_2$, Mn(III)$_2$ and Mn(III)–Mn(IV). In the enzyme isolated from *T. thermophilus* the Mn(II)Mn(III) species is also present.

Structural information for the MnCATs from *L. plantarum* and *T. thermophilus* has been obtained via high-resolution X-ray crystallography [14,15]. Both enzymes are homohexamers (molecular weight ~210 kDa) with two Mn ions located in a catalytic core within a four-helix bundle domain in each of the six identical subunits. The *L. plantarum* enzyme crystallized predominantly in the oxidized Mn(III)$_2$ form. The manganese ions in the active site are separated by 3.03 Å and bridged by a μ-1,3-carboxylato group from a glutamate and two structurally distinct oxygen atoms (Fig. 1). One oxygen (*trans* to the coordinated histidines, Fig. 1) is protonated (hydroxo/aqua), while the other is an unprotonated oxo anion [15]. The coordination environments of both manganese ions are completed by one histidine and one glutamate residue. In one of the manganese binding sites this glutamate is a monodentate ligand in both the *L. plantarum* and *T. thermophilus* enzymes. This glutamate (Glu35 in *L. plantarum* MnCAT; Fig. 1) forms a hydrogen bond with the μ-hydroxo bridge. In the other manganese binding site, the relevant
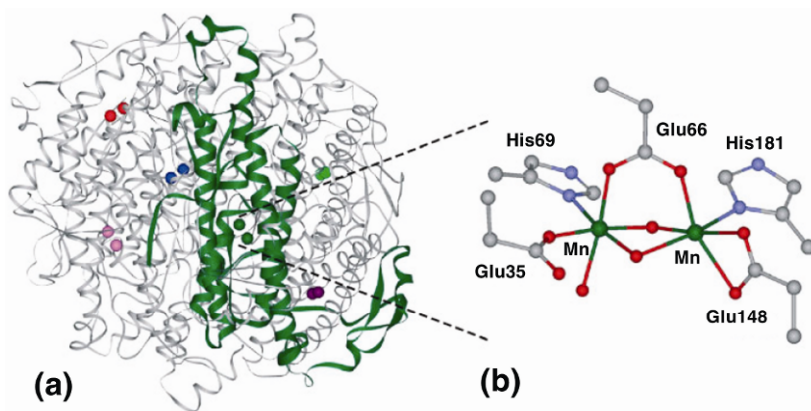
Figure 1. (a) Structure of the hexameric MnCAT protein from *L. plantarum*, one subunit highlighted in green (dark gray in grayscale version). (b) Active site of catalase (oxidized form). Reprinted with permission from [31]. Copyright © 2005, John Wiley & Sons. Please visit http://www.springer.com/978-1-4419-1138-4 to view a high-resolution full-color version of this illustration.

glutamate residue (Glu148 in *L. plantarum* MnCAT; Fig. 1) coordinates mono- and bidentately in the *T. thermophilus* and *L. plantarum* enzymes, respectively. Each manganese ion has a distorted octahedral geometry, and the Mn_2O_2 core is nonplanar, displaying a "butterfly" structure [15]. The active site is connected via a network of hydrogen bonds to the outer coordination sphere, creating a specialized environment for redox catalysis, by permitting the protein to respond to redox changes within the core with a rapid electrostatic polarization over the hydrogen bonding network [15]. The importance of the outer sphere for the catalytic efficiency of MnCATs is demonstrated by a mutagenesis study whereby a highly conserved outer sphere tyrosine residue in *L. plantarum* MnCAT has been replaced by a phenylalanine resulting in greatly reduced activity [16]. The mutation does not affect the overall fold of the active site, but it perturbs the hydrogen bond network, resulting in a change in coordination of one of the oxygen ligands from a bridging, bidentate to a non-bridging, monodentate position [16].

 T. thermophilus MnCAT has been crystallized in both the oxidized and reduced forms. While the two forms are structurally similar, one of the bridging oxygen ligands in the reduced enzyme appears to toggle between bridging and terminal coordination [17]. Interestingly, the active site access channel is broader in the *T. thermophilus* enzyme than in that obtained from *L. plantarum*, which may be responsible for the more rapid autoxidation of the *T. thermophilus* enzyme [18].

 MnCATs are inhibited by various anions such as azide, cyanide, chloride, and fluoride [19]. Halide inhibition results in trapping of the enzyme in the reduced state and shows significant pH dependence, with stronger inhibition at lower pHs [20]. In contrast, the enzymatic activity of the *T. thermophilus* and *L. plantarum* enzymes is independent of pH between pH 7 and 10 [6,19]. The crystal structure of

L. plantarum MnCAT has also been solved as a complex with azide and chloride; in the former complex azide displaces the terminal water ligand in the oxidized enzyme (Fig. 1) [15], while in the latter chloride binds in a bridging mode and the enzyme remains in the reduced oxidation state [14].

2.2. Spectroscopic Characterization

Much of the information about the electronic structure of MnCATs gained from EPR-related techniques has relied on comparison with corresponding data measured for appropriate model complexes. Here we will focus only on the protein systems, but the reader interested in biomimetics is guided toward [21,22] and the references therein. Table 2 summarizes the EPR data reported for some of the studied forms of MnCAT. Although only the Mn(II)–Mn(II) and Mn(III)–Mn(III) states are catalytically relevant [20], the intermediate Mn(II)–Mn(III), and superoxidized Mn(III)–(IV) states can be readily accessed chemically.

Table 2. g- and Hyperfine Coupling Values Used in Simulations of the $S = \frac{1}{2}$ Ground States of Mn(II)Mn(III) and Mn(III)Mn(IV) Catalase

Enzyme	g_x	g_y	g_z	$A_{xII/IV}$	$A_{yII/IV}$	$A_{zII/IV}$	A_{xIII}	A_{yIII}	A_{zIII}
Mn(II)Mn(III)									
T. thermophilus	1.958	1.965	2.025	–529	–502	–730	222	210	236
Mn(II)Mn(III)									
T. thermophilus	1.935	1.995	2.016	–523	–514	–722	217	218	217
Mn(III)Mn(IV)									
L. plantarum	2.008	2.008	1.990	228	228	250	–425	–425	–312
Mn(III)Mn(IV)									
T. thermophilus	2.014	2.014	2.000	235	224	252	–410	–425	–315
Mn(III)Mn(IV)									
T. thermophilus	2.0048	2.0040	1.9876	224	233	253	–427	–412	–298

$A_{II/IV}$ (MHz) refers to the hyperfine coupling of the divalent or tetravalent manganese; A_{III} (MHz) refers to the hyperfine coupling of the trivalent center.

2.2.1. Mn(II)Mn(II)

The EPR spectra for the Mn(II)$_2$ form of MnCAT in the absence of added anions are extremely broad (*T. thermophilus*) [23] and may require very low temperatures for detection (*L. plantarum*) [24]. Although integral spin systems are typically not observable in perpendicular mode detection, Mn(II)$_2$ species are an exception. In the presence of added anions and/or under optimized conditions, spectra attributed to the triplet ($S_T = 1$) and quintet ($S_T = 2$) excited states are observed in both perpendicular ($B_1 \perp B_0$) and parallel ($B_1 \parallel B_0$) polarizations [24,25]. Spectra arising

from both spin states are complex, and only recently a quantitative method for the analysis of spectra of this type has been reported [26].

Deconvolution of the variable temperature EPR spectra has enabled the features arising from each spin state to be determined, and fitting the signal intensities to the appropriate Boltzmann expressions, the exchange coupling constant ($H = -2J$ $S_1 \cdot S_2$) can be exctracted. (N.B. The spin Hamiltonian $H = -2J$ $S_1 \cdot S_2$ is used throughout this text unless otherwise specified.) Applying this technique to the *L. plantarum* MnCAT yields $J = -20$ cm^{-1} and -5.25 cm^{-1} for the native and fluoride-bound enzyme respectively, while the phosphate adduct of *T. thermophilus* MnCAT yields an a exchange constant of $J = -5.6$ cm^{-1} [25]. These J values are typical of Mn(II) dimers and slightly larger than some of the values determined via magnetic susceptibility studies [27,28]. By comparison with model complexes, these coupling values suggest a (μ-OH)(μ-carboxylato) bridging mode in the reduced enzyme. The relatively large change to J upon fluoride binding suggests that the fluoride may bind in a bridging mode, as has been observed for chloride crystallographically [17,24]. Magnetization studies suggested even smaller coupling constants, indicative of a μ-aqua bridge [27].

Additionally, the metal–metal distance has been determined from the EPR parameters. The zero field splitting of the $S = 2$ state was used to determine a value of ~3.6 Å for the phosphate adduct of *T. thermophilus* MnCAT. From the dipolar coupling of the fluoride adduct of *L. plantarum* catalase a metal–metal distance of 3.4 Å was calculated, in reasonable agreement with the values determined from extended X-ray absorption fine structure (EXAFS) [3] and crystallography [17].

2.2.2. Mn(III)Mn(III)

The wild-type enzyme is characterized by an absorption band at ~500 nm [18], but lacks any significant EPR resonances, due to strong antiferromagnetic coupling mediated by the two bridges (μ-oxo and μ-hydroxo) ($J \sim -100$ cm^{-1}) [18,29]. As previously mentioned, however, the mutation of an outer sphere tyrosine in *L. plantarum* results in the cleavage of a solvent bridge, and the resulting Mn(III)$_2$ species has been investigated spectroscopically. Loss of the solvent bridge not only dramatically decreases catalytic activity, but also alters the electronic structure of the binuclear manganese core. EPR of the enzyme in parallel and perpendicular polarizations enables differentiation of Mn(II) impurities and the even-electron transitions. Comparison of the two polarizations indicates two resonances arising from an even-electron system (mononuclear Mn(II) impurities are also apparent). An intense, low-field resonance ($g_{eff} = 20$; consistent with a transition between sublevels of a non-Kramers ground state with $\delta = 0.3$ cm^{-1} (X-band microwave energy), which in parallel polarization shows a hyperfine splitting ($A/g\beta$) of 3.7 mT (approximately half the value expected for an Mn(III) center) is consistent with a binuclear coupled site. The feature is strongly temperature dependent, implying that other states are thermally accessible at low temperatures (10–25 K). Coupled with the observation of intense low-temperature magnetic circular dichroism (MCD) spectra, the EPR spectra indicate that the manganese ions are ferromag-

netically coupled in the strong exchange regime ($J > D$), giving rise to an $S_T = 4$ ground state. A sextet resonance near $g_{eff} = 6$ with a hyperfine coupling of 8.5 mT indicates an Mn(III) monomeric impurity. At high pH, the mutant enzyme has only weak low-field resonances in both parallel and perpendicular polarizations. This, and the absence of substantial MCD intensity, supports the restoration of the second bridge at higher pH, consistent with the return of catalytic competence, and strong antiferromagentic coupling between the metal ions [16].

Additionally, in *L. plantarum*, but not *T. thermophilus*, addition of fluoride to the Mn(III)Mn(III) MnCAT (pH 9) results in a ferromagnetic ground state identified by EPR and MCD. This has been interpreted in terms of fluoride binding either in a terminal or bridging mode and perturbing the structure around the active site. That this is observed in only one of the enzymes indicates that there are electronic differences between the two enzymes, despite the structural similarities [18].

Magnetization studies have identified two forms of the Mn(III,III) enzyme in *T. thermophilus* — (μ-oxo)(μ-carboxylato) and bis(μ-oxo)(μ-carboxylato) — which are in a pH-dependent equilibrium [29].

2.2.3. Mn(II)Mn(III)

The Mn ions in the mixed valent Mn(II,III) state of MnCAT are antiferromagnetically coupled, with an $S_T = \frac{1}{2}$ ground state. The spectrum is shown in Figure 2 and is similar to that of the NO adduct of photosystem II [30]. The simulation parameters are reported in Table 2 [31,32]. The hyperfine coupling values diverge from the calculated spin projection factors, which can be attributed to the failure of the species to satisfy the strong exchange regime, with the zero field splitting contributing to the effective hyperfine coupling tensors (the magnitude of the exchange coupling constant is estimated to be <20 cm^{-1} [32]). Simulation of the zero field splitting associated with the Mn(III) results in a negative value, consistent with tetragonal elongation due to Jahn-Teller distortion, and the J/D ratio is determined as 0.47 [32]. Additionally, the spectrum can only be observed at low temperatures, which is consistent with rapid relaxation due to a small exchange coupling [31]. The small exchange coupling constant also makes EPR spectrosocopy of the enzyme difficult at high frequencies and fields. Specifically, at W-band, marked broadening of the high-field side of the spectrum is observed, largely due to g-strain, which is likely due to the axial Jahn-Teller distortion of the Mn(III) ion [31].

The model systems to which the Mn(III)Mn(II) forms have been compared typically contain one bridging water based ligand (typically hydroxo), and two carboxylate ligands ($|J| < 10$ cm^{-1}), resulting in small J values. Their EPR spectra are very similar to those reported for MnCAT, suggesting that the (μ-hydroxo)bis(μ-carboxylato) bridging mode may be relevant in the intermediate Mn(III)Mn(II) state, in contrast to the bis(μ-oxo)(μ-carboxylato) bridging mode observed crystallographically for the Mn(III)Mn(III) enzyme. By extrapolation, this would suggest the presence of a similar mode of bridging in the Mn(II,II) form
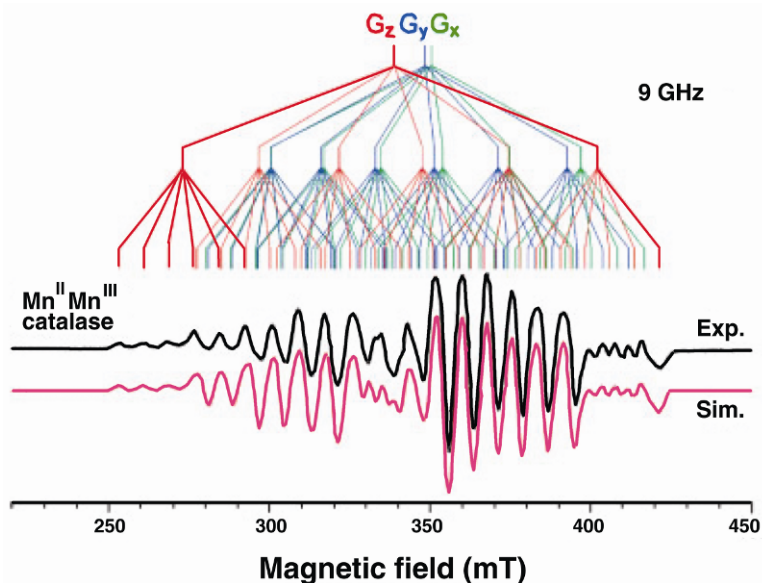
Figure 2. EPR spectrum of Mn(II)Mn(II) catalase and simulation, measured at X-band. Reprinted with permission from [31]. Copyright © 2005, John Wiley & Sons. Please visit http://www.springer.com/978-1-4419-1138-4 to view a high-resolution full-color version of this illustration.

of MnCAT, consistent with metal–metal distances found by EXAFS studies and crystallography [31], and the bridging mode predicted on the basis of the exchange coupling in the reduced enzyme (*vide supra*).

2.2.4. Mn(III)Mn(IV)

The Mn(III)Mn(IV) oxidation state of MnCAT from both *L. plantarum* and *T. thermophilus* has been investigated by EPR [31–37]. For all studied systems of this type, a 16-line spectrum is observed at X-band frequencies, as shown in Figure 3, indicative of a system in the strong exchange regime with trapped valencies [31]. The exchange coupling has been estimated as ~ -150 cm^{-1} [38]. At X-band freqencies the anisotropy of the hyperfine coupling and the g-matrix are of similar magnitude, making reliable elucidation of the spectral parameters difficult [37]. Haddy et al. first employed a multifrequency EPR approach to the Mn(III)Mn(IV) state of MnCAT, using P-, S-, and X-band frequencies [34]; however, higher frequencies (Q- and W-band) are required to obtain a unique set of g- and A-values due to increased g-value resolution and the different scaling of the g- and hyperfine values with frequency [31,37]. While Schäfer et al. [37] observed a similar X-band spectrum to that of Zheng et al. [32], computer simulation of a multifrequency dataset indicated that the simulation of the g-matrix was somewhat inaccurate when only
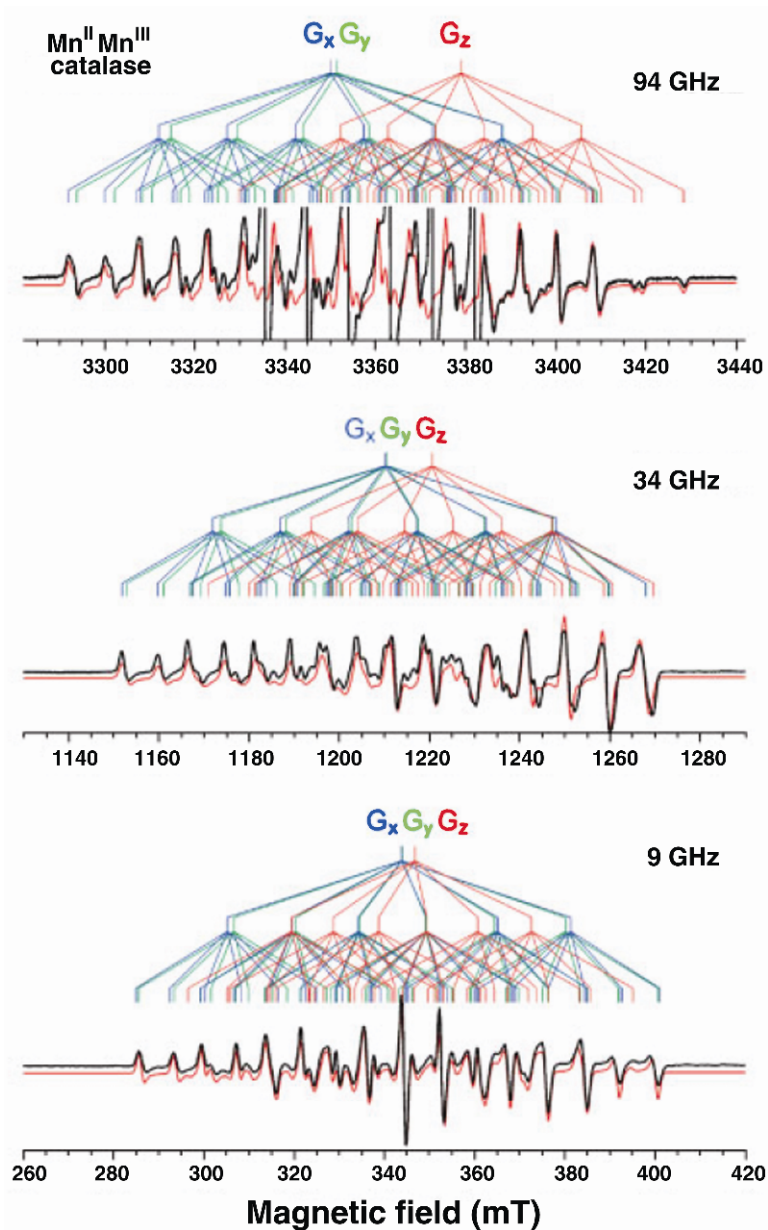
Figure 3. 16-line EPR spectrum of Mn(II)Mn(IV) catalase recorded at X-band. Reprinted with permission from [31]. Copyright © 2005, John Wiley & Sons. Please visit http://www.springer.com/978-1-4419-1138-4 to view a high-resolution full-color version of this illustration.

X-band spectra were used. Specifically, the g-matrix has very close to axial symmetry ($\Delta g_{xy} = 5 \times 10^{-4}\,\mathrm{cm}^{-1}$), so the increased resolution at higher frequency is essential for an accurate determination of the g-matrix [31,32,34]. Also of note is the decreased hyperfine anisotropy of the trivalent ion as compared with Mn(IV) [37]. One difficulty in the study of Mn(III)Mn(IV) complexes at high frequency is the presence of Mn(II) background signals that can be eliminated by the use of pulsed EPR techniques (based either on different T_1 or T_2 relaxation times or different transition moments) [37].

The Mn(III)Mn(IV) form of MnCAT has also been investigated by pulsed EPR techniques. [1]H electron nuclear double resonance (ENDOR) identified two exchangeable classes of proton, one corresponding to a water hydrogen bonded to the μ-oxo bridge, the other more closely associated with the Mn(IV) ion and attributed to a water molecule hydrogen bonded to a μ-carboxylate bridge, or a terminal Mn(IV) bound carboxylate [36]. While ENDOR failed to resolve any couplings from strongly coupled ^{14}N nuclei, electron spin echo envelope modulation (ESEEM), which is more sensitive to weak hyperfine couplings, resolved single and double quantum peaks attributable to hyperfine coupling to a single ^{14}N nucleus. Analysis of the ESEEM spectra of *L. plantarum* and *T. thermophilus* enzymes indicated similar hyperfine and electric quadrupolar couplings [35,39].

Addition of azide to the enzyme results in a decrease in the overall hyperfine splitting and subtle changes in the lineshapes [39]. Based on UV/Vis and EPR spectral titrations, a cooperative binding mode of the azide was proposed. The azide induced perturbation of the EPR spectra is strongly pH dependent, with no change apparent at pH 8.5, but binding affinity increased as the pH decreased. Addition of cyanide results in similar spectral changes, but with a lower binding affinity. The pH dependence of the binding may be attributed to either the binding of protonated anions or the requirement for protonation of an amino acid sidechain in the enzyme prior to anion binding. In contrast, addition of fluoride, also an inhibitor, resulted in no change to the spectrum [39]. The binding of azide and cyanide does not significantly change the UV/visible absorption spectrum, but does result in an increase in intensity, consistent with some flattening of the initially bent binuclear manganese core. The EPR perturbations are in agreement with this proposal. Anion (azide or cyanide) binding causes no significant changes in the g-values or A anisotropy. The major changes are a ~20% decrease in linewidth and a very slight (~3–4%) decrease in hyperfine couplings. Such a decrease in hyperfine coupling would be expected if the core was flattened, as there would be a slightly greater delocalization of the electron spin onto the oxo bridges. The two hyperfine coupling matrices are decreased equally, indicating that the anion-induced changes are not localized on either manganese ion. It is thus unlikely that the anions are coordinated directly to the manganese center [39]. ESEEM measurements support this conclusion, as the ^{14}N quadrupolar parameters are similar in the unligated and both anion-bound systems and are thus likely attributable to a coordinated histidine ligand [39]. Instead, the anions may replace one of the hydrogen-bonded water molecules identified in the proton ENDOR studies [36]. This

is in contrast to the observed binding mode in the azide-bound crystal structure of the oxidized enzyme [15].

By comparison to similar model complexes, the g- and A-values determined for Mn(III)Mn(IV) MnCAT are indicative of a tilted core geometry, consistent with that observed in the crystal structure of the Mn(III)Mn(III) state. In contrast to the Mn(III)$_2$ state, where one oxo and one hydroxo bridge is observed crystallographically, two oxo bridges are proposed for the Mn(III)Mn(IV) state based on the magnitude of the exchange coupling in comparison to model complexes and the metal–metal distance [40,41]. Additionally, ^{1}H ENDOR indicates that there is no bridging proton (vide supra) [36]. MCD spectroscopy supports these structural properties of the Mn(III)Mn(IV) active site [42].

Of note is that the Mn(III) hyperfine anisotropy is larger in the Mn(II)Mn(III) enzyme than the Mn(III)Mn(IV) enzyme, indicative of a larger asymmetry of the spin density surrounding Mn(III) in the former case. The existence of different bridging modes ((μ-OH)(μ-carboxylate) versus (μ-O)$_2$(μ-carboxylate)) in the two systems is consistent with this change in spin density [32].

2.3. Mechanistic Implications

EPR has been pivotal in the determination of the bridging and inhibitor binding modes in the various oxidation states, which is of substantial relevance to the catalytic mechanism (Fig. 4). In brief, the substrate binds terminally to the oxidized enzyme, replacing a water ligand, consistent with observations of preferential terminal binding of anions to the oxidized enzyme [18]. Two-electron oxidation of the
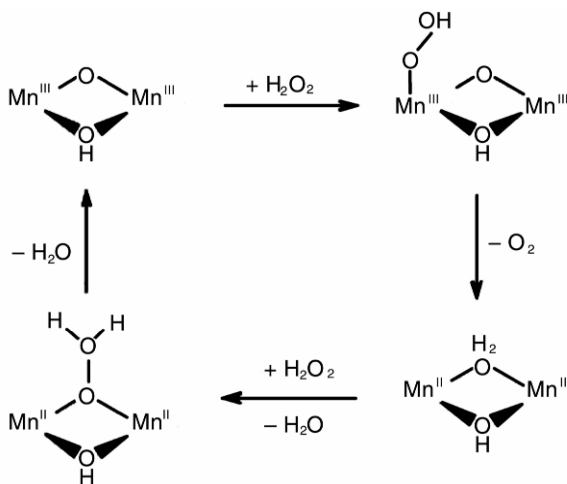
Figure 4. Catalytic mechanism of MnCAT. Reprinted with permission from [18]. Copyright © 1999, Elsevier.

terminally bound peroxide by the manganese cluster results in release of the dioxygen product and reduction of the manganese cluster. This step is facilitated by an active site glutamate that transfers the peroxidic protons, possibly to the solvent bridges, which are proposed to be protonated in the reduced cluster [15,16]. Alternatively, an active site lysine may act as a general base [43]. The protonated bridges in the reduced enzyme (particularly the proposed μ-aqua bridge) are relatively labile, allowing the second peroxide anion to insert in a bridging mode, similar to other anions [17,19,24]. The resulting peroxide complex is activated for O–O bond cleavage, and the concomitant reoxidation of the manganese core [15,16]. Further activation of the peroxide complex for cleavage may be accomplished by *vic* to *gem* isomerization of the peroxide protons facilitated by the active site glutamate [15]. In alternative mechanisms one of the bridges in each form of the enzyme is proposed to dissociate to convert the active site into a catalytically active, mono-bridged form [13,43]. This seems unlikely, however, given that the inactivity of the mono-bridged mutant oxidized protein is regained upon formation of the second bridge at high pH [16]. It is, however, possible that the aqua ligand in the reduced complex is terminally bound, rather than bridging, based on (i) the magnitude of the coupling, (ii) the proposed structure of the Mn(III)Mn(II) form of the enzyme, and (iii) the observation of an equilibrium between the bridging and terminal coordination mode in the crystal structure from *T. thermophilus* MnCAT [17]. Further EPR studies of the enzyme trapped at various stages of the catalytic cycle will be informative to elucidate the precise structure of the active site during catalysis.

3. RIBONUCLEOTIDE REDUCTASE

3.1. Biochemical and Structural Characterization

Ribonucleotide reductases (RNRs) (E.C. 1.17.4.1) are enzymes that catalyze the reduction of ribonucleotides to their corresponding 2′-deoxyribonucleotides, thus providing precursors that are necessary for DNA biosynthesis and repair [44–46]. General classification of RNRs groups them into three major classes (I–III) based on their amino acid sequence similarities, metal and radical cofactor requirements, composition, and pathways for radical generation [47]. Class I RNRs are further subdivided into subclasses Ia and Ib, and, only more recently, subclass Ic [48], based on their amino acid sequence identity, allosteric properties, and their reductant requirements under physiological conditions [49–51]. Class Ia and Ic RNRs from eukaryotes, bacteria, viruses, and bacteriophages were reviewed in detail previously in this series [1]. In our recent article in this book series we have extensively reviewed conventional class I RNRs, which are comprised of two homodimeric subunits: R1 (containing the site of ribonucleotide reduction, allosteric binding sites and redox active cysteines involved in substrate reduction) and R2 (containing the cofactor, the carboxylate-bridged non-heme Fe(III)–Fe(III) cluster) [1]. The R2 cofactor is generated by addition of O_2 to the reduced Fe(II)–

Fe(II) cluster via formation of intermediate X (Fe(IV)–Fe(III) cluster) to generate a stable tyrosyl radical (Y$^•$) in the vicinity of the di-iron cluster, which in turn oxidizes a cysteine residue located in the R1 subunit, yielding a cysteine thiyl radical (C$^•$) via a long-range (~35 Å) proton-coupled electron transfer (PCET). This cysteine radical is the initiator of the ultimate ribonucleotide reduction in the R1 subunit. Inhibition of RNRs is particularly important with respect to development of anticancer and antiviral drugs [52,53]. Furthermore, some of the existing drugs that target RNRs are based on reduction of the catalytically important tyrosyl radical found in the R2 subunit [54,55]. Recently, a new subclass of RNRs (known as class Ic) has been discovered in some species of *Chlamydiae*, which, although highly homologous to their conventional R2 counterparts (for example, those from *E. coli* and *Mus musculus*), seem to contain a phenylalanine residue in place of the corresponding radical-harbouring tyrosine residue found in other R2 proteins [56]. Furthermore, sequence analysis of R2 genes from other organisms indicated the presence of a phenylalanine residue instead of tyrosine in some other bacteria including *Mycobacterium tuberculosis* and *M. bovis*, and archaea like *Sulfolobus solfataricus* [48]. Hence, in class Ic RNRs the R2 component seems to operate and function catalytically without the use of this essential tyrosyl radical. A crystal structure of the R2 protein from *C. trachomatis* has been recently reported, confirming the presence of a phenylalanine residue at the site corresponding to the conserved tyrosine residue crucial for catalysis in other R2 proteins (F127 in *C. trachomatis* R2 vs. Y122 in *E. coli* R2) [48]. Furthermore, the two Fe(III) ions found in R2 of *C. trachomatis* (*Ct*) are bridged by two hydroxides and a μ-1,3 carboxylate from Glu120. Fe1 is also coordinated by Glu89 and His123, while Glu193, Glu227, and His230 complete the coordination sphere of Fe2. Earlier biochemical, kinetic, and EPR studies of *C. trachomatis* RNR have demonstrated the formation of a catalytically competent Fe(IV)–Fe(III) cluster in the presence of R1, substrate, and allosteric effectors [57], as well as the generation of this reactive species under turnover conditions from the diferric center [58]. Therefore, it was proposed that the Fe(IV)–Fe(III) species may be responsible for directly generating the cysteine radical in the R1 subunit. Initial specific activity measurements of di-iron-containing *C. trachomatis* R2 were much smaller in comparison to the corresponding *E. coli* R2 protein and ranged between less than 75 and ~230 U/mg [57,58]. Further biochemical and kinetic characterization of this enzyme involving protein expression under various conditions has led to the conclusion that the actual catalytically active R2 in *C. trachomatis* is a mixed heterobinuclear Fe/Mn center [59,60]. While a small percentage of moderately active Fe(II)–Fe(II) centers are also present in *C. trachomatis* R2 [48,58], the maximum specific activity of the protein expressed in the presence of varying metal ion concentrations is achieved for a 1:1 Mn(II):Fe(II) ratio with two metal ions per R2 monomer [59]. Exposure of the Mn(II)–Fe(II) *Ctr* R2 to dioxygen has been shown to activate this protein subunit [59]. In addition, activity studies performed with the Fe(III)–Fe(III) form of this enzyme by Bollinger and coworkers confirmed that the Fe(IV)–Fe(III) species of *Ctr* R2 is catalytically incompetent for the radical generation process [59]. Furthermore, the previous reports on the activity of the Fe(IV)–Fe(III) center by the Grässlund group are

most likely due to undetected Mn(IV)–Fe(III) species [59]. In vitro activity measurements with the Mn(IV)–Fe(III) form of *Ctr* R2 imply that this heterobinuclear cofactor is also likely to operate in vivo in the RNR of *C. trachomatis*. The use of a heterobinuclear Mn–Fe center instead of a homobinuclear Fe–Fe center may be the result of the immune response of the pathogen's host (increased oxidative stress) [48,59].

3.2. Spectroscopic Characterization

3.2.1. Mn(III)–Fe(III) and Mn(IV)–Fe(III)

EPR spectroscopy in combination with Mössbauer spectroscopy has been a major tool for characterizing various oxidation states of the heterobinuclear Mn–Fe center in the *Ctr* R2 protein subunit and to probe the chemical, electronic, and spectroscopic properties of the intermediate species responsible for catalysis. The active form of *Ctr* R2 (generated in the presence of O_2) exhibits no characteristic signal in the X-band perpendicular mode EPR spectrum, while Mössbauer characterization of this species shows the iron site to be trivalent and the ground state for this complex to have an overall paramagnetic integer spin [59]. In contrast, the EPR spectrum of the reduced form of this enzyme complex exhibits hyperfine coupling to both the ^{55}Mn nucleus ($I = 5/2$) and the ^{57}Fe nucleus ($I = ½$), indicative of an $S_T = ½$ ground state, and the Mössbauer spectrum ($\delta = 0.43$ mm s^{-1} and $\Delta E_Q = 0.81$ mm s^{-1}) suggests that the iron site remains in its Fe(III) oxidation state [59]. Correlation of these spectroscopic data implies that the active form of *Ctr* R2 contains an EPR-silent Mn(IV)–Fe(III) center (antiferromagnetic coupling of an Mn(IV) with $S_{Mn} = 3/2$ and Fe(III) with $S_{Fe} = 5/2$ gives rise to a triplet $S_{tot} = 1$ ground state), while the reduced species contains an Mn(III) ($S = 2$) antiferromagnetically coupled to an Fe(III) ($S = 5/2$), resulting in $S_T = ½$ (see Fig. 5A). The effects of several substrates and substrate analogues on the electronic structure of the Mn–Fe cluster of *Ctr* R2 have also been investigated by EPR spectroscopy. Addition of the R1 subunit and the nucleotides cytidine 5′-diphosphate (CDP) and adenosine 5′-triphosphate (ATP) perturbs the EPR spectrum of R2–Mn(III)–Fe(III) (Fig. 5) [59]. Simulations of the EPR spectra were consistent with the presence of an Mn(III)–Fe(III) species (significant anisotropy of the ^{55}Mn hyperfine coupling matrix, A_{Mn} [(269, 392, 314) MHz]) and an isotropic ^{57}Fe hyperfine coupling matrix, A_{Fe} [(–64.5, –64.5, –64.5) MHz] (see Fig. 5). Addition of the substrate analogue 2′-azido-2′-deoxyadenosine-5′-diphosphate (N$_3$–ADP) to the EPR-silent Mn(IV)–Fe(III) cluster of *Ctr* R2 led to an EPR spectrum identical to that of Mn(III)–Fe(III) (generated by dithionite reduction of Mn(IV)–Fe(III)) with additional features in the region of 333–342 mT, characteristic of a nitrogen-centered free radical species (Fig. 5) [61,62]. This substrate analogue has been used previously in studies on iron-containing R2 proteins and is known to inactivate them by irreversibly reducing radicals (Y$^•$) necessary for catalysis [61,63]. Therefore, the
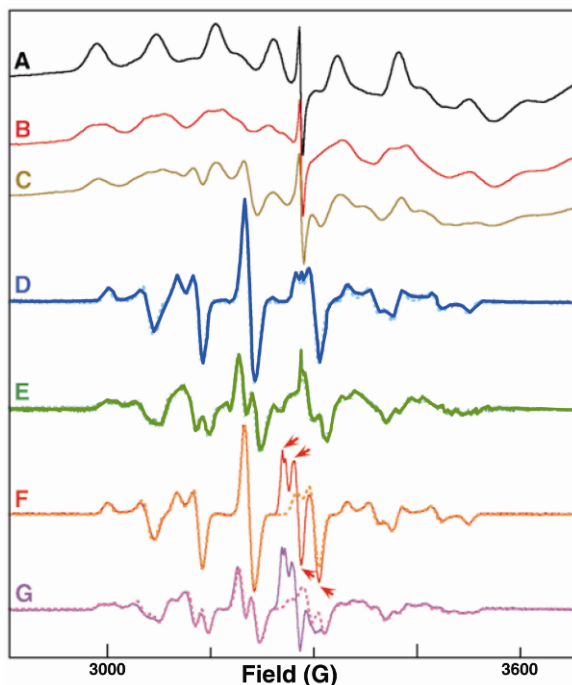
Figure 5. X-band EPR spectra (v = 9.45 GHz) demonstrating formation of Mn(II)–Fe(III) cluster by dithionite reduction of Mn(IV)–Fe(III)–R2 in *Chlamydia trachomatis*: (A,B) dithionite-reduced Mn(IV)–Fe(III) at 4 K; (C,D,E) dithionite-reduced Mn(IV)–Fe(III) in the presence of R1, CDP, and ATP at 4 K, and 14 K respectively; (F,G) dithionite-reduced Mn(IV)–Fe(III) in the presence of N_3–ADP at 14 K. Samples in A, C, D, and F were prepared with natural abundance ^{56}Fe (91.7%, I = 0), while samples B, E, and G were prepared with ^{57}Fe-enriched (95%, I = ½). Reprinted with permission from [59]. Copyright © 2007, AAAS. Please visit http://www.springer.com/978-1-4419-1138-4 to view a high-resolution full-color version of this illustration.

above EPR evidence of the formation of the Mn(III)–Fe(III) species upon addition of N_3–ADP to the Mn(IV)–Fe(III) species further substantiates the catalytic activity of the latter in *Ctr* R2.

In parallel with Bollinger's group, Grässlund and coworkers have also investigated the nature of the metal cofactor of R2 responsible for catalysis. EPR studies of *Ctr* RNR (the R1 and R2 subunits; ATP and CDP were incubated for 10 min at 25°C and frozen at –120°C in isopentane) has confirmed the presence of a resonance at g = 2 due to intermediate X (known as the Fe(IV)–Fe(III) species) and a weak and broad (70 mT) six-line signal at (Fig. 6). In the presence of the inhibitor hydroxyurea the intensity of the signal due to the intermediate X species was reduced twofold, while the six-line signal was enhanced (Fig. 6). The latter has been
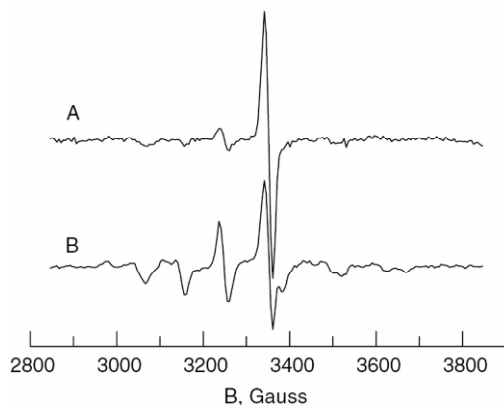
Figure 6. (A) EPR spectrum at 40 K of a catalytic mixture of *Chlamydia trachomatis* RNR, frozen (–120°C) in isopentane after 20-min incubation at 20°C. (B) EPR spectrum of the same catalytic mixture as in (A) but in the presence of 1 mM hydroxyurea. Reprinted with permission from [60]. Copyright © 2007, Elsevier.

attributed to an $S_T = \frac{1}{2}$ spin system and was interpreted as arising from the inactivated state of the protein containing Mn [60]. This six-line EPR spectrum was investigated further by preparing samples in the presence of higher Mn concentrations and incubating the enzyme in liquid nitrogen for 72 hours prior to recording spectroscopic data (eliminates intermediate X), as well as in the presence of both ^{57}Fe (nuclear spin, $I = \frac{1}{2}$) and ^{56}Fe ($I = 0$). In the case of normal isotope substitution, ^{55}Mn(III)–^{56}Fe(III), only hyperfine splitting from the ^{55}Mn nucleus is observed ($I_{Mn} = 5/2$). In the case of ^{55}Mn(III)–^{57}Fe(III), additional hyperfine coupling to the ^{57}Fe nucleus was observed (Fig. 7). EPR simulations have allowed determination of the principal components of the g, ^{55}Mn and ^{57}Fe hyperfine matrices (g[2.015, 2.009, 2.024], A_{Mn} [395, 315, 272 MHz] and A_{Fe} [68, 70, 62 MHz]; [x,y,z]) of the Mn(III)–Fe(III) center in *Ctr* R2 [60]. These observations have led to the conclusion that the six-line EPR spectrum (shown in Fig. 7) is indeed associated with the Mn(III)–Fe(III) center, where the Mn(III) and Fe(III) are antiferromagnetically coupled, giving rise to the observed $S_T = \frac{1}{2}$ ground state. Correlation of the relative number of pure di-iron centers relative to the mixed metal centers in the EPR samples supports the hypothesis that the major catalytically active form of *Ctr* R2 is the mixed metal ion Mn–Fe center, with only a small contribution of activity attributed to the di-iron center [2].

3.2.2. Mn(IV)–Fe(IV)

The reaction between the Mn(II)–Fe(II) center in *Ctr* R2 with dioxygen has been investigated using stopped-flow absorption, rapid-freeze-quench EPR, and Mössbauer spectroscopies. Stopped-flow absorption measurements indicated the
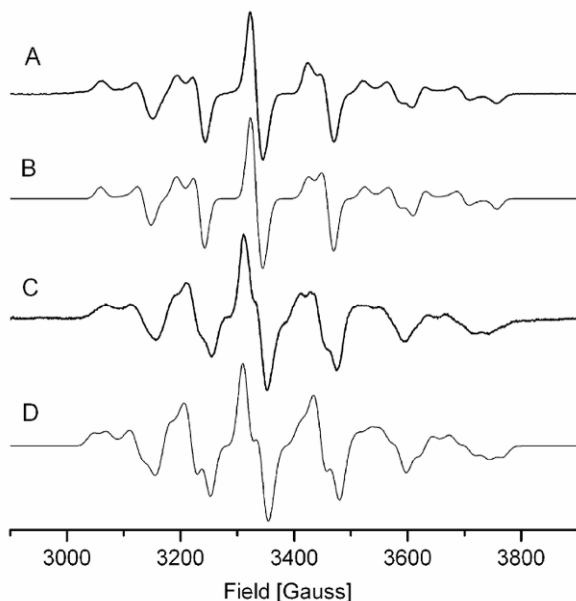
Figure 7. EPR spectra with their simulations of the Mn(II)–Fe(III) cluster of *Chlamydia trachomatis* RNR catalytic mixtures stored at 77 K for 72 hours (to suppress contribution of the signal due to the Fe(IV)–Fe(III) cluster. (A) ^{55}Mn(II)–^{56}Fe(III) and (B) its EPR-simulated spectrum; (C) ^{55}Mn(II)–^{57}Fe(III) and (D) its EPR-simulated spectrum. Reprinted with permission from [60]. Copyright © 2007, Elsevier.

rapid formation (k = 13 mM^{-1} s^{-1}) of an intermediate species with an intense absorption feature at ~390 nm [64]. This species decays slowly to form a green Mn(IV)–Fe(III) product [2]. Addition of the one-electron reductant ascorbate accelerates the decay of the intermediate to this Mn(IV)–Fe(III) species without having an effect on the kinetics of its formation. Time-dependent X-band EPR spectra were also collected for samples that were freeze-quenched at different reaction times (see Fig. 8). These experiments also demonstrate the rapid formation of an intermediate species with a sharp g ~ 2 EPR signal at 4.2 K and 20 mW, which decays slowly and shows hyperfine coupling to both ^{55}Mn and ^{57}Fe nuclei (Fig. 8). The EPR signal of this intermediate species consists of six resonances separated by ~8 mT, indicative of hyperfine coupling to a single ^{55}Mn nucleus. Furthermore, enrichment of this intermediate by ^{57}Fe led to an EPR spectrum where hyperfine coupling to a ^{57}Fe nucleus was also observed in addition to the sextet signal (Fig. 8). Simulations of these EPR spectra together with data from Mössbauer spectroscopy have allowed the determination of the ^{55}Mn and ^{57}Fe hyperfine coupling matrices, thereby providing insight into the electronic and structural properties of this heterobinuclear intermediate species. The $A_{Mn}(x,y,z)$ is found to be nearly isotropic
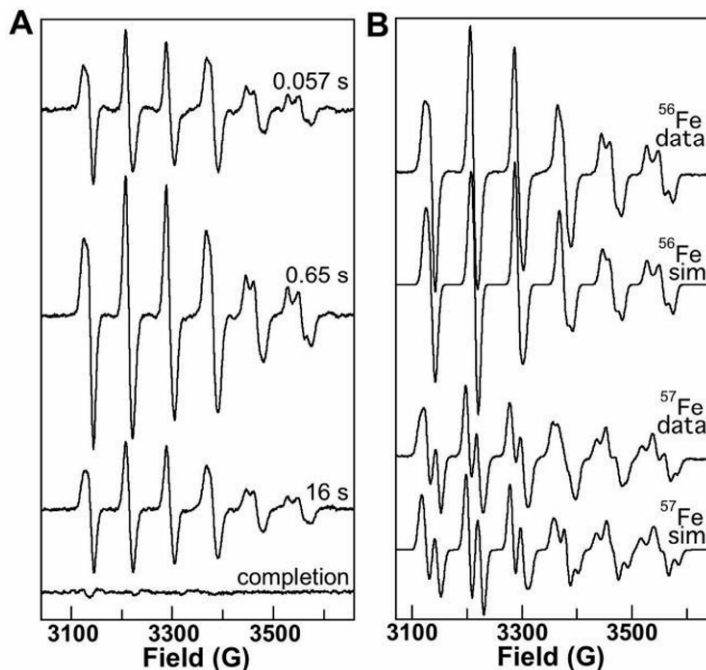
Figure 8. X-band EPR spectra collected at 14 K, 9.45 GHz for the Mn(IV)–Fe(IV) interme-
diate during O_2 activation of *Chlamydia trachomatis* R2 subunit, and their simulations. All
EPR samples in (A) were freeze quenched at various reaction times as shown after mixing
anaerobically prepared solution (free of O_2) of Mn(II)–Fe(II)–R2 (0.40 mM monomer), 0.5
equivalents of Fe(II), and 1.5 equivalents of Mn(II)) with an equal volume of O_2-saturated
buffer. Samples shown in (B) were prepared by mixing Mn(II)–Fe(II)–R2 (3.0 mM mono-
mer), 0.75 equivalents of Fe and Mn, with O_2-saturated buffer (samples frozen after 20 sec-
onds). Reprinted with permission from [64]. Copyright © 2007, American Chemical Society.

(247, 216, 243 MHz), very similar to the A_{Mn} determined for the Mn(IV) site in
Mn(III)–Mn(IV) catalase [32,65], thus supporting the presence of Mn(IV) in the
intermediate species [64]. Mössbauer simulations have supported the assignment of
the iron site in the structure of the intermediate as high–spin Fe(IV) based on (i) an
isomer shift δ of 0.17 mm/s, close to the previously reported value for Fe(IV) in the
intermediate Q of methane monooxygenase [66,67], and (ii) a quadrupole splittting
parameter ΔE_Q of –0.75 mm/s [64]. Hence, the combined EPR and Mössbauer data
collected for the reaction of the Mn(II)–Fe(II) center of *Ctr* R2 with O_2 indicates
that the intermediate has an $S_T = \frac{1}{2}$ electronic ground state as a result of antiferro-
magnetic coupling between Mn(IV) ($S_{Mn} = 3/2$) and Fe(IV) ($S_{Fe} = 2$) centers [64].
Thus, the functional cofactor in *Ctr* R2 responsible for catalysis is the heterobinu-
clear Mn(IV)–Fe(III) center that forms via an Mn(IV)–Fe(IV) intermediate. The
Mn(IV) site acts as the radical initiator in *Ctr* RNR instead of the tyrosyl radical
serving the same purpose in the conventional class I RNRs.
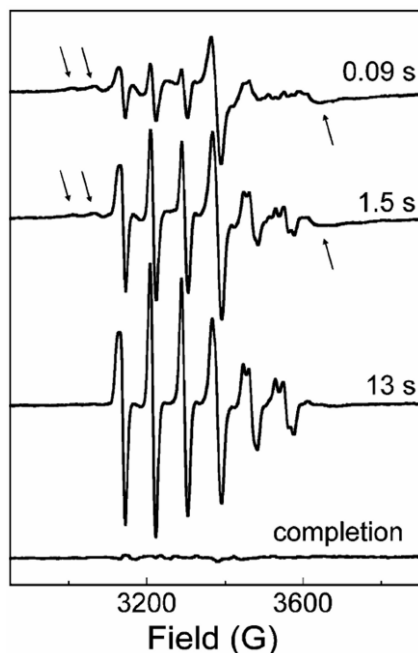
Figure 9. X-band EPR spectra collected at 14 K, 9.45 GHz for freeze-quenched samples of the reaction of Mn(II)–Fe(II)–R2 complex with H_2O_2. Samples were prepared by mixing Mn(II)–Fe(II)–R2 (0.90 mM monomer, containing 0.5 equivalents of Fe(II), 1.0 equivalents of Mn(II)) with 0.5 equivalent volume of 45 mM H_2O_2. Arrows shown in the figure indicate the features attributed to Mn(III)–Fe(III)–R2 intermediate. Reprinted with permission from [68]. Copyright © 2008, American Chemical Society.

3.2.2. Interaction of H_2O_2 with Mn(II)–Fe(II), Mn(III)—Fe(III), and Mn(IV)–Fe(III)

It has been speculated that the reason for employing a heterobinuclear Mn/Fe center by *Ctr* R2 is to make this enzyme more resistant to reactive oxygen and nitrogen species, a hypothesis that was further investigated by stopped-flow absorption, rapid-freeze-quench-EPR, and Mössbauer spectroscopies [68]. Three forms of the *Ctr* R2 cofactor in various stable oxidation states — (Mn(II)–Fe(II), Mn(III)–Fe(III), and Mn(IV)–Fe(III) — were examined with respect to their reactivity in the presence of H_2O_2. It was found that all three oxidation states can be efficiently activated by H_2O_2. EPR spectra (Fig. 9) of freeze-quenched samples of the reaction between the Mn(II)–Fe(II) center and H_2O_2 are consistent with the sequential accumulation of Mn(III)–Fe(III) (broad features shown by arrows around the sharp six-line EPR spectrum) and Mn(IV)–Fe(IV) species (sharp six-line EPR spectrum) to form the final product Mn(IV)–Fe(III) (EPR silent). Examination of the Mn(III)–Fe(III) center by EPR (broad resonance at $g \sim 2$) in the presence of H_2O_2 confirms
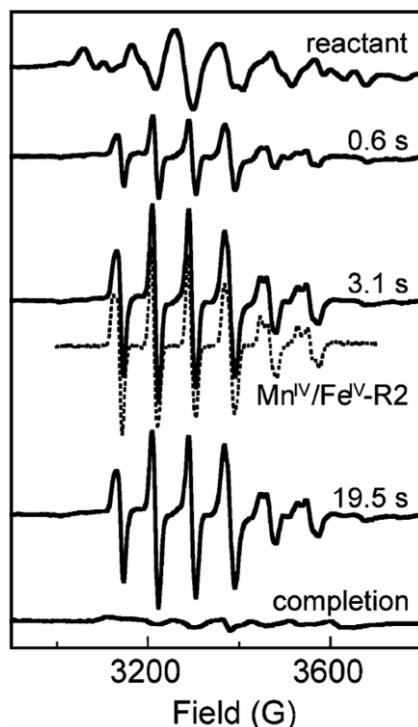
Figure 10. X-band EPR spectra collected at 14 K, 9.45 GHz for freeze-quenched samples of the reaction of Mn(II)–Fe(III)–R2 complex with H_2O_2. Samples were generated by mixing Mn(II)–Fe(III)–R2 complex (0.90 mM monomer, containing 0.75 equivalents of Mn(II) and Fe(III)) with 0.5 equivalent volume of 150 mM H_2O_2 and frozen at various reaction times (shown in the figure). Reprinted with permission from [68]. Copyright © 2008, American Chemical Society.

the rapid formation of the Mn(IV)–Fe(IV) species (sharp six-line spectrum at $g \sim 2$) before it slowly starts to decay to Mn(IV)–Fe(III) (Fig. 10). Finally, the Mn(IV)–Fe(III) form of the cofactor was found to remain stable during prolonged incubation (>1 hour) with 5 mM H_2O_2 [68]. Mössbauer spectroscopy was also employed to verify various forms of the binuclear center formed in the reaction with H_2O_2, and the kinetics of formation of all observed species was investigated by stopped-flow absorption spectroscopy. When the Fe(III)–Fe(III) derivative of *Ctr* R2 was generated, it showed small reactivity toward H_2O_2 when compared to that of the heterobinuclear center [68]. It is thus speculated that *C. trachomatis* has evolved to utilize the Mn/Fe cluster instead of an Fe/Fe cluster as a part of its efficient defense strategy in response to RO(N)S.

Finally, rapid-freeze-quench-EPR spectroscopy has also been used to probe the formation of the Mn(IV)–Fe(IV) intermediate species upon O_2 activation by the

Mn(II)–Fe(II) form of three *Ctr* R2 variants: Y122F, Y338F, and W51F [69] (*vide infra*).

3.3. Mechanistic Implications

Kinetic and spectroscopic studies, including those discussed in the previous section, of *Ctr* R2 have led to a proposal for the reaction mechanism for the activation of the R2 cofactor. Unlike the *E. coli* R2 subunit, which utilizes the Fe(III)–Fe(III)/Y$^•$ cofactor to generate a Cys$^•$ in the R1 subunit necessary for the initiation of ribonucleotide reduction, the R2 subunit of *C. trachomatis* uses an Mn(IV)–Fe(III) cofactor in its place (*vide supra*). The Mn(II)–Fe(II) cluster interacts with O_2 to generate an Mn(IV)–Fe(IV) intermediate, which subsequently gets reduced to the active Mn(IV)–Fe(III) form (Fig. 11). It is speculated that the structure of the Mn(IV)–Fe(IV) intermediate is likely to resemble that of intermediate *Q* (with a "diamond core" structure) found in soluble methane monooxygenase [70]. Similar to *E. coli* R2, *Ctr* R2 also uses a tryptophan residue (W51) in the vicinity of its Mn/Fe active site to reduce the Mn(IV)–Fe(III) to an Mn(III)–Fe(III) species [64].
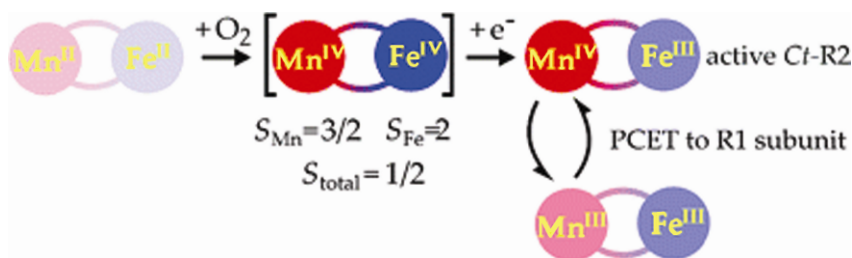
Figure 11. Overall reaction mechanism proposed for activation of the R2 subunit of *Chlamydia trachomatis* showing various different oxidation states of the Mn–Fe cluster. Reprinted with permission from [68]. Copyright © 2008, American Chemical Society. Please visit http://www.springer.com/978-1-4419-1138-4 to view a high-resolution full-color version of this illustration.

Recently, attempts have been made to deconvolute the plausible amino acid residues involved in the intersubunit PCET pathway between the *Ctr* R2 and R1 components. Several variant forms of the *Ctr* R2 subunit have been generated (W51F, Y122F, and Y338F) to map the residues that mediate reduction of the binuclear center and facilitate electron relay between the two protein subunits. While substitution of Y122 with F did not affect the formation of the Mn(IV)–Fe(IV) intermediate, it did slow down its decay (reduction) ~10-fold and also reduced the efficiency of ascorbate reduction ~65-fold, implicating residue Y122 as a mediator in the reduction step of Mn(IV)–Fe(IV) [69]. The Y338F mutation (Y338 corresponding to the interfacial residue Y356 in *E. coli* R2) has been shown to abolish

catalytic activity with no effect on the decay of the Mn(IV)–Fe(IV) intermediate, thus demonstrating that this residue is essential in the PCET pathway between R1 and R2 subunits. Finally, the W51F-R2 variant (W51 corresponds to W48 residue in *E. coli* R2) also exhibited no catalytic activity and slowed down the reduction of the Mn(IV)–Fe(IV) intermediate, thereby suggesting involvement of residue W51 in the catalytic PCET pathway between the two subunits [69]. Based on the previous observations for the O_2 activation of the Fe(II)–Fe(II) and Mn(II)–Fe(II) forms of *Ctr* R2, a plausible reaction mechanism is shown in Figure 12. In the case of the di-iron cluster of *Ctr* R2, rapid accumulation of intermediate X (Fe(IV)–Fe(III) cluster) with a tryptophan radical (W51$^{+•}$), X-W51$^{+•}$ occurs [48,58], whereas in the case of Mn(IV)–Fe(IV)–R2 there is no evidence for the formation of a transient radical during reduction of the Mn(IV)–Fe(III) cofactor, suggesting no coupling of an amino acid oxidation to O–O bond cleavage [69]. In summary, the *Ctr* R2 subunit seems to employ Y122 and W51 as likely residues that facilitate electron transfer to the Mn(IV)–Fe(IV) intermediate during the activation process, and utilizes both W51 and Y338 for the efficient electron relay pathway during catalysis.

Figure 12. Proposed mechanism for electron relay to the binuclear Mn–Fe cofactor of the R2 subunit of *Chlamydia trachomatis* during O_2 activation by Fe(II)–Fe(II) form (top) of R2 and the Mn(II)–Fe(II) (bottom) form of R2. Reprinted with permission from [69]. Copyright © 2008, American Chemical Society.

4. CLASS IB RIBONUCLEOTIDE REDUCTASES

4.1. Biochemical and Structural Characterization

As mentioned above, RNRs are enzymes that employ free radical chemistry to catalyze ribonucleotide reduction to the corresponding deoxyribonucleotides, thus providing precursors for DNA replication and repair [44]. The focus in this section is on class Ib RNRs, which are found mostly in prokaryotes and consist of two homodimeric protein subunits — R1E and R2F (containing the binuclear metal center) — a small redox protein similar to thioredoxin as well as an additional protein whose function is not yet fully known [71,72]. Although the class Ib RNR is present in *S. typhimurium* and *E. coli*, for example, it is not essential in these organisms [73]. However, they have attracted considerable attention due to their oc-

currence in pathogenic bacteria such as *Mycobacterium tuberculosis*, *Bacillus subtilis*, and *Mycoplasma pneumonia* [74–76]. The metal-coordinating residues, as well as residues involved in the radical transfer pathway, are highly conserved among class Ia and Ib RNRs [77]. The first crystal structure of a class Ib R2F protein reported was that from *S. typhimurium* [78], followed by the holocomplex of this RNR [79]. The two ferric ions are both octahedral, bridged by Glu98, an O^{2-} ion, and a water molecule. In addition, one of the irons is also ligated by a histidine (His101), an aspartate (Asp67), and a water molecule, with the second iron being coordinated by another histidine (His195) and two glutamates (Glu158 and Glu192). Three-dimensional structures of another class Ib R2F protein from *Corynebacterium ammoniagenes* has been reported more recently in the oxidized and reduced di-iron forms and a manganese-substituted one [80]. The overall structures of the *S. typhimurium* and *C. ammoniagenes* R2Fs are similar. In the oxidized form of the *C. ammoniagenes* enzyme, the two irons in *C. ammoniagenes* R2F are bridged by a μ-oxo bridge and a carboxylate group from Glu108. In addition, the five-coordinate Fe site is coordinated by an aspartate (Asp77), a histidine (His111), and a water molecule, while the second Fe is six-coordinate and its coordination sphere is completed by a bidentate glutamate (Glu202), Glu168, a histidine (His205), and a water molecule. In the Mn-substituted enzyme (Fig. 13), the two Mn ions are bridged by Glu202 and Glu108, with the four-coordinate Mn being also coordinated by His111 and Asp77, while the five-coordinate Mn is coordinated by His 205 and Glu168 in a bidentate fashion. For some time there has been some debate about the nature of the metal cofactor in class Ib RNRs. Initial studies with the R2F subunit from *C. ammoniagenes* have led to the proposal that manganese rather than iron is essential for catalytic activity [81,82]. This hypothesis was based on (i) the manganese requirement for growth, (ii) the inability of *C. ammoniagenes* to reduce ribonucleotides upon manganese depletion, (iii) the release of Mn(II) upon enzyme denaturation, and (iv) the reconstitution of enzyme activity upon supplementing Mn in vivo [81–83]. It was speculated that RNR from *C. ammoniagenes* belonged to a separate class of Mn-dependent RNRs. Establishing an efficient recombinant expression system for this enzyme in *E. coli* has facilitated its characterization. Surprisingly, enzyme activity measurements indicated that maximum specific activity is obtained in the presence of iron (1.5 Fe/monomer) and no manganese [84]. Specific activity of the enzyme expressed in media with supplemented iron and manganese was found to contain 0.5 Fe/monomer and 0.09 Mn/monomer and had higher specific activity than enzyme expressed in media supplemented with manganese only. Hence, in contrast to initial studies, catalytic measurements with *C. ammoniagenes* R2F protein imply that the active form of this enzyme is iron dependent.

4.2. Spectroscopic Characterization

Q-band EPR spectra of the R2F subunit of *C. ammoniagenes* (generated by careful dissociation of the holoenzyme) at 40 K was consistent with the presence of
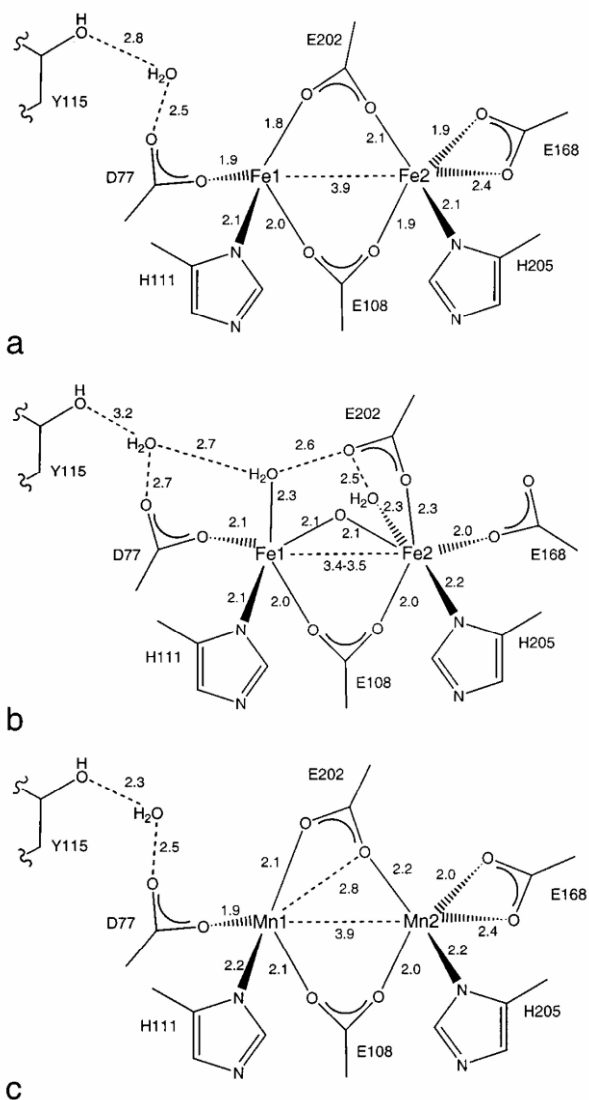
Figure 13. Schematic representation of the active site structure of the R2 subunit of *Coryne-bacterium ammoniagenes*. (A) Reduced form of the iron-containing cluster; (B) oxidized form of the iron-containing cluster; and (C) Mn-substituted form of enzyme. Reprinted with permission from [80]. Copyright © 2002, American Chemical Society.

an isolated Mn(II) in an octahedral environment (EPR signal with hyperfine couplings of 9.2–9.6 mT, centered at $g \sim 2$) [85]. Weak features are also observed both at the low- and high-field end of the sextet signal, indicating a small zero field splitting with rhombic distortion. There was no evidence for any spectral broaden-

ing, splitting, or multiline features characteristic for binuclear manganese systems as a result of exchange or strong dipolar coupling [86,87]. Sjöberg and coworkers reported that in the X-band EPR spectrum of the active R2F protein no signal is observed [88]. Upon denaturation of the enzyme, a six-line EPR signal at $g \sim 2$, characteristic of an isolated Mn(II), was observed. Metal ion analysis indicated the presence of 0.5 Mn/monomer and eliminated the presence of iron. Therefore, contrary to the results from the activity measurements (*vide supra*), it has been proposed that manganese ions could potentially be coupled in the native R2F, but the presence of substoichiometric amounts of Mn in protein samples was insufficient to support this hypothesis.

More recent spectroscopic characterizations of R2F from *C. ammoniagenes* have attempted to deconvolute the above conflicting results and shed insight into the nature of the metal cofactor of this enzyme. Cells grown in LB medium with no added metal ions have yielded an EPR signal characteristic of a tyrosyl radical at $g = 2.00$ (see Fig. 2 in Huque et al. [84]), and the amount of tyrosyl radicals increased twofold when cells were grown in Fe-supplemented medium [84]. Interestingly, cells grown in Mn-supplemented medium produced no tyrosyl radicals (see Fig. 2 in Huque et al. [84]). The R2F protein purified from Mn-supplemented medium had 1.6 Mn/monomer and displayed a complex multiline signal at $g \sim 2$ (more than 30 resolved lines separated by ~4.6 mT) on top of a broad signal (see Fig. 4 in Huque et al. [84]), characteristic of coupled Mn(II) sites in other proteins, but had minimal catalytic activity [25]. This EPR spectrum resembles that of arginase (see §10 below) with two Mn(II) ions being bridged by two carboxylates and a water/hydroxide [89]. Thus, the above metal reconstitution studies with *C. ammoniagenes* R2F have correlated enzyme activity with the presence of a tyrosyl radical ($g = 2.005$, $A(^1H)/g\beta = 0.9$ mT, $A(^1H)/g\beta = 0.7$ mT), which in turn can be correlated to the iron content in protein samples [84]. Similarly, manganese reconstitution studies performed with *S. typhimurium* apo-R2F resulted in completely inactive protein, although EPR spectroscopy confirmed the presence of a binuclear Mn(II) site in the enzyme (1.6 Mn/monomer); no tyrosyl radical was formed, similar to the Mn-derivative of *C. ammoniagenes* R2F [84]. In contrast, iron and iron/manganese reconstitution of *S. typhimurium* R2F generated a fully active enzyme. The observed tyrosyl radical is identical to that in the di-iron-containing *S. typhimurium* R2F subunit [90,91]. The microwave power saturation behavior of the tyrosyl radicals in R2F proteins of both *C. ammoniagenes* and *S. typhimurium* were examined in order to evaluate the different electronic environments in the vicinity of the radical. The EPR saturation behavior of the tyrosyl radicals was monitored at 95 K. The plots of the normalized double integral of the EPR signals vs. microwave power allowed for determination of $P_{1/2}$ (the power of half saturation), thereby measuring the magnetic interaction between the tyrosyl radical and the corresponding metal center [84]. The EPR signal observed for *C. ammoniagenes* was saturated at lower power ($P_{1/2} = 1.3$ mW) relative to that for *S. typhumurium* ($P_{1/2} = 3.7$ mW), indicative of the slightly weaker coupling of the tyrosyl radical in *C. Ammoniagenes* R2F. In contrast, the tyrosyl radical of the *E. coli* R2 subunit ($P_{1/2} = 91$ mW at 95 K) exhibits a much faster relaxation, a consequence of the

interaction with the di-iron active site [92]. While the tyrosyl radicals of the R2F subunits from *C. ammoniagenes* and *S. typhumurium* are also clearly interacting with their neighboring di-iron active sites, the high-field EPR studies of single crystals of R2F from *S. tyrphimurium* containing the tyrosyl radical (Y105$^\bullet$) have indicated that this radical is further away from the di-iron center, undergoing a different sidechain rotation relative to that of the *E. coli* R2 tyrosyl radical (Y122$^\bullet$) [93]. The exact nature and origin of the differences in magnetic coupling for the three tyrosyl radicals observed in *C. ammoniagenes*, *S. typhimurium*, and *E. coli* need further analysis by high-field EPR. However, the crystal structures of *C. ammoniagenes* and *S. typhimurium* R2F support the spectroscopic evidence that the radical-harboring tyrosine residues (Y115 and Y105 in *C. ammoniagenes* and *S. Typhimurium* R2F, respectively) are indeed located further from the binuclear metal active site (7 Å in *C. ammoniagenes* R2F relative to 5 Å in *E. coli R2*).

4.3. Mechanistic Implications

While EPR spectroscopic studies were able to demonstrate the formation of a coupled binuclear Mn(II) center in the R2F proteins from *C. ammoniagenes* and *S. typhimurium* (1.6 Mn/monomer in both proteins), both enzymes exhibited no catalytic activity and could not generate the tyrosyl radical required for catalytic activity [84]. The initial hypothesis that suggested the *C. ammoniagenes* R2F protein to be Mn dependent is thus no longer valid. Combined biochemical, spectroscopic, and crystallographic data on the R2F enzymes from *C. ammoniagenes* and *S. typhimurium* strongly support the idea that these are iron-dependent enzymes and fully functional in their di-iron form, similar to R2 from *E. coli*. Thus, their catalytic mechanisms are also likely to be similar, following the mechanistic model described in our previous article [1]. While the Mn-subsituted R2F is inactive, it represents a useful spectroscopic tool for the study of this enzyme. It may still be possible that manganese is necessary in class Ib RNRs for efficient formation of the holoenzyme complex and further studies are necessary to examine the overall role of manganese in this class of RNRs.

5. MANGANESE-IRON OXYGENASES

5.1. Biochemical and Structural Characterization

Non-heme di-iron containing oxygenases that catalyze a diverse and wide range of oxidative transformation reactions important in biological chemistry have been extensively studied, and we have covered these in great detail earlier [1]. Recently, a novel metalloenzyme known as arylamine oxygenase, or *N*-oxygenase AurF, from *Streptomyces thioluteus* has been isolated [94]. This enzyme, responsible for the biosynthesis of aureothin, a metabolite with antifungal anticancer and antifungal properties [95], catalyzes the selective six-electron oxidation of the amino group of *p*-aminobenzoic acid to *p*-nitrobenzoic acid [96]. AurF exhibits

high *para* regioselectivity and is also able to catalyze a number of other *para*-substituted substrates, such as *para*-aminophenyl sulfonic acid, and *para*-aminophenyl acetic acid, thus making it useful in biotechnology applications [97]. There has been an extensive debate in the literature as to whether this enzyme utilizes Mn, Fe, or both ions for its activity. Sequence alignment of AurF has identified a very low sequence homology (15–35% sequence identity) with several hypothetical proteins of unknown function, and found two putative conserved structural motifs, **EX**$_{28–37}$**DEXXH** (conserved residues shown in bold) [94], reminescent of the conserved structural motif found in carboxylate-bridged binuclear non-heme iron oxygenases [77,98]. Initial biochemical studies involving site-directed mutagenesis of each of the eight conserved residues of AurF have confirmed the absolute requirement of all of these residues for catalytic activity [94]. Metal ion analysis by ICP atomic emission spectrometry has revealed 2.18 *g* atoms of iron/enzyme, suggesting AurF to be a di-iron-containing oxygenase. When the protein was overexpressed in Mn-supplemented medium, it was able to incorporate two Mn ions/enzyme, but exhibited no activity. However, it was also proposed by Hertweck's group that AurF (expressed as soluble MBP–AurF fusion protein) was likely to function catalytically as an Mn-dependent enzyme based on significant amounts of Mn present in their samples (using colorimetric assays of enzyme solutions, the ratio of Mn:Fe found was 20:1) [97]. They were also able to restore enzyme activity by addition of H_2O_2, thereby implying that similar to the "peroxide shunt" process observed for other di-iron oxygenases [99], H_2O_2 can indeed form a catalytically active species while omitting the reduction step. Mechanistic studies of AurF have shown the formation of a hydroxylamine intermediate via incorporation of an oxygen atom [100]. In addition, ^{18}O labeling studies were used to follow the conversion of the hydroxylamine intermediate to a nitroso intermediate via a dehydrogenation step [94]. The three-dimensional structure of the first *N*-oxygenase AurF from *S. thioluteus* has been reported only recently [101]. The overall fold of AurF is similar to that of the *E. coli* ribonucleotide reductase R2 subunit [102]. The active site of AurF contains a binuclear manganese cluster (Fig. 14), where the two six-coordinate manganese ions are bridged by Glu227 in a μ-1,1 mode, Glu136 in a μ-1,3 fashion and a water molecule. In addition, one Mn ion is coordinated by Glu101, His223, His139, and a water molecule while the coordination environment of the second Mn ion is completed by His230 and bidentately coordinated Glu196. This study also suggested that the enzyme has a ~20-fold selectivity preference for manganese over iron. However, crystallographically characterized Mn-containing AurF contained ~15% iron as a contaminant, potentially giving rise to the observed enzyme activity. The Hertweck group has reexamined the immediate coordination environment of the AurF metal cofactor and the importance of specific residues for catalytic activity by carrying out experiments with rationally designed AurF variants (by site-directed mutagenesis of the three histidine and four glutamate residues found in the active site) [103]. Seven residues in the active site (3 His and 4 Glu) are necessary for catalytic activity of the enzyme.
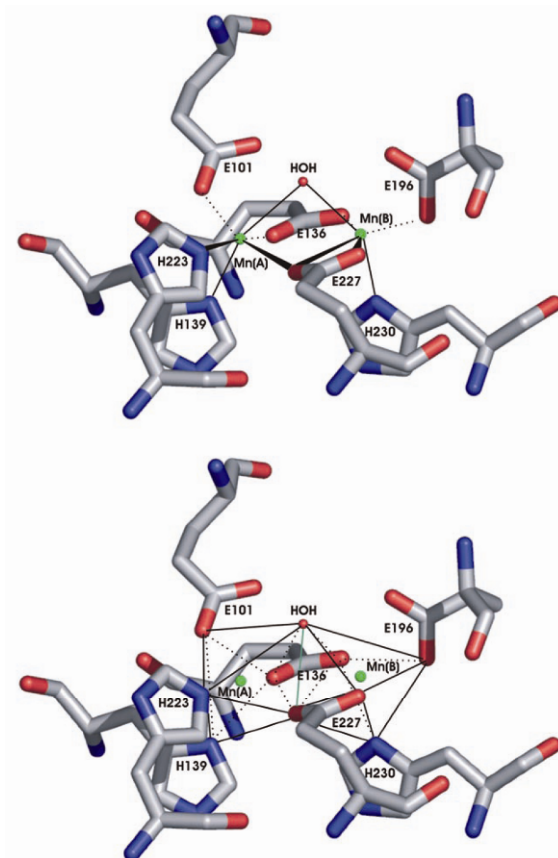
Figure 14. Active site structure of the Mn-containing AurF from *Streptomyces thioluteus*. Reprinted with permission from [103]. Copyright © 2006, Wiley-VCH. Please visit http://www.springer.com/978-1-4419-1138-4 to view a high-resolution full-color version of this illustration.

5.2. Spectroscopic Characterization

Some contradictory observations have been reported concerning the metal content of AurF and the activity of the enzyme. EPR spectroscopy has so far been a major tool in probing the nature of the metal cofactor in AurF N-oxygenase. The initial EPR study of AurF expressed in Fe-supplemented minimal medium by Zhao and coworkers has reported an X-band EPR spectrum with g values of 1.94, 1.79, and 1.70, suggesting the presence of a mixed-valent Fe(III)–Fe(II) center with an $S_T = \frac{1}{2}$ ground state, while fully reduced AurF was EPR silent [94]. This group also used oxidized AurF expressed in LB medium to record an EPR spectrum, which
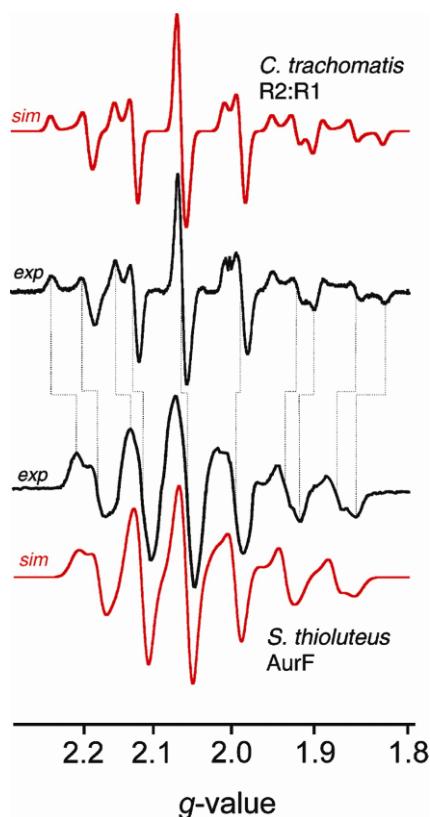
Figure 15. Comparison of the X-band EPR spectra and their simulations of the Mn(III)–Fe(III) cluster of the *Chlamydia trachomatis* Mn(III)–Fe(III)–R2–R1–CDP–ATP complex (top) and the oxidized form of AurF from *Streptomyces thioluteus* (bottom). Reprinted with permission from [106]. Copyright © 2007, American Chemical Society. Please visit http://www.springer.com/978-1-4419-1138-4 to view a high-resolution full-color version of this illustration.

showed features characteristic of mononuclear Mn(IV) ions [104] and the Fe(III)–Mn(III) center, which has been previously found in *E. coli* ribonucleotide reductase [105]. The authors interpreted their data in terms of AurF being able to incorporate Mn ions in addition to Fe, but argued that AurF was an iron-dependent enzyme. In support of this hypothesis, AurF expressed in Mn-supplemented minimal medium was found to incorporate two Mn ions per enzyme, but no catalytic activity was detected. Bollinger and coworkers have reevaluated and reanalyzed the EPR spectroscopic data reported for the resting form of AurF and proposed that it may use a heterobinuclear Mn/Fe center as the metal cofactor in catalysis [106]. In fact, the EPR spectrum of AurF resembled that of Mn(III)–Fe(III)–R2–R1–CDP–ATP observed for *C. trachomatis* RNR, with a similar hyperfine pattern, but somewhat smaller coupling (Fig. 15). The values of the A_{Mn} and g matrices were estimated from the simulations of the experimental EPR spectrum [$A_{Mn} = (210, 270,$

322) MHz; g = (2.030, 2.014, 2.015)]. The simulations reveal an anisotropic A_{Mn}, and the absolute magnitude of A_{Mn} in AurF is found to be smaller than that for *C. trachomatis* RNR. Evaluation of the intrinsic hyperfine matrices for AurF [A_{Mn} = (–158, –205, –213) MHz] proved to be consistent with those estimated earlier for catalase [A_{Mn} = (–158, –203, –213) MHz] [32]. In conclusion, EPR data for AurF strongly suggest the presence of a heterobinuclear Mn(III)–Fe(III) site, where Mn(III) (S_{Mn} = 2) and Fe(III) (S_{Fe} = 5/2) are antiferromagnetically coupled resulting in an S_T = ½ ground state. This AurF metal cofactor (Mn(III)–Fe(III)), is consistent with the biochemical studies carried out by the Zhao and Hertweck groups, which reported the presence of both iron and manganese in their protein samples [94,97]. Additional EPR experiments on AurF alone, and in the presence of oxidant and substrate, have recently shown some evidence for the involvement of Mn-containing AurF in *N*-oxygenation reactions [103]. The purified AurF exhibits a typical six-line EPR spectrum (g = 2.05) of an S = 5/2 high-spin Mn(II) ion in the region from 307.6 to 354.0 mT. An approximate hyperfine splitting of 8.9 mT ($A/g\beta$) is indicative of a mononuclear Mn(II) ion. The authors have argued that binuclear Mn centers often appear as a mononuclear Mn depending on pH. The weak signal (from iron contaminant) was observed for Fe(III) (g_{eff} = 4.3). Upon activation with H_2O_2, the Mn(II) sextet signal disappears and a sharp radical signal at g = 2.003 is formed (peak-to-peak width of 2.4 mT), suggesting a possible change in the oxidation state of Mn(II) and a possible Mn-based radical mechanism. In contrast, when both substrate and H_2O_2 are added, the radical signal disappears and the typical Mn(II) sextet EPR signal reemerges. This observation suggests Mn as the likely candidate implicated in catalysis rather than Fe. Final agreement has not been reached on the metal ion composition of AuF required for its activity. More detailed spectroscopic characterization is required to probe the specific states of this enzyme.

5.3. Mechanistic Implications

As mentioned above, due to the various metal ion content found in AurF from different sample preparations, it has been difficult to carry out any detailed mechanistic studies. The Hertweck group has recently proposed a radical-based mechanism in light of their recent EPR studies and peroxide shunt experiments [97,103]. This radical-based mechanism is analogous to that previously proposed for soluble methane monooxygenase [107], where the radical is close to the binuclear manganese cluster. So far, a radical similar to the tyrosyl radical operating in ribonucleotide reductases has not been observed for AurF. The Mn(II)–Mn(II) AurF is expected to react with dioxygen to generate a high-valent Mn(IV)–Mn(IV) intermediate similar to intermediate Q found in sMMO. While it is known that sMMO employs other protein components for efficient electron transfer, no such components have yet been associated with AurF. Finally, the proposal by the Bollinger group that AurF may utilize an Mn–Fe cofactor for its activity (Fig. 16) (based on the
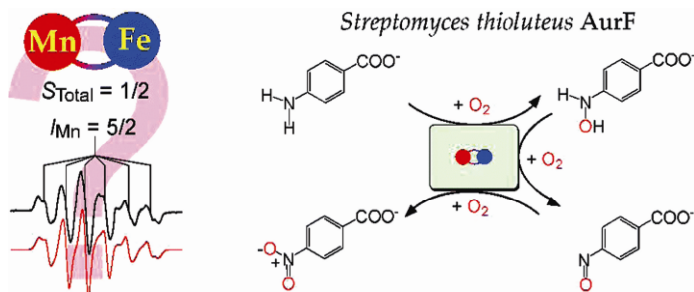
Figure 16. Proposed Mn–Fe cluster of AurF from *Streptomyces thioluteus* involved in catalysis of *N*-oxygenation reaction. Reprinted with permission from [106]. Copyright © 2007, American Chemical Society. Please visit http://www.springer.com/978-1-4419-1138-4 to view a high-resolution full-color version of this illustration.

EPR similarities between AurF and the *C. trachomatis* R2 RNR subunit) is attractive, as this would make AurF the first known Fe–Mn *N*-oxygenase [106]. In order to refine the reaction mechanism of AurF, the specific metal requirement of this enzyme and generation of its metal cofactor must first be established.

6. SOXB

6.1. Biochemical and Structural Characterization

Oxidation of inorganic sulfur to sulfuric acid represents the oxidative half of the global sulfur cycle [108,109]. Sulfur oxidation is performed by various aerobic chemotrophic and anaerobic phototrophic prokaryotes. Four soluble proteins — SoxAX, SoxYZ, SoxB, and SoxCD — comprise the sulfur-oxidizing enzyme system in vitro [108,109]. This system mediates hydrogen sulfide-, sulfur-, thiosulfate-, and sulfite-dependent cytochrome *c* reduction. Each protein alone is catalytically inactive [110,111]. The material balance of the thiosulfate oxidation by this system is given by

$$\text{}^-\text{S-SO}_3^- + 5\text{H}_2\text{O} + 8\text{Cyt } c^{3+} \rightarrow 2\text{SO}_4^{2-} + 8\text{Cyt } c^{2+} + 10\text{H}^+. \tag{3}$$
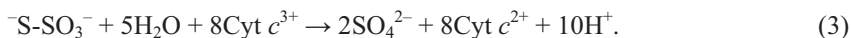
According to the current model, thiosulfate is covalently bound by the copper–heme enzyme complex SoxAX and to the thiol of the cysteine residue of the SoxY protein to form cysteine–thiosulfonate. The sulfonate moiety is proposed to be hydrolyzed by the dimanganese SoxB protein to yield sulfate and SoxY–cysteine persulfide. The sulfane sulfur of the SoxY–cysteine persulfide is then oxidized by the molybdoprotein cytochrome complex sulfur dehydrogenase Sox(CD)$_2$, and the sulfonate moiety is again hydrolyzed by SoxB to regenerate the cysteine residue of SoxY [108]. The monomeric SoxB protein contains two manganese atoms, pyroglutamate (cycloglutamate) as the N-terminus, with a molecular weight of 58.6 kDa [109]. SoxB has been shown to interact strongly with the SoxYZ complex. Its structure has been modeled based on *E. coli* 5′-nucleotidase (5′-NT), with which the enzyme shares 42% sequence similarity, due to which SoxB has been proposed to be a member of the metallophosphoesterase family [112,113].
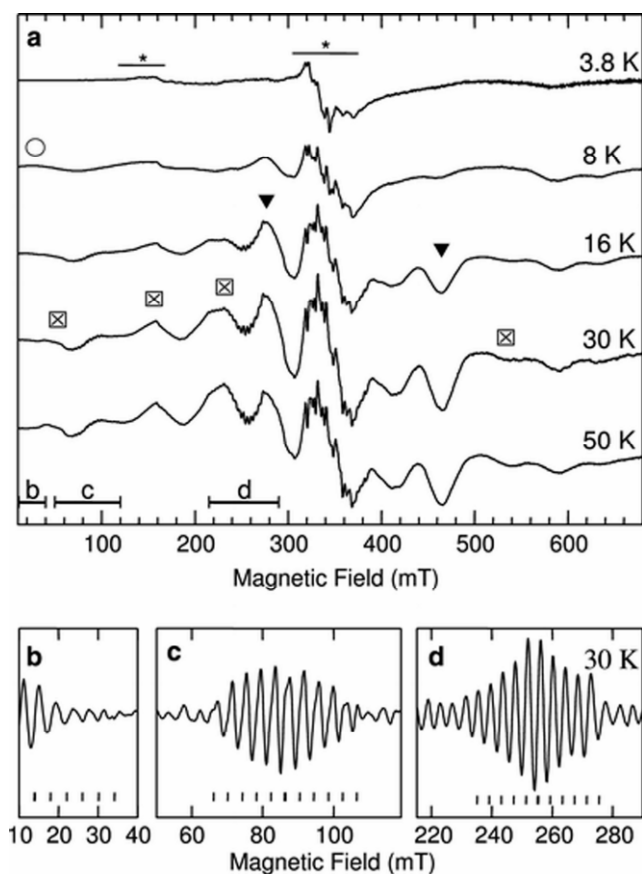
Figure 17. X-band spectrum of SoxB. (a) The range of the impurity signals (at 3.8 K) are indicated and marked with asterisks. Features arising from spin states $S_T = 1$ (○), 2 (▼), and 3 (⊠) are marked. (b–d) Extracted hyperfine patterns at the selected regions of the spectrum (a) recorded at T = 30 K. The 11-line patterns, split by 4.05 mT, are indicated by vertical bars at the bottom of the figure (b–d). Reprinted with permission from [110]. Copyright © 2005, Springer.

6.2. Spectroscopic Characterization

The first EPR spectrum of SoxB from *Thiobacillus verstus* was reported by Cammack et al. and was attributed to a binuclear Mn(II) center, due to the broad features and superimposed hyperfine splitting [114]. Subsequently, a multifrequency EPR analysis of Sox B from *Paracoccus pantotrophus* was carried out [110]. X-band (Fig. 17) and Q-band spectra revealed a broad signal with hyperfine structure superimposed, which was better resolved at Q-band frequencies. At Q-band, the main resonances are located within 900 to 1400 mT, and resonances at

1170, 1240, and 1300 mT exhibit resolved hyperfine structure, with ~40 hyperfine lines with a splitting of $A/g\beta \sim 4.2$ mT [115]. Simulations indicated that the resolved hyperfine structure originates only from the $S_T = 3$ state, with features arising from an $S_T = 1$ being very broad. Zero field splitting parameters $|D(S_T = 3)| = 0.07$ cm^{-1} and $E/D(S_T = 3) = 0.06$ correspond to a metal–metal distance of 3.3–3.46 Å. An exchange coupling of $J = -7$ cm^{-1} was used in the simulations and reproduced reasonably the intensity of the features from each spin state as a function of temperature as predicted by the Boltzmann distribution. A comparison of these parameters with model complexes suggests a bis(μ-hydroxo)(μ-carboxylato) bridging motif in the binuclear manganese core [110].

6.3. Mechanistic Implications

As mentioned above, SoxB is proposed to function as a sulfate thio-esterase, and the monomer possesses 42% similarity with 5′-NT, suggesting mechanistic similarities between the two metallohydrolases and other members of this family of enzymes, including λ protein phosphatase (§7) and purple acid phosphatases (§8). To date, EPR studies have been limited to determining the likely bridging mode in the active site of the resting enzyme. Further studies in the presence of substrates and/or inhibitors may help elucidate mechanistic details such as the identity of the nucleophile and the binding mode of the substrate.

7. BACTERIOPHAGE λ PROTEIN PHOSPHATASE

7.1. Biochemical and Structural Characterization

Bacteriophage λ protein phosphatase (E.C. 3.1.3.16) (λPP) is a member of the family of serine/threonine protein phosphatases based on sequence homology, and kinetic and spectroscopic properties [113,116,117]. The enzyme hydrolyzes phosphoserine/threonine substrates as well as tyrosine phosphoproteins and phosphopeptides [118], and model substrates such as *para*-nitrophenolphosphate (*p*-NPP) [117], but their biological role is unknown. Although its catalytic activity can be reconstituted with a variety of bound metal ions, such as iron [117], calcium [119], nickel and manganese [118], the observation that the recombinant expression of λPP in *E. coli* leads to a dramatic increase in intracellular manganese concentrations has been interpreted in terms of manganese being the most likely in vivo metal ion for this enzyme [120].

The crystal structure of λPP (Fig. 18) has been determined in the presence of manganese and sulfate (a very weak inhibitor [121]) [122]. The two metal ions are separated by 3.5 Å and are bridged monodentately by an oxygen atom of a conserved aspartate (Asp49). Additional ligands to the manganese site M1 are His22, Asp20, and three water molecules (or one water molecule and a bidentately bound sulfate ligand). The manganese M2 site is coordinated by nitrogen atoms from
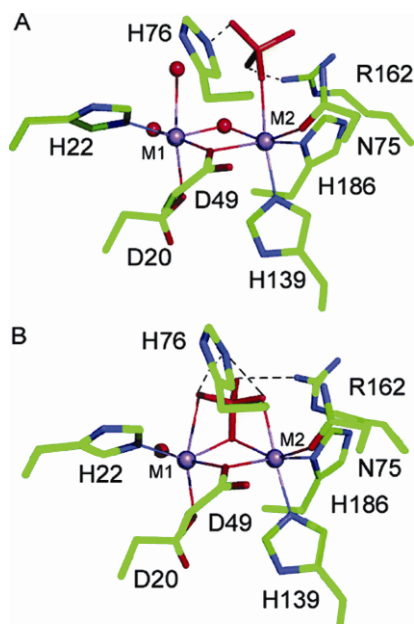
Figure 18. The active site of λPP complexed with sulfate (PDB code 1G5B). Sulfate binds in two different modes to the active site: (A) monodentately to the metal ion in site M2 and (B) tridentately, with two of its oxygen atoms forming a μ-1,3 bridge and one coordinating in μ-1,1 mode. Reprinted with permission from [113]. Copyright © 2005, American Chemical Society. Please visit http://www.springer.com/978-1-4419-1138-4 to view a high-resolution full-color version of this illustration.

His138 and His186, and three oxygen atoms, one of which is provided by Asn75. The remaining two oxygens are either from bridging water and a monodentate sulfate or from a bidentate sulfate. The asymmetric unit contains three enzyme molecules; in two of them the sulfate is bound terminally to manganese M2, in the other it binds in a bridging mode [122].

7.2. Spectroscopic Characterization

Following the reconstitution of λPP with manganese, and the removal of excess metal ions by dialysis, only one manganese ion remains tightly bound to the protein [123]. The EPR spectrum of this species shows a nearly isotropic six-line feature centered around $g = 2$, typical of Mn(II). The spectrum shows additional features, such as a peak at $g_{eff} = 2.73$, a six-line pattern at $g_{eff} = 4.05$ (a forbidden $\Delta M_s = \pm 2$ transition, characteristic of Mn(II) ions with a relatively large zero field splitting) and a weak, near zero field transition at $g_{eff} > 17$ [123].

An EPR titration of λPP with Mn(II) has demonstrated that the active site can accommodate a binuclear Mn(II)Mn(II) center. The two metal binding sites, similar to many other binuclear metalloenzymes [113], are characterized by substantial
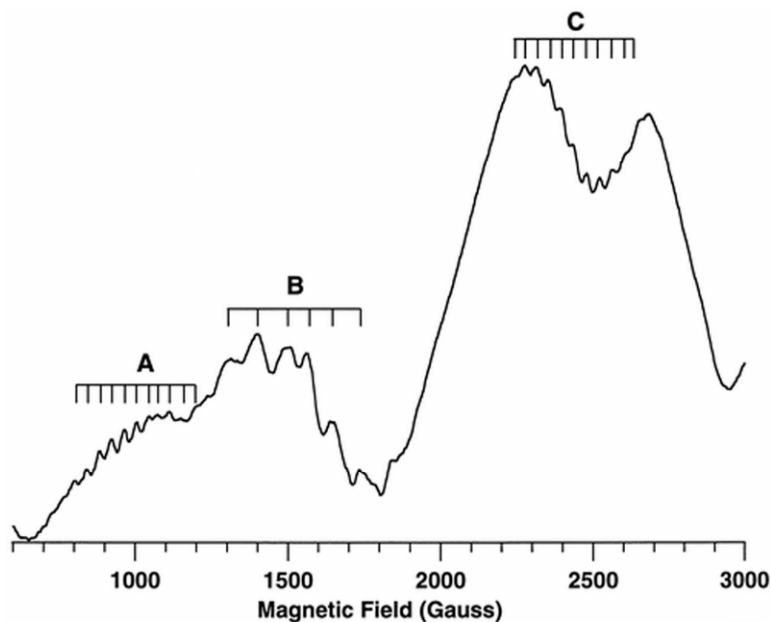
Figure 19. Multiline hyperfine pattern of λPP arising from an exchange-coupled binuclear Mn(II) center. A and C denote the positions of the hyperfine split resonances due to a coupled cluster with an average splitting of 3.9 mT, while B corresponds to a residual 6-line spectrum arising from the mononuclear enzyme. Reprinted with permission from [123]. Copyright © 1999, American Chemical Society.

differences in their affinities for the metal ions, with K_D values of ~2 and ~160 μM [123]. When less than 0.8 equivalents are added to the enzyme, the spectrum resembles that described above for the mononuclear manganese species. However, as the Mn(II) concentration is increased further, a spectrum attributed to a spin-coupled Mn(II)$_2$ cluster emerges (Fig. 19). Specifically, at 3.7 K the intensity of the g_{eff} = 4.05 resonance diminishes significantly, the near zero field transition disappears, and the feature at g_{eff} ~ 2.7 is replaced by a similar but broad and unresolved transition [123]. Unfortunately, hexaaqua Mn(II) obscures the g = 2 region of the spectrum. With increasing temperature (≥7 K), new features appear in the spectrum. At 31 K there are distinct resonances at g_{eff} = 14.6, 2.93, and 2.51, a shoulder at g_{eff} = 1.45, and a very broad feature at high field. Two of the features display 11-line hyperfine patterns with a splitting ($A/g\beta$) of 3.9 mT, characteristic of exchange-coupled binuclear Mn(II) ions. Fitting the temperature dependence of some of the features to an S_T = 2 state yields an exchange coupling constant of 1–3 cm^{-1} [123]. The spectra have not been simulated, but the manganese M2 site has been identified as the higher-affinity site via site-directed mutagenesis studies [124]. In all mutants involving active site and surrounding residues, the capacity for forming a binuclear center was retained, but the EPR spectra showed some differences [124].

The EPR spectra of various inhibitor-bound complexes have also been investigated. In the presence of tungstate, vanadate, phosphate, arsenate, and phosphonoacetohydroxamic acid (PhAH), the binuclear-type spectrum was apparent at low temperature (3.5 K), indicating that the binding of the inhibitors has effected a decrease in the exchange coupling constant in comparison to the unligated enzyme, suggesting a change in the bridging interaction between the metal ions. Consideration of the spectra of the inhibitor-bound species indicates some small, but possibly significant differences between the bound enzymes. In the vanadate-bound enzyme in particular there are numerous hyperfine lines resolved, which may be attributable to a superhyperfine interaction with the ^{51}V nucleus. However, simulations of these spectra have not yet been undertaken [121]. It has been proposed that PhAH may interact with the active site via a bridging carboxylate. Tungstate and vanadate, which are capable of adopting trigonal bipyramidal geometries, may also provide an additional μ-oxo bridge, explaining the change in the observed exchange coupling [121]. Interestingly, the spectra are unaffected by the presence of sulfate, suggesting that the sulfate bridging mode observed crystallographically may be irrelevant in solution [121,122].

In the di-iron derivative of λPP, a rhombic EPR signal with $g < 2$ is observed, indicative of the formation of a heterovalent, coupled Fe(III)Fe(II) center [117]. Upon mutation of a non-ligating active site histidine (His76), the spectrum changes, indicative of some perturbation of the ligand environment, possibly via disruption of a hydrogen bond between the histidine and a metal-coordinated water molecule. The observation of the heterovalent iron cluster is in contrast to the homovalent binuclear Mn(II) active site and is attributed to an $E^{0\prime}$ of >128 mV for the Fe(III)Fe(II)–Fe(II)Fe(II) couple. Consequently, a homovalent binuclear iron active site is likely in vivo [125].

7.3. Mechanistic Implications

The reaction mechanism of λPP is similar to that proposed for other metallophosphoesterases, as discussed in a number of recent review articles [1,113]. Based on the difference in the metal ion affinities of the two sites, it has been suggested that the second metal ion may enter the active site along with the substrate, as is observed, for instance, for the 3′-5′ proofreading exonuclease activity [126]. It remains unclear how the dianionic phosphoester binds to the active site, with both monodentate and bridging binding modes being proposed [124,127]. The bridging mode is favored because it requires a minimal rearrangement to accommodate the leaving group. A metal-bound hyroxide has been identified as the hydrolysis-initiating nucleophile, but it is unclear whether this nucleophile is terminally bound to one of the metal ions, or bridging the metal ions [119,124,127]. A bridging nucleophile appears ideally positioned for an in-line attack on the phosphorus atom of the phosphate group of the substrate (bound in a μ-1,3 mode). The kinetic pK_a attributed to the nucleophile is ~7.7 in the dimanganese enzyme [119], which is similar to the pK_a value attributed to a bridging water ligand in arginase (§10) [13.129].

His76 is likely to act as a proton donor to the leaving group [119,122,127]. Following release of the leaving group, the phosphate is likely to remain bound to the active site, either in a bidentate or tripodal mode, before being released, with regeneration of the active site [129].

8. PURPLE ACID PHOSPHATASE

8.1. Biochemical and Structural Characterization

Purple acid phosphatases (PAPs) have recently been reviewed in a number of articles [1,113,130]. In brief, PAPs are the only binuclear metallohydrolases with an established heterovalent binuclear metal center required for hydrolysis of a large range of predominantly monoester substrates. The biological functions of PAPs are organism dependent. In mammals, PAPs are involved in bone metabolism [131], bacterial killing [132], and possibly iron transport [133]. Plant PAPs may also be important for bacterial killing, but may also play an important role in phosphate uptake [134–136]. The metal ion composition for the catalytically active enzyme extracted from mammalian organisms is Fe(III)Fe(II) [137], whereas the plant counterparts have Fe(III)Zn(II) or Fe(III)Mn(II) centers [138–140]. Crystal structures for several animal and plant PAPs have been reported over the last decade, including those for the human, rat, pig, red kidney bean, and sweet potato enzymes [129,141–147]. Mammalian PAPs form ~35 kDa monomers, whereas the plant enzymes are homodimeric with ~55 kDa subunits. Each subunit in plant PAPs has two domains: a C-terminal one that accommodates the binuclear active site and is structurally closely related to animal PAPs, and an N-terminal domain of unknown function.

A PAP from sweet potato has been shown to require an Fe(III)Mn(II) center for optimal activity, and reconstitution experiments of the Fe(III) half apo enzyme with divalent metal ions other than manganese have been unsuccessful to date [4]. The crystal structure of this enzyme indicates that phosphate binds to the two metal ions, forming an unusual tripodal complex [144]. Recently, the apo form of this enzyme could be generated, and activity could be reconstituted by adding only manganese. While the enzyme is still an efficient catalyst, it has lost its ability to operate under acidic conditions [148]. Through EPR studies described below it was shown that an Mn(II)Mn(II) center was formed, this being the first homovalent catalytically active binuclear metal ion center in a PAP.

8.2. Spectroscopic Characterization

A PAP from sweet potato has been shown to have a specific requirement for manganese, forming an unusual, antiferromagnetically coupled Fe(III)Mn(II) center [4]. The X-band EPR spectrum of this enzyme shows no resonances from the Fe(III)Mn(II) center at temperatures up to ~200 K. From magnetic susceptibility measurements it was estimated that the exchange coupling constant was larger
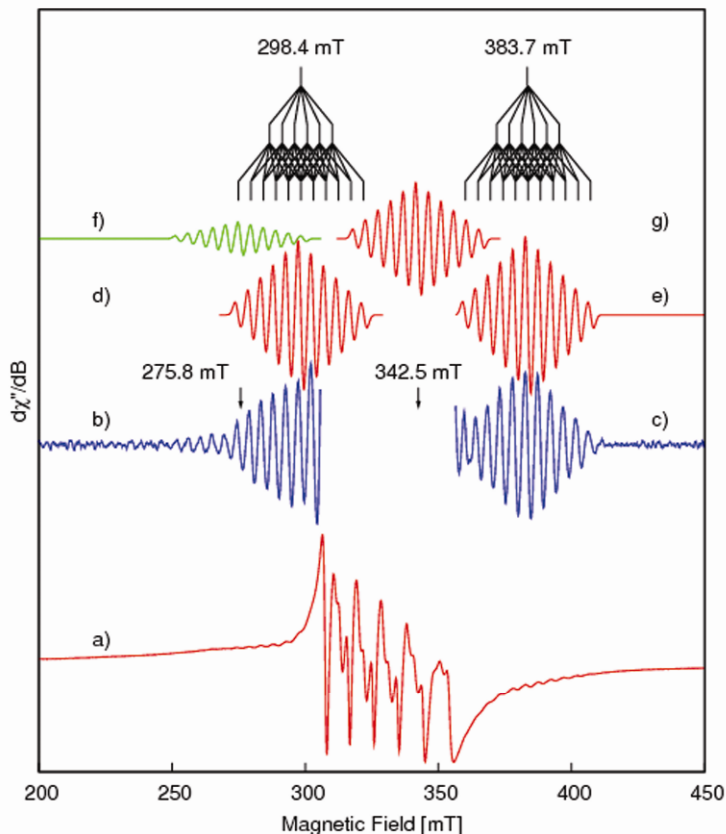
Figure 20. EPR spectrum of MnMn–spPAP at pH 6.5. ν = 9.382041 GHz, T = 4.7 K. The insets show an expansion of the experimental (b,c) resonances associated with the binuclear Mn(II) center after baseline correction with a cubic 55-point (low- and high-field sections) Savitsky-Golay filter [150]. (d,e) Computer simulation of (b) and (c), respectively, with the parameters g_S = 2.0023, A_1 = A_2 = 44.5 × 10^{-4} cm^{-1}, D_S = 410 × 10^{-4} cm^{-1}. (f,g) Fitting of the 11-line multiplets at 275.8 and 342.5 mT, respectively. Reprinted with permission from [148]. Copyright © 2009, American Chemical Society. Please visit http://www.springer.com/978-1-4419-1138-4 to view a high-resolution full-color version of this illustration.

than 150 cm^{-1}. While this enzyme appears to have a specific requirement for Mn(II), the Fe(III) site can be replaced by manganese. The enzyme was colorless and with the X-band EPR spectrum reveals resonances arising from an extraneous mononuclear Mn^{II} (S = 5/2, I = 5/2; g = 2, $A/g\beta$ = ~9.3 mT) center (<5%) and Mn hyperfine resonances on either side of this feature (Fig. 20). These hyperfine resonances are separated by $A/g\beta$ = 4.45 mT, which is half that expected for a mononuclear Mn(II) species, and characteristic of an exchange-coupled binuclear Mn(II) center [25,26,110,123,149]. Since resonances from the mononuclear Mn(II) center overlap with these resonances in the spectrum (Fig. 20) and are themselves inhomogenously broadened by a distribution of D and E values, a cubic Savitsky-Golay

filter [150] based on 55 points has been fitted to the low- and high-field regions (Fig. 20) to establish the relative intensities of the manganese hyperfine resonances, and they do indeed have the expected ratio (1:2:3:4:5:6:5:4:3:2:1) for a binuclear Mn(II) center (Fig. 20). Interestingly, the only resonances observed in the EPR spectrum of MnMn–spPAP are those centered at 275.8, 298.4, 342.5, and 383.7 mT. This can be readily explained by the presence of a large distribution of zero field splitting parameters, which broadens out the resonances from the other spin states (see numerical projection coefficients, Table 3.3 in [151]).

In order to gain an insight into the origin of the resonances, Molecular Sophe [152] (MoSophe) and Octave [153] were employed to simulate (fit) each of the four eleven-line multiplets (Fig. 20) with an effective $S_T = 1/2$ spin Hamiltonian to determine the resonant field positions for each of the multiplets and hyperfine couplings. Once the resonant field positions were determined, computer simulations (spectra, energy level diagrams, and roadmaps) using MoSophe [152] and an $S_T = 1/2$ spin Hamiltonian were used to fit the resonant field positions, assuming the resonances arise from an $S_T = 3$ spin state. The following spin Hamiltonian parameters ($g = 2.0023$, $A_1 = A_2 = 44.5 \times 10^{-4}\,\text{cm}^{-1}$, $D_S = 410 \times 10^{-4}\,\text{cm}^{-1}$) were found to reproduce the resonant field positions at 298.4 and 383.7 mT (Fig. 20). From the value of Ds ($D_S = D_1 + D_2 + D_{12}$) could be estimated by the dipole–dipole contribution (D_{12}) to be $745 \times 10^{-4}\,\text{cm}^{-1}$, which leads to an internuclear distance of 4.05 Å using the point dipole–dipole approximation. This represents an upper limit for the internuclear distance as the values of D_1 and D_2 will be nonzero, and without additional spectroscopic information their contribution cannot be defined as their magnitude, orientation of their principal axes, and sign remain unknown. A comparison of the internuclear Mn–Mn distance with a range of representative model complexes and metalloenzymes indicates that the most likely bridging ligands consist of one or more μ-OH, μ-OH$_2$, and μ-RCO$_2$ functional groups. This interpretation is in agreement with the alkaline shift in the pH optimum for the Mn(II)Mn(II) derivative when compared to the native enzyme, and identifies a chromphoric Mn(II)-bound hydroxide as the likely nucleophile [148].

8.3. Mechanistic Implications

The catalytic mechanism of PAPs has been reviewed extensively in recent articles [1,113]. The generation of a catalytically active Mn(II)Mn(II) center in a PAP, and the pH dependence of its catalytic parameters highlights the relevance of the bridging hydroxide as the likely hydrolysis-initiating nucleophile in this enzyme, but it also raises the interesting possibility that PAPs may have evolved from homodivalent binuclear ancestral metallohydrolases.

9. PHOSPHOTRIESTERASE

9.1. Biochemical and Structural Characterization

Phosphotriesterases (E.C. 3.1.8.1.) belong to the amidohydrolase superfamily of enzymes and are involved in the hydrolysis of a broad range of organophosphate

esters [154–158]. The ability to degrade these compounds has become increasingly important due to the widespread agricultural use of organophosphate pesticides. Likewise, the application of phosphoesterases in the degradation of nerve agents such as sarin or VX also gains increasing interest [155,159].

A number of phosphotriester-degrading enzymes have been isolated and characterized. The phosphotriesterase (PTE) from *Pseudomonas diminuta* is the best-studied example [154,160]. Others include the organophosphate-degrading PTE from *Agrobacterium radiobacter* (OPDA) [157,161–163] and methyl parathion hydrolase (MPH; from *Pseudomonas* sp.) [164,165]. PTE is a homodimeric protein and has a molecular weight of ~36 kDa/monomer [166]. The protein forms a TIM-barrel $(\alpha\beta)_8$ fold and the active site is located at the C-terminal end of the β-barrel. In its native form PTE binds two zinc ions in the active site, but metal ion replacement studies indicate that catalytic activity can be reconstituted with Mn(II), Co(II), Cd(II), and Ni(II) [167]. Crystal structures of PTE with a variety of metal ions and the substrate analog diethyl 4-methylbenzylphosphonate have been reported [168,169]. The catalytic center of PTE comprises a more buried α-metal ion that is coordinated in a trigonal bipyramidal arrangement, and a solvent exposed β-metal ion that is either octahedral or trigonal bipyramidal depending on the metal ion derivative. The two metal ions are bridged by a μ-1,3-carboxylated-lysine residue and one μ-H_2O/OH molecule [166].

9.2. Spectroscopic Characterization

A range of spectroscopic techniques, including [113]Cd NMR [170], X-ray crystallography [166], and EPR [171–173], have been employed to characterize the binuclear active site of PTE. EPR studies of Mn(II)-substituted PTE have been highly informative and have aided in the development of the currently proposed mechanism of catalysis.

X- and Q-band EPR spectra of Mn(II)–PTE at pH 8.3 exhibit features predominantly near $g = 2$ with more than 26 hyperfine resonances separated by $(A/g\beta)$ ~ 4.5 mT, half the magnitude expected for isolated Mn(II) [160]. This supports the presence of two spin-coupled Mn(II) ions in the active site. Initial studies assumed that the EPR signals arise from the $S_T = 1$ state of the coupled system, and an analysis of the temperature dependence of these signals yielded an isotropic Heisenberg exchange interaction of $J = -5 \pm 1$ cm^{-1} [160]. A subsequent study proposed, however, that the signals most likely arise from the quintet ($S_T = 2$) state ($J > D$) based on a comparison to more recent work and also the temperature dependence of a separate, broad resonance that is a better candidate for an $S_T = 1$ transition. The reevaluation of the exchange coupling based on this conclusion yielded $J = -2.7 \pm 0.2$ cm^{-1} [172]. In conjunction with metal-bridge distances determined by X-ray crystallography (2.0 and 2.1 Å) and comparison of the coupling to other known Mn(II) complexes, the magnitude of the exchange interaction suggests the presence of a bridging μ-hydroxide ligand at pH 8.3. The EPR parameters have also been determined by simulation of the experimental spectra. The simulation parameters for the best fit were: $g = 2.01$, $D = -0.055$ cm^{-1}, and $E = -0.0067$

cm^{-1}. These values are consistent with X-ray crystallographic studies suggesting less than axial symmetry [172].

The pH dependence of the EPR spectra has been studied in order to correlate spectral changes associated with the binuclear Mn center to the catalytic properties of the enzyme. Mn(II)–PTE is activated by the deprotonation of a species with a pK_a of 7.1, as observed in the pH-rate profile for the hydrolysis of paraoxon [172]. EPR spectra were collected at various pHs between pH 6.0 and 8.5. These reveal a gradual and reversible transition from a fully coupled binuclear Mn spectrum at high pH (as described above) to resonances that are typical of mononuclear Mn(II) at pH 6.0. The fraction of coupled binuclear Mn at each pH was calculated by double integration of the derivative EPR signal. A fit to this data resulted in an apparent pK_a of 7.3 [172]. This corresponds to the protonation of a bridging hydroxide, which, in turn, results in the loss of the Mn–Mn exchange interaction. The similarity of the pK_a values obtained by kinetic analysis (7.1) and EPR (7.3) provides strong evidence for the role of the bridging hydroxide as the hydrolysis-initiating nucleophile.

Further insight into the mechanism of hydrolysis by PTE has been achieved through EPR analysis of enzyme–inhibitor or enzyme–product complexes (Fig. 21). The addition of the reaction product diethylphosphate (DEP) and inhibitors diisopropylmethylphosphonate (DIMP) and triethylphosphate (TEP) produce several changes in the EPR spectrum compared with the native enzyme [173]. All three compounds cause a decrease in the binuclear Mn signals at $g = 2.2$ and an increase in the mononuclear Mn signals at $g = 2.0$. This observation is interpreted in terms of the loss of the hydroxide bridge upon binding of the inhibitor. No further perturbations are observed in the DEP bound sample. In the case of DIMP, additional hyperfine split resonances appear at $g_{eff} = 4.3$ and 3.8 (Fig. 21). The hyperfine resonances are separated by 4.5 mT ($A/g\beta$) and 9.0 mT ($A/g\beta$), respectively, and therefore indicate the presence of both coupled and uncoupled centers in the DIMP-bound sample. These higher field resonances are double quantum transitions between the M_S –1 and +1 levels within the $S_T = 1$ spin state. Emergence of these forbidden transitions occurs due to an increase in the zero field splitting, which is caused by a reduction in symmetry upon DIMP binding. TEP-bound PTE also displays an additional resonance at $g_{eff} = 4.3$, split by 11 hyperfine lines of 4.5 mT ($A/g\beta$) (Fig. 21). No half-field resonance from uncoupled Mn(II) is observed, suggesting higher symmetry in the uncoupled center of the TEP-bound sample than for PTE-DIMP. In addition to the half-field formally forbidden ($\Delta M_S = \pm 2$) transitions, TEP also induces the appearance of resonances at $g_{eff} = 1.7$ with hyperfine splittings of $A/g\beta = 8.8$ mT. The origin of this signal is unclear, but the hyperfine splittings indicate that it evolves from a distorted mononuclear Mn(II) center [173].

9.3. Mechanistic Implications

EPR has facilitated the elucidation of several key features in the mechanism of phosphotriester hydrolysis by PTE. Comparison of the kinetic pK_a values with
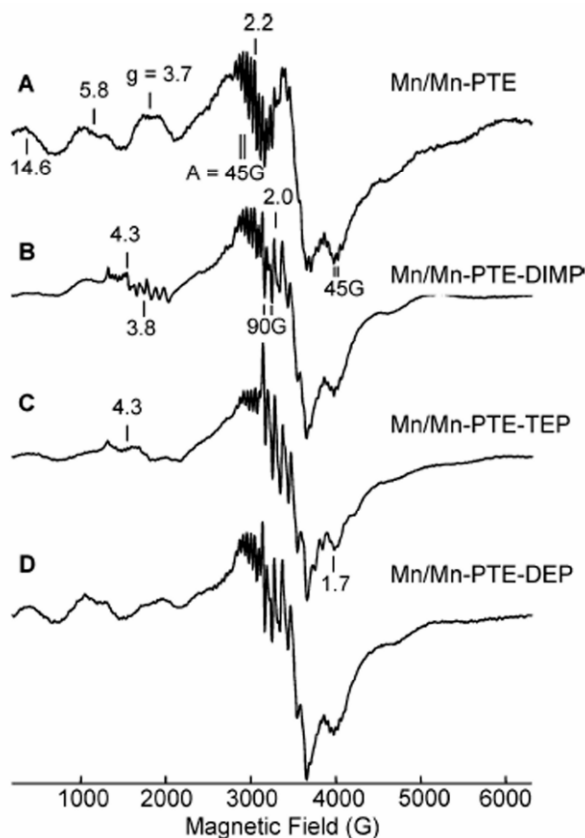
Figure 21. EPR spectra at 10 K of Mn$_2$–PTE with inhibitors and product bound. (A) 200 μM Mn$_2$–PTE; (B) 200 μM Mn$_2$–PTE with 171 mM DIMP; (C) 130 μM Mn$_2$–PTE with 350 mM TEP; (D) 115 μM Mn$_2$–PTE with 350 mM DEP. Reprinted with permission from [172]. Copyright © 2007, American Chemical Society.

those obtained from the analysis of EPR spectra has provided strong support for a bridging hydroxide as the rate-initiating nucleophile. EPR studies involving the binding of inhibitor and product molecules indicate a shift in equilibrium from primarily a bridged hydroxide species towards a nonbridged hydroxide species. In conjunction with kinetic and crystallographic data, this observation suggests that the phosphoryl oxygen of the substrate binds to the β-metal ion. As a result, the coordination of the hydroxyl bridge to the β-metal ion is weakened and its nucleophilic character is enhanced. A similar mechanism has been proposed for PAPs [129] and a glycerophosphodiesterase from *Enterobacter aerogenes* (GpdQ) [174]. The catalytic mechanism described by Aubert et al. [175] is shown in Figure 22.
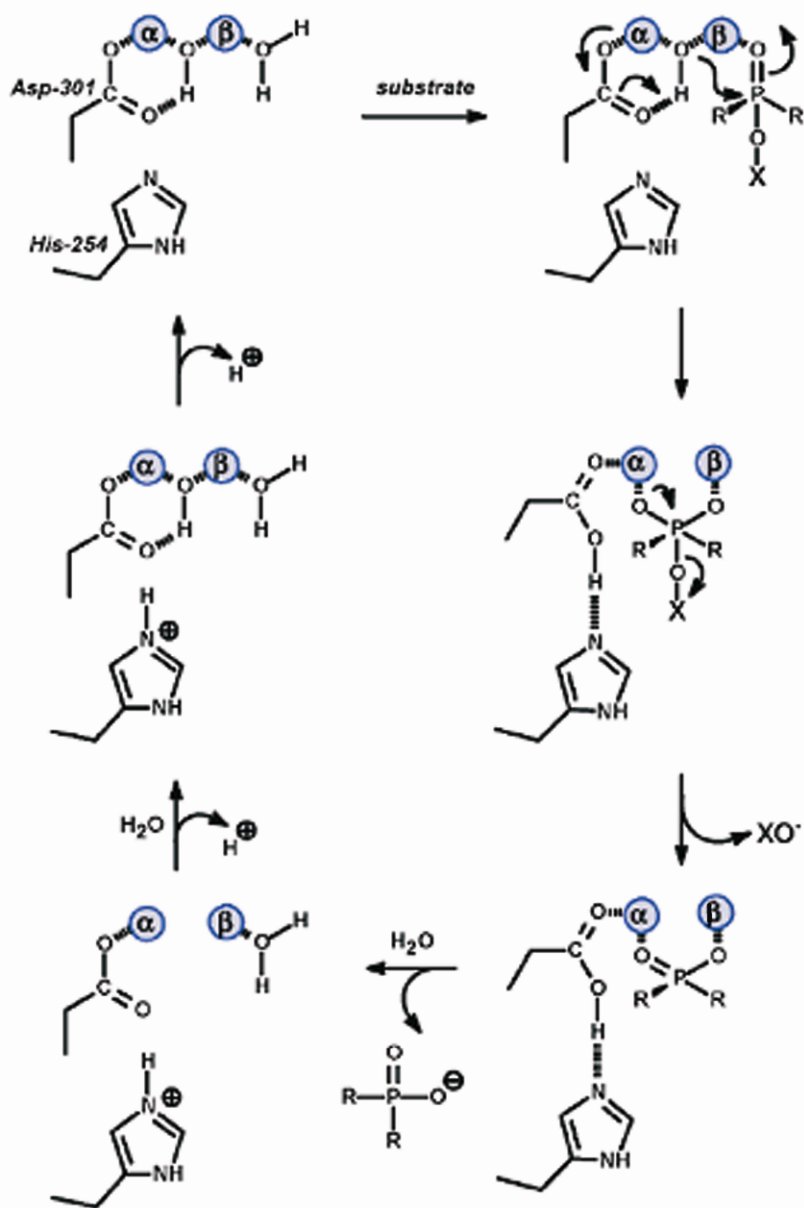
Figure 22. Mechanism of hydrolysis of PTE. Reprinted with permission from [174]. Copyright © 2007, American Chemical Society. Please visit http://www.springer.com/978-1-4419-1138-4 to view a high-resolution full-color version of this illustration.

10. ARGINASE

10.1. Biochemical and Structural Characterization

Arginase (E.C. 3.5.3.1) is an exclusively dimanganese enzyme that catalyzes the hydrolysis of L-arginine to L-ornithine and urea [5,13,176]. Two genetically distinct isozymes have been identified in vertebrates, and these differ in their tissue distribution and immunological reactivity [177]. Type I arginase is abundant in the liver and to a lesser extent in extra-hepatic tissue. It has a key role in nitrogen metabolism as it is responsible for the final cytosolic reaction that generates urea, the primary metabolite for disposal of nitrogen in the body. Deficiency of type I arginase in humans is a rare autosomal recessive disorder and results in hyperargininemia [178]. Symptoms of this disease include mental and growth retardation, seizures, and spastic tetraplegia [179]. The cause of hyperargininemia is thought to involve point mutations of the type I arginase gene [180]. Type II arginase is a mitochondrial enzyme that is present in extra-hepatic tissue, kidney, brain, skeletal muscle, heart, and pancreas [181]. This isozyme has been implicated in functioning as a regulator of L-arginine concentration for the biosynthesis of polyamines, proline, glutamate, and nitric oxide (NO) [182,183]. The ability of arginase type II to control NO levels has provided motivation for the design and understanding of arginase inhibitors as drugs that may control NO-dependent physiological processes such as erectile function [176].

A variety of X-ray crystal structures of the free enzyme and substrate/inhibitor complexes of both type I and II arginases are available (Fig. 23) [89,184–190]. Arginase I from rat liver was the first reported and has been the subject of the majority of EPR-related studies. It forms a homotrimeric protein with molecular mass of 35 kDa/subunit. Belonging to the α/β family of enzymes, it consists of a parallel, eight-stranded β-sheet flanked on both sides by numerous α helices. The binuclear center is located at the base of a ~15-Å deep active site cavity [182]. Each manganese ion is coordinated by a bridging (μ-aqua/hydroxo)(μ-1,3 carboxylato)(μ-1 carboxylato) moiety and to terminally bound histidine and aspartate residues (Fig. 23). The Mn–Mn internuclear separation as determined from the crystal structure is 3.3 Å.

In addition to the hydrolysis of L-arginine, arginase has also been shown to catalyze the disproportionation of hydrogen peroxide (catalase activity). The catalytic efficiency (k_{cat}/K_M) of arginase is 10^5–10^6 slower than in bacterial catalases [191]. It has been suggested that this is due to large differences in the redox potential of arginase compared with catalase and/or differences in the identity of proton transfer groups in the active site [13,191].

10.2. Spectroscopic Characterization

EPR-related studies of arginase have primarily focused on characterization of the solution structure and the binding modes of inhibitors. Fully activated rat liver
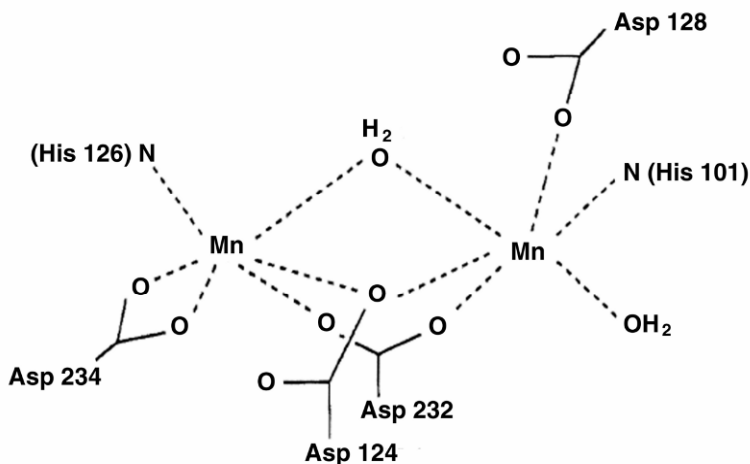
Figure 23. The active site of rat liver arginase. Reprinted with permission from [220]. Copyright © 2002, Elsevier.

arginase does not give rise to discernible X-band EPR signals at 4.2 K [25]. At 20 K a multiline spectrum is observed consisting of several regions that exhibit hyperfine resonances with a coupling constant ($A/g\beta$) of ~4.5 mT (Fig. 24) [192]. These spectral features are consistent with two exchange coupled Mn(II) ions with a diamagnetic ground state. A comparison of the EPR features with model complexes suggests that the signals arise from the triplet and quintet spin states, although predominantly the latter at 20 K [25]. Recent studies of unrelated model complexes propose that hyperfine coupling in exchange coupled binuclear Mn(II) systems is only observed for $S_T \geq 3$ transitions [26]. Further studies, possibly involving parallel mode EPR, may help to clarify the origin of these EPR transitions.

Temperature dependence of the tentative quintet ($S_T = 2$) state confirms that the manganese centers are antiferromagnetically coupled with a Heisenberg exchange interaction of $J \approx -2.0 \pm 0.5$ cm^{-1} [193]. Based on a comparison with other bridged binuclear manganese species, it is inferred that an exchange coupling of this size is mediated by a μ-aqua ligand. The description of the bridging solvent molecule as a μ-aqua ligand also agrees with EXAFS studies [3] and X-ray crystallography, which depicts a symmetrical Mn–O distance of 2.4 Å [89]. The internuclear manganese distance can be calculated from the zero field splitting of the quintet state, which can be determined from the high-field resonances in the experimental spectrum. In the native enzyme, three high-field transitions of this nature are observed, and a distribution of distances (3.4 to 3.6 Å) has been deduced [25]. This has been interpreted as the enzyme having multiple forms in solution at neutral pH, where the aqua ligand can freely migrate between the bridging and terminal positions [13]. The Heisenberg exchange coupling appears to be constant from pH 6.3
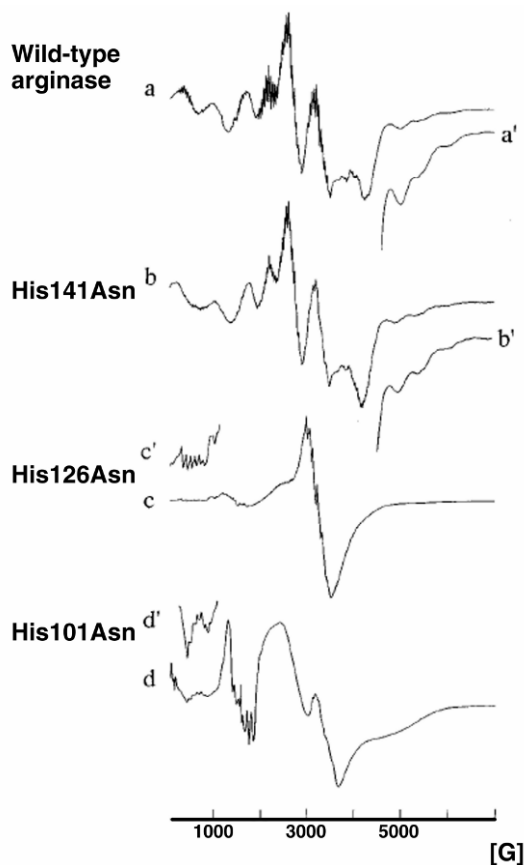
Figure 24. EPR spectra of wild-type arginase (a), His141Asn mutant (b), His126Asn mutant (c and c'), and His 101Asn mutant (d and d'). Spectra were recorded at 14.0 K, 15.0 K, 16.0 K, and 17.0 K, respectively. Reprinted with permission from [192]. Copyright © 1998, American Chemical Society.

to 9.2, and therefore it has been inferred that the solvent bridge does not undergo ionization over this range [193]. This result is in disagreement with other studies that conclude that the observed pK_a of 7.9 in the kinetic rate profile is attributed to deprotonation of μ-H_2O to form a nucleophilic μ-OH species [13,89,176,194]. Khangulov et al. attribute the observed protonation equilibria at $pK_a \approx 7.9$ to His141 that acts as a base when deprotonated [193]. This hypothesis is based on kinetic and EPR characterization of the His141Asn mutant, which exhibits a 10-fold reduction in hydrolytic activity and an unperturbed EPR spectrum of the binuclear Mn center (Fig. 24).

A number of enzyme–inhibitor complexes have been characterized by EPR, and this has led to identification of two classes of arginase inhibitors (Fig. 25). Class I inhibitors include L-ornithine (K_i = 1.0 mM), L-citrulline, L-isoleucine,

borate ($IC_{50} > 50$ mM), and hydroxylamine ($IC_{50} = 2$ mM) [191]. These produce minor changes in the lineshape of the Mn_2 signal, suggesting only a weak or outer sphere interaction with the Mn center (Fig. 25). Borate and L-ornithine have been
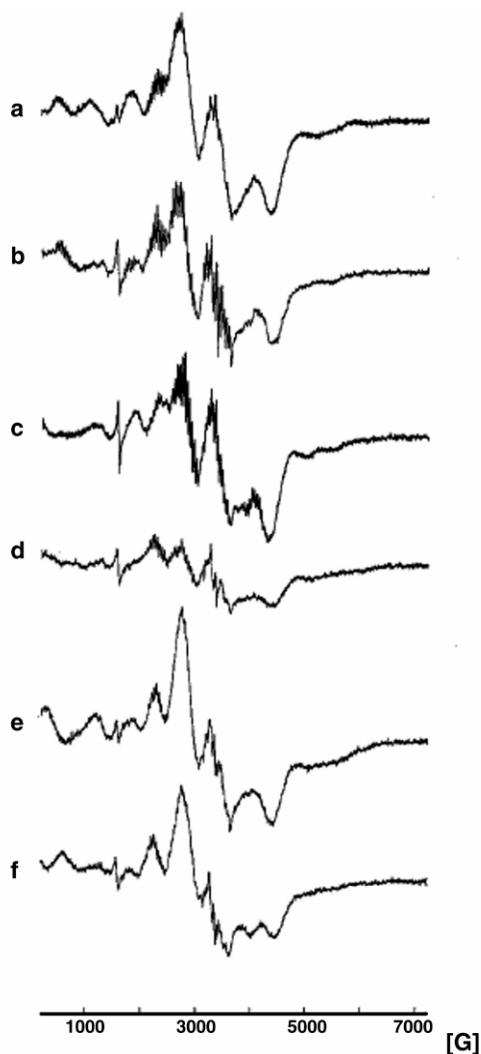
Figure 25. Effect of inhibitors of the EPR spectrum of wild-type arginase at 22 K. Uninhibited (a); 4.0 mM L-ornithine (b); 1.2 mM L-citrulline (c); and 3.0 mM L-lysine (d). Traces (e) and (f): the EPR signal from (d) is restored by addition of 1.8 mM isoleucine (e) and 2.2 mM borate (f). Reprinted with permission from [192]. Copyright © 1998, American Chemical Society.

shown to convert the three high-field resonances that appear in the free enzyme to a single broad resonance that corresponds to a unique Mn–Mn distance of 3.50 Å [193]. The exact mode in which these inhibitors bind is uncertain. A crystal structure of arginase complexed with borate depicts the displacement of the bridging solvent molecule in the free enzyme by an oxygen atom of the tetrahedral borate anion [195]. An alternative X-ray structural model has been proposed based on the magnitude of the exchange coupling for the borate-inhibited species. This involves a Lewis acid complex between a μ-OH$^-$ and boric acid, forming a μ–HO–B(OH)$_3^-$ bridge [193].

Class II inhibitors of arginase include L-lysine, L-valine, and N^{ω}-hydroxy-L-arginine (NOHA), and these induce the loss of the binuclear Mn EPR signal and appearance of a minor mononuclear Mn(II) signal (Fig. 25) [191]. These changes have been attributed to either (i) an increase in the zero field splitting (ZFS > J) of the binuclear Mn centers, rendering the EPR transitions extremely broad and difficult to detect at X-band, or (ii) as a result of decoupling of the two Mn ions [193]. The former interpretation is supported by EPR data of the His101Asn mutant that contains only one manganese ion. In this case, the EPR signal is almost completely eliminated in the L-lysine inhibited form due to an increase in the zero field splitting of the Mn ion. However, the authors of the study favor decoupling of the Mn electron spins as the mechanism for loss of the EPR signal [193]. The exchange interaction is reduced to $J \approx 0$, and any EPR signal arising from the individual Mn ions is broadened by the remaining magnetic dipole–dipole interaction. It has been suggested that decoupling could occur as a result of the breakage of the μ-aqua bridge and subsequent migration of the aqua ligand to a terminal position. This binding mode, however, is inconsistent with those proposed on the basis of inhibitor binding affinities and models for the binding of substrate to the enzyme [196,197].

One of the most potent inhibitors (K_i = 0.5 μM) of arginase is N^{ω}-hydroxy-nor-L-arginine (nor-NOHA), having one less –CH$_2$– group than NOHA [196]. Membership of this inhibitor to class I or class II has not been established, however, EPR measurements of the enzyme–inhibitor complex exhibits many class I-like characteristics. Almost all EPR features of free arginase were altered upon treatment with nor-NOHA, including a reduction in intensity or loss of the 272 and 183 mT signals and an increase in intensity of the 413 mT signal [198]. The three zero field splitting resonances at high field in native arginase were replaced by one resonance, also reminiscent of a class I inhibitor. It was proposed that nor-NOHA interacts with the binuclear Mn cluster, altering the Mn–Mn distance, possibly due to replacement of the bridging solvent ligand by its N–OH moiety. Further studies are required to clarify the structural and spectroscopic interaction of these inhibitors with arginase.

EPR spectroscopy has also been used as a tool to help elucidate the role of several active site residues in the catalytic mechanism. Replacement of His126 and His101 for asparagine results in predominantly mononuclear Mn(II) EPR resonances (Fig. 24) [193]. Catalytic activity in these mutant species is also lost, con-

firming the requirement of a binuclear Mn center for catalysis. Characterization of the Gly235Arg, one of the mutations identified in humans that leads to hyperargininemia, has also been performed by EPR [199]. Gly235 is the neighboring amino acid to Asp234, which is coordinated terminally to one manganese ion. Upon addition of Mn(II) to Gly235Arg, only signals attributed to free Mn(II) were observed in the EPR spectrum, indicating an inability of this mutant to bind Mn(II). Without an intact binuclear center, the enzyme is rendered inactive and therefore unable to perform its biochemical function.

The ability of arginase to catalyze disproportionation of hydrogen peroxide (catalase activity) has also been investigated. A fourfold weaker exchange coupling exists in the case of arginase when compared with catalase, and X-ray crystallography has confirmed these enzymes have different bridging structures [17]. Hydroxylamine, a known inhibitor of catalases, has been shown to inhibit both the hydrolytic and redox activity of arginase. EPR spectra indicate that hydroxylamine binds to arginase in a similar fashion to known class I inhibitors, reducing the three high-field resonances to one single trough [191]. In contrast to catalase, EPR indicates that arginase cannot be superoxidized to an Mn(III)–Mn(IV) form by treatment with hydroxylamine and hydrogen peroxide and persists in the Mn(II)–Mn(II) oxidation state [191].

10.3. Mechanistic Implications

There are two distinct proposals for the catalytic mechanism of arginase [89,193]. The mechanism based on EPR studies depicts four key steps (Fig. 26) [193]. The first step entails deprotonation of the guanidinium proton of L-arginine(H^+) by His141 prior to binding of the terminal imino N atom to one Mn(II) ion. L-arginine is proposed to bind in a similar fashion to known class II inhibitors, resulting in breakage of the μ-aqua bridge and decoupling of the binuclear center. The second step involves transfer of a proton from a terminally bound aqua ligand to the N^δ-guanidinium atom of the substrate and, as a consequence, the nucleophilic hydroxide evolves (Fig. 26). The third step is the nucleophilic attack on the guanidinium carbon atom, forming a tetrahedral intermediate. The final step of catalysis involves transfer of a second proton to N^δ and the subsequent cleavage of the C^ε–N^δ bond forming the products L-ornithine(H^+) and urea. L-ornithine(H^+) can diffuse immediately from the active site; however, proton transfer from His141 is required prior to release of urea [193].

An alternative mechanism proposed based primarily on X-ray crystal structure data of arginase with bound inhibitors also exists and opposes the EPR-based mechanistic strategy in several key aspects (Fig. 27) [89]. In brief, the differences include: (i) the binding mode of L-arginine to Glu277 and not to the binuclear Mn(II) center; (ii) deprotonation of the substrate by His141 is not required subsequent to substrate binding; and (iii) the bridging μ-hydroxide acts as the catalytic nucleophile, attacking the guanidinium carbon and forming a trivalent μ₃-oxo bridge (Fig. 27) [89].
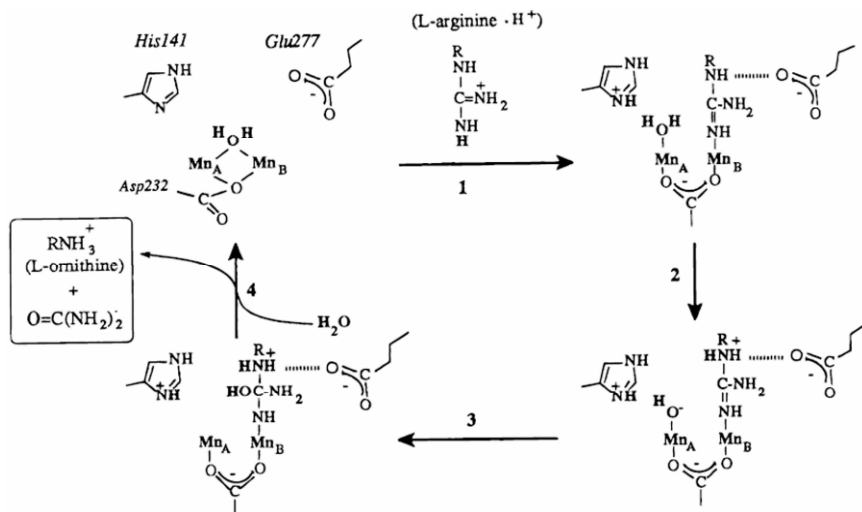
Figure 26. Mechanism of L-arginine hydrolysis proposed by Dismukes et al. based on research involving EPR. Reprinted with permission from [192]. Copyright © 1998, American Chemical Society.
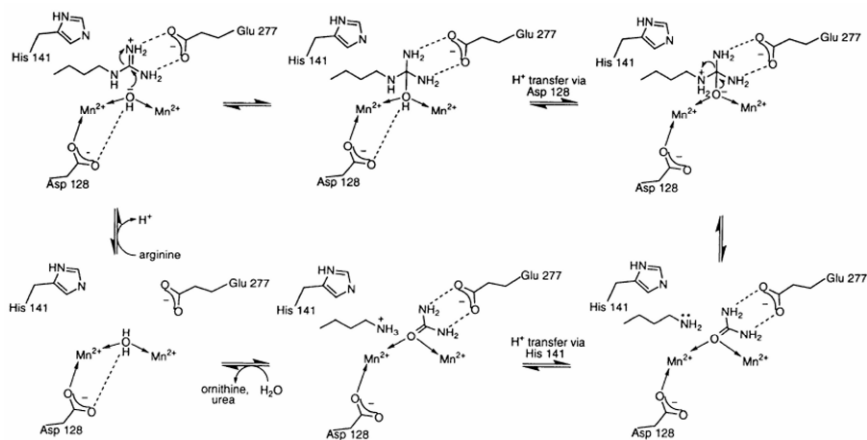
Figure 27. Mechanism of L-arginine hydrolysis proposed by Christianson et al. based primarily on X-ray crystallographic data. Reprinted with permission from [89]. Copyright © 1996, Macmillan Publishers Ltd.

11. METHIONYL AMINOPEPTIDASE

11.1. Biochemical and Structural Characterization

Methionyl aminopeptidases (MetAP) (E.C. 3.4.11.18) catalyze the removal of N-terminal methionine residues from polypeptide chains [200,201]. While the biological significance of this reaction is not fully understood, it is known that cleavage of methionine is required for biological activity, subcellular localization, and to groom proteins for degradation by other enzymes. MetAP is known to have a major role in the development of new blood vessels, tumor growth and metastasis, and for these reasons considerable interest has been directed toward the design of inhibitors and understanding the mechanism of MetAP [202,203]. Two anti-angiogenesis drugs, ovalicin and fumagillin, have both been shown to target MetAP, as well as TNP-470, a novel drug that is currently in phase III clinical trials [204–207].

MetAPs are classified into two distinct types that are characterized by the absence (type I) or presence (type II) of a sequence of 62 amino acids of unknown function near the C terminus [202]. Eurkaryotes have been shown to possess both types of MetAPs; however, bacteria and archaea appear to contain only type I or type II, respectively. Crystal structures are available for type I forms from *E. coli*, *Staphylococcus aureus*, and for type II forms found in *Homo sapiens* and *Pyrococcus furiosus* [207–210]. These structures depict a set of five invariant amino acid residues that bind two metal ions at the active site. A bis(μ-carboxylato)(μ-aqua/hydroxo)dimetal(II) moiety is observed at the core. There is some debate as to (i) the identity of the metal ions in vivo, and (ii) whether the enzyme operates in a mononuclear or binuclear form in vivo. MetAP was originally believed to be a Co(II)-containing enzyme, based on the availability of crystal structures of the Co(II) form and the ability of Co(II) to activate all metal-free MetAPs. Other studies have refuted this suggestion, and Zn(II), Fe(II), and Mn(II) have all been implicated as possible candidates for the in-vivo metal ion [211–213]. The number of metal ions involved in the catalytic mechanism is also a point of contention. MetAP-I from *E. coli* and MetAP-II from *P. furious* are both fully active with one equivalent of metal ion, and a combination of calorimetry, EXAFS, EPR, and NMR experiments support that these enzymes are mononuclear in vivo [214,215].

As mentioned above, the interaction of inhibitors such as fumagillin with MetAP is of interest due to its relevancy in treating tumors. Type II MetAPs are known to be the target for such drugs; however, fumagilin has also been shown to inhibit MetAP-I from *E. coli* [216]. Fumagilin interacts with the enzyme by forming a covalent bond to an active-site histidine residue. A crystal structure of MetAP-II from *H. sapiens* complexed with fumagilin illustrates this mode of binding and also reveals an additional interaction between an alkoxide moiety on fumagilin and the binuclear center [207].

11.2. Spectroscopic Characterization

EPR studies of Mn(II)-loaded MetAP have focused on the binding of fumagilin and the reaction product L-methionine. Spectra of uninhibited Mn(II)–MetAP-I from *E. coli* at 4 K exhibits six resonances at $g \sim 2$ with ^{55}Mn hyperfine splittings of $A/g\beta = 9.3$ mT, characteristic of mononuclear Mn(II) [217]. Other features that are attributable to mononuclear Mn(II) transitions are also present. These include six resonances centered at $g_{eff} = 4.15$, arising from a formerly forbidden ($\Delta M_S = \pm 2$) transition, a weak six-line pattern at $g_{eff} = 9.0$, and a signal extending out of zero field. The latter two features have been assigned to inter-Kramer doublet transitions where $M_S = \pm 5/2 \leftrightarrow 3/2$ or $M_S = 3/2 \leftrightarrow 1/2$. EPR resonances that originate from a coupled binuclear Mn(II) center become evident with increasing temperature. At 41 K, additional features at $g_{eff} = 3.19, 2.85, 2.39, 1.60, 1.43$, and 1.31 are observed, and multiline hyperfine structure consistent with two exchange-coupled Mn(II) ions is evident [217]. The appearance of these features with increasing temperatures implies that they are due to transitions from within the $S_T = 1, 2, 3, 4,$ or 5 non-Kramer doublets that arise from two antiferromagnetically coupled Mn(II) ions in the strong exchange regime ($J > D$) with a diamagnetic ground state. Confirmation that these signals originate from integer spin states was achieved by the use of parallel mode EPR [217]. The temperature dependence of spectra collected in parallel mode suggest the assignment of a signal at $g_{eff} = 18$ to either an $S_T = 4$ or 5 transition, a shoulder at $g_{eff} = 12$ to an $S_T = 3$ spin state transition, and a feature at $g_{eff} = 4.2$ to an $S_T = 1$ transition. The resonances at $g_{eff} = 2.39$ and 1.60 in perpendicular mode were fitted to a Boltzmann distribution for the quintet $S_T = 2$ state of an exchange-coupled Mn(II) system and gave $J \approx 7$ cm^{-1}. The zero field splitting of the quintet state is correlated with the inter-manganese distance, and comparison of this parameter (-0.175 cm^{-1}) with other compounds provided an internuclear distance of 3.1 Å. This is in good agreement with the cobalt–cobalt distance of 3.2 Å obtained by X-ray crystallography [208,218]. The EPR spectra of Mn(II)–MetAP-II from *P. furiosus* are virtually identical to that of the Mn(II)–MetAP-I from *E. coli*, as described above. Although deconvolution of the EPR signals arising from the coupled dimer was more complicated in the enzyme from *P. furiosus* due to overlap in both the spectral and temperature domains, it was noted that the temperature dependence was consistent with antiferromagnetically coupled Mn(II) ions exhibiting modest exchange coupling ($J \ll 50$ cm^{-1}) [219].

Complexation of Mn(II)–MetAP-I from *E. coli* with fumagillin results in only small perturbations of the spin-coupled Mn(II) EPR resonances. A small shift of 2.0 mT and an increase in intensity of 30% in the multiline signals at ~260–315 mT, in addition to the appearance of an additional multiline pattern in the 387–434 mT region were observed [217]. These changes imply a reduction in the *g*-strain broadening upon binding with fumagillin to the Mn(II) center and a possible decrease in the vibrational freedom compared with the free enzyme. Moreover, the EPR spectra strongly discounts the report [207] that the alkoxide oxygen of fumagillin is directly coordinated to the Mn(II) center of MetAP-I in solution.
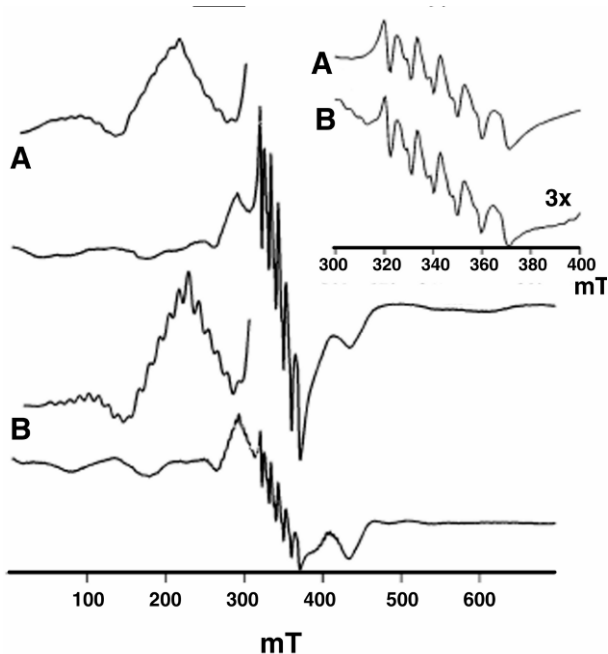
Figure 28. EPR spectrum of Mn$_2$–MetAP from *E. coli* (A) and from *P. furiosus* (B) with L-methionine bound. Spectra are recorded at 40 K. Reprinted with permission from [218]. Copyright © 2005, American Chemical Society.

EPR studies of MetAP from *E. coli* and *P. furiosis* complexed with the reaction product L-methionine have further highlighted the similarities and differences between type I and type II MetAPs (Fig. 28). L-methionine appears to increase either the resolution or relative amplitude of the multiline binuclear Mn signals in both species of enzyme due to a reduced lability of the Mn(II) ions or a reduced distribution of the zero field splitting parameters [219]. The hyperfine resonances in the EPR spectra of L-methionine-bound enzymes are also better resolved, indicating a smaller distribution in the zero field splitting or *g* values (Fig. 28). The relative intensity of the resonances from mononuclear and binuclear Mn(II) transitions in both perpendicular and parallel mode indicate a different mode of binding of L-methionine to MetAP. In particular, an increased amount of mononuclear Mn(II) is observed in MetAP-II from *P. furiosis* as compared to the type I enzyme from *E. coli* [219]. With support of electronic absorption data and X-ray crystallography, it was proposed that in the case of type II MetAPs a carboxylate oxygen of L-methionine binds to only one Mn(II) ion, whereas in type I MetAPs the equivalent oxygen atom forms a bridge. In both cases, the L-methionine molecule is bound to the second Mn(II) ion by an N-terminal amine nitrogen atom [219].

11.3. Mechanistic Implications

Given the uncertainty of whether MetAP operates as a mononuclear or binuclear enzyme, investigations into the catalytic mechanism of MetAP have considered a distinct mechanism for both possibilities. EPR-related studies have made a large contribution to our understanding of the catalytic cycle of the binuclear form of both type I and type II MetAPs and have also been useful in understanding the interaction of fumagillin with the enzyme. While these studies have led to the suggestion that the mechanism of action for MetAPs with only one metal ion bound is identical for the type I and II forms, there appear to be differences when two metal ions are present. On the basis of kinetic, X-ray crystallographic, and spectroscopic data including EPR, a mechanism for type II MetAPs has been proposed (Fig. 29) [219]. In brief, catalysis is initiated by recognition of the N-terminal methionine sidechain by the hydrophobic pocket adjacent to the active site of the enzyme. The peptide carbonyl oxygen of methionine then coordinates to the histidine-ligated divalent metal ion [219]. When both metal binding sites are occupied, the N-terminal amine is coordinated to the second metal ion. Hydrolytic cleavage of the
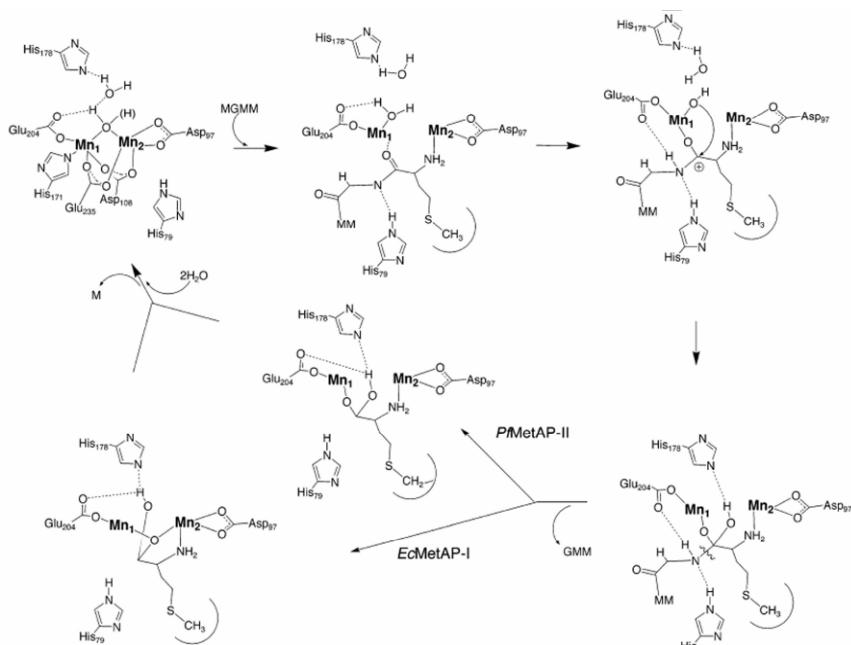
Figure 29. Proposed mechanism of hydrolysis of Mn_2–MetAP enzyme. Reprinted with permission from [218]. Copyright © 2005, American Chemical Society.

C–N bond occurs by nucleophilic attack by the hydroxide molecule bound terminally to the histidine-ligated metal ion (Fig. 29). Hydrogen bonding between His79 and the backbone N–H scissile peptide bond acts to stabilise the leaving group and Glu204 has been proposed to act as a proton acceptor/donor in catalysis. After release of the cleaved peptide, the L-methionine bound form of the enzyme transpires. As discussed, the structure of this species is distinct for type I and type II forms of the enzyme, and therefore the catalytic mechanisms diverge at this point. The final catalytic stage is release of L-methionine by addition of two water molecules [219].

REFERENCES

1. Mitić N, Hanson GR, Schenk G. 2009. Multinuclear non-heme iron enzymes. In *Biological magnetic resonance*, Vol. 28: *High resolution EPR: applications to metalloenzymes and metals in medicine*, pp. 269–395. Ed GR Hanson, LJ Beliner. New York: Springer.

2. Jiang W, Bollinger JM, Krebs C. 2007. The active form of *Chlamydia trachomatis* ribonucleotide reductase R2 protein contains a heterodinuclear Mn(IV)/Fe(III) cluster with $S = 1$ ground state. *J Am Chem Soc* **129**:7504–7505.

3. Stemmler TL, Sossong TM Jr, Goldstein JI, Ash DE, Elgren TE, Kurtz DM, Penner-Hahn JE. 1997. EXAFS comparison of the dimanganese core structures of manganese catalase, arginase, and manganese-substituted ribonucleotide reductase and hemerythrin. *Biochemistry* **36**:9847–9858.

4. Schenk G, Boutchard CL, Carrington LE, Noble CJ, Moubaraki B, Murray KS, de Jersey J, Hanson GR, Hamilton S. 2001. A purple acid phosphatase from sweet potato contains an antiferromagnetically coupled binuclear Fe–Mn center. *J Biol Chem* **276**:19084–19088.

5. Ash DE, Cox JD, Christianson DW. 1999. Arginase: a binuclear manganese metalloenzyme. In *Metal ions in biological systems*, pp. 407–428. Ed A Sigel, H Sigel. New York: Marcel Dekker.

6. Yoder DW, Hwang J, Penner-Hahn JE. 2000. Manganese catalases. In *Manganese and its role in biological processes*, pp. 527–557. Ed A Sigel, H Sigel, New York: Marcel Dekker.

7. Kono Y, Fridovich I. 1983. Isolation and characterization of the pseudocatalase of *Lactobacillus plantarum*. *J Biol Chem* **258**:6015–6019.

8. Barynin VV, Vagin AA, Melik-Adamyan WR, Grebenko AI, Khangulov SV, Popov AN, Andrianova ME, Vainshtein BK 1986. Three-dimensional structure of the T-catalase with a 3-Å resolution. *Dokl Akad Nauk SSSR* **288**:877–880.

9. Robbe-Saule V, Coynault C, Ibanez-Ruiz M, Hermant D, Norel F 2001. Identification of a non-haem catalase in Salmonella and its regulation by RpoS (σS). *Mol Microbiol* **39**:1533–1545.

10. Kagawa M, Murakoshi N, Nishikawa Y, Matsumoto G, Kurata Y, Mizobata T, Kawata Y, Nagai J 1999. Purification and cloning of a thermostable manganese catalase from a thermophilic bacterium. *Arch Biochem Biophys* **362**:346–355.

11. Allgood GS, Perry JJ. 1986. Characterization of a manganese-containing catalase from the obligate thermophile *Thermleophilum album*. *J Bacteriol* **168**:563–567.

12. Amo T, Atomi H, Imanaka T. 2002. Unique presence of a manganese catalase in a hyperthermophilic archaeon, *Pyrobaculum calidifontis* VA1. *J Bacteriol* **184**:3305–3312.

13. Dismukes GC. 1996. Manganese enzymes with binuclear active sites. *Chem Rev* **96**:2909–2926.

14. Antonyuk SV, Melik-Adamyan WR, Popov AN, Lamzin VS, Hempstead PD, Harrison PM, Artymyuk PJ, Barynin VV. 2000. Three-dimensional structure of the enzyme dimanganese catalase from *Thermus thermophilus* at 1 Å resolution. *Crystallogr Rep* **45**:105–116.

15. Barynin VV, Whittaker MM, Antonyuk SV, Lamzin VS, Harrison PM, Artymiuk PJ, Whittaker JW. 2001. Crystal structure of manganese catalase from *Lactobacillus plantarum*. *Structure* **9**:725–738.

16. Whittaker MM, Barynin VV, Igarashi T, Whittaker JW. 2003. Outer sphere mutagenesis of *Lactobacillus plantarum* manganese catalase disrupts the cluster core: mechanistic implications. *Eur J Biochem* **270**:1102–1116.

17. Barynin VV, Hempstead PD, Vagin AA, Antonyuk SV, Melik-Adamyan WR, Lamzin VS, Harrison PM, Artymiuk PJ. 1997. The three-dimensional structure of the di-Mn catalase, and the environment of the di-Mn sites in different redox states. *J Inorg Biochem* **67**:196.

18. Whittaker MM, Barynin VV, Antonyuk SV, Whittaker JW. 1999. The oxidized (3,3) state of manganese catalase. Comparison of enzymes from *Thermus thermophilus* and *Lactobacillus plantarum*. *Biochemistry* **38**:9126–9136.

19. Khangulov SV, Goldfeld MG, Gerasimenko VV, Andreeva NE, Barynin VV, Grebenko AI 1990. Effect of anions and redox state on the activity of manganese containing catalase from *Thermus thermophilus*. *J Inorg Biochem* **40**:279–292.

20. Waldo GS, Penner-Hahn JE. 1995. Mechanism of manganese catalase peroxide disproportionation: determination of manganese oxidation states during turnover. *Biochemistry* **34**:1507–1512.

21. Mukhopadhyay S, Mandal SK, Bhaduri S, Armstrong WH. 2004. Manganese clusters with relevance to photosystem II. *Chem Rev* **104**:3981–4026.

22. Wu AJ, Penner-Hahn JE, Pecoraro VL. 2004. Structural, spectroscopic, and reactivity models for the manganese catalases. *Chem Rev* **104**:903–938.

23. Khangulov S, Barynin VV, Voevodskaya NV, Grebenko AI. 1990. ESR spectroscopy of the binuclear cluster of manganese ions in the active center of Mn-catalase from *Thermus thermophilus*. *Biochim Biophys Acta* **1020**:305–310.

24. Meier AE, Whittaker MM, Whittaker JW. 1996. EPR polarization studies on Mn catalase from *Lactobacillus plantarum*. *Biochemistry* **35**:348–360.

25. Khangulov S, Pessiki PJ, Barynin VV, Ash DE, Dismukes GC. 1995. Determination of the metal ion separation and energies of the three lowest electronic states of dimanganese(II,II) complexes and enzymes: catalase and liver arginase. *Biochemistry* **34**:2015–2025.

26. Golombek AP, Hendrich MP. 2003. Quantitative analysis of dinuclear manganese(II) EPR spectra. *J Magn Reson* **165**:33–48.

27. Jacquamet L, Michaud-Soret I, Debaecker-Petit N, Barynin VV, Zimmermann J-L, Latour J-M. 1997. Magnetization studies of the reduced active form of the catalase from *Thermus thermophilus*. *Angew Chem, Int Ed* **36**:1626–1629.

28. Le Pape L, Perret E, Michaud-Soret I, Latour J-M. 2002. Magnetization studies of the active and fluoride-inhibited derivatives of the reduced catalase of *Lactobacillus plan-*

tarum: toward a general picture of the anion-inhibited and active forms of the reduced dimanganese catalases. *J Biol Inorg Chem* **7**:445–450.

29. Michaud-Soret I, Jacquamet L, Debaecker-Petit N, Le Pape L, Barynin VV, Latour J-M. 1998. The existence of two oxidised Mn(III)Mn(III) forms of *Thermus thermophilus* manganese catalase. *Inorg Chem* **37**:3874–3876.

30. Sarrou J, Ioannidis N, Deligiannakis Y, Petrouleas V. 1998. A Mn(II)–Mn(III) EPR signal arises from the interaction of NO with the S1 state of the water oxidising complex of photosystem II. *Biochemistry* **37**:3581–3587.

31. Teutloff C, Schäfer K-O, Sinnecker S, Barynin V, Bittl R, Wieghardt K, Lendzian F, Lubitz W. 2005. High-field EPR investigations of Mn^{III}Mn^{IV} and Mn^{II}Mn^{III} states of dimanganese catalase and related model systems. *Magn Reson Chem* **43**:S51–64.

32. Zheng M, Khangulov SV, Dismukes GC, Barynin VV. 1994. Electronic structure of dimanganese(II,III) and dimanganese(III,IV) complexes and dimanganese catalase enzyme: a general EPR spectral simulation approach. *Inorg Chem* **33**:382–387.

33. Fronko RM, Penner-Hahn JE, Bender CJ. 1988. EPR spectral evidence for a dinuclear active site in the *Lactobacillus plantarum* manganese catalase. *J Am Chem Soc* **110**:7554–7555.

34. Haddy A, Waldo GS, Sands RH, Penner-Hahn JE. 1994. Simulation of multifrequency EPR spectra from Mn(III)/Mn(IV) catalase of *Lactobacillus plantarum* using a new approach based on perturbation theory. *Inorg Chem* **33**:2677–2682.

35. Ivancich A, Barynin VV, Zimmermann J-L. 1995. Pulsed EPR studies of the binuclear Mn(III)Mn(IV) center in catalase from *Thermus thermophilus*. *Biochemistry* **34**:6628–6639.

36. Khangulov S, Sivaraja M, Barynin VV, Dismukes GC. 1993. The dimanganese(III,IV) oxidation state of catalase from *Thermus thermophilus*: electron nuclear double resonance analysis of water and protein ligands in the active site. *Biochemistry* **32**:4912–4924.

37. Schäfer K-O, Bittl R, Lendzian F, Barynin V, Weyhermueller T, Wieghardt K, Lubitz W. 2003. Multifrequency EPR investigation of dimanganese catalase and related Mn(III)Mn(IV) complexes. *J Phys Chem B* **107**:1242–1250.

38. Sinnecker S, Neese F, Noodleman L, Lubitz W. 2004. Calculating the electron paramagnetic resonance paramaters of exchange coupled transition metal complexes using broken symmetry density functional theory: application to a Mn^{III}Mn^{IV} model compound. J Am Chem Soc **126**:2613–2622.

39. Stemmler TL, Sturgeon BE, Randall DW, Britt RD, Penner-Hahn JE. 1997. Spectroscopic characterization of inhibitor interactions with the Mn(III)/Mn(IV) core in *Lactobacillus plantarum* manganese catalase. *J Am Chem Soc* **119**:9215–9225.

40. Schäfer K-O, Bittl R, Zweygart W, Lendzian F, Haselhorst G, Weyhermueller T, Weighardt K, Lubitz W. 1998. Electronic structure of antiferromagnetically coupled dinuclear manganese (Mn^{III}Mn^{IV}) complexes studied by magnetic resonance techniques. *J Am Chem Soc* **120**:13104–13120.

41. Waldo GS, Yu S, Penner-Hahn JE. 1992. Structural characterization of the binuclear Mn site in *Lactobacillus plantarum* manganese catalase. *J Am Chem Soc* **114**:5869–5870.

42. Gamelin DR, Kirk ML, Stemmler TL, Pal A, Armstrong WH, Penner-Hahn JE, Solomon EI. 1994. Electronic structure and spectroscopy of manganese catalase and di-μ-oxo [Mn^{III}Mn^{IV}] model complexes. *J Am Chem Soc* **116**:2392–2399.

43. Boelrijk AEM, Dismukes GC. 2000. Mechanism of hydrogen peroxide dismutation by a dimanganese catalase mimic: dominant role of an intramolecular base on substrate binding affinity and rate acceleration. *Inorg Chem* **39**:3020–3028.

44. Nordlund P, Reichard P. 2006. Ribonucleotide reductases. *Annu Rev Biochem* **75**:681–706.

45. Stubbe J. 2003. Di-iron-tyrosyl radical ribonucleotide reductases. *Curr Opin Chem Biol* **7**:183–188.

46. Stubbe J, Nocera DG, Yee CS, Chang MCY. 2003. Radical initiation in the class I ribonucleotide reductase: long-range proton-coupled electron transfer? *Chem Rev* **103**:2167–2202.

47. Jordan A, Reichard P. 1998. Ribonucleotide reductases. *Annu Rev Biochem* **67**:71–98.

48. Högbom M, Stenmark P, Voevodskaya N, McClarty G, Gräslund A, Nordlund P. 2004. The radical site in chlamydial ribonucleotide reductase defines a new R2 subclass. *Science* **305**:245–248.

49. Jordan A, Gilbert I, Barbé J. 1994. Cloning and sequencing of the genes from *Salmonella typhimurium* encoding a new bacterial ribonucleotide reductase. *J Bacteriol* **176**:3420–3427.

50. Jordan A, Pontis E, Åslund F, Hellman U, Gilbert I, Reichard P. 1996. The ribonucleotide reductase system of *Lactococcus lactis*. *J Biol Chem* **271**:8779–8785.

51. Jordan A, Pontis E, Atta M, Krook M, Gilbert I, Barbé J, Reichard P. 1994. A second class I ribonucleotide reductase in Enterobacteriaceae: characterization of the *Salmonella typhimurium* enzyme. *Proc Natl Acad Sci USA* **91**:12892–12896.

52. Baker CH, Banzon J, Bollinger JM, Stubbe J, Samano V, Robins MJ, Lippert B, Jarvi E, Resvick R. 1991. 2'-Deoxy-2'-methylenecytidine and 2'-deoxy-2',2'-difluorocytidine 5'-diphosphates: potent mechanism-based inhibitors of ribonucleotide reductase. *J Med Chem* **34**:1879–1884.

53. Mayhew CN, Phillips JD, Greenberg RN, Birch NJ, Elford HL, Gallicchio VS. 1999. In vivo and in vitro comparison of the short-term hematopoietic toxicity between hydroxyurea and Trimidox or Didox, novel ribonucleotide reductase inhibitors with potential anti-HIV-1 activity. *Stem Cells* **17**:345–356.

54. Lori F, Malykh A, Cara A, Sun D, Weinstein JN, Lisziewicz J, Gallo RC. 1994. Hydroxyurea as an inhibitor of human immunodeficiency virus-type 1 replication. *Science* **266**:801–805.

55. Van der Donk WA, Yu G, Pérez L, Sanchez RJ, Stubbe J, Samano V, Robins MJ. 1998. Detection of a new substrate-derived radical during inactivation of ribonucleotide reductase from *Escherichia coli* by gemcitabine 5-diphosphate. *Biochemistry* **37**:6419–6426.

56. Roshick C, Iliffe-Lee ER, McClarty G. 2000. Cloning and characterization of ribonucleotide reductase from *Chlamydia trachomatis*. *J Biol Chem* **275**:38111–38119.

57. Voevodskaya N, Lendzian F, Gräslund A. 2005. A stable Fe^{III}–Fe^{IV} replacement of tyrosyl radical in a class I ribonucleotide reductase. *Biochem Biophys Res Commun* **330**:1213–1216.

58. Voevodskaya N, Narvaez A-J, Domkin V, Torrents E, Thelander L, Graeslund A. 2006. Chlamydial ribonucleotide reductase: tyrosyl radical function in catalysis replaced by the Fe^{III}–Fe^{IV} cluster. *Proc Natl Acad Sci USA* **103**:9850–9854.

59. Jiang W, Yun D, Saleh L, Barr EW, Xing G, Hoffart LM, Maslak M-A, Krebs C, Bollinger JM. 2007. A manganese(IV)/iron(III) cofactor in *Chlamydia trachomatis* ribonucleotide reductase. *Science* **316**:1188–1191.

60. Voevodskaya N, Lendzian F, Ehrenberg A, Graeslund A. 2007. High catalytic activity achieved with a mixed manganese–iron site in protein R2 of Chlamydia ribonucleotide reductase. *FEBS Lett* **581**:3351–3355.

61. Fritscher J, Artin E, Wnuk S, Bar G, Robblee JH, Kacprzak S, Kaupp M, Griffin RG, Bennati M, Stubbe J. 2005. Structure of the nitrogen-centered radical formed during inactivation of *E. coli* ribonucleotide reductase by 2'-azido-2'-deoxyuridine-5'-diphosphatase: trapping of the 3'-ketonucleotide. *J Am Chem Soc* **127**:7729–7738.

62. Stubbe J, van der Donk WA. 1998. Protein radicals in enzyme catalysis. *Chem Rev* **98**:705–762.

63. Eliasson R, Pontis E, Eckstein F, Reichard P 1994. Interactions of 2'-modified azido- and haloanalogs of deoxycytidine 5'-triphosphate with the anaerobic ribonucleotide reductase of *Escherichia coli*. *J Biol Chem* **269**:26116–26120.

64. Jiang W, Hoffart LM, Krebs C, Bollinger JM. 2007. A manganese(IV)/iron(IV) intermediate in assembly of the manganese(IV)/iron(III) cofactor of *Chlamydia trachomatis* ribonucleotide reductase. *Biochemistry* **46**:8709–8716.

65. Sinnecker S, Neese F, Lubitz W. 2005. Dimanganese catalase-spectroscopic parameters from broken-symmetry density functional theory of the superoxidized MnIII/MnIV state. *J Biol Inorg Chem* **10**:231–238.

66. Lee SK, Fox BG, Froland WA, Lipscomb JD, Munck E. 1993. A transient intermediate of the methane monooxygenase catalytic cycle containing an $Fe^{IV}Fe^{IV}$ cluster. *J Am Chem Soc* **115**:6450–6451.

67. Liu KE, Wang D, Huynh BH, Edmondson DE, Salifoglou A, Lippard SJ. 1994. Spectroscopic detection of intermediates in the reaction of dioxygen with the reduced methane monooxygenase/hydroxlase from *Methylococcus capsulatus* (Bath). *J Am Chem Soc* **116**:7465–7466.

68. Jiang W, Xie J, Nørgaard H, Bollinger JM, Krebs C. 2008. Rapid and quantitative activation of *Chlamydia trachomatis* ribonucleotide reductase by hydrogen peroxide. *Biochemistry* **47**:4477–4483.

69. Jiang W, Saleh L, Barr EW, Xie J, Gardner MM, Krebs C, Bollinger JM. 2008. Branched activation- and catalysis-specific pathways for electron relay to the manganese/iron cofactor in ribonucleotide reductase from *Chlamydia trachomatis*. *Biochemistry* **47**:8477–8484.

70. Shu L, Nesheim JC, Kauffmann K, Münck E, Lipscomb JD, Que L. 1997. An $Fe_2^{IV}O_2$ diamond core structure for the key intermediate Q of methane monooxygenase. *Science* **275**:515–518.

71. Jordan A, Aragall E, Gibert I, Barbé J. 1996. Promoter identification and expression analysis of *Salmonella typhimurium* and *Escherichia coli* nrdEF operons encoding one to two class I ribonucleotide reductases present in both bacteria. *Mol Microbiol* **19**:777–790.

72. Jordan A, Åslund F, Pontis E, Reichard P, Holmgren A. 1997. Characterization of *Escherichia coli* NrdH: a glytaredoxin-like protein with a thioredoxin-like activity profile. *J Biol Chem* **272**:18044–18050.

73. Jordan A, Gibert I, Barbé J. 1995. Two different operons for the same function: comparison of the *Salmonella typhimurium* nrd AB and *nrdEF* genes. *Gene* **167**:75–79.

74. Himmelreich R, Plagens H, Hilbert H, Reiner B, Herrmann R. 1997. Comparative analysis of the genomes of the bacteria *Mycoplasma pneumoniae* and *Mycoplasma genitalium*. *Nucleic Acids Res* **25**:701–712.

75. Scotti C, Valbuzzi A, Perego M, Galizzi A, Albertini AM. 1996. The *Bacillus subtilis* genes for ribonucleotide reductase are similar to the genes for the second class I NrdE/NrdF enzymes of *Enterobacteriaceae*. *Microbiology* **142**:2995–3004.

76. Yang F, Rubin H. 1994. Isolation of ribonucleotide reductase from *Mycobacterium tuberculosis* and cloning, expression, and purification of the large subunit. *J Bacteriol* **176**:6738–6743.

77. Nordlund P, Eklund H. 1995. Di-iron-carboxylate proteins. *Curr Opin Struct Biol* **5**:758–766.

78. Eriksson M, Jordan A, Eklund H. 1998. Structure of *Salmonella typhimurium* nrdF ribonucleotide reductase in its oxidized and reduced forms. *Biochemistry* **37**:13359–13369.

79. Uppsten M, Färnegårdh M, Domkin V, Uhlin U 2006. The first holocomplex structure of ribonucleotide reductase gives new insight into its mechanism of action. *J Mol Biol* **359**:365–377.

80. Högbom M, Huque Y, Sjöberg B-M, Nordlund P. 2002. Crystal structure of the di-iron/radical protein of ribonucleotide reductase from *Corynebacterium ammoniagenes*. *Biochemistry* **41**:1381–1389.

81. Schimpff-Weiland G, Follmann H. 1981. A new manganese-activated ribonucleotide reductase found in gram-positive bacteria. *Biochem Biophys Res Commun* **102**:1276–1282.

82. Willing A, Follmann H, Auling G. 1988. Ribonucleotide reductase of *Brevibacterium ammoniagenes* is a manganese enzyme. *Eur J Biochem* **170**:603–611.

83. Auling G, Thaler M, Diekmann H. 1997. Parameters of unbalanced growth and reversible inhibition of deoxyribonucleic acid synthesis in *Brevibacterium ammoniagenes* ATCC 6872 induced by depletion of Mn^{2+}: inhibitor studies on the reversibility of deoxyribonucleic acid synthesis. *Arch Microbiol* **127**:105–114.

84. Huque Y, Fieschi F, Torrents E, Gibert I, Eliasson R, Reichard P, Sahlin M, Sjöberg B-M. 2000. The active form of the R2F protein of class Ib ribonucleotide reductase from *Corynebacterium ammoniagenes* is a diferric protein. *J Biol Chem* **275**:25365–25371.

85. Griepenburg U, Blasczyk K, Kappl R, Hüttermann J, Auling G. 1998. A divalent metal site in the small subunit of the manganese-dependent ribonucleotide reductase of *Corynebacterium ammoniagenes*. *Biochemistry* **37**:7992–7996.

86. Antanaitis BC, Brown RD, Chasteen ND, Freedman JH, Koenig SH, Lilienthal HR, Peisach J, Brewer CF. 1987. Electron paramagnetic resonance and magnetic susceptibility studies of dimanganese concanavalin A: evidence for antiferromagnetic exchange coupling. *Biochemistry* **26**:7932–7937.

87. Dismukes GC, Siderer Y. 1982. Intermediates of a polynuclear manganese center involved in photosynthetic oxidation of water. *Proc Natl Acad Sci USA* **78**:274–278.

88. Fieschi F, Torrents E, Toulokhonova L, Jordan A, Hellman E, Barbe J, Gibert I, Karlsson M, Sjöberg B-M. 1998. The manganese-containing ribonucleotide reductase of *Corynebacterium ammoniagenes* is a class Ib enzyme. *J Biol Chem* **273**:4329–4337.

89. Kanyo ZF, Scolnick LR, Ash DE, Christianson DW. 1996. Strucutre of a unique binuclear manganese cluster in arginase. *Nature* **383**:554–557.

90. Allard P, Barra AL, Andersson KK, Schmidt PP, Atta M, Gräslund A. 1996. Characterization of a new tyrosyl free radical in *Salmonella typhimurium* ribonucleotide reductase with EPR at 9.45 and 245 GHz. *J Am Chem Soc* **118**:895–896.

91. Graslund A, Sahlin M. 1996. Electron paramagnetic resonance and nuclear magnetic resonance studies of class I ribonucleotide reductase. *Annu Rev Biophys Biomol Struct* **25**:259–286.

92. Sahlin M, Petersson L, Graeslund A, Ehrenberg A, Sjoeberg B-M, Thelander L. 1987. Magnetic interaction between the tyrosyl free radical and the antiferromagnetically coupled iron center in ribonucleotide reductase. *Biochemistry* **26**:5541–5548.

93. Galander M, Uppsten M, Uhlin U, Lendzian F. 2006. Orientation of the tyrosyl radical in *Salmonella typhimurium* class Ib ribonucleotide reductase determined by high field EPR of R2F single crystals. *J Biol Chem* **281**:31743–31752.

94. Simurdiak M, Lee J, Zhao H. 2006. A new class of arylamine oxygenases: evidence that *p*-aminobenzoate *N*-oxygenase (AurF) is a di-iron enzyme and further mechanistic studies. *ChemBioChem* **7**:1169–1172.

95. Schwartz JL, Tishler M, Arison BH, Shafer HM, Omura S. 1976. Identification of mycolutein and pulvomycin as eureothin and labilomycin respectively. *J Antibiot* **29**:236–241.

96. Ziehl M, He J, Dahse H-M, Hertweck C. 2005. Mutasynthesis of aureonitrile: an eureothin derivative with significantly improved cytostatic effect. *Angew Chem, Int Ed Engl* **44**:1202–1205.

97. Winkler R, Richter MEA, Knüpfer U, Merten D, Hertweck C. 2006. Regio- and chemoselective enzymatic N-oxygenation in vivo, in vitro and in flow. *Angew Chem, Int Ed Engl* **45**:8016–8018.

98. Fox BG, Shanklin J, Ai J, Loehr TM, Sanders-Leohr J. 1994. Resonance raman evidence for an Fe–O–Fe center in stearoyl-ACP desaturase: primary sequence identity with other diiron-oxo proteins. *Biochemistry* **33**:12776–12786.

99. Andersson KK, Froland WA, Lee SK, Lipscomb JD. 1991. Dioxygen independent oxygenation of hydrocarbons by methane monooxygenase hydroxylase component. *New J Chem* **15**:411–415.

100. Winkler R, Hertweck C. 2005. Sequential enzymatic oxidation of aminoarenes to nitroarenes via hydroxylamines. *Angew Chem, Int Ed Engl* **44**:4083–4087.

101. Zocher G, Winkler R, Hertweck C, Schulz GE. 2007. Structure and action of the *N*-oxygenase AurF from *Streptomyces thioleteus*. *J Mol Biol* **373**:65–74.

102. Nordlund P, Eklund H. 1993. Structure and function of the *Escherichia coli* ribonucleotide reductase protein R2. *J Mol Biol* **232**:123–164.

103. Winkler R, Zocher G, Richter I, Friedrich T, Schulz GE, Hertweck C. 2007. A binuclear manganese cluster that catalyzes radical-mediated N-oxygenation. *Angew Chem, Int Ed Engl* **46**:8605–8608.

104. Mukherjee S, Weyhermüller T, Bothe E, Weighardt K, Chaudhuri P. 2004. Dinuclear and mononuclear manganese(IV)-radical complexes and their catalytic catecholase activity. *Dalton Trans* **22**:3842–3853.

105. Pierce BS, Elgren TE, Hendrich MP. 2003. Mechanistic implications for the formation of the diiron cluster in ribonucleotide reductase provided by quantitative EPR spectroscopy. *J Am Chem Soc* **125**:8748–8759.

106. Krebs C, Matthews ML, Jiang W, Bollinger JM. 2007. AurF from *Streptomyces thioluteus* and a possible new family of manganese/iron oxygenases. *Biochemistry* **46**:10413–10418.

107. Wallar BJ, Lipscomb JD. 1996. Dioxygen activation by enzyme containing binuclear non-heme iron clusters. *Chem Rev* **96**:2625–2658.

108. Friedrich C, Rother D, Bardischewsky F, Quentmeier A, Fischer J. 2001. Oxidation of reduced inorganic sulfur compounds by bacteria: emergence of a common mechanism? *Appl Environ Microbiol* **67**:2873–2882.

109. Quentmeier A, Hellwig P, Bardischewsky F, Grelle G, Kraft R, Friedrich CG. 2003. Sulfur oxidation in *Paracoccus pantotrophus*: interaction of the sulfur-binding protein SoxYZ with the dimanganese SoxB protein. *Biochem Biophys Res Commun* **312**:1011–1018.

110. Epel B, Schaefer KO, Quentmeier A, Friedrich C, Lubitz W. 2005. Multifrequency EPR analysis of the dimanganese cluster of the putative sulfate thiohydrolase SoxB of *Paracoccus pantotrophus*. *J Biol Inorg Chem* **10**:636–642.

111. Friedrich C, Quentmeier A, Bardischewsky F, Rother D, Kraft R, Kostka S, Prinz H. 2000. Novel genes coding for lithotrophic sulfur oxidation of *Paracoccus pantotrophus* BG17. *J Bacteriol* **182**:4677–4687.

112. Bagchi A, Ghosh TC. 2005. A structural study towards the understanding of interactions of SoxY, SoxZ and SoxB, leading to the oxidation of sulfur anions via the novel global sulfur oxidising (*sox*) operon. *Biochem Biophys Res Commun* **335**:609–615.

113. Mitić N, Smith SJ, Neves A, Guddat LW, Gahan LR, Schenk G. 2006. The catalytic mechanisms of binuclear metallohydrolases. *Chem Rev* **106**:3338–3363.

114. Cammack R, Chapman A, Lu W-P, Karagouni A, Kelly DP. 1989. Evidence that protein B of the thiosulfate-oxidizing system of *Thiobacillus versutus* contains a binuclear manganese cluster. *FEBS Lett* **253**:239–243.

115. Schäfer K-O. 2002. Exchange coupled manganese complexes: model systems for the active centres of redox proteins investigated with EPR techniques. PhD thesis. Max-Volmer-Laboratory, Institute for Chemistry, Technical University Berlin.

116. Lohse DL, Denu JM, Dixon JE 1995. Insights derived from the structures of the Ser/Thr phosphatases calcineurin and protein phosphatase 1. *Structure* **3**:987–990.

117. Mertz P, Yu L, Sikkink R, Rusnak F. 1997. Kinetic and spectroscopic analyses of mutants of a conserved histidine in the metallophosphatases calcineurin and λ protein phosphatase. *J Biol Chem* **272**:21296–21302.

118. Zhuo S, Clemens JC, Hakes DJ, Barford D, Dixon JE. 1993. Expression, purification, crystallization, and biochemical characterization of a recombinant protein phosphatase. *J Biol Chem* **268**:17754–17761.

119. Hoff RH, Mertz P, Rusnak F, Hengge AC. 1999. The transition state of the phosphoryl-transfer reaction catalysed by the lambda Ser/Thr protein phosphatase. *J Am Chem Soc* **121**:6382–6390.

120. Reiter TA, Reiter NJ, Rusnak F. 2002. Mn^{2+} is a native metal ion activator for bacteriophage lambda protein phosphatase. *Biochemistry* **41**:15404–15409.

121. Reiter NJ, White DJ, Rusnak F. 2002. Inhibition of bacteriophage lambda protein phosphatase by organic and oxoanion inhibitors. *Biochemistry* **41**:1051–1059.

122. Voegtli WC, White DJ, Reiter NJ, Rusnak F, Rosenzweig AC. 2000. Structure of the bacteriophage lambda ser/thr protein phosphatase with sulfate ion bound in two coordination modes. *Biochemistry* **39**:15365–15374.

123. Rusnak F, Yu L, Todorovic S, Mertz P. 1999. Interaction of bacteriophage lambda protein phosphatase with Mn(II): evidence for the formation of a $[Mn(II)]_2$ cluster. *Biochemistry* **38**:6943–6952.

124. White DJ, Reiter NJ, Sikkink RA, Yu L, Rusnak F. 2001. Identification of the high affinity Mn^{2+} binding site of bacteriophage lambda phosphoprotein phosphatase: ef-

fects of metal ligand mutations on electron paramagnetic resonance spectra and phosphatase activities. *Biochemistry* **40**:8918–8929.

125. Reiter T, Rusnak F. 2004. Electrochemical studies of the mono-Fe, Fe–Zn and Fe–Fe metalloisoforms of bacteriophage lambda protein phosphatase. *Biochemistry* **43**:782–790.

126. Park AY, Mitic N, Jessop LL, Urathamaku T, Carr PD, Ollis DL, Beck JL, Hanson GR, Schenk G, Dixon NE. 2009. Assembly of the binuclear metallocenter in the proof-reading (ε) subunit of *Escherichia coli* DNA polymerase III. Unpublished results.

127. Swingle MR, Honkanen RE, Ciszak EM. 2004. Structural basis for the catalytic activity of human serine/threonine protein phosphatase-5. J Biol Chem **279**:33992–33999.

128. Kuhn NJ, Ward S, Piponski M, Young TW. 1995. Purification of human hepatic arginase and its manganese(II)-dependent and pH-dependent interconversion between active and inactive forms: a possible pH-sensing function of the enzyme on the ornithine cycle. *Arch Biochem Biophys* **320**:24–34.

129. Schenk G, Elliott TW, Leung E, Carrington LE, Mitic N, Gahan LR, Guddat LW. 2008. Crystal structures of a purple acid phosphatase, representing different steps of this enzyme's catalytic cycle. *BMC Struct Biol* **8**:6.

130. Leung EWW, Teixeira M, Guddat LW, Mitic N, Schenk G. 2007. Structure, function and diversity of plant purple acid phosphatases. *Curr Top Plant Biol* **8**:21–31.

131. Oddie GW, Schenk G, Angel NZ, Walsh N, Guddat LW, de Jersey J, Cassady AI, Hamilton SE, Hume DA. 2000. Structure, function and regulation of tartrate-resistant acid phosphatase. *Bone* **27**:575–584.

132. Räisänen SR, Alatalo SL, Ylipahkala H, Halleen JM, Cassady AI, Hume DA, Vaananen HK. 2005. Macrophages overexpressing tartrate-resistant acid phosphatase show altered profile of free radical production and enhanced capacity of bacterial killing. *Biochem Biophys Res Commun* **331**:120–126.

133. Nuttleman PR, Roberts RM. 1990. Transfer of iron from uteroferrin (purple acid phosphatase) to transferrin related to acid phosphatase activity. *J Biol Chem* **265**:12192–12199.

134. Bozzo GG, Raghothama KG, Plaxton WC. 2002. Purification and characterization of two secreted purple acid phosphatases izozymes from phosphate-starved tomato (*Lycopersicon esculentum*) cell cultures. *Eur J Biochem* **269**:6278–6286.

135. Bozzo GG, Singh VK, Plaxton WC. 2004. Phosphate or phosphite addition promotes the proteolytic turnover of phosphate-starvation inducible tomato purple acid phosphatase isozymes. *FEBS Lett* **573**:51–54.

136. Rao MA, Gianfreda L, Palmiero F, Violante A. 1996. Interactions of acid phosphatase with clays, organic molecules and organo-mineral complexes. *Soil Sci* **161**:751–760.

137. Campbell HD, Dionysius DA, Keough DT, Wilson BE, de Jersey J, Zerner B. 1978. Iron-containing acid-phosphatases—comparison of enzymes from beef spleen and pig allantoic fluid. *Biochem Biophys Res Commun* **82**:615–620.

138. Beck JL, McConachie LA, Summors AC, Arnold WN, de Jersey J, Zerner B. 1986. Properties of a purple acid phosphatase from red kidney bean: a zinc-iron metalloenzyme. *Biochim Biophys Acta* **869**:61–68.

139. Durmus A, Eicken C, Sift BH, Kratel A, Kappl R, Huttermann J, Krebs B. 1999. The active site of purple acid phosphatase from sweet potatoes (*Ipomoea batatas*): metal content and spectroscopic characterization. *Eur J Biochem* **260**:709–716.

140. Schenk G, Ge Y, Carrington LE, Wynne CJ, Searle IR, Carroll BJ, Hamilton S, de Jersey J. 1999. Binuclear metal centers in plant purple acid phosphatases: Fe–Mn in sweet potato and Fe–Zn in soybean. *Arch Biochem Biophys* **370**:183–189.

141. Guddat LW, McAlpine AS, Hume D, Hamilton S, de Jersey J, Martin JL. 1999. Crystal structure of mammalian purple acid phosphatase. *Structure* **7**:757–767.

142. Klabunde T, Sträter N, Fröhlich R, Witzel H, Krebs B. 1996. Mechanism of Fe(III)–Zn(II) purple acid phosphatase based on crystal structures. *J Mol Biol* **259**:737–748.

143. Lindqvist Y, Johansson E, Kaija H, Vihko P, Schneider G. 1999. Three-dimensional structure of a mammalian purple acid phosphatase at 2.2 Å resolution with a μ-(hydr)oxo bridged di-iron center. *J Mol Biol* **291**:135–147.

144. Schenk G, Gahan LR, Carrington LE, Mitic N, Valizadeh M, Hamilton SE, de Jersey J, Guddat LW. 2005. Phosphate forms an unusual tripodal complex with the Fe–Mn center of sweet potato purple acid phosphatase. *Proc Natl Acad Sci USA* **102**:273–278.

145. Sträter N, Jasper B, Scholte M, Krebs B, Duff AP, Langley DB, Han RL, Averill BA, Freeman HC, Guss JM. 2005. Crystal structures of recombinant human purple acid phosphatase with and without an inhibitory conformation of the repression loop. *J Mol Biol* **351**:233–246.

146. Sträter N, Klabunde P, Tucker P, Witzel H, Krebs B. 1995. Crystal structure of a purple acid phosphatase containing a dinuclear Fe(III)–Zn(II) active site. *Science* **268**:1489–1492.

147. Uppenberg J, Lindqvist F, Svensson C, Ek-Rylander B, Andersson G. 1999. Crystal structure of a mammalian purple acid phosphatase. *J Mol Biol* **290**:201–211.

148. Mitic N, Noble CJ, Gahan LR, Hanson GR, Schenk G. 2009. Metal ion mutagenesis—conversion of a purple acid phosphatase from sweet potato to a neutral phosphatase with the formation of an unprecedented catalytically competent $Mn^{II}Mn^{II}$ active site. *J Am Chem Soc*. DOI:10.1021/ja900797u..

149. Howard T, Telser J, de Rose VJ. 2000. An electron paramagnetic resonance study of $Mn_2(H_2O)(OAc)_4(tmeda)_2$ (tmeda = *N,N,N',N'*-tetramethylethylenediamine): a model for dinuclear manganese enzyme active sites. *Inorg Chem* **39**:3379–3385.

150. Savitzky A, Golay MJE. 1964. Smoothing and differentiation of data by simplified least squares procedures. *Anal Chem* **36**:1627–1639.

151. Bencini A, Gateschi D. 1990. *EPR of exchange coupled systems*. Berlin: Springer-Verlag.

152. Hanson GR, Noble CJ, Benson S. 2009. Molecular Sophe: an integrated approach to the structural characterization of metalloproteins: the next generation of computer simulation software. In *Biological magnetic resonance*, Vol. 28: *High resolution EPR: applications to metalloenzymes and metals in medicine*, pp. 105–174. Ed GR Hanson, LJ Beliner. New York: Springer.

153. Octave is open source software and can be downloaded from http://www.gnu.org/software/octave/.

154. Donarski WJ, Dumas DP, Heitmeyer DP, Lewis VE, Raushel FM. 1989. Structure–activity relationships in the hydrolysis of substrates by the phosphotriesterase from *Pseudomonas diminuta. Biochemistry* **28**:4650–4655.

155. Ghanem E, Raushel FM. 2005. Detoxification of organophosphate nerve agents by bacterial phosphotriesterase. *Toxicol Appl Pharmacol* **207**:S459–S470.

156. Holm L, Sander C. 1997. An evolutionary treasure: unification of a broad set of amidohydrolases related to urease. *Proteins* **28**:72–82.

157. Jackson CJ, Carr PD, Kim H-K, Liu J-W, Herrald P, Mitic N, Schenk G, Clyde A, Ollis DL. 2006. Anomalous scattering analysis of *Agrobacterium radiobacter* phosphotriesterase: the prominent role of iron in the heterobinuclear active site. *Biochem J* **397**:501–508.

158. Raushel FM, Holden HM. 2000. Phosphotriesterase: an enzyme in search of its natural substrate. *Adv Enzymol Relat Areas Mol Biol* **74**:51–93.

159. Raushel FM. 2002. Bacterial detoxification of organophosphate nerve agents. *Curr Opin Microbiol* **5**:288–295.

160. Chae MY, Omburo GA, Lindahl PA, Raushel FM. 1993. Antiferromagnetic coupling in the binuclear metal cluster of manganese-substituted phosphotriesterase. *J Am Chem Soc* **115**:12173–12174.

161. Jackson C, Kim H-K, Carr PD, Liu J-W, Ollis DL. 2005. The structure of an enzyme-product complex reveals the critical role of a terminal hydroxide nucleophile in the bacterial phosphotriesterase mechanism. *Biochim Biophys Acta* **1752**:56–64.

162. Jackson CJ, Foo J-L, Kim H-K, Carr PD, Liu J-W, Salem G, Ollis DL. 2008. In crystallo capture of a Michaelis complex and product-binding modes of a bacterial phosphotriesterase. *J Mol Biol* **375**:1189–1196.

163. McLoughlin SY, Jackson C, Liu J-W, Ollis DL. 2004. Increased expression of a bacterial phosphotriesterase in *Escherichia coli* through directed evolution. *Protein Expression Purif* **41**:433–440.

164. Dong Y-J, Bartlam M, Sun L, Zhou Y-F, Zhang Z-P, Zhang C-G, Rao Z, Zhang X-E. 2005. Crystal structure of methyl parathion hydrolase from *Pseudomonas sp*. WBC-3. *J Mol Biol* **353**:655–663.

165. Wu X-P, Liu W-D, Cao H, Li S-P, Cui Z-L. 2005. Determination of the catalytic structures of methyl parathion hydrolase. *Chin J Biotechnol* **21**:998–1002.

166. Benning MM, Kuo JM, Raushel FM, Holden HM 1994. Three-dimensional structure of phosphotriesterase: an enzyme capable of detoxifying organophosphate nerve agents. *Biochemistry* **33**:15001–15007.

167. Omburo GA, Kuo JM, Mullins LS, Raushel FM. 1992. Characterization of the zinc binding site of bacterial phosphotriesterase. *J Biol Chem* **267**:13278–13283.

168. Benning MM, Shim H, Raushel FM, Holden HM. 2001. High resolution X-ray structure of different metal-substituted forms of phosphotriesterase from *Pseudomonas diminuta*. *Biochemistry* **40**:2712–2722.

169. Vanhooke JL, Benning MM, Raushel FM, Holden HM. 1996. Three-dimensional structure of the zinc-containing phosphotriesterase with the bound substrate analog diethyl 4-methylbenzylphosphonate. *Biochemistry* **35**:6020–6025.

170. Krauss M, Olsen L, Antony J, Hemmingsen L. 2002. Coordination geometries of Zn(II) and Cd(II) in Phosphotriesterase: influence of water molecules in the active site. *J Phys Chem B* **106**:9446–9453.

171. Chae MY, Omburo GA, Lindahl PA, Raushel FM. 1995. Utilization of copper as a paramagnetic probe for the binuclear metal center of phosphotriesterase. *Arch Biochem Biophys* **316**:765–772.

172. Samples CR, Howard T, Raushel FM, DeRose VJ. 2005. Protonation of the binuclear metal center within the active site of phosphotriesterase. *Biochemistry* **44**:11005–11013.

173. Samples CR, Raushel FM, DeRose VJ. 2007. Activation of the binuclear metal center through formation of phosphotriesterase–inhibitor complexes. *Biochemistry* **46**:3435–3442.

174. Hadler KS, Tanifum EA, Yip SH-C, Mitic N, Guddat L, Jackson CJ, Gahan LR, Nguyen K, Carr PD, Ollis DL, Hengge AC, Larrabee JA, Schenk G. 2008. Substrate-promoted formation of a catalytically competent binuclear center and regulation of reactivity in glycerophosphodiesterase from *Enterobacter aerogenes*. *J Am Chem Soc* **130**:14129–14138.

175. Aubert SD, Yingchun L, Raushel FM. 2004. Mechanism for the hydrolysis of organo-phosphates by the bacterial phosphotriesterase. *Biochemistry* **43**:5707–5715.

176. Christianson DW. 2005. Arginase: structure, mechanism, and physiological role in male and female sexual arousal. *Acc Chem Res* **38**:191–201.

177. Herzfeld A, Raper SM. 1976. The heterogeneity of arginases in rat tissues. *Biochem J* **153**:469–478.

178. Crombez EA, Cederbaum SD. 2005. Hyperargininemia due to liver arginase deficiency. *Mol Genet Metab* **84**:243–251.

179. Brusilow SW, Horwich AL. 2001. Urea cycle enzymes. In *The metabolic and molecular basis of inherited disease*, pp. 1909–1970. Ed CR Scriver, AL Beaudet, WS Sly, D Valle. New York: McGraw-Hill

180. Ash DE, Scolnick LR, Kanyo ZF, Vockley JG, Cederbaum SD, Christianson DW. 1998. Molecular basis of hyperargininemia: structure–function consequences of mutations in human liver arginase. *Mol Genet Metab* **64**:243–249.

181. Morris SM Jr, Bhamidipati D, D Kepka-Lenhart, 1997. Human type II arginase: sequence analysis and tissue-specific expression. *Gene* **193**:157–161.

182. Ash DE. 2004. Structure and function of arginases. *J Nutr* **134**:2760S–2764S.

183. Shi O, Morris SM Jr, Zoghbi H, Porter CW, O'Brien WE. 2001. Generation of a mouse model for arginase II deficiency by targeted disruption of the arginase II gene. *Mol Cell Biol* **21**:811–813.

184. Bewley MC, Jeffrey PD, Patchett ML, Kanyo ZF, Baker EN. 1999. Crystal structures of *Bacillus caldovelox* arginase in complex with substrate and inhibitors reveal new insights into activations, inhibition and catalysis in the arginase superfamily. *Structure* **7**:435–448.

185. Cama E, Colleluori DM, Emig FA, Shin H, Kim SW, Kim NN, Traish AM, Ash DE, Christianson DW. 2003. Human arginase II: crystal structure and physiological role in male and female sexual arousal. *Biochemistry* **42**:8445–8451.

186. Cama E, Pethe S, Boucher J, Han S, Emig FA, Ash DE, Viola RE, Mansuy D, Christianson DW. 2004. Inhibitor coordination interactions in the binuclear manganese cluster of arginase. *Biochemistry* **43**:8987–8999.

187. Cox JD, Kim NN, Traish AM, Christianson DW. 1999. Arginase-boronic acid complex highlights a physiological role in erectile function. *Nat Struct Biol* **6**:1043–1047.

188. Di Costanzo L, Pique ME, Christianson DW. 2007. Crystal structure of human arginase I complexes with thiosemicarbazide reveals an unusual thiocarbonyl μ-sulfide ligand in the binuclear manganese cluster. *J Am Chem Soc* **129**:6388–6389.

189. Kim NN, Cox JD, Baggio RF, Emig FA, Mistry SK, Harper SL, Speicher DW, Morris SM Jr, Ash DE, Traish A, Christianson DW. 2001. Probing erectile function: *S*-(2-boronoethyl)-L-cysteine binds to arginase as a transition state analogue and enhances smooth muscle relaxation in human penile corpus cavernosum. *Biochemistry* **40**:2678–2688.

190. Shin H, Cama E, Christianson DW. 2004. Design of the amino acid aldehydes as transition-state analogue inhibitors of arginase. *J Am Chem Soc* **126**:10278–10284.

191. Sossong TM Jr, Khangulov SV, Cavalli RC, Soprano DR, Dismukes GC, Ash DE. 1997. Catalysis of dinuclear Mn(II) centers: hydrolytic and redox activites of rat liver arginase. *J Biol Inorg Chem* **1997**:433–443.

192. Reczkowski RS, Ash DE. 1992. EPR evidence for binuclear Mn(II) centers in rat liver arginase. *J Am Chem Soc* **114**:10992–10994.

193. Khangulov SV, Sossong TM Jr, Ash DE, Dismukes GC. 1998. L-arginine binding to liver arginase requires proton transfer to gateway residue His141 and coordination of the guanidinium group to the dimanganese(II,II) center. *Biochemistry* **37**:8539–8550.

194. Kuhn NJ, Talbot J, Ward S. 1991. pH-Sensitive control of arginase by manganese(II) ions at submicromolar concentrations. *Arch Biochem Biophys* **286**:217–221.

195. Baggio R, Elbaum D, Kanyo ZF, Carroll PJ, Cavalli RC, Ash DE, Christianson DW. 1997. Inhibition of Mn_2(II)-arginase by borate leads to the design of a transition state analog inhibitor, 2-(*S*)-amino-6-boronohexanoic acid. *J Am Chem Soc* **119**:8107–8108.

196. Custot J, Boucher J-L, Vadon S, Guedes C, Dijols S, Delaforge M, Mansuy D. 1996. N^{ω}-hydroxyamino-α-amino acids as a new class of very strong inhibitors of arginases. *J Biol Inorg Chem* **1**:73–82.

197. Daghigh F, Fukuto JM, Ash DE. 1994. Inhibition of rat liver arginase by an intermediate in NO biosynthesis, NG-hydroxy-L-arginine: implications for the regulation of nitric oxide biosynthesis by arginase. *Biochem Biophys Res Commun* **202**:174–180.

198. Custot J, Moali C, Brollo M, Boucher JL, Delaforge M, Mansuy D, Tenu JP, Zimmermann JL. 1997. The new α-amino acid N^{ω}-hydroxy-nor-L-arginine: a high-affinity inhibitor of arginase well adapted to bind to its manganese cluster. *J Am Chem Soc* **119**:4086–4087.

199. Lavulo LT, Emig FA, Ash DE. 2002. Functional consequences of the G235R mutation in liver arginase leading to hyperargininemia. *Arch Biochem Biophys* **399**:49–55.

200. Lowther WT, Matthews BW. 2000. Structure and function of the methionine aminopeptidases. *Biochim Biophys Acta* **1477**:157–167.

201. Lowther WT, Matthews BW. 2002. Metalloaminopeptidases: common functional themes in disparate structural surroundings. *Chem Rev* **102**:4581–4607.

202. Bradshaw RA, Yi E. 2002. Methionine aminopeptidases and angiogenesis. *Essays Biochem* **38**:65–78.

203. Folkman J. 1995. Angiogenesis in cancer, vascular, rheumatoid and other disease. *Nat Med* **1**:27–31.

204. Bernier SG, Westlin WF, Hannig G. 2005. Fumagillin class inhibitors of methionine aminopeptidase-2. *Drugs Future* **30**:497–508.

205. Griffith EC, Su Z, Turk BE, Chen S, Chang Y-H, Wu Z, Biemann K, Liu JO. 1997. Methionine aminopeptidase (type 2) is the common target for angiogenesis inhibitors AGM-1470 and ovalicin. *Chem Biol* **4**:461–471.

206. Kruger EA, Figg WD. 2000. TNP-470: an angiogenesis inhibitor in clinical development for cancer. *Expert Opin Invest Drugs* **9**:1383–1396.

207. Liu S, Widom J, Kemp CW, Crews CM, Clardy J. 1998. Structure of human methionine aminopeptidase-2 complexed with fumagillin. *Science* **282**:1324–1327.

208. Lowther WT, Orville AM, Madden DT, Lim S, Rich DH, Matthews BW 1999. *Escherichia coli* methionine aminopeptidase: implications of crystallographic analyses of the native, mutant and inhibited enzymes for the mechanism of catalysis. *Biochemistry* **38**:7678–7688.

209. Oefner C, Douangamath A, D'Arcy A, Häfeli S, Mareque D, MacSweeney A, Padilla J, Pierau S, Schulz H, Thormann M, Wadman S, Dale GE. 2003. The 1.15 Å crystal structure of the *Staphylococcus aureus* methionyl-aminopeptidase and complexes with triazole based inhibitors. *J Mol Biol* **332**:13–21.

210. Tahirov TH, Oki H, Tsukihara T, Ogasahara K, Yutani K, Ogata K, Izu Y, Tsunasawa S, Kato I. 1998. Crystal structure of methionine aminopeptidase from hyperthermophile, *Pyrococcus furiosus*. *J Mol Biol* **284**:101–124.

211. D'souza VM, Holz RC. 1999. The methionyl aminopeptidase from *Escherichia coli* can function as an iron(II) enzyme. *Biochemistry* **38**:11079–11085.

212. Walker KW, Bradshawe RA. 1998. Yeast methionine aminopeptidase I can utilise either Zn(II) or Co(II) as a cofactor: a case of mistaken identity? *Protein Sci* **7**:2684–2687.

213. Wang J, Sheppard GS, Lou P, Kawai M, Park C, Egan DA, Schneider A, Bouska J, Lesniewski R, Henkin J. 2003. Physiologically relevant metal cofactor for methionine aminopeptidase-2 is manganese. *Biochemistry* **42**:5035–5042.

214. Cosper NJ, D'souza VM, Scott RA, Holz RC. 2001. Structural evidence that the methionyl aminopeptidase from *Escherichia coli* is a mononuclear metalloprotease. *Biochemistry* **40**:13302–13309.

215. Meng L, Ruebush S, D'souza VM, Copik AJ, Tsunasawa S, Holz RC. 2002. Overexpression and divalent metal binding properties of the methionyl aminopeptidase from *Pyrococcus furiosus*. *Biochemistry* **41**:7199–7208.

216. Lowther WT, McMillen DA, Orville AM, Matthews BW. 1998. The anti-angiogenic agent fumagillin covalently modifies a conserved active-site histidine in the *Escherichia coli* methionine aminopeptidase. *Proc Natl Acad Sci USA* **95**:12153–12157.

217. D'souza VM, Brown RS, Bennett B, Holz RC. 2005. Characterization of the active site and insight into the binding mode of the anti-angiogenesis agent fumagillin to the manganese(II)-loaded methionyl aminopeptidase from *Escherichia coli*. *J Biol Inorg Chem* **10**:41–50.

218. Lowther WT, Zhang Y, Sampson PB, Honek JF, Matthews BW. 1999. Insights into the mechanism of *Escherichia coli* methionine aminopeptidase from the structural analysis of reaction products and phosphorus-based transition-state analogues. *Biochemistry* **38**:14810–14819.

219. Copik AJ, Nocek BP, Swierczek SI, Ruebush S, Jang SB, Meng L, D'souza VM, Peters JW, Bennett B, Holz RC. 2005. EPR and X-ray crystallographic characterization of the product-bound form of the Mn[II]-loaded methionyl aminopeptidase from *Pyrococcus furiosus*. *Biochemistry* **44**:121–129.

220. Pethe S, Boucher J-L, Mansuy D. 2002. Interaction of anions with rat liver arginase: specific inhibitory effects of fluoride. *J Inorg Biochem* **88**:397–402.

NOVEL METALLOENZYMES

AND METALLOPROTEINS

EPR of Cobalt-Substituted Zinc Enzymes

Brian Bennett

*Department of Biophysics, Medical College of Wisconsin,
Milwaukee, Wisconsin*

Co(II) is sometimes utilized as a spectroscopically active substitute for Zn(II) in enzymes. Metal binding sites in enzymes that contain catalytically active Zn(II) generally yield high-spin $S = {}^3/_2$ Co(II) ions when substituted with cobalt, and these provide EPR spectra rich in information. Extracting this information involves an appreciation of the extent to which the properties of Co(II) mirror those of Zn(II), careful sample preparation and biochemical characterization, careful recording of the EPR data, and the ability to interpret spectra in a quantitative way. Here, the applicability of Co(II) as a structural and functional mimic of Zn(II) in enzymes is considered and a brief update of EPR studies in the literature is presented. Methods of substitution of Zn(II) by Co(II) are described. Recording EPR spectra of high-spin Co(II) that will provide useful information is not a trivial exercise, and experimental considerations are discussed in some detail. The analysis of EPR spectra in terms of spin-Hamiltonian parameters is described, along with their interpretation in structural terms. Complementary techniques to EPR are very briefly discussed, and a case study is presented as an example of how EPR of Co(II) can provide mechanistic information on a zinc enzyme that is unavailable by other techniques.

1. INTRODUCTION

Cobalt has long been used as a spectroscopic probe of the active sites of metalloproteins [1]. Co(II) is a particularly useful probe of the active sites of naturally zinc-containing enzymes that exhibit no optical electronic absorption or paramagnetic resonance. Zinc enzymes have been reported to outnumber any other group of metalloenzymes [2], and the existence of a spectroscopic probe is of major biochemical significance. Cobalt is often an excellent structural and functional model

Address all correspondence to Brian Bennett, Department of Biophysics, Medical College of Wisconsin, 8701 Watertown Plank Road, Milwaukee, WI 53226-0509, USA, 414 456-4787, 414 456-6512 (fax), <bbennett@mcw.edu>.

for zinc with higher coordination numbers; the ionic radii for octahedral Zn(II) (0.88 Å) and high-spin octahedral Co(II) (0.89 Å) are similar, their Alfred-Rochow electronegativities are comparable (Zn, 1.66; Co, 1.70), and Co(II) substitution often furnishes catalytically active forms of zinc enzymes [3,4]. Tetrahedral catalytically active Zn(II) centers can also be substituted with Co(II). In some cases, tetrahedral Co(II) centers directly adopt the original Zn(II) coordination [5–7]. In other zinc-dependent metalloenzymes, four-coordinate Zn(II) is replaced by five-coordinate [5,8,9], or even six-coordinate [10] Co(II). The general propensity of Co(II) to adopt higher coordination in a hitherto four-coordinate Zn(II) site [11] is underappreciated and has doubtless led to the incorrect assignment of $M_S = |\pm^1/_2\rangle$, $S = ^3/_2$ Co(II) EPR signals in some cases. Nevertheless, substitution of tetrahedral Zn(II) by higher-coordinate Co(II) still often results in catalytically active species, sometimes with catalytic properties perhaps unexpectedly similar to those of the native enzyme. In the vast majority of cases, no other transition ion than Co(II) provides a better substitute for Zn(II).

The present chapter is restricted largely to the description of cobalt-substituted zinc enzymes where Zn(II) is catalytically active; zinc finger proteins and metallothioneins do not fall into this class, although the discussion of EPR of Co(II) as a Zn(II) substitute is equally relevant to these proteins. Also, the focus here is on electron paramagnetic resonance (EPR) spectroscopy. Co(III) and Co(I) are EPR-silent, and EPR of low-spin Co(II) is straightforward; accordingly, only high-spin Co(II) will be considered in detail. Finally, the use of Co(II) as a spectroscopic probe of Zn(II) sites was reviewed in 1993 [4], and the reader is referred particularly to that article for references to earlier studies, as well as to two subsequent short reviews [12,13]. Here, a brief review of studies of Co(II)-substituted enzymes since 1993 will be presented, methods for the preparation of cobalt-substituted enzymes will be reviewed, practical concerns regarding the acquisition and quantitative analysis of Co(II) EPR data will be considered, a case study will be presented, and techniques complementary to EPR will be considered.

2. REVIEW OF COBALT-SUBSTITUTED ENZYMES

A list of some 37 examples of cobalt-substituted metalloproteins was provided in Table II of the review by Maret and Vallee [4]. Of these, 24 are native zinc-containing proteins and the enzymes include hydrolases (lactamases, phosphatases, phospholipases, peptidases, orotases, nucleases, polymerases, bacterial toxins), dehydrogenases, and dehydratases. Notable among earlier EPR studies are those of carbonic anhydrase [14], carboxypeptidase A [15], transcarboxylase [16], phospholipase C [17], and hemocyanin]18]. The roles of Zn(II) have long been assumed to include the activation of a nucleophilic hydroxyl in many of the hydrolases. In Class II aldolase, however, the role of the Zn(II) ion is to electrophilically activate the substrate carbonyl for nucleophilic attack [19]. Recent theoretical work on a β-lactamase [20] and experimental work on an aminopeptidase (see the case study) both suggest that this may be the primary role of Zn(II) in some of the

hydrolytic enzymes, with a role in nucleophile activation being either indirect or nonexistent.

Since 1993, the list of reports of studies of Co(II)-substituted enzymes has continued to grow. The most extensively characterized Co(II)-substituted enzyme is the dizinc-containing aminopeptidase (VpAP; formerly referred to as "AAP") from *Vibrio proteolyticus* (formerly *Aeromonas proteolytica*). This enzyme is structurally and functionally similar to many mammalian proteins involved in tumorigenesis and tumor growth and, particularly, to the carboxypeptidatic domain of the prostate-specific membrane antigen [21]. In addition, VpAP homologues are virulence factors of many pathogenic bacteria including *Vibrio, Aeromonas, Streptomyces*, and *Clostridium* species [22–27]. Extensive spectroscopic studies on cobalt-substituted VpAP have provided much mechanistic information, in conjunction with x-ray crystallographic studies, and the EPR work up until 2001 was the focus of a minireview by the present author [12]. Of particular utility were studies on the distinct heterodimetallic forms of the enzyme, [CoZn(VpAP)] and [ZnCo(VpAP)] [28–31]. The potential pitfalls of the use of other transition ions as zinc substitutes were exemplified by the observation by EPR that Cu(II), which also activates VpAP, forms a structurally dissimilar dinuclear site to that in the Zn(II) and Co(II) enzymes [32]. Further studies have characterized the interactions of VpAP with anticancer drugs and drug design templates [33–35], and these studies, along with others on metallo-β-lactamases [5], appear to have unveiled an effect of introducing a sulfur ligand in promoting fourfold rather than fivefold coordination of Co(II). Studies on site-directed variants of VpAP have shed light on the roles of active site residues [36,37]. More recently, EPR studies of catalytic intermediates of VpAP, trapped by rapid-freeze quenching (RFQ), have provided direct evidence that the nucleophile in VpAP-catalyzed hydrolysis is not delivered by the metal center (see the case study).

Another biomedically important class of enzymes for which the study of the Co(II)-substituted forms is providing new mechanistic information is that of the zinc-dependent metallo-β-lactamases and peptidases that confer bacterial antibiotic resistance. These enzymes include the D–Ala–D–Ala dipeptidase VanX, and the metallo-β-lactamases ImiS, L1, and CcrA [5,9,38,39]; EPR of Co(II) has provided information on the structure and assembly of the active metal sites and RFQ-EPR studies have proven fruitful in obtaining mechanistic information.

Other biologically interesting enzymes have been studied upon substitution with Co(II) since the last major review appeared. 3-Deoxy-D-*arabino*-heptulosonate-7-phosphate synthase (DAHPS) catalyzes the first committed step in the shikimate pathway; it is variously isolated with Cu(II), Fe(II), and Zn(II) and can be activated by Co(II). EPR of Cu(II)–DAHPS and Mn(II)–DAHPS are suggestive of two distinct metal binding sites and EPR of Fe(III)–DAHPS is suggestive of some spin coupling, indicating the proximity of these sites [40]. EPR of Co(II)–DAHPS, however, gave only a single, slightly rhombic $M_S = |\pm^1/_2\rangle$ signal. EPR of cobalt-substituted ribonucleotide reductase identified a ferromagnetically coupled dinuclear Co(II) site similar to that in VpAP [41]. EPR of Co(II) in native

and inhibited forms of the 174-kDa homotetrameric herbicide-degrading hydrolase AtzC from pseudomonads suggested that the enzyme monomer contained a catalytic Zn(II) ion with fivefold coordination [42]. The combination of EPR and electronic absorption spectroscopies of deuterolysin, a zinc protease with a novel "HEXXH + D" or "aspzincin" motif, appears to show that the Co(II) ion resides in a trigonal bipyramidal geometry; the authors of this report do not rule out an alternative distorted tetrahedral geometry, despite the axial $M_S = |\pm^1/_2\rangle$ slow-relaxing EPR signal [43]. Magnetic circular dichroism (MCD) and EPR were used to characterize the tetrahedral $M_S = |\pm^3/_2\rangle$ ground state Co(II) ion in liver alcohol dehydrogenase [7], and EPR has been brought to bear on the Co(II)-substituted zinc-containing hydrolases DapE [44,45] and ArgE [46]; these latter two enzymes are potential antibacterial targets.

In addition to the Co(II)-substituted zinc enzymes, another group of enzymes has emerged in which either Co(II) has been claimed to be a native metal ion or for which the native metal ion is unknown, but Co(II) remains a candidate. Of these, one of the better studied is methionine aminopeptidase (MAP). It is unclear whether the native metal ion for MAPs is Fe(II) [47], Co(II) [48] or, perhaps most likely, Mn(II) [49,50], though it is highly unlikely that it is Co(III), as originally proposed [51]. A prolidase from *Pyrococcus furiosus* has also been proposed to be a cobalt-dependent enzyme as it cannot be activated by iron, zinc, copper, nickel, calcium, or magnesium; it is, however, activated by Mn(II), and the identity of the native metal ion thus remains unclear [52]. Co(II) has been proposed as a cofactor in lysine-2,3-aminomutase and gives a distinctive $I = {}^7/_2$ hyperfine split EPR spectrum, though the relative contents of Co(II), Cu(II), and Zn(II) in the enzyme were dependent on the amount of Co(II) added to the cell growth medium [53]. Co(II) was detected in ATP sulfurylases, isolated from their native sulfate-reducing *Desulfovibrio* hosts, and was proposed to adopt tetrahedral coordination with three cysteine-S ligands on the bases of optical and x-ray absorption spectroscopies, and a well-defined $M_S = |\pm^3/_2\rangle$ EPR signal [54].

3. METHODS OF Co(II) INSERTION

As pointed out in an earlier review [55], the three strategies for introducing Co(II) into zinc (or other transition metal) proteins are (i) displacement of the original metal ion, (ii) preparation of the apoprotein followed by addition of Co(II), and (iii) biosynthetic incorporation. That review also cautioned about the possible need for anaerobic conditions, particularly with thiolate ligands. Given the volumes of buffers used during dialysis or direct exchange, an anaerobic glove box is advisable if anaerobic conditions are necessary.

Of the methods for Co(II) insertion, incorporation into apoprotein is the most controllable and is the only method readily applicable to the preparation of site-directed heterometallic forms such as heterodimatallic CoZn and ZnCo clusters [28,56]. Exhaustive dialysis of the native protein against a suitable chelator (EDTA; 1,10-phenanthroline, etc.) is often sufficient to remove the native metal

ion, as can be verified by loss of catalytic activity. The most difficult step is the subsequent removal of chelator, and this entails dialysis against metal-free buffer solution. Solutions should be prepared with metal-free water, using high-purity acids or bases to adjust the pH, and, if necessary, pretreatment of the buffer solution with a metal-chelating resin such as Chelex-100 should be carried out. It is worth bearing in mind that one liter of a solution containing 1 µM metal ion contains enough metal to provide a 1:1 ratio with 1 ml of 1 mM apoprotein. The affinity of some metalloenzymes for transition ions is sufficient that trace contamination from glassware can, over time, be significant. Dialyses should, therefore, be as short in duration as possible (2–4 h), with at least three changes of buffer, and the present author's experience is that unused "disposable" plastic beakers are the best vessels in which to carry out dialysis. Dialysis vessels should be covered and well stirred. Apoproteins are sometimes less stable than their metal-containing counterparts, and, of course, they are highly susceptible to contamination by metal ions. Therefore, manipulation of the apoprotein should be kept to an absolute minimum. For monometallic proteins, insertion of Co(II) merely involves the addition of Co(II) as a solution. The solution should be added slowly or as a relatively dilute solution, with stirring, to avoid local concentrations that could precipitate the protein. Dilute mono-Co(II) protein solutions can be safely concentrated further after metal addition. Alternatively, the Co(II) addition can be made in the EPR tube. A small (~10 µL) drop of Co(II) solution can be dispensed onto the inner wall of an X-band EPR tube, about 4 cm from the bottom, and then the apoenzyme introduced as a 2 cm "plug," about 10 cm from the bottom of the tube; a violent flick of the EPR tube, which forces the contents to the bottom of the tube, provides good mixing of the contents [57]. The preparation of specific heterodimetallic clusters is less straightforward, and some "trial and error" is to be expected. Where, for example, Co(II), as the spectroscopically active metal ion, is to be added first, it is recommended that substoichiometric Co(II) is added (0.9 eq) followed by a balance of the nonspectroscopic metal (e.g., 1.1 eq Zn(II)). This avoids the formation of unwanted CoCo if there are small errors in protein concentration or losses due to mechanical handling. If the binding constants of two sites are either unknown or are both tight, then local high concentrations of added metal ion should be avoided as far as possible for any length of time. Slow addition of metal ion to apoprotein with as much stirring as can be tolerated and very rapid, vigorous addition of a larger volume of apoprotein solution to a small volume of metal ion are two strategies that minimize the exposure of apoprotein to high local concentrations of metal ion; the use of an RFQ/stopped-flow-type mixer for very rapid mixing should be considered where practicable. Unlike monometallic enzymes, the final heterodimetallic form may also be unstable; even where thermodynamic binding constants are tight, kinetic exchange of metal ions can be significant, leading to "scrambling" of metal clusters [58]. This effect is accelerated significantly by excess metal ions.

Direct displacement of the metal ion may be the simplest method for substituting a mono-Zn(II) protein with Co(II), though if both Zn(II) and Co(II) forms are

active, catalytic assays cannot be used to judge the extent of substitution and metal analysis is required.

Biosynthetic incorporation involves growing the host organism on a Co(II)-supplemented and Zn(II)-deficient medium. The latter requirement may necessitate the use of a supplemented minimal medium such as that described for the expression of Co(II)-substituted VanX dipeptidase [38]. As pointed out earlier [4], pH needs to be considered, and the authors of the report on VanX substitution stated that the pH of the growth medium had to be lowered from 7.5 to 6.8 to optimize Co(II)–VanX yield. As with direct replacement, metal analysis is essential to verify and quantitate substitution.

Finally, it should be appreciated that "His-tagged" proteins from bacterial expression systems are generally not amenable to metal substitution for spectroscopy, and either the hexahistidine extension must be removed or alternative methods of expression explored.

4. EPR EXPERIMENTAL TECHNIQUES AND CONSIDERATIONS

The literature is, unfortunately, littered with examples of high-spin Co(II) EPR spectra that have been recorded under such conditions, and presented in such a manner, that useful information cannot be extracted. Some of the deficiencies in good practice include: (i) inappropriate temperature and microwave power, (ii) poor signal-to-noise, (iii) lack of attention to background signals, (iv) failure to detect hyperfine structure, (v) lack of attention to $M_S = |\pm^3/_2\rangle$ signals, and (vi) lack of attention to integer spin signals. Some experimental considerations are, therefore, reviewed here.

$S = {}^3/_2$ Co(II) EPR signals are often observable without significant distortion over only a very narrow range of temperatures and powers. $M_S = |\pm^3/_2\rangle$ signals may exhibit very fast relaxation times and be observable at only the lowest temperatures obtainable with liquid helium flow cryostats, using high microwave powers. In general, at higher than optimum temperatures, relaxation introduces significant broadening of Co(II) EPR spectra; at lower than optimum temperatures, saturation and rapid passage effects result in a spectrum containing both derivative ($\partial\chi''/\partial B$) and absorption-like components in standard 100-kHz field-modulated EPR. These components may appear to be of either the same or of opposite sign, and the magnitude of these effects often differs across the EPR spectral envelope. While advanced techniques, including dispersion-detected cw EPR and electron-spin-echo pulsed EPR at very low temperatures [59] and multi-quantum EPR [60], circumvent some of the deficiencies of field-modulated absorption-detected EPR, the instrumentation is not generally available to biochemical researchers, nor is it generally necessary. Further, the nonlinearity (relaxation dependence) of these techniques precludes their ready use for quantitation. The remainder of this discussion, therefore, pertains to field-modulated, absorption-detected EPR, as found on most EPR spectrometers, with temperature control from liquid helium temperature upwards. In general, three simple protocols can be used to ensure that, as near as pos-

sible, the standard EPR spectrum is recorded under appropriate conditions. First, a temperature dependence should be carried out from 4 to 40 K using the lowest microwave power for which a signal can be clearly seen. Under nonsaturating conditions, the signal intensity is proportional to (i) the inverse of the absolute temperature and (ii) the square root of the incident microwave power. To maximize the signal intensity but remain under nonsaturating conditions, therefore, at the temperature at which the product of the temperature (in K) and the signal intensity is a maximum using low microwave power, the highest microwave power at which the intensity remains proportional to the square root of the microwave power should then be identified. This combination of temperature and microwave power makes for good starting conditions. It is perhaps noteworthy that, for Co(II) in proteins, the ZFS is sufficiently large and the relaxation sufficiently fast that only the ground state doublet is generally observable; at temperatures where the excited state doublet is populated (1 cm^{-1} corresponds to 1.44 K), fast relaxation prohibitively broadens the spectrum. Second, after background subtraction (*vide infra*), when the spectrum is integrated, the baseline at low and high field should be level (Fig. 1). Third, when the modulation phase is set to 90° from the optimum (quadrature detection), no significant signal should be observable. If these latter two conditions are not met, the temperature should be incrementally increased and/or the microwave power reduced until they are.

High-spin Co(II) EPR signals can be very broad (the $M_S = |\pm^3/_2\rangle$ envelope can be infinitely broad), and, consequently, the signal intensities can be very small. Most commercially available field modulation units are restricted to ~10 G, which is usually significantly less than the width of the narrowest line in the spectrum. Therefore, sample concentrations need to be high, generally ≥0.2 mM, and sometimes significantly higher. These considerations are particularly important for rapid-freeze-quench (RFQ) sample preparation, where a starting concentration of 1 mM enzyme translates to a final effective concentration in the EPR tube of "only" 0.25 mM. In most cases, signal averaging over many minutes or even hours may be necessary and a stable environment (with respect to temperature, microwave frequency, spectrometer tuning/cavity coupling, and mechanical stability) is essential. A sample holder to accommodate wider tubes should be considered; the S/N advantage of a 4-mm I.D. tube over a 3-mm I.D. tube is $^{16}/_9$, or around 2, and corresponds to fourfold less acquisition time.

The presence of background signals is often a bigger hindrance to the collection of high-quality EPR data on $S = {}^3/_2$ Co(II) than absolute signal-to-noise limitations. Background signals from resonant cavities, cryostat components, and quartzware are virtually unavoidable, and the choice of cavity may depend more on the nature and intensity of the background signals than on the Q-factor. Other signals may derive from adventitious metal ions bound to the protein or from the use of spectroscopically impure Co(II). The narrow lines and spectral widths of the usual culprits (rhombic $M_S = |\pm^3/_2\rangle$, $S = {}^5/_2$ Fe(III); Cu(II); $M_S = |\pm^1/_2\rangle$, $S = {}^5/_2$ Mn(II); free radicals) result in high intensities of these signals compared to Co(II), even when
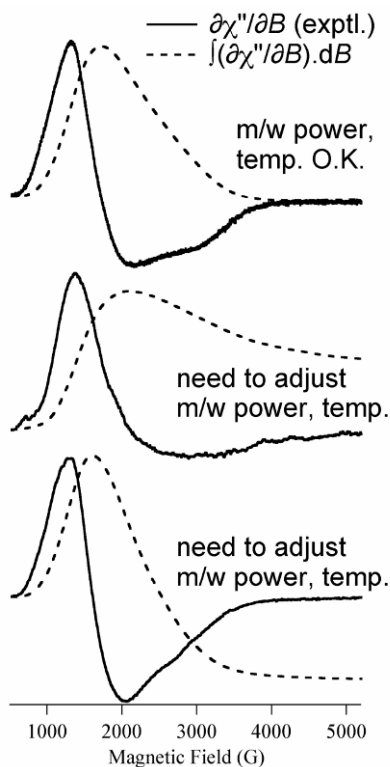
Figure 1. The figure illustrates how integration of spectra of Co(II)-substituted proteins can be used as a check that the appropriate recording conditions have been chosen. The top spectrum has been recorded under conditions that avoid saturation and rapid passage effects and the integral begins and ends at the baseline. The two spectra below are shown recorded under unsuitable conditions, as is clear from the asymmetric baselines of the integrals. Experimental $\partial\chi'/\partial B$ spectra are shown solid and integrated spectra are shown dashed. The spectra are of a methionine aminopeptidase (top, bottom), and a metallo-β-lactamase (middle) recorded at 13, 5, and 6 K, respectively.

the level of contamination in terms of the number of spins is low. These signals can often obscure the region from $g \sim 4$ to $g \sim 2$ to the extent that a reliable discrimination between $M_S = |\pm^1/_2\rangle$ and $M_S = |\pm^3/_2\rangle$ cannot be made [53]. It is thus essential that a background spectrum is recorded, of at least as high quality as the Co(II) spectrum, and subtracted. Ideally, the background consists of buffer in the same EPR tube to be used for the Co(II) sample, under the same experimental conditions; not only does this ensure that signals inherent in the EPR tube can be subtracted, but the equivalent sample geometries and dielelctric loads will ensure that the microwave frequencies and fields will closely match. For proteins derived from organisms grown on Co(II)-supplemented media, a sample of the protein obtained

from the cultured organism without added Co(II) is a useful control as Cu(II), Mn(II), or Fe(III) may differentially occupy sites in the two preparations.

Also worthy of comment are EPR signals due to molecular oxygen. Signals observed at very low field along with signals at 7000–8000 G and at 11,000 G (at 9.6 GHz) may occur due to oxygen and can be mistaken for $M_S = |\pm^3/_2\rangle$ Co(II) resonances. Exhaustive anaerobiosis is usually not necessary to prevent these signals provided that the sample height is sufficient to fill the active region of the cavity. For long EPR tubes that extend from the cryostat into the environment, the tubes should be hermetically sealed prior to freezing (a short piece of silicone tubing, knotted at one end and placed condom-like over the open end of the EPR tube, is a safe, cheap, and effective solution — hard plastic caps supplied by manufacturers may leak and rapid expansion of condensed gases can cause the tube to explode upon removal from the cryostat or from liquid nitrogen). Short EPR tubes that are entirely contained within the cryostat need not be sealed at all and can be annealed for 5 min at 110 K under helium to remove oxygen signals if necessary.

One of the more important pieces of information available from the EPR spectrum is the magnitude of the ^{59}Co hyperfine coupling. This may be poorly resolved or overlaid on a broad feature and is easily missed, particularly if insufficient data are collected (a 1024-point 10-kG spectrum with A (^{59}Co) = 80 G corresponds to only 8 points for each hyperfine line and its adjacent trough combined, i.e., ~4 points per line). Each of the spectral features should be investigated at high resolution. The use of higher-than-optimum microwave power and lower temperature may provide significantly better S/N for the detection of hyperfine structure, at the expense of faithful representation of the main spectral lineshape. Second-derivative ($\partial^2\chi''/\partial B^2$) spectra provide significantly enhanced resolution at the expense of S/N and can reveal hitherto unresolved lines. The utility of low-frequency EPR for detection of hyperfine structure in high-spin Co(II) was recently demonstrated in the present author's laboratory, and examples of the hyperfine enhancement are shown in Figure 2.

In the absence of other EPR signals, signals from Co(II) due to transitions in the $M_S = |\pm^3/_2\rangle$ doublet are generally very characteristic, with an isolated absorption-shaped feature at $g_{eff} > 6.0$ and often with no other resonances visible, due to either resonance positions at too high a field to be accessible by the laboratory magnet, or due to the extensive broadening of the line due to the scaling of the field-swept spectrum compared to the more fundamental frequency domain spectrum. This phenomenon is exacerbated where the linewidth is dominated by effective strains in g_{eff}, where g_{eff} itself is low. However, the intensity of the $g_{eff} > 6$ resonance can also be low because of the large field range spanned by the $M_S = |\pm^3/_2\rangle$ signal, and the signal can be very difficult to detect if it overlaps with an $M_S = |\pm^1/_2\rangle$ signal due to Co(II) in another environment (Fig. 3). The difficulty in detection of $M_S = |\pm^3/_2\rangle$ signals can be exacerbated by the often very fast relaxation of $M_S = |\pm^3/_2\rangle$ systems. Where $M_S = |\pm^3/_2\rangle$ (tetrahedral) Co(II) is even suspected, spectra should be collected at low temperatures and high powers, e.g., 3.5–5 K and
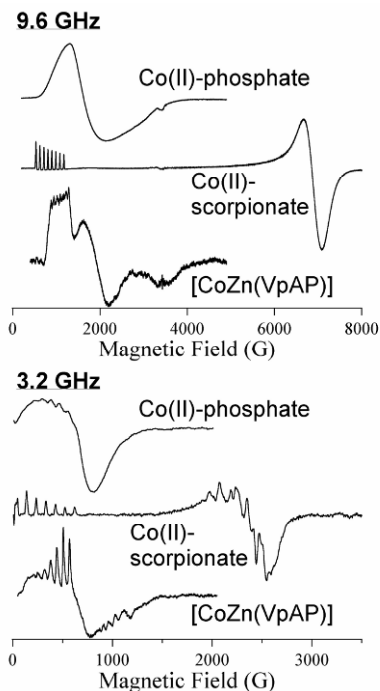
Figure 2. The EPR spectra of Co(II) in phosphate buffer, a Co(II)-scorpionate complex in acetonitrile, and the heterodimetallic Co(II)-substituted [CoZn(VpAP)] form of an amin-opeptidase are shown, as labeled, recorded at 9.6 GHz (12 K) and 3.2 GHz (14 K). Hyperfine structure is clearly apparent on all three spectra at 3.2 GHz that is absent in the spectra recorded at 9.6 GHz, due to the diminished effects of strains in **g** and **D**, and cancellations in *A*- and *g*-strains.

0 dB microwave attenuation; higher microwave powers than advertised can be obtained by switching the microwave bridge leveler off (550 mW was obtained with a commercial Bruker bridge [33]), though *caveat emptor* applies! An added benefit of the use of such extreme conditions is that the $M_S = |\pm^1/_2\rangle$ signals are often driven into rapid passage conditions and the $M_S = |\pm^3/_2\rangle$ signals are much easier to deconvolute; otherwise, the $M_S = |\pm^3/_2\rangle$ signal can be obtained by subtraction (Fig. 3) [5,33,34].

Dinuclear Co(II) centers have been encountered or generated in some enzyme systems and, where the exchange coupling is sufficiently small, give rise to an integer spin EPR signal [8,18,29,41]. g_{eff} values of 10–12 are generally seen, suggesting that the signals arise from either or both of the $S' = 2$ and $S' = 3$ states of an $S = 3$, $S' = 3, 2, 1, 0$ spin ladder. In some cases, the lack of an $S = ^3/_2$ EPR signal (with $\mathbf{B}_0 \perp \mathbf{B}_1$, where $\mathbf{B}_0$ is the static magnetic field and $\mathbf{B}_1$ the microwave magnetic field) alerts the investigator to the existence of a spin-coupled system [29], but in
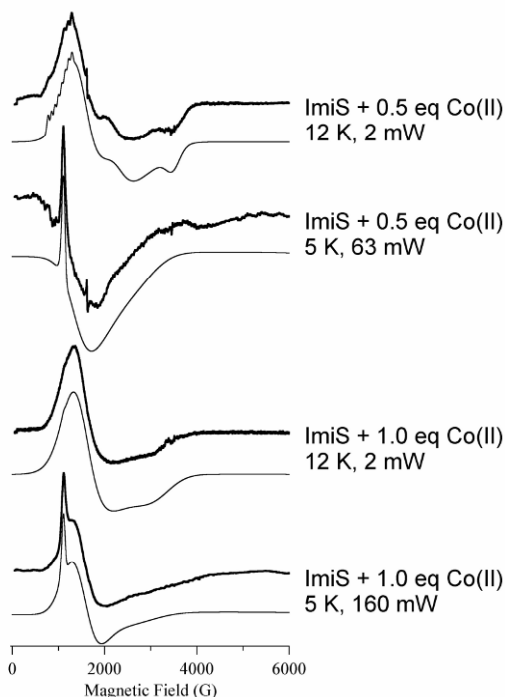
Figure 3. The traces show EPR spectra from the metallo-β-lactamase ImiS recorded during titration with Co(II). Experimental spectra are shown with heavy lines and simulations with light lines. The use of multiple recording conditions allowed the deconvolution of multiple species in the spectra, including an $M_S = |\pm\,^3/_2\rangle$ component that was almost undetectable under conditions optimum for $M_S = |\pm\,^1/_2\rangle$. Details of the simulations are given in [5].

other cases the presence of a substantial $S = \,^3/_2$ signal can easily mask the weak resonance due to the integer spin system (Fig. 4). Clues to the presence of an integer spin signal include the presence of low field absorption, particularly if it appears during a Co(II) titration beyond 1 eq Co(II) [8]. Where an integer spin signal is suspected, the use of parallel mode EPR ($\mathbf{B}_0 \parallel \mathbf{B}_1$) is essential to confirm this assignment; while parallel mode may result in some enhancement of the integer spin resonance, the overwhelming benefit is the very high attenuation of the Kramers signals [61,62]. Parallel mode EPR is most conveniently carried out at X-band using a dual mode cavity (e.g., Bruker ER 4116 DM TE$_{012}$/TE$_{102}$). At higher frequencies, resonators are sufficiently small to reorient the resonator in the field, whereas at lower frequencies it may be easier to retain the microwave geometry and to use a solenoid to generate the low fields necessary. This latter arrangement is particularly suited to a loop-gap resonator, which is of narrow diameter and can be designed to accept X-band sample tubes for 1–4 GHz EPR [63].
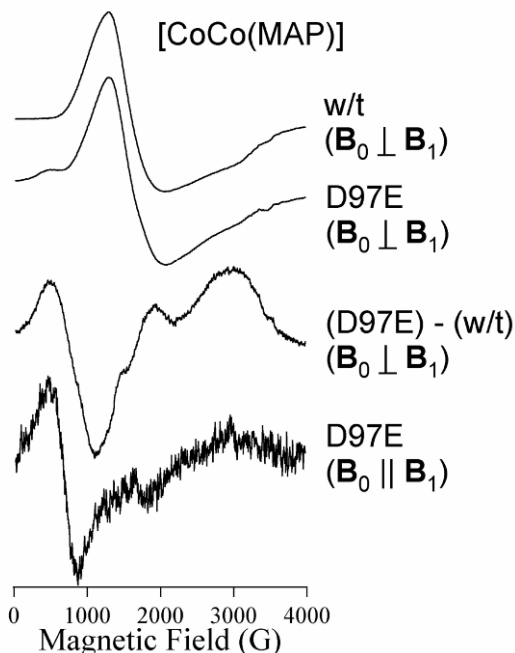
Figure 4. Traces show EPR spectra recorded on the Co(II)-homodisubstituted wild-type and D79E mutant forms of methionine aminopeptidase in perpendicular and parallel mode, as indicated. The third trace down is a difference spectrum; the other three spectra are experimental spectra.

5. SPECTRAL INTERPRETATION

"Interpretation" of EPR spectra can be divided into two separate categories. Interpretation of spectra in quantitative terms, particularly in terms of spin-Hamiltonian parameters, relaxation times, and spin concentrations, can be carried out without further knowledge of the chemical nature of the spin system. Interpretation of EPR spectra in terms of the structure and function of a catalytic entity such as a metalloprotein active site, on the other hand, requires not only a sound interpretation of the EPR in terms of quantitative spin system parameters, but also a good understanding of the chemical and biological nature of the system.

High-spin Co(II) is an $S = \frac{3}{2}$ system by virtue of its $3d^7$ electronic configuration. The two allowed EPR transitions are within the $M_S = |\pm\frac{1}{2}\rangle$ and $M_S = |\pm\frac{3}{2}\rangle$ Kramers doublets (Fig. 5), which are separated in energy at zero field by the zero field splitting energy (ZFS), Δ. In turn, Δ is a function of the axial ZFS term, D,
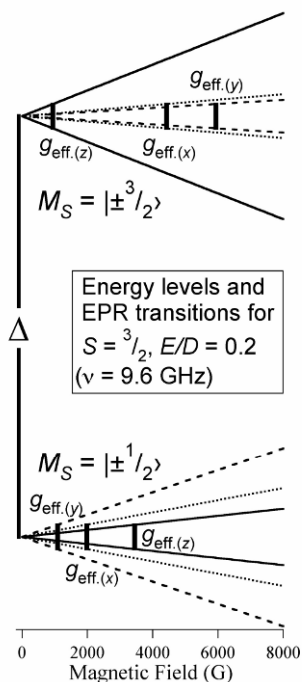
Figure 5. Schematic energy levels for Co(II), $S = {}^3/_2$ in a magnetic field. 9.6-GHz EPR transitions are shown for a system with an $M_S = |\pm{}^1/_2\rangle$ ground state, ZFS $= \Delta$, and $E/D = 0.2$ (these correspond to the third and fifth spectra of Fig. 7).

and the "rhombic" ZFS term, E, where $\Delta = 2D\sqrt{[1 + 3(E/D)^2]}$. (A comment regarding the use of "rhombic" is perhaps appropriate here. In a strict crystallographic sense, it relates to orthorhombic point symmetry. In cases where the **g** matrix and the **D** tensor have the same principal axes, even when the local symmetry is triclinic, then one cannot distinguish between true orthorhombic symmetry and triclinic [and also monoclinic] from the powder EPR spectrum. In general, **g** and **D** will have different principal directions, neither of which is determined by the symmetry if it is lower than orthorhombic. In the present article, the term "rhombic" is applied to **D** of a system where $E/D \neq 0$, though the reader should be aware that orthorhombic symmetry of such systems is not implied.) For all cases studied of high-spin Co(II) in proteins, $\Delta \gg g\beta BS$, and the $M_S = |\pm{}^1/_2\rangle$ and $M_S = |\pm{}^3/_2\rangle$ Kramers doublets can be considered as isolated effective $S = {}^1/_2$ systems. A practical consequence of the large ZFS is that Co(II) EPR spectra can be simulated to a first approximation using the relatively straightforward perturbation approach for $S = {}^1/_2$ (Bruker WINSIM, QPOW, EPRSim, etc. [64–66]), though spin-Hamiltonian parameters must then be calculated from those g-values, "$g_{eff(x,y,z)}$," used to obtain the $S = {}^1/_2$ simulation [8,28]. More sophisticated matrix diagonalization programs such as XSophe [67] exactly and explicitly calculate the $S = {}^3/_2$ spectrum from the

spin-Hamiltonian parameters, and not only provide fully described simulations but are a valuable teaching aid in understanding the origins of the spectra in terms of the spin-Hamiltonian parameters. The resonance positions on the EPR spectrum, $g_{\text{eff}(x,y,z)}$, are related to the real g-values and the ZFS (68) by

$$g_{\text{eff}(x)} = g_{\text{real}(x)}[1\pm[1+3(E/D)]/\sqrt{[1+3(E/D)^2]}\,,$$

$$g_{\text{eff}(y)} = g_{\text{real}(y)}\left[1\pm[1-3(E/D)]/\sqrt{[1+3(E/D)^2]}\right],$$

$$g_{\text{eff}(z)} = g_{\text{real}(z)}\left[1\pm-2\sqrt{[1+3(E/D)^2]}\right].$$

It is immediately obvious from these relationships that D, E, and Δ cannot be obtained from the EPR spectra. (In fact, there is only one report of direct EPR determination of Δ, carried out at multiple very high fields and on a complex with unusually low ZFS, where $\Delta \sim g\beta BS$ [69].) The quantities that can be obtained from the above equations are E/D and $g_{\text{real}(x,y,z)}$, and the relationships between g_{eff}, g_{real}, and E/D are graphically illustrated in the "Rhombogram" [61] of Figure 6. It is also
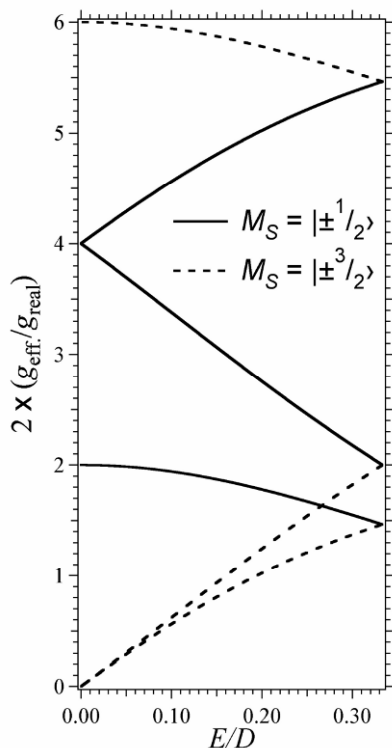
Figure 6. "Rhombogram" for $S = {}^3/_2$, $\Delta \gg g\beta BS$. $M_S = |\pm {}^1/_2\rangle$ is shown solid and $M_S = |\pm {}^3/_2\rangle$ dashed.

M_S; E/D

$\pm^1/_2$; 0

$\pm^1/_2$; 0.10

$\pm^1/_2$; 0.20

$\pm^1/_2, ^3/_2$; 1/3

$\pm^3/_2$; 0.20

$\pm^3/_2$; 0.10

$\pm^3/_2$; 0.05
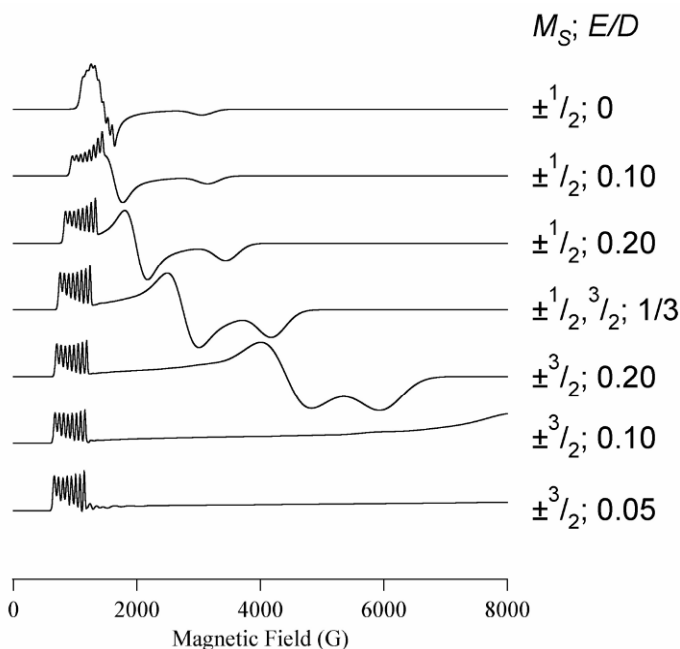
Figure 7. Traces show calculated EPR spectra of Co(II) as a function of E/D. Other parameters are $g_{x,y,z}$ = 2.5, 2.5, and 2.25 and A_y = 8.1 × 10^{-3} cm^{-1} for $M_S = |\pm\,^1/_2\rangle$. As the ground state changes from $M_S = |\pm^1/_2\rangle$ to $M_S = |\pm^3/_2\rangle$ at $E/D = ^1/_3$, the sign of D changes. This corresponds to a relabeling of the principal g_{eff} axes if the sign of E is changed with that of D such that E/D remains positive and the parameters $g_{x,y,z}$ = 2.25, 2.5, and 2.5 and A_z = 8.1 × 10^{-3} cm^{-1} were used here for $M_S = |\pm^3/_2\rangle$. With this relabeling of **g**, the $E/D = ^1/_3$ spectra with $M_S = |\pm^1/_2\rangle$ and $M_S = |\pm^3/_2\rangle$ are identical; if the sign of E is not changed with that of D, the spectrum with $E/D = ^1/_3$ and $M_S = |\pm^1/_2\rangle$ ($D > 0$) is identical to that with $E/D = -^1/_3$ and $M_S = |\pm^3/_2\rangle$ ($D < 0$).

immediately obvious that there are infinitely many solutions for $g_{eff(x,y,z)}$ in terms of $g_{real(x,y,z)}$ and E/D (one cannot uniquely determine four independent quantities from three observations). Something needs to be fixed, therefore, and if g_{real} is taken to be axial ($g_{real(x)} = g_{real(y)} \neq g_{real(z)}$), then unique solutions in terms of $g_{real(x,y)}$ ($g_\perp$), $g_{real(z)}$ ($g_\parallel$), and E/D can be found. This is a reasonable assumption since non-d^5 $S = ^1/_2$ transition ions with appreciable g anisotropy are generally axial. Spin Hamiltonian parameters are best obtained, therefore, by explicit $S = ^3/_2$ simulation of the Co(II) EPR spectrum, varying the parameters $g_\perp$, $g_\parallel$, and E/D ($^1/_3 \geq E/D \geq 0$), while fixing $|D| \gg g\beta BS$ (e.g., 50 cm^{-1}). The sign of D determines the ground state Kramers doublet (in XSophe, $D > 0 \rightarrow M_S = |\pm^1/_2\rangle$ ground state). Hyperfine coupling can be included where observed. A selection of computed spectra are shown in Figure 7.
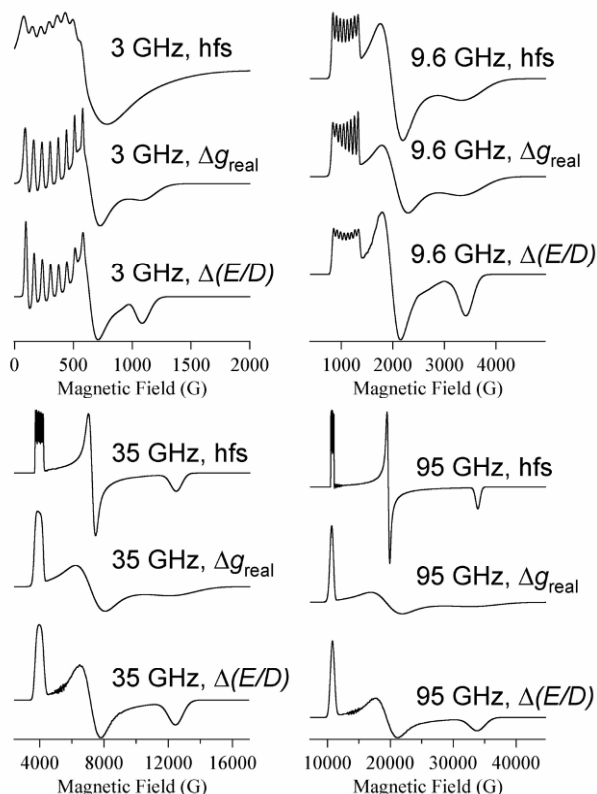
Figure 8. The effects of different linewidth-generating mechanisms on EPR spectra of Co(II) calculated at different frequencies is illustrated. Linewidths due to unresolved hyperfine coupling (labeled "hfs") show no frequency dependence. The X-band hfs spectrum was modeled as closely as possible using strains in g_{real} (labeled "Δg_{real}") and strains in E/D (labeled "$\Delta(E/D)$"), and the spectra were recalculated at the other frequencies with the same parameters. The calculation of $\Delta(E/D)$ is given in the text.

In addition to the Zeeman and ZFS interaction, Co(II) often exhibits $I = {}^7/_2$ hyperfine structure due to ^{59}Co. This can be easily measured where it is resolved, but in other cases where it is only partially resolved or not resolved at all it can be estimated by simulation. The other useful piece of information available concerns the linewidths. Linewidths can be due to either unresolved hyperfine couplings or else strains in **g** and ZFS due to structural microheterogeneities in the sample [70]. EPR at two or more frequencies can be used to determine the relative contributions to the linewidth of unresolved hyperfine coupling, the magnitude of which is field independent, and strains in the **g**-matrix and **D**-tensor (Fig. 8). While the spectra are insensitive to D and, therefore, to strains in D ("σD"), when $D \gg \sigma D$ and $D \gg g\beta BS$ strains in E/D result in a distribution of g_{eff} that is very difficult to deconvolute from any distribution in g_{eff} due to strains in g_{real}; in Figure 8 an example is shown that includes strain in E/D calculated using XSophe (the linewidths at a

given orientation for $i = x,y,z$ with direction cosines l_i are given in frequency terms by σ_v, where $\sigma_v = \sqrt{[\sigma_i = \sigma D^2 a^2 + \sigma(E/D)^2 D^2 b^2]}$, $\sigma_I = \lambda_i^2 + g_i^2 l_i^2/g^2$, λ_i is the intrinsic linewidth, a is the derivative of the energy difference between the two eigenvalues with respect to D, $a = d(E_i - E_j)/dD$, and b is the derivative of the energy difference between the two eigenvalues with respect to E, $a = d(E_i - E_j)/dE)$. Strain effects on linewidths are, in contrast, very easy to separate from line broadening due to unresolved hyperfine coupling because of the field dependence of the former.

$M_S = |\pm^1/_2\rangle$ EPR signals can be quantitated with reference to an appropriate standard (such as Co(II)-EDTA), providing that a clearly nonsaturating set of conditions can be found for both sample and standard, and that the background signals and/or baselines are subtracted. Noisy spectra or spectra with broad baselines are much more reliably quantitated by simulation followed by integration of the simulated spectra. $M_S = |\pm^3/_2\rangle$ signals can only be quantitated where *all three resonances are detected.* In some cases, $M_S = |\pm^3/_2\rangle$ signals relax too quickly to be "fully developed," even at liquid helium temperatures.

Because of the sensitivity of Co(II) EPR to temperature and microwave power, multicomponent spectra can often be deconvoluted by plotting the differential sensitivities of spectral features or by direct subtraction of spectra recorded under different conditions (or with different amounts of added Co(II), +/– substrate, different pH, etc.). Confirmation that the resultant is a single species must be confirmed by simulation of the component extracted, and of the experimental spectrum by linear combination of the individual component simulations.

Having obtained the spin-Hamiltonian parameters, spin concentration, and some information on the mechanism and extent of line broadening, interpretation of these in some structural or functional sense is desirable. This kind of interpretation will vary on a case-by-case basis, but some general rules of thumb are emerging as EPR is collected on more systems for which structural information from other techniques is available, and the structural inferences described in an earlier minireview appear to be general [12].

The identity of the ground state doublet has been used to assign the geometry of high-spin Co(II) centers, though calculation of the sign of D by DFT or other sophisticated methods from atomic coordinates is intrinsically difficult. Ligand field considerations suggest that tetrahedral Co(II) will exhibit $M_S = |\pm^3/_2\rangle$ ground state EPR spectra, whereas five-coordinate trigonal bipyramidal and octahedral geometries will exhibit an $M_S = |\pm^1/_2\rangle$ ground state. To the author's knowledge, there is no reliable report of a violation of this rule for Co(II) in substituted zinc enzymes. Tetrahedral zinc has been substituted by Co(II) that exhibits an $M_S = |\pm^1/_2\rangle$ spectrum but, where crystallographic, EXAFS, or optical spectroscopy has been carried out, Co(II) has been found to adopt higher coordination in each case. Catalytic zinc sites in enzymes are typically liganded by carboxylate oxygen atoms, histidine nitrogen, cysteine sulfur, and/or solvent water or hydroxyl. Substrates of the enzymes generally bind either to a coordinatively unsaturated Zn(II) ion or via displacement of a labile ligand(s), through oxygen and/or nitrogen, and substrate

binding usually results in a decrease in symmetry. Therefore, Co(II) is usually encountered in substituted zinc enzymes in lower than idealized symmetry and in modest ligand field strengths. It is perhaps worthy of comment that some tetrahedral inorganic complexes appear to exhibit $M_S = |\pm^1/_2\rangle$ spectra, or even $S = {}^1/_2$ spectra, and some octahedral complexes appear to exhibit $M_S = |\pm^3/_2\rangle$-like spectra. Inorganic complexes with very high symmetry, with unusually strong ligand fields, or with tailored magnetic properties can exhibit very high spin–orbit couplings (g_{real} values both $>>2$ and $<<2$), very low ZFS, and even $S = {}^1/_2 \Leftrightarrow S = {}^3/_2$ spin–state flipping [71–74]; for example, the 20-K frozen toluene solution spectrum of [PhBP$^{iPr}_3$]CoOSiPh$_3$ exhibits spectral features due to $S = {}^1/_2$, and both $M_S = |\pm^3/_2\rangle$ and $M_S = |\pm^1/_2\rangle$ doublets of $S = {}^3/_2$ [72]. In the case of very-high-symmetry complexes, the magnetic properties, such as the orientation of **g**, can be *extremely* sensitive to ligand orientation (to $^1/_{100}$ of an Ångström). A discussion of the magnetic properties of such complexes is well beyond the scope of this chapter, but the point is worth making that high-spin Co(II) in substituted zinc enzymes is sufficiently asymmetric [75], even in "high-symmetry" environments, that it, is "well-behaved"; i.e., $D >> g\beta BS$, ~$2.9 \geq g_{real} \geq 2.0$, and the expected ground state Kramers doublet is observed. Thus can EPR discriminate between four- and higher-coordinate Co(II). Discrimination of five- and six-coordinate Co(II) can often be made on the basis of the intensities of d–d optical transitions, and a strong correlation between fivefold coordination and very rhombic ($E/D \geq 0.2$) $M_S = |\pm^1/_2\rangle$ EPR spectra is emerging, whereas axial spectra ($E/D \leq 0.1$) are usually associated with sixfold coordination.

A final comment regarding coordination geometry regards the use of hyperfine splittings and, particularly, ZFS (Δ), as indicators of Co(II) coordination geometry. It has been shown that $A({}^{59}Co)/g_{eff}$ is independent of coordination number, and A is therefore not a marker of coordination number. The magnitude of the ZFS, Δ, has been used as an indicator of coordination number in a number of studies, e.g., [76,77]. A thorough and compelling treatment by Larrabee and colleagues, including a review of the data from available literature, along with optical absorption studies, MCD spectroscopy, and angular overlap method [AOM] calculations, concludes that "ZFS is rendered useless as a sole indicator of coordination number in Co(II)-substituted proteins" [75]. Some investigators continue to invoke Δ when considering geometrical interpretation of EPR data [43]. However, given that a demonstrably reliable determination of Δ by EPR is a difficult exercise (sometimes impossible), and given that even a reliable estimate of Δ clearly does not provide an unambiguous indication of coordination number in protein sites, great caution should be exercised in the structural interpretation of Δ. M_S and E/D, and d–d band intensities, are much more convenient and reliable methods of estimating Co(II) coordination number in the absence of direct structural data.

Further structural data can, in principle be obtained from Co(II) EPR spectra. Crystal field analysis of Co(II)(acac)$_2$(H$_2$O)$_2$ indicates an effect of axial elongation or compression on g_{eff} through the "axial splitting factor," δ [73], where δ is the splitting factor between ^4E_g and $^4A_{2g}$ in idealized D$_{4h}$ symmetry and is represented in the effective Hamiltonian $H_{axial} = -\delta(L_z^2 - {}^2/_3)$; positive δ under this convention

corresponds to a splitting with ^4E_g above $^4A_{2g}$ and reflects axial compression, whereas negative δ corresponds to axial elongation. In practice, it appears that the spectra from Co(II) in proteins fall well into the "axially elongated" region, where the dependence upon δ is very small and g_{eff} is dictated by the rhombic splitting (i.e., E/D). It is possible that structural information may be extracted from g_{real} values, particularly g_z, for which no assumptions have been made (g_y must be assumed to be equal to g_x for a unique solution). However, g_z is often poorly defined due to strains; while comparisons from sample to sample may suggest qualitative trends, no rigorous description of analysis of **g** in structural terms for Co(II) in proteins exists.

Linewidths can provide information, especially when considered along with E/D. High strains are generally associated with a flexible (in solution) ligand geometry, from which heterogeneous subpopulations are frozen out at cryogenic temperatures. Protein-derived ligands in enzymes with catalytic metal centers are generally rigid, as their function is to promote an "entatic" state, i.e., a high-energy site primed for catalysis, but coordination sites for substrate binding may be occupied by solvent ligands, and additional solvent may be present that is required for hydrolysis. These solvent ligands provide geometrical flexibility in enzyme sites, and extensive line broadening is a good indicator of one or more solvent ligands. Further, solvent ligands adopt a mean coordination geometry that minimizes the energy of the site, i.e., that increases the electronic symmetry of the site. Thus, axial spectra with extensive line broadening are often observed from Co(II)-substituted hydrolytic enzymes in the resting state [5,9,15,39,48]. Conversely, narrow spectral linewidths, allowing observation of resolved hyperfine structure, are more often observed on very rhombic spectra, suggestive of fivefold coordination. Fivefold coordination is less favorable than four- or sixfold and is maintained either by rigid ligands from the protein in the resting state, or by rigid substrate or inhibitor ligands in catalytic intermediate and analog complexes [15,28–31,33–35,38,44]; in the latter, the geometry is often very asymmetric and E/D approaches $^1/_3$. While resolved hyperfine structure is not indicative of geometry per se, it does indicate a very constrained metal ion coordination sphere, with chemical and structural implications.

The magnitude of the hyperfine interaction can also provide structural information. Where resolved, $A(^{59}Co)$ in Co(II)-substituted proteins is generally 70–90 G (7–9 mT; 7.6–9.6×10^{-3} cm^{-1}) and is best observed at the lowest-field g_{eff} resonance of $M_S = |\pm^1/_2\rangle$ due to the nature of the field-swept spectrum. Significant deviations from this may indicate either electron delocalization onto a ring system provided by a bidentate ligand, or onto an electrophilic substituent [12,28–31]. The narrower lines in the part of the spectrum exhibiting resolved hyperfine structure render this region particularly sensitive to the spin-Hamiltonian parameters in simulations and to changes in the Co(II) environment during reaction with substrates. Whether or not specific structural information can be obtained, changes in the hyperfine pattern can provide potentially important information during RFQ-EPR spectrokinetic studies (Fig. 9).
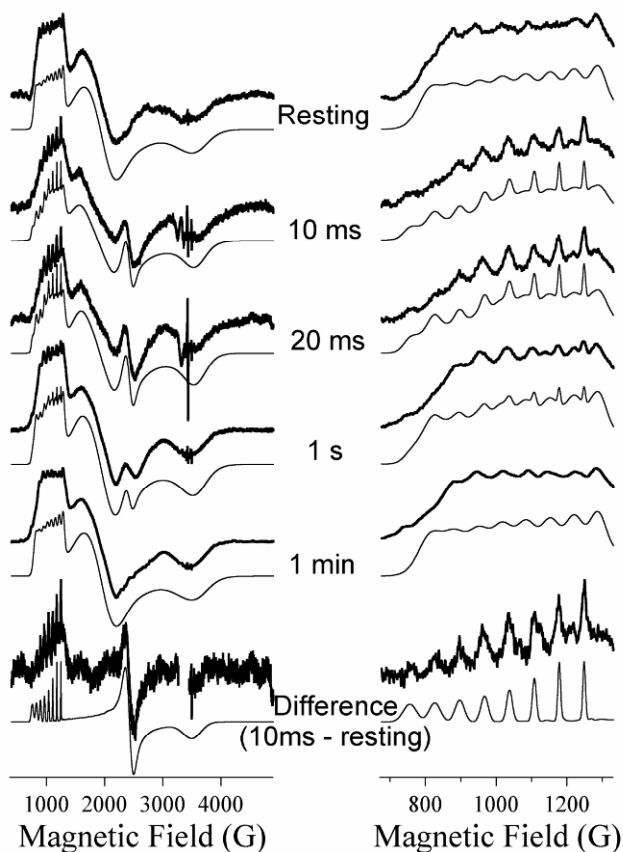
Figure 9. Traces show experimental (heavy) and simulated (light) spectra of aminopeptidase reacted with LeuLeuLeu at 2°C for reaction times shown. The hyperfine region is shown expanded on the right. Details of the simulations will be published elsewhere.

Information on whether Co(II) is incorporated into a dinuclear site can come from either the observation of a parallel mode signal at $g_{eff} \sim 10$–12 or by quantitation showing that the intensity of the $S = {}^3/_2$ spectrum does not account for all of the added Co(II). In the latter case, care must be taken to exclude the possibility of either a very fast relaxing or high-symmetry EPR-silent $M_S = |\pm{}^3/_2\rangle$ signal [9] by optical spectroscopy, and the possibility that Co(II) is being oxidized to Co(III).

6. SPECTRAL INTERPRETATION: A CASE STUDY

The data of Figure 9 show EPR signals from the Co(II)-substituted heterodimetallic form of aminopeptidase from *Vibrio proteolyticus*, [CoZn(VpAP)], in the

resting form and upon reaction with a substrate, LeuLeuLeu. From electronic absorption studies [32,56] and crystallography [78], the Co(II) ion is five coordinate in the resting state, and there is a bridging solvent molecule. Consistent with this, the resting EPR signal is rhombic and displays some poorly resolved hyperfine structure. Upon initial reaction (10 ms), two new signals appear. A broad, axial signal is present in the spectrum (not shown isolated), indicative of a six-coordinate Co(II) ion with a flexible solvent ligand, consistent with the observation that the solvent-derived bridge is broken upon substrate binding [30,32]. This signal is diminished at 20 ms reaction time and thereafter, and is therefore an early catalytic intermediate. The second signal (shown in Fig. 9 as the "difference" signal) is more rhombic than the resting signal and has very narrow lines. It is therefore five coordinate, and the Co(II) ion is ligated solely by rigid ligands. This signal persists during the reaction, though it shows maximum intensity at 20 ms. and, after the exhaustion of substrate, the signal returns to the resting form. Simulation of the spectra allowed determination of the relative contributions of the Co(II) ions as a function of reaction time and indicated a reaction mechanism

E (5-coord #1) + S → ES1 (6-coord) → ES2 (5-coord #2) (→ ES‡) → E + P.
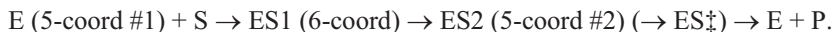
Because of the narrow lines of the EPR spectrum of ES2 and its similarity to those from crystallographically characterized inhibitor complexes [35], it was clear that (i) ES2 is a pretransition state, substrate-bound complex, and (ii) there is no Co(II)-bound water in ES2. The startling indication from EPR, then, was that the nucleophile in the hydrolytic reaction is *not* provided by the metal ion. Subsequent crystallographic [79] and theoretical studies [20] have provided further support for this mechanism, a new paradigm for metallohydrolases. The time-dependent EPR data were a crucial factor in elucidating this mechanism.

7. COMPLEMENTARY TECHNIQUES

There are many techniques that provide complementary information to EPR of Co(II)-substituted proteins. Crystallography is an obvious and important one and provides structural data on resting and inhibited forms of Co(II)-substituted enzymes that can be correlated with and compared to EPR. EXAFS can be useful, particularly in identifying sulfur as a ligand or in characterizing inter-metal distances in dinuclear centers. Optical absorption can be useful along with EPR in distinguishing 5- and 6-coordinate Co(II). Stopped-flow spectrophotometry is a valuable counterpart to RFQ-EPR studies where d–d absorption bands can be monitored and provides a second time-resolved technique with which to study the Co(II) ion. MCD can provide information on D and J in spin-coupled centers that may be unavailable from EPR.

8. CONCLUSIONS

EPR of Co(II)-substituted zinc enzymes can provide important structural and mechanistic information, particularly when combined with other techniques, provided that the samples are carefully prepared and biochemically characterized, the spectroscopy is carried out carefully, the caveats pertaining to Co(II) as a structural mimic of Zn(II) are appreciated, and the interpretation is carried out with regard to all the available information regarding the system and to the characteristics of EPR spectra exhibited by Co(II) in the active sites of metalloenzymes. Important in the future improved exploitation of EPR to the study of Co(II) in enzymes will be (i) the continued growth of a database of systems for which both structural and EPR data are available, (ii) the further development and evaluation of EPR methods that do not rely on field modulation, and (iii) application and continued development of computational techniques that can correlate spin-Hamiltonian parameters of Co(II) with structural features.

REFERENCES

1. Vallee BL, Rupley JA, Coombs TL, Neurath H. 1958. The release of zinc from carboxypeptidase and its replacement. *J Am Chem Soc* **80**:4750–4751.
2. Vallee BL, Galdes A. 1984. The metallobiochemistry of zinc enzymes. *Adv Enzymol* **56**:283–430.
3. Huheey JE. 1983. *Inorganic chemistry*. New York: Harper & Row.
4. Maret M, Vallee BL. 1993. Cobalt as probe and label of proteins. *Methods Enzymol* **226**:52–71.
5. Crawford PA, Yang K-W, Narayan S, Bennett B, Crowder MW. 2005. Spetroscopic studies on Co(II)-substituted metallo-beta-lactamase ImiS from *Aeromonas veronii bv. sobria*. *Biochemistry* **44**:5168–5176.
6. Wang J, Stieglitz A, Kantrowitz ER. 2005. Metal specificity is correlated with two crucial active site residues in *Escherichia coli* alkaline phosphatase. *Biochemistry* **44**:8378–8386.
7. Werth MT, Tang S-F, Formicka G, Zeppezauer M, Johnson MK. 1995. Magnetic circular dichroism and electron paramagnetic resonance studies of cobalt-substituted horse liver alcohol dehydrogenase. *Inorg Chem* **34**:218–228.
8. Bennett B, Holz RC. 1997. EPR Studies on the mono- and dicobalt(II)-substituted forms of the aminopeptidase from *Aeromonas Proteolytica*: insight into the catalytic mechanism of dinuclear hydrolases. *J Am Chem Soc* **119**:1923–1933.
9. Garrity JD, Bennett B, Crowder MW. 2005. Direct evidence that the reaction intermediate of metallo-lactamase L1 is metal bound. *Biochemistry* **44**:1078–1087.
10. Kleifeld O, Rulfísek L, Bogin O, Frenkel A, Havlas Z, Burstein Y, Sagi I. 2004. Higher metal–ligand coordination in the catalytic site of cobalt-substitiuted *Thermoanaerobacter brockii* alcohol dehydrogenase lowers the barrier for enzyme catalysis. *Biochemistry* **43**:7151–7161.
11. Kremer-Aach A, Kläui W, Bell R, Strerath A, Wunderlich H. Mootz D. 1997. Cobalt as a probe for zinc in metalloenzyme model compounds? A comparison of spectroscopic features and coordination geometry of four- and five-coordinate complexes. *Inorg Chem* **36**:1552–1563.

12. Bennett B. 2002. EPR of Co(II) as a structural and mechanistic probe of metalloprotein active sites: characterisation of an aminopeptidase. *Curr Topics Biophys* **26**:49–57.

13. Kobayashi M, Shimizu S. 1999. Cobalt proteins. *Eur J Biochem* **261**:1–9.

14. Grell E, Bray RC. 1971. Electron paramagnetic resonance spectroscopy of bovine cobalt carbonic anhydrase B. *Biochim Biophys Acta* **236**:503–506.

15. Martinelli RA, Hanson GR, Thompson JS, Holmquist B, Pilbrow JR, Auld DS, Vallee BL. 1989. Characterization of the inhibitor complexes of cobalt carboxypeptidase a by electron paramagnetic resonance spectroscopy. *Biochemistry* **28**:2251–2258.

16. Fung C-H, Mildvan AS, Leigh JS. 1974. Electron and nuclear magnetic resonance studies of the interaction of pyruvate with transcarboxylase. *Biochemistry* **13**:1160–1169.

17. Bicknell R, Hanson GR, Holmquist B, Little C. 1986. A spectral study of Cobalt(II)-substituted *Bacillus cereus* phospholipase C. *Biochemistry* **25**:4219–4223.

18. Bubacco L, Magliozzo RS, Beltramini M, Salvato S, Peisach J. 1992. Preperation and spectroscopic characterization of a coupled binuclear center in cobalt(II)-substituted hemocyanin. *Biochemistry* **31**:9294–9303.

19. Horecker BL, Tsolas O, Lai CY. 1972. Aldolases. In *The enzymes*, Vol. 7, 3rd ed, pp. 213–258. Ed PD Boyer. New York: Academic Press.

20. Xu D, Xie D, Guo H. 2006. Catalytic mechanism of class B2 metallo-β-lactamase. *J Biol Chem* **281**:9740–8747.

21. Davis MI, Bennett MJ, Thomas LM, Bjorkman PJ. 2005. crystal structure of prostate-specific membrane antigen, a tumor marker and peptidase. *Proc Natl Acad Sci USA* **102**:5981–5986.

22. Kaznowski A, Wlodarczak K. 1991. Enzymatic characterization of *Vibrionaceae* strains isolated from environment and cold-blooded animals. *Acta Microbiol Pol* **40**:71–76.

23. Maras B, Greenblatt HM, Shoham G, Spungin-Bialik A, Blumberg S, Barra D. 1997. Aminopeptidase from *Streptomyces griseus*: primary structure and comparison with other zinc-containing aminopeptidases. *Eur J Biochem* **236**:843–846.

24. Merkel JR, Traganza ED, Mukherjee BB, Griffin TB, Prescott JM. 1964. Proteolytic activity and general characteristics of a marine bacterium, *Aeromonas proteolytica* Sp. N. *J Bacteriol* **87**:1227–1233.

25. Scoglio ME, DiPietro A, Picerno I, Delia S, Mauro A, Lagana P. 2001. Virulence factors in vibrios and aeromonads isolated from seafood. *New Microbiol* **24**:273–280.

26. Stevens DL, Bryant AE. 2002. The role of clostridial toxins in the pathogenesis of gas gangrene. *Clin Infect Dis* **35**:S93–S100.

27. Toma C, Honma Y. 1996. Cloning and genetic analysis of the *Vibrio cholerae* aminopeptidase gene. *Infect Immun* **64**:4495–4500.

28. Bennett B, Holz RC. 1997. Spectroscopically distinct cobalt(II) sites in heterodimetallic forms of the aminopeptidase from *Aeromonas proteolytica*: characterization of substrate binding. *Biochemistry* **36**:9837–9846.

29. Bennett B, Holz RC. 1998. Inhibition of the aminopeptidase from *Aeromonas proteolytica* by L-leucinephosphonic acid, a transition state analogue of peptide hydrolysis. *J Am Chem Soc* **120**:12139–12140.

30. De Paola CC, Bennett B, Holz RC, Ringe D, Petsko GA. 1999. 1-butaneboronic acid binding to *Aeromonas proteolytica* aminopeptidase: a case of arrested development. *Biochemistry* **38**:9048.

31. Stamper C, Bennett B, Edwards T, Holz RC, Ringe D, Petsko G. 2001. Inhibition of the aminopeptidase from *Aeromonas proteolytica* by L-leucinephosphonic acid: spectro-

scopic and crystallographic characterization of the transition state of peptide hydrolysis. *Biochemistry* **40**:7035–7036.

32. Bennett B, Antholine WE, D'souza VM, Chen G, Ustinyuk L, Holz RC. 2002. Structurally distinct active sites in the copper(II)-substituted aminopeptidase from *Aeromonas proteolytica*. *J Am Chem Soc* **124**:13025–13034.

33. Bienvenue D, Bennett B, Holz RC. 2000. Inhibition of the aminopeptidase from *Aeromonas proteolytica* by L-leucinethiol: kinetic and spectroscopic characterization of a slow, tight-binding inhibitor–enzyme complex. *J Inorg Biochem* **78**:43–54.

34. Huntington KM, Bienvenue D, Wei Y, Bennett B, Holz RC, Pei D. 1999. Slow-binding inhibition of the aminopeptidase from *Aeromonas proteolytica* by peptide thiols: synthesis and spectral characterization. *Biochemistry* **38**:15587–15596.

35. Stamper CC, Bienvenue DL, Bennett B, Ringe D, Petsko G, Holz RC. 2004. Spectroscopic and x-ray crystallographic characterization of bestatin bound to the aminopeptidase from *Aeromonas (Vibrio) proteolytica*. *Biochemistry* **43**:9620–9628.

36. Bzymek K, Moulin A, Swierczek SI, Ringe D, Petsko G, Bennett B, Holz RC. 2005. Kinetic, spectroscopic, and x-ray crystallographic characterization of the functional E151H aminopeptidase from *Aeromonas proteolytica*. *Biochemistry* **44**:12030–12040.

37. Bzymek KP, Swierczek SI, Bennett B, Holz RC. 2005. Spectroscopic and thermodynamic characterization of the E151D and E151A altered leucine aminopeptidases from *Aeromonas proteolytica Inorg Chem* **44**:8574–8580.

38. Breece RM, Costello A, Bennett B, Sigdel TK, Matthews ML, Tierney DL, Crowder MW. 2005. A five-coordinate metal center in Co(II)-substituted VanX. *J Biol Chem* **280**:11074–11081.

39. Periyannan GR, Costello AL, Tierney DL, Yang KW, Bennett B, Crowder MW. 2006. Sequential binding of cobalt(II) to metallo-β-lactamase CcrA. *Biochemistry* **45**:1313–1320.

40. Jordan PA, Bohle DS, Ramilo CA, Evans JNS. 2001. New insights into the metal center of 3-deoxy-D-*arabino*-heptulosonate-7-phosphate synthase. *Biochemistry* **40**:8387–8396.

41. Strand KR, Karlsen S, Andersson KK. 2002. Cobalt substitution of mouse R2 ribonucleotide reductase as a model for the reactive diferrous state. *J Biol Chem* **37**:34229–34238.

42. Shapir N, Osborne JP, Johnson G, Sadowsky MJ, Wackett LP. 2002. Purification, substrate range, and metal center of AtzC: the N-isopropylammelide aminohydrolase involved in bacterial atrazine metabolism. *J Bacteriol* **184**:5376–5384.

43. Doi Y, Lee BR, Ikeguchi M, Ohoba Y, Ikoma T, Tero-Kubota S, Yamauchi S, Takahashi K, Ichishima E. 2003. Substrate specificities of deuterolysin from aspergillus oryzae and electron paramagnetic resonance measurement of cobalt-substituted deuterolysin. *Biosci Biotechnol Biochem* **67**:264–270.

44. Bienvenue DL, Gilner DM, Davis RS, Bennett B, Holz RC. 2003. Substrate specificity, metal binding properties and spectroscopic characterization of the DapE-encoded N-succinyl-L,L-diaminopimelic acid desuccinylase from *Haemophilus influenzae*. *Biochemistry* **42**:10756–10763.

45. Davis RM, Bienvenue DL, Swierczek SI, Gilner D, Rajagopal L, Bennett B, Holz RC. 2006. Kinetic and spectroscopic characterization of the E134A- and E134D-altered DapE-encoded N-succinyl-L,L-diaminopimelic acid desuccinylase from *Haemophilus influenzae*. *J Biol Inorg Chem* **11**:206–216.

46. McGregor WC, Swierczek SI, Bennett B, Holz RC. 2005. ArgE-encoded N-acetyl-L-ornithine deacetylase from *Escherichia coli* contains a dinuclear metalloactive site. *J Am Chem Soc* **127**:14100–14107.

47. Copik AJ, Waterson S, Swierczek SI, Bennett B, Holz RC. 2005. Both nucleophile and substrate bind to the catalytic Fe(II) center in the type-II methionyl aminopeptidase from *Pyrococcus furiosus*. *Inorg Chem* **44**:1160–1162.

48. D'souza VM, Bennett B, Holz RC. 2000. Characterization of the divalent metal binding properties of the methionyl aminopeptidase from *Escherichia coli*. *Biochemistry* **39**:3817–3826.

49. Copik AJ, Nocek BP, Swierczek SI, Ruebush S, Jang SB, Meng L, D'souza VM, Peters JW, Bennett B, Holz RC. 2005. EPR and x-ray crystallographic characterization of the product-bound form of the MnII-loaded methionyl aminopeptidase from *Pyrococcus furiosus*. *Biochemistry* **44**:121–129.

50. D'souza VM, Brown RS, Bennett B, Holz RC. 2005. Characterization of the active site and insight into the binding mode of the anti-angiogenesis agent fumagillin to the manganese(II)-loaded methionyl aminopeptidase from *Escherichia coli*. *J Biol Inorg Chem* **10**:41–50.

51. Lowther WT, Matthews BW. 2000. Structure and function of the methionine aminopeptidases. *Biochim Biophys Acta* **1477**:157–167.

52. Ghosh M, Grunden AM, Dunn DM, Weiss R, Adams MWW. 1998. Characterization of native and recombinant forms of an unusual cobalt-dependent proline dipeptidase (prolidase) from the hyperthermophilic archaeon *Pyrococcus furiosus*. *J Bacteriol* **180**:4781–4789.

53. Petrovich RM, Ruzicka FJ, Reed GH, Frey PA. 1991. Metal cofactors of lysine-2,3-aminomutase. *J Biol Chem* **12**:7656–7660.

54. Gavel OY, Bursakov SA, Calvete JJ, George GN, Moura JJG, Moura I. 1998. ATP sulfurylases from sulfate-reducing bacteria of the genus *Desulfovibrio*: a novel metalloprotein containing cobalt and zinc. *Biochemistry* **37**:16225–16232.

55. Maret W, Vallee BL. 1993. Cobalt as probe and label of proteins. *Methods Enzymol* **226**:52–71.

56. Prescott JM, Wagner FW, Holmquist B, Vallee BL. 1985. Spectral and kinetic studies of metal-substituted *Aeromonas* aminopeptidase: nonidentical, interacting metal-binding sites. *Biochemistry* **24**:5350–5356.

57. Bennett B, Benson N, McEwan AG, Bray RC. 1994. Multiple states of the molybdenum centre of dimethylsulphoxide reductase from *Rhodobacter capsulatus* revealed by EPR spectroscopy. *Eur J Biochem* **225**:321–331.

58. Siemann S, Badiei HR, Karanassios V, Viswanatha T, Dmitienko GI. 2006. [68]Zn isotope exchange experiments reveal an unusual kinetic lability of the metal ions in the di-zinc form of IMP-1 metallo-β-lactamase. *Chem Commun* **2006**:532–534.

59. Walsby CJ, Krepkiy D, Petering DH, Hoffman BH. 2003. Cobalt-substituted zinc finger 3 of transcription factor IIIA: interactions with cognate DNA detected by 31P ENDOR spectroscopy. *J Am Chem Soc* **125**:7502–7503.

60. Mchaourab HS, Pfenninger S, Antholine WA, Felix CC, Hyde JS, Kroneck PMH. 1993. Multiquantum EPR of the mixed valence copper site in nitrous oxide reductase. *Biophys J* **64**:1576–1579.

61. Hagen WR. 1982. EPR spectroscopy of iron sulfur proteins. *Adv Inorg Chem* **38**:165–222.

62. Hendrich MP, Debrunner PG. 1989. Integer-spin electron paramagnetic resonance of iron proteins. *Biophys J* **56**:489–506.

63. Froncisz W, Hyde JS. 1982. The loop-gap resonator: a new microwave lumped circuit ESR sample structure. *J Magn Reson* **47**:515–521.

64. Belford RL. 1979. *Computer simulation of powder spectra*, EPR Symposium, 21st Rocky Mountain Conference, Denver, Colorado.

65. Maurice AM. 1980. PhD dissertation. University of Illinois, Urbana.

66. Nilges MJ. 1979. PhD dissertation. University of Illinois, Urbana.

67. Hanson GR, Gates KE, Noble CJ, Griffin M, Mitchell A, Benson S. 2004. XSophe-Sophe-XeprView®: a computer simulation software suite (v. 1.1.3) for the Analysis of continuous wave EPR spectra. *J Inorg Biochem* **98**:903–916.

68. Pilbrow JR. 1978. Effective *g* values for *S* = 3/2 and *S* = 5/2. *J Magn Reson* **31**:479–489.

69. Krzystek J, Zvyagin SA, Ozarowski A, Fiedler AT, Brunold TC, Telser J. 2004. Definitive spectroscopic determination of zero-field splitting in high-spin cobalt. *J Am Chem Soc* **126**:2148–2155.

70. Hagen WR, Hearshen DO, Sands RH, Dunham WR. 1985. A statistical theory for powder EPR in distributed systems. *J Magn Reson* **61**:220–232.

71. Jenkins DM, Di Billio AJ, Allen MJ, Betley TA, Peters JC. 2002. Elucidation of a low spin cobalt(II) system in a distorted tetrahedral geometry. *J Am Chem Soc* **124**:15336–15350.

72. Jenkins DM, Peters JC. 2005. Spin-state tuning at pseudotetrahedral d7 ions: examining the structural and magnetic phenomena of four-coordinate [BP3]CoII–X systems. *J Am Chem Soc* **127**:7148–7165.

73. Lohr LL, Miller JC, Sharp RR. 1999. Electronic structure and magnetic properties of high-spin octahedral Co(II) complexes: Co(II)(Acac)$_2$(H$_2$O)$_2$. *J Chem Phys* **111**:10148–10158.

74. Ozarowski A, Lee HM, Balch AL. 2003. Crystal environments probed by EPR spectroscopy. *J Am Chem Soc* **125**:12606–12614.

75. Larrabee JA, Alessi CM, Asiedu ET, Cook JO, Hoerning KR, Klingler LJ, Okin GS, Santee SG, Volkert TL. 1997. Magnetic circular dichroism spectroscopy as a probe of geometric and electronic structure of cobalt(II)-substituted proteins: ground-state zero-field splitting as a coordination number indicator. *J Am Chem Soc* **119**:4182–4196.

76. Makinen MW, Maret W, Yim MB. 1983. Neutral metal-bound water is the base catalyst in liver alcohol dehydrogenase. *Proc Natl Acad Sci USA* **80**:2584–2588.

77. Makinen MW, Yim MB. 1981. Coordination environment of the active-site metal ion of liver alcohol dehydrogenase. *Proc Natl Acad Sci USA* **78**:6221–6225.

78. Munih P, Moulin A, Stamper CC, Bennett B, Ringe D, Petsko GA, Holz RC. 2007. X-ray crystallographic characterization of the Co(II)-substituted Tris-bound form of the aminopeptidase from *Aeromonas proteolytica*. *J Inorg Biochem* **101**(8):1099–1107.

79. Kumar A, Periyannan GR, Narayanan B, Kittell AW, Kim JJ, Bennett B. 2007. Experimental evidence for a metallohydrolase mechanism in which the nucleophile is not delivered by a metal ion: EPR spectrokinetic and structural studies of aminopeptidase from *Vibrio proteolyticus*. *Biochem J* **403**(3):527–536.

HYPERFINE AND QUADRUPOLAR INTERACTIONS IN VANADYL PROTEINS AND MODEL COMPLEXES: THEORY AND EXPERIMENT

Sarah C. Larsen[1] and N. Dennis Chasteen[2]

[1]*Department of Chemistry, University of Iowa, Iowa City*
[2]*Department of Chemistry, University of New Hampshire, Durham*

The oxycation VO^{2+} has been employed for many years as an EPR spin probe of the metal binding sites in proteins. Its utility in these investigations has increased markedly with the advent and widespread use of high-resolution techniques such as ENDOR, ESEEM, and HYSCORE to measure isotropic and dipolar components of ligand hyperfine couplings. Measurements with model complexes in conjunction with DFT calculations have provided new insights into the dependence of *g*-factors and ligand and ^{51}V nuclear hyperfine couplings on the electronic structure and coordination geometries of VO^{2+} chelates. These studies have greatly enhanced the information that can be derived from data with proteins. In the past fifteen years, high-resolution techniques have been applied to a variety of VO^{2+}-containing proteins and tissues samples, a number of which are reviewed here.

Address all correspondence to N. Dennis Chasteen, University of New Hampshire, Department of Chemistry, Parsons Hall, 23 College Road, Durham, NH 03824 USA, 603 862-2520, 603 862-4278 (fax), <ndc@cisunix.unh.edu>.

1. INTRODUCTION

1.1. Coordination Chemistry of VO^{2+}

The oxycation vanadyl(IV), VO^{2+}, is one of the most studied of the electron paramagnetic resonance (EPR) active transition metal ion species. Its appeal as a spin probe resides in its useful coordination and spectroscopic properties [1–7]. In addition to numerous investigations of small oxovanadium(IV) chelates, the vanadyl ion has been used as a probe of metal ion coordination and the conformational and kinetic properties of some twenty proteins. The biochemistry of vanadium has been extensively reviewed elsewhere, and the reader is referred to these authoritative papers for coverage of much of the earlier literature [3,8–12]. Most oxovanadium complexes have a square bipyramidal geometry in aqueous solution where L′ is usually H_2O (Fig. 1A) or a square pyramidal geometry in noncoordinating solvent (Fig. 1B). These complexes are dominated by the short (~1.6 Å) V=O bond (Fig. 1A) and have four equatorial bonds of length 1.9–2.0 Å, whereas the bond to the axial ligand L′ *trans* to the vanadyl oxygen is typically somewhat longer (~2.2–2.4 Å). The vanadium atom itself usually sits ~0.5 Å above the plane defined by four equatorial ligands. However, there are many examples of deviations from this idealized geometry as governed by the structural properties of the ligands. In the classic example of the vanadyl uridine inhibitor complex of ribonuclease A, a five-coordinate trigonal bipyramidal geometry is observed [13]. The dichlorobis(N,N-dimethylacetamide) oxovanadium(IV) complex has a near trigonal bipyramidal structure as in Figure 1C [14]. A more recently reported series of shift base VO^{2+} complexes has geometries ranging from square pyramidal (Fig. 1B) to trigonal bipyramidal (Fig. 1C), as dictated by steric effects of the ligands [15]. The coordination flexibility of the VO^{2+} ion contributes to its versatility as a

(A)   (B)   (C)
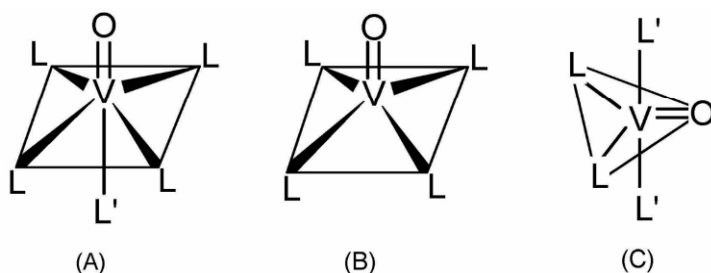
Figure 1. Idealized geometries of vanadyl complexes: (A) square bipyramidal, (B) square pyramidal, and (C) trigonal bipyramidal.

spin probe and undoubtedly accounts for its ability to complex with such a large variety of proteins where the coordination geometry is determined in part by the structure of the metal site.

1.2. EPR Properties

Oxovanadium(IV) complexes have an outer electron configuration of $3d^1$, a modest spin–orbit coupling constant of ~170 cm^{-1}, and no excited electronic states nearby in energy. These are the requirements for sharp EPR lines since relaxation broadening through spin–orbit coupling mechanisms is minimized. EPR spectra of room-temperature solution as well as frozen solid matrices are readily observed in most instances. The ability to make liquid solution measurements, and hence ascertain the degree of motional freedom of the VO^{2+} ion, enables one to unequivocally establish whether the probe is coordinated to the macromolecule being investigated [2]. Since high-resolution studies involve the use of frozen solutions or powdered samples at reduced temperatures (4 or 77 K), rotational diffusion is absent and "powder-pattern" EPR spectra are obtained that are rich in fine structure from coupling of the unpaired electron with the 100% ^{51}V nucleus (Fig. 2).
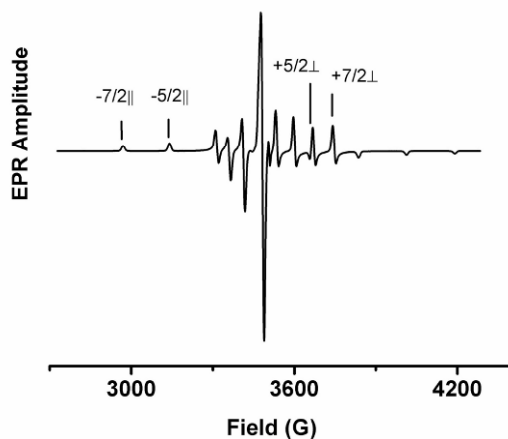
Figure 2. Room-temperature cw-EPR spectrum of powdered vanadyl(IV) tetraphenylporphyrin doped in Zn(II) tetraphenylporphyrin. The spectrum was measured with a peak-to-peak modulation amplitude of 3.0 G.

In solid-state magnetically dilute samples (frozen solutions or doped minerals), the EPR spectra of VO^{2+} chelates consist of overlapping patterns of 8 hyperfine lines ($2I + 1$ rule), as shown in Figure 2 by the X-band spectrum of a powdered sample of vanadyl tetraphenylporphyrin (VOTPP) doped in the corresponding Zn^{2+} lattice. The short V=O bond axis of vanadyl complexes invariably defines the

magnetic z-axis. Allowed transitions ($\Delta m_s = +1$, $\Delta m_I = 0$) corresponding to the magnetic field along or approximately along the z-axis give rise to the less intense lines appearing in the wings of the spectrum. The more intense pattern of 8 lines in the central region of the spectrum arises from transitions where the field is perpendicular to the z-axis. Thus, through careful selection of field in an electron nuclear double resonance (ENDOR) or electron spin echo envelope modulation (ESEEM) experiment, one can obtain "single-crystal" spectra from a powder pattern and hence orientation information on observed couplings. The principles of such an analysis as applied to VO^{2+} have been recently reviewed [6]. A pedagogical treatment of the high-resolution techniques of ENDOR and ESEEM can be found in Chasteen and Snetsinger [16]. A comprehensive coverage of pulsed electron resonance is given by Schweiger and Jeschke [17].

1.3. The Additivity Relationship for Predicting Ligand Environments

The lack of "superhyperfine" splittings from ligand nuclei in the cw EPR of most vanadyl complexes has historically led workers to rely on indirect methods to identify first-coordination sphere ligands in unknown complexes such as those with proteins or catalytic surfaces. The g-factors and ^{51}V hyperfine couplings are sensitive to the identity and geometry of the ligands coordinated to the vanadium. "Truth diagrams" show correlations between values for $g_{||}$ and $A_{||}(^{51}V)$ or g_0 and $A_0(^{51}V)$ with points clustering in domains according to ligand donor type (oxygen, nitrogen, sulfur, mixed, etc.) [1,2]; however, there is significant overlap between domains. Nevertheless, these diagrams provided some information about the ligand environment of the vanadium in VO^{2+}–protein complexes. A more refined approach was subsequently developed, employing additivity relationships in which each type of equatorial donor contributes a defined amount to the measured value of $A_{||}(^{51}V)$. The contributions for different donors (oxygen of carboxylate, oxygen from phenolate, hydroxide, water, imidazole, primary amine, etc.) were originally compiled by Chasteen [2] based on measurements with model compounds [18] and subsequently updated by Smith et al. [7]. This approach by itself cannot unequivocally define the coordination sphere of the vanadium since more than one combination of equatorial ligand donor set can lead to nearly the same predicted value of $A_{||}(^{51}V)$. Moreover, the effect of the identity of the axial ligand L′ on the observed coupling can be significant [7]. Nevertheless, additivity calculations can be helpful, especially when combined with measurement of couplings from ligand nuclei using ENDOR or ESEEM.

1.4. The Ground State and Ligand Hyperfine Couplings

The failure to observe ligand superhyperfine splittings in the cw-EPR spectra of the majority of VO^{2+} complexes is a consequence of the ground state molecular orbital in which the unpaired electron resides. This orbital is mostly d_{xy} in character where the x- and y-axes are chosen to lie approximately along the sigma bonds of
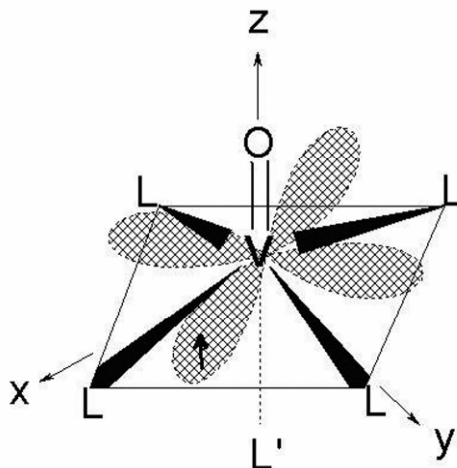
Figure 3. Ground state "nonbonding" $3d_{xy}$ orbital of VO^{2+} complexes.

the equatorial ligands (Fig. 3). This orbital is largely nonbonding or participates in in-plane π bonding with ligand orbitals of correct symmetry. In either case, the resultant hyperfine couplings are typically small. This situation is unlike that with $3d^9$ Cu^{2+}, where the odd electron is in a d_{x2-y2} orbital that participates in σ-bonding with the ligands. Couplings, especially with ^{14}N, are commonly seen in cw EPR of Cu^{2+}. They are often well resolved at S-band frequency, where g-strain is minimized for this ion [19].

The difference in ground states for Cu^{2+} and VO^{2+} ions is particularly revealed by comparison of the EPR spectra of their tetraphenylporphyrin (TPP) complexes where ^{14}N hyperfine splittings from the in-plane nitrogen donor atoms are observed. These splittings of $a_0(^{14}N) \sim 15$ G are relatively large in the Cu^{2+} case, corresponding to a hyperfine coupling of $A_0(^{14}N) \sim 44$ MHz, and exceed the cw-EPR linewidth [20]. In contrast, the fivefold smaller ^{14}N splittings of VOTPP can be easily missed during routine scanning of the cw spectrum at a modulation amplitude of 3.0 G (Fig. 2). However, careful scanning of the $m_I = -5/2$ parallel and the $m_I = + 5/2$ perpendicular lines at a reduced modulation amplitude of 0.5 G reveals evidence of fine structure (Fig 4, curves a and c). The structure can be significantly enhanced by postprocessing the spectrum using first-harmonic pseudo-field modulation (Fig. 4., curves b and d) [21,22]. VOTPP doped into the corresponding ZnTPP lattice is a particularly favorable case since the peak-to-peak linewidths of the 9 components of the ^{14}N superhyperfine patterns of both the parallel and perpendicular lines are only ~1.6 G, enabling the hyperfine splitting of $a_0(^{14}N) \sim 2.7$ G to be resolved, a value in agreement with that calculated from the isotropic coupling $A_0(^{14}N) = 7.3$ MHz determined from ESEEM [23].
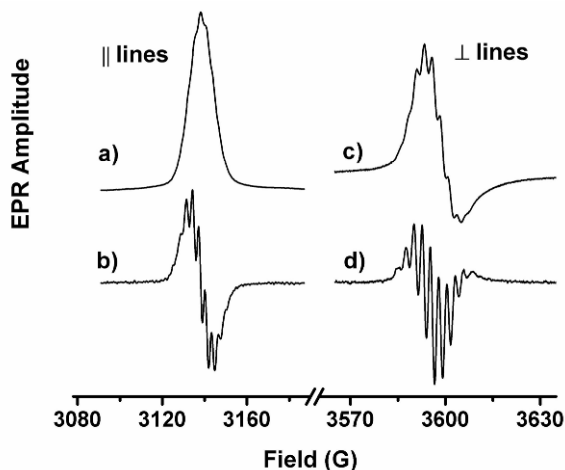
Figure 4. Effect of pseudomodulation on resolution of fine structure from ^{14}N couplings in the cw-EPR spectrum of vanadyl(IV) tetraphenylporphyrin. Spectrum a: –5/2 ∥ line. Spectrum b: –5/2 ∥ line pseudomodulated. Spectrum c: +5/2 ⊥ line. Spectrum d: +5/2 ⊥ line pseudomodulated. Original spectrum measured with 0.5 G peak-to-peak field modulation. Pseudomodulation postprocessing of the spectra was carried out using Bruker Xepr software employing a first-harmonic pseudomodulation with an amplitude of 0.5 G.

Resolution of superhyperfine structure is typically not observed with frozen aqueous samples of VO^{2+} where unresolved proton couplings, g-strain, and A-strain contribute significantly to the observed inhomogeneously broadened linewidths of 5–10 G. Hence the development of high-resolution electron resonance techniques for measuring superhyperfine couplings lost in the width of the EPR line has been of great value in investigations of VO^{2+}–protein complexes. Here we review cw and pulsed ENDOR and ESEEM studies of VO^{2+} model complexes, DFT calculations of hyperfine couplings, and the application of ENDOR and ESEEM to proteins. We largely focus on the literature of the past 15 years. The reader should consult several other reviews for coverage of other model compounds and protein complexes and much of the earlier literature [2,4–7,24,25].

2. ENDOR AND ESEEM OF VANADYL MODEL COMPLEXES

2.1. [14]N Hyperfine and Quadrupole Coupling Constants

[14]N is a quadrupolar nucleus with a nuclear spin $I = 1$. [14]N hyperfine and quadrupole coupling constants in vanadyl model complexes and proteins are routinely measured by ESEEM and ENDOR [2,4–7,25–31]. In both ENDOR and ESEEM, the spectrum is obtained at a specific field position within the EPR spectrum so that molecules with specific orientations will be interrogated in the ENDOR or

ESEEM experiment. Varying the EPR line position in an ENDOR or ESEEM experiment is referred to as *orientation selection* because only molecules with specific orientations will be excited [6].

ENDOR spectroscopy is most effectively used to measure strong ^{14}N hyperfine couplings $A_0(^{14}\text{N})$ with ENDOR frequencies given by the following expression [7,16]:

$$\nu_{\text{ENDOR}} = \left| \frac{A_0(^{14}\text{N})}{2} \pm \nu_N \pm 3K \right|. \tag{1}$$

ESEEM methods are used to measure relatively weak nitrogen hyperfine coupling constants (HCCs) typically in the range of ~1–10 MHz. Nuclear quadrupole coupling constants (QCCs) can be directly measured by ESEEM spectroscopy under conditions of *exact cancellation* [23,29,32,33]. Exact cancellation for nitrogen nuclei occurs when the nuclear Zeeman interaction and the hyperfine coupling interaction cancel in one electron spin manifold, and pure quadrupole eigenstates remain. Under conditions of exact cancellation, three pure quadrupole peaks are observed in the ^{14}N ESEEM spectrum at frequencies of $K(3 + \eta)$, $K(3 - \eta)$, and $2K\eta$, where $K = e^2qQ/4$ is the QCC and η is the asymmetry parameter (Table 1, footnote b). Singel and coworkers have demonstrated that the microwave frequency can be varied to achieve exact cancellation, such that the quadrupole coupling constants can be determined directly from the positions of the lines in the FT-ESEEM spectrum [30,32,41]. When the ESEEM experiment is performed far from exact cancellation, the predominant features of the ESEEM spectrum will be double quantum peaks that appear at the following frequencies:

$$\nu_{dq,\pm} = 2\left[\left(\nu_N \mp \left(\frac{A_0(^{14}\text{N})}{2} \right) \right)^2 + K^2\left(3 + \eta^2\right) \right]^{1/2}. \tag{2}$$

Recently, a two-dimensional ESEEM experiment employing hyperfine sublevel correlation spectroscopy (HYSCORE) has been widely used to investigate a range of systems [26,42,43]. The advantage of the HYSCORE experiment relative to standard ESEEM methods is that spectral assignments are simplified due to cross-peaks in the two-dimensional spectrum that correlate nuclear frequencies from different electron spin manifolds, simplifying spectral assignments and decreasing spectral overlap [17].

Numerous ESEEM and ENDOR studies of VO^{2+} model complexes have been conducted in order to elucidate the ligand environment in vanadyl proteins [4,6,7,25]. In vanadyl protein systems, ligands such as histidine and glycine can be identified by characteristic ^{14}N HCCs and QCCs. Dikanov and coworkers studied ^{15}N-labeled VO^{2+}–imidazole and histidine model complexes using ESEEM and HYSCORE [34,38]. The coordinated and remote nitrogen HCCs are clearly resolved in the HYSCORE spectrum of VO^{2+}-((^{15}N)imidazole)$_4$ and differ in magnitude by a factor of ~20, as for Cu^{2+} [34]. These findings are in contrast to those of

Table 1. Nitrogen-14 Nuclear Hyperfine Coupling Constants and Quadrupole Coupling Parameters for VO^{2+} Protein and Model Complexes[a,b]

VO^{2+}–complex[c]	Method	Nitrogen type[d]	$A_0(^{14}N)$	$A_z(^{14}N)$	$Q_z(^{14}N)$	η	Reference
VO–LF–CO$_3$	ESEEM	His	6.6	–	0.75	0.5	[28]
VO–XylI	ESEEM	N3 His	5.7	5.7	0.64	~1.0	[34]
VO–IGDP	ESEEM	His	7.2	7.5	0.88	~1.0	[35]
VO–TF1	ESEEM	N3 His	6.5	–	1.0 – 1.2	–	[36]
VO(Im)$_4$	ENDOR	N3 Im	6.4	6.6	0.80	–	[37]
VO(Im)$_4$	ESEEM	N1 Im	0.3	–	–	–	[38]
VO–TF1	ESEEM	ε-amino Lys	4.8	–	1.4 – 1.6	–	[36]
E–VO–AdoMet–K	ESEEM	α-amino Met	5.3	5.5	1.5	0.3	[39]
E–VO–ATP–Met–K	ESEEM	ε-amino Lys	4.3	4.3	1.85	0.3	[39]
VO–PK–PEP	ESEEM	ε-amino Lys	4.9	5.1	1.28	0.5	[40]
VO–gly$_2$	ESEEM	α-amino	4.8	–	1.3 – 1.5	–	[36]
VO–gly$_2$	ESEEM	α-amino	5.0	5.3	1.28	0.5	[40]
VO–(H$_2$O)–nta	ESEEM	Amino (axial)	1.3	2.3	1.2	0.86	[31]

[a]Values of $A_0(^{14}N)$, $A_z(^{14}N)$, and $Q_z(^{14}N)$ are expressed in MHz.
[b]There is no accepted practice for reporting quadrupole parameters. The following equations relate the different quadrupole parameters (K, e^2Qq, Q_x, Q_y, Q_z, P_x, P_y, P_z, and η) commonly reported in the literature: $K = e^2Qq/4$, $Q_z = e^2Qq/2$, $\eta = (Q_x - Q_y)/Q_z$ and $Q_x + Q_y + Q_z = 0$, i.e., the quadrupole tensor is traceless. The principle values of the quadrupole coupling tensor, Q_x, Q_y, and Q_z, are also frequently designated P_x, P_y, and P_z. η is the asymmetry parameter, e^2Qq is the quadrupole coupling constant (QCC), Q is the electric quadrupole moment of the ^{14}N nucleus, and eq. is the electric field gradient at the ^{14}N nucleus. When necessary, we have converted the parameters reported in the literature to those given in the table using the above equations.
[c]Abbreviations: E–VO^{2+}–ATP–met–K, the VO^{2+} enzyme complex of S-adenosylmethionine synthetase with ATP and methionine coordinated; gly, glycine; IGDP, imidazole glycerol phosphate dehydratase; LF, lactoferrin; nta, nitrilotriacetate; PEP, phosphoenolpyruvate; PK, pyruvate kinase; TF1, wild-type F1 ATPase from thermophilic *Bacillus* PS3; XylI, D-xylose isomerase.
[d]Coordination is assumed equatorial to the V=O bond axis unless specified otherwise.

earlier ENDOR work [37]. For the VO^{2+}–((^{15}N)histidine)$_2$ complex, equatorial coordination by both imine and amine nitrogens was observed [34]. Table 1 summarizes HCCs and QCCs for a number of model and protein complexes.

Lobrutto and coworkers have measured the ESEEM spectra for several oxovanadium model complexes with axial nitrogen ligands so that axial versus equatorial ligation could be distinguished in VO^{2+} systems [31]. An isotropic hyperfine coupling constant for a vanadyl model complex with an axial amine ligand was deter-

mined to be 1.3 MHz, in contrast to the isotropic hyperfine coupling constant of ~5.0 MHz for an equatorially coordinated amine [31] (Table 1).

Fukui and coworkers demonstrated that the nitrogen hyperfine coupling constants for equatorially coordinated amine (~5 MHz), imine (~6–7 MHz), and thiocyanate (~7.5 MHz) ligands in vanadyl complexes can be differentiated using ESEEM spectroscopy [44]. Previous measurements of vanadium–amine HCCs for nitrogen adducts of $VO(acac)_2$ [45] and $VO(gly)_2$ [40], and vanadium–imine HCCs for $VO(meox)_2$ [46], $VO(mim)_4$ Cl^+ [46], pyridine, and imidazole adducts of VO–(hexafluoroacetylacetonate)$_2$ [28], and a VO–histidine complex [34] support the trend in amine, imine, and thiocyanate nitrogen HCCs [acac = acetylacetonate; gly = glycinate; meox = oxobis(2-methylquinolin-8-olato); and mim = 1-methyl imidazole].

2.2. ^1H and ^{17}O Coupling Constants

ENDOR [47–49] and ESEEM [50–52] have been used extensively to measure the proton hyperfine coupling constants of $[VO(H_2O)_5]^{2+}$ in a single crystal [47] and in frozen solution and powder samples [49,50,52]. The single-crystal proton ENDOR results for the equatorial water ligands of $[VO(H_2O)_5]^{2+}$ in an $Mg(NH_4)_2(SO_4)_26H_2O$ single crystal led Atherton and Shackleton to conclude that two water molecules were oriented approximately in the equatorial plane while the other two water molecules were located approximately perpendicular to the equatorial plane [47]. Frozen solution ENDOR data were also obtained in which the first coordination sphere with water (and methanol) was probed [48,49]. The dipolar approximation was the basis for the ENDOR analysis, thus yielding distance information for the proton relative to the vanadium center. Use of the dipolar part of proton hyperfine coupling constants to elucidate the structure of VO^{2+} complexes has been reviewed [5].

A transition metal complex with a terminal hydroxy ligand is an important moiety in metalloproteins, such as vanadium haloperoxidase [27]. In a recent study, cis-$[VO(OH)]^+$ complexes containing bidentate ligands, such as 2,2′-bipyridine (bipy) and 1,10-phenanthroline (phen), were prepared and characterized by ESEEM spectroscopy [52]. A characteristic proton isotropic hyperfine coupling constant of $A_0(^1H) = 2.2$ MHz with a large anisotropic component of $A_D(^1H) = 3.5$ MHz was observed using HYSCORE spectroscopy. Based on the proton coupling constants, the signal was assigned to the hydroxy proton of an equatorially bonded OH group [52].

^{17}O ($I = 5/2$) can be a difficult nucleus to probe with ESEEM and ENDOR due to its low natural abundance and large quadrupole moment. The large quadrupole interaction often leads to significant line broadening. Spectral overlap with proton signals can also be problematic. These effects can be mitigated somewhat at high frequencies such as Q- and W-bands. For example, in a recent high-field ENDOR study, Baute and Goldfarb measured ^{17}O hyperfine and quadrupole coupling constants of $[VO(H_2O)_5]^{2+}$ [53]. The equatorial water ligands had ^{17}O iso-

tropic hyperfine couplings of $A_0(^{17}O) = 6.4$ MHz compared to $A_0(^{17}O) = -1.9$ MHz for the axial oxygen in the oxovanadium bond. The corresponding e^2qQ/h values for ^{17}O were 10.7 and 3.3 MHz for the equatorial and vanadyl oxygen atoms. Corresponding DFT calculations of $[VO(H_2O)_5]^{2+}$ reproduced the experimental ^{17}O hyperfine and quadrupole coupling constants very well, thus confirming the spectral assignments.

2.3. ^{31}P Hyperfine Coupling Constants

Binding of VO^{2+} to phosphate in biological systems is of great interest in studies of the interaction of vanadium with nucleotides such as adenosine diphosphate (ADP) and adenosine triphosphate (ATP). ESEEM and ENDOR studies have elucidated ^{31}P hyperfine couplings for VO^{2+}–ADP (adenosine monophosphate AMP) [54], VO^{2+}–ATP [36], and triphosphate complexes [55]. Mustafi and coworkers [54] used ENDOR and EPR to determine that adenine nucleotides (ATP, ADP, and AMP) bind the VO^{2+} center via the phosphate groups. Proton ENDOR indicated that solvent molecules were only present in axial coordination and that for all three nucleotides the species formed was $[VO(nucleotide)_2{}^{eq}(solvent)^{ax}]$. In HYSCORE experiments of $VO(ATP)_2$, Buy et al. [36] observed two pairs of correlation peaks that were identified as ^{31}P couplings with $^{31}P_\beta$ and $^{31}P_\gamma$ of ATP with ^{31}P hyperfine coupling constants $A_{zz}(^{31}P) = 9$ and 14.8 MHz, respectively. The model complex results were used to interpret the HYSCORE data for the VO–TF1–ATP ternary protein complex (TF1 = soluble part of ATP synthetase) and suggested equatorial coordination of the two phosphates. Dikanov and colleagues [55,56] studied the binding of VO^{2+} with triphosphate as a model for in-vivo vanadyl phosphate interactions. For the VO^{2+}–triphosphate complex, three sets of ^{31}P cross-peaks were observed in the HYSCORE spectrum with coupling constants of ~15, 9, and 1–2 MHz [55]. The results suggested tridentate coordination of the triphosphate with the weakest coupling constant of 1–2 MHz attributed to an axially coordinated ^{31}P.

2.4. ^{51}V Nuclear Quadrupole Coupling Constants

^{51}V is a quadrupolar nucleus with $I = 7/2$. The ^{51}V nuclear quadrupole moment in vanadyl model complexes has been measured using electron spin echo-electron nuclear double resonance (ESE-ENDOR), as demonstrated by Britt and coworkers in several studies [57–60]. The ^{51}V QCC was found to be sensitive to the coordination geometry of the vanadyl complex, i.e., square bipyramidal, square pyramidal, and trigonal bipyramidal (Fig. 1). Only small changes in the QCC were observed for *cis* ligand binding [57], whereas the ^{51}V QCC was significantly reduced when ligands were bound *trans* to the oxovanadium bond as in square pyramidal vs. bipyramidal complexes. For example, the ^{51}V QCC for VO(acac) was experimentally determined to be –0.429 MHz compared to –0.250, –0.224, and –0.110 MHz for VO(acac) with axially bound ethanol, DMSO, and pyridine, respectively [58]. For five-coordinate vanadyl complexes containing Schiff base ligands, the ^{51}V

QCCs decreased linearly in magnitude as the distortion parameter increased toward a trigonal bipyramidal geometry [59]. This work demonstrates the potential of ESE-ENDOR measurements of ^{51}V QCCs for identifying ligands coordinated *cis* or *trans* to the oxovanadium bond, a finding that has important implications for studies of vanadium-containing proteins.

3. DENSITY FUNCTIONAL THEORY CALCULATIONS OF EPR PARAMETERS IN VANADYL MODEL COMPLEXES

3.1. Overview of DFT Methods for Calculations of EPR Parameters

Recent advances in computational chemistry have led to the development of quantum chemical methods based on density functional theory (DFT) for calculating transition metal EPR parameters. The underlying principle of DFT is the Kohn-Sham theorem, which states that the exact ground state energy of a nondegenerate ground state is a unique functional of the electron density. The choice of the electron density functional, ρ, is key to the accuracy of the DFT method for calculating the energies, structures, and properties of chemical systems. DFT methods require much less computational time (and therefore cost) relative to *ab initio* methods.

The relationship between the isotropic hyperfine coupling constant and the ground state wavefunction, neglecting spin–orbit coupling, is given by Munzarova and Kaupp [61]:

$$A_0 = \frac{4\pi}{3} g_e \beta_e g_N \beta_N \left\langle S_z \right\rangle^{-1} \rho_N^{\alpha-\beta},$$

where

$$\rho_N^{\alpha-\beta} = \sum_{\mu,\nu} P_{\mu,\nu}^{\alpha-\beta} \left\langle \phi_\mu \left| \delta(R_N) \right| \phi_\nu \right\rangle, \tag{3}$$

where ρ is the spin density at the position of the nucleus, R_N, and P is an element of the spin density matrix. β_e is the Bohr magneton, β_N is the nuclear magneton, g_e is the free electron g-value (2.002319), and g_N is the g-value of the nucleus, N. $\left\langle S_z \right\rangle$ is the expectation value of the z-component of the electron spin. The components of the anisotropic hyperfine tensor are given by Munzarova and Kaupp [61]:

$$T_{kl}(N) = \frac{1}{2} g_e \beta_e g_N \beta_N \left\langle S_z \right\rangle^{-1} \sum_{\mu,\nu} P_{\mu,\nu}^{\alpha-\beta}$$

$$\times \left\langle \phi_\mu \left| r_N^{-5} \left(r_N^2 \delta_{kl} - 3 r_{N,k} r_{N,l} \right) \right| \phi_\nu \right\rangle, \tag{4}$$

where $r_N = r - R_N$.

In diagonal form, the matrix elements of **T** are $A_{D,x}$, $A_{D,y}$, and $A_{D,z}$. The **g**-tensor is calculated as a correction, Δg, to the free electron value. Δg includes contribu-

tions from several Breit-Pauli terms, with the largest contribution typically due to a second-order spin–orbit/orbital Zeeman cross-term [62].

In a DFT calculation of EPR parameters, the molecular structure (either input from experimental data or calculated by geometry optimization) is used to calculate the ground state wavefunction, ϕ_0, which is in turn used to determine the hyperfine coupling constants using Eqs. (3) and (4). Therefore, the correct molecular structure is important to the success of the DFT calculation. The choice of exchange-correlation functional also affects the accuracy of hyperfine coupling constants calculated with DFT methods and has been systematically investigated in several studies [61–63].

Several DFT-based computational methods for calculating EPR parameters for transition metals have been reported in the literature [61,64–74]. The relativistic methods for calculation of g- and A-values developed by van Lenthe [65,66] have been incorporated into a commercial software package, ADF (Amsterdam Density Functional Theory) [75,76], which uses Slater type orbitals (STOs) [77]. Three approaches can be used for **A**-tensor calculations with ADF: the scalar-relativistic spin-unrestricted open shell Kohn Sham (SR UKS) calculation, the spin–orbit coupling and scalar-relativistic spin-restricted open shell Kohn Sham (SO + SR ROKS) calculation, and the scalar relativistic spin unrestricted calculation (SO + SR UKS) with spin–orbit coupling effects. In the SR UKS method, spin–orbit coupling is not included, but spin polarization effects are included, making this the preferred method for calculating isotropic hyperfine coupling constants (A_0). In the SO + SR ROKS method, spin–orbit coupling effects are included, but not spin polarization effects. The SO + SR ROKS method is used for calculating **g**-tensors and the anisotropic contribution to the hyperfine coupling constants (A_D). In the most recent version of ADF (2004.1), the implementation of a scalar relativistic spin unrestricted calculation (SO + SR UKS) with spin–orbit coupling effects was introduced for g- and A-value calculations, and this method is now preferred for hyperfine coupling tensor calculations.

Another DFT method for calculating hyperfine tensors has been incorporated into commercial Gaussian software [78]. This method does not include relativistic effects and uses Gaussian type orbitals (GTOs) [79]. All-electron unrestricted Kohn-Sham calculations of hyperfine tensors can be conducted using Gaussian software [78]. Relativistic effects and spin–orbit contributions are not included in the Gaussian calculations. However, Gaussian software provides a much wider choice of exchange and correlation functionals and basis sets than ADF. Other computational programs, such as ORCA [73,80] and MAGReSpect [81], are also available for relativistic DFT calculations of EPR parameters.

Ultimately, DFT calculations of transition metal hyperfine coupling constants can be used to correlate experimentally determined hyperfine coupling constants with molecular structure. Experimental spectral assignments can be verified using DFT calculations of model complexes. The reactivity of metalloenzymes and model complexes can then be probed by elucidating the geometric and electronic structures [82]. In this section, the use of DFT methods to calculate vanadium and ligand hyperfine and quadrupole coupling constants of model complexes will be

described. The results will be compared with experimental EPR and pulsed EPR data for VO^{2+} model complexes.

3.2. DFT Calculations of Vanadium EPR Parameters

DFT calculations of vanadium EPR parameters for VO^{2+} complexes with known crystal structures and experimentally determined EPR parameters have been conducted by several groups [53,61,62,83–88]. The approach has been to use model complexes with known geometries to evaluate the efficacy of DFT methods for calculating vanadium hyperfine coupling constants and **g**-tensors.

The vanadium hyperfine coupling tensor can be parsed into two contributions: an isotropic or Fermi contact interaction, A_0, and an anisotropic or dipolar hyperfine interaction, A_D [89]. A_0 and A_D can be calculated from the principal values of the **A**-tensor using the following relationships: $A_0 = (A_{11} + A_{22} + A_{33})/3$ and $A_{D,x} = A_{11} - A_0$, $A_{D,y} = A_{22} - A_0$, $A_{D,z} = A_{33} - A_0$. The vanadium g-values are given as the diagonal elements of the **g**-tensor.

DFT methods have been utilized to calculate the **g**-tensor for $[VO(H_2O)_5]^{2+}$ [53,83]. DFT results for g-value calculations for $[VO(H_2O)_5]^{2+}$ are included in Table 2, along with experimental g-values from the literature for comparison. Reasonably good agreement between the experimental and DFT calculated g-values is observed.

Table 2. DFT Calculations of g-Values for $[VO(H_2O)_5]^{2+}$

	g_{xx}	g_{yy}	g_{zz}	Program	Method	Reference
Exp.	1.978	1.978	1.933	–	–	[2]
DFT	1.9852	1.9852	1.9495	ORCA coupled pert. SCF eqs [88]	B3LYP,	[53]
DFT	1.986	1.986	1.930	ADF	BP86, SO+SR ROKS	[83]

The corresponding calculated and experimental vanadium hyperfine coupling constants for $[VO(H_2O)_5]^{2+}$ are presented in Table 3. The vanadium isotropic hyperfine coupling constant calculated with ADF or Gaussian and the BP86 functional underestimates the experimental value by approximately 80 MHz. The hybrid functionals, such as BHPW91 and B3PW91, incorporate Hartree-Fock exchange, and provide more accurate vanadium hyperfine coupling tensors relative to the GGA functionals [61,85,86]. As shown in Table 3, the vanadium isotropic hyperfine coupling constant calculated with the hybrid functional B3PW91 is –304 MHz, which deviates by only 20 MHz from the experimental value. DFT calculated vanadium isotropic coupling constants from other research groups are also

Table 3. DFT Calculations of the Vanadium-51 Hyperfine
Coupling Constants for $[VO(H_2O)_5]^{2+}$ [a]

	$A_0(^{51}V)$	$A_{D,x}(^{51}V)$	$A_{D,y}(^{51}V)$	$A_{D,z}(^{51}V)$	Method	Reference
Exp.	−324	112	112	−224	–	[90]
DFT	−246	95	96	−192	Gaussian, BP86	[63]
DFT	−236	89	90	−180	ADF, BP86, SR UKS	[63]
DFT	−304	97	98	−198	Gaussian, B3PW91	[63]
DFT	−268	96	105	−201	ORCA, B3LYP	[85]
DFT	−249	91	101	−193	ORCA, BP86	[85]
DFT	−293	103	103	−207	ORCA, B3LYP	[85]

[a] All A-values are given in MHz.

presented in Table 3 for comparison, with the realization that some of the variability of results is due to the fact that all groups did not use the same structural coordinates for $[VO(H_2O)_5]^{2+}$. For VO^{2+} systems, with small spin–orbit coupling contributions, the nonrelativistic DFT calculations provide very good accuracy for isotropic hyperfine coupling constants with hybrid functionals. Currently, hybrid functionals cannot be used in relativistic calculations with ADF, thus limiting the accuracy of these calculations. The implications for transition metals with significant spin–orbit coupling such as Cu^{2+} are much greater.

In a comprehensive investigation of DFT calculations of transition metal hyperfine coupling constants, Munzarova and Kaupp concluded that quantitative agreement with experimental transition metal hyperfine coupling constants is hindered by the inability of currently available exchange-correlation functionals to accurately describe spin polarization, which is essential for an accurate calculation of the isotropic hyperfine component [61]. In DFT calculations of hyperfine tensors using Generalized Gradient Approximation (GGA) functionals, such as BP86 [91], the spin polarization for VO^{2+} complexes is systematically underestimated [61,62,83,86]. To demonstrate the impact of the exchange correlation functional on the computational accuracy, DFT calculations of vanadium hyperfine tensors were conducted for a series of VO^{2+} complexes including: $[VO(H_2O)_5]^{2+}$, $VO(acac)_2$, $[VO(mal)_2]^{2−}$, $[VO(ox)_2]^{2−}$, and $VO(gly)_2$ [acac = acetylacetonate, mal = malonate, ox = oxalate, and gly = glycinate]. The A_0-values were calculated for the VO^{2+} complexes using the Gaussian software package and 9 different functionals, and using ADF and 3 different functionals. The complete set of DFT results for all of the complexes can be found in Saladino and Larsen [86]. Selected computational results for a representative complex, $VO(gly)_2$ are given in Table 4. The A_0-values calculated for $VO(gly)_2$ using ADF (SR UKS, GGA functionals) are approximately 70% of the experimental value of –275 MHz. This is not surprising since GGA functionals have been previously shown to underestimate the spin polarization of the s-type metal core orbitals, as discussed above [61,69]. Nonrelativistic Gaussian

Table 4. Calculated (DFT) and Experimental Isotropic and Dipolar
Hyperfine Coupling Constants for VO(gly)$_2$[a,b]

	BP86 (ADF, SR UKS)	BP86 (ADF, SO+SR ROKS)	BP86 (Gaussian)	BHP86 (Gaussian)	Exp.
A_0	−145	19	−161	−277	−275[c]
$A_{D,x}$	97	117	106	114	115
$A_{D,y}$	75	77	79	93	105
$A_{D,z}$	−172	−193	−185	−207	−220

[a] All A-values are given in MHz.   [b] Data are from [63].   [c] From [18].

calculations with the same functionals yielded similar results. However, the Gaussian DFT calculations of A_0 with the hybrid functionals (BHLYP, BHP86, and BHPW91) exhibited the best agreement with experimental results. As illustrated in Table 4, the A_0-value calculated with the BHP86 functional provide the best quantitative agreement with the experimental data. The calculated anisotropic hyperfine coupling constants are also listed in Table 4.

The A_D-values calculated using the SO + SR ROKS method provide the best quantitative agreement with experimental results relative to the SR UKS method. The ^{51}V A_D-values calculated for VO(gly)$_2$ using Gaussian are also quite close to the experimental results (~85–95% of experimental value) and are much less sensitive to the choice of functional than the corresponding A_0 calculations. Similar agreement is observed for $A_{D,x}$ and $A_{D,y}$.

These results are in agreement with previous studies by Munzarova and Kaupp, who observed that the calculated A_0-value for transition metal complexes is sensitive to the choice of functional [69]. For A_0-value calculations of vanadyl complexes containing Schiff bases, Munzarova and Kaupp [62] found that the best quantitative agreement with experimental data was found for the hybrid functionals B3PW91 and BHPW91. The same general trends in calculated values were observed for all of the VO^{2+} complexes examined, as previously suggested by Kaupp, who pointed out that the deficiencies in density functionals are systematic for complexes of related electronic structure [62].

In the next example, the structural insight that can be obtained from DFT calculations by taking into account that the deviations from experimental values are systematic for complexes with similar electronic structure will be illustrated. As discussed in section 1.3, the EPR spectra of VO^{2+} complexes (square pyramidal or bipyramidal) in which different equatorial ligands are present can be interpreted using an empirical additivity relationship [2,7]. The additivity relationship can be used to calculate the vanadium hyperfine coupling constant, $A_{||}$, for a VO^{2+} complex when the number and identity of the equatorial ligands are known.

In a recent study, Pecoraro and coworkers reported the use of the additivity relationship to predict the orientation of equatorial imidazole rings relative to the VO^{2+} bond in VO^{2+} model complexes [92]. The results of Pecoraro's study suggested that the differences in additivity relationship values [2,15,37] for the coordinated imidazole could be due to different orientations of the imidazole ring relative to the equatorial plane. In Pecoraro's study, five new VO^{2+} imidazole model complexes with the imidazole rings in different orientations with respect to the VO^{2+} bond were synthesized [92]. They found that $A_{||}(^{51}V)$ (imidazole contribution) varied from 120 to 138 MHz for parallel- and perpendicular-oriented imidazole ligands, respectively.

Saladino and Larsen used DFT methods and model VO^{2+}–imidazole complexes to investigate the dependence of the vanadium hyperfine coupling constant on ligand orientation [84]. A model complex, $[VO(imid)(H_2O)_4]^{2+}$, was constructed and optimized so that the effect of imidazole ligand orientation on vanadium hyperfine coupling constant could be investigated using DFT calculations. The dihedral angle, θ, that characterizes the orientation of the imidazole ring relative to the V=O bond was varied from 0 to 345°. For each value of the dihedral angle, the vanadium hyperfine coupling constant, $A(\theta)$, was calculated using the relativistic methods of van Lenthe and coworkers [65]. The A-values were calculated using two different methods, the SR UKS method (A_0) and the SO + SR ROKS method (A_D). The most accurate A-values for transition metals when spin–orbit effects are small are currently obtained by combining A_0 values calculated using the SR UKS method and A_D calculated using the SO + SR ROKS method. The principal values of the **A**-tensors for the $[VO(imid)(H_2O)_4]^{2+}$ complexes were calculated with the different methods and as a function of the dihedral angle. The combined A_{33}-value (or $A_{||}$-value assuming axial symmetry) vs. the dihedral angle is plotted in Figure 5. The calculated $A_{||}(^{51}V)$ values vary systematically with the dihedral angle. The theoretical basis for the orientation dependence of the vanadium hyperfine coupling constant is the overlap between the unpaired electron in the vanadium d_{xy} orbital and the aromatic p orbital of the coordinated imidazole nitrogen [84]. As the imidazole ring is rotated through a dihedral angle of 0 to 90°, the overlap between the aromatic p orbital and the vanadium d_{xy} orbital (Fig. 3) decreases, leading to a decrease in the hyperfine coupling constant. Computationally, this was explained by examining the contributions of the d_{xy} and aromatic p orbitals to the singly occupied molecular orbital (SOMO), which trended accordingly [84].

Recently, Britt and colleagues conducted an ESE-ENDOR study of vanadyl complexes of Hcapca (N-{2-(2-pyridylmethylene(amino)phenyl]pyridine}-2-carboxamide) to experimentally measure the vanadium hyperfine and quadrupole coupling constants [60]. Complementary DFT calculations for various vanadyl complexes were also completed, and the results confirmed experimentally observed trends in the hyperfine and quadrupole coupling constants but were not quantitatively accurate. In part, this was attributed to the use of single-crystal structure coordinates for the calculations while the experiments were done on liquids or frozen solutions.
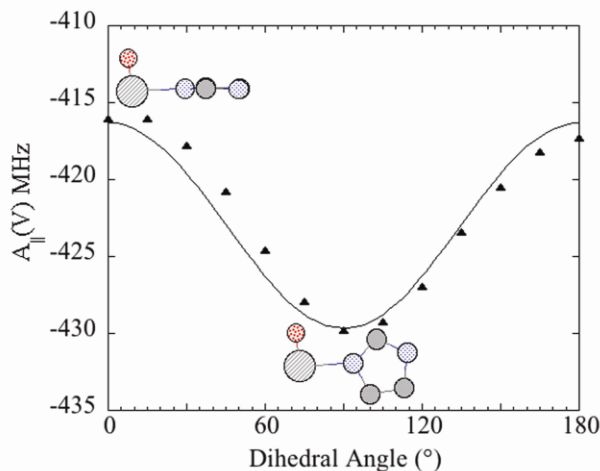
Figure 5. The calculated vanadium hyperfine coupling constant, $A_{||}(^{51}V)$, for $[VO(imid)(H_2O)_4]^{2+}$ as a function of the dihedral angle, θ, is plotted using the data in Saladino and Larsen (2002) [84]. $A_{||}(^{51}V)$ was calculated from $A_0(^{51}V)$ (SR UKS, BP86) + $A_D(^{51}V)$ (SR + SO ROKS, BP86). The data were fit to $A_{||} = A + B(\sin 2\theta - 90)$, where $A = -423$ MHz and $B = -6.7$ MHz. Adapted with permission from Saladino and Larsen [84]. Copyright © 2002, American Chemical Society. Please visit http://www.springer.com/978-1-4419-1138-4 to view a high-resolution full-color version of this illustration.

DFT methods can be effectively used to calculate vanadium hyperfine coupling constants for vanadyl complexes with the following caveat. Careful attention must be paid to the choice of functional since the DFT methods are often limited by the ability of the exchange and correlation functional to accurately predict spin polarization for transition metals. However, since deviations from experimental values are systematic for a series of complexes such as VO^{2+} complexes, DFT calculations can be used to investigate trends in vanadium hyperfine coupling constants with changes in structure. Similarly, trends in vanadium quadrupole coupling constants are reproduced by DFT calculations, but quantitative agreement with experiment is still not satisfactory.

3.3. DFT Calculations of Ligand Hyperfine and Quadrupole Coupling Constants

DFT methods can be used to calculate hyperfine coupling constants for ligands in vanadyl complexes. The ligand hyperfine coupling constants are generally 10 to 100 times smaller than metal hyperfine coupling constants, thus requiring increased quantitative accuracy from the DFT calculations. Experimentally, ligand hyperfine coupling constants for vanadyl complexes are usually too small to be resolved in cw-EPR experiments and are measured using ENDOR or ESEEM techniques [28–

30,37,38,46,49,93]. The data analysis for ENDOR and ESEEM experiments on vanadyl complexes can be significantly enhanced by the use of DFT calculations for ligand hyperfine and quadrupole coupling constants. Assignments of spectral features and the interpretation of the EPR spectra with respect to the structure can be strengthened by the application of DFT methods.

Recently, ^{17}O hyperfine coupling constants for the vanadyl aquo complex $[VO(H_2O)_5]^{2+}$ were measured using W-band ENDOR [53]. DFT calculations [80] of ^{17}O hyperfine tensors in $[VO(H_2O)_5]^{2+}$, were used to assign the experimental hyperfine couplings for the equatorial and vanadyl oxygen ligands. The agreement between the experimental and DFT results was very good and confirmed the exchangeable nature of the vanadyl oxygen [53]. In a study of vanadium complexes with tridentate bisphenol ligands containing various donor atoms, ^{31}P hyperfine coupling constants were calculated using DFT methods and were found to be in good agreement with experimental ^{31}P hyperfine coupling constants [87].

In the next example, this time examining proton hyperfine coupling constants for $[VO(H_2O)_5]^{2+}$, the effect of water ligand orientation on the hyperfine coupling constants was investigated using DFT methods [94]. Single-crystal ENDOR data [47] for the proton hyperfine coupling constants of $[VO(H_2O)_5]^{2+}$ were used for comparison with the DFT calculated values. In the DFT study, the $[VO(H_2O)_5]^{2+}$ complex was geometry optimized and then an SR UKS DFT calculation of the proton hyperfine coupling constants was completed [94]. Subsequently, one of the equatorial water molecules was systematically rotated by 15° (while the other water molecules remained in their original orientations), and the DFT calculation was repeated for each orientation so that the proton hyperfine coupling constants $(A_0(^1H))$ of the equatorial water ligand could be mapped as a function of orientation. The proton hyperfine coupling constants for each of the two protons, H_a and H_b, on the water molecule being rotated, are graphed in Figure 6. The proton hyperfine coupling constant is sensitive to orientation and varies from 10 to –1 MHz as a function of dihedral angle. These results can be rationalized by considering the overlap between the vanadium d_{xy} orbital and the hydrogen molecular orbitals, which is maximized when the hydrogen atoms are in the equatorial plane and minimized when the hydrogen atoms are rotated out of the equatorial plane.

The DFT results can be compared with experimental single-crystal ENDOR results for $[VO(H_2O)_5]^{2+}$ [47]. The single-crystal results indicate that there are two groups of protons with approximately equivalent proton hyperfine coupling constants. The first four protons have $A_0(^1H)$ values of –0.39, 4.08, –0.05, and 4.57 MHz. The second four protons have $A_0(^1H)$ values of 8.67, 7.14, 7.73, and 6.96 MHz. The interpretation supported by the DFT results in Figure 6 is that the first two water molecules are located approximately perpendicular to the equatorial plane and the second two water molecules are oriented in or nearly in the equatorial plane. This demonstrates the potential for using DFT calculations to obtain structural insight for vanadyl complexes.

Nitrogen–ligand hyperfine and quadrupole coupling constants for vanadyl model complexes can also be calculated using DFT methods. A series of nitrogen
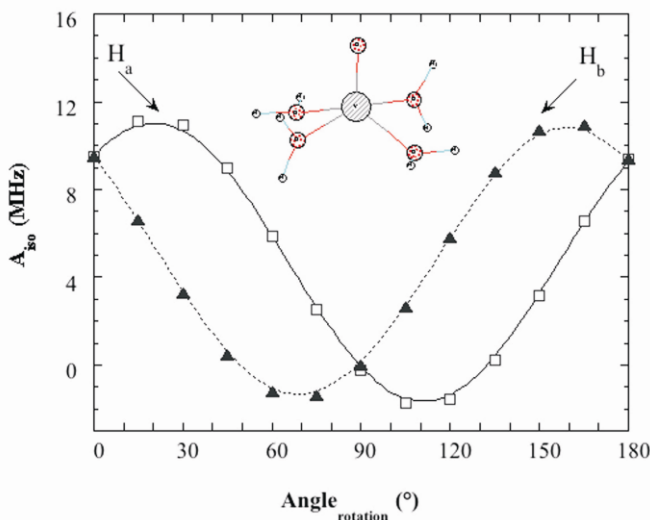
Figure 6. Calculated isotropic proton hyperfine coupling constants, $A_0(^1\text{H})$, plotted versus the angle of rotation of an equatorial water molecule in $[\text{VO}(\text{H}_2\text{O})_5]^{2+}$ relative to the equatorial plane. The variation of $A_0(^1\text{H})$ for each proton, H_a and H_b, on the water molecule is shown as a function of the rotation angle of the water molecule using data from Larsen [95]. Two of the possible orientations for the water molecule are illustrated schematically. Adapted with permission from Larsen [95]. Copyright © 2001, American Chemical Society. Please visit http://www.springer.com/978-1-4419-1138-4 to view a high-resolution full-color version of this illustration.

containing vanadyl model complexes for which experimental EPR data and in most cases, crystal structures, are available served as a testing ground for the application of DFT methods to the calculation of ligand hyperfine and quadrupole coupling constants. The nitrogen hyperfine and quadrupole coupling constants for a group of VO^{2+} complexes containing amine (VO(gly)$_2$, VO(edda)), imine (VO(meox)$_2$, VO(salen)) and isothiocyanate ($[\text{VO}(\text{SCN})_4]^{2-}$) groups were calculated using relativistic DFT calculations [63] [gly = glycinate, edda = ethylenediamine-N,N′-diacetate, meox = oxobis(2-methylquinolin-8-olato); and salen = N,N′-bis(salicylidene)ethylenediamine]. Selected results are listed in Table 5, and the complete results can be found in Saladino and Larsen [63]. The calculated values were compared with experimental data obtained from high-resolution EPR measurements. The agreement between the experimental and the calculated $A_0(^{14}\text{N})$-values was very good, with deviations ranging from <1% for VO(edda) to ~10% for VO(meox)$_2$, with an average deviation of ~4%. The calculated nitrogen A_0-values vary systematically with nitrogen type from ~−5 MHz for amine complexes, to −6 to −7 MHz for imine complexes to −7 to −8 MHz for isothiocyanate complexes, which reflects the experimental trend observed by Fukui and coworkers [44] and LoBrutto and coworkers [31] (Table 1).

Table 5. DFT Calculated and Experimental Hyperfine $A_0(^{14}N)$
and Quadrupole Coupling Constants (Q_z) for VO_2^+ Complexes
with Equatorially Coordinated Nitrogen Ligands[a]

Complex[b]	$A_0(^{14}N)$ SR UKS	$A_0(^{14}N)$ exp.	$Q_z(^{14}N)$ SR UKS[a]	$Q_z(^{14}N)$ exp.	η SR UKS[a]	η exp.
VO(gly)$_2$	−4.87	−5.10[c]	−1.68	−1.35[c]	0.27	0.48
VO(edda)	−4.97	−4.98[c]	−1.62	−1.55[c]	0.42	0.48
VO(meox)$_2$	−6.73	−6.18[d]	−1.33	−1.17[d]	0.09	0.13
VO(salen)	−6.06	−5.83[c]	−1.30	−1.20[c]	0.47	0.33
	−6.19	−	−1.24	−1.20[c]	0.52	−
VO(NCS)$_4^{2−}$	−7.09	−7.47[c]	−0.65	−0.50[c]	0.03	0.00

[a] The table is adapted from [63]. $Q_z(^{14}N)$ and $A_0(^{14}N)$ are expressed in MHz.
[b] Abbreviations: gly, glycinate; edda, ethylenediamine-N,N′-diacetate; meox, oxobis(2-methylquinolin-8-olato); and salen, N,N′-bis(salicylidene)ethylenediamine.
[c] Data from [44].
[d] Data from [29].

Both direct singly occupied molecular orbital (SOMO) and indirect spin polarization may contribute to the isotropic hyperfine coupling constant. For these vanadyl complexes, the unpaired electron on the vanadium atom occupies a d_{xy} orbital. Consequently, the overlap with the nitrogen ligand p orbitals is small and therefore direct spin polarization contributions are not expected to be significant. The primary contribution to the nitrogen isotropic hyperfine coupling constant is from an indirect spin transfer mechanism in which the nitrogen p orbital is polarized by an exchange interaction with the unpaired electron on the vanadium [95]. The SR UKS method includes spin polarization effects and therefore provides very good agreement with experimental data. The anisotropic contributions to the ^{14}N hyperfine coupling constant tensor, $A_{D,x}$, $A_{D,y}$, and $A_{D,z}$, were also calculated, but the quantitative agreement with experiment was not as good as for A_0.

The DFT computational results for Q_z for the vanadyl complexes with nitrogen ligands are listed in Table 5 and are in good agreement with the experimental data [63]. The deviation between the calculated and experimental values ranges from 5 to 25%, with an average deviation of 14%. Qualitatively, the computational results exhibit the same trend as the experimental Q_z values in that Q_z varies from amine (∼−1.6 MHz), to imine (∼−1.2 MHz), to isothiocyanate (∼−0.65 MHz). Recently, Warncke and coworkers reported a DFT computational study of the NQCCs of imidazole derivatives and the impact of the molecular environment [96].

3.4. Outlook

In this section, the use of DFT methods to calculate the EPR parameters for vanadyl model complexes was reviewed. Examples of DFT calculations of vana-

dium hyperfine coupling constants for vanadyl model complexes with water and glycine ligands were presented. DFT calculations of ligand hyperfine and quadrupole coupling constants were also included. The limitations of the current computational DFT methods were discussed as well as strategies for optimizing the performance of these methods. There are still deficiencies in the quantitative accuracy of the calculated vanadium hyperfine coupling constants due to the shortcomings of exchange and correlation functionals with respect to spin polarization. However, since the spin polarization is systematically underestimated for vanadium hyperfine couplings, trends in these parameters can be reproduced, thus providing valuable insight into how the vanadium hyperfine coupling constants vary with structure. The DFT calculations of ligand and quadrupole hyperfine coupling constants generally showed better quantitative agreement with experimental results relative to the vanadyl hyperfine coupling constant. Future advances in computational methods will improve the accuracy of the DFT methods so that the "holy grail" of using DFT calculations of EPR parameters to elucidate structure–function relationships in vanadyl protein complexes will eventually be realized.

4. SELECT PROTEIN STUDIES

4.1. Pyruvate Kinase

Pyruvate kinase (PK) is one of the most heavily studied enzymes that requires metal ion cofactors but is not a metalloenzyme itself [40]. PK catalyzes the phosphate transfer reaction between ADP and phosphoenolpyruvate (PEP) to form ATP and pyruvate. Oxalate is a competitive inhibitor of the enzyme [97]. The enzyme requires divalent and monovalent cations (e.g., Mg^{2+} and K^+) for activity. Normally Mn^{2+} ($S = 5/2$) is used as a surrogate probe for Mg^{2+} in magnesium-activated enzymes, but the use of VO^{2+} has some advantages. Since VO^{2+} is an $S = 1/2$ spin system, the interpretation of hyperfine couplings is more straightforward than with Mn^{2+}, making it easier to obtain structural information [40]. The VO^{2+} ESEEM study of PK by Tipton and coworkers [40] represents the richest system reported to date where a variety of couplings (i.e., from ^{13}C, ^{133}Cs, ^{23}Na, ^{14}N, and ^2H) has been measured. Relatively large couplings from $^{203,205}Tl$ and ^{17}O have been observed in cw-EPR spectra of PK as well as line broadening from unresolved ^{31}P hyperfine interactions [97,98].

The VO^{2+}–PK complex has only weak catalytic activity [97]. Nevertheless, studies of this complex with monovalent ion cofactor (Tl^+, Na^+, or Cs^+), substrate PEP, product pyruvate, and inhibitor oxalate have provided insight into assembly of the active site complex [40,97,98]. ^{14}N couplings in the ESEEM were assigned to the equatorial coordination of the ε-amino group of lysine to the VO^{2+} ion on the basis of the striking similarity to the spectrum of VO(glycine)$_2$, which is a model complex for primary amine coordination. These spectra were quite unlike that seen with VO(imidazole)$_4$, a model for imine coordination. Couplings of $A_0(^{14}N) = 4.9$

MHz and $Q_z(^{14}N) = 1.28$ MHz were obtained for the protein complex, values essentially identical to those for the glycine complex (Table 1).

Upon establishing that the metal binding site of PK involves a lysine residue, Tipton et al. [40] proceeded to examine other structural features of the metal site complex. An isotropic coupling of $A_0(^{31}P) = 4.1$–4.4 MHz from ^{31}P in the Mn^{2+} complex Mn–PK–MgATP–oxalate was observed, indicating direct coordination to phosphate. While such a coupling was not reported by Tipton et al. [40] for the corresponding VO^{2+} complex, line broadening in the cw-EPR spectrum indicates that phosphate is probably also coordinated in both the VO–PK–PEP and the VO–PK–PG complexes (PG ≡ phosphoglycolate) but not in the VO–PK–ATP complex, where line broadening is absent [97]. ^{17}O labeled pyruvate, oxalate, and glycolate produced resolved splittings of ~6 G in the cw EPR that were interpreted as bidentate coordination of the anion [97]. Such coordination was corroborated by ESEEM studies of the [1–^{13}C]pyruvate and [2–^{13}C]pyruvate complexes, i.e., VO–PK–pyruvate, showing ^{13}C couplings of $A_0(^{13}C) = 2.2$ and 2.0 MHz, respectively [40]. Dipolar interactions between ^2H of deuteromethylpyruvate, [$^2H_3$]pyruvate, and the electron spin of the VO^{2+} ion produced a signal at 2.2 MHz in the 3-pulse ESEEM spectrum. From simulation in which a point dipole model was assumed, a vanadium–deuterium distance of 4.0 Å was obtained. This value is reasonable for bidentate coordination through the α-oxo and carboxyl groups of pyruvate. Although the values of $A_{\parallel}(^{51}V)$ and $g_{\parallel}$ of the VO^{2+}-PK complex with various substrates are consistent with an equatorial ligand field of oxygen donor atoms [97], the magnitude of the isotropic ^{14}N coupling of lysine (4.9 MHz) indicates that it most likely occupies an equatorial position in the first coordination sphere since axially coordinated amines have isotropic couplings of only ~1.3 MHz [31].

Studies of the structural replacement of the monovalent ion K^+ using ^{23}Na and ^{133}Cs as probes produced modulations in the three-pulse ESEEM [40]. By ratioing the modulation patterns of the VO–PK–Na^+–oxalate and VO–PK–K^+–oxalate complexes, the decay function was eliminated and contributions from ^{23}Na to the ESEEM could be readily seen. The resultant ^{23}Na modulation pattern was Fourier transformed, a narrowed spectral region selected corresponding to the ^{23}Na absorbance, and the spectrum back transformed. The modulation pattern of the back-transformed spectrum could be adequately simulated using a VO^{2+}–^{23}Na distance of 4.8 ± 0.2 Å, indicating that the monovalent cation is in close proximity to the divalent metal ion and constitutes part of the active site complex. This finding is in accord with the earlier study showing resolved $^{203,205}Tl$ ($I = 1/2$) splittings of 26–31 G in the cw-EPR spectrum. The value of the splitting depended on the substrate or substrate analogue employed in the VO–PK–substrate complex (substrate = pyruvate, 2-fluoropyruvate, phosphoenolpyruvate, or acetopyruvate) and thus is sensitive to the identity of the substrate bound at the active site [98]. The work of Lord and Reed [97,98] and that of Tipton et al. [40] demonstrate the utility of both cw EPR and ESEEM of VO^{2+}–protein complexes for obtaining detailed structural information about the assembly of the active site.

4.2. S-Adenosylmethionine Synthetase

S-Adenosylmethionine synthetase catalyzes the transfer of the adenosyl group of ATP to the sulfur of L-methionine (Met) to produce S-adenosylmethionine (AdoMet). It is a homotetramer of molecular weight 180,000 Da. Each monomer unit has two divalent metal ion sites (normally Mg^{2+} or Mn^{2+}) and a monovalent metal ion site (e.g., K^+). Substrate binding is required for the binding of divalent metal ions at one site, while the other site is independent of substrate binding. VO^{2+} binds to the substrate-independent site. When the substrate-dependent site is occupied by Mg^{2+}, the VO^{2+} enzyme is catalytically active. Multifrequency 3-pulse ESEEM was employed to determine the coordination sphere in a number of different complexes [39].

All of the ESEEM spectra showed peaks characteristic of ^{14}N. To establish the identity of the nitrogen ligand(s) responsible, protein was prepared with ^{15}N-labeled ε-amino nitrogen of lysine and the various complexes examined. In all cases the ^{14}N peaks were lost, confirming that the ε-amino group of lysine is a ligand to the vanadium. However, modulations from ^{15}N, which are typically more difficult to observe, were absent from the spectra. Simulations of the spectra of E–VO–ATP–Met–K gave $A_0(^{14}N)$ = 4.3 MHz, e^2Qq = 3.7 MHz, corresponding to $Q_z(^{14}N)$ = 1.85 MHz, and η = 0.3. Similar measurements with E–VO–AdoMet–K gave ^{14}N parameters $A_0(^{14}N)$ = 5.5 MHz, e^2Qq = 3.0 MHz, corresponding to $Q_z(^{14}N)$ = 1.5 MHz, and η = 0.3 (Table 1). Isotopic labeling of AdoMet demonstrated that in this latter case the coupling arises from the ε-amino group of methionine. This specific study was of particular importance since it was the first documented case of coordination of ε-amino groups in a vanadyl–protein complex and helped to confirm the previous assignment of lysine coordination in pyruvate kinase [40]. Moreover, this study further established that the ^{14}N nuclear hyperfine couplings seen with primary amine coordination is typically 1–2 MHz smaller than those from imine of imidazole coordination (Table 1); the highest value for a primary amine coordination differs from the lowest value for imidazole coordination by ~0.5 MHz. Thus, based on the value of $A_0(^{14}N)$ one can reasonably assign the origin of the nitrogen donor ligand, the range of $A_0(^{14}N)$ values reported in this paper being 4.3–5.5 MHz [39].

A number of substitutions were made to look for couplings with other nuclei, i.e., Tl^+ (I = ½) substituted for K^+, and deuteration and ^{13}C enrichment of the methionine methyl group. The ESEEM spectra were unchanged. Moreover, no couplings from ^{31}P were observed. These negative results suggest that the methyl group is not "proximal" to the vanadium but is probably nearby. The observation of $^{203,205}Tl$ couplings in cw EPR indicates that the Tl^+ site is adjacent to the VO^{2+} site and is part of the active site [99], as noted above for pyruvate kinase. The EPR lines were narrowed in D_2O, possibly a consequence of coordinated H_2O [90] and/or exchangeable protons of the coordinated amino nitrogen. Through the use of additivity relationships and the ESEEM data, a probable set of equatorial ligands to the vanadium were proposed — namely, two phosphate oxygens, a water molecule, and a lysine ε-amino nitrogen.

4.3. Imidazole Glycerol Phosphate Dehydratase

Imidazole glycerol phosphate dehydratase (IGPD) is an enzyme involved in the biosynthesis of the amino acid histidine. It removes a water molecule from imidazole glycerol phosphate to produce imidazole acetol phosphate [100]. The activity, protomeric 24mer assembly, and quaternary structure of the enzyme depends on the binding of a divalent metal ion. Mn^{2+} activates IGPD most effectively. On the other hand, VO^{2+}, while facilitating the assembly of the protein, results in an enzyme that has activity only 0.3% of that of the Mn^{2+} form. The nature of the VO^{2+} binding site has been explored using cw-EPR, cw-ENDOR, and ESEEM spectroscopies [35,100]. The EPR spectra show the presence of at least three pH-dependent forms (α, β, and γ) of VO^{2+} binding to the protein that probably represent different conformational states of the metal bindings site. ^{1}H ENDOR shows numerous couplings ranging from 0.2 to 3.7 MHz, mostly from nonexchangeable protons since they are also observed in D_2O. An exchangeable ^{1}H with a coupling of ~0.5 MHz is observed when the field is on the $M_I = -3/2$ perpendicular line of the EPR spectrum and was tentatively assigned to an amide proton of equatorially coordinated histidine. The resonances from nonexchangeable ^{1}H were attributed to protein protons. Employing additivity relationships for the $A_{\parallel}(^{51}V)$ values for the α, β, and γ forms suggest that the equatorial ligand field is one of mostly nitrogen donors, i.e., histidyl residues, in all three species. The low pH = 6.0 α species appears to have an H_2O in place of histidine relative to the β species. The low-frequency region (<6 MHz) of the cw-ENDOR spectrum shows features ascribable to ^{14}N; however, its complexity precludes simple analysis, perhaps due to the presence of three vanadium subspecies and multiple coordinating histidyl groups. From the double quantum ($\Delta M_I = 2$) observed at 8.7 MHz in the ENDOR, a ^{14}N coupling of $A_{x,y}(^{14}N) \sim 7$ MHz was obtained [100]. Subsequent stimulated echo ESEEM measurements along with simulations provided an improved assessment of the ^{14}N parameters — namely, $A_{x,y}(^{14}N) \sim 7.0$ MHz and $A_z(^{14}N) \sim 7.5$ MHz — as well as the quadrupole parameters $Q_z(^{14}N) = 0.88$ MHz and $\eta \sim 1.0$ [35]. From considerations of ^{1}H ENDOR as well as the ^{14}N ENDOR data, models for the α and β forms of the binding site were proposed, the α form consisting of equatorial coordination of three His residues and a water molecule, with the axial position occupied by a fourth His residue. In the β form four histidine residues are coordinated equatorially with the axial ligand unidentified [100].

4.4. ATP Synthase

The ATP synthase from Bacillus PS3 couples the phosphorylation of ADP to form ATP through an H^+ ion gradient and requires Mg^{2+} as a cofactor. The soluble part (TF1) of the membrane-bound protein has ATPase activity and is similar to that (CF1) isolated from chloroplasts. VO^{2+} binding at the M1 site of TF1 was carried out to gain insight into the ligand environment of the vanadium and, by inference, that of the native metal Mg^{2+} [36]. While the cw-EPR spin Hamiltonian parameters were consistent with the presence of nitrogen ligands, 3-pulse ESEEM in

conjunction with HYSCORE clearly showed the presence of two nitrogen donor ligands, $A_0(^{14}N)$ = 4.75 and 6.5 MHz, respectively, assigned to ε-amino of lysine-164 and the imidazole of His-324 of the β subunit of the protein complex. This is the first example of both types of nitrogen coordination in a single vanadyl–protein complex. Again, the ^{14}N coupling of the amine nitrogen is smaller, whereas its quadrupole coupling $Q_z(^{14}N)$ is larger than those of imine nitrogen (Table 1). Previous studies with other metal derivatives of the protein had failed to detect histidine coordination in the metal–protein complex.

Significantly, the binding of ATP causes the appearance of correlation patterns in the HYSCORE that are assigned to hyperfine couplings from $^{31}P_\beta$ (A_0 = 15.5 MHz) and $^{31}P_\gamma$ (A_0 = 8.7 MHz) in the VO–TF1–ATP complex. Thus, the nucleotide binding site is next to the M1 site. The in-plane ligand environment is assigned to two nitrogens (amine of lysine and imine of histidine) and the β and γ phosphate groups of ATP. The implications of these findings with respect to the catalytic mechanism are discussed in [36].

4.5. D-Xylose Isomerase

D-xylose isomerase (XylI) is a homotetramer of subunits that catalyzes the isomerization of α-D-xylose to α-D-xylulose and D-glucose to D-fructose. The activity of the enzyme is dependent on two divalent metal ion binding sites per subunit, designated A and B. The enzyme is activated by Mg^{2+} and Mn^{2+} but inhibited by VO^{2+}, which binds at the B site when the A site is occupied by Cd^{2+} [101]. The ligands of the B binding site as derived from the crystal structure of the Mn^{2+} enzyme consist of three carboxylate groups of aspartate and glutamate residues and the imidazole group of a histidine residue along with a water molecule [101]. An early ENDOR study of the $4VO^{2+}/4Cd^{2+}$ protein complex with coordination at the B sites showed an unusually large ^{14}N coupling of 13.2 MHz for a protein or model complex [101].

An ESEEM study was undertaken to better understand the nuclear hyperfine coupling of VO^{2+} to histidine in this protein and to explore the use of orientationally selected spectroscopy to obtain structural information regarding the coordination to imidazole in the VO^{2+}–protein complex [34]. Two- and three-pulse ^{14}N ESEEM were conducted across the EPR powder-pattern envelope of transitions and the FT-ESEEM ^{14}N spectra simulated. Excellent correspondence between the experimental and simulated 2-pulse spectra was obtained for various values of the applied magnetic field (Fig. 7). From a detailed analysis of the spectra, the principal values of the ^{14}N electron–nuclear coupling constant were determined — namely, $A_{||}(^{14}N)$ = 5.7 MHz, $A_\perp(^{14}N)$ = 5.9 MHz, and $A_0(^{14}N)$ = 5.7 MHz — and quadrupole couplings of $Q_{||}(^{14}N)$ = 0.64 MHz, $Q_{\perp(1)}(^{14}N)$ = 0.17 MHz, and $Q_{\perp(2)}(^{14}N)$ = 0.83 MHz. Their relative orientations with respect to each other and with respect to the principal axes of the **g**-matrix of the VO^{2+} ion were established within a limited range of angles.
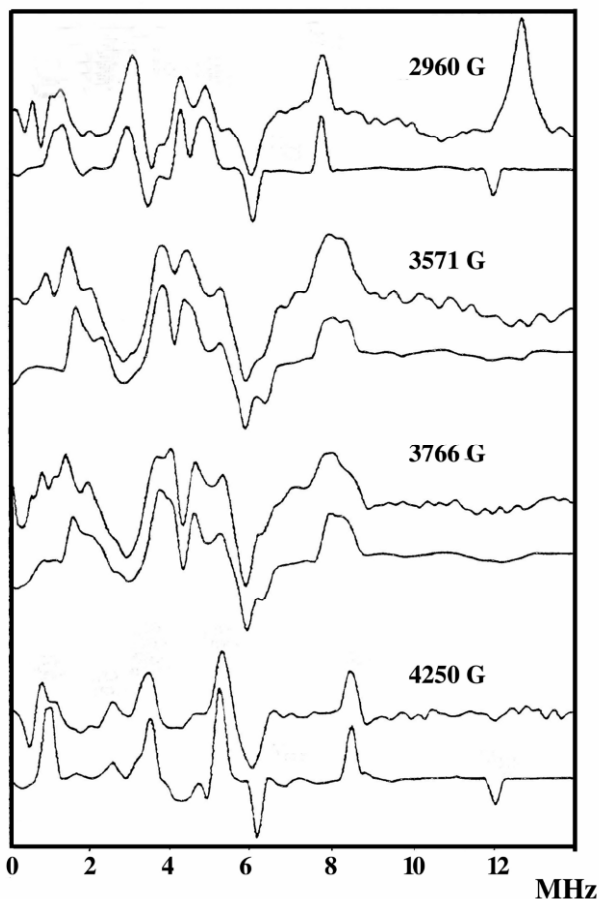
Figure 7. Cosine two-pulse FT-ESEEM spectra of $4VO^{2+}/4Cd^{2+}$ D-xylose isomerase obtained at various field positions in the EPR spectrum. Experimental (upper) and simulated (lower) curves are shown. Reproduced with permission from Dikanov et al. [34]. Copyright © 1995, American Chemical Society.

The proton sum-combination peaks in the four-pulse ESEEM were also measured as a function of applied field. Simulations of the spectra indicated the presence of two protons at distances of 3.25 and 2.8 Å based on the point–dipole approximation. The directions of the principal axes of the proton hyperfine tensors relative to the g-matrix of the complex were also determined. This orientation and distance information was used to assign protons to the nonexchangeable H1 and H2 protons of the imidazole ring. The combined ^{14}N and ^{1}H data led to the structure proposed in Figure 8, where coordination is through the N3 (imine) nitrogen of
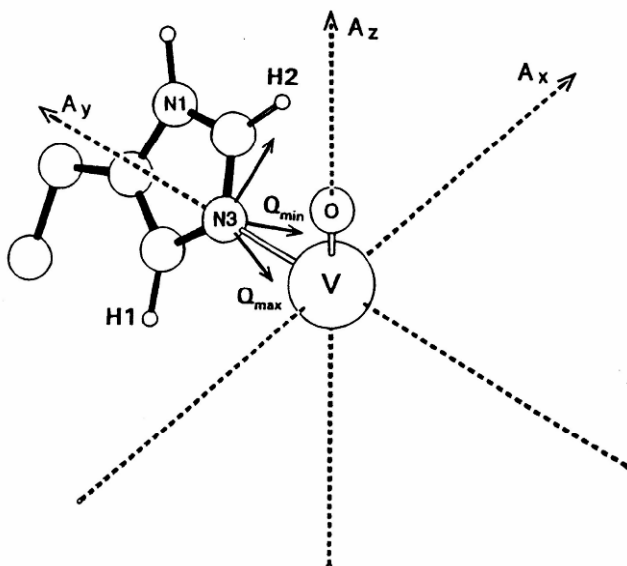
Figure 8. Proposed structure for histidine coordination in vanadyl D-xylose isomerase based on the ^{14}N quadrupole and nuclear hyperfine tensors. Reproduced with permission from Dikanov et al. [34]. Copyright © 1995, American Chemical Society.

the imidazole ring. The directions of the principal components of **Q** are indicated relative to the imidazole plane. Coordination is suggested to be along the *y*-axis of the ^{51}V nuclear hyperfine tensor. The ESEEM data on the VO^{2+} complex in conjunction with the x-ray structure of the Mn^{2+} enzyme are consistent with the structure in Figure 8.

The values of the electron–nuclear ^{14}N hyperfine coupling derived from the ESEEM data are ~6 MHz and are in accord with the couplings seen in model compounds and other protein complexes. The earlier report of a coupling of 13.2 MHz from ENDOR measurements [101] was suggested to be due to the observation of double quantum transitions in that work [34].

4.6. Transferrins

Human serum transferrin, lactoferrin, ovotransferrin, and melanotransferrin belong to a class of iron(III) binding proteins that stem from a common ancestral gene and are collectively known as the "transferrins" [102]. The primary function of serum transferrin is the transport of Fe(III) in blood plasma from the gut to bone marrow for the synthesis of heme and to other iron-requiring organs and cells. Lactoferrin has multiple functions, including involvement in the immune response and bactericidal effects. All the transferrins are composed of two similar binding sites located in separate N and C binding lobes of the protein in which the ligands are

two Tyr, one His, an Asp residue, and a bidentate carbonate. The synergistic anion carbonate is required for Fe^{3+} binding [102]).

     VO^{2+} was first employed many years ago as an EPR probe of the inequivalence of the N and C iron binding sites of the protein and their conformational properties [103]. A large number of other studies followed. ESEEM has been used to study the structure of the transferrin and lactoferrin complexes, particularly regarding the coordination of the histidine residues and the synergistic anion carbonate [28]. Two-pulse ESEEM showed pronounced low-frequency modulations attributed to ^{14}N of the imidazole group of His. Simulations gave $A_0(^{14}N) = 6.6$ MHz and $Q_z(^{14}N) = 0.75$ MHz, with $\eta = 0.5$ and $r = 2.0$ Å (the ^{14}N–V distance) for the lactoferrin complex with carbonate as the synergistic anion. These values are comparable to those for other VO^{2+} protein complexes involving histidine coordination in the equatorial plane of the vanadium (Table 1). Replacement of carbonate with oxalate causes $A_0(^{14}N)$ to increase from 6.6 to 7.0 MHz and probably reflects some small structural reorganization of the binding site when the synergistic anion is changed. Use of ^{13}C-enriched carbonate and oxalate revealed ^{13}C modulations, demonstrating coordination of the anion to the vanadium. Simulation of the ratio of $^{13}C/^{12}C$ modulation patterns indicated that the isotropic ^{13}C coupling is negligible, the interaction being adequately treated as point dipolar, giving $r \sim 2.7$–2.9 Å for the vanadium–carbon distance. The modulation depths for the oxalate complexes of transferrin and lactoferrin were twice as deep as for the carbonate complexes, an observation arguing for bidentate coordination of oxalate to the vanadium. A single exchangeable water molecule at approximately 2.9 Å was observed in D_2O/H_2O experiments, but its origin is obscure. There does not appear to be water in the first coordination sphere of the vanadium.

4.7. Ferritin

     Ferritin is an iron storage and detoxification protein found widely distributed among the plant, microbial, and animal kingdoms. Fe^{2+} and O_2 (or H_2O_2) are substrates for the protein-catalyzed ferroxidation reaction, which produces a hydrous ferric oxide mineral core of up to 4500 Fe inside the shell of the protein [104]. VO^{2+} was originally used as a probe to demonstrate the binding of Fe^{2+} and Fe^{3+} to the protein as well as the binding of Tb^{3+}, Zn^{2+}, and Cd^{2+}, which are known inhibitors of iron deposition [105,106]. Subsequent studies of rats on vanadium-supplemented diets revealed that vanadium as VO^{2+} becomes associated with ferritin of the liver, spleen, and kidney, its presence being evident from its characteristic EPR spectrum [107,108]. Thus, an understanding of the sites where VO^{2+} binds is of interest, not only because they are also the binding sites for iron, but also because they are important for understanding the metabolism of vanadium as well as the role that ferritin plays in vanadium detoxification.

     Based on the vanadium binding stoichiometry of ~16 VO^{2+}/ferritin, two VO^{2+} ions were proposed to bind in each of the 8 hydrophilic channels that run along the 3-fold axes leading to the interior of the protein [106]. However, subsequent ENDOR [109] and ESEEM [30] revealed ^{14}N electron–nuclear hyperfine couplings

that were not evident in the EPR spectrum. Since the channels contain only aspartate, glutamate, and serine residues as potential vanadium ligands, the earlier proposal [106] was shown to be incorrect. The ENDOR experiments showed couplings to two ^{14}N ($A_z \sim 7.1$ and ~6.3 MHz) that were tentatively assigned to the coordinated and remote nitrogens of the imidazole group of histidine [109] based on the early model compound work with $VO(Im)_4^{2+}$ and assignments made there [37]. Since subsequent work has shown that the coupling of the ^{14}N of the remote nitrogen is about 20 times smaller than that of the directly coordinated nitrogen [38], the two ^{14}N couplings of 7.1 and 6.3 MHz reported for VO^{2+} cannot be due to coordinated and remote nitrogens. They most likely arise from VO^{2+} binding to two types of sites on the protein or to two conformations of VO^{2+} binding at the same site. Subsequent studies of VO^{2+} binding to site-directed mutants of recombinant human H-chain ferritin have implicated His118 located at the outer opening to the 3-fold channel as the ligand for VO^{2+} [110] and not His128 located at the inner opening to the channel as originally suggested [30]. ESEEM shows only a single ^{14}N coupling of 7.1 MHz [30]. The smaller coupling of 6.3 MHz observed by ENDOR perhaps is not resolvable in the ESEEM spectrum or it represents a minor component in the different samples prepared for ESEEM.

The VO^{2+} spectrum with ferritin shows at least two environments of the metal called α and β, originally proposed to arise from two forms of the bound metal in different sites or regions of the protein, the β form being favored at high pH [105]. Much later 2-pulse ESEEM measurements of the proton sum-combination peak led to the proposal that the α and β forms of VO^{2+} arise from binding at the same site and are due to deprotonation of a *cis*-coordinated H_2O with V–H distances of ~2.6 Å [30]. Careful examination of the intensities of the α and β peaks of various site-directed mutants later showed that, while the two forms may differ by deprotonation of a coordinated H_2O to form coordinated OH^-, they most likely represent VO^{2+} binding to distinct sites on the protein and not from two forms of the same site [110]. Electron resonance studies of the VO^{2+}–ferritin complex is an example of a continually evolving story where the advent of high-resolution techniques in conjunction with site-directed mutagenesis has improved our understanding of vanadium interactions in this protein; however, much remains to be learned about this complicated metal binding system.

5. TISSUES

5.1. Kidney and Liver

Studies of the bioaccumulation of vanadium in tissues has a long history [3,111]. Early studies employed ^{48}V radioisotope to determine the tissue distribution of the metal. The proteins to which it was bound were typically separated by chromatography and electrophoresis of tissue homogenates and subsequently identified (see Chasteen et al. [107,108] and the references therein). However, these measurements provide no information regarding the oxidation state of

the vanadium or its ligand environment. Tissues of rats administered vanadium in various chemical forms exhibit EPR signals indicative of the presence of VO^{2+} [55,107,108,112–114]. Tissues showing VO^{2+} EPR signals include lung, kidney, liver, spleen, and bone as well as the duodenum plus contents, fecal pellets, and urine.

The EPR signals from liver and kidney of rats administered vanadium show a marked resemblance to those of VO^{2+} complexed with ferritin [107], a protein with which vanadium is known to be associated in vivo in these tissues. The first application of ESEEM to tissues was reported by Fukui et al. [112] in their study of vanadium in the kidney and liver of rats injected with vanadyl sulfate solution. This study employed 2-pulse ESEEM MEM (maximum entropy method) power spectra from which ^{14}N signals were extracted, yielding hyperfine couplings of $A_0(^{14}N) = 5.0$ MHz (liver) and 5.2 MHz (kidney), indicative of amine coordination. Estimates of the percentages of nitrogen-coordinating species in these tissues were obtained by comparing peak intensities with those of the VO^{2+}–histidine complex as a standard. Values of ~50–55% and ~70–80% were obtained for kidney and liver, respectively.

A more sophisticated and thorough study of the signals from kidneys of rats administered bis(ethylmaltolato)oxovanadium(IV) in drinking water was carried out by Dikanov et al. [114] using 3-pulse ESEEM and HYSCORE spectroscopies. Nuclear hyperfine and quadrupole coupling constants of $A_0(^{14}N) = 4.9$ MHz and $Q_z(^{14}N) = 1.2$ MHz were obtained [112]. Both the nuclear hyperfine and quadrupole couplings are in accord with amine coordination (Table 1), imine coordination having larger hyperfine couplings but smaller quadrupole couplings than observed for amine coordination. A somewhat higher estimate of the percentage of nitrogen-coordinated species in kidney was obtained by Dikanov et al. [114] compared to Fukui et al. [112], but the method of administration of vanadium and the analytical approach were different in the two studies.

The EPR parameters $g_{||} = 1.945$, $A_{||}(^{51}V) = 168 \times 10^{-4}$ cm^{-1}, $g_\perp = 1.98$, and $A_\perp(^{51}V) = 58 \times 10^{-4}$ cm^{-1} observed by Dikanov et al. [114] are essentially identical to those reported for the pH ~ 7.5 β form of VO^{2+} binding to horse spleen ferritin [105], a finding in accord with the previous assignment of the EPR signals in kidney to those of a VO^{2+}–ferritin complex [107]. However, whereas the tissue study showed amine coordination, ENDOR and ESEEM investigations of VO^{2+} complexed to pure ferritin reveal imine coordination from histidine [30,109]. As pointed out by Dikanov et al.[114], imine coordination is more difficult to observe by 2- and 3-pulse spectra than amine coordination, so it may have been missed in the tissue measurements. Furthermore, VO^{2+} EPR spectra of the ferritin complex show overlapping signals from multiple forms of metal binding to the protein [110]. Some of the coordinated species may involve imine coordination and others amine coordination.

5.2. Bone

Bone is one of the primary tissues for the bioaccumulation of vanadium. The bones of rats administered vanadium compounds show EPR signals from VO^{2+} ion [55,56,113]. ESEEM and HYSCORE spectroscopy revealed couplings from ^{31}P and ^{1}H [55,56]. Most notably, couplings from three distinct ^{31}P nuclei were observed. Single-frequency HYSCORE measurements do not allow the relative sign of isotropic coupling ($A_0(^{31}P)$) and anisotropic coupling ($T(^{31}P)$), which is dipolar in origin, to be determined. The following combinations of $A_0(^{31}P)$ and $T(^{31}P)$ for the three ^{31}P nuclei were reported: $A_0(^{31}P) = -14.25/12.38$ and $T(^{31}P) = 1.87$; $A_0(^{31}P) = -9.19/7.72$ and $T(^{31}P) = 1.47$; and $A_0(^{31}P) = -3.78/2.40$ MHz and $T(^{31}P) = 1.39$ MHz. Here $A_z(^{31}P) = A_0(^{31}P) + 2T(^{31}P)$ and $A_{x,y}(^{31}P) = A_0(^{31}P) - T(^{31}P)$. Regardless of the uncertainty in sign of $A_0(^{31}P)$ (which is probably negative [55]), the data indicate couplings of approximate magnitudes ~14, 9, and 3 MHz for the three phosphorus nuclei. The data at this point in time did not allow one to distinguish between the situation where a single VO^{2+} ion was simultaneously coordinated to three phosphate groups and the situation where VO^{2+} was coordinated to multiple sites. Regardless, the data demonstrated that VO^{2+} was bound to the inorganic phase of bone — namely, its phosphate-containing hydroxyapatite component. The observation of a ^{1}H hyperfine coupling of ~3 MHz from HYSCORE measurement was consistent with the equatorial coordination of H_2O or OH^-.

Major insights into the structure of the complex in bone were obtained from an extensive two- and four-pulse ESEEM and four-pulse two-dimensional HYSCORE spectroscopy study of the 1:1 complex of VO^{2+} with monoprotonated triphosphate (TPH) [55]. In this instance the couplings from three ^{31}P nuclei were observed — namely, $A_0(^{31}P) = -15.90/14.0$ and $T(^{31}P) = 1.94$; $A_0(^{31}P) = -8.82/7.33$ and $T(^{31}P) = 1.48$; and $A_0(^{31}P) = -2.01/0.88$ MHz and $T(^{31}P) = 1.14$ MHz, corresponding to isotropic hyperfine couplings of approximately 15, 9, and 1–2 MHz. The largest couplings of ~14 and 9 MHz correspond well with the couplings of 14.8 and 9.0 MHz reported for the β and γ phosphorus nuclei of $VO^{2+}(ATP)_2$, where equatorial coordination of the phosphate groups occurs [36]. The smallest coupling of 1–2 MHz in VO–TPH was assigned to axial coordination of a terminal phosphate from PPPi. A combination of HYSCORE and proton sum-combination peaks in the 4-pulse 1D ESEEM reveal the presence of protons associated with the ligands, most likely from two H_2O molecules in equatorial positions. The water proton counts derive from comparison of the intensities of the sum-combination peak (relative to the matrix proton at $2\nu_H$) of the VO–TPH complex with that of $VO(H_2O)_5^{2+}$. The close correspondence between the spectral properties of the VO–TPH complex and that of bone strongly suggested that in bone the VO^{2+} is bound to the surface of the hydroxyapatite, and hence is solvent coordinated, and that the three phosphates coordinate in a facial complex with two phosphates coordinated equatorially and one axial to the V=O bond axis, with the remaining two equatorial positions occupied by H_2O.

6. CONCLUSIONS

VO^{2+} was originally introduced as a spin probe of metal binding sites in proteins some thirty years ago. At that time, the ligand environment of the metal was inferred through measurements of *g*-factors and vanadium hyperfine coupling constants and compared with those of model complexes. cw-EPR enabled the detection of multiple binding sites on several proteins and to measure conformational changes in these sites. In the intervening years, the development and application of high-resolution techniques have permitted the binding sites in proteins to be defined in much greater detail. ENDOR — particularly pulsed ENDOR, ESEEM, and HYSCORE — have found widespread use in VO^{2+}–protein and model complex studies. Through the use of these techniques, the isotropic and anisotropic components of ligand nuclear hyperfine coupling constants have been measured, allowing nearby nuclei to be identified and their distances determined. HYSCORE has greatly facilitated spectral assignments through separating complex patterns of ESEEM lines and aiding in interpreting the nuclear transitions involved. HYSCORE has been especially useful in studying ^{31}P interaction in complexes involving phosphate. DFT calculations have assisted in making spectral assignments of model complexes and aided in understanding the dependence of the electronic structure of VO^{2+} complexes on geometry, as reflected in their spin Hamiltonian parameters. Multifrequency ESEEM measurements have become commonplace, which, when combined with spectral simulations, have increased the spectral information obtained. Proton sum-combination peaks in 2D ESEEM have proven useful in determining the number of weakly coupled ^{1}H nuclei and their distances from the vanadium. Measurements of ^{51}V quadrupole coupling constants show promise for studies of VO^{2+} coordination in proteins.

ACKNOWLEDGMENTS

REFERENCES

1.   Boucher LJ, Tynan EC, Yen TF. 1969. Properties of oxovanadium(IV) complexes, IV: correlations of ESR spectra with ligand type. In *Electron spin resonance of metal complexes*. pp. 111–130. Ed TF Yen. New York: Plenum.
2.   Chasteen ND. 1981. Vanadyl(IV) EPR spin probes: Inorganic and biochemical aspects. In *Biological magnetic resonance*, Vol. 3, pp. 53–119. Ed LJ Berliner, J Reuben. New York: Plenum.
3.   Chasteen ND. 1983. The biochemistry of vanadium. In *Structure and bonding*, Vol. 53, pp. 107–138. Berlin: Springer-Verlag.

4. Eaton SS, Eaton GR. 1990. Biological applications of EPR, ENDOR and ESEEM spectroscopy. In *Vanadium in biological systems: physiology and biochemistry*, pp. 199–222. Ed ND Chasteen. Dordrecht: Kluwer Academic.

5. Makinen MW, Mustafi D. 1995. The vanadyl ion: molecular structure of coordinating ligands by electron paramagnetic resonance and electron nuclear double resonance. In *metal ions in biological systems: vanadium and its role in life*, Vol. 31, pp. 89–127. Ed H Sigel, A Sigel. New York: Marcel Dekker.

6. Mustafi D. Makinen MW. 2005. Application of angle-selected electron nuclear double resonance to characterize structured solvent in small molecules and macromolecules. In *Biological magnetic resonance*, Vol. 24: *Biomedical EPR, part B: methodology, instrumentation and dynamics*. pp. 89–144. Ed SS Eaton, GR Eaton, LJ Berliner. New York: Kluwer Academic/Plenum.

7. Smith II TS, LoBrutto R, Pecoraro VL. 2002. Paramagnetic spectroscopy of vanadyl complexes and its applications to biological systems. *Coord Chem Rev* **228**:1–18.

8. Chasteen ND, ed. 1990. *Vanadium in biological systems*, pp. 1–225. Dordrecht: Kluwer Academic.

9. Butler A, Carrano CJ. 1991. Coordination chemistry of vanadium in biological systems. *Coord Chem Rev* **109**:61–105.

10. Sigel H, Sigel A, eds. 1995. *Metal ions in biological systems: vanadium and its role in life*, Vol. 31. New York: Marcel Dekker.

11. Tracy AS, Crans DC, eds. 1998. *Vanadium compounds: chemistry biochemistry and therapeutic applications*. ACS Symposium Series 711, pp. 1–381. Washington, DC: American Chemical Society.

12. Rehder D. 2003. Biological and medicinal aspects of vanadium. *Inorg Chem Commun* **6**:604–617.

13. Linquist RN, Lynn Jr JL, Lienhard GE. 1973. Possible transition-state analogs for ribonuclease: complexes of uridine with oxovanadium(IV) ion and vanadium(V) ion. *J Am Chem Soc* **95**:8762–8768.

14. Priebsch W, Rehder D. 1990. Dichlorobis(N,N-dimethylacetamide) oxovanadium(IV). *Acta Cryst* **C46**(4): 568–570.

15. Cornman CR, Geiser-Bush KM, Rowley SP, Boyle PD. 1997. Structural and electron paramagnetic resonance studies of the square pyramidal to trigonal bipyramidal distortion of vanadyl complexes containing sterically crowded schiff base ligands. *Inorg Chem* **36**:6401–6408.

16. Chasteen ND, Snetsinger PA. 2000. ESEEM and ENDOR spectroscopy. In *Physical Methods of Bioinorganic Chemistry: Spectroscopy and Magnetism*, pp. 187–231. Ed L Que Jr. Sausalito, CA: University Science Books.

17. Schweiger A, Jeschke G. 2001. *Principles of pulse electron paramagnetic resonance*. New York: Oxford UP.

18. Holyk NM. 1979. An electron paramagnetic resonance study of model oxovanadium(IV) complexes in aqueous solution: correlation of magnetic properties with ligand type and metal chelate structure, pp. 1–121. MS thesis, University of New Hampshire.

19. Hyde JS, Froncisz W. 1982. The role of microwave frequency in EPR spectroscopy of copper complexes. *Ann Rev Biophys Bioeng* **11**:391–417.

20. Manoharan PT, Rogers MT. 1969. ESR study of copper(II) and silver(II) tetraphenylporphyrin. In *Electron spin resonance of metal complexes*, pp. 143–173. Ed TF Yen. New York: Plenum.

21. Hyde JS, Pasenkiewicz-Gierula M, Jesmanowicz A, Antholine WE. 1990. Pseudo-field modulation EPR spectroscopy. *Appl Magn Reson* **1**:483–496.

22. Hyde JS, Jesmanowicz A, Pake JJ, Antholine WE. 1992. Pseudomodulation: a computer-based strategy for resolution enhancement. *J Magn Reson* **96**:1–13.

23. Fukui K, Ohya-Nishiguchi H, Kamada H. 1993. Electron spin echo envelope modulation study of oxovanadium(IV)–porphyrin complexes: reinvestigation of hyperfine and quadrupole couplings of pyrrole nitrogen. *J Phys Chem* **97**:11858–11860.

24. Chasteen ND. 1993. Vanadyl(IV) electron nuclear double resonance/electron spin echo envelope modulation spin probes. In *Methods in enzymology*, Metallobiochemistry, Part E: Physical and spectroscopic methods for probing metal ion environments in metalloproteins, Vol. 227, pp. 232–244. Ed JF Riordan, BL Vallee. New York: Academic Press.

25. Chasteen ND. 1995. Vanadium–protein interactions. In *Metal ions in biological systems: vanadium and its role in life*, Vol. 31, pp. 231–247. Ed H Sigel, A Sigel. New York: Marcel Dekker.

26. Hofer P, Grupp A, Nebenfuhr H, Mehring M. 1986. Hyperfine sublevel correlation (HYSCORE) spectroscopy: a 2D ESR investigation of the squaric acid radical. *Chem Phys Lett* **132**(3):279–282.

27. de Boer E, Keijzers CP, Reijerse EJ, Collison D, Garner CD, Wever R. 1988. N-14 Coordination to VO^{2+} in reduced vanadium bromoperoxidase: an electron–spin echo study. *FEBS Lett* **235**:93–97.

28. Eaton SS, Dubach J, More KM, Eaton GR, Thurman G, Ambruso DR. 1989. Comparison of the electron spin echo envelope modulation (ESEEM) for human lactoferrin and transferrin complexes of copper(II) and vanadyl ion. *J Biol Chem* **254**:4776–4781.

29. Reijerse EJ, Tyryshkin AM, Dikanov SA. 1998. Complete determination of nitrogen quadrupole and hyperfine tensors in an oxovanadium complex by simultaneous fitting of multifrequency ESEEM powder spectra. *J Magn Reson* **131**:295–309.

30. Gerfen J, Hanna PM, Chasteen ND, Singel DJ. 1991. Characterization of the ligand environment of vanadyl complexes of apoferritin by multifrequency electron spin–echo envelope modulation. *J Am Chem Soc* **113**:9513–9519.

31. LoBrutto R, Hamstra BJ, Colpas GJ, Pecoraro VL, Frasch WD. 1998. Electron spin echo envelope modulation spectroscopy reveals and distinguishes equatorial and axial nitrogen ligands bound to VO^{2+}. *J Am Chem Soc* **120**:4410–4416.

32. Larsen SC, Singel DJ. 1992. Multifrequency ESEEM spectroscopy of ammonia adsorbed on silica-supported reduced molybdenum oxide. *J Phys Chem* **96**:10594–10597.

33. Magliozzo RS, Peisach J. 1993. Evaluation of nitrogen nuclear hyperfine and quadrupole coupling parameters for the proximal imidazole in myoglobin-azide, -cyanide, and -mercaptoethanol complexes by electron spin echo envelope modulation spectroscopy. *Biochemistry* **32**:8446–8456.

34. Dikanov SA, Tryshkin AM, Hüttermann J, Bogumil R, Witzel H. 1995. Characterization of histidine coordination in VO^{2+}-substituted D-xylose isomerase by orientationally-selected electron spin-echo envelope modulation spectroscopy. *J Am Chem Soc* **117**:4976–4986.

35. Peterson J, Hawkes TR, Lowe DJ. 1998. Nitrogen coordination in VO^{2+}-substituted imidazole glycerol phosphate dehydratase studied by electron spin-echo envelope modulation spectroscopy. *J Am Chem Soc* **120**:10978–10979.

36. Buy C, Matsui T, Andrianambinintsoa S, Sigalat C, Girault G, Zimmermann J-L. 1996. Binding sites for Mg(II) in H^+-ATPase from *Bacillus* PS3 and the $\alpha_3\beta_3\gamma$ subcomplex studied by one-dimensional ESEEM and two-dimensional HYSCORE spectroscopy of

the oxovanadium(IV) complexes: a possible role for β-His-324. *Biochemistry* **35**:14281–14293.

37. Mulks CF, Kirste B, van Willigen H. 1982. ENDOR Study of VO^{2+}–imidazole complexes in frozen aqueous solution. *J Am Chem Soc* **104**:5906–5911.

38. Dikanov SA, Burgard C, Hüttermann J. 1993. Determination of the hyperfine coupling with the remote nitrogen of the VO^{2+}–(imidazole)$_4$ complex by ESEEM spectroscopy. *Chem Phys Lett* **212**:493–498.

39. Zhang C, Markham GD LoBrutto, R. 1993. Coordination of vanadyl(IV) cation in complexes of S-adenosylmehtionine synthetase: multi-frequency electron spin echo envelope modulation study. *Biochemistry* **32**:9866–9873.

40. Tipton PA, McCracken J, Cornelius JB, Peisach J. 1989. Electron spin echo envelope modulation studies of pyruvate kinase active site complexes. *Biochemistry* **28**:5720–5728.

41. Flanagan HL, Singel DJ. 1987. Analysis of nitrogen-14 ESEEM patterns of randomly oriented solids. *J Chem Phys* **87**:5606–5616.

42. Shane JJ, Hofer P, Reijerse EJ, Deboer E. 1992. Hyperfine sublevel correlation spectroscopy (HYSCORE) of disordered solids. *J Magn Reson* **99**:596–604.

43. Dikanov SA, Tyryshkin AM, Bowman MK. 2000. Intensity of cross-peaks in HYSCORE spectra of $S = 1/2$, $I = 1/2$ spin systems. *J Magn Reson* **144**:228–242.

44. Fukui K, Ohya-Nishiguchi H, Kamada H. 1997. ^{14}N coupling parameters in oxovanadium(IV)–amine, –imine, –isothiocynate complexes studied by electron spin echo envelope modulation spectroscopy. *Inorg Chem* **36**:5518–5529.

45. Astashkin AV, Dikanov SA, Tsvetkov YD. 1985. Coordination of vanadyl acetylacetonate with nitrogen-containing donor bases. *J Struct Chem* **26**:363–368.

46. Reijerse EJ, Shane J, de Boer E, Collison D, eds. 1989. ESEEM of nitrogen coordinated oxo-vanadium(IV) complexes: electron magnetic resonance of disordered systems. Singapore: World Scientific.

47. Atherton NM, Shackleton JF. 1980. Proton ENDOR of $VO(H_2O)_5^{2+}$ in $Mg(NH_4)_2(SO_4)_2 6H_2O$. *Mol Phys* **39**:1471–1485.

48. van Willigen H. 1980. Proton ENDOR on $VO(H_2O)_5^{2+}$ in solid solution. *J Magn Reson* **39**:37–46.

49. Mustafi D, Makinen MW. 1988. ENDOR-determined solvation structure of VO^{2+} in frozen solution. *Inorg Chem* **27**:3360–3368.

50. Dikanov SA, Yudanov VF, Tsvetkiv YD. 1979. Electron spin-echo studies of weak hyperfine interactions with ligands in some VO^{2+} complexes in frozen glassy solution. *J Magn Reson* **34**:631–645.

51. Tryshkin AM, Dikanov SA, Evelo RG, Hoff AJ. 1992. Properties of the combination harmonic spectra of primary electron spin echo envelope modulation of orientationally selected disordered systems: application to aqua–oxovanadium complexes. *J Chem Phys* **97**:42–49.

52. Tolis EJ, Manos MJ, Tasiopoulos AJ, Raptopoulou CP, Terzis A, Sigalas MP, Deligiannakis Y, Kabanos TA. 2002. Monomeric compounds containing the cis-[V(=O)(OH)]$^+$ core. *Angew Chem Int Ed* **41**(15):2797–2801.

53. Baute D, Goldfarb D. 2005. The ^{17}O hyperfine interaction in $[(V^{17}O)(H_2{}^{17}O)_5]^{2+}$ and $[Mn(H_2{}^{17}O)_6]^{2+}$ determined by high field ENDOR aided by DFT calculations. *J Phys Chem A* **109**(35):7865–7871.

54. Mustafi D, Tesler J, Makinen MW. 1992. Molecular geometry of vanadyl-adenine nucleotide complexes determined by EPR, ENDOR and molecular modeling. *J Am Chem Soc* **114**(16):6219–6226.

55. Dikanov SA, Liboiron BD, Orvig C. 2002. Two-diminsional (2D) pulsed electron paramagnetic resonance study of VO^{2+}–triphosphate interactions: evidence for tridentate triphosphate coordination, and relevance to bone uptake and insulin enhancement by vanadium pharmaceuticals. *J Am Chem Soc* **124**:2969–2978.

56. Dikanov SA, Liboiron BD, Thompson KH, Vera E, Yuen VG, McNeill JH, Orvig C. 1999. In vivo electron spin-echo envelope modulation (ESEEM) spectroscopy: first observation of vanadyl coordination to phosphate in bone. *J Am Chem Soc* **121**(47):11004–11005.

57. Grant CV, Ball JA, Hamstra BJ, Pecoraro V, Britt RD. 1998. [51]V ESE–ENDOR studies of oxovanadium(IV) complexes: investigation of the nuclear quadrupole interaction. *J Phys Chem B* **102**:8145–8150.

58. Grant CV, Cope W, Ball JA, Maresch GG, Gaffney BJ, Fink W, Britt RD. 1999. Electronic structure of the aqueous vanadyl ion probed by 9 and 94 GHz EPR and pulsed ENDOR spectroscopies and density functional theory calculations. *J Phys Chem B* **103**:10627–10631.

59. Grant CV, Geiser-Bush KM, Cornman CR, Britt RD. 1999. Probing the molecular geometry of five-coordinate vanadyl complexes with pulsed ENDOR. *Inorg Chem* **38**:6285–6288.

60. Aznar CP, Deligiannakis Y, Tolis EJ, Kabanos T, Brynda M, Britt D. 2004. ESE–ENDOR study and DFT calculations on oxovanadium compounds: effect of axial anionic ligands on the V-51 nuclear quadrupolar coupling constant. *J Phys Chem A* **108**(19):4310–4321.

61. Munzarova M, Kaupp M. 1999. A critical validation of density functional and coupled cluster approaches for the calculation of EPR coupling constants in transition metal complexes. *J Phys Chem A* **103**:9966–9983.

62. Munzarova ML, Kaupp M. 2001. A density functional study of EPR parameters for vanadyl complexes containing Schiff base ligands. *J Phys Chem B* **105**:12644–12652.

63. Saladino AC, Larsen SC. 2003. Density functional theory calculations of nitrogen hyperfine and quadrupole coupling constants in oxovanadium(IV) complexes. *J Phys Chem A* **107**:4735–4740.

64. Schreckenbach G, Ziegler T. 1997. Calculation of g-tensor of electron paramagnetic resonance spectroscopy using gauge-including atomic orbitals and density functional theory. *J Phys Chem A* **101**:3388–3399.

65. van Lenthe E, Wormer PES, van der Avoird A. 1997. Density functional calculations of molecular g-tensors in the zero-order regular approximation for relativistic effects. *J Chem Phys* **107**:2488–2498.

66. van Lenthe E, van der Avoird A, Wormer PES. 1998. Density functional calculations of molecular hyperfine interactions in the zero order regular order approximation for relativistic effects. *J Chem Phys* **108**:4783–4796.

67. Patchkovskii S, Ziegler T. 1999. Predicion of electron paramagnetic resonance g tensors of transition metal complexes using density functional theory: first applications to some axial d^1 MEX$_4$ systems. *J Chem Phys* **111**:5730–5740.

68. Malkina OL, Vaara J, Schimmelpfennig B, Munzarova M, Malkin VG, Kaupp M. 2000. Density functional calculations of electronic g-tensors using spin-orbit pseudopotentials and mean-field all-electron spin-orbit operators. *J Am Chem Soc* **122**:9206–9218.

69. Munzarova ML, Kubacek P, Kaupp M. 2000. Mechanisms of EPR hyperfine coupling in transition metal complexes. *J Am Chem Soc* **122**:11900–11913.

70. Patchkovskii S, Ziegler T. 2000. Prediction of EPR g-tensors in simple d^1 metal porphyrins with density functional theory. *J Am Chem Soc* **122**:3506–3516.

71. Kaupp M, Reviakine R, Malkina OL, Arbuznikov A, Schimmelpfennig B, Malkin VG. 2002. Calculation of electronic g-tensors for transition metal complexes using hybrid density functionals and atomic meanfield spin-orbit operators. *J Comput Chem* **23**:794–803.

72. Arbuznikov AV, Kaupp M. 2005. Localized hybrid exchange-correlation Potentials for Kohn-Sham DFT calculations of NMR and EPR parameters. *Int J Quant Chem* **104**(2):261–271.

73. Neese F. 2005. Efficient and accurate approximations to the molecular spin-orbit coupling operator and their use in molecular g-tensor calculations. *J Chem Phys* **122**(3):1–13.

74. Remenyi C, Munzarova ML, Kaupp M. 2005. Comparative density-functional study of the electron paramagnetic resonance parameters of amavadin. *J Phys Chem B* **109**(9): 4227–4233.

75. Te Velde G, Bickelhaupt FM, van Gisbergen SJA, Fonseca Guerra C, Baerends EJ, Snijders JG, Ziegler T. 2001. Chemistry with ADF. *J Comput Chem* **22**(22):931–967.

76. Baerends EJ, Autschbach JA, Bérces A, Bo C, Boerrigter PM, Cavallo L, Chong DP, Deng L, Dickson RM, Ellis DE, Fan L, Fischer TH, Fonseca Guerra C, van Gisbergen SJA, Groeneveld JA, Gritsenko OV, Grüning M, Harris FE, van den Hoek P, Jacobsen H, van Kessel G, Kootstra F, van Lenthe E, Osinga VP, Patchkovskii S, Philipsen PHT, Post D, Pye CC, Ravenek W, Ros P, Schipper PRT, Schreckenbach G, Snijders JG, Sola M, Swart M, Swerhone D, Te Velde G, Vernooijs P, Versluis L, Visser O, van Wezenbeek E, Wiesenekker G, Wolff SK, Woo TK, Ziegler T. ADF 2005. Amsterdam: Netherlands, Vrije Universiteit, http://www.scm.com.

77. Slater JC. 1930. Atomic shielding constants. *Phys Rev* **36**:57–64.

78. Frisch MJ, Trucks GW, Schlegel HB, Scuseria GE, Robb MA, Cheeseman JR, Montgomery Jr JA, Vreven T, Kudin KN, Burant JC, Millam JM, Iyengar SS, Tomasi J, Barone V, Mennucci B, Cossi M, Scalmani G, Rega N, Petersson GA, Nakatsuji H, Hada M, Ehara M, Toyota K, Fukuda R, Hasegawa J, Ishida M, Nakajima T, Honda Y, Kitao O, Nakai H, Klene M, Li X, Knox JE, Hratchian HP, Cross JB, Bakken V, Adamo C, Jaramillo J, Gomperts R, Stratmann RE, Yazyev O, Austin AJ, Cammi R, Pomelli C, Ochterski JW, Ayala PY, Morokuma K, Voth GA, Salvador P, Dannenberg JJ, Zakrzewski VG, Dapprich S, Daniels AD, Strain MC, Farkas O, Malick DK, Rabuck AD, Raghavachari K, Foresman JB, Ortiz JV, Cui Q, Baboul AG, Clifford S, Cioslowski J, Stefanov BB, Liu G, Liashenko A, Piskorz P, Komaromi I, Martin RL, Fox DJ, Keith T, Al-Laham MA, Peng CY, Nanayakkara A, Challacombe M, Gill PMW, Johnson B, Chen W, Wong MW, Gonzalez C, Pople JA. 2004. *Gaussian 03, revision C.02*. Wallingford CT: Gaussian Inc.

79. Boys SF. 1950. Electronic wave functions, I: a general method of calculation for the stationary states of any molecular system. *Proc R Soc* (*London*) *A* **200**:542–554.

80. Neese F. 2004. ORCA—an ab inito density functional and semi-empirical program package, version 2.4, revision 13. Mülheim an der Ruhr: Max Planck Institute for Bioinorganic Chemistry.

81. Malkin VG, Malkina OL, Reviakine R, Arbuznikov A, Kaupp M, Schimmelpfennig B, Malkin I, Helgaker T, Ruud K. 2003. *MAG-ReSpect program package, version 1.1*.

82. Neese F. 2003. Quantum chemical calculations of spectroscopic properties of metallo-proteins and model compounds: EPR and Mossbauer properties. *Curr Opin Chem Biol* **7**:125–135.

83. Carl PJ, Isley SL, Larsen SC. 2001. Combining theory and experiment to interpret the EPR Spectra of VO^{2+}-exchanged zeolites. *J Phys Chem B* **105**:4563–4573.

84. Saladino AC, Larsen SC. 2002. Computational study of the effect of the imidazole ring orientation on the EPR parameters for vanadyl–imidazole complexes. *J Phys Chem A* **106**:10444–10451.

85. Neese F. 2003. Metal and ligand hyperfine couplings in transition metal complexes: the effect of spin–orbit coupling as studied by coupled perturbed Kohn-Sham theory. *J Chem Phys* **118**:3939–3948.

86. Saladino AC, Larsen SC. 2003. Density functional theory calculations of the EPR parameters for VO^{2+} complexes. *J Phys Chem A* **107**:1872–1878.

87. Paine TK, Weyhermuller T, Slep LD, Neese F, Bill E, Bothe E, Wieghardt K, Chaudhuri P. 2004. Nonoxovanadium(IV) and oxovanadium(V) complexes with mixed O, X, O-donor ligands (X = S, Se, P, or PO). *Inorg Chem* **43**(23):7324–7338

88. Neese F. 2001. Prediction of electron paramagnetic resonance g value using coupled perturbed Hartree-Fock and Kohn-Sham theory. *J Chem Phys* **115**:11080–11096.

89. Weil JA, Bolton JR, Wertz JE. 1994. Electron paramagnetic resonance: elementary theory and practical applications. New York: John Wiley & Sons.

90. Albanese NF, Chasteen ND. 1978. Origin of the electron paramagetic resonance line widths in frozen solutions of the oxovanadium(IV) ion. *J Phys Chem* **82**:910–914.

91. Perdew JP, Burke K, Wang Y. 1996. Generalized gradient approximation for the exchange-correlation hole of a many-electron system. *Phys Rev B* **54**:16533–16539.

92. Smith II TS, Root CA, Kampf JW, Rasmussen PG, Pecoraro VL. 2000. Reevaluation of the additivity relationship for vanadyl-imidazole complexes: correlation of the EPR hyperfine constant with ring orientation. *J Am Chem Soc* **122**:767–775.

93. Larsen SC, Singel DJ. 1992. Multifrequency and orientation selective ESEEM spectroscopy of ammonia adsorbed on a silica supported vanadium oxide catalyst. *J Phys Chem* **96**:9007–9013.

94. Larsen SC. 2001. DFT calculations of proton hyperfine coupling constants for $[VO(H_2O)_5]^{2+}$: comparison with proton ENDOR data. *J Phys Chem A* **105**:8333–8338.

95. Scholes CP, Falkowski KM, Chen S, Bank J. 1986. Electron nuclear double resonance (ENDOR) of bis(imidazole) ligated low-spin ferric heme systems. *J Am Chem Soc* **108**:1660–1671.

96. Torrent M, Musaev DG, Morokuma K, Ke SC, Warncke K. 1999. Calculation of nuclear quadrupole parameters in imidazole derivatives and extrapolation to coenzyme B12: a theoretical study. *J Phys Chem B* **103**:8618–8627.

97. Lord KA, Reed GH. 1990. Vanadyl(IV) complexes with pyruvate kinase: activation of the enzyme and electron paramagnetic resonance properties of ternary complexes with the protein. *Arch Biochem Biophys* **281**:124–131.

98. Lord KA, Reed G.H. 1987. Vanadyl(IV)–thallium(I)–205,203 superhyperfine coupling in complexes with pyruvate kinase. *Inorg Chem* **26**:1464–1466.

99. Markham GD, Leyh TS. 1987. Superhyperfine couplings between metal ions at the active site of S-adenosylmethionine synthetase. *J Am Chem Soc* **109**:599–600.

100. Peterson J, Hawkes TR, Lowe DJ. 1997. The metal-binding site of imidazole glycerol phosphate dehydratase; EPR and ENDOR studies of the oxo-vanadyl enzyme. *J Biol Inorg Chem* **2**:308–319.

101. Bogumil R, Hüttermann J, Kappl R, Stabler R, Sudfeldt C, Witzel H. 1991. Visible EPR and electron nuclear double resonance spectroscopic studies on the two metal-binding sites of oxovanadium(IV)-substituted D-xylose isomerase. *Eur J Biochem* **196**:305–312.

102. He QY, Mason AB. 2002. Molecular aspects of iron release from transferrin. In *Molecular and cellular iron transport*, pp. 95–123. Ed DM Templeton. New York: Marcel Dekker.

103. Cannon JC, Chasteen ND. 1975. Nonequivalence of the metal binding sites in vanadyl labeled human serum transferrin. *Biochemistry* **14**:4573–4577.

104. Liu X, Theil EC. 2005. Ferritins: dynamic management of biological iron and oxygen chemistry. *Acc Chem Res* **38**:167–175.

105. Chasteen ND, Theil EC. 1982. Iron binding by horse spleen apoferritin: a vanadyl(IV) EPR spin probe study. *J Biol Chem* **257**:7672–7677.

106. Wardeska JG, Viglione B, Chasteen ND. 1986. Metal ion complexes of apoferritin: evidence for initial binding in the hydrophilic channels. *J Biol Chem* **261**:6677–6683.

107. Chasteen ND, Lord EM, Thompson HJ, Grady JK. 1986. Vanadium complexes of transferrin and ferritin in the rat. *Biochim Biophys Acta* **884**:84–92.

108. Chasteen ND, Lord EM, Thompson HJ. 1986. Vanadium metabolism: vanadyl(IV) electron paramagnetic resonance spectroscopy of selected tissues in the rat. In *Frontiers in bioinorganic chemistry*, pp. 133–144. Ed A Xavier. Weinheim: VCH Publishers.

109. Hanna PM, Chasteen ND, Rottman GA, Aisen P. 1991. Iron binding to horse spleen apoferritin: a vanadyl ENDOR spin probe study. *Biochemistry* **30**:9210–9216.

110. Grady JK, Shao J, Arosio P, Santambrogio P, Chasteen ND. 2000. Vanadyl(IV) binding to mammalian ferritins: an EPR study aided by site-directed mutagenesis. *J Inorg Biochem* **80**:107–113.

111. Martin DM, Chasteen ND. 1987. Vanadium. *Methods Enzymol* **158**:402–421.

112. Fukui K, Ohya-Nishiguchi H, Nakai M, Sakurai H, Kamada H. 1995. Detection of vanady-nitrogen interaction in organs of the vanadyl-treated rat: electron spin echo envelope modulation study. *FEBS Lett* **368**(1):31–35.

113. Fukui K, Fujisawa Y, Ohy-Nishiguchi H, Kamada H, Sakurai H. 1999. In vivo coordination structural changes of a potent insulin-mimetic agent, bis(picolinato)oxovanadium(IV), studied by electron spin-echo envelope modulation spectroscopy. *J Inorg Biochem* **77**:215–224.

114. Dikanov SA, Liboiron BD, Thompson KH, Vera E, Yuen VG, McNeill JH, Orvig C. 2003. One- and two-dimensional pulsed electron paramagnetic resonance studies of in vivo vanadyl coordination in rat kidney. *Bioinorg Chem Appl* **1**:69–83.